

mnb

Journal of
**Geophysical
Research**

VOLUME 65

MAY 1960

NUMBER 5

**THE SCIENTIFIC PUBLICATION
OF THE AMERICAN GEOPHYSICAL UNION**

Journal of Geophysical Research

An International Scientific Publication

OFFICERS OF THE UNION

LLOYD V. BERKNER, *President*
F. W. REICHELDERFER, *Vice President*
A. NELSON SAYRE, *General Secretary*
WALDO E. SMITH, *Executive Secretary*

OFFICERS OF THE SECTIONS

Geodesy

CHARLES PIERCE, *President*
FLOYD W. HOUGH, *Vice President*
BUFORD K. MEADE, *Secretary*

Seismology

LEONARD M. MURPHY, *President*
JAMES A. PEOPLES, JR., *Vice President*
BENJAMIN F. HOWELL, JR., *Secretary*

Meteorology

THOMAS F. MALONE, *President*
GORDON E. DUNN, *Vice President*
WOODROW C. JACOBS, *Secretary*

Geomagnetism and Aeronomy

L. R. ALLREDGE, *President*
C. T. ELVEY, *Vice President*
J. HUGH NELSON, *Secretary*

Oceanography

WALTER H. MUNK, *President*
DONALD W. PRITCHARD, *Vice President*
EUGENE C. LAFOND, *Secretary*

Volcanology, Geochemistry, and Petrology

ALFRED O. C. NIER, *President*
FRANCIS J. TURNER, *Vice President*
IRVING FRIEDMAN, *Secretary*

Hydrology

WALTER B. LANGBEIN, *President*
WILLIAM C. ACKERMANN, *Vice President*
CHARLES C. McDONALD, *Secretary*

Tectonophysics

PATRICK M. HURLEY, *President*
LOUIS B. SLICHTER, *Vice President*
H. RICHARD GAULT, *Secretary*

BOARD OF EDITORS

Editors: PHILIP H. ABELSON and J. A. PEOPLES, JR.

ASSOCIATE EDITORS

1960

HENRY G. BOOKER	WALTER B. LANGBEIN
E. C. BULLARD	ERWIN SCHMID
JULE CHARNEY	HENRY STOMMEL
GEORGE T. FAUST	J. TH. THIJSSSE
DAVID G. KNAPP	A. H. WAYNICK

J. TUZO WILSON

1960-1961

HENRI BADER	T. NAGATA
K. E. BULLEN	FRANK PRESS
CONRAD P. MOOK	A. NELSON SAYRE
WALTER H. MUNK	MERLE A. TUVE

JAMES A. VAN ALLEN

1960-1962

JULIUS BARTELS	TOR J. NORDENSON
E. G. BOWEN	E. N. PARKER
JOHN E. CHAPPELEAR	GEORGE P. RIGSBY
G. D. GARLAND	WALTER O. ROBERTS
GORDON J. F. MACDONALD	C. N. TOUTAT
L. A. MANNING	JAMES R. WAIT

This Journal welcomes original scientific contributions on the physics of the earth and its environment. Manuscripts should be transmitted to J. A. Peoples Jr., Geology Department, University of Kansas Lawrence, Kansas. Authors' institutions, if in the United States or Canada, are requested to pay a publication charge of \$25 per page, which, if honored, entitles them to 100 free reprints.

Subscriptions to the *Journal of Geophysical Research and Transactions*, AGU are included in membership dues.

Non-member subscriptions, *Journal of Geophysical Research*. . . \$30 for back Volume of 1959, \$4 for this issue; \$20 for the calendar year 1960.

Non-member subscriptions, *Transactions, AGU*. . . \$4 per calendar year, \$1.25 per copy. Subscriptions, renewals, and orders for back numbers should be addressed to American Geophysical Union, 1515 Massachusetts Ave., Northwest, Washington 5, D. C. Suggestions to authors are available on request. Advertising Representative: Howland and Howland, Inc., 230 Park Ave., New York 17, N. Y.

Beginning with the January 1959 issue (Vol. 64, No. 1) the *Journal of Geophysical Research* is published monthly by the American Geophysical Union, the U. S. National Committee of the International Union of Geodesy and Geophysics organized under the National Academy of Sciences-National Research Council as the U. S. national adhering body. Publication of this journal is supported by the National Science Foundation and the Carnegie Institution of Washington. The new monthly combines the type of scientific material formerly published in the bi-monthly *Transactions, American Geophysical Union*, and the quarterly *Journal of Geophysical Research*. The *Transactions, American Geophysical Union* will continue as a quarterly publication for Union business and items of interest to members of the Union.

Published monthly by the American Geophysical Union from 1407 Sherwood Avenue, Richmond, Virginia. Second class postage paid at Richmond, Virginia.



Expanding the Frontiers of Space Technology in **SPACE PHYSICS**

Lockheed Missiles and Space Division is broadening its studies in space physics to keep pace with this rapidly growing field of fundamental research.

Positions are available for physicists with advanced degrees, at our Palo Alto facilities in the Stanford Industrial Park, for work in basic research on the physics of the earth's upper atmosphere and beyond.

Typical research projects include: measurement of atmospheric composition and density at satellite altitudes; laboratory experiments on upper atmospheric atomic and molecular reactions; hydromagnetic interactions with the earth's magnetic fields; simulation and study of meteor impacts; and particle radiation.

The successful solution to problems such as these calls for advancement of the state of the art to unknown environments and the maximum of scientific effort.

Engineers and Scientists — We invite you to join us in this challenging effort and to share in the future of a company that has an outstanding record of achievement.

Write: Research and Development Staff, Dept. E-59,
962 W. El Camino Real, Sunnyvale, California. U.S. citizenship
or existing Department of Defense clearance required.

Lockheed / **MISSILES AND SPACE DIVISION**

*Systems Manager for the Navy POLARIS FBM; the Air Force
AGENA Satellite in the DISCOVERER, MIDAS and
SAMOS Programs; Air Force X-7; and Army KINGFISHER*

SUNNYVALE, PALO ALTO, VAN NUYS, SANTA CRUZ, SANTA MARIA, CALIFORNIA
CAPE CANAVERAL, FLORIDA • ALAMOGORDO, NEW MEXICO • HAWAII

ASKANIA - GRAVIMETER

Type Gs 11 with Recording Equipment

The Gravity Meter most used for earth tidal measurements

Type Gs 12

The extremely reliable instrument with built-in ball system

Sea Gravimeter Gss 2 after Graf

with direct recording for uninterrupted measurements on board ship



ASKANIA - WERKE · AKTIENGESSELLSCHAFT

U. S. Branch Office, 4913 Cordell Ave., Bethesda, Maryland

Research by Soviet Experts—Translated by Western Scientists

CALCULATION OF THE BRIGHTNESS OF LIGHT IN THE CASE OF ANISOTROPIC SCATTERING

by E. M. Feigelson, et al.

Designed to present new data which effectively approximate the real conditions of the propagation of light in the terrestrial atmosphere—and uncover the extent to which the anisotropy in scattering should be taken into account. The authors are all members of the staff of the Atmospheric Physics Laboratory of the Academy of Sciences of the USSR, where this research was initiated.

Although previous solutions to this problem have produced accurate results, the authors regard those conclusions as being of too specific a nature. (Optical characteristics of a real atmosphere change with light—and particularly rapidly with respect to time.) The authors felt, therefore, that the problem of the scattering of light in the atmosphere must be solved under more general assumptions pertaining to the laws of scattering than had been done in prior investigations. Those calculations involving the most characteristic cases of the optical state of the atmosphere are presented with accompanying graphs, charts, tables, and literature references.

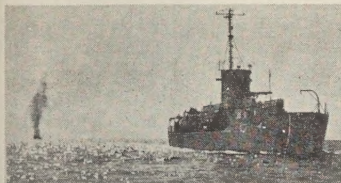
Cloth

104 pages

\$8.00

CONSULTANTS BUREAU ENTERPRISES, INC.

227 West 17th St. • New York 11, N. Y.



TO THE OCEAN'S FLOOR ... AND BELOW

Daily aboard TI's 405-ton, 158-foot SONIC—uniquely a complete sea-going seismic and acoustic investigation center—geoscientists are studying and mapping the structure of the earth below the ocean's floor. Illustrated above is the seismic reflection method, with explosive charges detonated nearby for detailed study of energy travel through water and rock. Technicians aboard the SONIC also record refracted seismic energy, measuring signals through the ocean



floor from charges exploded on land or in water as much as 35 miles away. Similar land-based TI geophysical parties are now working in more than 22 countries of the world.



INNER-SPACE KNOWLEDGE FOR OUTER-SPACE TECHNOLOGY ADVANCED BY TI'S

scientific key to Davy Jones' locker!

At a time when the focus is on outer space—a time when we know more about the moon's surface than we know about 70% of the earth's surface—geophysicists such as this sea-going scientist from Texas Instruments are furthering space-age technology with studies of inner space—the oceans.

He represents one of more than 60 global TI geophysical investigation parties who are applying 30 years' experience in earth sciences to measurement of earth's land and sea physical characteristics. Fundamental to modern defense, earth sciences have extended their traditional role in petroleum exploration to gathering information vital to programs in *underwater warfare, missile accuracy, seismic communications, detection/surveillance of nuclear tests, and design of underground defense structures.*

TI's talent for these "down-to-earth" studies dates back to 1930, when the company was formed as Geophysical Service Inc.—the first independent company to perform seismic reflection surveys for oil exploration. And from GSI's early need for sensitive electronic seismic equipment

came an engineering skill that was applied to Anti-Submarine Warfare systems in World War II, and resulted in TI's Apparatus division becoming a leading ASW equipment manufacturer today. This rare blending of earth sciences knowledge and experience with skills in systems and components gives TI a *unique capability in space-age technology.*

The founding company (GSI) is now the geophysical exploration arm of TI's Geosciences & Instrumentation division, and these capabilities are extended to governmental agencies by the Geosciences department. Designing and manufacturing advanced instruments and systems in wide use by these parties and others is the Instrumentation Product group, with such products as *WORDEN** gravity meters, *EXPLOREX** seismograph systems and *seisMAC** seismic computers.

For more about geosciences at TI, write to Central Merchandising for Bulletin DM-101.

*Trademark of Texas Instruments

TEXAS  **INSTRUMENTS**
INCORPORATED

HEADQUARTERS: 6000 LEMMON AVENUE, DALLAS 9, TEXAS **PLANTS:** ATTLEBORO, MASS. • DALLAS, TEXAS • HOUSTON, TEXAS • VERSAILLES, KY. • ELIZABETH SOUTH, AUSTRALIA • ALMELO, HOLLAND • AVERSA, ITALY • BEDFORD, ENGLAND • BONNEVILLE, FRANCE • BUENOS AIRES, ARGENTINA • MEXICO CITY, MEXICO

OFFICES IN 75 PRINCIPAL CITIES OF THE WORLD

Please mention JOURNAL OF GEOPHYSICAL RESEARCH, when writing to advertisers

NEW BOOKS FROM INTERSCIENCE

Methods and Techniques in Geophysics—Volume 1

edited by S. K. RUNCORN, *King's College, University of Durham*

Modern advances in physical techniques in this field are presented here by an international group of experts to help fill a relative void in the literature of pure geophysical research. The topics discussed in this first volume include *Measurement of: Temperature Gradient in the Earth, Heat Flow over Land, Gravity at Sea. The Geomagnetic Elements; also Bore-Hole Surveying, Measurements in Paleomagnetism, The Detection of Earth Movements, Earth Currents, Properties of Rocks under High Pressure and Temperature, Latitude and Longitude, and the Secular Motion of the Pole.*

Approx. 385 pages Ready Summer 1960

Lead Isotopes in Geology

by R. D. RUSSELL, *University of British Columbia*, and R. M. FARQUHAR, *University of Toronto*

The application of isotopic studies to geophysics has developed rapidly in very recent years, and there is need for this extensive detailed description. The authors, who have contributed much to rock dating by lead isotope determinations, have surveyed the field and given a coherent and up-to-date account of the various ideas that they and other investigators have expressed on the subject. A feature is the very extensive tabulation of lead isotopic abundances, from the authors' own work in Toronto and from other centers of geophysical studies in many parts of the world.

Approx. 240 pages Ready Summer 1960

Methods and Techniques in Geochemistry

edited by A. A. SMALES, *United Kingdom Atomic Energy Research Establishment, Harwell*, and L. R. WAGER, *Oxford*

In this single volume, experts consider all the analytical methods used in geochemistry. Recent advances are discussed, as well as older techniques and their new developments. Each major method, with various related techniques, is treated in a separate contributed chapter, including a discussion of the underlying theory. Thoroughly practical, an early chapter deals with the preliminary examination and treatment of the material before analysis begins.

Approx. 460 pages Ready Summer 1960

**INTERSCIENCE
PUBLISHERS, INC.**

250 Fifth Ave., New York 1, N. Y.

GEOTECH GROUND-BASED ANALOG DATA—TRANSMISSION EQUIPMENT

- ▶ **CAPACITY**—1 to 7 channels of low-frequency analog data.
- ▶ **TRANSMISSION CIRCUIT**—a single voice-frequency telephone, radio, or microwave circuit.
- ▶ **TRANSMISSION RANGE**—coast to coast if required.
- ▶ **DEPENDABILITY**—proven, continuous year-round operation.
- ▶ **ECONOMY**—building-block components; ± 100 volt output of discriminator eliminates need of DC amplifier; can use a leased commercial circuit.
- ▶ **COMPONENTS**—FM telemetering multiplexer: output $z=600$ ohms, $8\frac{3}{4}"$ h x $19"$ w x $15"$ d; voltage—controlled oscillators: RDB/IRIG subcarrier channels, $\pm 2\frac{1}{2}$ volts input produces $\pm 7\frac{1}{2}\%$ deviation, $4\frac{7}{8}"$ h x $3\frac{3}{8}"$ w x $1\frac{5}{8}"$ d; discriminators: input $z=\text{over } 1$ megohm, output $z=0$ ohms, $5\frac{1}{4}"$ h x $19"$ w x $16\frac{3}{8}"$ d.



RUGGED SENSITIVE GALVANOMETERS

SERIES 2980

- ▶ **PERIODS**—1 to 90 seconds.
- ▶ **SENSITIVITY**— 9×10^{-11} amps/mm/meter typical at 90 seconds.
- ▶ **STABILITY**—new fast-stabilizing design provides extremely small drift.
- ▶ **ADJUSTABLE**—CDRX, sensitivity, leveling, and horizontal light spot position.

SERIES 4100

- ▶ **FREQUENCIES**—1 to 50 cps.
- ▶ **SENSITIVITY**—up to 3×10^{-9} amps/mm/meter.
- ▶ **SUSPENSION**—separate, insulated suspension frame rotates, does not disturb ribbon.
- ▶ **ADJUSTABLE**—air gap, natural frequency, horizontal and vertical light spot position.

FOR INFORMATION WRITE:

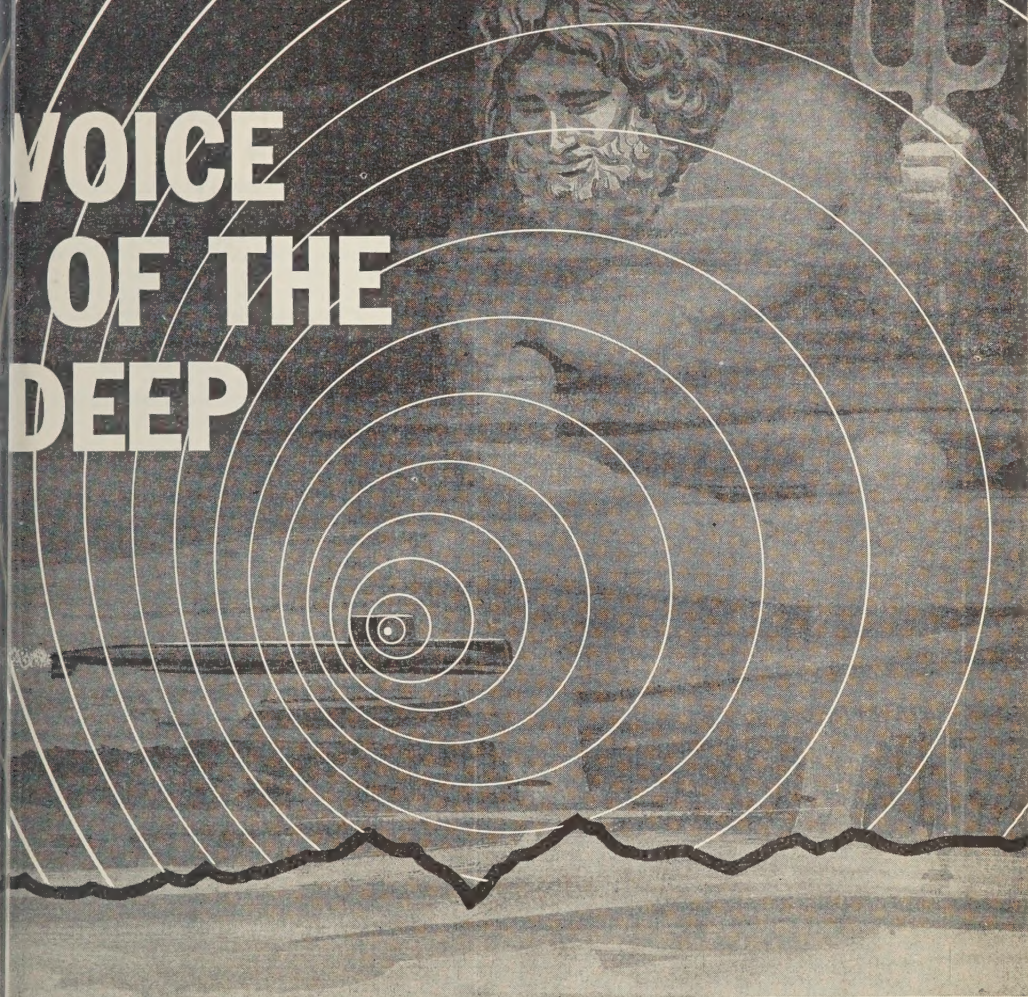


THE GEOTECHNICAL CORP.

3401 Shiloh Road • Garland, Texas

P. O. Box 28277 • Dallas 28, Texas

VOICE OF THE DEEP



Neptune, the mythological ruler of the deep, holds all the waters of the earth as his domain. His son, Triton, was assigned the vital task of communicating his father's commands to submarines in all parts of the ocean.

The U. S. Navy has need of a counterpart for Triton. RCA is now assisting in this role through development of a communication link to our

new nuclear powered Polaris-carrying submarines, anywhere on the seven seas.

RCA, in addition to its Polaris developments, is also working on many new Undersea Warfare systems such as detection, classification and destruction of enemy submarines as well as coordination of our friendly air, surface, and subsurface effort.



Tmk(s) ®

RADIO CORPORATION of AMERICA

DEFENSE ELECTRONIC PRODUCTS

CAMDEN, NEW JERSEY

Please mention JOURNAL OF GEOPHYSICAL RESEARCH, when writing to advertisers

GEOPHYSICAL MONOGRAPH SERIES

AMERICAN GEOPHYSICAL UNION

1515 MASSACHUSETTS AVENUE, N.W.

WASHINGTON 5, D. C., U.S.A.

Antarctica in the International Geophysical Year—Geophysical Monograph No. 1 (Publication No. 462, National Academy of Sciences—National Research Council); Library of Congress Catalogue Card No. 56-60071; 133 pp. and large folded map of the Antarctic, 1956, 7" x 10", \$6.00. Contains 16 papers by various American authorities on the Antarctic under the headings: General, Geographic and Meteorological, Geological and Structural, Upper Atmospheric Physics, and Flora and Fauna. Map (41" x 41") compiled by the American Geographical Society. Introduction by L. M. Gould.

Geophysics and the IGY—Geophysical Monograph No. 2 (Publication No. 590, National Academy of Sciences—National Research Council); Library of Congress Catalogue Card No. 58-60035; 210 pp., 1958, 7" x 10", \$8.00. Contains 30 papers by leading American authorities under the headings: Upper Atmospheric Physics, The Lower Atmosphere and the Earth, and The Polar Regions. Preface by Joseph Kaplan.

Atmospheric Chemistry of Chlorine and Sulfur Compounds—Geophysical Monograph No. 3 (Publication No. 652, National Academy of Sciences—National Research Council); Library of Congress Catalogue Card No. 59-60039; 129 pp., 1959, 7" x 10", \$5.50. Based on a symposium held jointly with the Robert A. Taft Sanitary Engineering Center of the U. S. Public Health Service in Cincinnati in November, 1957. Contains 23 papers (some as summaries) with discussion. Preface by James P. Lodge, Jr.

Contemporary Geodesy—Geophysical Monograph No. 4 (Publication No. 708, National Academy of Sciences—National Research Council); Library of Congress Catalogue Card No. 59-60065; 96 pp., 7" x 10", 1959, \$5.50. Based on a Conference held at Cambridge, Massachusetts, in December 1958 jointly by the AGU with the Smithsonian Astrophysical Observatory and the Harvard College Observatory. Contains 14 papers by leading authorities, with verbatim discussions on topics ranging from classical geodesy to trilateration by underwater sound to space navigation in the solar system. Edited by Charles A. Whitten and Kenneth H. Drummond.

Physics of Precipitation—Geophysical Monograph No. 5 (Publication No. 746, National Academy of Sciences—National Research Council); Library of Congress Catalogue Card No. 60-60010; about 425 pp., 7" x 10", to be published in the early spring, 1960, \$12.50. Based on a Conference held at Woods Hole, Massachusetts, in June 1959. Contains 48 papers by leading authorities, with verbatim discussions on topics ranging from planetary-scale phenomena to microanalysis including hail formation and precipitation control. Edited by Helmut Weickmann.

Postage is to be added to prices shown unless payment accompanies order. Quantity discounts (count each Monograph separately): 5-19 copies, 10%; 20-49 copies, 15%; 50 or more copies 20%.

Purchase Order

TO AMERICAN GEOPHYSICAL UNION

1515 Massachusetts Avenue, N.W., Washington 5, D. C., U.S.A.

Please enter our order for the following:

_____ copies of Geophysical Monograph No. 1, at \$6.00*	\$ _____
_____ copies of Geophysical Monograph No. 2, at \$8.00*	\$ _____
_____ copies of Geophysical Monograph No. 3, at \$5.50*	\$ _____
_____ copies of Geophysical Monograph No. 4, at \$5.50*	\$ _____
_____ copies of Geophysical Monograph No. 5, at \$12.50*	\$ _____

☐ Payment of \$ _____ is enclosed.

☐ Please send invoice, adding postage charges.

☐ Enter our standing order for _____ copies of subsequent Geophysical Monographs at the special prepublication rates, e.g., prepublication rate for Monograph No. 4 for non-members was \$4.00, payment in advance, or \$4.75 (plus postage) on invoice.

* List price is net for quantities up to four; see above for discounts on quantity purchases. Special discounts to members.

Typed name _____ Signature _____

Address _____

Physicists, Geophysicists,
Astronomers:

National Aeronautics and
Space Administration

GODDARD
SPACE FLIGHT
CENTER

Space Sciences Program

The space sciences program of the Goddard Space Flight Center covers all phases of experimental and theoretical physics associated with the exploration of space. The program emphasizes the following areas:

■ EXPERIMENTAL RESEARCH

FIELDS AND PARTICLES: Measurements on gravitational, magnetic, and electric fields; ionospheres of the earth and other planets; interplanetary plasma, auroral and radiation belt particles, and cosmic rays.

PLANETARY ATMOSPHERES: Pressure, temperature, density and composition of the earth's atmosphere; atmospheres of the moon and planets; meteors.

ASTRONOMY: Interstellar and intergalactic media; stellar structure; terrestrial air glow; development of astronomical instruments for rockets, satellites, and space probes.

SOLAR PHYSICS: Measurements in the ultraviolet and x-ray regions of the spectrum.

METEOROLOGY: Satellite and rocket-sonde meteorology.

■ THEORETICAL RESEARCH

PLANETARY SCIENCES: Physics of the Moon and planets; ionospheric physics; upper atmosphere physics; theoretical meteorology; atomic and electronic interactions.

ASTRONOMY: Astrophysics; gravitational astronomy, including celestial mechanics and geodesy; cosmology and relativity.

PLASMA PHYSICS: Magneto-fluid flow; particles and magnetic fields in space; cosmic rays.

■ OPPORTUNITIES exist for physicists, geophysicists, and astronomers who wish to do fundamental research in these fields. Pre-doctoral as well as postdoctoral applicants will be considered. Applicants without a Ph.D. should include a transcript of college and graduate training. Continuation of graduate work will be encouraged. Those interested should address their inquiries to:

Personnel Director
NASA, Goddard Space Flight Center, Dept. L.
Washington 25, D. C.

NASA

National Aeronautics and Space Administration

**ACF ELECTRONICS DIVISION
ELECTRO-PHYSICS
LABORATORIES**

Responsible assignments in furthering the state-of-the-art of Ionospheric Physics, combining competitive salaries and unusual growth potential, are offered to men who can contribute. Our present needs are for:

Physicists

**FOR RESEARCH PROGRAMS IN
IONOSPHERIC
PROPAGATION &
HF COMMUNICATIONS**

**SENIOR IONOSPHERIC
PHYSICISTS**

Ph.D. preferred, with several years' experience in the study of Ionospheric phenomena. Should be familiar with present knowledge of upper atmosphere physics and possess an understanding of current programs using rockets and satellites for studies in F-region and beyond. Qualified individuals with supervisory abilities will have an exceptional opportunity to assume project leadership duties on HF projects already under way involving F-layer propagation studies backed by a substantial experimental program.

The Electro-Physics Laboratories are located in the suburban Washington, D.C. area, where post-graduate study is available in several nearby universities. Housing is plentiful in attractive, well-established neighborhoods. Our relocation allowance is liberal.

*All inquiries will be held
in strictest confidence and answered promptly.*

Please send resume to:
**ROBERT REID, PROFESSIONAL
EMPLOYMENT SUPERVISOR**

ACF ELECTRONICS DIVISION

acf

Industries, Incorporated

Riverdale, Maryland

WARfield 7-4444

**ARE YOU A MEMBER
of
AGU?**

If you are a reader or user of either of the publications noted below, you should look into this matter.

Members regularly receive
the monthly

**Journal of
Geophysical
Research**

the quarterly

**Transactions
American
Geophysical
Union**

Members are entitled to special discounts on other publications of AGU such as

- **Geophysical Monograph Series** (Nos. 1 to 5 available)
- **Izvestiya of the Academy of Sciences, USSR; Geophysics Series** for the years 1957, 1958, and 1959
- Annual meeting in Washington in late April or early May each year
- Regional meeting in the Pacific Northwest in autumn
- Regional meeting in the Pacific Southwest in winter
- Others as opportunity permits

For application forms and other information regarding membership, meetings, and other matters, write to

AMERICAN GEOPHYSICAL UNION

**1515 Massachusetts Ave., N.W.
Washington 5, D. C.**

(An application form is also inserted in the closing pages of this issue.)

Please mention JOURNAL OF GEOPHYSICAL RESEARCH, when writing to advertisers

SPRENGNETHER LONG PERIOD HORIZONTAL SEISMOMETER

GENERAL SPECIFICATIONS:

- Period Range: 6 to 70 seconds.
- Magnification: Up to 15,000, depending on operating period.
- Damping: Electromagnetic.
- Transducer-moving coils in circular magnetic gaps.
- Coils approximately 500 ohms. or to your specifications.
- Pendulum steady mass weight 22 lbs.

PHYSICAL SPECIFICATIONS:

Length.....25"
Width.....25"
Height.....22"
Net Weight.....90 lbs. approx.
Shipping Weight.....155 lbs. approx.

COVER:

Light weight aluminum with rubber gasket seal to base.
Provided with viewing window to observe pendulum centering.

*To compliment this instrument,
a long period vertical seismometer is also available.*

Internationally Known Mfrs. of Seismological, Geophysical Instruments.

W. F. SPRENGNETHER INSTRUMENT CO., INC.

4567 SWAN AVENUE

ST. LOUIS 10, MO.



WRITE FOR DETAILED
INFORMATION ON THESE
INSTRUMENTS.

Back issues available . . .

Journal of Geophysical Research • 1959 • Volume 64

Complete set of 12 (2488 pp.)—\$30.00

January (132 pp.) \$2.00	May (98 pp.) \$2.00	September (230 pp.) \$3.00
February (138 pp.) \$2.00	June (110 pp.) \$2.00	October (284 pp.) \$4.00
March (112 pp.) \$2.00	July (168 pp.) \$2.00	November (390 pp.) \$5.00
April (106 pp.) \$2.00	August (268 pp.) \$4.00	December (452 pp.) \$6.00

Scientific Effects of Artificially Introduced Radiations at High Altitudes (74-page Symposium reprinted from the August issue) \$1.50

International Symposium on Fluid Mechanics in the Ionosphere (202-page Symposium reprinted from the December issue) \$4.50

Subscriptions to Journal of Geophysical Research, Calendar Year 1960..... \$20.00

AMERICAN GEOPHYSICAL UNION

1515 Massachusetts Avenue, N.W. • Washington 5, D. C.

Note: The former publisher of the Journal of Geophysical Research has turned over the stock of back numbers, 1958 and earlier, to Walter J. Johnson, Inc., 111 Fifth Avenue, New York 3, New York.



Western Conducts More Marine Seismic Surveys Than All Other Contractors Combined!

Since 1954, Western Geophysical Company's techniques, instrumentation and professional excellence have won over half of *all* contracts for offshore seismic exploration.

The Western Marine Seismometer, a low-impedance, pressure-sensitive device, is unequalled for high output, low-frequency response, and ruggedness. Western records the entire spectrum from $\frac{3}{4}$ -cps to 10-Kc, plus. Western's high speed cable permits normal production of up to 200 recording locations a day. The story of Western's current activities—"Panorama of a World Wide Organization"—will be sent to you upon request.



Additionally,
Western's land seismic parties
and gravity crews
are at work on four continents.

Western

GEOPHYSICAL COMPANY
AND ITS AFFILIATES

Principal Office: 523 WEST SIXTH STREET • LOS ANGELES 14, CALIFORNIA

AFFILIATE AND REGIONAL OFFICES THROUGHOUT THE WORLD

Journal of GEOPHYSICAL RESEARCH

VOLUME 65

MAY 1960

No. 5

Balloon Study of High-Altitude Radiations during the International Geophysical Year¹

J. R. WINCKLER

*School of Physics, University of Minnesota
Minneapolis, Minnesota*

Abstract. The results of a series of 85 constant level balloon flights conducted during the IGY period to measure cosmic rays and other types of radiation at high altitude are summarized. Each flight carried an ionization chamber, a Geiger counter, and nuclear emulsions, and remained at approximately 10 g/cm^2 depth for times between 2 and 24 hours. The majority of flights were made at Minneapolis, Minnesota. The large decrease in primary cosmic-ray intensity between 1956 and 1958 was observed at high altitude. The high-altitude measurements correlate with sea-level neutron instruments. Many special events were detected, including X rays produced by electrons incident on the atmosphere during strong aurorae and solar cosmic rays detected on ten occasions and correlating with other known observations made in the polar regions. In one case γ rays originating on the solar surface were detected in a short burst. Several cases of radioactive layers in the atmosphere at low level resulting from nuclear explosions were found. This paper summarizes the entire program, and gives the instrumental details, a summary of published information, and detailed analysis of many data not heretofore published.

1. *Introduction.* This paper will summarize the results of an extensive series of balloon flights carried out as part of the United States program for the International Geophysical Year. The balloon flights carried instruments suitable for studying cosmic rays and other types of radiation found in the atmosphere up to heights of 30 km, or 10 mb pressure level. The balloons were of the constant-level polyethylene type, so that about 2 hours of each flight is required for the equipment to be carried to high altitude, and after that it remains at constant level for up to 20 hours. Most of the flights were launched from Minneapolis, Minnesota, and drifted in the prevailing winds in an east or west direction.

Some were launched from other locations, including Cuba, Texas, and Alaska, and near-by sites in Missouri and South Dakota. Some of the measurements were made by attaching the radiation units to ONR 'Skyhook' balloons whose principal purpose was high-altitude experiments for other laboratories.

The equipment on these flights consisted of a spherical integrating ionization chamber, a Geiger counter, a recording package containing a small aerial camera and a pressure transducer, a telemetering transmitter, and a package of nuclear emulsions. The details of the apparatus have been described in a number of publications [Ney and Winckler, 1958; Winckler, Peterson, and Arnoldy, 1958; Peterson, Howard, and Winckler, 1958]. The equipment is sensitive to primary cosmic rays and their time variations associated with radioactive clouds from

¹This research was supported by the U. S. National Committee for the IGY through the National Science Foundation, and by the ONR.

nuclear weapons tests. Detailed analyses of a number of such events have been published and will be referred to later.

This summary of the results of the flights will be grouped into a number of categories as follows:

1. The high-altitude ionization rate and the total atmospheric energy integral as a function of time during the period of the IGY.

2. Changes of intensity observed as a function of latitude.

3. Observations of solar cosmic rays.

4. Observations of X rays associated with aurorae.

5. An observation of solar γ rays.

6. Observation of radioactivity from the testing of nuclear weapons.

This paper will discuss the data obtained with the various electronic detecting instruments. The results of the nuclear emulsion analysis have been recorded in a number of publications by Ney and others [Freier, Ney, and Waddington, 1959a, 1959b; Freier, Ney, and Winckler, 1959; Fowler, Freier, and Ney, 1958]; this analysis is continuing. An extensive analysis of the upper winds obtained from trajectories from the aerial camera photographs has been carried out by Mantis [1959]. The balloon trajectories thus obtained have been used for correlation with the cosmic-ray radiation data.

TABLE 1. Balloon Flight Summary

Flight	Date, UT	Launch Time, UT	Launch Location	Duration, launch to termination	Instrumentation*
	1957				
1	May 23	1201	Minneapolis, Minn.	11 hr 30 min	SC, IC, NE
2	June 6	0220	Minneapolis, Minn.	21 hr 40 min	SC, IC, NE
3	July 1	0107	Minneapolis, Minn.	21 hr 35 min	SC, IC, NE
4	July 4	0416	Minneapolis, Minn.	15 hr 40 min	SC, IC, NE
5	July 28	0217	Minneapolis, Minn.	16 hr 48 min	SC, IC, NE
6	Aug. 1	1037	Minneapolis, Minn.	10 hr 44 min	SC, IC, NE
7	Aug. 10	0150	Minneapolis, Minn.	8 hr	SC, IC, NE
8	Aug. 13	0200	Minneapolis, Minn.	9 hr 47 min	SC, IC, NE
9	Aug. 17	0118	Minneapolis, Minn.	19 hr 40 min	SC, IC, NE
10	Aug. 20	0818	Minneapolis, Minn.	14 hr 17 min	SC, IC, NE
11	Aug. 24	0315	Minneapolis, Minn.	1 hr 40 min	SC, IC, NE, PC
12	Sept. 1	0126	Minneapolis, Minn.	17 hr 50 min	IC, NE, PC
13	Sept. 4	1459	Minneapolis, Minn.	5 hr 30 min	Double IC
14	Sept. 10	1729	Minneapolis, Minn.	9 hr 43 min	Double IC, NE
15	Sept. 13	0207	Minneapolis, Minn.	4 hr 30 min	SC
16	Sept. 21	0040	Minneapolis, Minn.	4 hr 43 min	SC
17a	Sept. 22	0542	Minneapolis, Minn.	3 hr	SC
17b	Sept. 22	0344	Minneapolis, Minn.	1 hr 30 min	SC, IC, NE, PC
18	Sept. 23	0558	Minneapolis, Minn.	11 hr 50 min	SC, IC, NE, PC
19	Sept. 30	0315	Minneapolis, Minn.	8 hr 45 min	SC, IC, NE
20	Oct. 19	0445	Huron, S. D.	6 hr	SC, IC, NE
21	Nov. 6	1339	Minneapolis, Minn.	3 hr 45 min	Triple IC, NE
22	Dec. 3	1406	Minneapolis, Minn.	>4 hr 45 min	SC, IC, NE
	1958				
23	Jan. 2	1545	Sioux Falls, S. D.	8 hr 9 min	SC, IC, NE
24	Jan. 22	1129	Minneapolis, Minn.	9 hr 11 min	SC, IC, NE
25	Feb. 9	0202	Minneapolis, Minn.	19 hr 35 min	SC, IC, NE
26	Feb. 11	0440	Minneapolis, Minn.	14 hr 45 min	SC, IC, NE
27	Mar. 21	0745	Minneapolis, Minn.	6 hr 35 min	SC, IC, NE
28	Mar. 26	1136	Minneapolis, Minn.	6 hr 38 min	SC, IC, NE
29	Apr. 8	1109	Minneapolis, Minn.	9 hr	SC, IC, NE
30	Apr. 18	0329	Minneapolis, Minn.	6 hr 50 min	SC, IC, NE
31	May 16	1213	Minneapolis, Minn.	>14 hr	SC, IC, NE
32	May 30	0033	Minneapolis, Minn.	21 hr 58 min	SC, IC, NE
33	June 18	0235	Minneapolis, Minn.	18 hr 30 min	SC, IC, NE
34	June 20	0505	Minneapolis, Minn.	20 hr	SC, IC, NE
35	June 21	0100	Minneapolis, Minn.	21 hr	SC, IC, NE

TABLE 1. (Continued)

Flight	Date, UT	Launch Time, UT	Launch Location	Duration, launch to termination	Instrumentation*
36	June 27	1153	Minneapolis, Minn.	13 hr 25 min	SC, IC, NE
37	July 10	0757	Minneapolis, Minn.	2 hr 3 min	SC, IC, NE
38	July 11	0137	Minneapolis, Minn.	20 hr 40 min	SC, IC, NE
39	July 13	0049	Minneapolis, Minn.	19 hr 30 min	SC, IC, NE
40	July 18	2201	Minneapolis, Minn.	22 hr 15 min	SC, IC, NE
41	July 22	0040	Minneapolis, Minn.	16 hr 10 min	SC, IC, NE
42	July 25	0215	Minneapolis, Minn.	19 hr 16 min	SC, IC, NE
43	July 26	0041	Minneapolis, Minn.	23 hr	SC, IC, NE
44	July 27	0251	Minneapolis, Minn.	19 hr 24 min	SC, IC, NE
45	Aug. 17	0528	Minneapolis, Minn.	1 hr 30 min	SC, IC, NE
46	Aug. 22	0816	Minneapolis, Minn.	14 hr 40 min	SC, IC, NE
47	Aug. 24	0420	Minneapolis, Minn.	17 hr 45 min	SC, IC, NE
48	Aug. 27	0436	Minneapolis, Minn.	40 hr	SC, IC, NE
49	Sept. 4	0424	Minneapolis, Minn.	11 hr (approx.)	SC, IC, NE
50	Sept. 22	0518	Minneapolis, Minn.	9 hr	SC, IC, NE
51	Oct. 13	1332	Minneapolis, Minn.	7 hr 20 min	SC, IC, NE
52	Oct. 21	1115	Minneapolis, Minn.	6 hr 10 min	SC, IC, NE
53	Oct. 23	0644	Minneapolis, Minn.	6 hr	SC, IC, NE
54	Oct. 31	1148	Minneapolis, Minn.	17 hr (approx.)	SC, IC, NE, PIC
55	Nov. 22	0838	Minneapolis, Minn.	2 hr 15 min	SC, IC, NE
56	Nov. 24	0827	Minneapolis, Minn.	13 hr 30 min	SC, IC, NE
57	Nov. 27	0058	Minneapolis, Minn.	20 hr 42 min	SC, IC, NE
58	Dec. 18	1248	Minneapolis, Minn.	7 hr	SC, IC, NE, SCI
A	8/14/56	2138	Minneapolis, Minn.	>2 hr 22 min	SC, IC
B	9/18/56	1225	Crosby, Minn.	9 hr 36 min	IC, NE
C	10/16/56	1300	Minneapolis, Minn.	11 hr 10 min	SC, IC, NE
D	2/12/57	2110	Guam	2 hr 56 min	SC, IC
E ₁	2/19/57	1549	Guam	5 hr 40 min	SC, IC
E ₂	4/8/57	1334	Minneapolis, Minn.	41 min	SC, IC
F	4/27/57	1348	Minneapolis, Minn.	7 hr 10 min	SC, IC
G	9/5/57	1306	South St. Paul, Minn.	>2 hr	IC, NE
H	11/10/57	Unknown	Huron, S. D.	Unknown	IC
I	10/27/57	1301	South St. Paul, Minn.	6 hr 38 min	SC, IC
J	10/19/57	1240	Brownwood, Tex.	10 hr 20 min	SC, IC, NE
K	2/16/58	1410	South St. Paul, Minn.	7 hr 12 min	SC, IC, NE
L	12/19/57	0832	Guantanamo, Cuba	7 hr 13 min	SC, IC, NE
M	3/20/58	0842	Guantanamo, Cuba	8 hr	SC, IC, NE
N	3/21/58	0740	Guantanamo, Cuba	9 hr	SC, IC, NE
O	3/21/58	0911	Brownwood, Tex.	Negligible	SC, IC, NE, GT
P	3/26/58	1204	Brownwood, Tex.	7 hr 20 min	SC, IC, NE
Q	6/27/58	1047	Moberly, Mo.	11 hr 55 min	SC, IC, NE
R	7/2/58	1220	Minneapolis, Minn.	10 hr 40 min	SC, IC, NE
S	8/23/58	0545	Fairbanks, Alaska	17 hr 30 min	SC, IC, NE
T	8/24/58	1045	Fairbanks, Alaska	17 hr 50 min	SC, IC, NE
U	8/27/58	0655	Fairbanks, Alaska	38 hr 50 min	SC, IC, NE
V	9/22/58	1944	Fairbanks, Alaska	2 hr	SC, IC, NE, PIC
W	9/10/58	2236	Fairbanks, Alaska	>16 hr	SC, IC, NE
X	9/23/58	0330	Fairbanks, Alaska	1 hr 40 min	SC, IC, NE

* Key:

SC = single Geiger counter.

IC = ion chamber.

NE = nuclear emulsion.

PC = photon counter.

PIC = pulse ion chamber.

SCI = scintillation counter.

GT = Geiger telescope.

> = termination time not known accurately at time of this report.

The lettered flights are hitchhikes on ONR 'Skyhook' flights, or flights made by our project at field locations (Cuba, Fairbanks, etc.).

In Table 1 are summarized the flights made up to December 31, 1958. It will be of use for persons interested in comparing other types of data with the radiation data obtained on the balloon flights, and accordingly gives the time and latitude at which balloon exposures were obtained. Most flights carried the standard equipment of ionization chamber, counter, and emulsions, but in the last column of the table a notation is made of the exact instrumentation. A tabulation of all the balloon data obtained with the counting instruments is being completed and will be available as a Technical Report; it will also be made available to the IGY Data Centers. In general, the balloon flights rise in about 2 hours from launch to the floating altitude in the vicinity of 10 mb and remain approximately at this altitude until the indicated cut-down of the flight. A few of the flights have indefinite terminations, owing to a timer failure. The numbered flights are those made on our standard program at Minneapolis; lettered

flights are those flown from field locations or as 'hitchhike' loads on Skyhook balloon flights.

2. *Summary of high-altitude intensities during the IGY.* One of the principal objects of the program was to observe the day-to-day intensity of galactic cosmic radiation at high altitude. For this purpose the counting rates of the ion chamber and Geiger counter have been standardized using a Co^{60} γ -ray source which provides photons of about 1-Mev energy. The geometry of the Geiger counter and ion chamber is closely the same from flight to flight, and this fact alone might be used for normalization. In the case of the ion chamber, however, the electrometers differ considerably from one chamber to another, which necessitates careful calibration with the radiation source. In Figure 1 is a scale drawing of the two instruments. It will be noted that the Geiger counter has a sensitive length less than its diameter, and this is so chosen that the response of the counter to particles is approximately isotropic. The omnidirectional projected area of the counter is 24.2 cm^2 . The rates of the two instruments under the calibration source after correction for the decay of the cobalt were normalized to a standard rate of 50 c/sec for the counter and 50×10^{-8} pulse/sec for the ion chamber. The normalization factors thus derived were then applied to the flight data. The rates of the instruments after normalization were plotted as a function of pressure for the ascending part of the flight up to the point where the balloon floats level at ceiling altitude.

From these soundings the high-altitude intensity was read off at 10 mb for each flight. Figure 2 shows a set of soundings chosen as an example during the period of the March 25, 1958, intensity decrease. With the normalization factors and scale chosen, the counter curve generally lies above the ion chamber in rate but crosses somewhere near the ceiling altitude. The counter on all the IGY flights shows a considerable Pfozter maximum in intensity, and the ion chamber likewise shows a mild maximum. It was noted that, on several of the very earliest flights in the series made in the fall of 1956, this maximum was absent and at the same time the intensity was much larger. In Figure 2, the curve of flight IGY-27 on March 21, 1958, is typical of the lowered level of intensity at solar

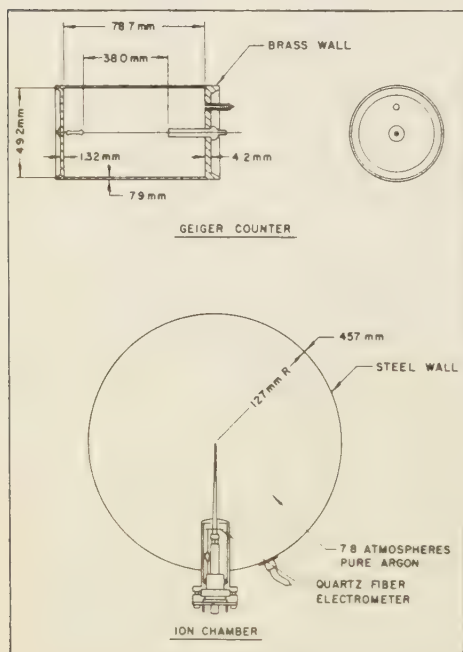


Fig. 1. Scale drawing of Geiger Müller counter and ionization chamber. See the text and Table 2 for further detailed specifications of these instruments.

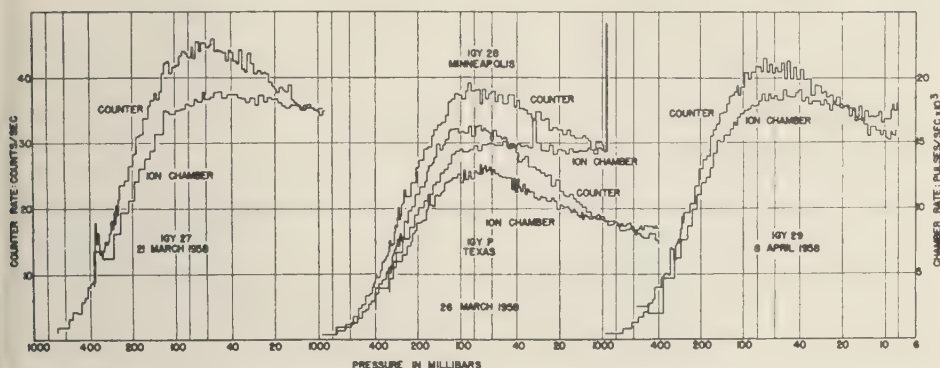


Fig. 2. A group of ion-chamber and counter soundings during the Forbush decrease and low-energy solar cosmic-ray event of March 26, 1958. Left-hand curves typical of solar maximum before the Forbush decrease. Note the spike on both instruments at about 350 mb, which is a radioactive layer in the atmosphere. Center set of soundings: upper, Minneapolis ion chamber and counter during the Forbush event; lower, ion chamber and counter at Texas at the same time. Right-hand sounding: ion chamber and counter after the recovery of the Forbush event.

maximum. On the ascent part of this flight, at about 350 mb, both the ion chamber and the counter show an increase associated with a radioactive layer from a bomb test. This event will be discussed in section 5. On March 26, the center set of soundings in Figure 2, both the ion chamber and the counter at Minneapolis show a decreased intensity, throughout the atmosphere, due to the Forbush event then in progress. Shortly after reaching ceiling, this particular flight encountered a large increase in flux which has been analyzed as incident solar protons in the low cosmic-ray energy range. This and similar events are discussed in section 3. On this flight some large spikes were observed on the ion chamber, and one of these occurs, as can be seen, at about 10 mb. The origin of these spikes is not at present understood.

Simultaneously with the Minneapolis flight IGY-28, a balloon was launched in Texas numbered IGY-P; the sounding is shown on the same pressure scale in Figure 2. It will be observed that there is a large latitude effect between Minneapolis and Texas. At Texas the intensity measured with both instruments is lower and the transition effects are bigger, which is to be expected as the average energy is higher. The Texas flight reached a considerably higher altitude of 4 mb, further displaying the atmospheric transition effect. A later flight, IGY-29,

on April 8, is also shown (in Fig. 2) to illustrate the recovery of the high-altitude intensity from the Forbush-type event which occurred on March 25. In this figure, and in the graphs that follow, the counter rate is given in counts per second and the ion-chamber rate in pulses per second multiplied by 10^3 , each on the normalized scale. The average omnidirectional flux may be obtained from the normalized Geiger counting rate according to the equation

Flux = Normalized rate (c/sec)

$$\times 0.00725 \text{ Particles}/(\text{cm}^2 \cdot \text{sec} \cdot \text{ster}) \quad (1)$$

This assumes upper hemisphere response only.

The number of ion pairs per second, per cubic centimeter of standard air (76 cm Hg, 24°C), may be obtained from the normalized ion-chamber rates, R_m (pulses/sec $\times 10^3$), according to the expression

$$N = 12.3 \times R_m \quad (2)$$

In determining the 10-mb rates, in a few cases a short extrapolation is needed. In others, changes of intensity encountered at high altitude associated with various kinds of temporary radiation often made the ion-chamber rate increase as the balloon reached ceiling. In such cases an attempt was made to estimate the galactic cosmic-ray background. In addition, we have

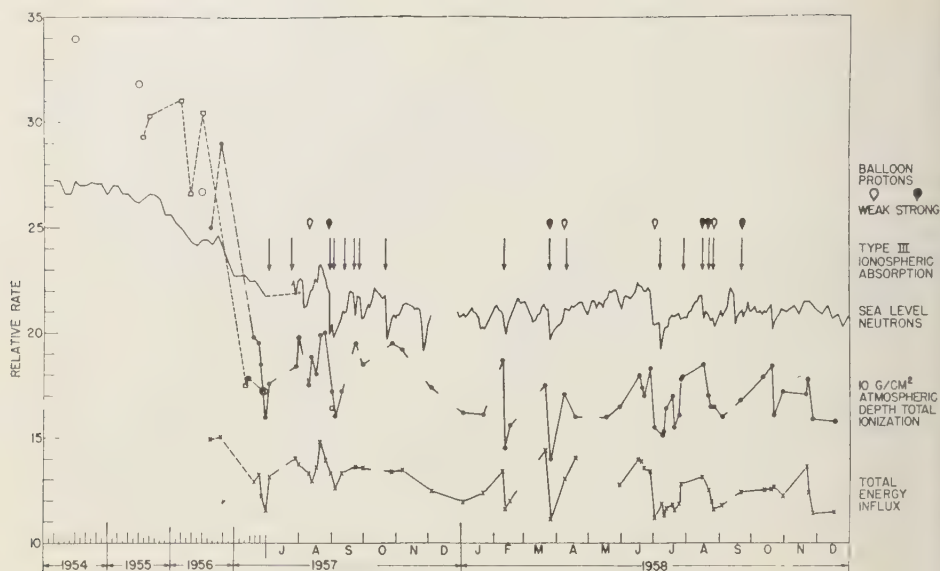


Fig. 3. Summary of high-altitude measurements during the IGY period compared with sea-level cosmic-ray detectors. Upper curve, neutron monitor intensities; middle curve, total cosmic-ray ionization at 10 g/cm² atmospheric depth; bottom curve, total energy influx measured as ionization. The dotted curve covering the period July 1955 to January 1957 with the data indicated as square points was obtained with small Geiger coincidence telescopes. We have normalized to our data the values obtained by Neher close to the geomagnetic pole and extending back to solar minimum in 1954 (circles). The arrows at top represent times when solar-generated low-energy cosmic rays were known to be incident over the polar region. The balloon above the arrow indicates a direct measurement of these solar cosmic rays with balloons, either at Minneapolis or at high latitude.

computed the atmospheric integral of the ionization according to the relation

$$P = 2.5 \int_0^{\infty} R dp \quad (3)$$

for each of the ion-chamber curves. R is the normalized chamber rate in pulses/sec $\times 10^8$, and dp the pressure increment measured in millibars. The value P of these atmospheric integrals is plotted along with the high-altitude values in Figure 3. The total energy dissipated in an atmospheric column 1 cm² in cross section is given by the relation

$$E = P \times 1.42 \times 10^8 \text{ ev/cm}^2 \cdot \text{sec} \quad (4)$$

The ratio (normalized ion rate)/(normalized count rate) is proportional to the mean omnidirectional ionization of the combined cosmic-ray primaries and secondaries in the atmosphere. In Table 2 are given average observed values

under 'normal' conditions at various depths in the atmosphere. The calculated value for isotropic minimum ionizing particles is 3.19. Observed values are higher, and increase with altitude, as would be expected.

Figure 3 presents a summary of the high-altitude data obtained in the manner described

TABLE 2. Normalized Ion Rate/Normalized Count Rate under Various Conditions

Atmospheric Depth, g/cm ²	Ratio $\times 10^4$
300	3.36
200	3.84
100	4.03
50	4.21
10	5.02
Isotropic minimum ionizing particles calculated	3.19
Co ⁶⁰ γ rays uniform flux	4.03

above. We have compared our absolute values of ionization with those obtained by Neher, and this is discussed later in this section. During the IGY from July 1, 1957, to December 31, 1958, we have used a wide scale but for comparison have included some values reaching back to solar minimum in 1954, and this part of the scale is contracted. The flights on this program began in the fall of 1956 and extended through the IGY period. In Figure 3 is seen, at the bottom, the atmospheric integral for each of the flights; next above, the 10-mb total ionization rate; and on the top line, for comparison, the Deep River neutron monitor rates for the period. These last data were furnished through the IGY Data Center A for Cosmic Rays by courtesy of Hugh Carmichael. For comparison with the earlier values, back to solar minimum, we have used a summary prepared by *Forbush* [1958]. The neutron monitor data are those of the Ottawa neutron monitor, normalized to the Carmichael monitor about August 1, 1957. High-altitude ionization points with ion chambers similar to the ones used on this program and obtained by H. V. Neher are also plotted for comparison. They are normalized to our ionization points in June 1957. The justification for normalizing together Neher's Thule data with our Minneapolis data is the absence of a latitude effect between these points in 1957. This is discussed in later paragraphs.

In addition to the data of Rose and Neher as summarized by *Forbush*, we have also plotted data obtained at Minnesota with small Geiger counter coincidence telescopes flown at the 10-mb level. The results of this series of flights have been reported in the literature [*Winckler and Anderson*, 1957; *Winckler and Peterson*, 1958]. These Geiger-telescope points have likewise been normalized to the high-altitude ionization values in June 1957. One striking feature shown in Figure 3 is the large decrease in intensity accompanying the solar maximum period. This is shown by the data in Figure 3 prior to July 1, 1957, both by the high-altitude ionization and counting rate and by the sea-level neutron monitor. By comparing Neher's data, it is seen that the solar-cycle modulation between June 1954 and June 1957 is a factor of 2 in the high-altitude ionization. The change in the sea-level neutron rate over the same interval

is about 20 per cent. The atmospheric ionization integral, although the data extend back only to August 1956, appears to agree more closely with the neutron monitor data, and the effect is not nearly as large as the high-altitude ionization effect. The anticorrelation of galactic cosmic-ray intensities with solar activity or sunspot numbers has been much discussed in the literature; see, for example, *Forbush* [1958], *Lockwood* [1958], *Simpson and Meyer* [1957], *Neher* [1956].

Another striking feature of the data is the many large, sudden intensity decreases which show in all the instruments. In examining the data in Figure 3, one must keep in mind that, although many balloon flights were made, the intensity record is nevertheless crude compared with the continuous sea-level monitoring instruments, and so some of the intensity decreases as shown by the neutron monitor will be missed on the high-altitude record. An attempt has been made to draw the high-altitude lines broken where it is obvious that details are lost, but a number of the high-altitude intensity decreases have good balloon data before, during, and after the decrease, and these show a striking correlation with the neutron monitor data. The arrows at the top of the figure refer to measurements of solar-generated cosmic rays; they are discussed in section 3. An examination of solar data shows that all the large *Forbush* decreases shown here are associated with intense solar flares that occurred between 1 and 2 days before the decrease.

It is important to examine the data to see what quantitative facts can be obtained about the nature of the modulation of the galactic cosmic rays over the period of the solar cycle and also during the sudden intensity decreases. The relative data as shown by the various instruments during these types of decreases are summarized in Table 3. We tabulate the fractional decrease in the sea-level neutrons, in the 10-mb-level total ionization, and in the total atmospheric integral ionization. These values are read off for a selected number of events for which data are available. Unfortunately, our balloon flight sequence does not extend back to solar minimum, but we have compared the 10-mb ionization with Neher's data that are available to that time.

TABLE 3. Comparison of Measurements during Cosmic-Ray Intensity Decreases

Date UT	Event	Fractional Decrease			Ratios		
		Sea-Level Neutrons	10-mb Total Ionization	$\int I \, dp$	Ions/Neutrons	$\int I \, dp$ /Neutrons	Ions/ $\int I \, dp$
7/54-7/57	Solar-cycle decrease	0.18	0.50	...	3.7
8/56-7/57	Solar-cycle decrease	0.10	0.32	0.17	3.1	1.6	1.9
8/29/57	Forbush decrease	0.11	0.20	0.089	1.8	1.2	2.2
2/11/57	Forbush decrease	0.05	0.22	0.13	4.6	2.8	1.6
3/25/58	Forbush decrease	0.06	0.20	0.23	3.3	3.7	0.90
6/28/58	Forbush decrease	0.07	0.15	0.16	2.1	2.3	0.92
8/17/58	Forbush decrease	0.05	.11	0.13	2.4	2.8	0.84

The last three columns of Table 3 give, respectively, the ratio of the 10-mb ionization to the sea-level neutrons, the ratio of the total atmospheric integral to the neutrons, and, last, the ratio of the 10-mb ionization to the atmospheric integral. The change in the 10-mb ionization for all seven cases discussed shows a factor of increase over the change in sea-level neutrons of approximately 3. There does not seem to be a striking difference in this case between the solar cycle decrease between 1954 and 1957 and the sudden intensity decreases, although some of the latter show smaller ratios. But, for example, the highest ratio observed is for the February 10, 1958, solar storm, where the relative value between 10-mb and sea-level neutrons is 4.0. This reflects the rather small change in the sea-level neutrons during this event. The average ratio of 10-mb ionization change to sea-level neutron changes for decreases throughout the IGY period is 2.8.

The ratio of the atmospheric integral to the sea-level neutrons seems to show a tendency to increase during the progression of the solar cycle through maximum. On the other hand, the 10-mb ionization compared with the atmospheric integral shows a tendency to decrease during the solar cycle, reflecting the fact that the atmospheric integral energy is sensitive to the high-energy part of the primary spectrum. A considerable fraction of the value of the

integral is obtained from the low-altitude part of the flight, where the pressure is high and the intensities due to high-energy primaries are not negligible. The 10-mb ionization level, on the other hand, is sensitive to primaries down to the geomagnetic cutoff at Minneapolis. One must note that most of the ionization produced in the chamber floating at 10 mb, or about 100,000 feet of altitude, is caused by secondary particles in the atmosphere. Some effect is produced by the heavy elements in the primary spectrum because of their high Z and high relative ionization. These components, however, are rapidly attenuated at large zenith angles, where the chamber has its largest solid angle, and therefore do not contribute a very large fraction of the total effect.

As was also pointed out earlier, the 10-mb ionization level is sensitive to various kinds of soft particles such as the solar cosmic rays discussed in the next section, auroral X rays, and other types of radiation. Because these effects often appear during geomagnetic storms when the intensity of galactic cosmic rays is depressed, this contributes an error in the direction of increasing the high-altitude ionization at a time when the galactic cosmic-ray effect is to decrease the ionization. It appears that such effects may account for some of the fluctuations in the ratio, for example, of ionization to sea-level neutrons. The August 29 event, listed in

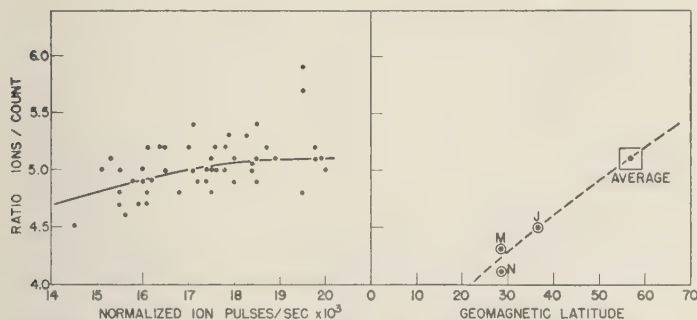


Fig. 4. Comparison of the ratio (normalized ion rate)/(normalized counter rate) as a function of ion-chamber intensity at Minneapolis, left curve; as a function of geomagnetic latitude, right curve. The fluctuations seen on the left curve are principally due to Forbush-type events during the IGY. The maximum change in ratio of such events is seen to be equivalent to a latitude change on the average of about 12°.

Table 3, shows a very low ratio, and the February 10 one a high ratio.

The most self-consistent data are those contained in the last column, where the high-altitude ionization is compared with the atmospheric integral. This ratio is sensitive to the extremes of the cosmic-ray spectrum, and it shows a progressive hardening as the solar cycle proceeds. The sudden intensity decreases, coupled with whatever continuous decrease may be superposed, flatten the spectrum more and more as the solar cycle progresses. The reader should remember, however, that considerable errors creep into the ratios given in Table 3. For example, the fractional decreases of the 10-mb total ionization given during the sudden intensity decreases are often in error because the time of the decrease coincides with the geomagnetic storm when solar cosmic rays, auroral X rays, or other effects are present at high altitudes, and this perturbs the readings due to the galactic cosmic-ray background. Errors creep into the measurement of the integral of ionization in the atmosphere on both the high-altitude and the low-altitude end, because in the former we have to integrate to infinity using the observed value at the last pressure point at the ceiling of the balloon. Also at the high-pressure end at low altitude the pulsing rate of the chamber is low enough so that an extrapolation is necessary, based on an average for many curves to fill out the ionization integral. These procedures lead to appreciable uncertainties. The error is

difficult to estimate, but, in general, in the last column of Table 3 a significant effect is observed above the errors. That is, the continual decrease of the high-altitude ionization divided by the atmospheric integral appears to have a significant trend.

Some further information is available from the flight series on the intensity decreases. For example, we have compared the ratio of the 10-mb ionization rate to the 10-mb Geiger counter rate. In Figure 4 this ratio is plotted as a function of the level of intensity read by the ion chamber. There is considerable scatter of the points, and only a small trend is noticeable at the lowest values of ion-chamber rates. A much clearer effect is observed if the ratio of the ionization chamber to the counter is plotted as a function of the geomagnetic latitude for the few flights made on the program at lower latitudes compared with Minneapolis. This is shown also in Figure 4 in the right-hand section. The trend toward lower ratios at lower latitudes reflects the higher average energy and the decrease in heavily ionizing secondaries in high atmosphere. By comparing the two parts of Figure 4, the change in primary energy at Minneapolis during Forbush decreases is seen to be, at most, equivalent to a shift in latitude of about 12°, under the cosmic-ray conditions at solar maximum.

The same value is obtained from Figure 5, where the total ionization at 10 g/cm² is plotted as a function of latitude during normal levels

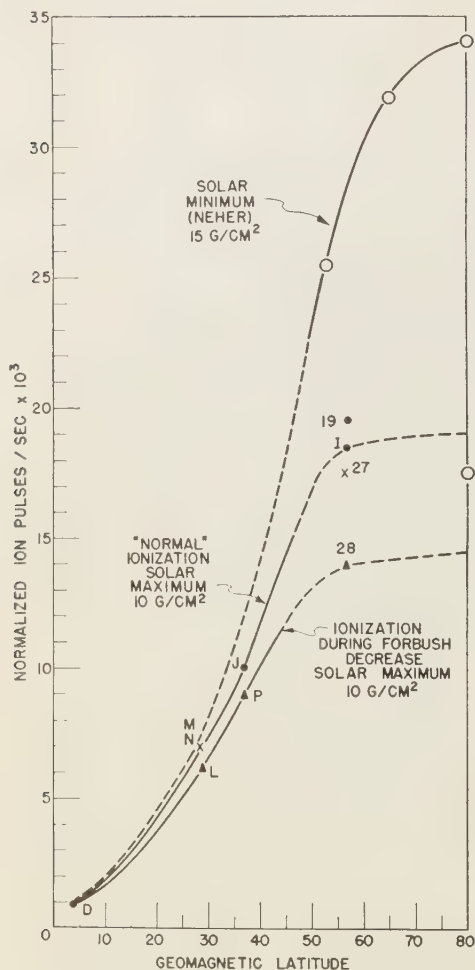


Fig. 5. Total ionization at 10 g/cm² depth as a function of geomagnetic latitude at solar minimum and for normal and Forbush decrease intensities measured at solar maximum. The numbers and letters refer to the various applicable flights of the present series. The circles are data obtained by Neher.

at solar maximum and during depressed levels following Forbush decreases. Unfortunately, the points on the two curves are not all for the same decrease, but on account of the paucity of data it was not possible to fill out complete latitude curves with the balloon data during a single intensity decrease. Also shown in Figure 5 are the high-latitude values of total ionization

measured by Neher in 1954 at solar minimum at 15 g/cm² [Neher, 1956]. An approximate latitude curve is shown dotted, which normalizes with our data at the equatorial point, flight D, where it is known that the solar-cycle and intensity-decrease effects are of such size as to be inconspicuous on the present plot. Figure 5 shows immediately that both the solar-cycle effect and the Forbush-decrease effect operate selectively on the low-energy end of the spectrum. The question is whether the basic mechanism of these two is the same, that is, whether it is possible that the solar-cycle effect is compounded of many Forbush decreases from which recovery is not complete or whether the two mechanisms are basically different in their action on the primary cosmic-ray spectrum. The difficulty of getting good answers to this problem is obvious if the data shown in Figure 5 are carefully considered. First of all, the solar-cycle modulation removes the majority of the low-energy particles in the spectrum, and the effect of the Forbush decrease on these particles cannot, therefore, be studied in detail, at least with these data. It does appear that the qualitative effect of the solar cycle is similar to the effect of the sudden intensity decrease on the rest of the spectrum, but because of the crudeness of the data shown in Figure 5 this is not a very firm conclusion. It should be noted that Figure 5 is plotted as a function of geomagnetic latitude, which means that the data are representative in some way of the integral rigidity spectrum. However, the 10-mb ionization measured by the integrating ion chambers consists mostly of secondary particles in equilibrium with the primaries in the high atmosphere, and in some complicated way is related to the number energy spectrum of the primaries. It is very difficult to get point-by-point relations between the 10-mb ionization and the flux of particles because of the large effect of the secondaries. It does not seem wise to try to extract further information of this type from these data.

We have attempted several other means of comparing the different parts of the primary energy spectrum during the IGY period. One additional method is to plot the 10-mb ionization against the total energy influx calculated as the ion chamber ascends into the atmosphere. The results for all the flights are shown in

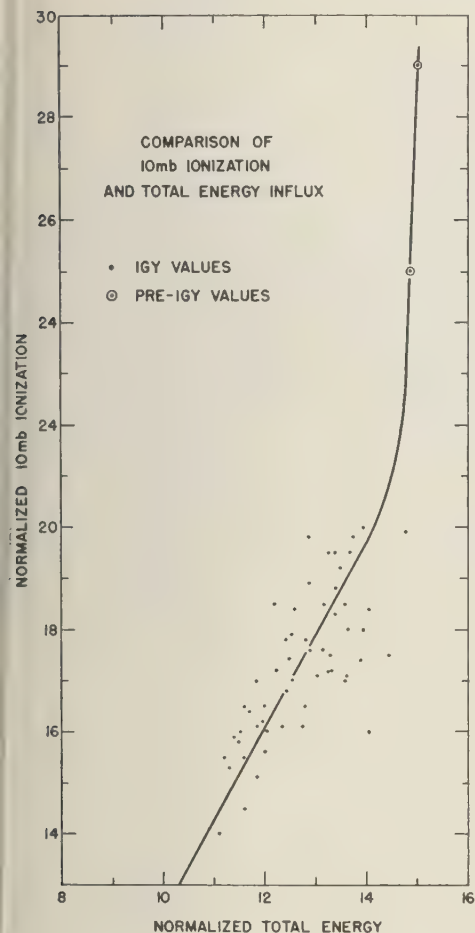


Fig. 6. The comparison of two parts of the primary energy spectrum obtained from 10-mb ionization and the normalized total atmospheric energy integral. Most of the points are during the IGY period, but the two high points represent pre-IGY values before the intensity had dropped to the low value during sunspot maximum.

Figure 6. Two points are available before the main solar cycle decrease in the winter of 1956–1957; all the other points are during 1957–1958. It can be seen that there is a rough proportionality during 1957–1958 but that the curve steepens a very large amount at the high-intensity values of the 10-mb ionization. These high-intensity values refer to points taken in the fall and winter of 1956. Figure 6 reflects again

netic latitude effect, although generally present, the depletion of the low-energy part of the spectrum relative to the high-energy part.

We have also compared the 10-mb total ionization with ground-level neutron monitors as shown in Figure 7. The upper part of Figure 7 is for the Churchill neutron monitor (Churchill neutron rates obtained from U. S. Data Center A for Cosmic Rays, courtesy of D. C. Rose, 1958). The lower part of Figure 7 is for the Climax neutron monitor (Climax neutron monitor neutron data through U. S. Data Center A for Cosmic Rays, courtesy of J. A. Simpson, 1958). In the lower figure we have connected the points in temporal sequence by straight lines. We see that there is a general proportionality but that there are large excursions, for example those connected with flights 18, 19, I, and 21, which occur in a fairly short region of time and show deviations from the neutron monitor in the same sense, in this case corresponding to the temporary return of a more highly ionizing but lower than average energy radiation. In the upper part of Figure 7 the encircled points refer to pre-IGY values comparing the Ottawa monitor and the 10-mb ionization. The Ottawa and Churchill monitors are on the same scale. This curve, showing the large change in the relative spectrum between fall 1956 and summer 1957, is very similar to Figure 6. (Note difference in scale proportion in abscissas of Figure 6 and 7.)

Since the balloons frequently drift somewhat in geomagnetic latitude during a particular flight, and since the trajectories are known accurately over a considerable part of each flight from the aerial camera photographs, it is possible to measure differential latitude effects from many of the flights as long as the altitude remains sufficiently constant so that an altitude effect is not superposed. Figure 8 shows data from a number of flights which meet satisfactory criteria of having trajectories at constant level. The geographic latitude and longitude have been converted to geomagnetic latitude using the earth's centered dipole approximation.

From these differential segments is noted a trend from the latitude of Minneapolis, where most of the flights cluster, toward latitude 41° in Texas, where several flights were made. However, at the latitude of Minneapolis the geomag-

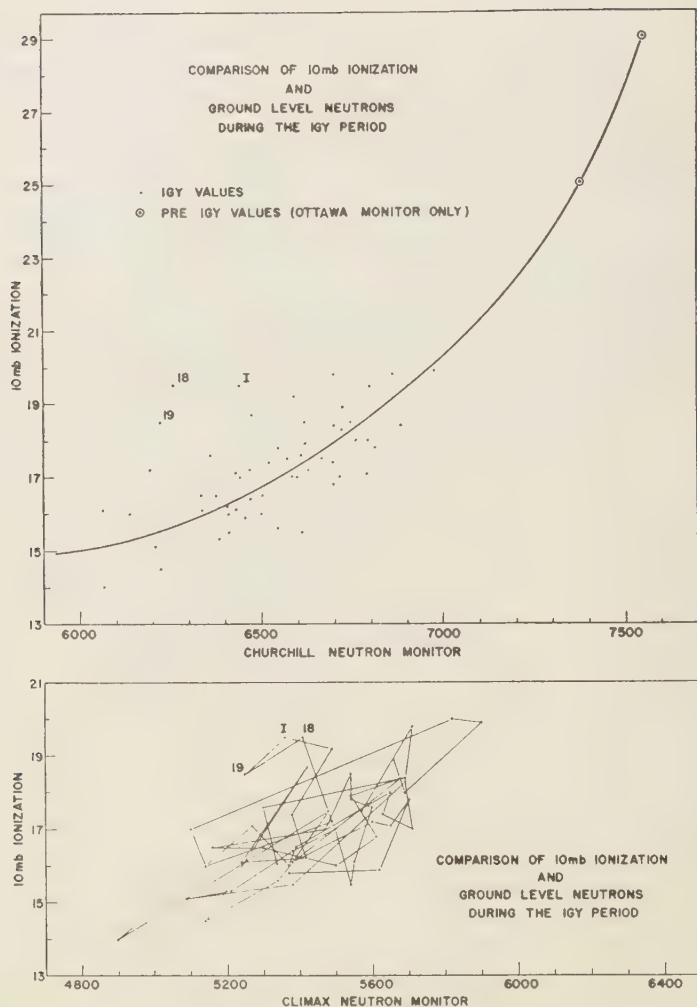


Fig. 7. Comparison of two parts of the primary energy spectrum using the 10-mb ionization and the sea-level neutron data.

is highly variable. The absolute intensity fluctuates a great deal in accordance with the maxima and minima in the over-all cosmic-ray intensity, and the latitude effect varies strikingly from one flight to another. For example, flights 19, 27, and 28 show very steep latitude effects attributable to the presence of some low-energy solar particles, which, having a very steep spectrum, produce such a latitude effect. This is in contrast, for example, with flight I over the same region,

which shows no latitude effect at all and was during a time when solar particles were absent and the intensity was fairly high for the sunspot maximum period. Several high points shown in Figure 8 at values of 25 and 29 on the normalized rate scale which date back to the fall of 1956 show some features of the large intensity decrease with the solar-cycle effect. The weight of the evidence is that, except for times when low-energy solar cosmic rays are present, the

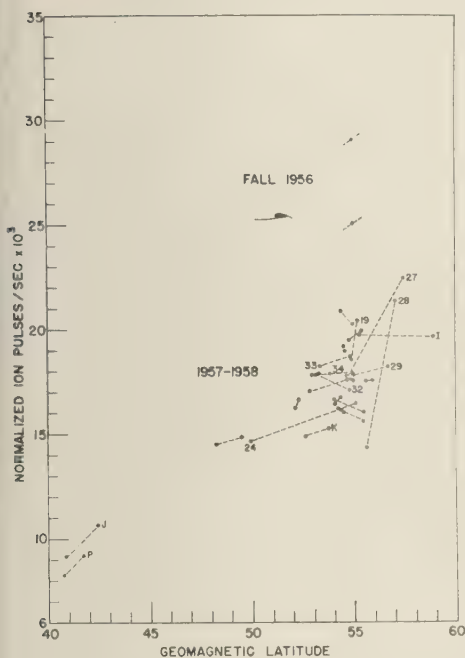


Fig. 8. Differential latitude effects from single balloon flights which remain at constant altitude. Two flights were made in the fall of 1956 as shown in the upper part of the figure. All the other flights were made in 1957 and 1958 following the large decrease at solar maximum. There is a general latitude-effect trend, but for the flights in the neighborhood of Minneapolis large differences are observed on different days. In particular, flights 27 and 28 seem to show the presence of very latitude-sensitive radiation. Flight I shows no latitude effect.

latitude effect is negligible at Minneapolis or at more northerly points during the period of the low intensity at solar maximum. Some flights show even a negative latitude effect, probably due to a specific time variation during the flight.

During the summer of 1958 Neher [1958] conducted a series of sounding flights at Bismarck, N. D., using integrating ionization chambers. The atmospheric ionization rate was given at the location of the ionization maximum (approximately 50 g/cm²). In Table 4 Neher's results are compared with flights made in this series on the same or adjacent days. The values have been read from our curves also at the ionization maximum, and are computed using equa-

tion 2. Table 4 thus represents an absolute comparison between the two investigations. In the last column, giving the ratios of the measurements, we note that the Minnesota values are on the average 16 per cent lower than Neher's. We do not believe that this discrepancy is caused by the geographical difference of Minneapolis and Bismarck, as cosmic-ray latitude effects were essentially zero over this range of latitudes in 1958. The packaging of the Minnesota ion chamber for night flights required several inches of Santo Cell powder and an exterior aluminum can. For very soft radiation a small effect might be produced, as the thickness was about 0.5 g/cm², but it does not seem possible to account for more than a few per cent by this means. In December 1959 we directly compared the standardization of the California Institute of Technology and the University of Minnesota laboratories by measuring the rate of the same ion chamber under the Co⁶⁰ calibration sources at the two locations. Again we found the same 16 per cent discrepancy. The two laboratories are rechecking all fundamental calibration procedures to determine the cause of the difference. The absolute work at Minnesota has been carried out by Hoffman [1960].

It is interesting to examine the flights for regular diurnal variation; the large number of flights which stay at high altitude during the night and day hours give an opportunity to set limits on such a variation. The result is very simple: none has been found under normal conditions, and the upper limit to the effect is of the order of about 2 per cent in the total ionization or counting rate of the Geiger counter. On at least one occasion, however, a strong diurnal effect was observed during a geomagnetic disturbance in the low-intensity period of a Forbush-type decrease. This diurnal wave is shown in Figure 12 in section 3. Diurnal variations of this type following the sudden intensity decreases have been known in the past. They are apparently connected with an anisotropy of outer space to the galactic cosmic rays, and in time, with proper analysis, it may be possible to examine the causes of the anisotropy in terms of solar magnetic fields. During the time of measurement of the low-energy solar cosmic rays, discussed in a later section, the geomagnetic storm variations on these particles at

TABLE 4. Comparison of California Institute of Technology and University of Minnesota Ionization Measurements at High Altitudes

Bismarck (Neher)			Minneapolis (Univ. Minn.)				Ratio, UM/CIT
Date	Time	I , ion pair/ $\text{cm}^2 \cdot \text{sec}$	Date	Time	Normalized Rate	I , ion pair/ $\text{cm}^2 \cdot \text{sec}$	
6/22	1323	251	6/21	0200	18.2	218	} 0.83
6/24	1301	256					
6/26	1431	260					
6/27	1310	259	6/27	1310	19.0	228	0.85
6/29	1313	256					
6/30	1402	252					
7/2	1828	248	7/2	1330	17.5	210	} 0.85
			7/10	0900	16.6	199	
			7/11	0250	16.6	199	
7/12	1522	241	7/13	0200	18.0	216	} 0.89
7/14	1527	243					
7/15	1531	246					
7/17	1536	247					
			7/18	0240	16.8*	202	} 0.805
7/19	1527	251					
7/20	1550	251	7/20	0145	17.0	204	
						Average	0.839

* Shows increase to 10 g/cm^2 .

Minneapolis are unfortunately so large that they mask any regular diurnal effect, and it has not been possible to determine whether solar particles vary as a function of local time.

3. *Solar cosmic rays.* Probably the single most significant finding of the entire series was the frequent occurrence of intense low-energy solar cosmic rays. They originated from large solar flares but had an energy spectrum so steep that the particles were not detected by the extensive network of sea-level cosmic-ray monitors established during the IGY. The particles were measured directly, however, by means of balloons at altitudes greater than 20 or 25 km; they showed very strong ionospheric effects over the polar-cap regions. The recognition of the relationship between the high-latitude ionospheric blackouts and these influxes of solar cosmic rays has been extremely useful in predicting the time at which balloon soundings could be made to study these events in detail.

Before the solar cosmic-ray events described here, five other solar increases observed at sea level were known; they occurred on February

28 and March 7, 1942, July 25, 1946, November 19, 1949, and the largest increase of all, on February 23, 1956. This last event received world-wide study from numerous sea-level observatories, and some high-altitude experiments were carried out. It has generally been thought that such cosmic-ray flares are infrequent, as shown by the above-mentioned dates, namely, about once every 3 years on the average. The development of high-altitude ballooning techniques and riometer-type integrated absorption measurement over the polar regions has brought to light many additional cases, smaller in intensity and with a maximum energy less than that of the sea-level events. The speculations based on the first five events, to the effect that the cosmic-ray outbursts were either very large or not present at all, have not been confirmed, and as more sensitive measurements are made it is found that many flares generate solar cosmic rays over a wide range of intensity.

One of the remarkable features of the great cosmic-ray increase of February 23, 1956, was the observation that ionospheric absorption was

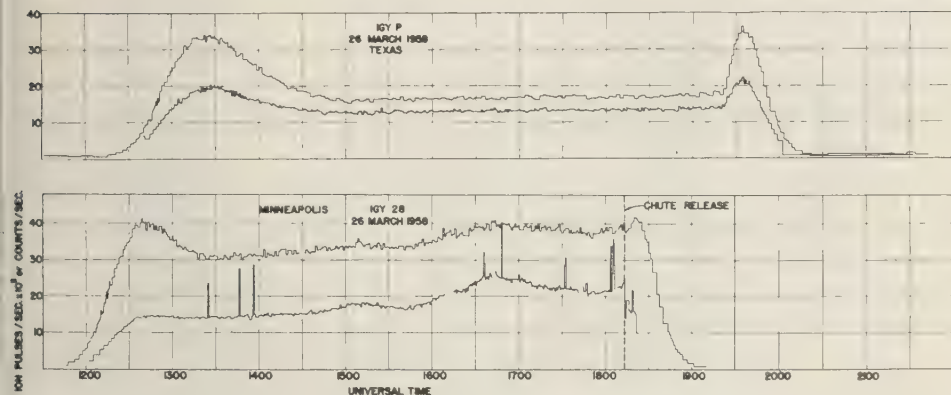


Fig. 9. Ionization and counter measurements at two latitudes, showing the increase due to low-energy solar cosmic rays measured at Minneapolis on March 26, 1958 (see also Fig. 2). The Texas flight, upper, shows a normal undisturbed behavior and the Pfozter maximum on ascent, and on parachute descent both show clearly. The Minneapolis flight shows the Pfozter maxima on ascent and then, at constant level, a continual increase in the ionization and counting rate until the time of parachute release at about 1830 UT. The relative ionization is consistent with the low-energy protons.

generated on the dark side of the earth which could only be caused by the cosmic-ray particles entering the *D* layer of the ionosphere. An excellent analysis of the manner in which the cosmic-ray-particle spectrum is related to the electron density of the ionosphere has been carried out by *Bailey* [1959].

The first direct evidence for the solar cosmic rays with IGY balloon programs was an event occurring on March 26, 1958. A preliminary analysis of this event has been published [*Freier, Ney, and Winckler*, 1959]. The event occurred during a coordinated series of balloon flights between Minneapolis, Texas, and Cuba. A simultaneous pair of flights was made at Texas and Minneapolis, which by chance occurred about a day after the start of a very large Forbush-type intensity decrease. When the Minneapolis instruments were analyzed, it was found that the ionization and counting rate, which at the beginning of the flight was at a low level corresponding to that of the low intensity during the Forbush decrease, increased during the 5-hour period of the flight in a fairly smooth manner to a value about twice the normal cosmic-ray-ionization and counting-rate background. An analysis of the simultaneous flight at Texas showed no detectable effects.

The ionization and counting rates during

these two flights are shown in Figure 9. The readings of the ionization chamber and counter on the March 26 flight were at first interpreted as a possible X-ray event. The peculiar behavior of this event compared with other X-ray events, however, cast some uncertainty on the assumption that the increase was due to X rays. When the nuclear emulsions recovered from this flight were examined several months later, it was immediately apparent that a large increase had occurred in the low-energy proton flux present at high altitudes. This event was discussed informally with other investigators, and other geophysical measurements pertinent to the event were accumulated, including: (1) the magnetic records of a magnetic storm in progress at the time of the balloon flight; (2) the great intensity decreases of sea-level cosmic rays, shown by sea-level cosmic-ray neutron monitors; (3) the presence over the polar cap of very strong *D*-layer ionospheric absorption—the absorption has been measured by *Leinbach and Reid* [1959] using the riometer technique at Fairbanks, Alaska; (4) the probable source of the event in a large flare occurring March 23, 1958, beginning at 0950 UT.

The association with this flare was suggested by J. S. Denisse of Meudon Observatory. The flare was observed and studied by the Belgian

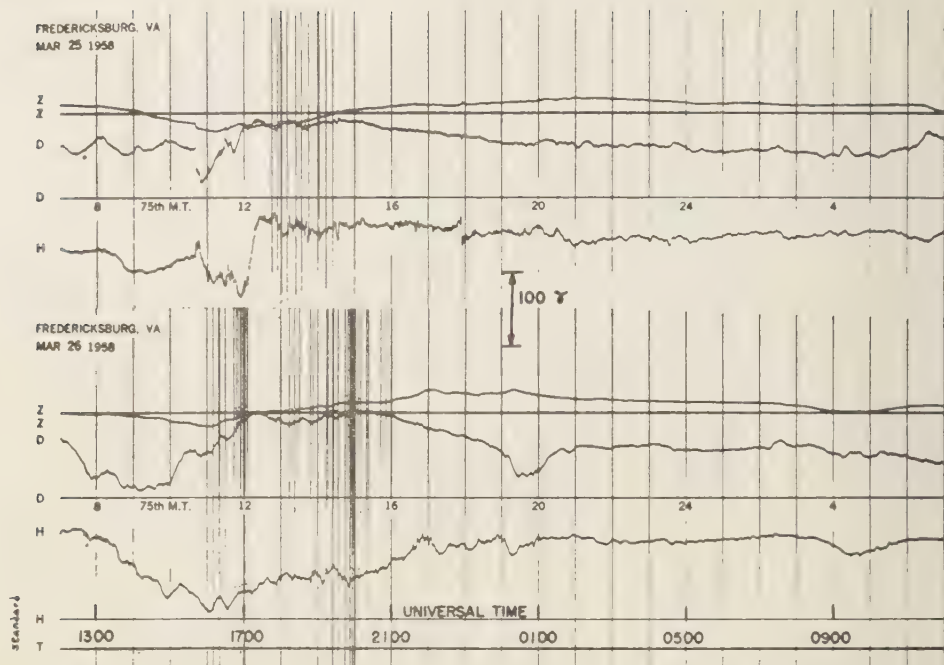


Fig. 10 Fredericksburg magnetic record during the magnetic storm of March 25-26, 1958, when low-energy solar cosmic rays were observed at Minneapolis. The sudden commencement is at about 1540 UT on March 25. The cosmic rays at Minneapolis were observed during the balloon flight which was in the air on March 26, and the increases coincided with the bay disturbance in H , beginning at 1300 UT and lasting until 2100 on March 26.

Royal Observatory [Koeckelenbergh, 1958]. A search was made for solar-activity time coincident with the balloon event, but none could be found; therefore it seemed necessary to attribute it to an event occurring earlier, and with the presence of delayed emission or storage of the observed particles. In Figure 10 is shown the magnetic record obtained from Fredericksburg Observatory. The sudden commencement at 1540 UT on March 25 is quite evident, followed by a disturbed condition, and on March 26 a considerable negative phase developed in the storm at the time at which the protons were seen on the Minneapolis balloon flight. Figure 11, reproduced from our first publication on this event, shows the temporal sequence of events associated with the cosmic-ray increase. The sudden increase in polar-cap cosmic noise absorption is seen to occur, not at the time of the flare, but at the time of the magnetic sudden commencement. This is a very unusual occur-

rence for these events, as further detailed analysis will show, and may be taken to indicate that the protons arrived trapped in a beam from the flare which was in transit from the sun for about 2 days. The Forbush-intensity decrease comes with the usual association with the magnetic sudden commencement and occurs within a few hours of it.

The ionization points in Figure 11 on March 21 and 26 and on April 8 were obtained from the soundings shown in Figure 2 above. The energy spectrum of the protons observed in this event is obtained from the emulsion analysis, which is discussed in a previous publication [Freier, Ney, and Winckler, 1959]. The protons were observed down to an energy of 120 Mev, which is the air and apparatus cutoff for the balloon flight at Minneapolis. One of the important features of the event is that the energy seems to be much lower than any assumed geomagnetic cutoffs for this latitude. We shall

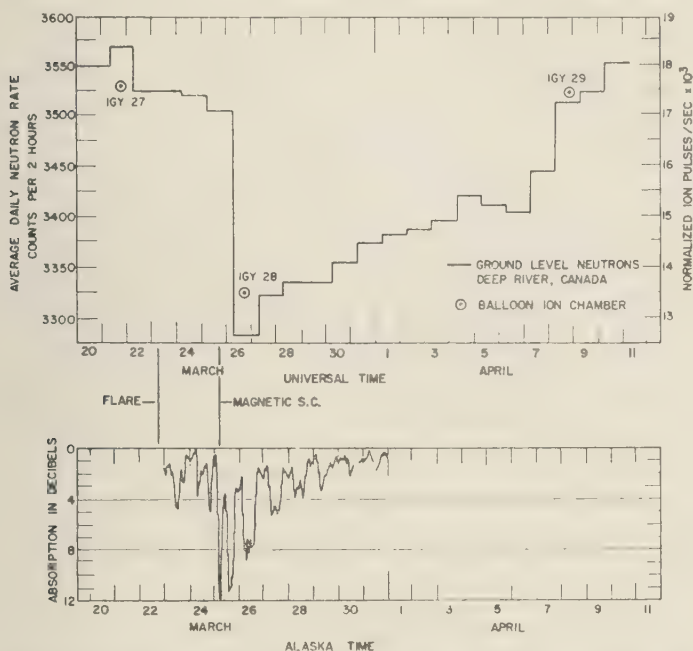


Fig. 11. Temporal sequence of events during the solar cosmic-ray event of March 25-26, 1958. Upper curve, ground-level neutrons compared with the balloon ionization-chamber readings for galactic cosmic radiation on this occasion, showing the large Forbush-type decrease. Lower curve, absorption in decibels of the riometer at Fairbanks, Alaska (courtesy of Leinbach and Reid). The lower curve represents a complete time history of the solar cosmic rays over the polar cap and shows that they began at the time of the sudden commencement on March 25 and lasted for 5 or 6 days afterwards.

see that this is a characteristic of these events, that the presence of the protons at Minneapolis is associated with the geomagnetic storm, which in some way alters the cutoffs and allows the solar particles to enter into otherwise forbidden ranges of latitude. The complete lack of an effect on the Texas flight is consistent with the strong connection between these particles and the presence of the aurora. The latitude of Texas is definitely below the latitude of most auroras. The lack of an effect at Texas also permits the deduction that less than 10 per cent of the effect at Minneapolis could have been due to direct solar photons (γ rays).

If the observed increase is assumed to be due to protons, it is possible to deduce their flux and mean energy from the ionization chamber and counter readings. If we assume isotropic incidence above the atmosphere, and monoenergetic protons of range R_0 , g/cm², the solid angle in

which particles may be received by the ion chamber and counter at depth h is a cone of semiapex angle θ_0 , such that $R_0 = h \sec \theta_0$. The mean ionization compared with minimum ionization measured by the instruments is then

$$\frac{\bar{I}}{I_{\min}} = \frac{1}{1 - \cos \theta_0} \int_0^{\theta_0} \frac{I}{I_{\min}}(\theta) \sin \theta d\theta \quad (5)$$

$I/I_{\min}(\theta)$ is determined from range-ionization curves for protons for each value of θ and R , using the fact that the residual range $R = R_0 - h \sec \theta$. Numerical integration of the above equation for various values of R_0 shows that the observed \bar{I}/I_{\min} of three times minimum corresponds to protons of $R_0 = 33$ g/cm² range, 220 Mev energy, and 0.69 bv rigidity. The peak flux at 1810 UT is then 0.11/cm²·sec·ster, and the average flux during the flight period is 0.058/cm²·sec·ster.

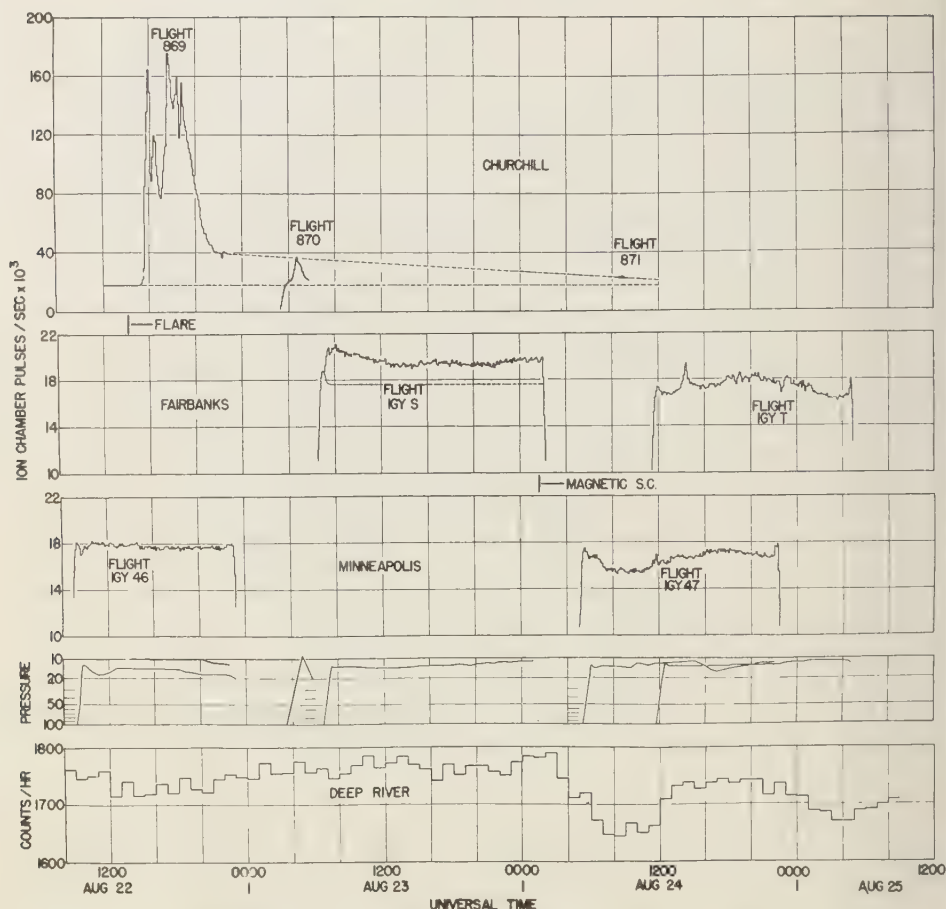


Fig. 12. Balloon observations and correlated data during the cosmic-ray event of August 22, 1958. Top line, observations at Churchill; next lower, observations at Fairbanks; center, observations at Minneapolis; next lower, balloon pressure curve; and bottom, Deep River sea-level neutron monitor.

As was pointed out in our previous paper [Freier, Ney, and Winckler, 1959], these values are in good agreement with those obtained from the emulsion data on this flight. The understanding of the March 26 event was greatly aided by a direct observation by Anderson of similar solar-flare protons during a balloon flight at Churchill on August 22, 1958. In this event a considerably larger increase was observed, which was directly associated with a very large solar flare. A preliminary report has been made by Anderson [1958]. Simultaneous flights during the event were being conducted by the Minne-

sota group at Fairbanks, Alaska, and also at Minneapolis, and a complete correlation of all these experiments on this occasion has been published [Anderson, Arnoldy, Hoffman, Peterson, and Winckler, 1959]. We reproduce here from this paper the figure showing the balloon observations at various times and various latitudes (Fig. 12). The direct flare increase observed at Churchill is not accompanied by any observable effects at Minneapolis. This is consistent with the known energy spectrum for the flare particles and reasonable knowledge of the geomagnetic cutoffs at Minneapolis. It should

noted that the geomagnetic storm associated with this event occurred on August 24. At the time of the flare on August 22 there was no strong geomagnetic disturbance in progress. This event was also observed by Leinbach and Reid to produce *D*-layer ionospheric absorption. It is apparently of considerably lower inherent intensity than the event in March, although the balloon records, being at a more favorable time and latitude, show a larger effect. Also, the solar particles come with a delay from the flare consistent with their direct time of flight, not the long time delay of 2 days seen on the March event. This may be due to the more favorable location of the August 22 flare nearer the center of the disk. The flare that accelerated the particles on August 22 produced a strong geomagnetic storm and aurora on August 24, accompanied by a Forbush-type decrease in the galactic cosmic rays, as did the event in March. These features are well shown in Figure 12 both by the balloon flights at high altitudes and by the sea-level neutron intensities. In contrast to the March event, even during the geomagnetic storm flare particles were not seen at Minneapolis, probably on account of the much lower intensity of the August 22 event and the more rapid decrease of the particles.

Anderson's Churchill balloon flights did not carry emulsions, but, because one of the flights, No. 870, rose through the atmosphere into the flare radiation at a time when the intensity was reasonably constant, it is possible to unfold the omnidirectional ionization indicated by the ion chamber to give the spectrum of protons. The differential proton energy spectrum so derived may be written

$$N(E) dE = K(t)E^{-5.0 \pm 0.2} dE$$

(Particles/cm²·sec·ster·Mev) (6)

This spectrum is very steep and in that respect resembles the spectrum obtained on the March 26 event over a small energy interval by nuclear emulsion analysis [Freier, Ney, and Winckler, 1959]. The integral energy spectrum is found to be

$$N(>E) = 5 \times 10^3 E^{-4} \quad (\text{Particles/cm}^2 \cdot \text{sec}) \quad (7)$$

The energy *E* is expressed in Mev. An analysis of the United States satellite Explorer IV by

Rothwell and McIlwain [1959] has definitely shown increases in rates associated with the August 22 event. The particles were observed at high latitude, and the intensity increased with increasing latitude. The fluxes observed in the satellite, considering the stopping power of the Geiger counters used, fall on the same spectrum as derived from the balloon measurements. This correlation is discussed in the complete paper by Anderson, Arnoldy, Hoffman, Peterson, and Winckler [1959]. The Explorer satellite also detected two other occurrences of solar cosmic rays, on August 16 and on 26, which had similar properties. Both these events were associated with large flares similar to the events detected by the high-altitude balloon measurements.

In a recent compilation Reid and Leinbach [1959] list 20 type III ionospheric absorption events which they believe are associated with flare-produced cosmic-ray protons. For comparison with the type III tabulation of Leinbach and Reid we have examined all the IGY balloon flights for events in which the ionization increases at high altitudes as the balloon rises on the last part of its ascent. This provides a critical test for the presence of the low-energy protons, because of their rapid absorption in the atmosphere. Ten flights in all were found in which high-altitude increases occurred; they are listed in Table 5. For illustration, typical ionization rate soundings are shown in Figure 13, for the events on September 1, 1957, and August 17, 1958. The normal curve without low-energy protons (see for example Fig. 2) goes through a mild maximum and drops slightly toward the highest altitude reached. The curves of Figure 13, however, show an increase of ionization which on the September 1 event begins at 15 mb and on the August 17, 1958, event begins as deep as 30 mb. If the high-altitude increase is statistically accurate, the spectrum of protons may be unfolded using the atmospheric depth dependence. This procedure has been carried out for the August 22 event for the Churchill and Fairbanks, Alaska, data, and is discussed in detail in that reference [Anderson, Arnoldy, Hoffman, Peterson, and Winckler, 1959].

On August 17, the magnetic sudden commencement occurred at 0622 UT associated with the great flare on August 16 which produced the solar cosmic rays on this occasion. On the

TABLE 5. IGY Flights that Show Increases on Arrival at High Altitudes

IGY Flight	Location	Date, UT	Time of Observation, UT	Approximate Increase, %	Pressure, g/cm ²	Observed Polar Region Type III
7	Minneapolis	8/10/57	0345	10	10	No
12	Minneapolis	9/1/57	0300	10	12	Yes
28	Minneapolis	3/26/58	1315	100	10	Yes
29	Minneapolis	4/8/58	1300	5	8	No
R	Minneapolis	7/2/58	1400	5	6	No
45	Minneapolis	8/17/58	0700	15	8	Yes
S	Fairbanks, Alaska	8/23/58	0715	15	12	Yes
48	Minneapolis	8/27/58	0610	5	10	Yes
U	Fairbanks, Alaska	8/27/58	0845	5	14	Yes
V	Fairbanks, Alaska	9/22/58	2125	15	8	Yes

August 17 flight the solar cosmic rays were seen at Minneapolis after the beginning of the geomagnetic disturbance. Of the ten events listed in Table 5, seven were also reported by Leinbach and Reid as showing polar region type III absorption. Furthermore, all those listed by Leinbach and Reid in which balloons were at high altitude showed an increase attributable to solar protons. Table 5 includes, of course, the several occurrences discussed in detail such as those of March 26 and August 22, 1958.

In all the occasions on which the solar proton effects were seen at Minneapolis, a geomagnetic

storm was in progress. In at least one, on August 22, the event referred to previously, the effect was seen at Minneapolis when large high-latitude effects were in progress, and here the geomagnetic storm was absent. Most of the increases reported in this series in Table 5 are small, the largest one, which is twice cosmic-ray intensity, being the March 26 occasion. However, recently, in May and again in July 1958 very large increases of solar protons have been observed with omnidirectional intensities at balloon heights reaching several hundred times the ionization produced by normal cosmic rays. On

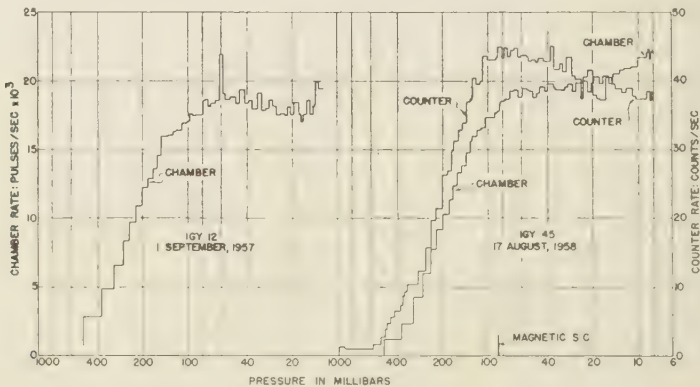


Fig. 13. Two events showing a detectable amount of low-energy radiation, presumably solar proton at high altitude at Minneapolis occurring during a time when ionospheric effects at high latitude showed the presence of the low-energy solar particles. These soundings are typical of a series of such weak events seen in balloons during the IGY period.

these events has been reported in the literature [Ney, Winckler, and Freier, 1959]. The phenomenally intense July 1959 series will be reported later. In many respects they have characteristics similar to the events discussed here and are evidently of the same variety but with enormously higher intensity.

During the IGY and IGC periods, Vernov, Charakhchian, and collaborators have made a large number of sounding flights using meteorological balloons and single Geiger counters or Geiger counter coincidence trains from three latitudes in the Soviet Union, 64° geomagnetic, 55° , and 41° . Extensive measurements were made on many of the solar cosmic-ray events that are on record. The Russian workers in particular have studied in detail the great events in May and July 1959 which were referred to earlier [Charakhchian, Tulinov, and Charakhchian, 1960; Rymko, Tulinov, and Charakhchian, 1959; Vernov, Tulinov, and Charakhchian, 1958]. The comparison of the Minnesota results and the results of Charakhchian and collaborators will yield much additional information about these events, but a discussion of the 1959 events will be reserved for later communications.

The balloon observation by Rymko, Tulinov, and Charakhchian [1959] on July 8, 1958, of a high-latitude increase in the cosmic rays corresponds to a polar-cap absorption event reported by Reid and Leinbach [1959]. The July 1958 event was of moderate intensity but exhibits in the balloons the very steep spectrum and sharp latitude dependence shown by the other events. The July event was observed by Rymko, Tulinov, and Charakhchian at latitude 4° but not at latitude 51° or 41° . These workers find that the incidence of the solar protons coincides with a large Forbush-type decrease in the geomagnetic cosmic radiation which appears at all the stations. They find that the directly measured cosmic rays at balloon altitudes are delayed from the time of the associated chromospheric solar flare by several hours but not as long as the geomagnetic storm delay. Evidently the time of passage of the cosmic rays from the sun is considerably longer than the straight transit time and must, therefore, involve a partial trapping even in the early stages of the event.

Continued study of these events shows clearly, however, that, in the overwhelming majority, one cannot consider that the solar-accelerated cosmic rays are contained with any degree of efficiency by the low-energy plasma from the flare. If they were, large changes in the solar cosmic rays would be observed at the highest latitudes over the polar cap of the earth at the time of the sudden commencement of magnetic storms. With one exception, such changes are not observed. On the other hand, as mentioned above, the particles do not come in a straight line from the source on the sun but travel over a tortuous path as if scattered by many minor irregularities in space between the sun and the earth. Further discussion of this question as well as the very interesting problem of the decay of the particles after the acceleration will be reserved for later publications.

4. *Analysis of auroral X rays.* The initial discovery of the X rays at balloon levels directly coincident with visible auroras occurred on July 1, 1957, during the strong storm at the beginning of the IGY. Several further observations of these auroral X rays were made during 1957 and 1958, some of which have been reported in detail in the literature [Winckler, Peterson, Arnoldy, and Hoffman, 1958; Winckler, Peterson, Hoffman, and Arnoldy, 1959]. The identification of the increased rates of the cosmic-ray detectors as X rays has been made on a number of occasions in which special counting devices were flown during auroras. These devices, including shielded Geiger counters, arranged to be sensitive only to photons, and scintillation counters, have a much higher relative efficiency for X rays than an ordinary Geiger counter and, as expected, showed a very much larger intensity during the auroral storms than the single Geiger counter or ionization chamber which was normally flown on the balloon flights.

We should like now to summarize all the occurrences of auroral X rays observed during the IGY and to discuss several of them in detail. Figure 14 summarizes the X-ray bursts observed in all events recorded during 1957 and 1958. The bursts are plotted with the cosmic-ray background subtracted and the ionization rates normalized to a common scale. Only the ionization-chamber data are shown in Figure

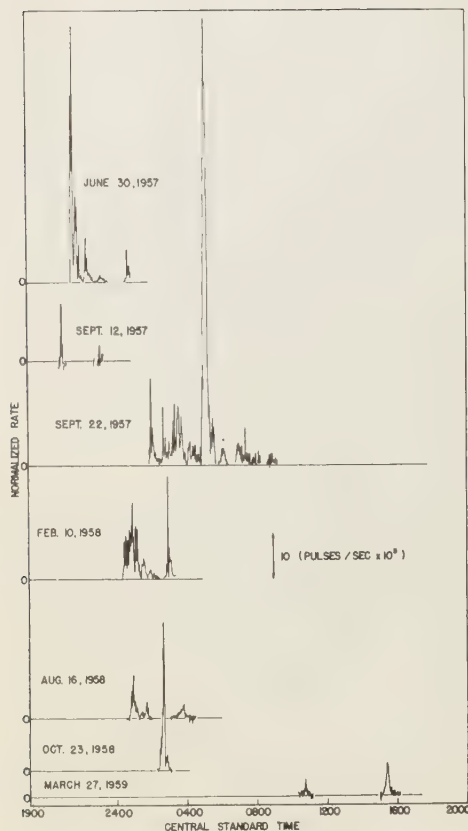


Figure 14. Summary of auroral X-ray bursts observed with ionization chambers during the IGY period. The bursts are plotted as a function of local time in the central standard time zone at Minneapolis. The ion-chamber rate is on the same normalized scale adopted throughout this paper with the cosmic-ray background subtracted. With the instrumental data given in Table 2, above, the absolute X-ray intensities can be computed. Cosmic-ray rates with the same chamber are between 15 and 20 pulses/sec 10^3 . Only the September 12 event represents the Geiger counter curve, as the ion chamber was not available on this flight.

14 (with one exception; see the figure legend). These data give some insight into the time distribution of energetic auroras measured at Minneapolis. It is seen that most X-ray bursts are observed during the night but that they can be observed during daylight. The sample is somewhat biased, as balloons are normally launched about sunset, so that activity starting before

that time would have been missed. All the storms are classified as very strong, with large magnetic fluctuations. It can be seen that the auroral X-ray burst vary enormously in size which is probably an indication in some way of the intensity of the solar bombardment. Although the characteristic of the time constant of the bursts is similar from one burst to another, being about half an hour, the bursts show considerable fine structure with variations down into the 1-minute range. The most intense X-ray burst observed occurred just before dawn CST on September 23, 1957.

The following general observations are of use in understanding the nature of the X-ray bursts.

1. When the skies are clear and visual observations can be made at the time of the balloon X-ray bursts, it is found that the bursts correspond to intensification of auroral luminosity close to the zenith at Minneapolis. This observation in effect associates the electrons producing the X rays with the visual forms of the aurora. This follows because the absorption coefficient for the observed X-ray energies of 50–100 keV is approximately 0.2 cm²/g. For example, at the nominal balloon ceiling height of 10 g/cm² the ratio of the expected intensity from the vertical compared with a 60° zenith angle for a uniform source of X rays is 7. This implies that X rays in general will be seen only from electron currents incident close to the zenith considering the nominal auroral height of 100 km. X rays will be seen from electrons striking the atmosphere only within a radius of about 100 km from the balloon.

2. A careful comparison between the X-ray bursts and auroral all-sky camera photographs shows that the time of the burst is associated within times of the order of 1 minute with the passage across the zenith of regions of high luminosity. See for example the discussion Winckler, Peterson, Hoffman, and Arnold [1959], Figure 3, for the aurora of February 10, 1958. Also see paragraphs below for a discussion of the September 22–23, 1957, aurora. The apparent velocity of the luminous region across the sky is often found to be of the order of 0.5 to 1 km/sec from the all-sky camera records. This is consistent with the agreement within a minute or so between the appearance

the luminosity and the X-ray bursts considering the 100-km-radius criterion mentioned in paragraph 1 above for detecting the X rays.

3. The energy of the X rays that is accessible to measurement at balloon levels begins at about 10 keV and extends upward; however, by examining the ratio of the instruments [Winckler, Peterson, Arnoldy, and Hoffman, 1958], the energy of the X rays at balloon levels in many cases is estimated to range from 50 to 100 keV. The shape of the spectrum cannot be determined from the ion chamber and Geiger counter, but it is believed to be that of a bremsstrahlung spectrum of electrons striking air plus the energy-sensitive absorption of the atmosphere which attenuates strongly the very low-energy X rays. This in effect produces a maximum in the spectrum at about the energies mentioned above. From the observed sizes of the bursts in the ion chamber it is possible to estimate the electron flux, assuming that the flux is uniform over the restricted region near the zenith to which the instruments are sensitive. The relation between the electron flux incident on the atmosphere and the normalized ion-chamber rate shown in Figure 14 is discussed below.

4. The X-ray bursts studied at Minneapolis are associated with subauroral zone auroras. None of the observations therefore, are associated with the phenomenon called a 'quiet arc,' as such phenomena are rarely seen at the zenith at Minneapolis. Rather, the X rays are associated with rayed forms such as rayed arcs, rayed bands, and corona which represent a phase of the auroral storm accompanying the motion of the luminosity either in latitude or in longitude.

5. There is known to be a close association between the presence of magnetic bays at a given latitude and the advance or retreat of the aurora across that latitude [Gartlein, Bless, Kimball, and Sprague, 1959]. It is therefore understandable that the presence of the auroral X rays is associated with the presence of bays in the magnetic records. We have already pointed out such an association for the February 10 aurora [Winckler, Peterson, Hoffman, and Arnoldy, 1959]. Other such cases are known [Akasofu, 1959].

6. The power available in the electrons inferred from the X rays is very large, comparable with that required to produce the visual lumi-

nosity of an aurora. It is therefore probable that the electrons are a major contributor to the excitation of the auroral spectrum as observed.

7. The observation of electrons at 100-keV energy as a direct part of the visual aurora raises an interesting question about the origin of these electrons. It is known that strong auroral storms are frequently associated with violent solar flares occurring about a day earlier; in fact, such was the case in the storms summarized in this paper. The 100-keV electrons cannot have come directly from the flare with a speed characteristic of their velocity, which is about 0.9 the speed of light. Therefore, either (a) the electrons were trapped in the plasma cloud and traveled around in this cloud during its transit from the sun, perhaps because of magnetic fields or electrostatic forces; or (b) the electrons are discharged from the Van Allen regions around the earth, in which event they would constitute part of the semipermanent flux of such electrons observed in the outer Van Allen region [Van Allen, 1959]; or (c) electrons are locally accelerated in the earth's magnetic field at the time of incidence of the solar cloud and are discharged down the lines of force as part of the auroral phenomenon.

In a recent publication [Winckler, Peterson, Hoffman, and Arnoldy, 1959], we have considered the detailed correlation between the X-ray bursts, the magnetic records, the auroral all-sky camera photographs, and other types of information for the great storm of February 10-11, 1958.

We will now consider another event in a similar way, namely, the very strong aurora of September 22-23, 1957. This was a time of extremely high solar activity, probably representing the peak in the sunspot numbers for the present solar cycle. The number of flares of all sizes recorded each day was so great that it is very difficult to correlate the storm with a specific flare. However, the magnetic records from Fredericksburg Observatory show that a typical strong storm with sudden commencement occurred coincidentally with the observed aurora (see Fig. 15).

The sudden commencement occurred on September 23 at approximately 0235 UT. There was a very sharp positive excursion followed by



Fig. 15. Fredericksburg Observatory record for the strong magnetic storm of September 23, 1957. The sudden commencement occurred at approximately 0240 UT on September 23. After a very short positive phase, the storm exhibited large bay disturbances. Disturbances on this and other magnetograms show correlation with the balloon X rays for this event.

a negative region at the beginning of the storm. After a disturbed period, a large disturbance which developed into a negative bay began at 0438 UT on September 23. The bay disturbance ended by 0630 UT on September 23, and then, after a long disturbed period, the main phase of the storm ended by 2400 UT on September 23.

The balloon flight IGY-18, the record of which is shown in Figure 16, was launched about 0600 UT on September 23. It was observed that

great auroral activity had been present for several hours before launch, and this is undoubtedly associated with the large disturbance shown on the Fredericksburg magnetogram. The balloon reached high altitude at about 0745 UT, and as can be seen in Figure 16, X-ray bursts of considerable magnitude developed immediately. In the legend for the figure, the various auroral effects observed at Minneapolis close to the balloon are described. The most prominent feature, however, is an extremely large burst

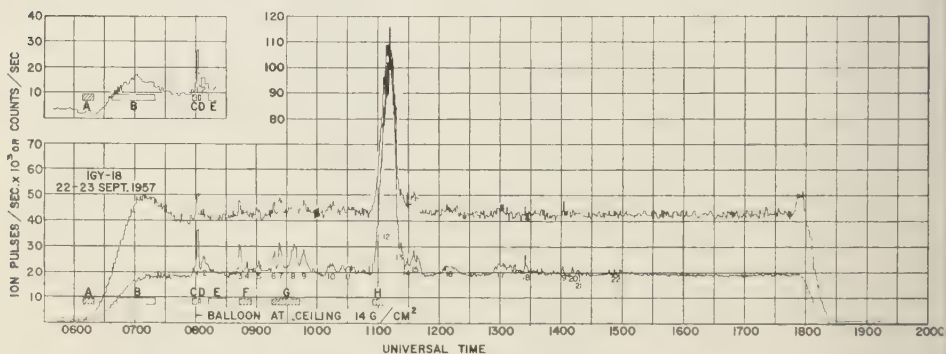


Fig. 16. Ion chamber (bottom), single counter (top), and photon counter (upper left, separate curve) response during the intense auroral storm of September 22-23, 1957. The balloon was launched about midnight CST during a lull in auroral activity, which had been very high in the earlier evening. The letters refer to observed auroral phenomena as follows: A, flaming auroral rays reaching zenith from all points of compass; red color. B, curtains in north but activity generally decreasing overhead. B-C (0735 UT), arcs in narrow bands extending across zenith and almost to horizon in east and west directions; north dark; no rays. C, extremely strong ray buildup from all directions; intense red patches at 30° elevation in west. D, red patches intense again after decrease. E, flaming rays; no red; activity decreased. F, strong rays in northwest; red color; strong flaming in west; general activity increasing. G, major ray buildup in west, north, and east, with corona; red color reappeared at 0945 UT; following G, general intensity decreased with flaming rays. H, very strong ray structure at 30° elevation in east with intense red color; visible against predawn sky light.

X rays which began at about 1050 UT and which the response to X rays was about 5 times above the cosmic-ray background. This excursion constitutes the largest increase observed in our series of balloon flights during the IGY. It lasted for approximately 30 minutes. In the Fredericksburg magnetogram, there is no definite correlating feature, which probably implies that the auroral phenomenon did not progress as far south as Fredericksburg at that time. Other stations in the auroral zone and below show a large bay disturbance at this time [Akasofu, 1959].

The large burst occurred just before dawn, local time, so that it is difficult to find all-sky camera records that show the aurora. However, a good record was found from a station at Choteau, Montana, which is on exactly the same geomagnetic latitude as Minneapolis. A series

from the Choteau station close to the time of the beginning of the burst is shown in Figure 17. A remarkably intense phenomenon makes its appearance at that time and is evidently one loop of a very large rayed arc which is sliding in longitude from west to east and moving almost directly across the station at Choteau. It passes the zenith at 1048 UT. In Figure 18 is shown an enlarged view of the frame in which the rayed arc is over head. The rayed arc is accompanied by other arcs to the south and by considerable ray structure which extends far around to the north, almost closing the loop. From the sequence of photographs in Figure 17, it is possible to measure the velocity across the station if the height is assumed. Using the known geometry of the all-sky camera [Elvey, 1957], the result of the measurement is shown in Figure 19, assuming both 100- and 120-km heights.

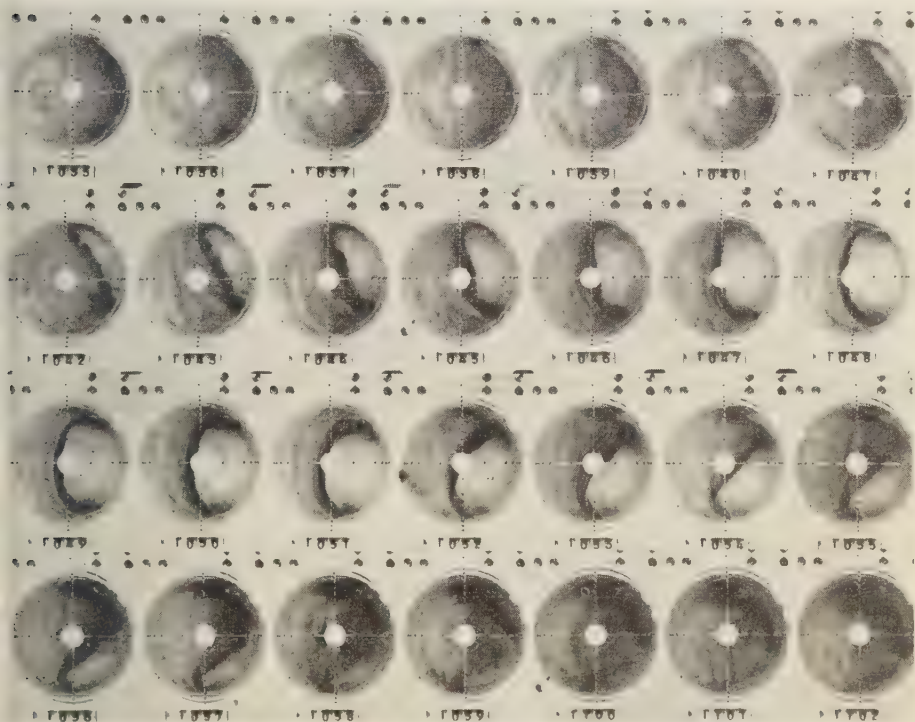


Fig. 17. Auroral all-sky camera records from Choteau, Montana, on September 23, 1957. The intense rayed band which moves across the station in these pictures is associated in time with the great X-ray burst observed at Minneapolis and is undoubtedly a part of the same auroral feature, which existed over a considerable range of longitudes at this time.

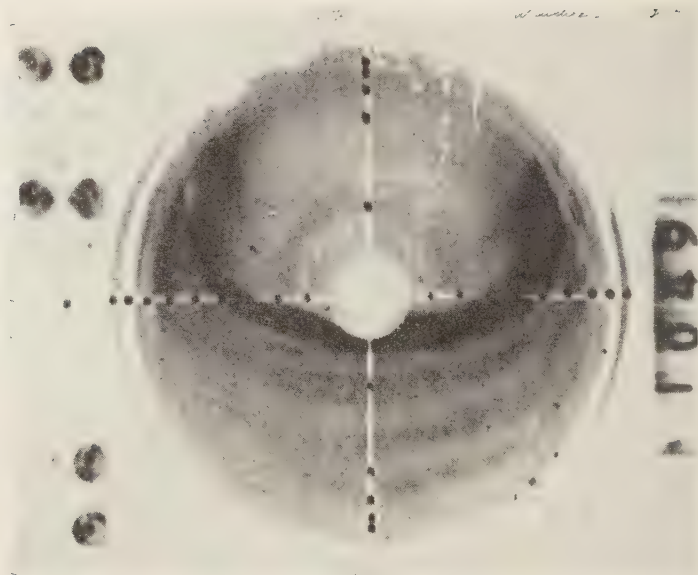


Fig. 18. Detail of the intense rayed band as observed over Choteau, Montana. The very intense band is accompanied by a succession of other, less intense arcs and by considerable ray structure which extends far around to the north.

The velocity obtained from this measurement is 0.5 km/sec. It seems certain that the intense X-ray burst observed at 1050 UT on the balloon near Minneapolis is associated with the auroral phenomenon shown in the Choteau records. The great intensity of the X-ray burst is consistent with the great luminous intensity of the concentrated rayed arc seen in Figure 18.

Under certain assumptions it becomes possible to compute the current of primary auroral electrons producing the X rays observed at balloon heights. We present here a brief outline along the lines of a previous discussion. The primary electron current is given by the expression

$$J = \frac{(dE/dx)_{\text{collision}}}{(dE/dx)_{\text{radiation}}} \times \frac{CI}{\text{energy/electron}} \times e \quad (8)$$

where I is the observed X-ray energy flux, e is the electronic charge, and the constant C depends on the geometry. For a uniform bombardment over the sky $C = 2$, as half the X-ray energy is propagated upward. For an auroral

arc the situation might be approximated by a line source of X rays extending a large distance in longitude and located at approximately 100-km altitude. The electron current would be a sheet aligned along the magnetic field, extending downward to the 100-km level, where the electrons stop. In this case $C = 2\pi h/w$, where $h = (100 \text{ km} - \text{balloon height}) = 70 \text{ km}$ approximately, and W is the thickness or width of the electron stream in the north-south direction. For the ratio of collision loss to radiation loss we may use the relation given, for example, by Fermi [1950]:

$$(dE/dx)_{\text{collision}}/(dE/dx)_{\text{radiation}} = 800/ZE \quad (9)$$

where Z is the atomic number of stopping material and E is the electron energy in Mev. The observed X-ray energy flux is computed from the ion-chamber rate according to the expression

$$I = \frac{R_n \cdot Q_n \cdot W}{e \cdot \mu \cdot M} \cdot K \quad \text{ev/cm}^2/\text{sec} \quad (10)$$

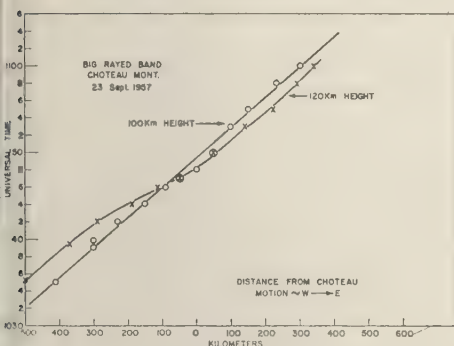


Fig. 19. Result of position measurements in the west-east direction over Choteau, Montana, of the center of the very intense rayed arc on September 23, 1957. The measurements are scaled from the all-sky camera records, and positions are given for two different heights of the auroral feature.

where R_n is the normalized ion-chamber rate in pulses per second, Q_n the normalized charge per pulse of the chamber, W the energy in electron volts required to form an ion pair in argon gas, e the electronic charge, μ the absorption constant in cm^2/g for X rays of the measured energy in argon, M the argon mass in grams, and K a correction for the energy in the form of X rays produced in the high atmosphere but not reaching the balloon level. This correction may be computed assuming a bremsstrahlung spectrum of X rays from the electrons coming to rest by ionization loss. As discussed previously, K has a value of approximately 10 [Winckler, Peterson, Hoffman, and Arnoldy, 1959].

Assuming $E = 100$ kev, and using known values for μ , Q_n , and M , we obtain the expressions

$$J = C \times R_n \times 3.0 \times 10^{-11} \text{ amp/cm}^2 \quad (11)$$

$$J = C \times R_n \times 1.9 \times 10^8 \text{ electrons/cm}^2/\text{sec}$$

For uniform bombardment over the top of the atmosphere where $C = 2$ we obtain

$$J = R_n 6.0 \times 10^{-11} \text{ amp/cm}^2 \quad (12)$$

$$J = R_n 3.8 \times 10^8 \text{ electrons/cm}^2/\text{sec}$$

For arc forms where $C = 2\pi h/w$ we obtain for 100-km aurora of thickness W cm in latitude

$$J = R_n (1.3 \times 10^{-6})/W \text{ amp/cm}^2/\text{cm} \quad (13)$$

$$J = R_n (8.3 \times 10^{15})/W \text{ electrons/cm}^2/\text{cm}$$

The large increase at 1050 UT on September 23 produced a peak normalized ion-chamber rate of $R_n = 0.1/\text{sec}$. From Figure 18 we estimate the thickness of the rayed arc to be not more than 10 km. The resulting electron flux is $J = 8 \times 10^9/\text{cm}^2 \cdot \text{sec}$. This appears to be a value comparable with fluxes reported in the outer trapped radiation zone of the earth [Van Allen, 1959], where typical values are 10^{10} – $10^{11}/\text{cm}^2 \cdot \text{sec}$. The aurora of September 13, 1957 (Fig. 14), was observed at great depth with an insensitive instrument. The *inferred* flux at high altitude in that event exceeded the September 23 event by 50 times.

5. *Measurement of solar γ rays and radioactive layers in the atmosphere.* In this section we shall discuss briefly two observations of quite different phenomena that are unique in that they were observed with the ion chambers and counters only over a very short time interval but became significant when correlated with other geophysical effects.

The first such event was a transitory increase—for an interval of only 18 seconds—in the counting rate of the ion chamber and Geiger counter observed on flight IGY-M on March 20, 1958, flown over the island of Cuba. The increases were significant above the low and rather steady background of the cosmic radiation at the latitude of Cuba. They were found to coincide precisely with a very intense radio burst observed on 3 cm and on 21 cm by the radio astronomy group at Meudon. They also coincided with the maximum phase of a class II flare. The event has been analyzed in its entirety [Peterson and Winckler, 1959] as being due to a burst of high-energy X rays or γ rays coming from the sun and probably generated there by electrons accelerated in the flare and producing bremsstrahlung in the photosphere of the sun. It was concluded that 9.4×10^{10} electrons producing the bremsstrahlung on the sun were re-

quired to account for the observed burst. If the number of electrons required to produce synchrotron radiation is estimated, assuming that the radio observation is due to this source, the number of electrons of similar energy is 2.5×10^{30} . The discrepancy of 10^8 is not difficult to explain in terms of the opacity of the solar photosphere to the electromagnetic radiation. The event is self-consistent with the above interpretation but has one very puzzling feature, namely that the source of the radio waves observed by Denisse at Meudon [Denisse, 1959] was observed to be very large. The size was such that the effects would have had to spread across the solar disk with the velocity of light and produce the electromagnetic radiation in the radio-frequency spectrum from the whole region simultaneously. This region is about one-third the size of the solar disk. It appears that this observation of γ rays from outside the earth is the only one so far recorded of such a phenomenon. No other observation of solar γ rays has been made during the IGY period, although a number of balloon flights were at high altitude during strong solar flares. Increases associated with flares have been shown to be due to particle effects or have been otherwise accounted for.

The second observation occurred on balloon flight IGY-27 on March 21, 1958; it stems from an increase in both the ion chamber and the counter observed while the balloon was rising through the lower atmosphere at a pressure of about 350 mb (see Fig. 2 above for the instrumental soundings for this flight). The increases were almost certainly due to a strong radiation layer in the atmosphere. Another case tentatively assigned to a radioactive cloud layer was observed on flight IGY-54, on October 31, 1958. A detailed study has been made of these two events [Mantis and Winckler, 1960]. It was concluded that on the March 21, 1958, event the increases in the instruments were due to γ rays of approximately 1-Mev energy and having a specific activity of 0.8×10^{-4} disintegration per second per cm^3 of air at 30,000 feet. The layer containing the activity was located in the jet stream, and the trajectory could be followed backward with a time delay of about 5 days to a probable source in Siberia. In analyzing the event, the decay of the fission fragments and the loss of intensity by diffusion were estimated.

It should be noted that the radioactive layer was not observed on the descent of either of the balloons, although the descent occurred only a few hundred miles from the launch point. No other event intense enough to be detected was observed in the 83 IGY balloon flights on this program. The direct detection of radioactive debris in situ in the atmosphere is unusual. The fact that it is possible to make such measurements suggests that with more sensitive techniques the direct sounding measurement of radioactivity might be a useful tool for studying the distribution of radioactive material and drawing inferences about the large-scale circulation of the atmosphere.

Acknowledgments. A large number of people in the School of Physics, University of Minnesota have contributed in a major way to the successful carrying out of this program. Besides those who have on occasion been joint authors of the paper analyzing detailed events, which are referred to above, credit should be given to the enthusiastic and loyal group of undergraduate physics and electrical engineering students who took part in the flight operations and contributed to the analysis of the data. Rudolph Thorness made major contributions in the design of the instrumentation. Robert Howard and Raymond Maas in the design of the electronic components, and William Hue in the design of the balloons and the technique in conducting the launchings. James Stoddart successfully recovered many of the loads by airplan chase. We are appreciative of the support of the National Science Foundation operating under the U. S. National Committee for the IGY for the grant which set this project in operation, and also of the loyal and understanding support of the Office of Naval Research.

REFERENCES

- Akasofu, S. I., Large scale auroral motions and polar magnetic disturbances, I, Preprint, Geophysical Institute, University of Alaska, Fairbanks, in press 1959.
- Anderson, K. A., Ionizing radiation associated with solar radio noise storm, *Phys. Rev. Letters*, **1**, 335-337, 1958.
- Anderson, K. A., R. Arnoldy, R. Hoffman, I. Peterson, and J. R. Winckler, Observations of low-energy solar cosmic rays from the flare of 22 August 1958, *J. Geophys. Research*, **64**, 113:1147, 1959.
- Bailey, D. K., Abnormal ionization in the lower ionosphere associated with cosmic-ray flux enhancements, *Proc. IRE*, **47**, 255-266, 1959.
- Charakhchian, A. N., V. F. Tulinov, and T. N. Charakhchian, Cosmic rays emitted by the sun, *J. Exptl. Theoret. Phys. USSR*, in press, 1960.

- also *Proc. 1st Intern. Conf. Space Sci.*, Nice, January 1960, in press 1960.
- enisse, J. F., Relation entre les émissions de rayons cosmiques solaires et certains sursauts radioélectriques, *Paris Symposium on Radio Astronomy*, Ed. Bracewell, pp. 237-239, Stanford University Press, 1959.
- lvey, C. T., Auroral photography by all-sky camera, *Ann. IGY*, 5, part II, Pergamon Press, London, 244 pp., 1957.
- erni, Enrico, *Nuclear Physics*, p. 47, University of Chicago Press, 246 pp., 1950.
- orbush, Scott E., Cosmic-ray intensity variations during two solar cycles, *J. Geophys. Research*, 63, 651-669, 1958.
- owler, P., P. S. Freier, and E. P. Ney, The primary alpha particle spectrum over North America and geomagnetic cutoff energies, *Nuovo cimento, Suppl. to vol. 8*, ser. X, 492-499, 1958.
- reier, P. S., E. P. Ney, and C. J. Waddington, Flux and energy spectrum of cosmic-ray α -particles during solar maximum, *Phys. Rev.*, 114, 365-373, 1959a.
- reier, P. S., E. P. Ney, and C. J. Waddington, Lithium, beryllium, and boron in the primary cosmic radiation, *Phys. Rev.*, 113, 921-927, 1959b.
- reier, P. S., E. P. Ney, and J. R. Winckler, Balloon observation of solar cosmic rays on March 26, 1958, *J. Geophys. Research*, 64, 685-688, 1959.
- artlein, C. W., R. C. Bless, D. S. Kimball, and G. Sprague, Auroras, magnetic bays, and protons, *J. Geophys. Research*, 64, 949-953, 1959.
- offman, Robert A., Standardization of ionization chambers, *Tech. Rept. CR-27, Cosmic Ray Group*, University of Minnesota, Minneapolis, 1960.
- oeckelenbergh, André, L'Éruption solaire remarquable du 23 mars 1958 à 09h 49m TU, *Comms. Observatoire roy. Belg.*, no. 144, 1958.
- einbach, H., and G. C. Reid, Ionization of the upper atmosphere by low-energy charged particles from a solar flare, *Phys. Rev. Letters*, 2, 61-63, 1959.
- ockwood, J. A., Variations in the cosmic-ray nucleonic intensity, *Phys. Rev.*, 112, 1750-1758, 1958.
- antis, H. T., Winds and wind structure at 100,000 feet from constant altitude balloon trajectories, *Tech. Rept. AP-15, Atmospheric Physics*, University of Minnesota, Minneapolis, 1959.
- antis, H. T., and J. R. Winckler, Balloon observation of radiation layers in the stratosphere associated with nuclear explosions, in preparation, 1960.
- Neher, H. V., Low energy cosmic-ray particles in 1954, *Phys. Rev.*, 103, 228-236, 1956.
- Neher, H. V., *Latitude survey of high altitude cosmic rays*, preprint, California Institute of Technology, Pasadena, 1958.
- Ney, E. P., and J. R. Winckler, High altitude cosmic-ray measurements during the IGY, *Geophys. Monograph* 2, pp 81-91, Am. Geophys. Union, Washington, D. C., 210 pp., 1958.
- Ney, E. P., J. R. Winckler, and P. S. Freier, Protons from the sun on May 12, 1959, *Phys. Rev. Letters*, 3, 183-185, 1959.
- Peterson, L. E., R. L. Howard, and J. R. Winckler, Balloon gear monitors cosmic radiation, *Electronics*, 31, 76-79, 1958.
- Peterson, L. E., and J. R. Winckler, Gamma-ray burst from a solar flare, *J. Geophys. Research*, 64, 697-708, 1959.
- Reid, G. C., and H. Leinbach, Low-energy cosmic ray events associated with solar flares, *J. Geophys. Research*, 64, 1801-1805, 1959.
- Rothwell, P., and C. McIlwain, Satellite observations of solar cosmic rays, *Preprint SUI-59-12*, State University of Iowa, Iowa City, 1959.
- Rymko, N. P., N. F. Tulinov, and A. N. Charakhchian, A case of a sharp increase in cosmic-ray intensity in the stratosphere, *J. Exptl. Theoret. Phys. USSR*, 36, 1687, 1959.
- Simpson, J. A., and P. Meyer, Changes in the low-energy particle cutoff and primary spectrum of cosmic rays, *Phys. Rev.*, 106, 568-571, 1957.
- Van Allen, J. A., The geomagnetically trapped corpuscular radiation, *J. Geophys. Research*, 64, 1683-1689, 1959.
- Vernov, S. N., V. F. Tulinov, and A. N. Charakhchian, The 27-day cosmic-ray period in the stratosphere, *Doklady Akad. Nauk SSSR*, 122, 788, 1958.
- Winckler, J. R., and K. A. Anderson, High altitude cosmic-ray latitude effect from 51° to 65°N geomagnetic latitude, *Phys. Rev.*, 108, 148-154, 1957.
- Winckler, J. R., and L. Peterson, A large cosmic-ray decrease accompanying the solar maximum of 1957, *Nature*, 181, 1317-1321, 1958.
- Winckler, J. R., L. Peterson, R. Arnoldy, and R. Hoffman, X rays from visible aurorae at Minneapolis, *Phys. Rev.*, 110, 1221-1231, 1958.
- Winckler, J. R., L. Peterson, R. Hoffman, and R. Arnoldy, Auroral X rays, cosmic rays, and related phenomena during the storm of February 10-11, 1958, *J. Geophys. Research*, 64, 597-610, 1959.

(Manuscript received February 15, 1960.)

Observations of the Van Allen Radiation Regions during August and September 1959, Part 1¹

R. L. ARNOLDY, R. A. HOFFMAN, AND J. R. WINCKLER

*School of Physics
University of Minnesota
Minneapolis, Minnesota*

Abstract. An integrating ionization chamber and a single Geiger counter were flown on United States satellite Explorer VI in an elliptical orbit extending to 48,000 km. In addition to the Van Allen inner zone and the great outer zone, a stable and distinct intermediate zone was detected throughout August and September 1959. The outer-zone intensity showed a large decrease following the sudden commencement of a geomagnetic storm. Later in the storm the outer zone increased to much in excess of its prestorm level. During stable periods the outer zone was fairly constant and less intense than it had been observed to be with Pioneer III or Pioneer IV or the first Soviet cosmic rocket. Cosmic-ray background counting rates were reached on most passes in August and September near apogee of the satellite. The radiation 'dumped' from the outer zone during the geomagnetic storm fits very well with the intensity and latitude distribution required to account for balloon observations of auroral X rays made during the IGY period. This paper is based on preliminary analysis of Explorer VI data.

Introduction and description of apparatus. The University of Minnesota provided a radiation-detection experiment for the payload of Explorer VI satellite, launched August 7, 1959, from Cape Canaveral, Florida. The program was under the auspices of the National Aeronautics and Space Administration, and the payload was engineered by the Space Technology Laboratories of Los Angeles. This paper is based on a preliminary analysis of data now available. Additional data may be available from magnetic tape playback during the period under discussion in this paper. The present paper is an extension of an earlier version presented at the first international space symposium at Nice, France, in January 1960 [Arnoldy, Hoffman, and Winckler, 1960].

Figure 1 shows the University of Minnesota package before the potting compound was inserted to fill the container. The instruments are an integrating ionization chamber and a Geiger counter. The ionization chamber operates on the pulsing electrometer principle, which has been extensively used by the balloon projects at the

University of Minnesota and was developed for cosmic-ray purposes by Neher and Millikan [Winckler, Peterson, Arnoldy, and Hoffman, 1958]. The specifications of the two instruments are given in Table 1.

The ionization chamber and counter are sensitive to all types of radiation, but in addition, the ratio of the counting rates of the two instruments gives a measure of the mean particle ionization and accordingly particle energies if the type of particle is known. For X rays, which are an important contribution to the radiation detected inside the satellite, the relative response of the two instruments is sensitive to the energy of the X rays encountered, and suitable calibrations have been carried out with X-ray machines. Table 2 lists the rms plate voltage of the a-c X-ray machine versus the ionizing power ratio expressed as number of times the ratio for minimum ionizing particles. The unit has also been exposed to protons in the energy range 10 to 30 Mev from the Minnesota linear accelerator. Using the observed ratio for protons, and the ratio for Co^{60} γ rays given in Table 2 as characteristic of minimum ionizing particles, very reasonable agreement is obtained with the known specific ionization of the Linac protons. We give in Figure 2 the response of the ion chamber and counter to known amounts of Co^{60}

¹ This work was supported by the National Aeronautics and Space Administration under contract NASw-56.

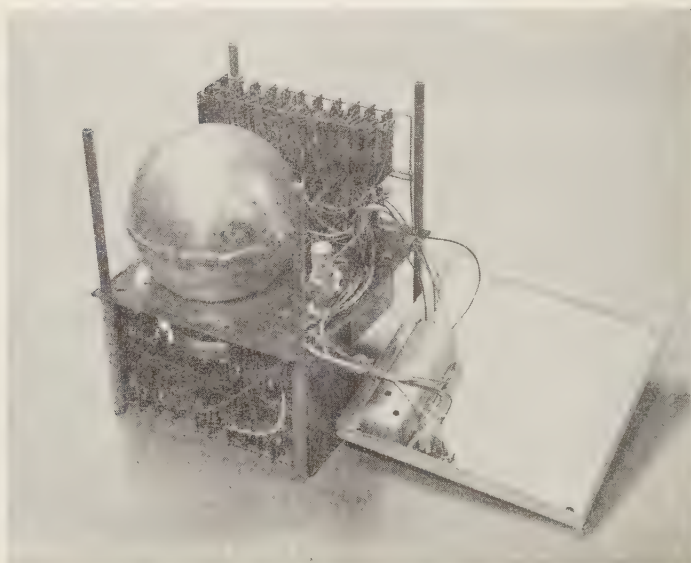


Fig. 1. View of the University of Minnesota radiation experiment containing the 3-inch-diameter aluminum ion chamber, left, and the small Anton infinite-life Geiger counter on the right side of the package. Note transistor scaling circuits and radio-frequency filter box on the cover of the package. This unit is completely filled with a polyurethane foaming plastic in its case.

γ radiation supplied by the high-intensity γ -ray facility at the University of Minnesota. The radiation dosage in roentgens is obtained from carefully calibrated Victoreen R meters exposed, along with the satellite package, to the cobalt radiation source. The ion chamber shows essentially a straight-line log-log plot with a slope differing slightly from unity. The Geiger counter shows a dropping off at high rates which occurs because of the dead time of the counter and circuitry. With the aid of this calibration curve, true counting rates can be inferred from the observed counting rate of the counter at high rates.

Both analog and digital telemetry were used, but only the former was analyzed for this report. The Geiger counter fed 17 binaries in series, samples being taken after the 8th and 17th. These were mixed, with different amplitudes, with the output of the 5th binary after the ionization chamber. The record could be read without difficulty, since usually only one of the scaling rates of the counter and the ion chamber was observed at the same time, owing to the action of a 3-cps filter network.

The radiation unit in the payload was surrounded by considerable material located mostly in the plane of the figure. A preliminary evaluation has been made of the complex shielding experienced in different directions by the unit, and in a simple way this may be expressed by the values in Table 3 covering different ranges of absorption. In general, the lower limit

TABLE 1. Specifications of Radiation Detectors

Ionization chamber	
Diameter	3.0 in.
Wall thickness of aluminum	0.020 in.
Filling pressure of argon	94 lb/in. ² absolute
Charge collected/pulse	2.14×10^{-10} coulomb/pulse
Geiger counter	
Anton type 302	
Wall thickness of stainless steel	0.020 in.
Efficiency for charged particles	80 per cent*
Omnidirectional factor	0.55-0.75 cm ^{††}

* As given by manufacturer.

† Computed from direct measurements on samples and from manufacturer's dimensions. A more accurate value for the flight unit will be reported later.

TABLE 2. Relative Photon Response of University of Minnesota Radiation Detectors
Exposure was made with experiment removed from satellite.

X-Ray Tube RMS Plate Voltage, kv	Approximate X-Ray Ratio/Minimum Ionizing Ratio
35	844
38	76
43	34
50	30
57	10

Isotropic Co ⁶⁰ γ Rays	1.33×10^{-4}
--	-----------------------

of detectability is about 16 Mev for protons and about 2 Mev for electrons directly. Low-energy electrons may be detected indirectly by the X rays generated when collisions occur with the skin and other parts of the payload. For such X rays the limit of detectability is approxi-

mately 30 kv, where the sensitivity of the detectors drops off to a negligible value. The efficiency of detection of such electrons is of course low on account of the intermediate bremsstrahlung process.

The payload was injected into an elliptical orbit positioned in space as shown in Figure 3 with the plane of the orbit making an angle of 38° with the ecliptic plane. The period of the satellite was about 12 hours and 42 minutes, and the payload was spun about its axis of greatest moment at a rate of $2\frac{1}{2}$ revolutions per second. Perigee was 6615 km and apogee 48,616 km from earth center. Successful telemetry of the channel carrying the University of Minnesota experiment was maintained for approximately 2 months, between August 7 and October 6, 1959. During this period a strong geomagnetic storm occurred on August 16-17 which will be discussed in detail below. A great solar radio noise storm took place at the end of August, and on September 4 and 23 disturbances

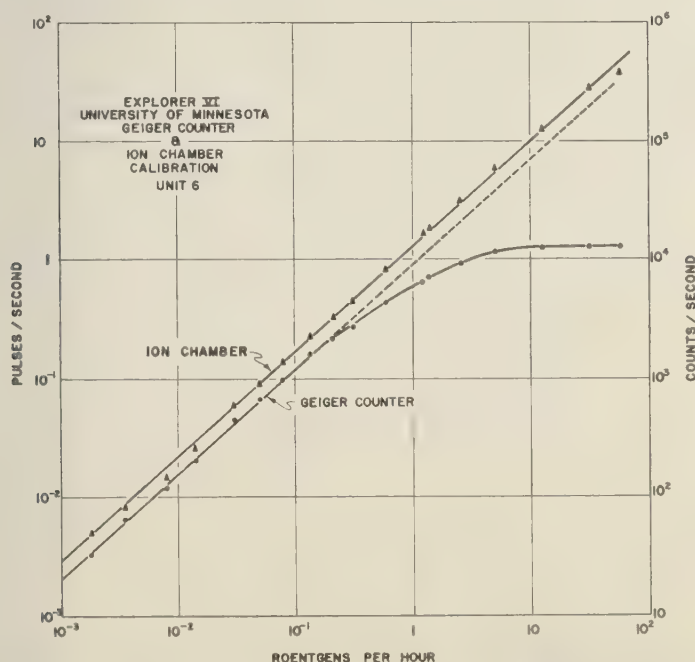


Fig. 2. Calibration curve for the ion chamber and Geiger counter used in the University of Minnesota Explorer VI experiment. The rates for the two instruments are plotted against the radiation in roentgens per hour as measured by calibrated Victoreen R. meters. The source of radiation was cobalt 60.

TABLE 3. Shielding Effect of Material in Satellite around Minnesota Package

Range Interval, g/cm ²	Percentage of Total Solid Angle	
	Counter	Chamber
0-0.5	16	26
0.5-5	54	46
>5	30	28

that may be of the recurrent *M*-region type were also observed. These latter storms will be discussed in full detail in a later communication when more data have been read.

Profile of the Van Allen regions during the first week of the satellite. Because the Explorer VI satellite was placed into a high-ellipticity orbit, and because with respect to the geomagnetic axis of the earth the orbits swing northward and southward in latitude, a large part of the radiation belts is swept out in a period of several days, affording an unusual opportunity to plot the details of the distribution of particles that are accessible to the instruments in this experiment. Figure 4 shows a series of typical orbits plotted in rectilinear form, in which the geomagnetic latitude appears as the

vertical coordinate and the range as the horizontal coordinate. These orbits were obtained from an ephemeris furnished by the Space Technology Laboratories. The geographic latitude, longitude, and range have been converted to geomagnetic latitude and range with the aid of the earth-centered dipole approximation of Vestine [1948]. Recently the orbits in geomagnetic coordinates from Vestine's analysis have also been furnished directly by the Space Technology Laboratories, in 1-minute intervals. In addition, the NASA, on the basis of data obtained by the minitrack net and analyzed under the Vanguard program, has furnished orbital data in 1-minute intervals. These various measurements are in good agreement. Figure 4 also includes lines of force of the earth's centered dipole field in the rectilinear form of plotting.

From the Geiger counter rate during the first 14 passes of Explorer VI, a contour plot of the radiation regions has been constructed, which appears in Figure 5 in rectilinear form. This period, the first week after launch, was fairly quiet magnetically, and the radiation regions were stable. The dotted parts of contour lines are extrapolations between regions where data are available. A more recent contour plot, making use of the geomagnetic data at 1-minute

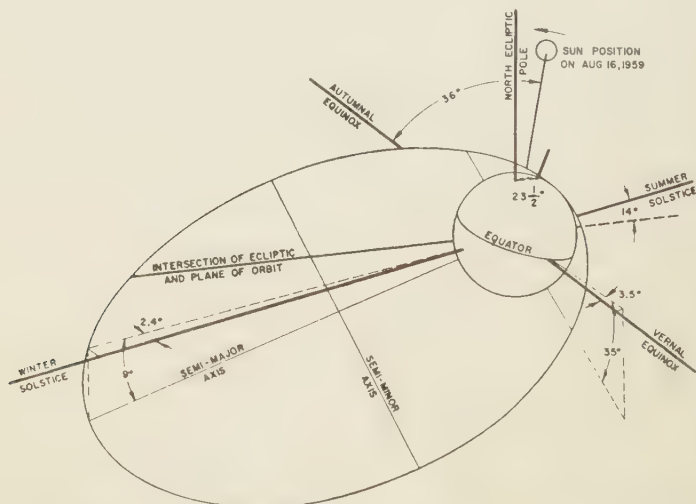


Fig. 3. The orbit of Explorer VI in space. The angle between the plane of the orbit and the earth's equatorial plane is 47° . The orbital plane is tipped 38° to the plane of the ecliptic. On August 16 during the geomagnetic storm the major axis was directed about 125° away from the sun.

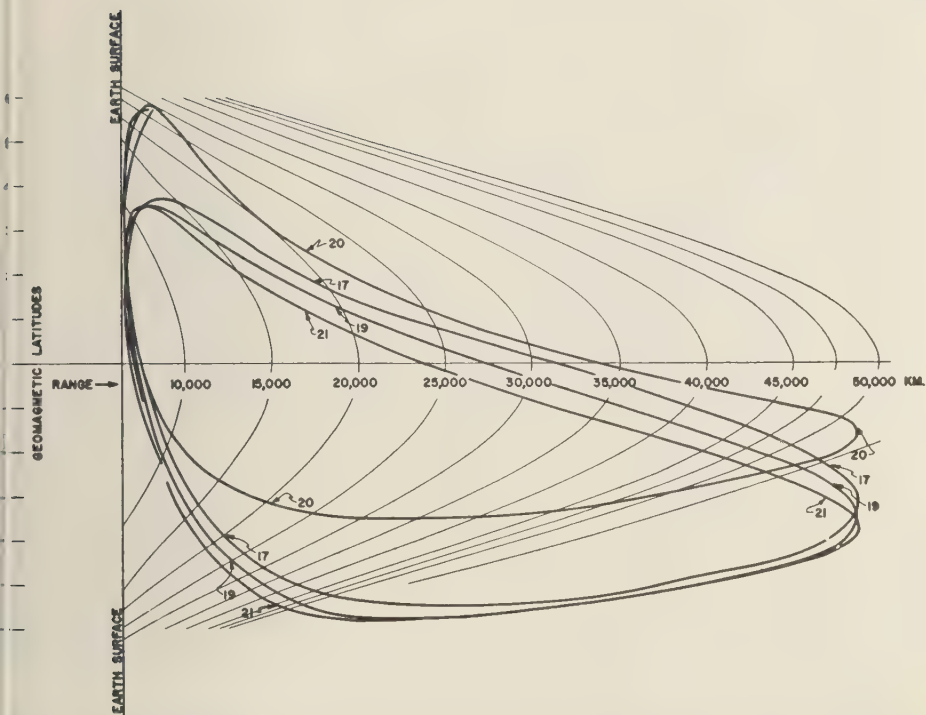


Fig. 4. Typical orbits of Explorer VI plotted in the geomagnetic meridian with the lines of force of the earth's field shown for comparison. A rectilinear plot is used, the earth's surface being represented by the Y coordinate and the range by the X coordinate. The particular passes shown are those occurring during the geomagnetic storm beginning August 16.

Intervals and additional data from the counter, shows considerably more detail at low altitudes, for example, the 'horns' derived from Explorer VI data by Van Allen [1959a].

In Figure 6, on a polar-type diagram which is more familiar to most readers, the extent and intensity of the radiation zones as given by Van Allen, upper [Van Allen, 1959a], and as derived from Explorer VI measurements, lower, are compared. The comparison is made on the basis of the same instrument, namely an Anton type 302 counter. Although the shielding of the surroundings of Explorer VI may not be quite the same as for the Explorer IV and Pioneer III and IV detectors used by Van Allen, they are not too dissimilar for the present purpose. It is apparent that since the time of the construction of the radiation zone figure by Van Allen the zones have shrunk considerably in intensity and extent. It is seen that during the first week of

August the counting rate reached the cosmic-ray background of 1.5 counts/sec at the outer extremity of the orbit of Explorer VI, whereas earlier in the year the radiation intensity as deduced from the Pioneer shots was still considerably above this value.

Throughout the time of observation, three distinct maxima in the trapped radiation region were measured by both detectors. The first of these three regions can be identified with the Van Allen inner zone and is closest to the earth. The second and third regions are seen at 17,000 and 23,000 km, respectively, near the equator. Only these last two are measured on outgoing passes, owing to the high latitude of the orbit. Many incoming passes display all three regions as they exist at southerly magnetic latitudes between 20° and 50°. Maxima observed on outgoing and incoming passes lie on connecting lines of force in the dipole field. An example of

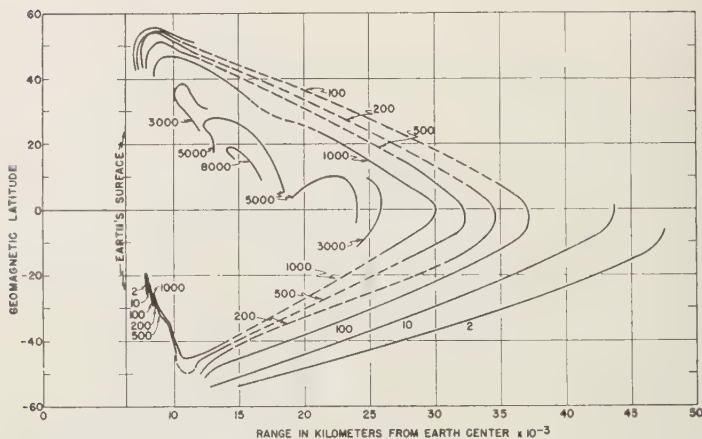


Fig. 5. Rectilinear plot of contours of equal counting rate for the Anton counter as obtained from the first week of Explorer VI.

such an incoming pass is shown in Figure 7 for pass 27, which has an incoming trajectory similar at low latitudes to that for pass 21 (see Fig. 4). The maximum rates for the two outer regions are somewhat larger than normal, since the pass occurred during a rising intensity following a magnetic storm. The two innermost maxima have average ionizing power as observed by the two instruments 5 to 6 times that for minimum ionizing particles. The outermost maximum has a ratio of approximately 16 times that for minimum ionizing particles. Such a large ratio is consistent with soft X rays produced by electrons bombarding the outer shell of the payload. Protons with this specific ionization would be stopped by the material surrounding the instruments.

Assuming that the soft outermost maximum is due to electrons, it is possible to estimate the flux incident upon the payload shell. Comparing the ratio of the ion-chamber rate to counter rate at this point with that from the X-ray calibration of the unit yields a value of 50 kev for the mean energy of the X rays. For the maximum value, observed during the first week, of 10 r/hr (1.9×10^8 ev/cm² · sec in air), the X-ray energy flux is given by

$$N = \frac{dN}{\lambda dx} = \frac{1.9 \times 10^8 \text{ ev/cm}^2 \cdot \text{sec}}{0.23 \text{ cm}^2/\text{g} \times 0.0013 \text{ g/cm}^3} \quad (1)$$

$$= 6.3 \times 10^{11} \text{ ev/cm}^2 \cdot \text{sec}$$

The mass absorption coefficient, λ , in the argon gas of the chamber is chosen for 50-kev X ray. The electron energy flux is about 10^4 times greater than the X-ray energy flux at 50 kev owing to the inefficiency of the bremsstrahlung process. The electron particle flux is then four to be

$$\frac{6.3 \times 10^{11} \times 10^4 \text{ ev/cm}^2 \cdot \text{sec}}{50 \times 10^3 \text{ ev}} = 1.2 \times 10^{11} / \text{cm}^2 \cdot \text{sec} \quad (2)$$

Another way to compare the various measurements of the radiation zones is shown in Figure 8, in which the counting rate of the Geiger counter is plotted as a function of range in kilometers for passes of the Pioneer III and IV, the Russian Mechta rocket [Vernov, Chudakov, Vakulov, and Logachev, 1959] and a typical pass (no. 6, August 10, 1959) of Explorer VI. It is seen in Figure 8 that the highest over-all intensity was that recorded by the space probe Pioneer IV launched March 3, 1959, in which the intensity in the central part of the outer region went off scale but was perhaps as much as 100 counts/sec. The Russian Mechta rocket, launched January 2, 1959, recorded intensities one to two orders of magnitude less intense. The Pioneer I data in December of 1958 are still lower, and the closest in intensity to the Explorer VI results. Explorer VI reached the cosmic-ray back-

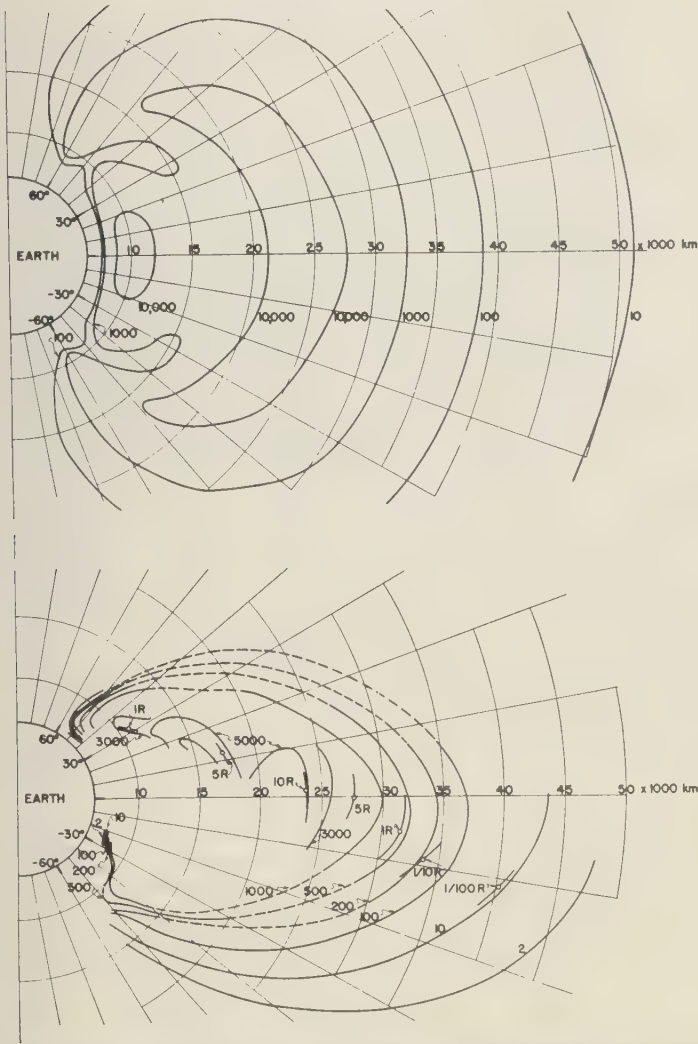


Fig. 6. Comparison of the counting-rate contours in the radiation zone as given by Van Allen (*upper*) and as given by analysis of Explorer VI (*lower*) shown on a polar plot. It is apparent that the radiation zones during the time of Explorer VI have shrunk considerably and changed form since those inferred from the Explorer IV and Pioneer III and IV data.

ground rate of about 1.5 counts/sec at approximately 42,000 km, and at that point had a rate 10^{-4} of the Pioneer IV rate. The intensity measured is strongly a function of the position of the trajectory. Figure 9 compares the trajectories of Pioneer III, Pioneer IV, and Mechta plotted on the same rectilinear scale on which the typical

passes of Explorer VI are shown in Figure 4. These trajectories are roughly similar, but the Mechtla probe crossed the equator at larger distances. It is clear that large temporal changes occur in at least the outer radiation regions surrounding the earth. The Iowa group reports that the enormous filling-up of the regions shown on

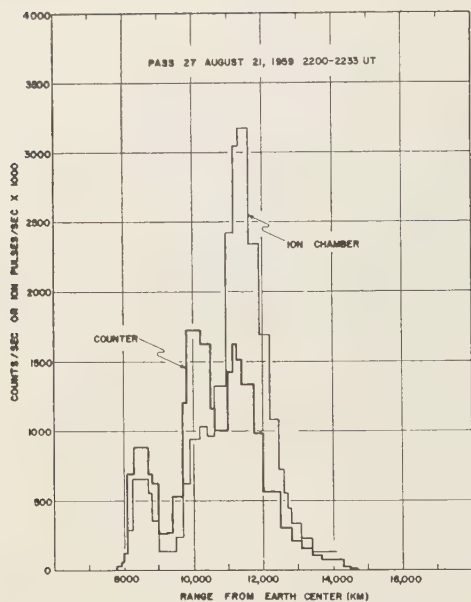


Fig. 7. Radiation levels on the incoming part of pass 27, which show three distinct radiation regions. The Van Allen inner zone appears at 8500 km, the outer zone at 11,500 km, and the new intermediate zone close to 10,000 km. The trajectory is closely similar to that for pass 21, Figure 4. The relative intensities are meaningful only when the position along the magnetic line of force is considered.

the March 3 pass of Pioneer IV is associated with an *M*-region solar-type disturbance [Van Allen, 1959b]. It will be shown that an analysis of Explorer VI data likewise shows strong dependence on solar activity but not in a simple manner.

To illustrate some of the time variations observed on Explorer VI, Table 4 lists the Geiger counter rates along the trajectories at the maximum of the soft outer region for magnetic latitudes within 8° of the equator. Also tabulated are the planetary magnetic indices A_p and the ionizing power of the trapped radiation expressed as number of times that for minimum ionizing particles (i.e., Co^{60} γ rays). No data were received from the ion chamber after August 21, and hence the ratios are missing during the high intensity and the subsequent decrease. This table will be discussed further in connec-

tion with the magnetic storm of August 16-19 1959. The table is incomplete but represents the present state of analysis of the data.

Observations during the geomagnetic storm of August 16-18, 1959. We shall now consider in detail the changes observed in the trapped radiation associated with a strong geomagnetic storm having a sudden commencement at about 0415 UT on August 16. The remarkable effect observed during the first 24 hours of this storm was a large loss of radiation from the outer region. It is shown in Figure 10, where pass 1' which occurred early in the disturbance, is compared with pass 19, which occurred 1 day later. In Figure 10 the ion-chamber rate and the corrected or true counter rate are plotted in pulses per second multiplied by 1000, and in counts per second, respectively. The ion-chamber rate dropped from a maximum of 9 to about 1 pulses/sec, and the counting rate from 4800 to about 1800 counts/sec. This means that about two-thirds of the detectable radiation existed in the outer zone during the first week of Explorer VI was lost during the first day of this geomagnetic storm. As is seen from Table 4 the trapped radiation remaining after the dumping was considerably harder than before the storm. Changes were also observed in the intermediate maximum occurring at around 13,000 km, but they have not yet been analyzed in detail.

If the change in the ion-chamber rates at different ranges as shown in Figure 10 is considered, and the location on the surface of the earth where this radiation must be precipitated is computed, on the assumption that it is discharged down along the corresponding lines of force, the precipitation or 'dumping' profile shown in Figure 11 is obtained. The radiation intensities have been corrected, because of the convergence of the magnetic lines of force, by the ratio of the surface field to the field along the orbit at the point from which the radiation disappeared. The radiation lost from the outer region is dumped between geomagnetic latitudes 52° and 62° with a peak intensity around 57° or 58° . This profile of precipitation lies definitely below the usual latitude of the auroral zone. The ratio of the ion chamber and counter for the dumped radiation suggests that the particles are electrons of approximately 50-kev energy. We

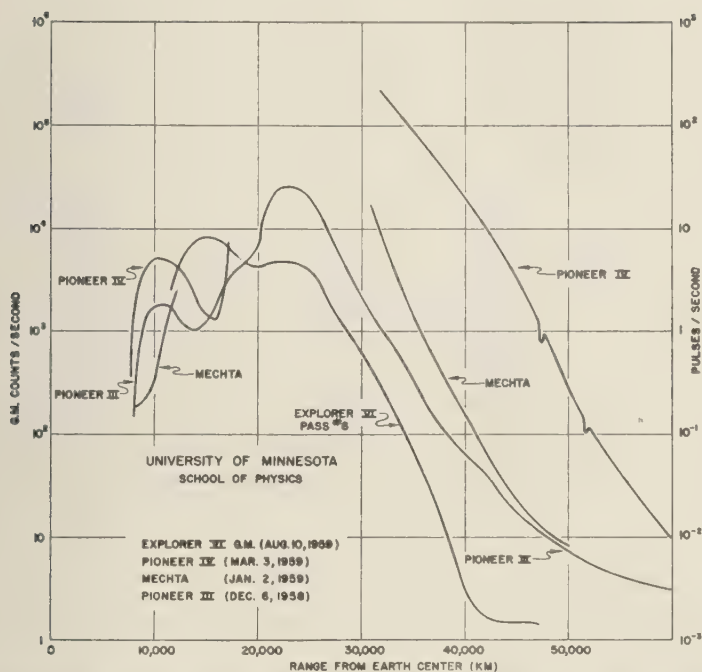


Fig. 8. Comparison of Giger counter rates for Explorer VI, Pioneer III, Pioneer IV, and the Russian Mechta space probe. The various counting rates are on a comparable basis within approximately 25 per cent. To compare orbits, see Figures 5 and 8. Explorer VI shows the lowest intensity of trapped radiation, and Pioneer IV the greatest enhancement of the radiation regions. These curves illustrate the time variability of the outer regions over long periods.

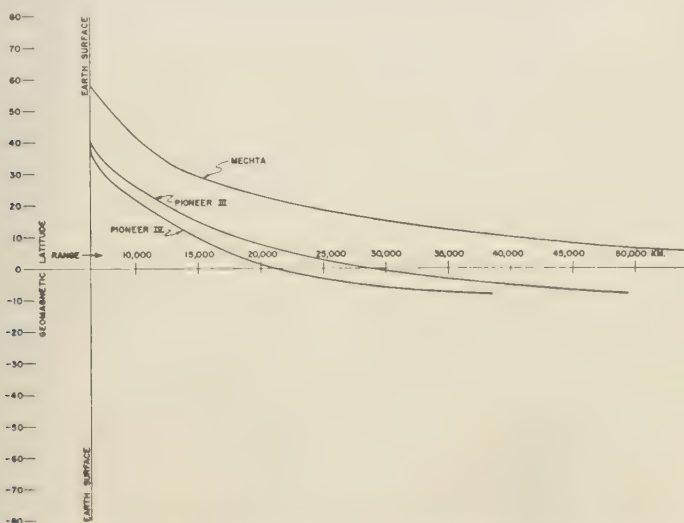


Fig. 9. Comparison of the outgoing trajectories of Pioneer III, Pioneer IV, and Mechta.

TABLE 4. Preliminary Summary of Measurements of Outer Zone Maximum during August and September 1959

Date	Time UT	Pass No.	Counts	X Minimum Ionizing	A_p Planetary Indices	Magnetic Latitude, degrees	Range from Earth Center, km
			Sec				
Aug 7	1538	1	5,050	15.5	14	7.5	22,000
Aug 9	0559	4	5,400	14.3	22	7	23,500
Aug 10	0727	6	4,700	14.5	14	2	22,600
Aug 11	0859	8	5,650	13.9	8	-1	22,500
Aug 12	1028	10	6,100	13.9	5	0	22,500
Aug 13	1200	12	5,500	14.3	6	-2	22,500
Aug 14	1330	14	6,250		6	1	22,600
Aug 17	0509	19	1,900	7.6	114	7	21,700
Aug 18	0645	21	8,150	15.7	28	0	23,500
Aug 19	0817	23	10,000	15.7	21	-3	23,500
Aug 20	0900	25	28,000	10.3	38	-1	21,700
Aug 21	1000	27	27,000	11.1	34	-1	21,500
Aug 22	1232	29	28,500		27	3	20,500
Aug 26	0542	36	27,000		8	4	21,000
Aug 27	0710	38	28,300		5	0	20,700
Aug 29	1005	42	27,500		13	0.5	20,500
Aug 30	1130	44	22,300		9	3	19,800
Aug 31	1302	46	17,200		9	3.5	20,500
Sep 2	0312	49	16,000		34	7.5	20,700
Sep 3	0438	51	16,000		33	6	20,000
Sep 4	0600	53	5,100		103	4	19,000
Sep 5	0730	55	7,600		34	2.5	18,500
Sep 12	0446	68	8,100		14	7.8	17,200
Sep 27	0116	96	3,800		21	-2	26,300
Sep 28	1524	99	4,100		18	2	25,500
Sep 29	0400	100	4,000		9	4	25,500

conclude that this source of electrons could well provide the auroral X rays seen on numerous occasions in balloon flights flown near the latitude of Minneapolis, which is about 56° geomagnetic [Winckler, Peterson, Arnoldy, and Hoffman, 1958]. In fact, a semiquantitative comparison can be made between the ion chambers flown on balloons measuring the X rays generated by the impact of the electrons on the atmosphere, and the ion chamber contained in the satellite measuring the X rays from the electrons bombarding the outer shell of the satellite. We estimate that for a typical strong balloon X-ray event, considered as extrapolated above the atmosphere, in a 24-hour period a dosage R_s of approximately 24 mr of X radiation would be produced. From the change in the satellite ion-chamber reading shown in Figure 10, it is estimated that 7 r/hr of radiation dosage rate was lost from the radiation belts at the place of maximum intensity at about 21,000 km. The

change in the number of electrons in the radiation zone at 21,000 km may be expressed by

$$\Delta N_{\text{loss}} = (\Delta r/\text{hr})/K \cdot T \quad (3)$$

The number of electrons required to produce the observed auroral X rays at balloon levels may also be expressed

$$\Delta N_{\text{precip}} = (R_s/K)(B/B_s) \quad (4)$$

where the constant K is the number of roentgens delivered in the form of X rays to the ionization chamber, either in balloon or satellite, by one electron, T is the period of an electron trapped in the radiation region and oscillating back and forth between the mirror points (approximately 1 second), B_s is the surface value of the geomagnetic field, and B is the value of the field at 21,000 km. The ratio of ΔN_{loss} to $\Delta N_{\text{precipitated}}$ is equal to approximately 4, which means that enough radiation is lost from the outer

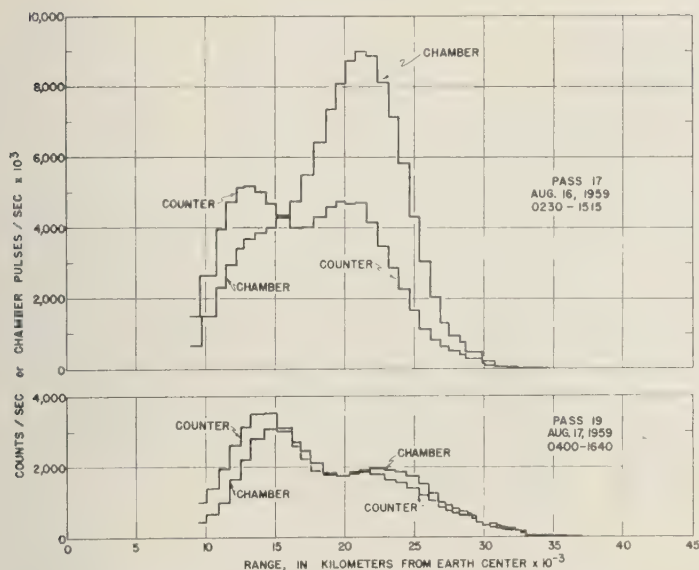


Fig. 10. Comparison of a pass at the very beginning of the geomagnetic storm and a pass 21 hours after the beginning of the geomagnetic storm. Note the large decrease in the radiation content of the outer region. From this disappearance of net radiation, it can be computed that the electrons discharged are sufficient to produce the auroral X rays observed at balloon altitudes in subauroral zone auroras.

zone to account completely for the bursts of X rays observed at balloon levels. A further remarkable observation is that on the night of August 16-17 a very strong aurora was observed by one of us (JRW) at approximately 57° geomagnetic latitude over the state of Minnesota. The aurora was a typical strong storm aurora with ray structure and visible forms extending as far south as 54° or 55° geomagnetic latitude. The visual observations indicated that this was the type of aurora, when observed with balloons at this latitude, which would produce strong X-ray bursts. A bright corona was observed, which has always been correlated with the presence of balloon X rays if the corona is seen near the balloon at these latitudes. It thus seems very reasonable that the balloon X rays can be due to the direct discharge of the soft radiation from the outer radiation zone.

This observation also may account for conclusions reached by Anderson [1959] that, although strong X-ray bursts are observed under visible auroras in latitudes below that of the auroral zone, balloon observations of auroras in

the auroral zone show only weak X rays. The line of force connecting to the auroral zone at approximately 65° geomagnetic latitude leads into the trapped radiation at a region where the soft radiation is at a very low intensity, at least as seen during August and September 1959. There is some evidence also from examination of Figure 8 that the radiation regions tend to return to a configuration similar to that observed in Explorer VI except for times when there is a large acceleration or injection from outside, and so the normal situation might be similar to that seen in August and September.

These observations are concerned with only one component of the aurora, namely electrons around 50 kev of energy. It is not certain what fraction of the total auroral energy is contained in these electrons. We have estimated from balloon X-ray data that some times sufficient energy is present in the X-ray electrons to supply all the energy of an auroral display. It is probable, however, that the solar plasma, which is presumably present but inaccessible to measurements with our instruments, or a similar

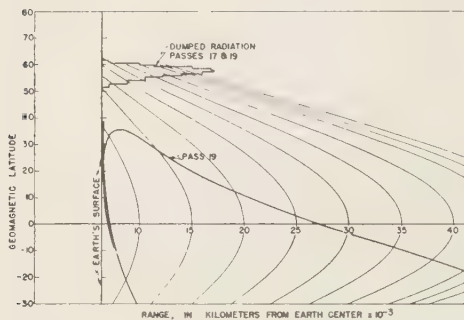


Fig. 11. Estimate of the precipitation of electronic radiation from the outer regions of the trapped radiation onto the surface of the earth inferred from the measurements before and during the geomagnetic storm of August 16-17. Note that the electrons strike the earth's surface at about 57° geomagnetic latitude, and that, at least with the profile of radiation intensity observed in August and September 1959, they are not discharged into the auroral zone.

type of low-energy radiation normally in the radiation regions, discharges to the surface and produces a large fraction of the visible auroral luminosity, both in the auroral zone and at latitudes below it. The association of the auroral X rays with the visible aurora occurs only in very strong auroras which sweep southward from the auroral zone and are characterized by magnetic indices of K7 to K9.

The exact mechanism of dumping in this case is not clear, but it seems certain that the increase in altitude of the atmosphere due to heating cannot remove enough particles. By following down the line of force with passes through the outer zone maximum, it is found that too large a fraction of the particles have turning points near the equator and hence at too high an altitude to be removed by scattering from a rising atmosphere. Therefore some other mechanism besides atmospheric heating must be invoked to explain the great loss of particle fluxes from the trapped radiation. Possibly perturbations of the magnetic field by the solar plasma exciting the geomagnetic storm may account for this, and the accompanying discharge of the particles into the atmosphere may perhaps cause the atmospheric warming and the scattering-out of trapped particles with low mirror points. Evidence for this latter phenomenon has been

obtained by the Iowa group [Rothwell and McIlwain, 1959] as the result of extensive observations with the Explorer IV satellite, which penetrates the outer zone at low altitudes up to 1000 km above the surface.

Another surprising observation is that, near the end of the storm on August 18, pass 21, as shown in Figure 12, recorded an increase in the intensity of radiation in the outer region to a value very much higher than that we have called normal, characteristic of prestorm conditions. Pass 22, as shown in Figure 13, showed a similar increase above normal, although the pass went through the trapped radiation at a very high latitude. Table 4 shows that the intensity in the soft outer maximum following the storm rapidly increased on August 20 to about 5 times prestorm levels, and remained at this value until August 30, when it began to decrease. While at peak intensity the radiation appeared harder than before the storm as given by the ratios on August 20 and 21. The magnetic storm of September 3-4 likewise diminishes the radiation in the soft maximum with a small intensity increase following it. The data for this storm are incomplete and will not be discussed further here.

During the peak intensity in the outermost maximum, a great long-lasting solar radio noise storm was observed. A plot of the intensity of radio emission at 169 Mc/s as determined by the Meudon Observatory group from the solar radio station at Nançay, France, is shown in Figure 14, which is taken from the Boulder reports [National Bureau of Standards, 1959]. The sun is scanned every day, and the intensities are plotted across the disk. Regions of moderate activity appear frequently, as shown by the small black and white spots, but on August 22 a region developed which on succeeding days reached very high intensity. The radio emission from this region extended beyond the limits of the disk (shown by the horizontal lines labeled W and E on the left margin). This long-lasting solar noise storm has been observed at several other stations, for example by Warwick (private communication, 1959) at Boulder and by Erickson (private communication, 1959), at the Convair radio astronomy station in California. Warwick's sweep frequency interferometer covering the approximate range 15 to 100 Mc/s

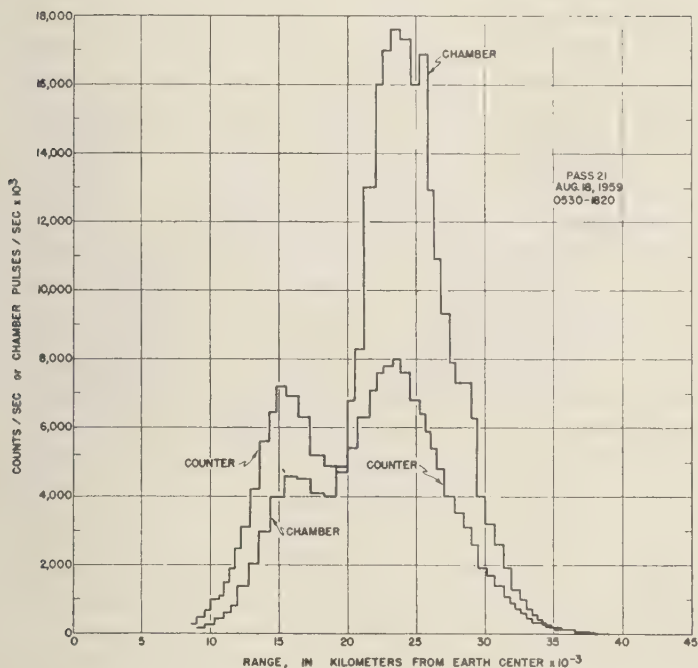


Fig. 12. Pass 21 occurring at the end of the second day of the strong geomagnetic storm on August 16. Note the great increase in intensity of the radiation regions following the dumping shown in the previous figure. This pass went out from the earth at a quite low latitude. The maximum at 15,000 km is the new intermediate zone, also shown on Figure 10.

showed that the emission was continuum radiation, definitely not thermal, and attributable to synchrotron radiation from electrons in a region that appeared to be at a very great distance from the surface of the sun.

The unusual nature of this noise storm is also made clear by observations of the Fraunhofer Institute, which showed numerous wide-band rapid intensity fluctuations during the period. Similar observations were reported by the Nera Observatory [Information Bulletin, 1960].

On the basis of incomplete data used in our earlier report [Arnoldy, Hoffman, and Winckler, 1960], a close association seemed to exist between the beginning of the intense part of this noise storm and the increase in the outer zone. The acquisition of additional data makes this association less certain.

During the time of observations of the first half of this radio noise storm, the trapped radiation was extremely stable and the magnetic

indices were low. Whether the build-up of the radiation is related to an unobserved initial phase of the solar radio noise storm or is an after-effect of the magnetic storm starting August 16 cannot be determined. Nevertheless, the injection of some particles into the trapped-radiation region during this period is suggested by Figure 15, which shows a pass during the high intensity in the outermost maximum. This pass has structure at apogee and a counting rate there about 5 times that observed for cosmic rays during undisturbed periods. A pass during the intensity build-up just after the magnetic storm displayed similar structure, as did several other passes during the enhanced intensity.

If the increase of electron flux is associated only with the geomagnetic storm beginning August 16, shown in Figure 12, a tentative conclusion is that somehow in the wake of the storm part of the low-energy matter that is normally

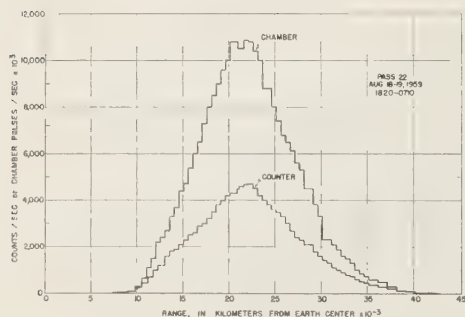


Fig. 13. Pass 22, showing the increase following the geomagnetic storm of August 16-17. This pass went out at high latitude and missed the new intermediate zone.

undetectable was elevated in energy and passed across the energy threshold of the ion chamber and counter carried in the Explorer VI satellite, appearing as an increase in the electronic component. Further studies of the details of the magnetic field during this storm and similar ones will be needed to decide on the exact mechanism of this acceleration process, if, in fact, it does exist.

Professor Sydney Chapman and his collaborator, S. Akasofu, have kindly furnished us with a preliminary D_{\perp} curve for the storm of August

16, obtained from eight selected equatorial stations. This curve, shown in Figure 16, has been corrected for the regular diurnal magnetic variation S_q , and for the effect of the underground current system (by taking 2/3 of the total H variation after S_q correction). With relation to this storm time field variation, which seems to be a more or less typical example of a strong storm, the behavior of the energetic trapped electrons in the outer zone may be described by the observations of Explorer VI. We show the times of the appropriate passes by the indicated bars on Figure 16. Data so far have been analyzed only for the outgoing parts of the passes.

The sudden commencement occurred during the outgoing part of pass 17, at about 25,600-km range from earth center (see Fig. 10). No appreciable changes from prestorm conditions are observed during this pass. The 'dumping' effect is observed after about 24 hours of the main phase have elapsed. The replacement or local acceleration effect coincides with the recovery of the field to its normal value. These relationships are probably extremely significant for understanding the morphology of the storm, but we will defer detailed discussion until a more complete analysis of the data has been made.

In conclusion, it must be emphasized that the data reported herein are preliminary, as a great

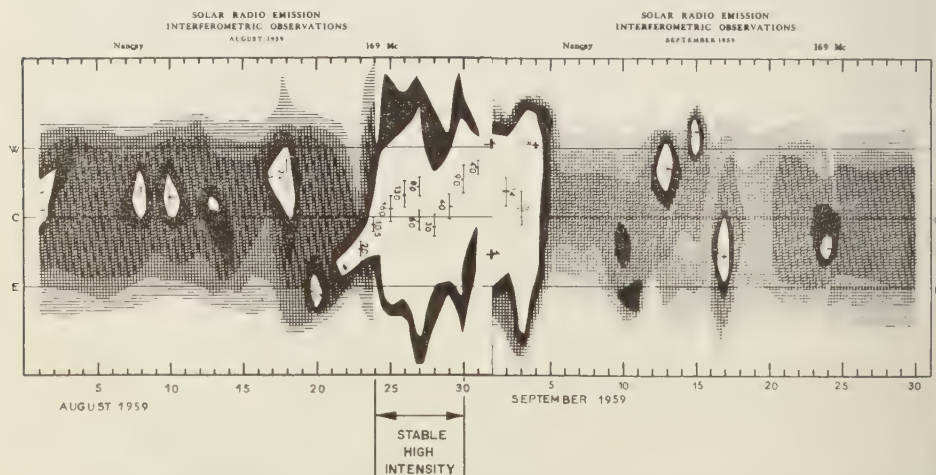


Fig. 14. Solar radio noise intensity measured in Nançay on 169 Mc/s during August and September 1959, showing the great long-lasting noise storm beginning on August 22. Between August 24 and 30 the outer radiation zone stabilized at a high intensity.

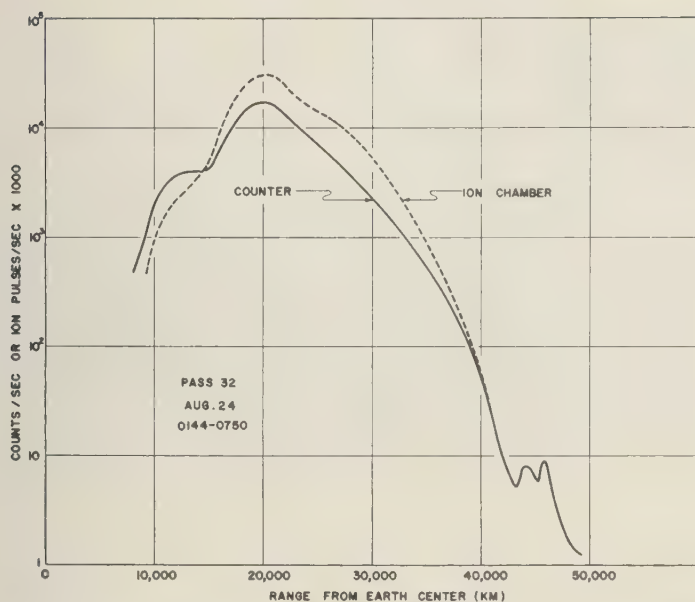


Fig. 15. Pass 32 on August 24 during the high-intensity period of the outer zone. Note the structure at 45,000 km and the enhanced ion chamber and counter at the maximum at 20,000-km range. The structure is soft radiation similar to the maximum outer zone.

amount of unanalyzed records yet remains. We think that the essential features of this discussion will, however, be preserved. It should also be noted that Explorer VI carried a variety of detectors from various laboratories, including a

scintillation counter, a magnetometer, a coincidence telescope train, a lead-shielded counter, and the present ion chamber and unshielded counter. A comparison of these instruments, when more complete data are available, is certain to yield a more definitive account of the types and intensities of particles in the radiation regions surrounding the earth.

Acknowledgments. We wish to acknowledge the coordinated efforts of the NASA and Space Technology Laboratories in successfully executing this complex experiment. The University of Minnesota effort was financed by a direct grant from the NASA, and the understanding support of Dr. John Lindsay of NASA is appreciated. The excellent work of Mr. Robert Howard of the University of Minnesota in the design of the electronic circuitry is also acknowledged. We have had numerous enlightening discussions about the interpretation of the results with Professor Paul Kellog of the University of Minnesota.

REFERENCES

- Anderson, K. A., Balloon observations of X rays in the auroral zone, I, *Preprint SUI-59-22*, Department of Physics and Astronomy, State University of Iowa, 1959.

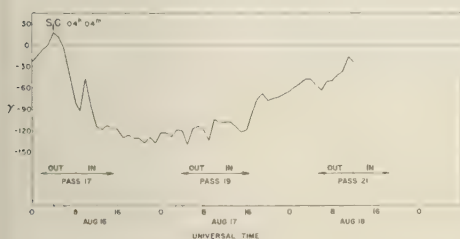


Fig. 16. The $Dst(H)$ curve for the August 16 storm as analyzed by Chapman and Akasofu. This analysis is based on 12 observatories well distributed in latitude and longitude between geomagnetic latitudes $30^\circ N$ and S. Each record was corrected to remove the quiet-day solar daily variation of H . About $2/3$ of the $Dst(H)$ variation is supposed to be of external origin. From Figures 10 and 12, on the outgoing portions pass 17 showed normal, pass 19 showed a large decrease, and pass 21 a large increase in the outer-zone intensity.

- Arnoldy, R., R. Hoffman, and J. R. Winckler, Observations of Van Allen radiation regions during geomagnetic storms, *Proc. COSPAR 1st Intern. Space Sci. Symposium*, Nice, January 1960.
- Information Bulletin of Solar Radio Observations in Europe*, no. 1, Section Ionosphere and Radio Astronomy, Netherlands PTT, The Hague, January 1960.
- National Bureau of Standards, *Solar and Geophysical Data*, September and October 1959, Central Radio Propagation Laboratory, Boulder, Colorado.
- Rothwell, P., and C. E. McIlwain, Magnetic storms and the Van Allen radiation belts: Observations from satellite 1958 epsilon (Explorer IV), *Preprint SUI-59-25*, Department of Physics and Astronomy State University of Iowa, 1959.
- Van Allen, J. A., The geomagnetically trapped corpuscular radiation, *J. Geophys. Research*, **64**, 1683-1689, 1959a.
- Van Allen, J. A., Radiation measurements to 658,300 kilometers with Pioneer IV, *Bull. Am. Phys. Soc.*, **4**, 402 1959b.
- Vernov, S. N., A. E. Chudakov, P. V. Vakulov, and Yu. I. Logachev, The study of the terrestrial corpuscular radiation and cosmic rays during the flight of a cosmic rocket, *Soviet Phys. JETP*, **4**, 338, 1959.
- Vestine, E. H., L. Laporte, C. Cooper, I. Lange, and W. C. Hendrix, Description of the earth's main magnetic field and its secular change, 1905-1945, *Carnegie Inst. Washington Publ.* **578**, pp. 28-39, 1948.
- Winckler, J. R., Balloon study of high-altitude radiation during the International Geophysical Year, *J. Geophys. Research*, **65**, 1331-1359, 1960.
- Winckler, J. R., L. Peterson, R. Arnoldy, and R. Hoffman, X rays from visible aurorae at Minneapolis, *Phys. Rev.*, **110**, 1221-1231, 1958.

(Manuscript received March 16, 1960.)

Particle Fluxes in the Inner Radiation Belt¹

STANLEY C. FREDEN AND R. STEPHEN WHITE

*Lawrence Radiation Laboratory, University of California
Livermore, California*

Abstract. Using the albedo neutron decay source, the energy spectrum of trapped protons in the inner belt has been calculated from 10 to 700 Mev. This calculation differs from those of Singer and Hess in that a nuclear interaction term, in addition to the energy loss term, has been used in the continuity equation for the steady-state condition. The spectrum agrees well with the published data. This agreement is strong evidence for the albedo neutron decay source. It also indicates that nonadiabatic losses are small for the particles measured here.

A second small stack of nuclear emulsions was flown at the lower edge of the inner radiation belt 11 days after the large solar flare of May 10, 1959. The ratio of the proton flux measured on the second flight to that on the first one is 0.8 ± 0.1 , indicating that the solar flare had little or no effect on the proton content of the inner belt. A flux of 2 ± 1 tritons/cm² sec between 126 and 200 Mev was observed; it is attributed to collisions of trapped protons with air nuclei. No other nuclei heavier than protons were seen.

1. Introduction. The albedo neutron decay mechanism has been used to account for the protons trapped in the earth's lower radiation belt [Singer, 1958; Hess, 1959]. According to this theory, neutrons produced by high-energy cosmic-ray collisions in the atmosphere leak out into space and decay. Some of the resulting protons and electrons then become trapped to form the inner radiation belt. These charged particles spiral around the magnetic field lines and are reflected at magnetic mirrors formed by the more concentrated magnetic field lines on each side of the magnetic equator. The particles continue to move back and forth until they are removed by the loss mechanisms. At equilibrium the rate of loss of particles is equal to the rate of injection.

In this paper we present experimental results and theoretical calculations for particles trapped in the inner radiation belt. This information is discussed by sections as follows: section 2, calculation of the equilibrium trapped proton spectrum; 3, additional experimental data recorded 11 days after the strong solar flare of May 10, 1959; 4, deuterons, tritons, and helium nuclei in the inner belt.

2. Proton spectrum. The energy spectrum

of trapped protons is calculated here using a computed neutron albedo flux [Hess, 1959] and the proton loss mechanisms of ionization and nuclear collisions. The nuclear collision loss mechanism is important for protons with energies above 80 Mev. The calculated equilibrium trapped proton spectrum is found to be in good agreement with our data [Freden and White, 1959], which extend from 60 to 700 Mev.

In previous calculations [Singer, 1958; Hess, 1959] the ionization loss mechanism was used. Singer [1959] also imposed the breakdown of the adiabatic condition, which removes the higher-energy protons. The results of his calculation [Lencheck and Singer, 1960] are in apparent disagreement with the measured spectrum. Hess [1959] predicted an equilibrium trapped proton spectrum which varies as $E_p^{-1.0}$ protons/Mev cm² sec. It is considerably flatter than the measured spectrum above 200 Mev.

The equation for the conservation of particles is

$$dN_p/dt + \nabla \cdot j = 0$$

Using ionization and nuclear interaction loss mechanisms this equation becomes

$$\frac{dN_p(E)}{dt} = S(E) - \frac{d}{dE} \left[N_p(E) \frac{dE}{dt} \right] - \eta \sigma N_p(E) \beta c = 0 \quad (1)$$

¹ This work was done under the auspices of the U. S. Atomic Energy Commission, contract W-7405-eng-48.

for the steady-state condition. Nonadiabatic losses are neglected. The last term represents protons lost as the result of nuclear interactions with the atoms of nitrogen and oxygen, η is the number of such atoms/cm³, and σ is the interaction cross section, which is taken to be 360 mb. This corresponds to nuclear area for oxygen or nitrogen. $N_p(E)$ is the number of protons/Mev cm³. The albedo neutron flux at the top of the atmosphere [Hess, 1959] as calculated from the measured flux in the atmosphere [Hess, Patterson, Wallace, and Chupp, 1959] is

$$\phi_n = 0.8E^{-2.0} \text{ neutrons/Mev cm}^2 \text{ sec}$$

$S(E)$ is the proton source due to albedo neutron decays and is therefore given by

$$(0.8E^{-2}/\beta\gamma c\tau_n)(R_*/R)^4 \text{ protons/Mev cm}^2 \text{ sec}$$

The neutron source spectrum, $E^{-1.3}$, used by Singer [1958] would not change the results significantly. A large fraction of the albedo neutrons leave the earth with large zenith angles, making the radial dependence of the source more like R^{-4} than R^{-3} at low altitudes. We assume that the trapping fraction is 1, independent of energy. Since the energy of the decay proton is nearly equal to the energy of the parent neutron, β and γ are the same for the neutron and proton. τ_n is the neutron mean life, 1000 seconds [Sosnovsky, Spiwak, Prokofiev, Kutikov, and Dobrinin, 1959]. The contribution to the source function of knock-on protons due to nuclear collisions is neglected.

From 80 to 700 Mev an approximate solution to equation 1 is of the form

$$N_p = (N_0 e^{-nE})/\beta c \text{ protons/Mev cm}^3$$

The flux to be directly compared with the experiments is

$$\phi_p = N_0 e^{-nE} \text{ protons/Mev cm}^2 \text{ sec}$$

In the same energy interval we use

$$\beta = 0.0896E^{0.344}$$

$$\gamma = 0.428E^{0.205}$$

$$dE/dx = 110.5\rho E^{-0.614} \text{ Mev/cm}$$

where ρ is the density of air in g/cm³. These values are valid to within 10 per cent. We use $(R_*/R) = 0.85$ for an altitude of 1100 km. This is only approximate, since some of the observed

protons could have been injected at higher altitudes. Substituting into equation 1, we have the identity

$$E^{-2.549} = 3.52 \times 10^{13} N_0 \rho e^{-nE} [5.30E^{-1.614} + 8.62nE^{-0.614} + 0.00120] \quad (2)$$

Setting $n = (170 \text{ Mev})^{-1}$ and $N_0 \rho = 6 \times 10^{-17}$, and substituting back into equation 2, we find that the equality is violated by a factor of about 2 from 80 to 700 Mev.

A more exact solution to equation 1 is found using

$$N_p = N_0 f(E)(e^{-nE}/\beta c) \equiv \phi_p/\beta c \quad (3)$$

where $f(E)$ is a slowly varying function of E and is plotted in Figure 1. Substitution back into equation 1 yields

$$\phi_p = \frac{4.55 \times 10^{-17} f(E) e^{-E/170}}{\rho} \text{ protons/Mev cm}^2 \text{ sec} \quad (4)$$

Equation 4 satisfies equation 1 to within 15 per cent from 80 to 700 Mev. It is plotted in Figure 2, along with the experimental data presented previously [Freden and White, 1959] and some new data which are discussed in section 3. The dashed line is the least-squares fit to the earlier data. The calculated curve has been normalized to the data in the region of 100 Mev, giving $N_0 = 8.3 \pm 1.2$ protons/Mev

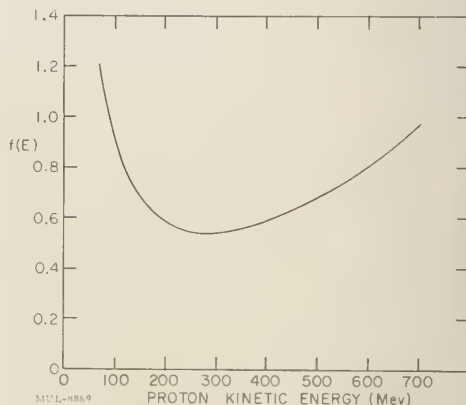


Fig. 1. Plot of $f(E)$ versus proton kinetic energy; $f(E)$ is defined in equation 4.

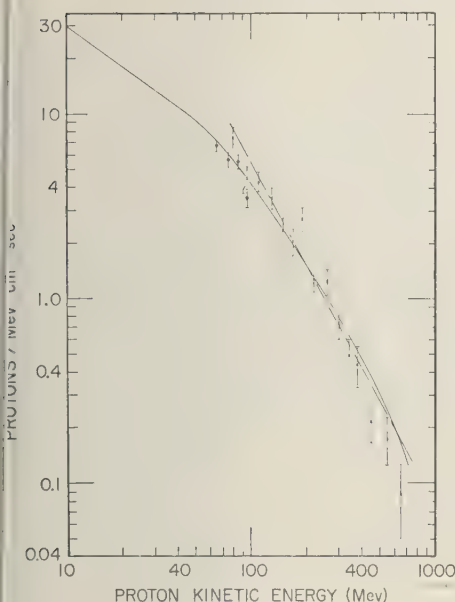


Fig. 2. The solid curve is a plot of ϕ_p , given by equations 4 and 6, as a function of proton kinetic energy. The crosses are the previously published data [Freden and White, 1959]. The dots are the new data. The dashed line is the least-squares fit to the earlier data.

$\text{cm}^2 \text{ sec}$. The resulting average air density over the trajectories of the particles is

$$\rho = 5.5 \times 10^{-18} \text{ g/cm}^3 \quad (2.3 \times 10^5 \text{ atoms/cm}^3)$$

From 10 to 80 Mev we use

$$\beta = 0.0484E^{0.477}$$

$$\gamma = 0.930E^{0.032}$$

$$dE/dx = 243.3\rho E^{-0.790} \text{ Mev/cm}$$

$$N_p = (N_1 E^{-n_1})/\beta c$$

Using the same neutron albedo source function and substituting into equation 1, neglecting the last term, we find

$$\phi_p = \frac{8.43 \times 10^{-16}}{\rho} E^{-0.72} \text{ protons/Mev cm}^2 \text{ sec} \quad (5)$$

At 80 Mev the interaction term is only about 10 per cent of the energy loss term, so that

neglecting it is justified. Using the value of ρ obtained above, we have

$$\phi_p = 1.55 \times 10^2 E^{-0.72} \text{ protons/Mev cm}^2 \text{ sec} \quad (6)$$

This curve is also plotted in Figure 2 and is joined smoothly in the region of 80 Mev to the higher-energy spectrum.

The lifetimes of the trapped protons may be calculated by means of the 'leaking bucket' equation

$$\begin{aligned} \tau_p &= \text{contents/input} \\ &= 8.5 \times 10^3 f(E) e^{-E/170} E^{2.20} \text{ sec} \quad (7) \end{aligned}$$

from 80 to 700 Mev.

In the interval from 10 to 80 Mev,

$$\tau_p = 3.5 \times 10^5 E^{1.31} \text{ sec} \quad (8)$$

Figure 3 is a plot of τ_p versus proton kinetic energy from 10 to 700 Mev. The lifetime rises from 10 Mev and reaches a maximum at about 500 Mev. This maximum lifetime is 2.7×10^8 seconds, or about 9 years.

The lifetimes for particles lost by multiple coulomb scattering have been calculated by Christofilos [1958] and Welch and Whitaker [1959]. For 10-Mev protons this lifetime is about 20 times that plotted in Figure 3. For higher-energy protons the ratio is even larger. Therefore it is justifiable to neglect this loss mechanism here.

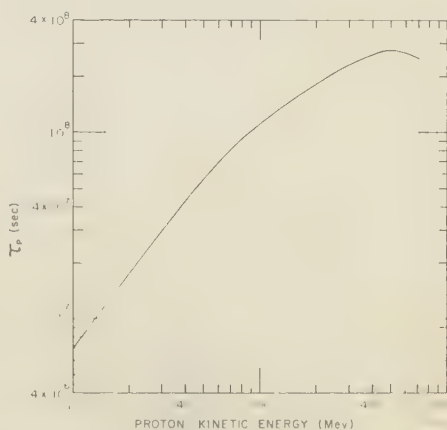


Fig. 3. Plot of the trapped proton lifetime, τ_p , versus kinetic energy. τ_p is calculated from equations 7 and 8.

3. *Additional experimental data.* In this section we show that solar activity has little or no effect on the flux of trapped protons in the inner belt. This is done by comparing the flux before and after the large solar flare of May 10, 1959. A small stack of nuclear emulsions was flown on April 7, 1959 [Freden and White, 1959]. A second exposure occurred on May 21, 1959. The second flight was identical to the first except that the thickness of the nose-cone wall was only 2.5 g/cm^2 . Before reaching the region of observation the particles penetrated a total of 3.9 g/cm^2 of material, including a protective stainless-steel container, the mounting supports, and 1 mm of nuclear emulsion. The minimum observable proton energy was therefore 58 Mev.

The scanning was done along a line 1 mm in from the edge of the stack nearest the nose-cone wall. Particles whose vertical angles were within $\pm 15^\circ$ of the plane of the emulsions, and whose horizontal angles in the plane of the emulsions were within $\pm 15^\circ$ of the normal to the nose-cone wall, were accepted for measurement. An ionization measurement [Fowler and Perkins, 1955] (g^*) was made on each track which crossed the scan line within the angle criteria. If the g^* was 4 or greater the track was followed until it ended or went out of the stack. The value 4 was chosen because protons with that ionization have a range less than the maximum path length available in the stack. A total of 497 tracks were followed.

The flux of protons in this stack is compared with that in the first one only in the region from 60 to 100 Mev, where the scanning efficiency is about 1. At $g^* \approx 4$, 115 Mev for protons, the scanning efficiency is significantly less than 1. The new data are plotted as dots on Figure 2 along with the results from the first flight. The ratio of the proton flux on the second flight to that on the first is 0.8 ± 0.1 , indicating that the large solar flare of May 10, 1959, had little or no effect on the proton content of the inner belt.

4. *Deuterons, tritons, and helium nuclei.* An independent method for determining whether the sun is a source for the inner belt is to measure the flux of trapped particles heavier than protons. If protons were injected by the sun at the time of solar flares, we would also expect the injection of He^+ and α particles and possibly

deuterons and tritons. We have looked in the second stack for these particles. A flux of 2 ± 1 tritons/cm² sec between 126 and 200 Mev was observed. No other particles heavier than protons were seen. This observed flux can be attributed to collisions of trapped protons with air nuclei. No evidence is found for solar injection.

In order to identify particles heavier than protons, we selected the 246 tracks having ranges greater than 8 mm. The g^* versus range for these tracks is plotted in Figure 4. One of them, track 60, is discussed separately later. The minimum useful range of 8 mm was chosen because mass measurements for shorter tracks are not considered reliable. The solid lines in Figure 4 are the theoretical curves for protons, deuterons, tritons, He^+ , and α particles. Additional g^* measurements at several different ranges as well as integral gap count measurements were made on each track whose initial ionization fell higher than half way between the proton and deuteron lines. A total of 15 tracks were selected for the additional measurements. The combined data showed that 12 of these are protons and 3 are tritons.

Track 60 is of special interest. The g^* at the scan line is 7.1 ± 0.7 , which predicts a range of $7.4^{+2.0}_{-1.4}$ mm for a proton. This particle went 28

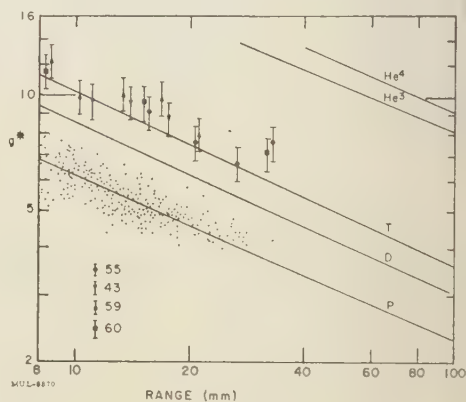


Fig. 4. Plot of ionization (g^*) versus range for the 246 tracks having ranges greater than 8 mm. The points for the 4 triton tracks are described by the legend on the figure.

mm, scattered from a free proton, and then went out the top of the stack. The scattering is coplanar to within $\pm 1^\circ$. The mass of the incident particle, calculated from kinematics, is 2.93 ± 0.41 proton masses. The error quoted is 1 standard deviation. The energy and residual range of the incident particle at the point of scatter were then calculated to be 42 Mev and 2.9 mm, respectively. This calculated range was added to the range to the point of scatter to give the total range. Additional g^* measurements were taken at various ranges, and all these data are also plotted in Figure 4.

The results may be summarized as follows. For particles with $g^* \geq 4$ and ranges from 8 to 33 mm the identification is good. This range interval corresponds to 78 to 116 Mev for protons, 106 to 168 Mev for deuterons, 126 to 200 Mev for tritons, 276 to 444 Mev for He^3 , and 312 to 504 Mev for α particles. Here we observed 4 tritons, 242 protons, no deuterons, and no helium nuclei. The triton energies were 156, 168, 195, and 195 Mev. These 4 tritons represent a flux of 2 ± 1 tritons/cm² sec, or about 2 per cent of the proton flux in the same energy interval. For ranges between 4 and 8 mm the identification is subject to larger statistical and systematic errors and cannot be regarded as positive. In this region we observed 115 tracks, of which 2 may be deuterons or tritons. For ranges < 4 mm, identification is not possible.

It is of interest to investigate local mechanisms that can give trapped tritons, namely: (1) interactions of trapped protons with air nuclei; (2) cosmic-ray interactions with air nuclei; (3) interactions of solar storm protons with air nuclei; (4) interactions of high-energy albedo neutrons with air nuclei. In addition, the tritons could have been produced in the nose cone by the trapped or cosmic-ray protons. Of these proposed mechanisms, the first represents a source at least an order of magnitude greater than any other. Therefore we shall concentrate on it alone.

The flux of tritons that should be observed can be estimated from the expression

$$F_t = F_p \sigma_t \eta v t f_{\Delta E} f_{\Delta \Omega} \quad (9)$$

where F_p is the number of incident protons/cm² sec; σ_t is the triton production cross section; η is the number of air nuclei per cm³; t is the

time during which the tritons can be observed, in seconds; and v is the triton velocity. $f_{\Delta E}$ is the fraction of tritons that fall in the correct energy interval to be observed, and $f_{\Delta \Omega}$ is the fraction of produced tritons that fall within the proper angles to be trapped and observed. The value of F_p , found by integrating equation 4 from 200 to 700 Mev, is 290 protons/cm² sec. The measured total cross section for tritium production on oxygen and nitrogen is about 30 mb [Currie, Libby, and Wolfgang, 1956; Fireman and Rowland, 1955]. For $\eta v t$ we take 3.1×10^{12} nuclei/cm² (7.2 g/cm²), which is the amount of air required to slow a 200-Mev triton down to 126 Mev, the energy region where tritons could be recorded in this experiment.

In calculating $f_{\Delta E}$ we must include tritons made with energies > 200 Mev, because some of them will be degraded down to 200 Mev and will contribute to the measured flux. $f_{\Delta E}$ is estimated to be about 0.2 averaged over the proton spectrum for protons > 200 Mev. This estimate is based on experimental evidence for tritons produced by 190-Mev cyclotron-accelerated protons [Bailey, 1956].

Since the high-energy tritons produced by proton bombardment will be emitted primarily in the direction of the incident protons, the fraction $f_{\Delta \Omega}$ will be very nearly 1 for production at the equator, and will approach zero at the mirror points. We estimate $f_{\Delta \Omega}$ to be 0.5 on the average.

Substituting into equation 9, we find $F_t = 0.3$ tritons/cm² sec. This is certainly an underestimate, because we have only considered triton production by protons which mirror in the region or below where the tritons were observed. Protons which mirror nearer the equator, and therefore could not be recorded in this experiment, are also effective in contributing to the measured triton flux. Thus the effective F_p is considerably larger than the value used here. We conclude that the expected number is consistent with the observed number of 2 ± 1 tritons/cm² sec.

The possibility that some of the tritons came from outside the earth's atmosphere cannot be ruled out. Since no increase in the proton flux was observed in the second stack the observed tritons could not have been injected by the solar flare unless the tritons are a large fraction

of the solar particles. These would be easy to detect with balloon-borne emulsion stacks.

We are now looking for tritons in the stack flown on the first flight. If the triton production mechanism is correct they should be present there in the same abundance.

We have yet to explain the absence of deuterons, He^3 , and α particles. Because of its double charge, He^2 will have $1/4$ the lifetime of a triton of the same energy if interaction loss is neglected. The same-energy α particle will have about $1/5$ the lifetime of the triton. The observable energy intervals for helium nuclei were considerably higher than for tritons: 276 to 444 Mev for He^3 and 312 to 504 Mev for He^4 . Thus the number of protons, F_p , that can produce these helium nuclei is down by a factor of about 4 from the number that can produce tritons. The production ratio of α particles to tritons at low energies is about 10 [Bailey, 1956]. Even if this ratio were the same at high energies, which is certainly an overestimate, the triton to α particle ratio would be 2. The triton to He^3 ratio would be more like 10. Therefore it is not surprising that no helium nuclei were seen.

The absence of deuterons is more difficult to understand. A deuteron should have about the same lifetime as a triton of the same energy. About the same number of protons are effective in producing observable deuterons. The ratio of the production cross sections for deuterons to tritons with energies below 40 Mev produced by 190- and 332-Mev protons is about 3 [Bailey, 1956; Deutsch, 1955]. In order to account for the lack of deuterons we must assume that this ratio becomes $\lesssim 1$ at high energies. It is also possible that the interaction cross section is larger for deuterons than for tritons.

This mechanism for producing tritons can account for no more than 10^{-3} tritons/cm² sec at the surface of the earth and therefore cannot be responsible for the flux of 1 triton/cm² sec which Craig [1957] concluded was necessary to explain the observed tritium content of sea water.

Conclusions. 1. The spectrum of trapped protons with energies from 10 to 700 Mev at 1100-km altitude has been calculated by assuming that energy loss and collision loss are the only loss mechanisms for the protons. The cal-

culated spectrum agrees with the data in the energy region where the flux has been measured. This implies that nonadiabatic losses are small for the protons sampled in our experiments.

2. The fact that the proton content of the inner belt was not increased by the exceedingly strong solar flare of May 10, 1959, is evidence against solar injection.

3. A flux of 2 ± 1 tritons/cm² sec between 126 and 200 Mev was observed in the stack exposed on the second flight. No other nuclei heavier than protons were seen. This flux of tritons can be attributed to collisions of high-energy trapped protons with air nuclei. The absence of helium nuclei is accounted for. The absence of deuterons can be explained by a low production or a high interaction cross section. We are now looking for tritons in the stack exposed on the first flight.

4. The above evidence demonstrates that most, if not all, of the protons trapped in the lower radiation belt are due to cosmic-ray albedo neutron decays.

Acknowledgments. It is a pleasure to acknowledge the assistance and cooperation of personnel in the Space Technology Laboratories both at Los Angeles and Cape Canaveral, General Electric Missile and Space Vehicle Department, and Avco Research and Development Division. We especially thank Dr. John Lindner of STL for coordinating the experiment with the missile requirements. We are grateful to Mr. Al Oliver and Mr. George Leipelt for assembly and processing of the stacks. We are especially indebted to Mrs. Barbara Allen, Miss Patricia Banks, Mrs. Irene Brown, Mrs. Theodora Hilliard, and Mrs. Nancy Stratton for locating the tracks and making measurements on them.

Note added in proof. One deuteron, one triton, and 250 protons have been identified in the stack flown on the first flight. The resulting fluxes are in agreement with the fluxes and the production mechanism given in this paper.

REFERENCES

- Bailey, L. E., Angle and energy distributions of charged particles from the high-energy nuclear bombardment of various elements, *Univ. Calif. Radiation Lab. Rept., UCRL 3334*, unpublished, 1956.
- Christofilos, N. C., Trapping and lifetime of charged particles in the geomagnetic field, *Univ. Calif. Radiation Lab. Rept., UCRL 5407*, unpublished, 1958.
- Craig, H., *Phys. Rev.*, **105**, 1125, 1957.

- Currie, Libby, and Wolfgang, *Phys. Rev.*, **101**, 1557, 1956.
- Deutsch, R. W., *Phys. Rev.*, **97**, 1110, 1955.
- Fireman, E. L., and F. S. Rowland, *Phys. Rev.*, **97**, 780, 1955.
- Gowler, P. H., and D. H. Perkins, *Phil. Mag.*, **46**, 587, 1955.
- Heden, S. C., and R. S. White, *Phys. Rev. Letters*, **3**, 9, 1959. These earlier data are multiplied by 4π for use in this paper.
- Jess, W. N., *Phys. Rev. Letters*, **3**, 11, 1959.
- Hess, Patterson, Wallace, and Chupp, *Phys. Rev.*, **116**, 445, 1959.
- Lenchek, A. M., and S. F. Singer, *Bull. Am. Phys. Soc.*, **5**, 47, 1960.
- Singer, S. F., *Phys. Rev. Letters*, **1**, 181, 1958.
- Singer, S. F., *Phys. Rev. Letters*, **3**, 188, 1959.
- Sosnovsky, Spivak, Prokofiev, Kutikov, and Dobrinin, *Nuclear Phys.*, **10**, 395, 1959.
- Welch, J. A., and W. A. Whitaker, *J. Geophys. Research*, **64**, 909, 1959.

(Manuscript received March 17, 1960.)

Cosmic-Ray Characteristics Registered in Chacaltaya during Unusually High Solar Activity

I. ESCOBAR¹ AND E. MALDONADO

*Laboratorio de Fisica Cósmica
Universidad Mayor de San Andrés, Bolivia, and Centro Brasileiro de Pesquisas Físicas
Brasil*

N. W. NERURKAR² AND R. ROMERO

*Laboratorio de Fisica Cósmica
Universidad Mayor de San Andrés, Bolivia*

Abstract. Cosmic-ray meson intensity at Chacaltaya (elevation 5220 meters above sea level and magnetic latitude 4°S) registered a 9.5 per cent decrease during three magnetic storms of July 1959. In addition a small increase of 1 to 2 per cent was observed in association with the first and last storms which commenced at Chacaltaya at about noon. These features have been discussed in relation to different magnetic field structures contained in the ionized gas ejected by the sun, and it is shown that the gas had partly turbulent and partly coherent magnetic fields in it when it arrived in the earth's vicinity.

On the Chacaltaya Mountain in Bolivia (elevation 5220 meters above sea level, geomagnetic latitude 4°S), the cosmic-ray meson intensity is being monitored by vertical narrow-angle (semiangles 20° × 20°) and by wide-angle cubical (semiangles 45° × 45°) telescopes. The narrow-angle telescope, with a triple coincidence arrangement, has an average counting rate of 9000 counts per hour, which includes 109 (1.2 per cent) accidental counts. The wide-angle one is derived from the double coincidence between the two trays of the narrow-angle telescope. It has a counting rate of 42,000 counts per hour, which includes all those registered by the narrow-angle telescope, and the accidental counting rate is 540 (1.3 per cent) per hour. In both telescopes an absorber of 9 cm of lead is used.

The barometric pressure at Chacaltaya shows very little fluctuation, the maximum change being about 2 mb on successive days and about 7 mb over a period of 6 months [Weil, 1959]. The large day-to-day changes in cosmic-ray in-

tensity, associated with high solar activity in the period of solar maximum, masked the small effect due to pressure, and it was difficult to determine a pressure coefficient from day-to-day changes in cosmic-ray intensity and pressure. The pressure was, however, found to exhibit prominently a semidiurnal wave with an amplitude of about 0.6 mb. Over a period of 6 months, a correlation of 0.96 was found between the semidiurnal periodicity of the cosmic-ray intensity and the pressure. The pressure coefficient derived from it was 0.4 per cent per mb. This is about double that found at sea level for meson intensity and is in rough agreement with the value expected from the intensity depth curve. Because of the lack of radiosonde observations near by, data on the distribution of temperature at different levels in the atmosphere were not available. The cosmic-ray intensity was, therefore, corrected for pressure only, using the above pressure coefficient.

During a period of 1 week, from July 10 to 17, a large sunspot group having magnetic fields of complex structure was extremely active. [Trotter, 1959]. It produced three solar flares of 3+ type on July 10, 14, and 16, respectively, each followed a day later by a magnetic storm of the sudden-commencement type.

Figure 1 shows the bihourly cosmic-ray in-

¹ Now on leave at the Department of Physics and the Fermi Institute of Nuclear Studies, University of Chicago.

² On leave from Physical Research Laboratory, India, under UNESCO Technical Assistance Program.

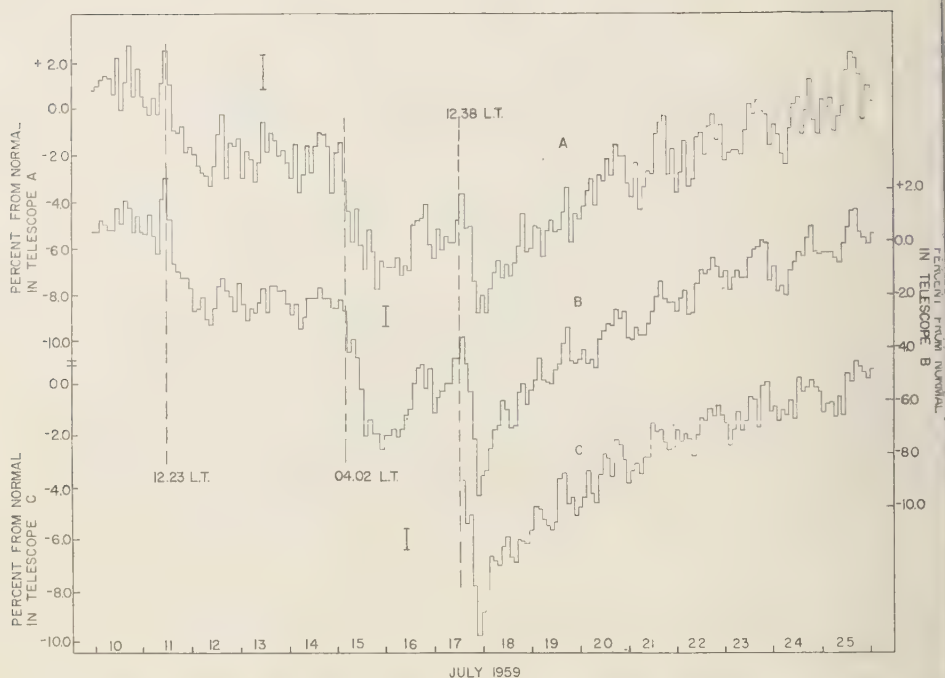


Fig. 1. Bihourly cosmic-ray meson intensity fluctuations in vertical telescopes at Chacaltaya associated with magnetic storms of July 11, 15, and 17, 1959. The semiangles of telescope A are $20^\circ \times 20^\circ$; of telescope B, $45^\circ \times 45^\circ$; and of telescope C, $45^\circ \times 45^\circ$. The dotted lines indicate the commencement of the magnetic storm at $60^\circ W$ longitude.

tensity observed by the narrow- and wide-angle telescopes at Chacaltaya during this period. The times of commencement of the magnetic storms are also indicated. The normal intensity for each telescope is assumed to be an average of the daily intensity observed 1 week before the beginning of the events discussed here and 1 week after July 25, when the cosmic-ray intensity appeared to have recovered from the magnetic storm effects.

The first storm, on July 11, produced in both telescopes about a 3 per cent decrease, which was gradual, the minimum being reached about 20 hours later. Although this storm finished on July 13, there was no appreciable sign of recovery of intensity until July 15. The magnetic storm of July 15 was the strongest storm in the present solar cycle, causing the daily magnetic *A* index to rise as high as 167 [Trotter, 1959]. The associated decrease in cosmic-ray intensity was about 5 per cent,

which was also gradual. This storm was of short duration, and the intensity showed the usual characteristics of recovery the next day.

The third storm, on July 17, caused another 3 per cent decrease in the meson intensity, which thereafter climbed gradually, reaching the normal by about July 25. These magnetic storms occurred so close together that there was not sufficient time for the intensity to recover from the decreases of the previous storm. Their effect was, therefore, cumulative, and the meson intensity at the equator in the cubical telescopes dropped to about 9.5 per cent below the normal level, this being the largest decrease ever recorded in the meson intensity at the equator. The neutron monitor intensity at Chicago and at Climax also exhibited similar features, although the decreases were three times larger and the intensity did not recover to the preactivity level but climbed only to the level of July 12 in the same period.

Apart from these decreases, an interesting feature shown in Figure 1 is that the first and last storms, which commenced at Chacaltaya about 1230 hours, were associated with 1 to 2 per cent increase lasting for 2 to 4 hours before the storm decrease set in. Such sharp increases have not been observed in neutron intensity at Climax and Chicago, although there is an indication that the neutron intensity during 12 hours before the storm decrease was about 1 per cent higher than normal. The second storm, which began at Chacaltaya at 0402, did not show any sharp increase in the meson intensity. Whether a slow increase in the neutron intensity at high latitudes was observed or not is difficult to ascertain, since the intensity before the storm had not recovered from the previous storm decrease.

If the above features are attributed to the presence, in the earth's vicinity, of an ionized gas ejected from the surface of the sun simultaneously with the 3+ solar flare, it is possible to derive some of the characteristics of the gas. In each case, such a flare occurred a day earlier than the commencement of the magnetic storm. The gas must, therefore, have been ejected in a cone wide enough to engulf the earth, and prior to the magnetic storm, the stream was moving towards the earth in a 12-hour direction. The usual picture of a stream of gas approaching the earth from the left side (18-hour direction) will not hold in this case.

Since this gas originated from an active region on the sun, it would have contained magnetic field. This field could not have been turbulent as suggested by Morrison [1956], since such a structure has been shown to be completely inadequate to cause the decreases of a few per cent observed with magnetic storms [Dorman, 1957]. Let us, therefore, assume the field to be completely coherent in nature and to resemble that of the general magnetic field of the sun or the regular field structure of the sunspots. Low-energy cosmic rays impinging on such a gas will be reflected so that, as the gas expands in the space, it will displace in part low-energy cosmic rays from the region it occupies. If there are interplanetary magnetic fields, these displaced particles will not wander far away, and long before the gas comes in the vicinity of the earth the intensity of low-energy

cosmic radiation on the earth will be greater than normal. The amount of this increase will depend on the dimensions of the gas and on the strength of the frozen magnetic field and interplanetary fields, and is, therefore, likely to vary with individual storms. Moreover, this additional radiation on the earth will have been made isotropic by the interplanetary magnetic fields so that its effect on the earth will not have appreciable longitude dependence. High-energy particles passing through the gas are accelerated in some directions and decelerated in others, and when the gas is far away from the earth, their effect is likely to be negligible. It is thus possible to understand an increase of ~ 1 per cent in neutron monitor data during about 12 hours before the commencement of the magnetic storms.

When the gas is near the earth, the effect of interplanetary magnetic fields between the earth's magnetic field and the advancing front of the gas can be neglected. Figure 2(a) shows the directions in which high-energy particles will be impinging on the earth's magnetic field after passing through the gas. It is seen that they are decelerated sometime before mid-day and accelerated thereafter, and the meson telescopes, responding to high-energy primaries from a wide range of directions from the front of the gas, will first show a small decrease and then an increase for a few hours before the final decrease due to the magnetic storm sets in.

Figure 2(b) shows the directions in which low-energy particles impinge on the earth's magnetic field after being reflected from the advancing front of the gas. Although these particles traverse a smaller part of the gas than high-energy particles, and hence have less energy gain, the relative increase in their energy is comparable to, or even more than, that of high-energy particles. Moreover, most of these particles striking the earth after emerging from the front of the gas are accelerated so that neutron monitors, accepting these particles from a wide range of directions, will show a larger increase than that in the meson telescopes. Such increases have not been observed, and it is rather unlikely that the gas had completely coherent magnetic field within it.

Dorman [1957, p. 443] has shown that the strength of the coherent frozen magnetic field,

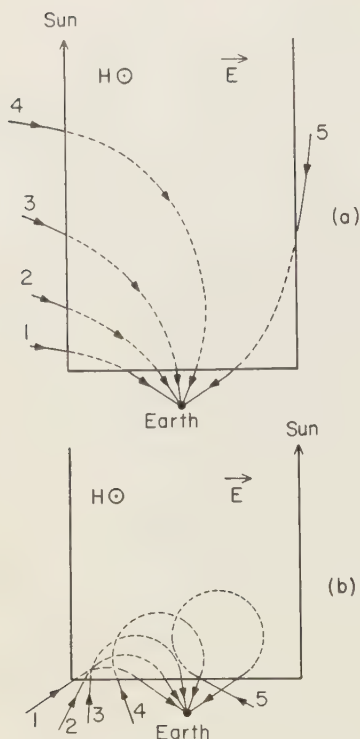


Fig. 2. Deflections of (a) high- and (b) low-energy particles (incident on the earth) in the magnetic field of the solar gas. High-energy particles are accelerated in directions 1 to 4 and are decelerated in direction 5; low-energy particles are accelerated in all directions shown in the figure.

derived from the magnitude of intensity decreases associated with magnetic storms, is not sufficient to ensure complete stability of the solar gas with respect to the appearance of turbulence. He points out, however, that the time to render the gas turbulent is of the order of passage time of the gas from the sun to the earth. It appears, therefore, that, although the gas carries coherent magnetic fields within it while emerging from the sun, in general the magnetic field will be rendered partly turbulent (i.e., the magnetic lines of force are not completely entangled so that there still exists a component in the direction of the original frozen field) when the gas comes near the earth.

Since this gas has a coherent magnetic field for the earlier part of the journey and a part

of this magnetic field until it reaches the earth, it will still displace low-energy particles on its way and cause a small increase in the intensity of neutron monitor for about 12 hours before the storm, as explained earlier. In respect to high-energy particles, the gas will behave more as though it had a coherent magnetic field, and when it comes in the vicinity of the earth, these particles are accelerated while striking the earth's magnetic field near 12-hour direction, as shown in Figure 2(a), and an anisotropic increase will be registered in meson detectors. Because of the partial turbulence, the trajectories of low-energy particles inside the gas will not be as regular as those shown in Figure 2(b). It is very likely that in some directions (which will not be fixed) these particles will be accelerated and in some others they will be decelerated, and a cosmic-ray neutron monitor, which responds mainly to low-energy cosmic-ray primaries and which accepts cosmic rays from a wide range of directions, will not show any appreciable anisotropic effect.

The characteristics of cosmic-ray fluctuations observed at Chacaltaya and at high latitudes can now be examined in the light of the above discussion. Since the gas was advancing toward the earth, its position was in the 12-hour direction. The first and the last storms started at Chacaltaya near noon, at Chicago at about 10 hours, and at Climax at about 09 hours. Hence only those primaries that suffered small deflections in the earth's magnetic field had passed through the gas. This condition was satisfied by high-energy primaries at Chacaltaya but by most of the primaries at high latitudes. There was therefore an increase in the meson intensity at Chacaltaya just before the storm decrease but no appreciable sharp increase was registered by neutron monitors, which are affected most by changes in low-energy primaries.

The second storm was the strongest of the three, and in the strength of the trapped magnetic field as well as in the turbulence in the associated solar gas could have been the greatest. In this case medium-energy particles (15 to 25 bev) would behave similarly to low-energy particles. This storm started at Chacaltaya at 0402, so that only medium-energy primaries incident at Chacaltaya, being deflected considerably in the earth's magnetic field

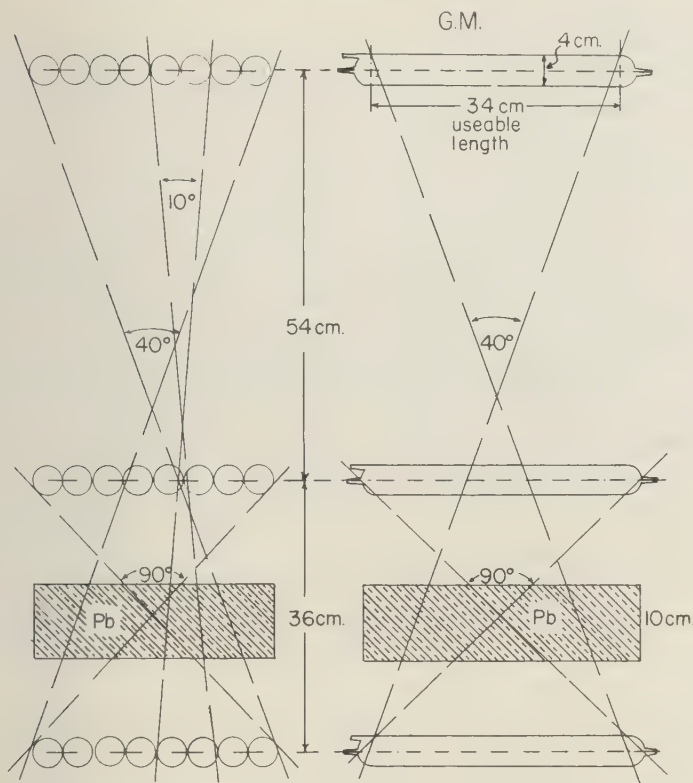


Fig. 3. Geometry of the cubical and narrow-angle meson telescope.

passed through the gas, but with no appreciable effect. Hence, no increase was registered at Chacaltaya. Only very low-energy primaries identical at Chicago and Climax were received from the front of the gas, and they too registered no anisotropic effect at these stations.

It is difficult to say from what distance in the interplanetary space the solar gas with magnetic field would cause an anisotropic effect to be registered on the earth. In this period of high solar activity, conditions in the interplanetary space would be quite chaotic, so that the trajectories of the primary particles far from the earth would be quite different from those just outside the earth's magnetic field, and the above picture might hold only when the solar gas is near the earth.

Because of some coherent magnetic field, such gas had a deficiency of cosmic-ray particles,

and when it engulfed the earth, it produced a decrease in cosmic-ray intensity there. This deficiency being more for low-energy particles, the decrease was greater in the cosmic-ray intensity observed by neutron monitors. It is thus seen that the ionized gas from the sun, containing coherent frozen magnetic fields which are rendered partly turbulent when it comes in the vicinity of the earth, explains most of the features in cosmic-ray intensity registered at Chacaltaya and high latitudes in association with the magnetic storms of July 1959.

Conclusion. The cosmic-ray meson intensity at Chacaltaya registered decreases in association with three magnetic storms, which took place between July 10 and 17, 1959. Because of the close proximity of the storms, their effect was cumulative, and the cosmic-ray intensity

in narrow- and wide-angle telescopes at the equator decreased to about 9.5 per cent below the normal.

The first and the last storms, which began at Chacaltaya near noon, were associated with a small increase of 1 to 2 per cent for 2 to 4 hours before the storm decrease. This feature was not observed in the cosmic-ray neutron intensity at high latitudes, but there is an indication that during 12 hours preceding the magnetic storms the cosmic-ray neutron intensity was slightly higher than normal. It is shown that an ionized gas, ejected by the sun and carrying within it completely coherent magnetic fields, could explain most of the above-mentioned features of cosmic-ray variations except that there would be a larger increase in the neutron intensity than that observed. If, however, the field structure was partly turbulent and partly coherent, all the above experimental observations could be satisfactorily explained. It is concluded that solar gas ejected during high solar activity of July 1959 had a mixed mag-

netic field when it arrived in the vicinity of the earth.

Acknowledgments. The Atomic Energy Department of the Government of India and UNESCO are due our thanks for the installation of meso-telescopes at Chacaltaya. We are also grateful to Professor J. A. Simpson of the University of Chicago for making the data of neutron monitor available to us before publication, to Dr. Dorothy Trotter of the High Altitude Observatory, Boulder, Colorado, for the solar and geophysical data and to Ing. R. Weil and Ing. J. Hersil for their helpful comments on this paper.

REFERENCES

- Dorman, L. I., *Cosmic Ray Variations*, p. 387, Statistical Publishing House for Technical and Scientific Literature, Moscow, 1957; Technical Document Liaison Office, Wright Patterson Air Force Base, Ohio.
Morrison, P., *Phys. Rev.*, **101**, 1397, 1956.
Trotter, D., Preliminary reports on solar activity No. TR 412, High Altitude Observatory, Boulder, Colorado, January 24, 1959.
Weil, R., Proceedings of cosmic-ray conference in Bariloche, Argentina, July 1959.

(Manuscript received January 14, 1960.)

The Influence of the Solar Radiation Pressure on the Motion of an Artificial Satellite

PETER MUSEN

*Theoretical Division, Goddard Space Flight Center
National Aeronautics and Space Administration
Washington, D. C.*

Abstract. This article reports an investigation of the effect of solar radiation pressure on the motion of an artificial satellite. The theory has been applied to the orbit of the Vanguard I satellite, and is found to produce significant perturbations in the perigee height of that satellite. In the case of a satellite with a large ratio of area to mass the major terms introduced by solar radiation pressure can reduce the perigee distance at the rate of 1 to 2 km per day, so that the lifetime of the satellite will become considerably shorter than it would be without this effect.

Introduction. The perturbing effects of solar radiation pressure on satellite orbits have been generally considered by celestial mechanicians to be negligible. However, the difference between observed and theoretical values of perigee height for the Vanguard I satellite have suggested a re-examination of radiation pressure as a possible source of the discrepancy. We have carried out an investigation of the radiation-pressure perturbation and developed an analytical theory of resonance for the case in which the perigee follows the motion of the sun. It is found that when resonance conditions are nearly satisfied the radiation pressure may produce substantial orbit perturbations over an interval of several months. For a satellite with a large ratio of area to mass the major terms introduced by solar radiation pressure can reduce the perigee distance at the rate of 1 to 2 km per day, so that the lifetime of the satellite becomes considerably shorter than it would be without this effect. Radiation pressure is also found to produce significant perturbations in the orbit of the Vanguard I satellite which remove the principal discrepancy between theory and observation in the analysis of the Vanguard I orbit [Musen, 1959; Musen, 1960; and Bryant, 1960].

The terms of long period make the principal contribution to the orbit perturbations. In the present investigation we have therefore neglected the effect of the earth's shadow which has the period of the satellite's mean motion. The shadow effect does not change the nature of

the perturbations, although it produces a change in their amplitudes. We have also neglected all other periodic terms having the mean anomaly of the satellite in the argument.

The vectorial method is used in the development to obtain several kinematical relations. The equations for the scalar elements are deduced from the equations for the vectorial elements. All elements except the semimajor axis contain long-period terms, but the semimajor axis is affected by short-period variations only and is therefore not subject to substantial perturbations.

Perturbations in the orbit plane. Let us designate the gravitational constant by G , the mass of the earth by M and its equatorial radius by ρ . Let \mathbf{R} be the unit vector directed along the normal to the orbit plane, \mathbf{P} be the unit vector directed from the center of the earth to perigee, and let $\mathbf{Q} = \mathbf{R} \times \mathbf{P}$. The position and the velocity vectors of the satellite are represented by \mathbf{r} and \mathbf{v} , respectively; the radius vector of the satellite will be designated by r , the true anomaly by f , the mean anomaly by l ; and the other elliptic elements will be designated, using the standard notations, by ω , Ω , i , e , a , n . The mean longitude of the sun on the ecliptic will be designated by λ' , and the mean motion of the sun will be designated by n' . Let ϵ be the inclination of the equator to the ecliptic, \mathbf{i} the unit vector directed from the center of the earth toward the vernal equinox, \mathbf{k} the unit vector normal to the earth's equator, and let $\mathbf{j} = \mathbf{k} \times \mathbf{i}$.

Finally, let \mathbf{u}^0 be the unit vector directed from the center of the earth toward the sun. Neglecting the eccentricity of the earth's orbit, we can put

$$\mathbf{u}^0 = \mathbf{i} \cos \lambda' + \mathbf{j} \cos \epsilon \sin \lambda' + \mathbf{k} \sin \epsilon \sin \lambda' \quad (1)$$

The solar radiation pressure will be

$$\mathbf{F} = F\mathbf{u}^0 \quad F < 0 \quad (2)$$

F = constant for a spherical satellite; for the satellite of nonspherical form we must make a certain assumption about the average value of F and use the average value in the development. We shall deal with the vectorial element

$$\mathbf{g} = \epsilon \mathbf{P} \quad (3)$$

and with the time variation of this vector with respect to a system of coordinates rigidly connected to the osculating orbit plane. In other words, we shall deal with the motion of \mathbf{P} in this plane. For that purpose it is convenient to use Herrick's equation [Herrick, 1948]

$$GM \, d\mathbf{g}/dt = \mathbf{\Gamma} \cdot \mathbf{F} \quad (4)$$

where

$$\mathbf{\Gamma} = 2\mathbf{r}\mathbf{v} - \mathbf{v}\mathbf{r} - \mathbf{r} \cdot \mathbf{v} \mathbf{I} \quad (5)$$

\mathbf{r} and \mathbf{v} in this case are given, not with respect to our inertial system, but with respect to a system rigidly connected to the osculating orbit plane. The notations $\mathbf{r}\mathbf{v}$ and $\mathbf{v}\mathbf{r}$ represent the dyadic products; in other words, they are the

column vector · row vector

and \mathbf{I} is the planar idemfactor (the planar unit matrix). Substituting

$$\mathbf{r} = \mathbf{P}r \cos f + \mathbf{Q}r \sin f \quad (6)$$

$$\mathbf{v} = -\mathbf{P} \frac{\sqrt{GM} \sin f}{\sqrt{a(1-e^2)}} + \mathbf{Q} \frac{\sqrt{GM} (\cos f + e)}{\sqrt{a(1-e^2)}} \quad (7)$$

$$\mathbf{I} = \mathbf{P}\mathbf{P} + \mathbf{Q}\mathbf{Q} \quad (8)$$

into (5), and, taking

$$GM = n^2 a^3 \quad (9)$$

in consideration, we deduce

$$\begin{aligned} \mathbf{\Gamma} = & \frac{na^2}{\sqrt{1-e^2}} \left\{ -\frac{r}{a} (e \sin f \right. \\ & + \frac{1}{2} \sin 2f) \mathbf{P}\mathbf{P} \\ & + \frac{1}{2} \frac{r}{a} \sin 2f \mathbf{Q}\mathbf{Q} \\ & + \left[\frac{r}{a} (\frac{1}{2} + e \cos f \right. \\ & + \frac{1}{2} \cos 2f) + 1 - e^2 \left. \right] \mathbf{P}\mathbf{Q} \\ & - \left[\frac{1}{2} \frac{r}{a} (1 - \cos 2f) \right. \\ & + 1 - e^2 \left. \right] \mathbf{Q}\mathbf{P} \left. \right\} \end{aligned} \quad (10)$$

In order to separate the long periodic part $\mathbf{\Gamma}$ from the short periodic one we must develop the coefficients of the dyadic products in Fourier series with respect to the mean anomaly and retain only the constant terms in the development. Using Cayley's tables, we find that the constant parts of the coefficients $\mathbf{P}\mathbf{Q}$ and of $\mathbf{Q}\mathbf{P}$ are equal to $\pm \frac{3}{2}(1-e^2)$. The constant parts of the other coefficients are equal to zero. Thus, we have for the long periodic part of $\mathbf{\Gamma}$

$$[\mathbf{\Gamma}] = \frac{3}{2} na^2 \sqrt{1-e^2} (\mathbf{P}\mathbf{Q} - \mathbf{Q}\mathbf{P})$$

but

$$\mathbf{R} \times \mathbf{I} = \mathbf{R} \times (\mathbf{P}\mathbf{P} + \mathbf{Q}\mathbf{Q}) = \mathbf{Q}\mathbf{P} - \mathbf{P}\mathbf{Q}$$

and we have a simple relation

$$[\mathbf{\Gamma}] = -\frac{3}{2} na^2 \sqrt{1-e^2} \mathbf{R} \times \mathbf{I} \quad (11)$$

Substituting (3) and (11) into (4) we deduce for the long periodic part in $\epsilon \mathbf{P}$

$$\frac{d(\epsilon \mathbf{P})}{dt} = -\frac{3}{2} \frac{na^2 \sqrt{1-e^2}}{GM} \mathbf{R} \times \mathbf{F} \quad (12)$$

We see that the time variation of $\epsilon \mathbf{P}$ is normal to the component of \mathbf{F} lying in the orbit plane. The vector \mathbf{P} in the moving system of coordinates is affected only by the rotation about \mathbf{R} . The angular velocity of rotation

$$\mathbf{R} \, d\pi/dt$$

and

$$\frac{d\mathbf{P}}{dt} = \frac{d\pi}{dt} \mathbf{R} \times \mathbf{P} = \frac{d\pi}{dt} \mathbf{Q} \quad (13)$$

follows from (12) and (13)

$$\frac{d\mathbf{P}}{dt} + e \frac{d\pi}{dt} \mathbf{Q} = -\frac{3}{2} \frac{na^2 \sqrt{1-e^2}}{GM} \mathbf{R} \times \mathbf{F}$$

$$\frac{de}{dt} = +\frac{3}{2} \frac{na^2 \sqrt{1-e^2}}{GM} \mathbf{Q} \cdot \mathbf{F} \quad (14)$$

$$e \frac{d\pi}{dt} = -\frac{3}{2} \frac{na^2 \sqrt{1-e^2}}{GM} \mathbf{P} \cdot \mathbf{F} \quad (15)$$

substituting

$$\begin{aligned} &= \mathbf{i} [+\cos^2(i/2) \cos(\omega + \Omega) \\ &\quad + \sin^2(i/2) \cos(\omega - \Omega)] \\ &\quad + \mathbf{j} [+\cos^2(i/2) \sin(\omega + \Omega) \\ &\quad - \sin^2(i/2) \sin(\omega - \Omega)] \\ &\quad + \mathbf{k} \sin i \sin \omega \end{aligned} \quad (16)$$

to (15) and

$$\begin{aligned} &= \mathbf{i} [-\cos^2(i/2) \sin(\omega + \Omega) \\ &\quad - \sin^2(i/2) \sin(\omega - \Omega)] \\ &\quad + \mathbf{j} [+\cos^2(i/2) \cos(\omega + \Omega) \\ &\quad - \sin^2(i/2) \cos(\omega - \Omega)] \\ &\quad + \mathbf{k} \sin i \cos \omega \end{aligned} \quad (17)$$

to (14), and taking (1)-(2) into account, we obtain

$$\begin{aligned} &= -\frac{3F}{2GM} na^2 \sqrt{1-e^2} \\ &\cdot \{ +\cos^2(i/2) \sin^2(\epsilon/2) \sin(\omega + \Omega + \lambda') \\ &\quad + \cos^2(i/2) \cos^2(\epsilon/2) \sin(\omega + \Omega - \lambda') \\ &\quad + \sin^2(i/2) \cos^2(\epsilon/2) \sin(\omega - \Omega + \lambda') \\ &\quad + \sin^2(i/2) \sin^2(\epsilon/2) \sin(\omega - \Omega - \lambda') \\ &\quad - \frac{1}{2} \sin i \sin \epsilon \sin(\omega + \lambda') \\ &\quad + \frac{1}{2} \sin i \sin \epsilon \sin(\omega - \lambda') \} \end{aligned} \quad (18)$$

$$e \frac{d\pi}{dt} = -\frac{3F}{2GM} na^2 \sqrt{1-e^2}$$

$$\begin{aligned} &\cdot \{ +\cos^2(i/2) \sin^2(\epsilon/2) \cos(\omega + \Omega + \lambda') \\ &\quad + \cos^2(i/2) \cos^2(\epsilon/2) \cos(\omega + \Omega - \lambda') \\ &\quad + \sin^2(i/2) \cos^2(\epsilon/2) \cos(\omega - \Omega + \lambda') \\ &\quad + \sin^2(i/2) \sin^2(\epsilon/2) \cos(\omega - \Omega - \lambda') \\ &\quad - \frac{1}{2} \sin i \sin \epsilon \cos(\omega + \lambda') \\ &\quad + \frac{1}{2} \sin i \sin \epsilon \cos(\omega - \lambda') \} \end{aligned} \quad (19)$$

Perturbations in the position of the orbit plane.
The angular velocity of rotation of the osculating orbit plane, considered as a rigid body,

$$\boldsymbol{\psi} = \frac{na^2}{\sqrt{1-e^2}} \frac{\mathbf{r} \cdot \mathbf{R} \cdot \mathbf{F}}{a \cdot GM} \quad (20)$$

The part of \mathbf{r} independent of l is

$$-\frac{3}{2} \mathbf{P} a e$$

and, consequently, the long periodic part of $\boldsymbol{\psi}$ is

$$[\boldsymbol{\psi}] = -\frac{3}{2} \frac{na^2 e}{\sqrt{1-e^2}} \frac{\mathbf{P} \cdot \mathbf{R} \cdot \mathbf{F}}{GM} \quad (21)$$

The variation of \mathbf{R} is caused only by the rotation of the osculating orbit plane, and we have then for the long periodic part in \mathbf{R}

$$d\mathbf{R}/dt = -\mathbf{R} \times [\boldsymbol{\psi}]$$

or

$$\frac{d\mathbf{R}}{dt} = +\frac{3}{2} \frac{na^2 e \mathbf{Q} \cdot \mathbf{R} \cdot \mathbf{F}}{GM \sqrt{1-e^2}} \quad (22)$$

and we conclude that the long-period time variation of \mathbf{R} , caused by the radiation pressure, consists of the rotation of \mathbf{R} about \mathbf{P} with the angular velocity proportional to the cosine of the angle between the direction to the sun and \mathbf{R} .

This time variation is zero at the moment when \mathbf{R} is normal to \mathbf{u}^s , in particular when \mathbf{R} is normal to the ecliptic. From equation (22) we can also deduce the equations for i and Ω . The angular velocity $[\boldsymbol{\psi}]$ can be decomposed into the geometrical sum of (1) the angular velocity di/dt of the rotation of the orbit plane around the

line of nodes and (2) the angular velocity $\sin i \omega$ $d\Omega/dt$ of the rotation around the vector $\mathbf{P} \sin \omega + \mathbf{Q} \cos \omega$. We have for the long-period variation in i and Ω , taking (21) into account,

$$\begin{aligned} & (\mathbf{P} \cos \omega - \mathbf{Q} \sin \omega) \frac{di}{dt} \\ & + (\mathbf{P} \sin \omega + \mathbf{Q} \cos \omega) \cdot \sin i \frac{d\Omega}{dt} \\ & = -\frac{3}{2} \cdot \frac{na^2 e}{\sqrt{1-e^2}} \cdot \frac{\mathbf{P} \cdot \mathbf{R} \cdot \mathbf{F}}{GM} \end{aligned}$$

We deduce from this last equation, after the scalar multiplication by $\mathbf{P} \cos \omega - \mathbf{Q} \sin \omega$ and by $\mathbf{P} \sin \omega + \mathbf{Q} \cos \omega$ and taking $(\mathbf{P} \cos \omega - \mathbf{Q} \sin \omega) \cdot \mathbf{k} = 0$ and $\mathbf{P} \cdot \mathbf{k} = \sin i \sin \omega$ into consideration,

$$\frac{di}{dt} = -\frac{3}{2} \cdot \frac{na^2 e \mathbf{R} \cdot \mathbf{F} \cos \omega}{GM \sqrt{1-e^2}} \quad (23)$$

$$\sin i \frac{d\Omega}{dt} = -\frac{3}{2} \cdot \frac{na^2 e \mathbf{R} \cdot \mathbf{F} \sin \omega}{GM \sqrt{1-e^2}} \quad (24)$$

Taking

$$\mathbf{R} = \mathbf{i} \sin i \sin \Omega - \mathbf{j} \sin i \cos \Omega + \mathbf{k} \cos i \quad (25)$$

and (1)-(2) into consideration, we have after some easy trigonometrical transformations

$$\begin{aligned} \frac{di}{dt} &= -\frac{3}{4} \cdot \frac{Fna^2 e}{GM \sqrt{1-e^2}} \\ &\cdot \{ +\sin i \sin^2 (\epsilon/2) \sin (\omega + \Omega + \lambda') \\ &- \sin i \sin^2 (\epsilon/2) \sin (\omega - \Omega - \lambda') \\ &+ \sin i \cos^2 (\epsilon/2) \sin (\omega + \Omega - \lambda') \\ &- \sin i \cos^2 (\epsilon/2) \sin (\omega - \Omega + \lambda') \\ &+ \cos i \sin \epsilon \sin (\omega + \lambda') \\ &- \cos i \sin \epsilon \sin (\omega - \lambda') \} \\ \sin i \frac{d\Omega}{dt} &= +\frac{3}{4} \cdot \frac{Fna^2 e}{GM \sqrt{1-e^2}} \\ &\cdot \{ +\sin i \sin^2 (\epsilon/2) \cos (\omega + \Omega + \lambda') \\ &- \sin i \sin^2 (\epsilon/2) \cos (\omega - \Omega - \lambda') \} \end{aligned} \quad (26)$$

$$\begin{aligned} & + \sin i \cos^2 (\epsilon/2) \cos (\omega + \Omega - \lambda') \\ & - \sin i \cos^2 (\epsilon/2) \cos (\omega - \Omega + \lambda') \\ & + \cos i \sin \epsilon \cos (\omega + \lambda') \\ & - \cos i \sin \epsilon \cos (\omega - \lambda') \} \end{aligned}$$

These equations could also be obtained in standard way.

The integration problem. If we assume that we do not have sharp resonance conditions, first-order perturbations can easily be obtained by the integration of equations (18), (19), (20) and (27), assuming that the elements in the right hand sides are replaced by their mean values. The oblateness of the earth produces the secular motions of the node and of the argument of perigee, for which we have

$$\omega = \omega_0 + \frac{6k_2 p^2 n \left(1 - \frac{5}{4} \sin^2 i\right)}{a^2 (1-e^2)^2} (t - t_0)$$

$$\Omega = \Omega_0 - \frac{3k_2 p^2 n \cos i}{a^2 (1-e^2)^2} (t - t_0)$$

The resonance case. The resonance case deserves special attention and a special treatment. The most interesting resonance occurs when the perigee of the satellite closely follows the sun, i.e., when the critical argument, in the terminology of celestial mechanics, is

$$\omega + \Omega - \lambda'$$

The term with this argument is the most influential one in the development of the radiative perturbations in the case of Vanguard I.

In order to simplify the exposition we shall adopt the system of units in use at the Vanguard Computer Center in the computation of the general oblateness perturbations. We put

$$G = 1 \quad M = 1 \quad \rho = 1$$

and we use the system of coordinates rotating uniformly in the equatorial plane with angular velocity equal to the mean motion of the sun about the ecliptic. In our exposition we follow the line of thought laid down by Brown in his planetary theory [Brown and Shook, 1933], modifying the form of the disturbing function to serve our purpose, and, as Brown did in the

anetary case, we will reduce our problem to an equation similar in form to the equation of the motion of a mathematical pendulum. The modified canonical set of Poincaré

$$\begin{aligned} x_1 &= \sqrt{a} (1 - \sqrt{1 - e^2}) \\ y_1 &= -\omega - \Omega + \lambda' \\ x_2 &= \sqrt{a} \quad y_2 = l + \omega + \Omega - \lambda' \quad (28) \\ x_3 &= \sqrt{a(1 - e^2)} (1 - \cos i) \\ y_3 &= -\Omega + \lambda' \end{aligned}$$

is especially convenient here. The corresponding Hamiltonian function consists of several parts:

1. The part

$$\frac{1}{2a}$$

is contributed by the elliptic motion of the satellite.

2. The part

$$n' \sqrt{a(1 - e^2)} \cos i$$

is generated by the motion of the sun.

3. The secular part

$$\frac{k_2(1 - \frac{3}{2} \sin^2 i)}{a^3(1 - e^2)^{3/2}}$$

is produced by the oblateness of the earth.

4. The periodic part

$$-\frac{3}{2} Fae \cos^2(i/2) \cos^2(\epsilon/2)$$

$$\cdot \cos(\omega + \Omega - \lambda')$$

comes from the development of the disturbing potential $-\mathbf{F} \cdot \mathbf{r}$ into a trigonometric series.

Thus, we have

$$\begin{aligned} H &= \frac{1}{2a} + n' \sqrt{a(1 - e^2)} \cos i \\ &+ \frac{k_2(1 - \frac{3}{2} \sin^2 i)}{a^3(1 - e^2)^{3/2}} - \frac{3}{2} Fae \cos^2(i/2) \\ &\cdot \cos^2(\epsilon/2) \cos(\omega + \Omega - \lambda') \quad (29) \end{aligned}$$

or, taking (28) into consideration,

$$H = \frac{1}{2x_2^2} + n'(x_2 - x_1 - x_3)$$

$$\begin{aligned} &+ \frac{k_2}{x_2^3} \left[\frac{1}{(x_2 - x_1)^3} - \frac{3x_3}{(x_2 - x_1)^4} \right. \\ &\left. + \frac{3x_3^2}{2(x_2 - x_1)^5} \right] + k_2 K \cos y_1 \quad (30) \end{aligned}$$

where we put

$$k_2 K = -\frac{3}{2} Fae \cos^2(i/2) \cos^2(\epsilon/2) > 0$$

We have

$$\frac{dx_1}{dt} = +\frac{\partial H}{\partial y_1} \quad \frac{dy_1}{dt} = -\frac{\partial H}{\partial x_1} \quad (31)$$

The arguments y_2 and y_3 are not present in (30), and from

$$\frac{dx_2}{dt} = +\frac{\partial H}{\partial y_2} = 0 \quad \frac{dx_3}{dt} = +\frac{\partial H}{\partial y_3} = 0$$

it follows that

$$x_2 = \alpha_2 = \text{constant}$$

$$x_3 = \alpha_3 = \text{constant}$$

and we also have the integral of Jacobi

$$H = h$$

If the satellite is approximately of the size and the form of Vanguard I, the perturbations in the eccentricity are small, even if the resonance is a sharp one. The ratio F/k_2 in this case is also small, and the coefficient K might be considered to be invariable. Let us introduce a new variable ξ instead of x_1 , and a new independent variable T instead of t , by putting

$$x_1 = \alpha_1 + \sqrt{k_2} \xi \quad (32)$$

$$\sqrt{k_2} dt = dT \quad (33)$$

where α_1 is a constant to be determined.

Equations 31, if transformed to the new variables, becomes

$$\frac{d\xi}{dT} = +\frac{\partial W}{\partial y_1} \quad \frac{dy_1}{dT} = -\frac{\partial W}{\partial \xi} \quad (34)$$

where

$$\begin{aligned} W &= \frac{1}{\sqrt{k_2}} \left(k_2 \frac{\partial \phi}{\partial \alpha_1} - n' \right) \xi \\ &+ k_2 \frac{\partial^2 \phi}{\partial \alpha_1^2} \xi^2 + K \cos y_1 \quad (35) \end{aligned}$$

and

$$\phi = \frac{1}{\alpha_2^3} \left[\frac{1}{(\alpha_2 - \alpha_1)^3} - \frac{3\alpha_3}{(\alpha_2 - \alpha_1)^4} + \frac{3 \cdot \alpha_3^2}{2(\alpha_2 - \alpha_1)^5} \right] \quad (36)$$

Let us determine the constant α_1 in such a way that the condition

$$n' - k_2 \frac{\partial \phi}{\partial \alpha_1} = 0 \quad (37)$$

is satisfied. This last equation says that in the first approximation the argument y_1 does not have a secular motion. In other words, to assert (27) is the same as to assert the existence of the resonant conditions. Equation (35) becomes

$$W = \frac{1}{2} k_2 \frac{\partial^2 \phi}{\partial \alpha_1^2} \xi^2 + K \cos y_1 \quad (35')$$

and

$$\phi''_{\alpha_1^2} = \frac{\partial^2 \phi}{\partial \alpha_1^2} > 0$$

for moderate inclinations. We deduce from (34) and (35')

$$\frac{d\xi}{dT} = -K \sin y_1 \quad (38)$$

$$\frac{dy_1}{dT} = -k_2 \phi''_{\alpha_1^2} \cdot \xi \quad (39)$$

From these two last equations we obtain

$$\frac{d^2 y_1}{dT^2} = k_2 \phi''_{\alpha_1^2} \cdot K \sin y_1 \quad (40)$$

The integration of this equation is given in treatises on analytical dynamics, and it is not necessary to reproduce it here. The following three cases exist

1. The critical argument y_1 oscillates around 180° ; we have the case of libration.
2. The critical argument has a secular motion.
3. The critical argument approaches zero asymptotically.

Despite the fact that the libration of the critical argument may be large, the perturbations in x_1 are always small.

In the case of libration we have

$$\cos \frac{1}{2} y_1 = k \operatorname{sn}(\nu T, k) \\ = k \operatorname{sn}(k_2 \sqrt{K \phi''_{\alpha_1^2}} t, k) \quad (41)$$

where

$$\nu^2 = k_2 K \phi''_{\alpha_1^2} \quad (42)$$

and $0 < k < 1$ is the constant of integration. We deduce

$$\frac{dy_1}{dT} = -2k\nu \operatorname{cn}(\nu T, k) \quad (43)$$

and, taking (32), (33), (42), and (43) into consideration, we obtain

$$x_1 = \alpha_1 + 2k \sqrt{\frac{K}{\phi''_{\alpha_1^2}}} \operatorname{cn}(\nu T, k)$$

If the motion of y_1 is progressive, i.e., if y_1 has a secular motion, then we deduce

$$y_1 = \pi - 2am(\nu T, k) \\ = \pi - 2am\left(\frac{k_2}{k} \sqrt{K \phi''_{\alpha_1^2}} t, k\right)$$

and

$$\nu^2 k^2 = k_2 K \phi''_{\alpha_1^2} \\ x_1 = \alpha_1 + \frac{2}{k} \sqrt{\frac{K}{\phi''_{\alpha_1^2}}} \operatorname{dn}(\nu T, k)$$

And, finally, in the case of the asymptotic approach,

$$tg \frac{y_1}{4} = C e^{-\nu T} \quad \nu^2 = k_2 K \phi''_{\alpha_1^2} \\ y_1 \rightarrow 0, \quad \xi \rightarrow 0, \quad x_1 \rightarrow \alpha_1$$

if $T \rightarrow +\infty$.

Acknowledgment. The author wishes to express his gratitude to Drs. Robert Jastrow and John A. O'Keefe of the Theoretical Division of Goddard Space Flight Center, who suggested the investigation of this effect and with whom the author had several valuable discussions.

REFERENCES

- Brown, E. W., and C. A. Shook, *Planetary Theory*, pp. 216-249, Cambridge, 1933.
 Herrick, S., *Publs. Astron. Soc. Pacific*, 60, 32, 1948.
 Musen, P., A. Bailie, and R. Bryant, Perturbation in perigee height of Vanguard I, *Science*, 13, 935-936, 1960.

(Manuscript received March 4, 1960.)

Properties of the Solar Wind during Sunspot Minimum¹

A. L. LICHT

*Theoretical Division
Goddard Space Flight Center
National Aeronautics and Space Administration
Washington, D. C.*

Abstract. Parker's model of a spherically expanding corona, the solar wind, is compared with D. E. Blackwell's observations of the 1954 minimum equatorial corona. A significant discrepancy is found between the predicted and the observed electron densities at distances from the sun greater than 20 solar radii. Blackwell's data are found to be consistent with a model in which the corona expands mostly within a thin disk, of thickness less than 25 solar radii, and lying within the sun's equatorial plane. The thickness of the disk as a function of distance from the sun is qualitatively explained in terms of magnetic pressure.

Recently Parker [1958] has suggested that the solar corona may be in a state of continual expansion, to which he refers as the solar wind. The Parker model of the corona appears to effect a reasonable description of its properties during sunspot maxima. In this paper we investigate the applicability of the Parker model during a sunspot minimum. We use the electron-density measurements obtained by Blackwell from the 1954 solar eclipse [Blackwell, 1956a] and from airplane observations of the inner zodiacal light [Blackwell, 1956b].

Equations of motion of the corona. In the presence of a magnetic field \mathbf{B} , and a gravitational potential V , the steady-state equations of motion of an ionized fluid of velocity \mathbf{u} , mass density ρ , and pressure P are:

$$\nabla \cdot \rho \mathbf{u} = 0 \quad (1)$$

expressing the conservation of mass, and

$$\rho \mathbf{u} \cdot \nabla \mathbf{u} = -\nabla P - \rho \nabla V + (1/4\pi) \nabla \times \mathbf{B} \times \mathbf{B} \quad (2)$$

expressing the conservation of momentum.

We also have the equations of flux preservation,

$$\nabla \times (\mathbf{u} \times \mathbf{B}) = 0 \quad (3)$$

flux continuity,

$$\nabla \cdot \mathbf{B}$$

and the equation of state,

$$P = NkT \quad (4)$$

in which T is the temperature and N is the particle density. The potential V is

$$V = GM_*/r \quad (5)$$

where G is the universal gravitational constant, M_* is the sun's mass, and r is the radial distance to the sun.

The densities ρ and N can be related to the electron density n if we suppose the corona to consist of 1/5 doubly ionized helium and 4/5 ionized hydrogen:

$$\rho = \alpha M_H n \quad (6)$$

$$N = 2\beta n$$

where M_H is the mass of a proton, and α, β are the constants

$$\alpha = 1.286$$

$$\beta = 0.929$$

The Parker corona model. Parker solved a simplified form of these equations and derived the velocity distributions for a series of assumed temperatures. We have repeated his calculations and derived the density distribution correspond-

¹ Portions of this report were presented at the COSPAR meeting in Nice, France, January, 1960.

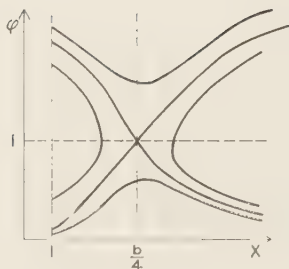


Fig. 1. The φ - x plane. $\varphi = \alpha M_{\text{H}} u^2 / 2\beta kT$;
 $x = r/r_0$

ing to the observed temperature. We have also calculated the temperature independently, by fitting his results to the observed electron density near the sun's surface.

In the Parker model a spherical expansion is assumed at a constant temperature, and the magnetic field is neglected. With these assumptions, equation 1 can be integrated immediately to give

$$nr^2u = \text{constant} \quad (7)$$

and equation 2 becomes

$$\frac{\alpha M_{\text{H}}}{2} n \frac{\partial u^2}{\partial r} = -2k\beta T \frac{\partial n}{\partial r} - \frac{GM \cdot \alpha M_{\text{H}} n}{r^2} \quad (8)$$

The abbreviations

$$\varphi = \frac{\alpha M_{\text{H}}}{\beta} \frac{u^2}{2kT} \quad (9)$$

$$x = r/r_0$$

$$n = n_0 \nu$$

where

$$r_0 = \text{the sun's radius and}$$

$$n = n \text{ at } r = r_0$$

permit us to write (7) as

$$x^2 \nu \sqrt{\varphi} = \sqrt{\varphi_0} \quad (10)$$

and with this (8) becomes

$$\frac{d\varphi}{dx} = \frac{\varphi}{x} \frac{4 - b/x}{\varphi - 1} \quad (11)$$

Figure 1 shows a sketch of the φ - x plane. We see that there is a saddle point at $\varphi = 1$, $x = b/4$. Parker picks the solution that goes

through the saddle point from low to high velocities. This is presumably the only stable solution. The other solutions require either too high velocities at $r = r_0$, or too high densities at ∞ . This fixes the constant of integration, and we get from (5) the equation

$$\varphi - \ln \varphi = (b/x) + 4 \ln(4x/b) - 3 \quad (12)$$

With (10) this is sufficient to determine the velocity and density, once b is known.

When x is near unity, u is very small. It is then possible to determine b from the observed density curve, using the hydrostatic equation valid for zero velocity,

$$\nu = \exp(b/2)([1/x] - 1) \quad (13)$$

From (13), and the values for ν given by de Jager [1959] for $x < 3$, we get $b = 18.70$, which corresponds to a temperature of $T = 1.70 \times 10^6$ degrees K.

Comparison of the Parker model with observation. The solid curve in Figure 2 shows the velocity calculated on the basis of the Parker model. It rises from 1.25 km/sec at the base of the corona to 560 km/sec at the orbit of the earth.

The solid curve in Figure 3 shows the electron density variation predicted by the Parker model. The dashed curve shows the density variation as observed by Blackwell. The two dotted lines show the margins of error estimated by Black-

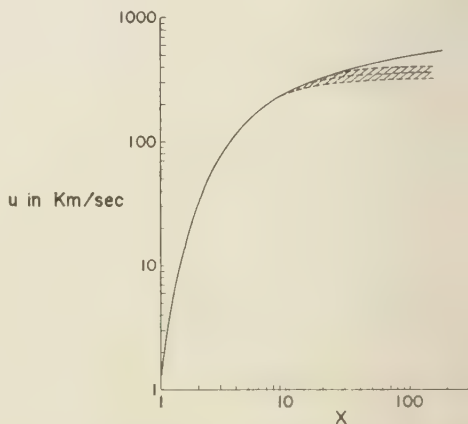


Fig. 2. Velocity distributions. Solid curve, Parker curve, calculated from observed density; broken

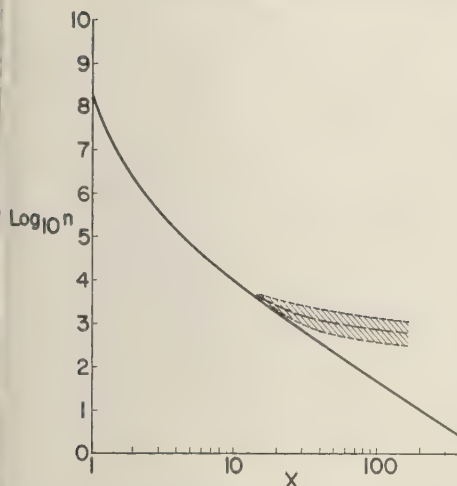


Fig. 3. Electron-density distributions. Solid curve, Parker model; broken curve, Blackwell's observations.

well, as the result of experimental error and the uncertain polarization of the F corona.

At 150 solar radii the Parker model predicts $1/30$ of the observed density.

Nonspherical model. We have found that it is possible to reconcile Blackwell's results with the concept of an expanding corona if we drop the hypothesis of a spherical expansion. From eclipse observations, it is well known that the minimum corona is greatly extended in the equatorial plane. We will therefore assume that most of the expanding gas moves nearly parallel to this plane, within a disk of thickness g . (We will normalize g so that $g(1) = 1$.)

If we interpret u as the mean radial velocity within this disk, we can still use equation 8. The first integral of this equation is the Bernoulli relation,

$$\begin{aligned} \frac{\alpha M_H}{2} u^2 + 2kBT \left(\ln v - \frac{b}{2x} \right) \\ = \frac{\alpha M_H}{2} u_0^2 - kBTb \end{aligned} \quad (14)$$

Equation 7, however, must now be replaced by

$$xg(x)u\nu = u_0 \quad (15)$$

The subscript zero refers to conditions at the base of the corona.

These equations are sufficient to determine u and g as functions of x if we use Blackwell's values for ν and assume a value for U_0 .

Our choice of U_0 is based on the condition that the corona expands spherically near the sun. On this basis U_0 has the value given by Parker model.

U is plotted as the dashed line in Figure 2. It is seen to be nearly constant at 380 km/sec near the earth's orbit. The thickness g is plotted as the solid line in Figure 4. The dotted lines in Figures 2 and 4 show the margins of error to be expected from the error in ν .

The thickness of the disk rises linearly to about $x = 10$, reaches a peak at $x = 25$, and falls slowly thereafter. If initially the disk is 1 solar radius in thickness, near the earth it will have a width of 5 radii.

Magnetic pressure. It is possible to obtain a qualitative explanation of the contraction of the disk in terms of magnetic pressure. We suppose the magnetic field B within the disk to be due to the blowing away of a dipole field. In order to obtain the order of magnitude of B , we assume it is nearly parallel to u . Writing

$$B = knu \quad (16)$$

we find that flux continuity requires that K be constant along a streamline. Thus, using (15), we can also write

$$B = B_0/xg \quad (17)$$

Here B_0 will be a function of the streamline, and will be determined by the original dipole field at the base of the corona. For instance, a field of 10^{-6} gauss at $x = 150$ would require a B_0 at the sun's equator of only 10^{-2} gauss.

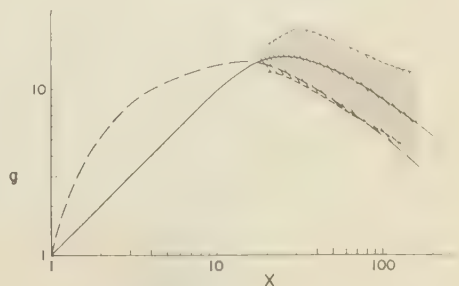


Fig. 4. Thickness of the coronal disk. Solid curve, calculated from observed density; broken curve, calculated from magnetic pressure.

These field strengths are sufficiently low to permit the neglect of the gradient of the magnetic pressure $B^2/8\pi$ along the streamlines in comparison with the gradient of kinetic pressure. The inclusion of a magnetic field of this magnitude will not seriously affect the validity of the Bernoulli equation 14. However, the magnetic field can produce a force transverse to the streamlines, which we will suppose to be balanced by a small transverse pressure gradient. That is,

$$\nabla_{\perp} B^2/8\pi = -\nabla_{\perp} P \quad (18)$$

If we integrate this between the center (c) and the edge (e) of the disk, holding x fixed, we get

$$\frac{1}{8\pi} (B_e^2 - B_c^2) = P_c - P_e \quad (19)$$

or

$$\Delta B^2/8\pi = \Delta P$$

From (17) we have

$$\Delta B^2/8\pi = \Delta B_0^2/[8\pi(xg)^2] \quad (20)$$

We will also assume that

$$\Delta P/P \approx \Delta P_0/P_0 \quad (21)$$

So that we have

$$\Delta B_0^2/[8\pi(xg)^2] = (\Delta P_0/P_0)P = \Delta P_0\nu \quad (22)$$

at

$$x = 1, \quad \Delta B_0^2/8\pi = \Delta P_0,$$

and we can eliminate ΔP_0 . Solving for g , we get

$$g = 1/x\sqrt{\nu} \quad (23)$$

This curve is plotted as the dashed line in Figure 4; it has a peak at $x \approx 15$, in qualitative agreement with the curve of thickness calculated from the density distribution; but it is too high for $x < 10$.

Discussion. Nothing has been said thus far about the polar corona, because of the lack of reliable density measurements at large polar distances from the sun. It is possible that the polar corona is in a state of spherical expansion. If so, its density at large distances will be considerably less than in the equatorial corona.

The sun's equator is known to be inclined at an angle of $7^\circ 15'$ to the plane of the ecliptic. During March and September, the earth is at its maximum distance, 27 solar radii, south and north of the sun's equator. According to figure 4, the earth during these months is at least 12 solar radii outside of the direct equatorial flow, and in the presumably turbulent fringe region of the coronal disk. Therefore, geomagnetic disturbances may be expected to be especially probable during these seasons, as they are in fact observed to be [Chapman and Bartels, 1951].

REFERENCES

- Blackwell, D. E., *Monthly Notices Roy. Astron. Soc.*, **116**, 56, 1956a.
 Blackwell, D. E., *Monthly Notices Roy. Astron. Soc.*, **116**, 365, 1956b.
 Chapman, S., and J. Bartels, *Geomagnetism*, Clarendon Press, Oxford, vol. I, 1951.
 de Jager, C., Structure and dynamics of the solar atmosphere, in *Encyclopedia of Physics*, **52**, Springer-Verlag, 1959.
 Parker, E. N., *Astrophys. J.*, **128**, 664, 1958.

(Manuscript received March 4, 1960.)

Observations of the Aurora Australis at New Zealand Antarctic Stations During IGY

T. HATHERTON AND G. G. MIDWINTER

*Geophysics Division, Department of Scientific and Industrial Research
Wellington, New Zealand*

Abstract. Intensive auroral observations at Scott Base and Hallett Station during IGY indicate that auroral activity is higher than has previously been estimated at these latitudes. The distribution of auroral activity is not simple; it appears to consist of two superimposed systems, one of isolated rays and the other of arcs and bands, symmetrical about different axes. Orientation of the principal arcs fits a zone which takes account of the nondipole field better than one based on the centered geomagnetic dipole, though the auroral frequencies conflict with this. Auroral activity increases with local geomagnetic disturbance at Hallett Station, but at Scott Base there is negligible increase in the probability of auroral occurrence until $K = 5$. However, the diurnal variation of auroral frequency, which is bimodal with the primary maximum at 04 hours local time and the secondary maximum at 17 hours local time, does not appear to be related to the diurnal trend of local geomagnetic disturbance, but the principal auroral events inside the zone seem to coincide with the principal magnetic events in the Stagg transition zone. The only characteristic colored form observed, a pale red glow on the horizon, is associated with high magnetic activity and ionospheric absorption. The latitude of auroral forms decreases with increase in K index. The results are compared with those of previous expeditions to Ross Island and Cape Adare.

Introduction. At both Scott Base and Hallett Station an intensive series of photographic and visual auroral observations was made during IGY. At least quarter hourly, but generally more often, visual observations of intensity, color, and position of all auroral forms were recorded. Photographs of the sky at 1-minute intervals were taken on 16-mm film with a Gartlein type 16-sky camera. The photographic and visual observations were found to be complementary in many respects. During the early part of the winter of 1957 while the cameras were being tested and modified for antarctic conditions continuity was obtained by means of visual observations. Only the camera can give a full and detailed record of the auroral forms present in the sky, but the photographic method did not permit the recording of color or short-period pulsations. Exposures were of 20-second duration at Scott Base and 15-second at Hallett Station on Tri-X film. Examination of the records indicates that many weak forms recorded visually, particularly isolated rays at low elevations, do not appear in the photographs.

The following analysis is based partly on the photographic records and partly on the visual

observations. The coordinates of the stations are given in Table 1. The two stations are inside the auroral zone and are ideally situated for the study of the relationship of auroral events to the geomagnetic and magnetic poles because of the comparatively large angles subtended by the poles at the stations (Fig. 6).

Frequencies of occurrence. The location and geometry of the auroral zones can be legitimately defined only on a frequency basis, although magnetic disturbance has been used as an indicator in the absence of auroral data [Vestine, 1944].

TABLE 1. Coordinates of New Zealand Antarctic Stations

Coordinates	Scott Base	Hallett Station
Geographical	77°51'S 166°48'E	72°19'S 170°13'E
Geomagnetic	79.0°S 294.4°E	74.7°S 278.2°E
Geomagnetic declination	58.7°E	40.0°E
Local magnetic dip	-82.0°	-84.8°
Local magnetic declination	156.5°E	103.1°E

In general the frequencies used have related the number of days on which auroras have been observed (either at the zenith in one method or in any part of the sky in the other) to the number of days when meteorological and darkness conditions allowed auroras to be seen.

These methods are relatively insensitive and because of the paucity of data have usually required the statistical inclusion of observations taken in the presence of cloud, twilight, and moonlight, whereas it may be preferable to neglect observations taken under these conditions. These factors have been discussed by Vestine [1944] and *McQuistan and Frankpitt* [1955]. Alternatively it has been suggested that the fraction of the number of hours of observation that aurora is visible, or is visible in the zenith, might be specified [*Evans and Thomas*, 1959]. This method, as will be seen, permits a more sensitive evaluation of relative frequency at high latitudes. Hourly cloud cover logs were kept throughout the year at both bases. Figure 1 shows the effect of cloud cover on visibility of the aurora at the two stations. At Hallett Station aurora is visible somewhere in the sky sometime during 80 per cent of totally clear dark hours. At Scott Base aurora is much less frequent, only 27 per cent of totally clear dark hours having activity. In 1957 (sunspot number 189.9) and 1958, however, auroras were visible from Scott Base on 84 and 82 per cent of clear dark nights respectively, a clear dark night having an average of less than $\frac{1}{8}$ cloud. Auroras overhead or within 0.5° latitude were visible on 95 per cent of clear dark nights at Hallett Station; at Scott Base auroras were overhead on 53 per cent (1957) and 56 per cent (1958) of clear dark nights. These frequencies are much

TABLE 2. Comparison of Auroral Occurrence Cape Evans, 1911, and Scott Base, 1957-1958

Place	Period	No. of Hours Favorable to Auroral Observation	No. of Hours When Aurora Seen	Percentage of Total Hours
Cape Evans	5/13-7/31/11	656	236	36
Scott Base	5/13-7/31/57	701	181	25
Scott Base	5/13-7/31/58	657	140	21

higher than the daily frequencies of occurrence of aurora anywhere in the sky of 60 per cent at Cape Hallett and <40 per cent for Ross Island, estimated by Vestine and Snyder [1945] from the data available at that time.

Comparison of the auroral frequencies of IGY expeditions with those of earlier expeditions is of more than passing interest. According to Vestine and Snyder the daily frequency of occurrence of aurora visible from Cape Royds 1908 (sunspot number 48.5) was 87 per cent, a figure very similar to that derived from the present observations. On the other hand, the frequency at Cape Evans in 1911 (sunspot number 5.7) was held by Vestine and Snyder to be 36 per cent. It is interesting to compare the actual hourly occurrence at Cape Evans in 1911 [Wright, 1921] and Scott Base during IGY. In observations on the hour only, between 4 P.M. and 8 A.M. (time of 180° meridian), on 'occasions for which conditions for observation were favourable' during 1911 and for cloud cover $\frac{3}{8}$ or less during 1957 and 1958, we obtain the occurrence of aurora shown in Table 2.

In view of these data it is surprising that the clear-dark-night frequency at Cape Evans in 1911 was assessed by Vestine and Snyder at 36 per cent. Nor does the higher frequency of observation ($\frac{1}{4}$ hourly minimum) during 1957 and 1958 account for the difference. Taking all visible observations into account, including those made between the hourly ones, aurora only occurred during 214 hours between May 13 and July 1, 1957, compared with 236 occurrences on the hour only during the same period in 19

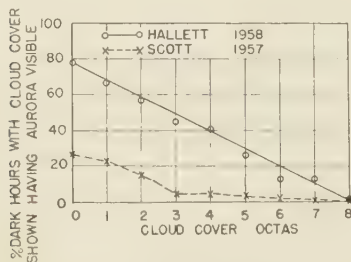


Fig. 1. Effect of cloud cover on visibility of aurora at Scott Base and Hallett Station.

Nearly the daily frequency at Cape Evans in 911 must have been comparable with and probably higher than that at Scott Base during IGY.

At Cape Adare in 1911 with bihourly observations auroras were noted at 72 per cent of the observations made on 'clear' even hours between May 26 and July 31. This is comparable with the frequencies for Hallett Station shown in Figure 1. Because of the lower density of observations, however, the 1911 figures probably represent a higher true occurrence.

In 1911 the sunspot number was very low (5.7), and in 1957 very high (189.9). That auroral incidence appears to have been higher in 1911 is some slight evidence in favor of the suggestion of *Tromholt* [1880] that inside the auroral zone auroral incidence is inversely related to sunspot number.

Diurnal frequency of occurrence. The diurnal variations of auroral incidence at Scott Base and Hallett Station during IGY are shown in Figure 2A. They indicate the frequency with which auroras occur during clear dark hours at the time stated for the entire annual auroral period (March to October). Frequencies derived by visual and photographic methods are plotted separately. Dark hours in which the cloud cover is $\frac{3}{8}$ or less have been considered clear for visual observations, and frames with the Southern Cross visible have been used for photographic observations. Hallett Station frequencies are given for 1958 only; those for Scott Base represent the mean of 1957 and 1958 values. The Scott Base curves and the Hallett photographic curve are based on observations or frames at every quarter hour. The Hallett visual curve is constructed from continuous observations.

The comparison of frequencies observed visually and those derived by photographic methods is of some interest because most future observations of auroras will be made photographically. It is important to know whether data derived in the past by visual methods are adequate enough to be incorporated into the future body of knowledge. The intensive observations made at Scott Base and Hallett Station during IGY enable the methods to be compared for frequency studies, and Figure 2A shows clearly that visual methods provide results comparable in this respect with those from photographic studies. The striking similarity between

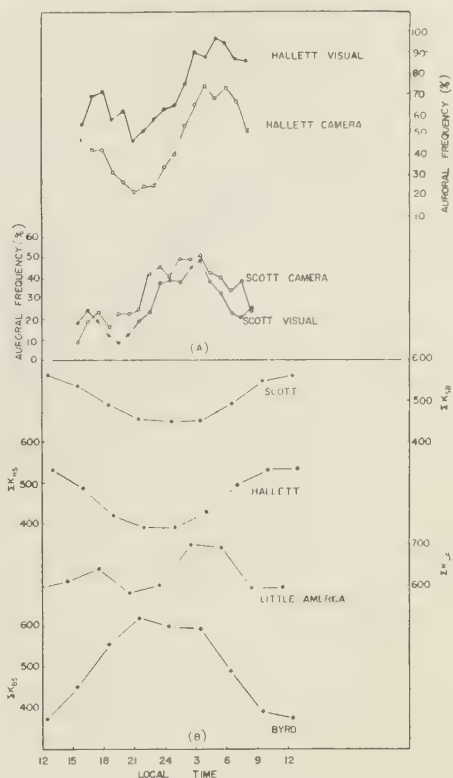


Fig. 2. A. Diurnal variation of auroral frequency, Scott Base (mean of 1957 and 1958) and Hallett Station (1958 only). Visual and photographic data shown separately. Values marked with a cross are based on a sample less than 30. B. Diurnal variation of local K index at four antarctic stations during 1958.

the visual results of the New Zealand IGY Expeditions and those of the earlier expeditions [Wright, 1921; Mawson, 1916] gives confidence to the use of visual data derived from properly conducted observations.

The two Scott Base diurnal curves lie fairly close together, with the photographic frequencies slightly higher, as might be expected. At Hallett the visual frequencies are much higher than the photographically derived ones. The higher density of the visual observations is only a partial explanation. Detailed comparison of the films and the visual records shows the greater effectiveness of the eye for detecting forms near the

horizon and forms present in moonlight, twilight, and thin cloud. That this discrepancy is not shown by the Scott Base results is due to a number of contributory factors. In particular at Hallett Station a large number of forms occur low down on the horizon and do not develop, and though they are recorded visually they are not seen on the films. At Scott Base, on the other hand, it is rare for a form on the horizon not to develop in elevation. Also it can be seen in Figure 1 for instance that auroras are often visible at Hallett Station during periods of quite high cloud cover, when photographic detection is difficult. At Scott Base they are almost never seen through cloud.

The diurnal variations of auroral incidence at Scott Base and Hallett Station are similar in form, with primary morning and secondary afternoon maxima. Such bimodal diurnal variations have been recognized before, and have been discussed by *Hulbert* [1931], who did not ascribe any significance to them. Obvious considerations prevent full diurnal curves from being obtained at all except at very high latitudes, and the value as a theoretical tool of a detailed description of the diurnal variation of auroral incidence at all latitudes has remained only potential. Recently, however, at the same time as *Hatherton and Midwinter* [1959] reported the existence of bimodal diurnal variations at the New Zealand antarctic stations, other authors reported similar variations in auroral frequency at the south pole [*Malville*, 1959] and at stations inside the northern auroral zone [*Lassen*, 1959].

Comparison of the diurnal variations of auroral incidence observed at Scott Base and

Hallett Station during IGY with those observed at Cape Evans and Cape Adare in 1911 is possible for limited periods. At Cape Evans observations were made on the hour, and at Cape Adare on the even hour. Similar data obtained from Scott Base and Hallett Station for the same periods (May 13–July 31) are shown in Figure 3, together with the results from Cape Evans and Cape Adare. The diurnal curves for Scott Base and Cape Evans are very similar despite the coincidence of sunspot minimum with the 1911 observations (sunspot number 5.7) and sunspot maximum with the 1957–1958 ones (sunspot number 1957, 189.9). The absence of aurora during the midday period in 1911 is due chiefly to the absence of observations. It is of interest to note, too, that the angle of magnetic dip at Cape Evans has changed from $-84^{\circ}55'$ in 1911 to $-81^{\circ}55'$ in 1958.

As Cape Adare is 80 miles north of Cape Hallett some dissimilarity in the curves might be expected, but Figure 3 shows that they have many features in common. The low observational density at Cape Adare makes it impossible to ascribe any significance to the difference in time of the maxima.

Distribution of the aurora in the sky. The sky has been divided into octants of 45° azimuth. Each octant contains three zones between the elevations, horizon– 20° , 20° to 50° , and 50° to 90° . The presence of the whole or part of an auroral form within any of the sections of the sky has been noted at each quarter-hourly inspection. Figure 4 shows the distribution of activity in the sky at Scott Base and Hallett Station during 1957. The maximum activity occurs

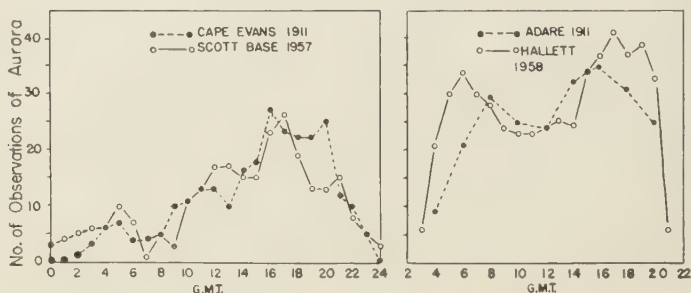


Fig. 3. Comparison of diurnal variation of auroral frequency, Scott Base, 1957, and Cape Evans 1911; and Hallett Station, 1958, and Cape Adare, 1911. Observations between May 13 and July 31 inclusive, only.

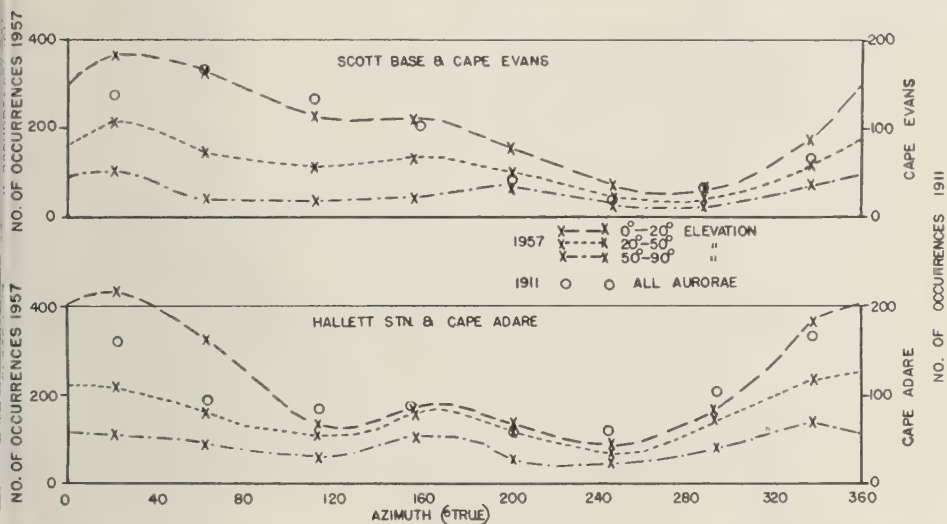


Fig. 4. Distribution of auroral activity in the sky, Scott Base and Hallett Station, 1957. Distribution of activity at Cape Adare and Cape Evans in 1911 is also shown.

at both stations in the NE octant. The subsidiary maximum which occurs at both bases in the SE octant is mainly due to the southern extensions of arcs and bands. The results of the British (Terra Nova) Expedition at Cape Evans and Cape Adare have been added for comparison.

The distributions of arc centers (or rather the highest points of arcs) at both stations derived from the quarter-hourly observations are shown in Figure 5. At Hallett Station arc centers at the horizon (050°) are little removed from the geomagnetic meridian (040°), but centers tend to move southward to 070° as the arcs rise in the sky. At Scott Base, on the other hand, arc cen-

ters are at 110° , which is 50° in azimuth from the geomagnetic meridian. Intersection of the radii of arcs at Hallett Station and Scott Base occurs at a point between the geomagnetic and dip poles and is in close agreement with the center of southern hemisphere isochasms derived by Gartlein and Sprague [1959]. Minimum auroral activity occurs at both stations in a direction 180° from the arc centers and toward the centers of the isochasms defined by Gartlein and Sprague.

The observations also fit extremely well a zone position predicted by Quenby and Webber [1959], who have considered the effect of the

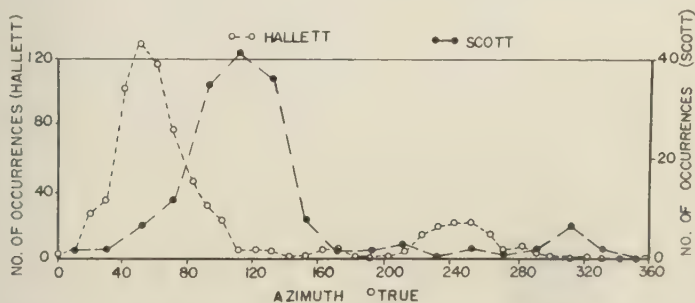


Fig. 5. Distribution of arc centers, Scott Base and Hallett Station, 1958.

nondipole parts of the field on cosmic-ray trajectories. They have obtained a latitude $\bar{\lambda}$ with respect to a tilted geomagnetic dipole adjusted to give the best fit to the horizontal and vertical components of the real field along the radius through any point. Figure 6 shows the isopleth of $\bar{\lambda} = -70.4^\circ$ corresponding to where Quenby and Webber would expect to find the southern auroral zone at sunspot minimum, and also included in the diagram are certain isochasms obtained by Gartlein and Sprague [1959] from IGY data.

In view of the theoretical prediction by Alfvén [1955] of an inner auroral zone at 5° to 10° , a prediction which has recently received some empirical confirmation from Lassen [1959], Fel'dshteyn [1959], and Aver'janov [1959], the distribution of auroral latitudes has been examined to see whether such an inner zone is present, or whether the frequencies decrease monotonously inward. Figure 7 shows the distribution of arc elevations in 1958 at the bases at the time the arcs were first observed. The day has been divided into two periods, one containing the morning maximum at 04 hours local time and the other containing the afternoon maximum at 17 hours local time, in view of Lassen's report of the coincidence of morning aurora with zenithal activity at Godhavn. Even allowing for the ten-

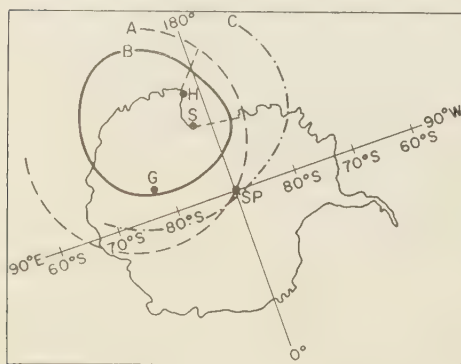


Fig. 6. Southern auroral zone at sunspot minimum after Quenby and Webber, (A). B and C are auroral zones for small and medium auroras, respectively, after Gartlein and Sprague. The dashed lines show the most frequent directions of arcs at the two bases. G, geomagnetic pole; H, Hallett Station; S, Scott Base; SP, south geographical pole.

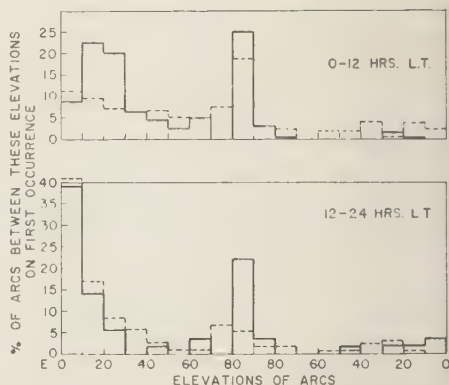


Fig. 7. Distribution of arc elevations on first sight, Scott Base (solid histogram) and Hallett Station (dotted histogram), 1958. The groups shown are for 0 to 12 hours and 12 to 24 hours local time.

dency of observers to classify any elevation above 60° as zenithal there is still a high proportion of arcs occurring virtually overhead. The possible dual nature of the zone is better shown by the afternoon results, when the main activity is at lower latitudes than during the morning. This shift is due to the decrease in latitude of auroral forms with increasing geomagnetic disturbance, the afternoon being more disturbed than the morning, reinforced by the poorer visibility of forms near the eastern horizon about the time of the morning maximum because of the sun's position. Otherwise there is little essential difference between the distribution of arc latitudes during the morning and afternoon periods.

That the maximum of auroral activity (Fig. 4) appears to the NNE at Scott Base, instead of ESE, which is the direction of the majority of arcs, is due to a large number of isolated rays or narrow pencils of rays which appear in that octant. Although rays have been observed at most azimuths they are most frequent in the region to the west of the geomagnetic meridian (Fig. 8) at a direction about 90° from the arc azimuth. A similar situation prevails at Hallett Station, where the angular separation of arc and ray azimuths is not quite so great.

In addition to the primary arc directions a second preferred direction of arcs occurs at 170° at Hallett Station and 180° at Scott Base.

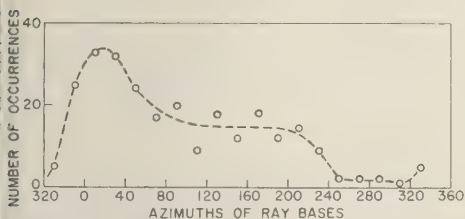


Fig. 8. Distribution of ray azimuths, Scott Base, 1958.

Though relatively few in number, these arcs are well-defined features of auroral activity at the two stations. At Scott Base 19 were photographed during IGY; all had centers between 165° and 195° , and all occurred between 0315 and 0915 GMT at a high elevation. At Hallett Station, during 1958 only, 14 similar arcs were observed, all (except one at 220°) with centers between 160° and 180° , and all occurring between 0400 and 1000 GMT. Consequently they contribute greatly to the afternoon secondary maximum of activity.

Color. Practically all the auroral forms observed at Scott Base and Hallett Station during IGY were, to the eye, of the 'normal' pale yellow-green color. Occasionally the greenness seemed to be accentuated. Occurrence of the only other visibly observed color, red, was rare, and (at Scott Base particularly) was almost invariably accompanied by intense magnetic activity and ionospheric absorption. In such cases a dusky pink glow low in the east was the characteristic and sometimes the only form.

It will be shown that for Scott Base the probability of occurrence of aurora is almost independent of local K index up to $K = 5$. 'Colored' aurora almost never occurred during periods of low magnetic activity. Conversely, the pale red glows almost invariably occurred sometime during a major geomagnetic storm. The previous expeditions to Ross Island, being on the western edge, were unfavorably situated with respect to observation of these glows. Of colored forms at Cape Royds in 1908 (sunspot number 48.5), Mawson [1916] says: 'This journal contains mention of only about 6 cases where such colours (crimson and greenish tints) were observed.' At Cape Evans [Wright, 1921], color (red and green) was recorded on only 14 out of 463 observations between April 24 and September 30,

1911. The mean magnetic character number for hours with occurrence of colored aurora was 1.82. At Scott Base during 1957 and 1958 the mean K index of 3-hourly intervals having red aurora was 5.0.

Sandford and Heiser [1959] have recently found that in fact color is present in the normal 'colorless' aurora. This interesting discovery however, does not invalidate the visual distinction between colorless and red auroras drawn here.

Aurora and geomagnetic disturbance. The probability of an occurrence of an auroral display during any hour which is part of a 3-hour interval with a particular K index is shown in Figure 9 for both stations. At Scott Base there is little increase in auroral activity with increase in K index until geomagnetic activity is high.

K indices measured during IGY have been used to derive the daily variations of magnetic disturbance at Scott Base and Hallett Station, and at two other places, Byrd Station and Little America 5 Station. The coordinates of the latter two stations are shown in Table 3. Local K indices from the four stations for each 3-hour period have been summed for the auroral months March to September 1958, inclusive. The diurnal variation of ΣK for each station is shown in Figure 2B.

Following the 1932-1933 International Polar Year an analysis of the irregular magnetic disturbance D at ten high-latitude stations led

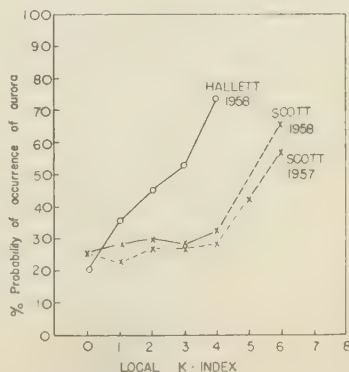


Fig. 9. Probability of auroral occurrence at Scott Base and Hallett Station for any value of K index. The last point on each of the Scott Base curves has a sample of less than 30.

TABLE 3. Coordinates of Byrd and Little America 5 Stations

Station	Geographical		Geomagnetic Latitude	Magnetic Dip
	Latitude	Longitude		
Byrd	80.0°S	120°W	-70.6°	Approx. -75°
Little America 5	78.2°S	161.9°W	-74.0°	-79.9°

Stagg [1935] to postulate three zones with different characteristics in the diurnal variation of D . The outer zone ($\phi_m < 70^\circ$) has primarily a 24-hour wave with a maximum in the evening, the maximum occurring at midnight at $\phi_m = 70^\circ$. For $\phi_m > 78^\circ$ the daily variation in D has again one dominant maximum, but it is invariably in the forenoon. The transitional zone ($\phi_m = 70^\circ$ to $\phi_m = 78^\circ$) has a daily variation in D marked by two maxima, one in the morning and the other in the evening. Nikolsky [1947] has discussed in detail the disturbance at Tikhaya Bay ($\phi_m = +71.5^\circ$), which is in the northern hemisphere transition zone and has the characteristic two maxima.

The data presented here show Little America 5 to be in the Stagg transition zone, Byrd Station to be in the outer zone, and both Scott Base and Hallett Station to be in the inner zone, though Hallett Station is of geomagnetic latitude similar to that of Little America 5.

The diurnal curves of auroral incidence and local geomagnetic disturbance at Scott Base and Hallett Station appear unrelated despite the marked relationship at Hallett Station between auroral probability and local K index. A computation of diurnal auroral occurrence from Figure 9 and the frequency spectra of K indices for each 3-hour interval gives a single wave with less than 10 per cent diurnal variation in probability even at Hallett. At the maximum and minimum on the observed diurnal curves auroral probabilities computed as above are almost identical, since the frequency spectra of K indices are almost identical. Hence any particular K index is more likely to be associated with aurora at 0300 hours local time than at 2000 hours, and the principal events of the diurnal variation of auroral incidence appear to be independent of

local magnetic activity. On the other hand, the principal maximum, secondary maximum, and minimum of geomagnetic disturbance at Little America 5 appear to be almost coincident with similar auroral events at Scott Base and Hallett Station.

An interesting difference occurs between the diurnal nature of magnetic disturbance at Little America 1 (1929-1930) and that reported above for Little America 5 from recent K indices. Davies [1935] found that at all seasons during 1929-1930 the magnetic-disturbance curve was of the single-maximum outer-zone type, the maximum being at 03.5 hours local time. This is approximately the time of the primary maximum in the 1958 observations, but the quite well-developed secondary maximum of 1958 is absent from the earlier observations. It should be stated that Little America 5 (Kainan Bay) is about 50 miles east of Little America 1 and paradoxically the geomagnetic latitude of Little America 5 is less than that of Little America 1. It should also be noted that the magnetic dip has decreased from $-82^\circ 20'$ at Little America 1 in 1929 to $-79^\circ 56'$ at Little America 5 in 1958. Sunspot numbers in 1929 were lower than in 1958, though 1928 was the maximum year of the cycle.

Position of displays and magnetic disturbance. The relationship between magnetic disturbance and the latitude of auroral forms was investigated by dividing the sky into two segments, one of elevations 0° to 20° (horizontal) and the other of elevations 21° to 90° (zenithal). Figure 10 shows the probability that a form is zenithal for each K index. At low K indices auroral forms are almost invariably 'overhead'; at higher K indices auroras tend to move outward to lower latitudes.

Radial velocities of arcs. The velocities of a number of arcs at both Scott Base and Hallett Station have been computed from the all-sky camera photographs. The velocity distribution of 184 measurements, assuming the aurora to be at 110 km, is shown in Table 4. The rate of movement of each arc is, of course, not uniform throughout its life.

Discussion. In this preliminary analysis of auroral data from Scott Base and Hallett Station during IGY little has been derived that could not have been obtained from the data of

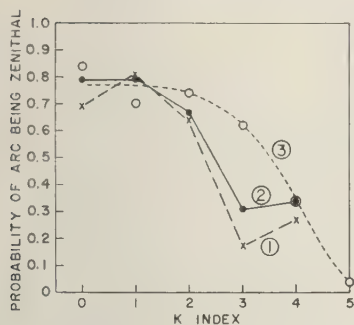


Fig. 10. Variation of latitude of aurora with local geomagnetic K index. 1, Scott Base aurora vs. Scott Base K index. 2, Hallett Station aurora vs. Hallett Station K index. 3, Scott Base aurora vs. Little America K index.

the earlier expeditions to Ross Island. The substantial agreement between the results of the IGY and previous expeditions is itself worthy of note, particularly since sunspot activity was widely variable.

Several points raised by the observations are of significance with respect to the morphology of auroral occurrence.

1. The radii of arcs do not lie along the geomagnetic meridians, and if the coincidence of arcs and isochasms is admitted the concept of geomagnetic latitude as an isopleth of auroral and magnetic behavior at high latitudes is inadequate. The directions of arc and band activity at Scott Base and Hallett Station fit very well with Quenby and Webber's postulated zone, which takes into account the nondipole parts of the field. Further, Quenby and Webber's $\lambda = -70.4^\circ$ zone passes almost through Little America, where the diurnal variation of magnetic disturbance has been shown to be similar to that of auroral disturbance inside the zone.

2. Though the distributions and directions of arcs at Scott Base and Hallett Station are consistent with the Quenby and Webber zone of maximum frequency with possibly an inner-zone population, there are inconsistencies in accepting such a picture. From Figure 6 it can be seen that the distances of Scott Base and Hallett Station from this zone are similar. In the section on frequency of occurrence above it has been shown that auroras occur at Hallett Station sometime during 80 per cent, and at Scott Base during

27 per cent, of all clear dark hours. These frequencies are not consistent with a simple concentric pattern. Further, the nature, types, behavior, and intensities of the auroras observed at the two stations have very marked differences. The picture is further complicated by the unusual characteristics of the aurora at Dumont d'Urville [Weill, 1958] ($\phi_m = -75.6^\circ$), where again the auroral behavior seems unique. In fact, auroral morphology and geometry inside the zone appear to be of the utmost complexity, and any attempt to synthesize pattern and theory from observations made in a limited part of the zone appears fruitless.

3. One consistent feature that has appeared in the published results of stations inside the zone is the bimodal diurnal variation of auroral frequency [Hatherton and Midwinter, 1959; Malville, 1959]. Lassen [1959] has published similar results for the northern zone, and has used them as evidence for the existence of an inner auroral zone as predicted by Alfvén [1955]. Lassen postulates the following: (a) stations near the main auroral zone have distributions with a single maximum near geomagnetic midnight; (b) stations between the zones often have, in addition, a weak morning maximum; (c) stations near the inner auroral zone show two maxima, one near geomagnetic midnight and one at about 06 hours L.T.; and (d) stations some degrees of latitude nearer the pole show a weak geomagnetic midnight maximum and a distinct morning maximum. These statements conflict with the observations at Scott Base and Hallett Station on several points. First, activity is a minimum at geomagnetic midnight

TABLE 4. Rate of Movement of Auroral Arcs

Velocity, km/min	No. of Observations
0-5	22
5-10	30
10-15	36
15-20	33
20-25	20
25-30	15
30-35	8
35-40	11
40-45	5
45-50	2
50-55	2

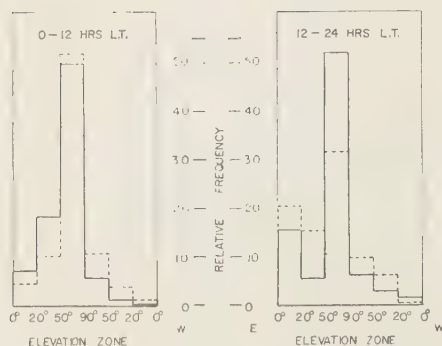


Fig. 11. Effective density of arc and band activity, Scott Base (solid histogram) and Hallett Station (dotted histogram), 1958.

though the afternoon maxima are close to a magnetic midnight taking the effective pole as the center of Quenby and Webber's zone. Second, although the frequency of occurrence of aurora at Hallett Station (80 per cent of clear, dark hours have aurora) is much higher than at Scott Base (27 per cent), suggesting that Hallett is much nearer the main zone, nevertheless the relative development of both maxima is similar at Hallett and Scott, and the absolute frequencies at Hallett are much higher than at Scott at both maxima. This could fit Lassen's scheme only if Scott Base were well inside the inner zone and Hallett Station just inside the inner zone, as in both cases the majority of auroras occur to the north and east. Thus a polar distance of at least 10° would be indicated for the inner zone if the concept of unicentricity of the zone is accepted.

In Figure 7 no account is taken of the effective increase in the area of the sky with decrease in elevation. Figure 11 shows the data converted to give the relative number of arcs per degree of geomagnetic latitude in the zones 0° to 20° , 21° to 50° , and 51° to 90° . If these curves could be corrected for decreasing visibility with distance the distribution of arcs with geomagnetic latitude could be obtained. It is difficult to obtain a basis for that correction, and hence difficult to construct a true picture of the latitudinal variation in arc frequency from observations at one station. However, Figure 11 shows that on an uncorrected basis arcs are most frequent overhead at Scott Base and Hallett Station on first

sighting. In the morning this is most marked, but during the afternoon there is a secondary population of aurora near the horizon at both bases. Again, it is difficult to interpret the zenithal occurrence as being due to an inner zone because of the wide disparity in frequencies at Scott and Hallett which requires that the bases occupy dissimilar positions with respect to the zone geometry; but this marked dissimilarity is not reproduced in Figure 11.

The difference in the frequencies of occurrence at Scott and Hallett is thus seen as the big obstacle to the construction of a simple zone geometry from observations at the two stations. As frequencies are the essential variable in zone geometry at present, it seems impossible to make a coherent picture from all the facts presented here.

4. A surprising result is the lack of correlation of the diurnal variation of geomagnetic disturbance with that of auroral occurrence despite other well-defined auroral-magnetic relationships. That the bimodal diurnal occurrence of geomagnetic disturbance at Little America is similar to the auroral occurrence at Hallett Station and Scott Base is interesting. An examination of the relationship of Stagg transition-zone magnetic events to the auroral zone is required.

Acknowledgments. The cooperation of many colleagues in the tedious task of obtaining visual observations of the aurora is gratefully acknowledged. In particular, thanks are due to C. E. Ingham and K. J. Salmon, who were responsible for the observations at the joint United States-New Zealand station at Cape Hallett during 1957 and 1958 respectively. The program was initiated by I. L. Thomsen, Director, Carter Observatory, for the New Zealand National Committee for IGY.

REFERENCES

- Alfvén, H., On the electric field theory of magnetic storms and aurorae, *Tellus*, 7, 50-64, 1955.
- Aver'janov, V. G., Preliminary auroral results from Vostok I., *Bull. Soviet Antarctic Expedition*, 5, 46-47, 1959.
- Davies, F. T., The diurnal variation in magnetic and auroral activity at three high latitude stations, *Terrestrial Magnetism and Atmospheric Elec.*, 40, 173-182, 1935.
- Evans, S., and G. M. Thomas, The southern auroral zone in geomagnetic longitude sector

- 20°E, *J. Geophys. Research*, *64*, 1381-1388, 1959.
- el'dshteyn, Ya. I., Distribution of auroras in the circumpolar region, *Izvest. Akad. Nauk SSSR, Ser. Geofiz.*, *1*, 170-171, 1959.
- artlein, C. W., and G. Sprague, *Newsletters from World Data Center IVa (Auroral Visual)*, Cornell University, 1959.
- atherton, T., and G. G. Midwinter, Diurnal variation of aurora and geomagnetic disturbance at New Zealand antarctic stations. *Nature*, *184*, 889-890, 1959.
- ulbert, E. O., On the diurnal variation of the aurora polaris, *Terrestrial Magnetism and Atmospheric Elec.*, *36*, 123-128, 1931.
- assen, K., Existence of an inner auroral zone, *Nature*, *184*, 1375-1377, 1959.
- alville, J. M., *Antarctic Auroral Observations, Ellsworth Station*, 1957, *J. Geophys. Research*, *64*, 1389-1393, 1959.
- icQuistan, G. W., and B. L. Frankpitt, Night cloud cover in New Zealand and its effect on auroral frequencies, *Carter Observatory Sci. Rept.* *4*, 1955.
- awson, D., Auroral observations at the Cape Royds Station, British Antarctic Expedition 1908, *Trans. Roy. Soc. S. Australia*, *40*, 151-212, 1916.
- ikolsky, A. P., Dual laws of the course of magnetic disturbance and the nature of mean regular variations, *Terrestrial Magnetism and Atmospheric Elec.*, *52*, 147-153, 1947.
- Quenby, J. J., and W. R. Webber, Cosmic-ray cut-off rigidities, *Phil. Mag.*, *4*, 90-113, 1959.
- Sandford, B. P., and P. Heiser, Colour photography of the aurora, *Nature*, *184*, 540, 1959.
- Stagg, J. M., The diurnal variation of magnetic disturbance in high latitudes, *Proc. Roy. Soc., A*, *149*, 298-311, 1935.
- Tromholt, S., *Danish Meteorological Yearbook*, 1880.
- Vestine, E. H., Geographic incidence of aurora and magnetic disturbance, northern hemisphere, *Terrestrial Magnetism and Atmospheric Elec.*, *49*, 77, 1944.
- Vestine, E. H., and E. J. Snyder, The geographic incident of aurora and magnetic disturbance, southern hemisphere, *Terrestrial Magnetism and Atmospheric Elec.*, *60*, 105-124, 1945.
- Weill, G., Aspects de l'aurore observée à la base Dumont d'Urville en Terre Adélie, *Compt. rend.*, *246*, 2925-2927, 1958.
- Wright, C. S., Observations of the aurora, *Sci. Rept. Brit. (Terra Nova) Antarctic Expedition 1910-13*, 1921.

(Manuscript received November 18, 1959; revised February 19, 1960.)

Observations of Geomagnetic Fluctuations in the Period Range 0.3 to 120 Seconds¹

HUGO BENIOFF

*Seismological Laboratory
California Institute of Technology
Pasadena, California*

Abstract. Data are presented from a 5-year series of observations of geomagnetic fluctuations in the period range 0.3 to 120 seconds, approximately. These were carried on with flux rate variographs using pickup coils with 1-second-period galvanometers recording photographically at a trace speed of 1 mm/sec with maximum sensitivities of 0.05 gamma/sec per trace millimeter. Four characteristic types of oscillations are included in this study:

Type A oscillations, approximately sinusoidal in form, range in period from 0.3 to 2.5 seconds and in southern California occur at night only. They exhibit a negative correlation with sunspot numbers. Type B oscillations are nearly sinusoidal in form with periods ranging from about 3 to 8 seconds. They appear to be associated with the local occurrence of auroras. Type C oscillations are nearly sinusoidal in shape with periods ranging from about 7 to 30 seconds. In southern California they occur in daylight and exhibit a strong correlation with sunspot numbers. Type D oscillations are transients in the form of single or multiple pulses or trains of several oscillations. The pulse breadths or oscillation periods range from about 40 to 120 seconds or more. They are strictly nocturnal in southern California with a sharp peak in the rate of occurrence at local midnight.

Some characteristics of sudden-commencement components in the observed period range are mentioned briefly.

INTRODUCTION

A program of continuous recording of geomagnetic fluctuations in the period range 0.3 to 120 seconds has been carried on since November 1954, using flux rate variographs. The original installation was located in Pasadena, California. Later it was moved to Palomar, California, and an additional variograph was set up in the quartz extensometer tunnel [Benioff, 1959] at Isabella, California. Since June 29, 1956, the program has been sponsored by the Office of Ordnance Research of the U. S. Army. Additional installations have been made at (a) Resolute Bay (November 1957) with the cooperation of the Canadian Government and Drs. John Hodgson and P. Willmore of the Dominion Observatory staff, (b) Uppsala, Sweden (July 1958), with the cooperation of Dr. Markus Båth of the University of Uppsala, (c) Reykjavik, Iceland, with the cooperation of Dr. Gunnar Bodvarsson of the State Electrical

Authority of Iceland (June 1958), and (d) Huancayo, Peru (October 1958), with the cooperation of Dr. Alberto Giesecke of the Instituto Geofísico de Huancayo.

INSTRUMENTATION

The flux rate variographs consist of pickup coils connected directly to galvanometers recording photographically, with standard seismograph recording drums. In the early installations the coils were wound with 750 turns on rectangular forms 4 feet by 7.5 feet with enameled insulated wire having a total resistance of 55 ohms. The coils were used in pairs connected in series and mounted coplanar. In these installations Moll galvanometers with periods of 1.3 seconds were used with optical lever arms of 1 meter. The galvanometer magnetic fields were adjusted for critical damping. In later installations, the wooden frame coils were replaced with others wound with 750 turns on circular aluminum forms, 192 cm in diameter. These are formed by bending aluminum channels into the required shape and fastening the

¹ Contribution 971, Division of Geological Sciences, California Institute of Technology.

ends to heavy Bakelite blocks to prevent the forms from acting as single-turn coils. The wire is saturated with a moistureproof cement, and leads are brought out through a gland mounted in the Bakelite block. The approximate resistance and inductance of each coil are 55 ohms and 2.75 henries, respectively. The turns area constant NA of each coil is approximately $2.17 \times 10^6 \text{ cm}^2$. The Moll galvanometers were later replaced with 1.0-second-period galvanometers designed by Francis Lehner and built by Lehner and Griffith of Pasadena. In the Palomar and Isabella installations two pickup coils are used with each galvanometer; all other installations are provided with one coil per galvanometer. For calibration purposes, a 1.0-ohm standard resistance is connected in series between the coil and galvanometer. Passing a current of constant amplitude and variable frequency through this resistance produces a standard emf in the circuit which with the known turns \times area constant of the coil provides the data for calculating the frequency response characteristic and sensitivity of the system. Periodic check of the calibration in the field is accomplished automatically by passing a measured direct current through the standard resistor once per day. Figure 1 shows a typical frequency response characteristic of the flux rate variograph with two coplanar pickup coils.

ORIENTATION

In the early stages of the program it was found that in southern California the largest response was usually obtained with the coil axis

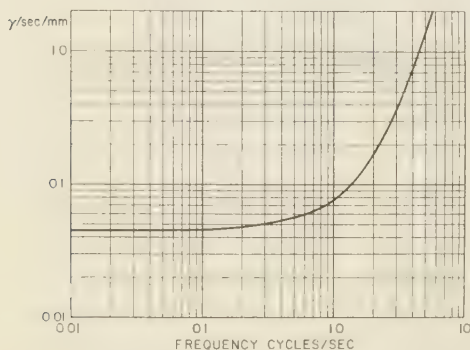


Fig. 1. Frequency response characteristic of flux rate variograph with two coplanar pickup coils.

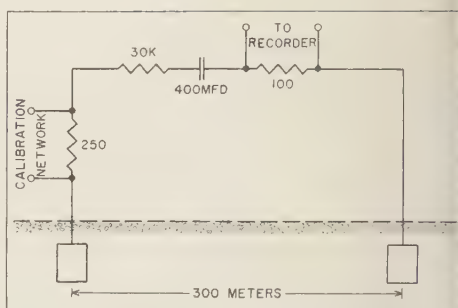


Fig. 2. Circuit for telluric current recorder.

horizontal and oriented in the north-south direction; accordingly, this configuration was settled on for all stations. Later a three-component variograph was installed at Isabella, and others are being contemplated.

RECORDERS AND TIMING

The photographic recorders include Geotechnical Corporation seismograph drums having trace speeds of 1 mm/sec on 30 by 90 cm sheets of photographic paper. Time marks offset the recorded lines once per minute. These are obtained from station clocks usually corrected daily by reference to radio time signals recorded directly on the records. On most of the recordings, event times can be determined to within ± 0.2 second.

A single heated stylus visible-writing recorder also manufactured by the Geotechnical Corporation is installed at Isabella. This has a frequency response characteristic corresponding to a galvanometer of 0.2-second period. Originally this operated from a standard coil pickup but in the last year it has been recording telluric current-generated emfs using two lead electrodes buried to a depth of about 1 meter and spaced 305 meters on an east-west line. Included in the circuit are a 30,000-ohm series resistance and a tantalum electrolytic condenser of 400-microfarad capacity for eliminating the d-c and low-frequency components. The circuit for this recorder is shown in Figure 2.

OBSERVATIONS

Early in the course of the program, it was found that most of the recorded disturbances were not random in form, but instead appeared

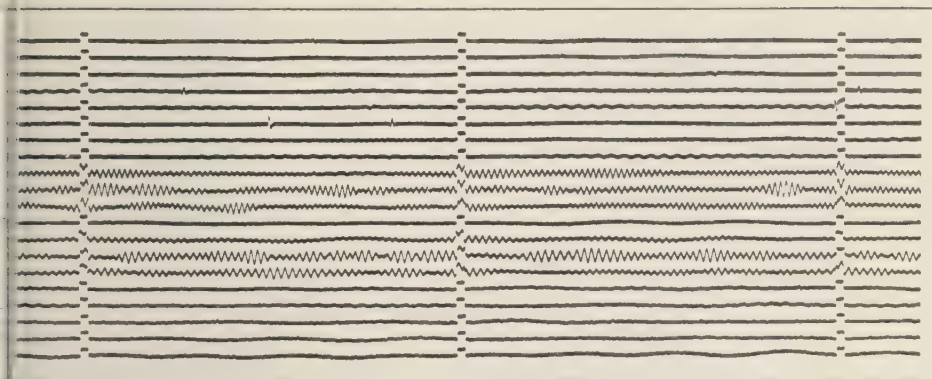


Fig. 3. N-S component, type A oscillations recorded at Isabella, California, December 10, 1959. The time marks are at 1-minute intervals. The successive lines are 15 minutes apart.

a number of definite types having easily recognizable characteristics. They are designated herein type A, type B, etc. Observations on four of these are reported in the following paragraphs together with a few remarks on sudden commencements.

Type A oscillations. Type A oscillations are nearly sinusoidal in shape with periods ranging from about 0.3 second to 2.5 seconds. The wave trains usually exhibit beats. They are designated 'pulsations of the pearl-beating type' by

Troitskaya [1957]. Portions of recordings of typical examples of these oscillations are shown in Figures 3, 4, and 5. They are recorded in southern California with peak amplitudes ranging up to about 0.2 γ /sec. At times the correlation between recordings at our Isabella and Palomar stations is nearly perfect, as shown in Figure 5. Comparison between recordings for these stations and others of our network indicate that the conditions are such as to show common activity fairly frequently within the

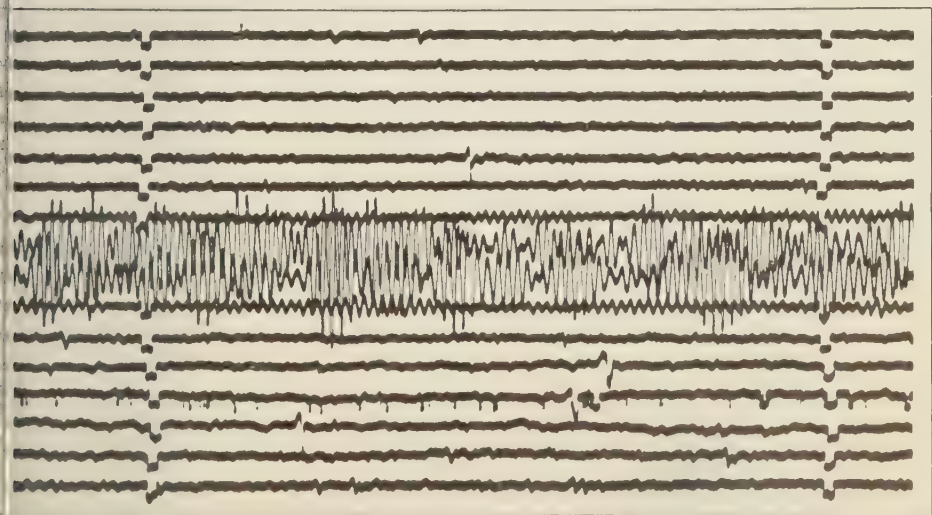


Fig. 4. Large amplitude N-S component type A oscillations recorded at Isabella, August 6, 1959. Maximum amplitudes about 0.61 γ /sec. Time marks are at 1-minute intervals.

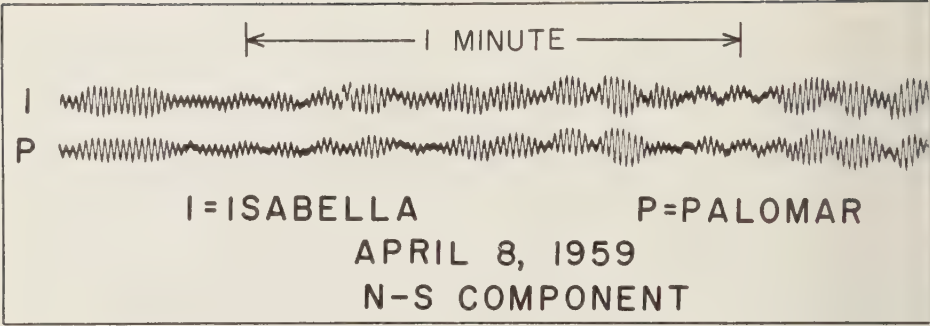


Fig. 5. Comparison type A oscillations recorded at Isabella and Palomar, California.

same 24 hours and, for Resolute Bay, within the same quarter hour. Figure 6 is a plot of the total number of observed daily occurrences in southern California from January 1, 1955,

accumulated to the indicated times. The curve appears to have a sinusoidal form with a period of about 4.25 years, but since only one cycle included, this appearance may be misleading.

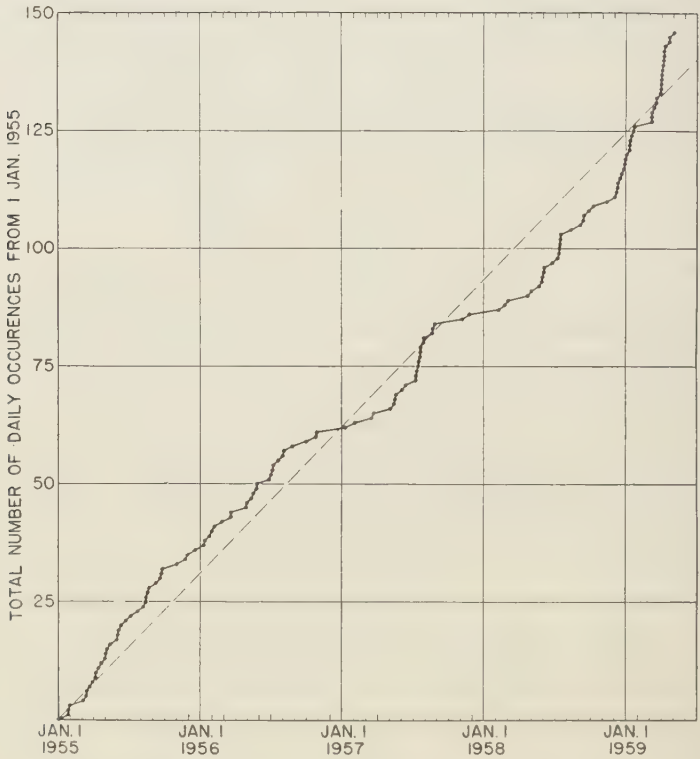


Fig. 6. Total number of daily occurrences in southern California of type A oscillations from January 1, 1955, to May 1, 1959.

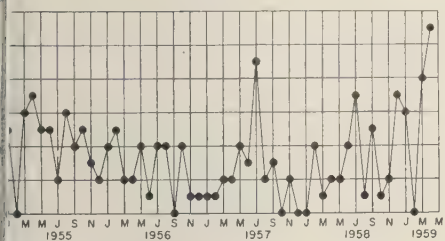


Fig. 7. Monthly rate of occurrences in southern California, type A oscillations, January 1955 to April 1959.

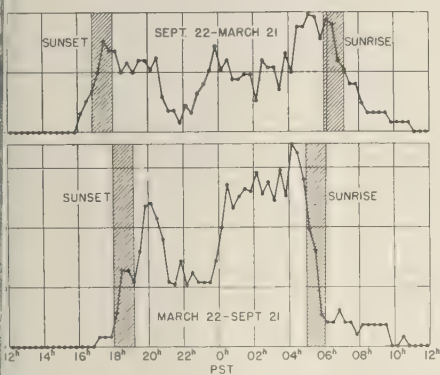


Fig. 8. Diurnal variations, type A oscillations, southern California, January 1955 to April 1959.

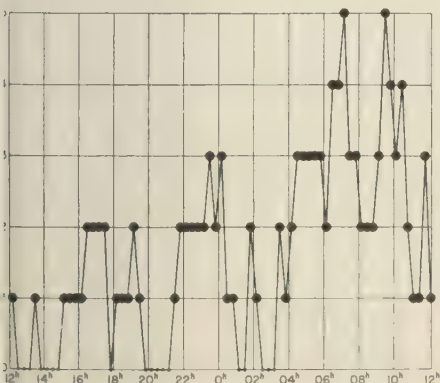


Fig. 9. Diurnal variations, type A oscillations, Uppsala, Sweden, December 1958 to June 1959.

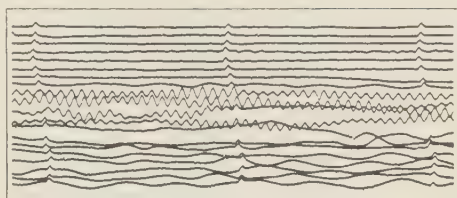


Fig. 10. Type B oscillations recorded at Palomar approximately 0638 to 0740, GCT, September 30, 1957. Time marks are at 1-minute intervals. The longer-period oscillations preceding and following are type C.

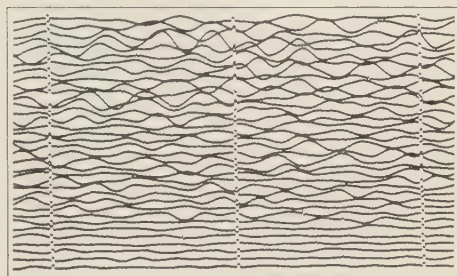


Fig. 11. Type C oscillations, N-S, recorded at Isabella, October 1959.

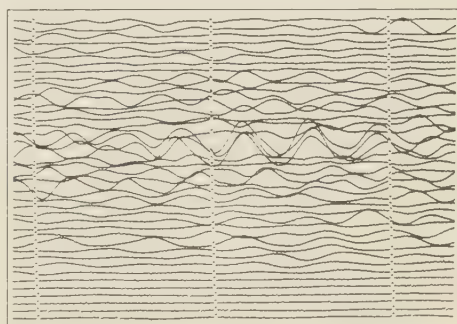


Fig. 12. Type C oscillations, N-S, recorded at Isabella, October 1959.

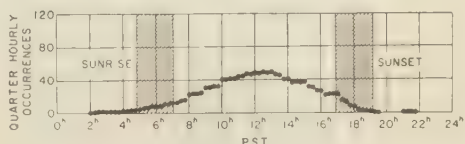


Fig. 13. Quarter-hourly occurrences, type C oscillations, southern California, 1955.

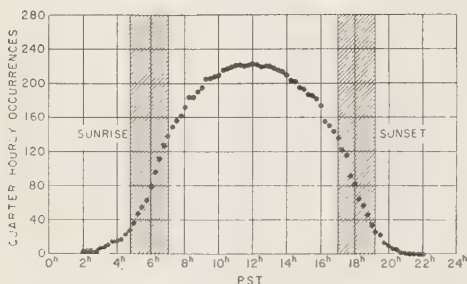


Fig. 14. Quarter-hourly occurrences, type C oscillations, southern California, 1956.

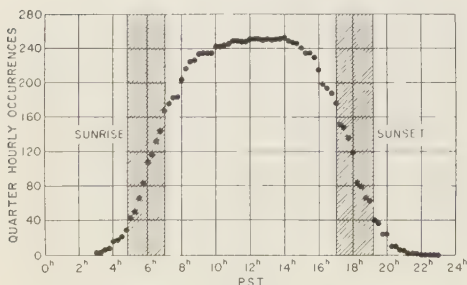


Fig. 15. Quarter-hourly occurrences, type C oscillations, southern California, 1957.

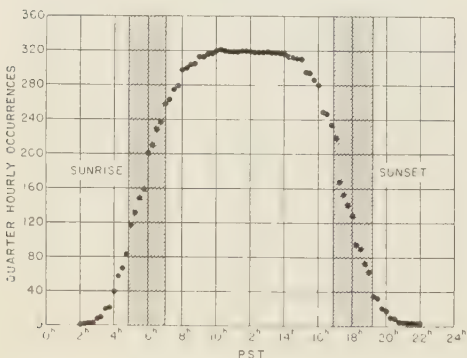


Fig. 16. Quarter-hourly occurrences, type C oscillations, southern California, 1958.

Figure 7 is a plot of the monthly rate of occurrence of these oscillations in southern California from January 1955 to May 1959. This figure indicates a rough inverse relationship to the solar sunspot cycle. In Figure 8 the diurnal

third-hourly rate of occurrences is plotted for the interval January 1, 1955, to September 1959, for the southern California stations. The upper curve refers to the winter half of the year from the autumnal equinox to the vernal equinox, and the lower figure to the summer half from the vernal to the autumnal equinox. Each point represents the total number of occurrences within the designated 20-minute interval and season for the whole period of observations. These oscillations are essentially nocturnal for this geographic location. They rise rapidly after sunset and fall rapidly after sunrise. Unlike the type D pulses described later, they show no peak at midnight, but rather a minimum at about 22^h local time and a maximum just before sunrise. Although in southern California the type A oscillations are strictly nocturnal in occurrence, at Uppsala, Sweden, they occur throughout the 24 hours but with a maximum frequency of occurrence between 7^h and 10^h local time. Figure 9 is a plot of the diurnal one-third-hourly occurrence rate for Uppsala from July 7, 1958, to June 2, 1959. The abscissas are local standard time. Gunnar Bodvarsson (private communication) found that in Southern California from 1955 to 1957 type C oscillations occurred only at times when the electron density of the F layer was at a minimum. Their appearances usually coincide with times when other disturbances within our observed period range are at a low level. Very likely the ionosphere is an opaque shield for waves of this frequency most of the time. Their

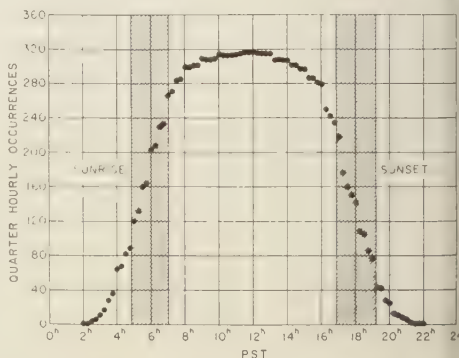


Fig. 17. Quarter-hourly occurrences, type C oscillations, southern California, 1959.

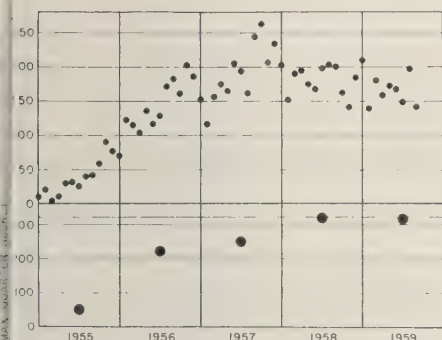


Fig. 18. Annual number of quarter-hourly sunspot occurrences, type C oscillations in southern California, 1955 to 1959, compared with sunspot numbers.

occasional appearances would, thus, correspond with intervals during which the ionosphere becomes transparent for oscillations in this period range.

Type B oscillations. Type B oscillations have nearly sinusoidal forms with periods ranging from about 3 to 8 seconds and occasionally longer. In southern California their peak amplitudes range up to about $2.0 \gamma/\text{sec}$. An example of this type is shown in Figure 10, taken at Palomar on September 30, 1957. Occurrences of these oscillations with large amplitudes have often noticed to coincide with times at which visible auroras are reported locally in the press. They occur at other times, however, usually with reduced amplitudes, when local auroras are not reported. Dr. Carl W. Gartlein has pointed out to me that, on the basis of his studies, auroras can be expected approximately overhead in San Francisco whenever the Cheltenham magnetic disturbance figure K is 8 or above and in Los Angeles part of the time whenever the figure is 9. In a list of 20 days on which the index was 8 or greater which he kindly lent me, type B oscillations recorded in south-

ern California were very strong (0.5 to $2.2 \gamma/\text{sec}$) on five of the days, average (0.05 to $0.16 \gamma/\text{sec}$) on nine days, weak ($0.025 \gamma/\text{sec}$) on four days, and absent on two days. The correlation of the occurrence of these oscillations with the large K figure is, thus, very good, and their relations to auroras must, therefore, also be a close one.

Type C oscillations. In southern California this type occurs throughout a greater part of the time than any other. It consists of oscillations having very nearly sinusoidal form with periods ranging roughly from 7 to 30 seconds. They are described by Troitskaya [1957] as 'steady regular pulsations.' Examples are shown in Figures 11 and 12. In southern California, the amplitudes range up to about $0.5 \gamma/\text{sec}$. They are essentially daylight phenomena there, with the maximum rate of occurrences coming at noon, as is evident from Figures 13, 14, 15, 16, and 17, which are plots of the southern California diurnal occurrences for the years 1955 to 1959. In these figures each point represents the number of occurrences per year within the indicated 15-minute diurnal interval. The shaded areas represent the annual range in times of sunrise and sunset, respectively. Similar behavior of type C oscillations was reported by Campbell [1959] for a series of observations extending over an interval of 7 months. He found that the flux density was maximum in the daytime with peaks at 0945 and 1400 hours local time. Over the 5-year observing period, these oscillations exhibit a strong correlation with the sunspot cycle, as shown in Figure 18, which is a plot of the annual number of noon occurrences taken from the five preceding figures together with a plot of monthly sunspot numbers. These oscillations appear to be a phenomenon of the local ionosphere, since, in spite of their low frequency, the phase relations between Palomar and Isabella, a distance of 291 km, frequently vary back and forth as much as sev-



Fig. 19. Single pulse type D oscillation recorded at Isabella, N-S, 1959 August 25, 0733, GCT.

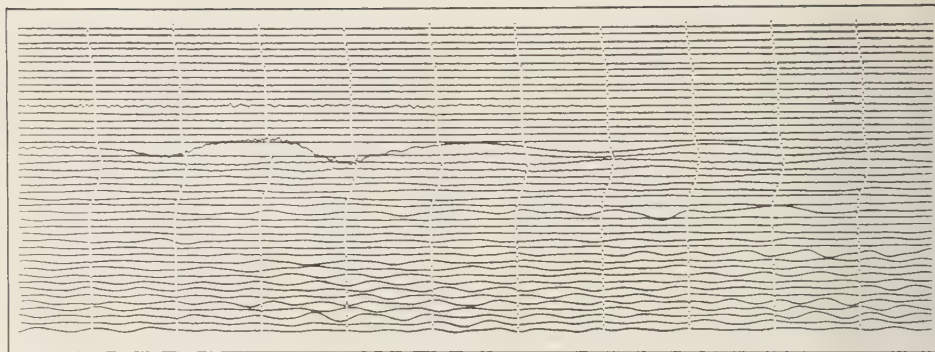


Fig. 20. One large type D oscillation of several cycles showing irregular short-period riders followed by several smaller ones. Several hours of type C oscillation are visible on the lower part of the record. Recorded at Palomar, January 29, 1960. Time marks are at half-minute intervals.

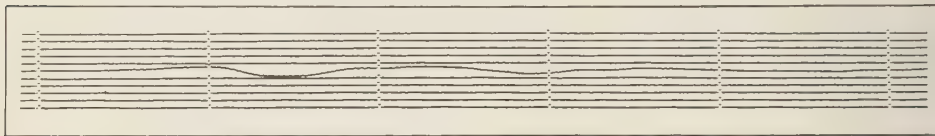


Fig. 21. Type D. oscillation which appears to be three single pulses. Recorded at Isabella 1959 October 10, 1002, GCT. Time marks at 1-minute intervals.

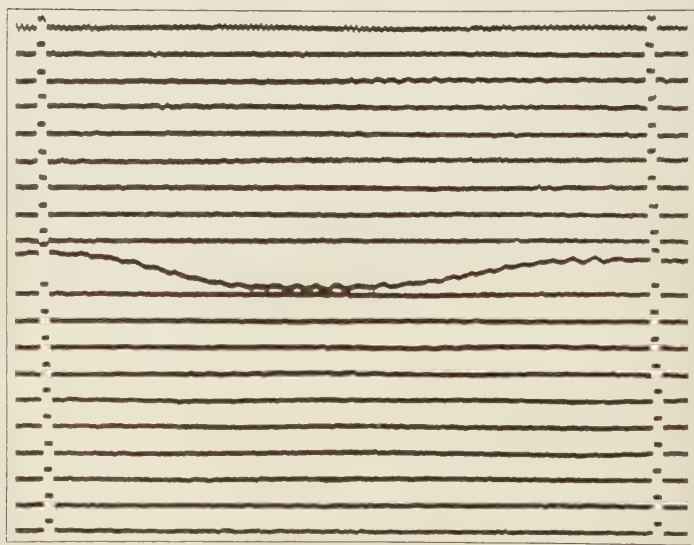


Fig. 22. Part of recording of Figure 21, showing regular short-period riders on type D oscillation. Type A oscillations can be seen on the first and sixth lines from the top.

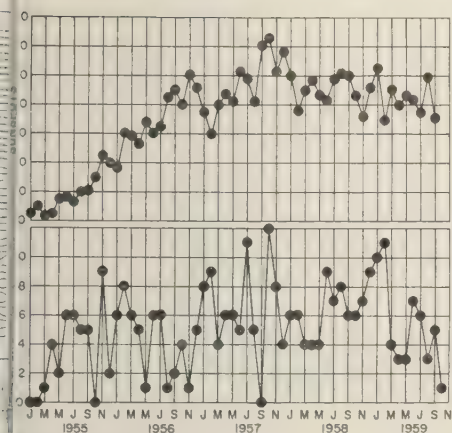


Fig. 23. Monthly occurrences, type D pulses, southern California, January 1955 to October 1959, compared with sunspot numbers.

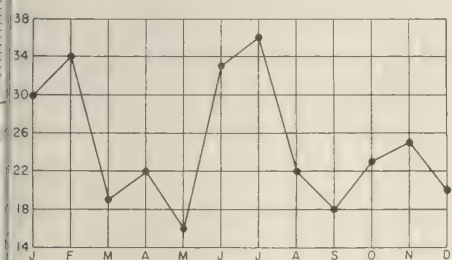


Fig. 24. Seasonal variations, type D pulses, southern California, January 1955 to September 1959.

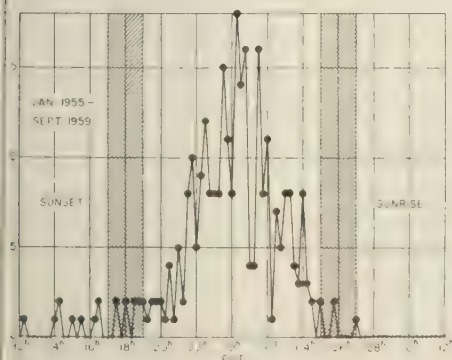


Fig. 25. Quarter-hourly diurnal variations, type D oscillations, southern California, January 1955 to September 1959.

eral seconds and at times the wave shapes differ significantly.

Type D oscillations. Disturbances of this type (Figs. 19, 20, and 21) are single pulses or wave trains of several oscillations with 'periods' or breadths lying between about 40 and 120 seconds (rarely to 300 seconds). (Period here refers to the time between two successive peaks or troughs.) The wave trains with several oscillations often, though not always, appear to be composed of a series of several pulses, rather than oscillations of a single system (Fig. 21). Type D pulses are recorded in southern California with peak amplitudes up to about 0.25 γ /sec. They frequently have riders with periods of 2 to 2.5 seconds, as evident in Figures 20, 21, and 22. Figure 23 shows the monthly rate of occurrences of these pulses in southern California from January 1955 to November 1959 compared with the sunspot numbers for the same interval. The type D pulses, thus, also appear to be related to the solar cycle, although fluctuations in the rate of occurrence are rather large. Figure 24 shows the seasonal variation in the monthly rate of occurrences for southern California over the interval from January 1, 1955, to November 1, 1959. Each point in the figure represents the total number of occurrences over the 5-year interval for the indicated month. This exhibits a semiannual period with maxima during the solstices and minima around the equinoxes. This seasonal distribution is just the inverse of that of auroras as reported by Gerson [1953], in which maximum occurrence rates occur during the equinoxes and minimum rates at the times of the solstices. Figure 25 is a plot of the diurnal variations in the quar-

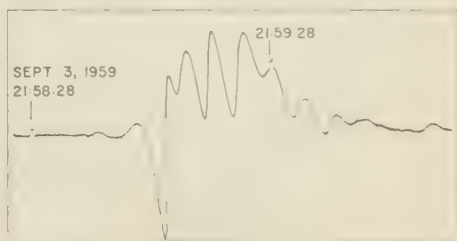


Fig. 26. Initial portion of the E-W recording of the sudden commencement of September 3, 1959, made at Isabella.

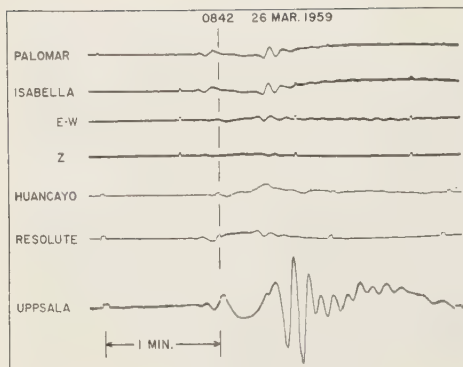


Fig. 27. Recordings of the initial portion of the sudden commencement of March 26, 1959, made at Palomar (N-S), Isabella (N-S, E-W, Z), Huancayo (N-S), Resolute Bay (N-S), and Uppsala (N-S). The traces are arranged with a common time base as indicated by the dashed vertical line at 0842.

ter-hourly rate of occurrences of the type D pulses in southern California. Each point represents the total number of occurrences within the indicated 15-minute interval for the period from January 1955 to September 1959. In southern California, these pulses are principally nocturnal, with no occurrences between sunrise and noon and only a few between noon and sunset. Their most striking characteristic is the sharp peak within 15 minutes of local midnight PST. The periods and wave forms associated with the single and multiple pulses and the sharp maximum rate of occurrence at midnight indicate a possible origin in the form of ionized clouds ejected from the sun and orbiting around the earth in eccentric orbits. For such clouds maximum velocity and nearest approach to the earth occur when they are opposite the sun on the dark side of the earth. Any observing site would, thus, exhibit maximum signal strength for those pulses which arrive at midnight. The shape of the single pulse (Fig. 19) requires the cloud to exhibit a substantial polarization component parallel to the direction of motion. This introduces dif-

ficulties, since the polarizing force is perpendicular to the direction of motion and also the magnetic field. Hence, unless a means can be found for introducing a phase delay in the effective polarization, the hypothesis is unsatisfactory.

Sudden commencements. Since the wave graphs of this network respond to rate of change of flux and, in addition, record at the rapid rate of 1 mm/sec they are particularly effective in recording the initial portions of sudden commencements. The onset of one which began at Isabella, 1959 September 215845, is shown in Figure 26 as recorded on the east-west instrument. The oscillatory beginning is typical. In this one, the oscillations begin gradually with small amplitudes and periods of about 9.5 seconds. After the arrival of the large-amplitude phase, the period shortens to about 7.1 seconds. The sharp discontinuity near the initial movement is a disturbance of local origin. Initial portions of the recordings of the sudden commencement of 1959 March 26, made at Palomar, Isabella, Huancayo, Resolute Bay, and Uppsala, are reproduced in Figure 27 with a common time base. Isabella is represented by three components. The rest are all north-south. The disturbance arrived first at Resolute Bay. The oscillation period is 7.0 seconds.

Acknowledgment. The writer is happy to acknowledge his appreciation for the help he received in the measurements from Dr. Gunnar Bodvarsson, Stewart Smith, and Jan Van Amerfoort.

REFERENCES

- Benioff, H., Fused-quartz extensometer for seismic, tidal and seismic strains, *Bull. Geol. Soc. Am.*, **70**, 1019-1032, 1959.
- Campbell, W. H., Studies of magnetic field micropulsations with periods of 5 to 30 seconds, *Geophys. Research*, **64**, 1819-1825, 1959.
- Gerson, N. C., A note on auroral interaction, *Atmospheric and Terrest. Phys.*, **4**, 81-88, 1959.
- Troitskaya, V., Earth current installations at the stations of the USSR, *Ann. IGY*, **4**, 322-325, 1957.

(Manuscript received February 19, 1960.)

Studies on Sudden Commencements of Geomagnetic Storms Using IGY Data from United States Stations

S. MATSUSHITA

*High Altitude Observatory
University of Colorado
Boulder, Colorado*

Abstract. This report contains studies of geomagnetic storm variations recorded at a network of seven IGY stations in the United States together with records for other observatories operated by the United States. The distance between adjacent stations of the network ranges from 360 to 510 km. Geomagnetic variations at these stations were usually quite similar, as would be expected. During magnetic storms, however, remarkable differences occurred even between adjacent stations.

About half of the sudden commencements of the horizontal component showed different shapes at adjacent stations for the same magnetic storm. From the data obtained from these results, and from observations at more distant stations, the behavior of sudden commencements is examined. The data also show that the variations of the vertical component of the sudden commencement differ in ways suggesting notable irregularities of the earth's conductivity in the central part of the United States. In addition, occasional examples of bay-shaped variations during magnetic storms, which are quite nonuniform over the closely spaced net, are illustrated and analyzed.

1. INTRODUCTION

As one of the United States programs of the IGY, measurements of the geomagnetic field were made by semiportable Askania variometers¹ at seven closely spaced stations under the operation of the Coast and Geodetic Survey. The names and locations of the stations are shown in the upper part of Table 1 and in Figure 1, on which are also shown both geographic (solid lines) and geomagnetic (broken lines) coordinates. The five stations of the east-west chain are all near 39.5°N geographic latitude. The three north-south stations, normal to the east-west chain, are near 106°W geographic longitude. However, neither line of stations is parallel either to a line of geomagnetic latitude or to a line of geomagnetic longitude. The whole net is located in the range 44° to 52°N geomagnetic latitude. The locations of Fredericksburg and Tucson, two permanent magnetic stations, and

of Boulder, where H is observed by a visually indicating magnetograph, are also shown in Figure 1 and the lower part of Table 1.

All these stations are close enough together so that the magnetic variations were usually quite similar. During magnetic storms, however, particularly at sudden commencements, different variations occurred. These variations were

TABLE 1. Geomagnetic Stations

Name	Geographic		Geomagnetic	
	Latitude	Longitude	Latitude	Longitude
Price	39°36'N	110°50'W	47.7°N	49.7°W
Leadville	39 17	106 17	48.0	44.5
Casper	42 50	106 22	51.5	45.6
Espanola	35 59	106 03	44.8	43.4
Burlington	39 23	102 15	48.6	39.9
Beloit	39 29	98 08	49.2	35.2
Carrollton	39 22	93 32	49.6	29.7
Fredericksburg	38°12'N	77°22'W	49.6°N	10.2°W
Tucson	32 15	110 50	40.4	47.8
Boulder	40 02	105 18	48.9	43.6

¹ Geomagnetic variations of all three components (horizontal H , vertical Z , and declination D) were recorded in the same 16-mm films. When the film magnification is 12, the length of a 1-hour period becomes 6 cm, and the scale value is 3.1 to 3.0 γ /mm for H and Z , and 0.81 to 0.91 γ /mm for D .

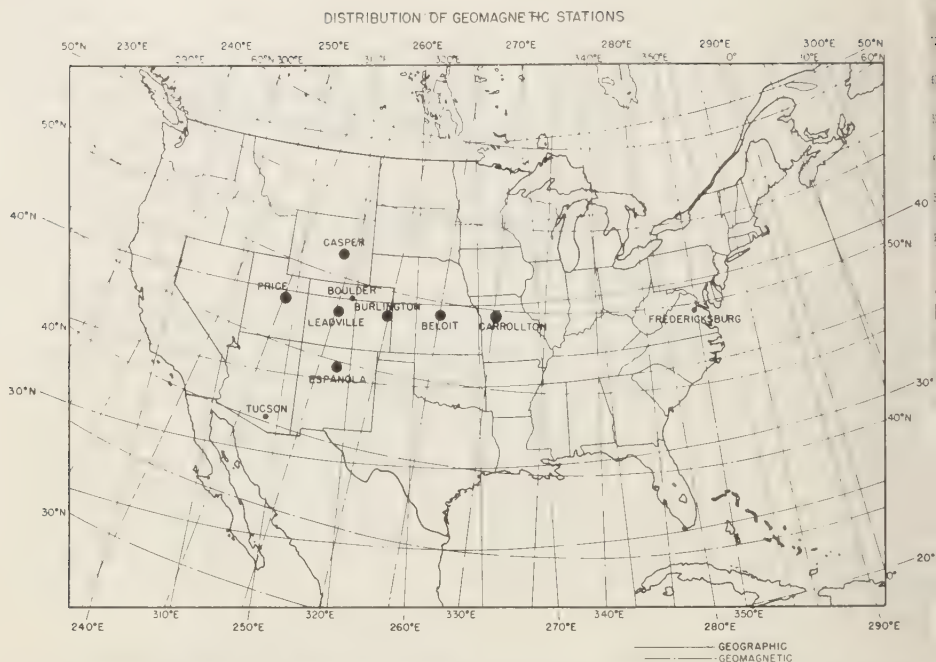


Fig. 1. Location of the net of seven geomagnetic stations and two permanent stations in the United States indicated by both geographic (solid lines) and geomagnetic (broken lines) coordinates.

sought from all the available data during 1 year starting from July 1, 1957.

2. SUDDEN COMMENCEMENT OF MAGNETIC STORMS

Horizontal Component H

Shape of the sudden commencement. The shapes of the sudden commencement (s.c.) of magnetic storms in the horizontal component will be classified into the following types, as previously suggested [Matsushita, 1957]:

(a) An s.c. characterized by definite negative impulses preceding the main positive impulse is designated as ^{-}SC (usually denoted by the symbol ssc^{*}).

(b) An s.c. characterized by an increase lasting from 0 to about 6 minutes followed by a decrease (to a level lower than the initial pre-s.c. level) lasting about 8 to 30 minutes is designated as SC^{-} . These ^{-}SC and SC^{-} occur frequently in high latitudes.

(c) The common type of s.c. in low latitudes,

having only a main positive impulse, is designated as SC .

In Figure 2 these three different types of s.c.'s, ^{-}SC , SC^{-} , and SC , at six permanent magnetic observatories during the pre-IGY period from July 1949 to March 1956, are plotted against local time of the occurrence. The two curves in the figure show the predominant regions of occurrence of ^{-}SC and SC^{-} . It will be noticed from this figure that in middle latitudes (say, $45^{\circ}N$) ^{-}SC often occurs in the afternoon and SC^{-} in the morning. In low latitudes the s.c. is almost always of the SC type. However, as is mentioned later, ^{-}SC occasionally occurs in the magnetic equatorial region between 7 and 18 h.

In a resolution (Toronto, 1957) of a special committee of the International Association of Geomagnetism and Aeronomy (IAGA) on rapid variations and earth current, geomagnetic s.c. are defined as follows:

ssc —A sudden impulse followed by an increase in activity lasting at least 1 hour.

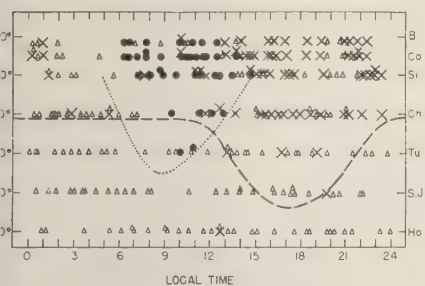


Fig. 2. The distribution in local time of the different types of sudden commencement, (triangle), $-SC$ (cross), and SC^- (dot), at row, College, Sitka, Cheltenham, Tucson, San Francisco, and Honolulu, during the period from July 1955 to March 1956. Two curves indicate the predominant regions of occurrence of $-SC$ and SC^- .

ssc^* —Similar to an ssc , except that the sudden pulse is immediately preceded, in at least one component, by one or more small reverse oscillations. In case the reverse movement has approximately the same amplitude as the principal movement, it is to be reported as ssc , rather than as ssc^* .

Thus the committee classifies s.c.'s into two types. The ssc^* in H is denoted by $-SC$ in the present classification. The preliminary reverse pulse of $-SC$ (ssc^*) shows local time effect in occurrence, as seen in Figure 2. Accordingly, we designate this type of s.c. as a different type from the ssc , as the IAGA did, an s.c. followed by a sharp reverse change (SC^- in the present classification), which also shows local time effect in its occurrence, must be designated as another type. For this reason the author offers the present classification of three types of s.c., taking into consideration both local and universal time effects.

Newton [1948] showed three types of the s.c. and a crochet in his work using the s.c.'s observed at Greenwich. However, he treated both the s.c. and s.i. (sudden impulse without preceding storms) as s.c.'s. All other early workers have treated the subject in a similar manner: for example, Rodés [1932] on Ebro, McNish [1933] on Watheroo, and Chakraborty [1951] on Alibag. Ferraro, Parkinson, and Unthank [1951] first analyzed the s.c. and separately and classified the s.c. into four types, ordinary SC , SC^* , inverted SC , and inverted SC^* . Both their inverted SC and inverted SC^* are SC^- in my classification. It will be

shown later in the discussions on the physical behavior of the s.c. that both types are in the same category. Results of local time changes in amplitude and shape of the s.c. obtained by Ferraro, Parkinson, and Unthank are clearly indicated in Figure 2, as explained later. McIntosh [1951] suggested three types of s.c., I, II, and III, which correspond with SC , $-SC$, and SC^- . His diagram on the occurrence frequency of different types of s.c. at Lerwick (geomagnetic $62.5^\circ N$, $88.6^\circ E$) agrees well with that at the same geomagnetic latitude in Figure 2. Jacobs and Obayashi [1956] showed nine idealized shapes of s.c.'s, but classified them only into SC and SC^* . The frequency of occurrence of SC and SC^* at Agincourt (geomagnetic $55.0^\circ N$, $347.0^\circ E$) obtained by them also agrees with what Figure 2 indicates at that latitude.

The boundary curves in Figure 2 cross the region of the network of IGY stations, located at about $50^\circ N$ geomagnetic latitude. Accordingly, we may expect some examples that show different types of s.c. among the IGY stations for the same storm. Thirteen out of thirty s.c.'s that occurred during the period of the present study showed this phenomenon, and some of them are shown in Figure 3A and B. The time variations of H are shown for each station, whose geomagnetic coordinates are indicated by a circle. The time scale is given in each figure, and the scale of intensity for each stations is shown beside the graph of H . The time and date in each figure refer to the occurrence of the s.c.

Figure 3A shows that the $-SC$ type occurred at Beloit and Carrollton, but not at Price, Espanola, and Tucson (nor at Fredericksburg). Figure 3B shows that the SC^- type occurred at Casper, Leadville, Espanola, Burlington, and Beloit (also at Fredericksburg), but did not occur at Tucson. The succeeding decrease of SC^- at Price reached only the initial pre-s.c. level, indicating that in this case Price was situated on a boundary of a region in which SC^- frequently occurred (see Fig. 4). Sometimes the SC^- 's for the same storm have different shapes at adjacent stations. Figure 3C, for example, shows that a needlelike sharp impulse occurred at Price, Casper, Leadville, and Espanola, but not at the other four stations. The s.c. at Fredericksburg showed $-SC$.

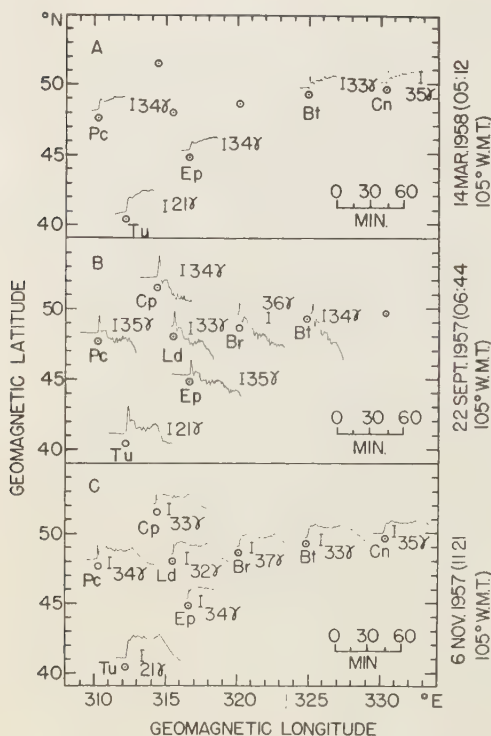


Fig. 3. Examples of geographic differences in the shapes of sudden commencement (H component) for three magnetic storms. Circles in this figure indicate geomagnetic locations of observed stations.

Figure 4 plots the s.c. type at different stations for the present thirty storms. The three different types of s.c.'s are shown by triangles (SC), crosses (\bar{SC}), and dots (SC^-). These symbols are placed at points indicating the geomagnetic latitude of the station and the local time of the s.c. Dotted lines connect the s.c. points for those storms in which the s.c. at one or more stations was not of the SC type. Seventeen out of thirty storms have this property. The storm numbers (see Table 2) are shown in the upper part (one in the bottom) of Figure 4 for those storms.

Two solid lines in Figure 4 show a predominant region of occurrence of \bar{SC} , which is indicated by the geomagnetic latitude and the local time. These lines coincide with the boundary line for \bar{SC} in Figure 2. At San Juan (geomagnetic 29.9°N , 3.2°E), SC^- occurred at 9:19 local

time on September 22, 1957 (storm 15). This is almost the point at which the above two lines would meet if prolonged downward.

A line for \bar{SC} is not drawn in Figure 4, since a definite \bar{SC} did not occur frequently. It may be noticed, however, that at Tucson and Fredericksburg rapid-run magnetograms (where recording speed is about 4 mm/min) often show a slight decrease of about 2γ or less preceding the main impulse, although normal-run magnetograms (speed about 20 mm/hr) show merely the SC type. In Figures 2 and 4, these s.c.'s are treated as the SC type. If \bar{SC} is defined to include this type of s.c., it seems to occur more frequently in middle latitudes than the frequency of \bar{SC} estimated from normal-run magnetograms would indicate.

In rapid-run magnetograms, the negative impulse of \bar{SC} occasionally shows two or more impulses. Two examples are shown in Figure 5. A W-shaped impulse occurred at Fredericksburg for storms 5, 21, and 28. The last one is shown in the upper part of Figure 5. In this storm, Campbell [1959] observed geomagnetic pulsations at California. In higher latitudes the pulse value between two negative impulses is occasionally higher than that at pre-s.c., as shown in the lower part of Figure 5. In normal-run magnetograms, these impulses are simply recorded as a single preceding negative impulse. Accordingly, early works of \bar{SC} by Nagata [1955], Nagata and Abe [1955], and Oguti [1956] using normal-run magnetograms should be re-examined using rapid-run data.

The s.c.'s in rapid-run magnetograms often show a superposed pulsation, with a period of 20 to 10 seconds in the first half stage of the main impulse. This was also noted by Kato and Saito [1959] using records of inductometer.

In low latitudes, as at Honolulu (geomagnetic 21.1°N , 266.5°E), the \bar{SC} is rare even in rapid-run magnetograms. In the equatorial region, however, a definite \bar{SC} occasionally occurs between 7 and 18 h local time. At Huancayo (geomagnetic 0.6°S , 353.8°E , dip 2°) storms 8, 23, 28, and 30 were of this type. At Kona (geomagnetic 3.2°S , 203.4°E , dip 0°) and Guam (geomagnetic 4.0°N , 212.9°E , dip 13°), storms 13 and 16 were \bar{SC} . At Jarvis Island (geomagnetic 0.6°S , 269.1°E , dip -2°), storm 16 was

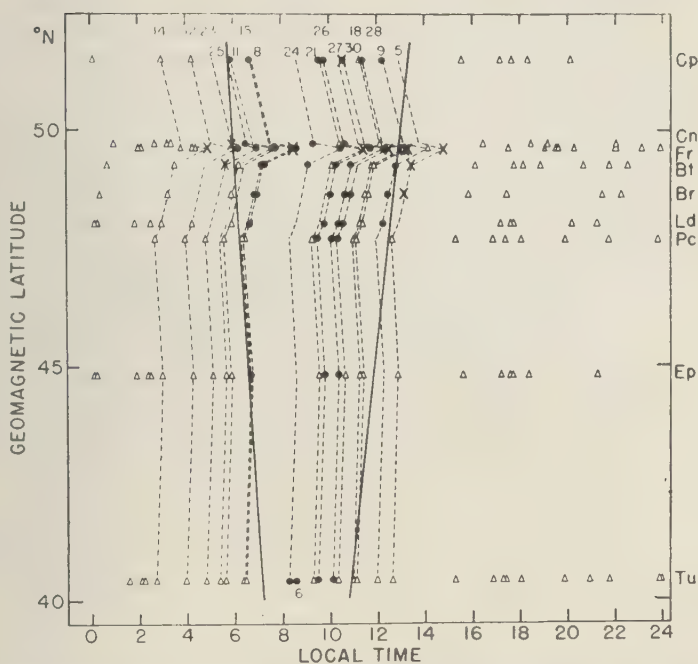


Fig. 4. Three different types of sudden commencements, SC (triangle), -SC (cross), and SC- (dot), at the network of seven stations and at Fredericksburg and Tucson, are shown at points indicating the geomagnetic latitude of the station and the local time of the s.c. The dotted line connecting the s.c. points indicates the storm in which the s.c., at one or more stations, was not of the SC type. The numbers given for these storms are those in Table 2. Two solid lines indicate a region at which the SC frequently occurs.

his type. Sugiura [1953], and Forbush and Festine [1955] obtained an outstanding daytime enhancement of s.c.'s at Huancayo. As shown in Figure 6, the daytime enhancement of the s.c. was also seen at Koror and Jarvis Island, although the amount of enhancement at these stations was less than that at Huancayo. The negative impulse of -SC is also enhanced in the equatorial region. For storm 18, the negative impulse at Huancayo was about seven times that at Fredericksburg, and the main impulse was about five times. Rapid-run magnetograms made in the equatorial region occasionally showed a slight negative change preceding the main impulse of s.c. As was mentioned before, similar phenomena occurred in the middle latitudes, but the occurrence was rare in low latitudes. Rapid-run magnetograms obtained in the equatorial region also indicated frequent super-

posed pulsations in the first half stage of the main impulse between 19 and 04 h.

Interpretation of different types of the sudden commencement. (a) Storm time and disturbance daily variations. In order to study the physical behavior of the s.c., we may assume that even at the initial stage of magnetic storms there are two types of variations: storm time variation, Dst, and disturbance daily variation, DS. Apparent differences in the shape of the s.c. are due to a combination of these two variations. The type SC- can be explained by assuming that the Dst first causes the initial impulse. Then the negative-phase part of the DS superposes and creates a larger effect than the Dst, thus causing the decrease of the SC. If the negative-phase part of the DS effect is quicker and larger than the Dst at the beginning of the s.c., the s.c. has no positive impulse, like Fer-

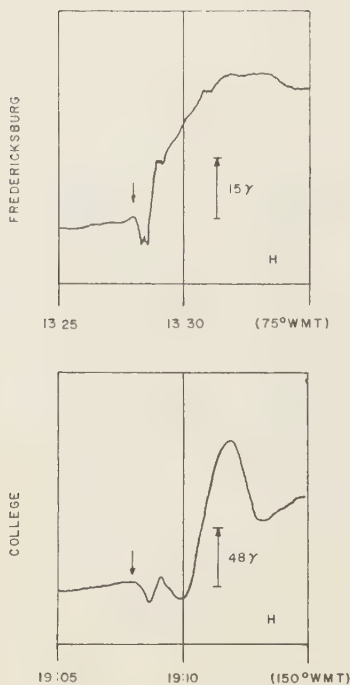


Fig. 5. Examples of preceding double reverse impulses of the ^{-}SC , in rapid-run magnetograms. The arrow indicates starting time of the s.c.

raro's reverse SC type. Accordingly, his reverse SC is merely an exceptional, hence rather rare, example of the SC^{-} . (In Ferraro's study it occurred only 13 times at six stations during 20 years.) This is the reason why the 'reverse SC' is included in the SC^{-} , and the s.c. is classified into three types of shapes instead of four. If this interpretation is correct, the SC^{-} region, at which the SC^{-} often occurs, in Figures 2 and 4, indicates generally a region where the negative-phase part of the DS variation occurs. Then, if the DS is a diurnal type of variation, the positive-phase part of the DS would be a region shifted about 12 hours from the negative-phase part. Roughly speaking, it is from 16 h meridian to 4 h meridian at about 65° latitude, from 18 to 01 h at about 50° , and from 19 to 23 h at about 40° (see the lower part of Fig. 7).

A result supporting the above estimate was obtained. The amplitude of the s.c. at Fredericksburg was usually similar to the amplitude of

the same s.c. at the net of seven stations where the s.c.'s at all these stations were of the S type. However, at storms 13 (which occurred at 17:46 105° WMT) and 20 (18:25 105° WMT), the amplitude of the SC at Fredericksburg was much larger (about 15γ larger for the former, and about 30γ larger for the latter) than the amplitude at the net. These differences in amplitude indicate that Fredericksburg was inside the positive DS region but other stations were outside. Thus the meridian of about 18° local time was a boundary of the positive DS region at about 50° latitude, as estimated above. Moreover, at storm 29 (00:13 105° WMT) the amplitude of the SC at Fredericksburg was about 10γ smaller than that at the net, indicating that Fredericksburg was outside the positive

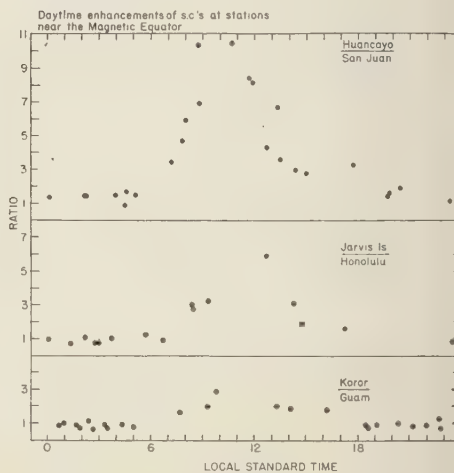


Fig. 6. Ratio of amplitudes of s.c.'s (ΔH) at two stations (Huancayo and San Juan, Jarvis Island and Honolulu, and Koror and Guam) for the same storm. The pairs of stations were selected as follows: one is situated near the magnetic equator and the other in the lower middle latitudes near the same meridian. The ratios are obtained from 30 s.c.'s of the present study. The abscissas in the top, middle, and bottom figures are local standard time 75° WMT, 150° WMT, and 135° EMT, respectively. The amplitude is defined as deviation of the first significant peak of s.c. from the pre-s.c. level. If the first significant peak is due mainly to the Dst (s.c.), the daytime enhancement in the magnetic equatorial region is caused by the Dst (s.c.) field in the high conductive zone of the ionosphere.

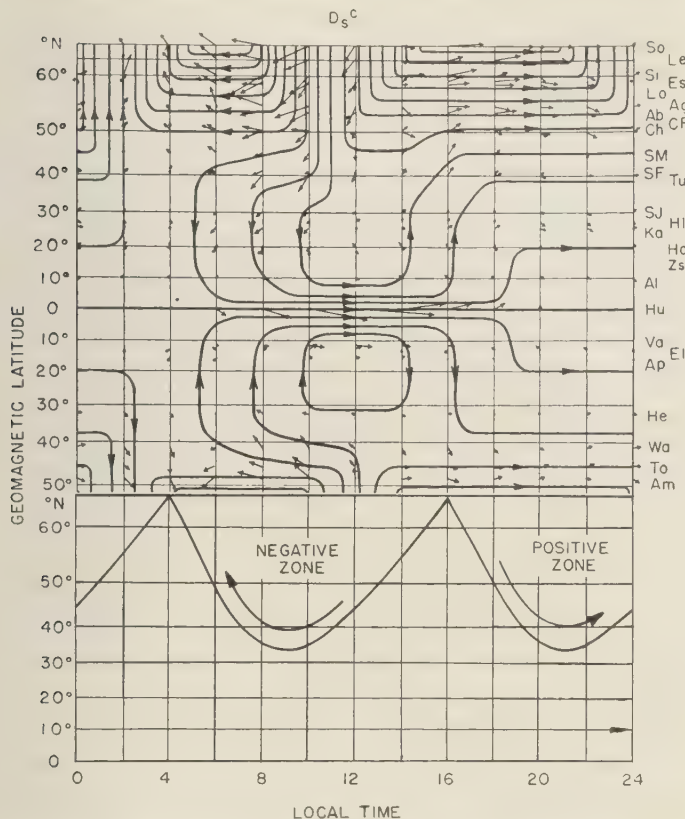


Fig. 7. The DS electric current system at sudden commencements obtained by Obayashi and Jacobs (upper part), and the DS deduced from the present study (lower part).

DS region but other stations were inside. Accordingly another boundary of the positive DS region was at about 01 h meridian in the vicinity of 50° latitude. These results nicely fit the above estimate of the positive-phase region of the DS. It must be mentioned, however, that these positive and negative-phase regions of the DS are given as an average, hence the exact shape for each storm would be slightly different from the average.

The occurrence of type SC in lower latitudes is mainly due to the Dst field. The SC which occurs in the SC⁻ region means that the Dst effect is stronger than the decrease due to the DS. The SC occurring in the estimated region of the positive-phase part of the DS is due to the combined effects of the Dst and the DS

increases. Accordingly, it is understandable that many workers have obtained the maximum occurrence frequency and largest amplitude of the SC sometime between the afternoon and the early morning. It is also easy to understand why the minimum amplitude of the SC occurred at about 08 h local time at Cheltenham, Tucson, San Juan, Honolulu, and Watheroo as obtained by Ferraro [1954]. It was due to the maximum decrease effect caused by the DS about that time at the above stations. Jackson [1952] compared the s.c. which occurred at about 08 h UT at Abinger with the same storm obtained at Cheltenham and Tucson, but he did not recognize differences in local time of the s.c. occurrence among these stations.

Obayashi and Jacobs [1957] showed electric

current systems responsible for the Dst and the DS variations at the s.c. (in fact, during about 10 minutes starting from the s.c.). In their diagram of the current system of the DS (see the upper part of Fig. 7), the westward current region indicates the negative-phase part of the DS, and the eastward indicates the positive phase. Then the above-obtained estimate of the DS from the shape of the s.c. in the H component (see the lower part of Fig. 7) generally agrees with this figure. Moreover, the electric current vectors along 12 h meridian in their figure indicate the westward component and should thus be included in the westward current zone. If this is done, the two pictures agree fairly well. The lower part of Figure 7 would indicate a more general scheme of the average DS current system than that in the upper part of Figure 7. This DS electric current seems to flow in the lower ionosphere.

In a narrow zone of about $\pm 7^\circ$ dip centering at the dip equator, the effective electrical conductivity at about the 100-km level is larger than that in middle latitudes [Matsushita, 1953, 1959b]. Accordingly it is reasonable to suppose that the daytime enhancement of the s.c. amplitude at Huancayo, Jarvis Island, and Koror is caused by s.c. electric currents in that highly conductive region. Forbush and Vestine, and also Obayashi and Jacobs, suggest that the current responsible for the enhancement is the DS current. However, the enhancement clearly appears at the first noticeable impulse of s.c.'s, as shown in Figure 6. This indicates that it is rather the Dst current that is mainly responsible for the enhancement. Naturally the enhancement of the DS variation of s.c.'s may occur in the magnetic equatorial region if the DS current flows there. However, as will be seen in the lower part of Figure 7, an expectable enhancement of the DS during the *day* is the *negative* phase of the DS. In other words, the enhancement may occur in the negative part of the SC⁻ and is certainly not in the positive sense in H . Obayashi and Jacobs' DS current diagram in the equatorial region, which is shown in the upper part of Figure 7, would lead to a misinterpretation by readers, because large current vectors at Huancayo would result mainly from the enhancement of the Dst instead of the DS. As is mentioned later, if hydromagnetic waves prop-

agated from the solar streamer and reach even the E layer, they could cause electric currents responsible for the Dst. Then it would be possible for the Dst current flowing in the highly conductive zone of the magnetic equatorial region to cause the enhancement of s.c.'s. A question remains concerning the amount of enhancement, because the s.c. enhancement is 6 to 10 times in the magnetic equatorial region whereas the daily variation in that region is only 2 to 3 times larger than that in lower latitudes. However, it is not difficult to answer this question if there are double layers of the equatorial electrojet, in which the direction of the jet is usually reversed.

(b) *The preceding negative impulse of SC⁻*
The negative part of the SC⁻ definitely shows the local time and latitude dependency, as seen in Figure 2. Thus Nagata [1952], Nagata and Abe [1955], Oguti [1956], Abe [1959], and Obayashi and Jacobs [1957] treated it as another DS, and even obtained its current system. This hypothetical current system is doubtful for the negative-phase part, because few stations were used; also it is in opposite phase to the Dst current system responsible for the SC⁻. Oguti has assumed that the phase change occurs in a very short time, and Obayashi has tried to explain it by a dynamo effect in double layers in which the wind direction is reversed. Neither explanation is quite satisfactory, for the following reasons. As was mentioned previously, the negative part of the SC⁻ in rapid-run magnetograms is usually a single negative impulse but occasionally shows multiple impulses. Also a short-period pulsation is often accompanied by the first half stage of the main impulse. Accordingly the phenomenon preceding the main impulse seems to be quite different from those succeeding the main impulse. Singer [1957] has suggested that the negative impulse of the SC⁻ is due to shock waves, and more recently that it is due to a diamagnetic effect caused by the solar gas. Neither of these suggestions is sufficient to explain the local time dependency of the SC⁻. As seen in Figure 2, about 17 h meridian is the center of the predominant region of occurrence of the SC⁻. In the simple geometry of a solar stream, which has a speed of about 10^8 cm/sec, Chapman [1929] showed that the first contact of the stream with the earth (or a

area of about 5 to 10 earth radii from the earth's center) is at about 17 h meridian plane. The coincidence of the times might be significant. In other words, the plasma responsible for the negative part of SC would have a possibility of reaching the auroral zone most frequently at about 17 h meridian, and also of reaching a latitude lower than the auroral zone at that meridian. An electric field brought by the plasma could be a cause of the negative part, as shown in high-altitude explosion effects observed at Apia [Matsushita, 1959a].

It must also be added that a definite SC in the equatorial region, which occurs only during daylight hours, seems to have some relation to the daytime high electric conductivity in the region of the magnetic equatorial zone.

(c) *Causes of the Dst and DS variations of the sudden commencement.* In the theory of Chapman and Ferraro [1931a, b; 1932a, b; 1933; 1940], the Dst of the s.c. is due to an electric current induced at the front of an approaching ionized cloud emitted from the sun, assuming that interstellar space is a vacuum. But, as interstellar space is not a vacuum, Dessler and Barker [1959], and also Piddington [1960], introduced hydromagnetic waves for the same effect suggested by Chapman and Ferraro. The hydromagnetic waves are generated by the impact of the solar plasma on the geomagnetic field. The Dst of the s.c. would be due to the hydromagnetic waves or shock front, which brings eastward electric currents in the ionosphere. As for the DS of the s.c., Chapman [1952, 1956] assumed incoming gas flow from the horns of the gas cloud. The gas flow may increase the electrical conductivity in the auroral zone. Then we may have the DS resulting from dynamo and drift effects. A question arises about the time lag between the Dst and the DS. Since the Dst usually precedes the DS, hydromagnetic waves responsible for the Dst must propagate faster or start earlier than the incoming gas flow, assuming that both are generated in almost the same region.

The speed of the hydromagnetic wave V is given by

$$V = H/(4\pi\rho)^{1/2}$$

where H is the magnetic field and ρ the effective density. Since the value of ρ at different alti-

tudes is uncertain, we cannot obtain exact values of V . In an approximate calculation, an average value of V is about 10^7 cm/s, and the maximum value is about 10^8 cm/s. The speed of the gas flow, which is responsible for the DS, must be at least 10^8 cm/s (for protons) in order to penetrate into the E region. Then it can be concluded from approximate calculations that hydromagnetic waves must be generated 1 to 10 minutes earlier than the gas flow.

There remains another problem of s.c.'s. Since the end of the last century, considerable investigation has been done to learn how nearly simultaneously s.c.'s occur over the world. Gerard [1959] recently showed that s.c.'s occur a few seconds earlier in the sunlit hemisphere than in the dark hemisphere. But Williams [1960] has come to a different conclusion—s.c.'s always occur first in high or middle latitudes. These time differences seem to be of the order of the time accuracy even in rapid-run magnetograms (about 4 mm/min). Dessler's [1958] calculation of the propagation velocity of the s.c. and also Francis, Green, and Dessler's [1959] recent work are not quite adequate for their assumed model of hydromagnetic propagation. We need more complete studies on this problem.

Vertical Component Z

During the period of the present study, thirty magnetic storms each with a s.c. occurred. The values of the ratio of the main deviation of Z at s.c., $[SC(\Delta Z)]$, to the positive deviation of H , $[SC(\Delta H)]$, calculated for each station for each storm, show the remarkable result given in Table 2. These values for different storms are consistent at each station, particularly for the sign of the ratio. The ratios at Price, Casper, Espanola, Carrollton, and Fredericksburg always show negative values; this means that ΔZ is always downward in magnetograms. Contrarily, the ratio at Leadville, Beloit, and Tucson is always positive; hence ΔZ is always upward in magnetograms. The value at Burlington shows that ΔZ is very small there. In other words, the sign of the ratio does not depend on the local time of occurrence of the s.c., or on the type of the s.c., but only on the station.

As discussed by Rikitake and Yokoyama

TABLE 2. Ratios of the Main Deviation of Z at the s.c. to the Positive Main s.c. Impulse of H at Nine Stations for Each Storm

Storm Number	Time of s.c.		$\Delta Z/\Delta H$, %								
	Date	105° WMT	Pc	Cp	Ld	Ep	Br	Bt	Cn	Fr	Tu
	1957										
1	7/2	01:57			8	-6			-13	-17	5
2	4	17:42			5	-6		7	-12	-13	6
3	16	00:14			4	-8		9	-8	-13	5
4	21	21:19			4	-5	0	9	-5	-10	9
5	27	12:59	-12			-6	2	2		-13	3
6	8/3	08:57									9
7	5	22:08	-15				-6	3		-18	10
8	9	06:47	-11				6	14		-20	10
9	29	12:20		-19	4					-14	6
10	9/1	20:14	-11	-7	2			6		-18	8
11	4	06:00	-17	-26	7	-11					12
12	6	04:21	-28	-19	0	-10					9
13	12	17:46	-26	-19	7	-6				-15	6
14	21	03:05	-17	-14	5	-8	0	9		-16	5
15	22	06:45	-86		13	-32	4			-5	2
16	28	17:16	-22	-13	8	-4	0	15		-16	5
17	10/21	15:41	-25			-12	0	13	-17	-14	3
18	11/6	11:21	-21	-26	3	-4	-5	15	-13	-30	6
19	12/19	02:37			4	-6			-13	-16	9
	1958										
20	2/10	18:25				-6		31	-22	-21	8
21	16	09:42	-59	-42		-24		6	-23	-26	5
22	3/3	02:31				-9			-13	-13	13
23	14	05:12	-37			-14		13	-23	-11	6
24	25	08:40						4	-13	-24	8
25	4/26	05:47				-18	-6	23	-32	-10	14
26	5/31	09:52	-16		5		0	5	-18	-16	12
27	6/8	10:28	-7		0	-5	-4	7		-16	5
28	14	11:28	-14	-12	7	-4	0	7		-17	13
29	28	00:13	-13	-11		-6	0			-14	5
30	28	10:42	-19	-8	10	-9	0			-12	11
	Mean		-24	-18	5	-10	-1	10	-16	-16	8

[1953] and also *Rikitake* [1959] for the observation in Japan, this phenomenon is not the result of the overhead electric current system, but seems to be the result mainly of an anomalous magnetic field caused by an induced earth current. An effective ground conductivity map for continental United States estimated by *Fine* [1953] suggests its plausibility. It must be added that according to this result we should not try to determine the overhead electric current system from short period variations of Z .

3. BAY-SHAPED VARIATIONS DURING MAGNETIC STORMS

Among the present magnetic stations in the United States, bay-shaped variations during

magnetic storms are usually quite similar. However, some differences occasionally occurred. For example, during the period from 01 to 02 h 105°WMT on September 13, 1957, variations at Espanola and Tucson were quite different from those at Price and Leadville.

During a strong magnetic storm on February 10 and 11, 1958, an even more interesting phenomenon occurred (see Fig. 8). In this figure, variations of the horizontal component and declination at six stations are shown for the same 105°WMT. Stations from west to east are arranged from the top to the bottom of the figure. At about 23:30 a large *positive* bay-shaped variation of H occurred at each of the first three stations, and contrarily a large *nega-*

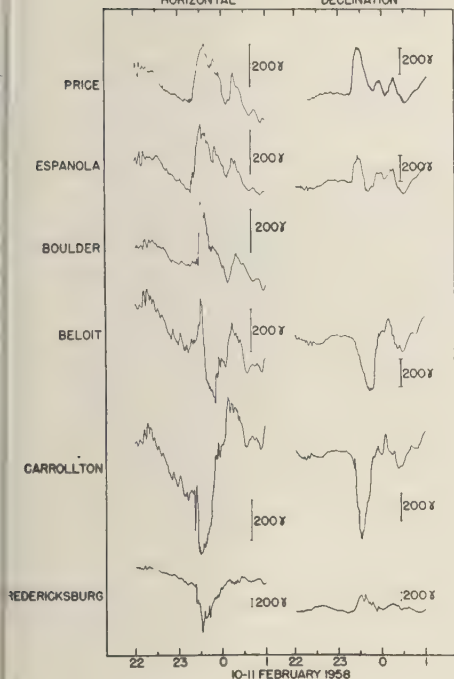
BAY-SHAPED VARIATIONS DURING MAGNETIC STORMS
HORIZONTAL DECLINATION

Fig. 8. Bay-shaped variations of the horizontal component (increase upward) and the declination eastward increase is upward) during a magnetic storm on February 10 and 11, 1958. The time scale of the abscissa is in 105° WMT.

ive variation occurred at Carrollton and Fredericksburg. At the intermediate station, Beloit, the variation was first an increase, then a decrease. A sequence of the change of declination from the western to the eastern station at about 23:30 is remarkable: from the top to the bottom in the figure, a large positive, a small positive, a large negative, a larger negative, and a large positive. If the H and D variations at Espanola are compared respectively with those at Carrollton, variations are almost exactly reversed.

Generally speaking, two-thirds of the magnitude of geomagnetic variations in the H and D components is due to the earth's external field, and one-third is due to the internal field of the earth. From the variations shown in Figure 8, deviations of H and D values from those at 23:00 (105° WMT) were obtained every 5 minutes

starting from 23:20, and the equivalent electric current arrows were calculated from them. Differences from the value at 23:00 were taken because the variation at that time seemed to be on the smoothed curve of the storm time variation. In other words, it is assumed that the storm time variation Dst during the main phase was roughly subtracted by this process.

The sequence of the equivalent electric current is represented in the top half of Figure 9 by arrows for every 5 minutes. If we assume that these current arrows show the overhead electric current with the unit $200 \times 2/3 \gamma$, instead of 200γ , the overhead current system at

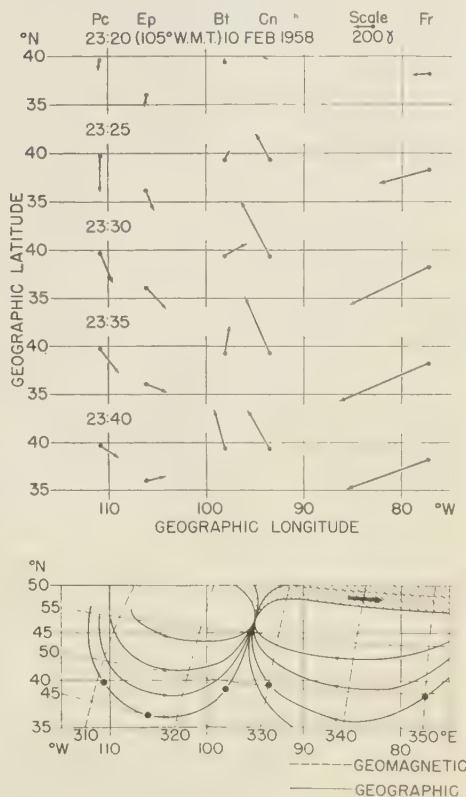


Fig. 9. Time sequence of the equivalent current vectors at Price, Espanola, Beloit, Carrollton, and Fredericksburg every 5 minutes. The bottom of the figure shows an overhead electric current system at about 23:35 (105° WMT). About 10^6 amperes flow between successive current lines.

about 23:35 would be as shown at the bottom of Figure 9. The five stations are given by both geographic and geomagnetic coordinates. The distribution of the current arrows at the five stations definitely suggests the existence of a strong flow of current around the auroral zone, which is hatched in the figure. In other words, the currents at these stations are the leak current from the strong auroral zone current. The latter results from mainly incoming auroral particles, which cause an increase of ionization there and thus a high electrical conductivity. Magnetic variations obtained at San Juan, Teoloyucan (geomagnetic 29.6°N, 327.1°E), and Huancayo also show that the leak current flowed even at these stations. Measurement of absorption of cosmic radio noise at that time by Warwick [1958] supports the hypothesis of an increase of ionization. Also vertical incidence ionospheric observations (frequency range 0.05 to 2.0 Mc/s) near Boulder clearly show the increase of ionization at 23:30 105° WMT. Auroral X rays measured at Minneapolis also started to increase at about 23:20 105° WMT, and reached a maximum at about 23:30 [Winckler, Peterson, Hoffman, and Arnoldy, 1959].

Acknowledgments. The author wishes to express his sincere gratitude to Dr. W. O. Roberts and Mr. A. H. Shapley for their kind help and valuable advice, to Dr. S. Chapman and Dr. E. H. Vestine for their discussion, and to Miss M. Sakamoto and Mr. S. J. Oh for their assistance. He wishes also to thank the IGY World Data Center A for Geomagnetism of the Coast and Geodetic Survey for use of geomagnetic data, and the Boulder Laboratories of the National Bureau of Standards for an appointment as guest worker and for extending their facilities to him. The work reported here was supported by the National Academy of Sciences as part of the IGY program, with the assistance of a grant from the Ford Foundation.

REFERENCES

- Abe, S., Morphology of ssc and ssc*, *J. Geomag. Geoelec.*, **10**, 153-163, 1959.
- Campbell, W. H., Studies of magnetic field micro-pulsations with periods of 5 to 30 seconds, *J. Geophys. Research*, **64**, 1819-1826, 1959.
- Chakrabarty, S. K., 'Sudden commencements' in geomagnetic field variations, *Nature*, **167**, 31, 1951.
- Chapman, S., Solar streams of corpuscles: their geometry, absorption of light and penetration, *Monthly Notices Roy. Astron. Soc.*, **89**, 456-470, 1929.
- Chapman, S., The morphology of geomagnetic storms. An extension of the analysis of DS, the disturbance local-time inequality, *Ann. geophys.*, **5**, 481-499, 1952.
- Chapman, S., The morphology of geomagnetic storms and bays. A general review, *Vistas in Astronomy*, **11**, 912-928, Pergamon Press, 1959.
- Chapman, S., and V. C. A. Ferraro, A new theory of magnetic storms, *Terrestrial Magnetism and Atmospheric Elec.*, **36**, 77-97, 1931a; part I, The initial phase, **36**, 171-185, 1931b; **37**, 147-156, 1932a; **37**, 421-429, 1932b; part II, The main phase, **38**, 79-96, 1933.
- Chapman, S., and V. C. A. Ferraro, The theory of the first phase of a geomagnetic storm, *Terrestrial Mag. Atmosph. Elect.*, **45**, 245-268, 1940.
- Dessler, A. J., The propagation velocity of world-wide sudden commencements of magnetic storms, *J. Geophys. Research*, **63**, 405-408, 1958.
- Dessler, A. J., and E. N. Parker, Hydromagnetic theory of geomagnetic storms, *J. Geophys. Research*, **64**, 2239-2252, 1959.
- Ferraro, V. C. A., Some remarks on recent notes by Drs. Sugiura and Vestine, *J. Geophys. Research*, **59**, 309-311, 1954.
- Ferraro, V. C. A., W. C. Parkinson, and H. W. Unthank, Sudden commencements and sudden impulses in geomagnetism: their hourly frequency at Cheltenham (Md.), Tucson, San Juan, Honolulu, Huancayo and Watheroo, *J. Geophys. Research*, **66**, 177-195, 1951.
- Fine, H., An effective ground conductivity map for continental United States, *Federal Communications Comm.*, *T. R. R. Rept.* **2.1.4**, 1953.
- Forbush, S. E., and E. H. Vestine, Daytime enhancement of size of sudden commencement and initial phase of magnetic storms at Huancayo, *J. Geophys. Research*, **60**, 299-316, 1955.
- Francis, W. E., M. I. Green, and A. J. Dessler, Hydromagnetic propagation of sudden commencements of magnetic storms, *J. Geophys. Research*, **64**, 1643-1645, 1959.
- Gerard, V. B., The propagation of world-wide sudden commencements of magnetic storms, *J. Geophys. Research*, **64**, 593-596, 1959.
- Jackson, W., World-wide simultaneous magnetic fluctuations and their relation to sudden commencements, *J. Atmospheric and Terrest. Phys.*, **2**, 160-172, 1952.
- Jacobs, J. A., and T. Obayashi, The sudden commencements of magnetic storms, *Univ. Toronto Sci. Rept.*, **3**, 1956.
- Kato, Y., and T. Saito, Preliminary studies on the daily behaviour of rapid pulsation, *J. Geomag. Geoelec.*, **10**, 221-225, 1959.
- Matsushita, S., Ionospheric variations associated with geomagnetic disturbances, *J. Geomag. Geoelec.*, **5**, 109-135, 1953.
- Matsushita, S., On sudden commencements of magnetic storms at higher latitudes, *J. Geophys. Research*, **62**, 162-166, 1957.
- Matsushita, S., On artificial geomagnetic and ion

- ospheric storms associated with high-altitude explosions, *J. Geophys. Research*, *64*, 1149-1161, 1959a.
- Matsushita, S., The equatorial ionosphere and the electrojet, USA-URSI, 1959, Fall Meeting Program, p. 25, 1959b.
- McIntosh, D. H., Geomagnetic 'sudden commencements' at Lerwick, *J. Atmospheric and Terrest. Phys.*, *1*, 223-232, 1951.
- McNish, A. G., Sudden commencement at Watheroo, *Compt. rend. assemblée de Lisbonne*, 1933, *IATME Bull.* 9.
- Nagata, T., Distribution of SC* of magnetic storms, *Rept. Ionosphere Research Japan*, *6*, 13-30, 1952.
- Nagata, T., and S. Abe, Notes on the distribution of SC* in high latitudes, *Rept. Ionosphere Research Japan*, *9*, 39-44, 1955.
- Newton, H. W., 'Sudden commencements' in the Greenwich magnetic records (1879-1944) and related sunspot data, *Monthly Notices Roy. Astron. Soc., Geophys. Suppl.*, *5*, 159-185, 1948.
- Obayashi, T., and J. A. Jacobs, Sudden commencements of magnetic storms and atmospheric dynamo action, *J. Geophys. Research*, *62*, 589-616, 1957.
- Oguti, T., Notes on the morphology of SC, *Rept. Ionosphere Research Japan*, *10*, 81-90, 1956.
- Piddington, J. H., Geomagnetic storm theory, *J. Geophys. Research*, *65*, 93-106, 1960.
- Rikitake, T., Anomaly of geomagnetic variations in Japan, *Geophys. J.*, *2*, 276-287, 1959.
- Rikitake, T., and I. Yokoyama, Anomalous relations between H and Z components of transient geomagnetic variations, *J. Geomag. Geoelec.*, *5*, 59-65, 1953.
- Rodés, L., Periodo diurno—en las perturbaciones súbitas, *Terrestrial Magnetism and Atmospheric Elec.*, *37*, 273-277, 1932.
- Singer, S. F., A new model of magnetic storms and aurorae, *Trans. Am. Geophys. Union*, *38*, 175-190, 1957.
- Sugiura, M., The solar diurnal variation in the amplitude of sudden commencements of geomagnetic storms at the geomagnetic equator, *J. Geophys. Research*, *58*, 558-559, 1953.
- Warwick, J. W., Absorption of cosmic radio noise during the great aurora of 11 February 1958, *Science*, *127*, 1047-1048, 1958.
- Williams, V. L., The simultaneity of sudden commencements of magnetic storms, *J. Geophys. Research*, *65*, 85-92, 1960.
- Winckler, J. R., L. Peterson, R. Hoffman, and R. Arnoldy, Auroral X-rays, cosmic rays, and related phenomena during the storm of February 10-11, 1958, *J. Geophys. Research*, *64*, 597-610, 1959.

(Manuscript received February 1, 1960; revised February 28, 1960.)

On the Position of the Focus of the Geomagnetic S_q Current System

M. HASEGAWA

*Fukui University
Fukui City, Japan*

Abstract. This paper reviews present knowledge about the S_q foci, discusses the cause of changes in the S_q field, and describes problems concerning the determination of the S_q focus. It is concluded that the foci in the potential fields of geomagnetic D_q variations may be taken as approximately indicating the positions of ionospheric S_q current foci.

1. THE FOCUS OF THE S_q CURRENT SYSTEM

The term ' S_q focus' may be defined in more than one way. Ionospheric workers use it to mean the daytime center of circulation of the overhead electric current system that is the primary cause of the S_q (quiet-day solar daily) magnetic variation. This varying current system induces electric currents within the earth, which also contribute to the S_q magnetic variations observed at the earth's surface. From the horizontal components of this variation the magnetic potential V of the total S_q field at the earth's surface can be determined. There is a point of minimum S_q potential in the northern hemisphere, and a point of maximum potential in the southern hemisphere. These points may be called the S_q potential foci.

The potential V can be expressed at any instant as the sum of a series of spherical harmonic terms. The S_q variation of the vertical magnetic intensity at the same instant can be expressed by another series of spherical harmonic terms. By comparing the two series V can be divided into two parts: V_e , the surface magnetic potential of the external electric current system; and V_i , the surface magnetic potential of the induced currents. Each part will have maximum and minimum points. From V_e it is possible to draw the current lines of the external system, supposed to flow at some chosen uniform height h above the earth. The positions of the northern and southern current foci will depend only slightly on the value of h for heights corresponding to the D , E , and F layers. Their radial projections on the earth's surface will be close to the V_e potential foci. (In this case the current lines coincide with the

equipotential lines. The current function is defined so that its maximum corresponds to a minimum of the potential.)

In a previous paper [Hasegawa, 1950] I have compared the V_e foci with the V and V_i potential foci, using *monthly or annual mean* data for S_q . The differences of position were not large. The same conclusion may be expected to apply also to the foci determined at particular *instants*. We may therefore take the V potential foci as approximately indicating the positions of the ionospheric S_q current foci. The V potential foci can be rather accurately determined graphically if recorded S_q data are available for several points suitably distributed along a meridian in the middle latitudes. We may then consider to what extent these potential foci are likely to differ from the ionospheric current foci.

2. SUMMARY OF PRESENT KNOWLEDGE ABOUT THE S_q FOCI

(a) *The average position of the foci.* Figure 1, from Chapman and Bartels [1940], shows the current lines of the ionospheric S_q system, drawn by Bartels from Chapman's spherical harmonic analysis (1919) of S_q for the minimum sunspot year 1902. It shows the daytime current foci at 40°N , 11h local time, at the equinoxes (the mean of the months March, April, September, October), and at 30°N , 11.5h, and 45°S , 11h, at the northern summer solstice (mean of the months May to August).

Other analyses of S_q , based on data for other times and observatories, have given fairly similar current diagrams.

These analyses were not specially directed to-

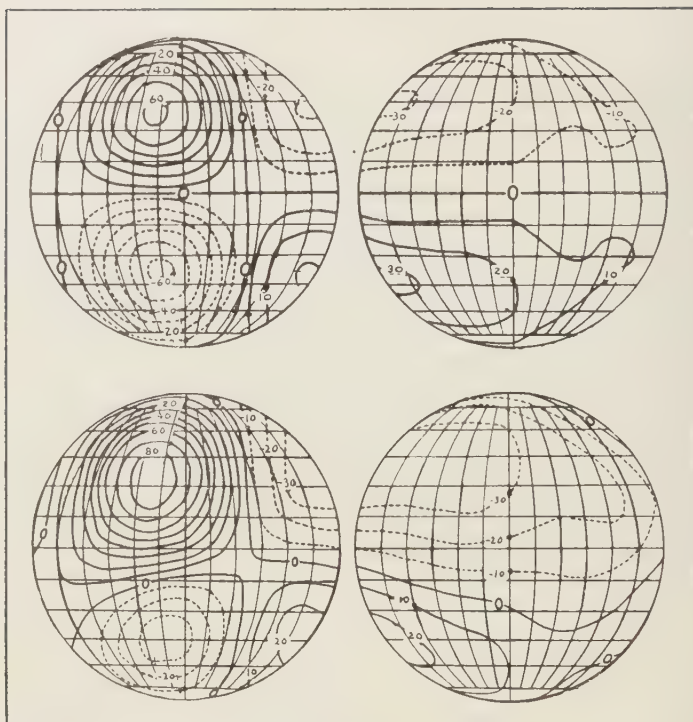


Fig. 1. The upper diagrams show the overhead electric current system corresponding to S_q (the solar daily magnetic variation on quiet days), over the sunlit hemisphere (left) and the night hemisphere (right), referring to sunspot minimum, at the equinox. The lower diagrams show the corresponding current system for the northern summer.

ward the accurate determination of the positions of the current foci. For this purpose more observations in middle latitudes, better distributed, were necessary. The Second International Polar Year, 1932-1933, supplied data for 46 observatories between the latitudes 60°N and 60°S . But even this was not quite adequate to determine the current foci accurately at individual epochs, especially in the southern hemisphere. However, the attempt was made to determine the most probable values of the S_q field vector over the belt of the earth's surface between 60°N and 60°S by taking account of the continuity of change of the S_q field as it progresses around the earth with respect to universal time (UT). For the mean of the summer and the winter solstice months twelve S_q current diagrams were obtained, for the epochs 0, 2, 4, . . . UT, that is, for twelve uniformly

spaced aspects of the earth relative to the sun [Hasegawa, 1950]. The potential was calculated by numerical integration. At epochs of UT at which several observatories are suitably located relative to a focus, the positions of the foci on these maps should be reasonably accurate. Figure 2 shows the (geographical) latitudes of the foci at the twelve UT epochs, estimated from the sequence of maps. The point associated with the northern focus are ringed by a full circle; those for the less-well-determined southern focus, by a broken circle. Figure 3 shows the corresponding (V) equipotential lines for the S_q field averaged over the twelve UT epochs; the coordinates of the base map are geomagnetic. The north daytime (V) focus is shown to be at 35°N , 11.0h, and the southern one at 35°S , 11.3h. These latitudes and local times are not necessarily the means of the

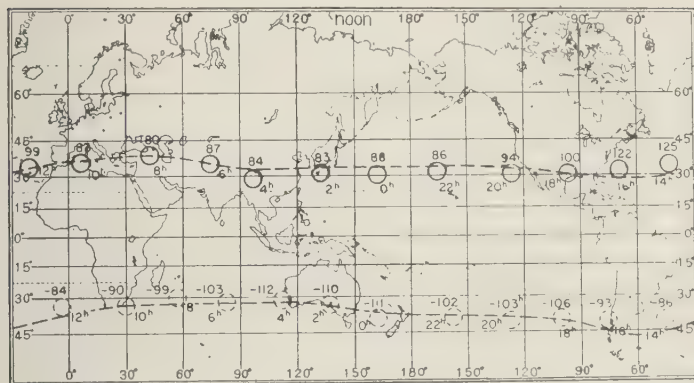


Fig. 2. The mean positions of foci in the equivalent current system of S_q every 2 hours, referring to the Second Polar Year (sunspot minimum), for the average of the summer and winter solstice months. Geographic coordinates. The number alongside each point indicates the potential (in units of 0.825×10^8 cgs) at each UT epoch. The broken curves in the two hemispheres show the boundaries at which the harmonic coefficient a_1 of the X variation changes sign.

twelve sets of values for the foci at the individual UT epochs, because the general intensity of the total surface potential V varies with UT in the course of a day; for 1932-1933 (solstice) the ratio maximum to minimum intensity was more than 3-2. In such diagrams as Figures 1 and 3, the mean positions of the foci will be especially influenced by the positions at the epoch of maximum V . Moreover, local peaks or other irregularities in the distribution of V , which influence the positions of the foci at particular UT's, will be smoothed out in the average S_q days.

In Figure 2 the focal latitudes are shown by

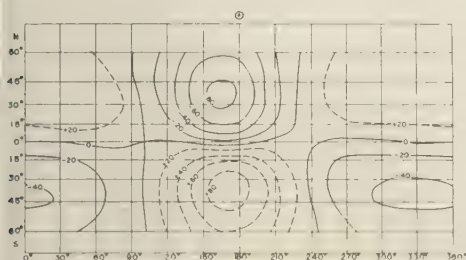


Fig. 3. Equipotentials of the S_q field (mean of solstitial months) referring to the Second Polar Year, in units of 0.825×10^8 cgs, which is equivalent to 1000 amperes in the overhead electric current at about 100-km height. The symbol shows the position of the sun.

points (on the map). The actual potential at each UT epoch is shown by a number along each point.

The north focus travels westward from North America across the Pacific Ocean at approximately 31°N (geographic): the latitude increases to a maximum in middle Asia, and, maintaining the average value of about 38°N over the Atlantic Ocean, declines to 31°N in North America; the average geographic latitude is about 34°N . The south focus is mostly in a somewhat higher latitude than the north focus, the average being about 36°S , but its position is less well determined. In both hemispheres, however, magnetic observatories adequate to determine the tracks of the foci are lacking. Only in five regions (Gulf of Mexico, South America, West Pacific, South Australia, and the Mediterranean region) are there adjacent observatories on both sides of the track, and even they are not most suitably located. The most favorable zones, which may be called European, Far Eastern, and American, give the following focal latitudes:

Latitudes of the S_q potential foci

Zone:	European	Far Eastern	American
North focus	37°	31°	31°
South focus	36°	32°	40°

As regards the local time or position in longi-

tude (relative to the meridian through the sun), the north focus, according to Figure 2, may be situated as early as about 1 hour before noon, and the south focus may be situated some 1/3 hour later than the north focus. But in view of the paucity of observatories suitably disposed near the focal tracks, these local times are rather uncertain, and there is need for further study based on better data.

It seems likely that on magnetically quiet days the focal latitudes can be estimated with fair accuracy by considering the S_q value of the horizontal intensity H on the meridian of 11h.

For comparison with the above results for S_q , a diagram, Figure 4, is taken from *Namikawa* [1957], showing the equipotential lines of the S_q field referring to the Second Polar Year (sunspot minimum) as the mean of the summer and winter solstice months. It is interesting to see that the positions of the daytime foci of S_q do not differ from those of S_q (Fig. 3) in the mean state. We will discuss this point later, in section 5(c).

(b) *The daily variation of intensity of the S_q field.* As the earth turns relative to the sun, there is a daily variation of the general intensity as well as of the form of the S_q field. A convenient general measure of the intensity is the value of the minimum or maximum potential at the north and south foci respectively. In the northern hemisphere the greatest numerical value of V is attained at 14h 16h UT, and the maximum potential at the south focus is numerically least around that epoch. The potential difference between the two foci has a smaller daily variation, as if the change at the south

focus nearly compensates for that at the north focus. This might be expected, as the S_q field will be largely controlled by the direction of the geomagnetic axis as this rotates with the earth.

The daily UT change of energy of the S_q field is greater than its mean energy.

(c) *The day-to-day S_q changes.* The S_q field undergoes active and complicated changes from day to day, which as yet have been but little studied. Bartels has given harmonic diads showing the daily diad vectors for the first and second components of $S_q(H)$ at Watheroo (not far from the south focal latitude). *Ota* [1949, 1950] has studied the north focal latitude in the Far Eastern zone for each day of the Second International Polar Year. The determination of the focal latitude on magnetically disturbed days requires that allowance be made for the presence of the additional disturbance field. This, not an easy problem, is discussed in section 5(c). Even during quiet periods the focal latitude may change considerably from one day to the next. Figures 5 and 6 illustrate this; they show the S_q equipotential lines (Fig. 5) and the external S_q current lines (Fig. 6) at 11h local time (2h UT) in the Far Eastern zone on June 21, 1934. Figures 7 and 8 are corresponding diagrams for the same hours on June 23, 1934. Both days were magnetically quiet, the daily character figures C being zero. On June 21 the main north focus was at $28^\circ N$, 11.2h; the weak south focus was at approximately $36^\circ S$, 12h. Forty-eight hours later the two foci were further north by about 15° (north focus) and 12° (south focus). At the observatories between the two positions of the

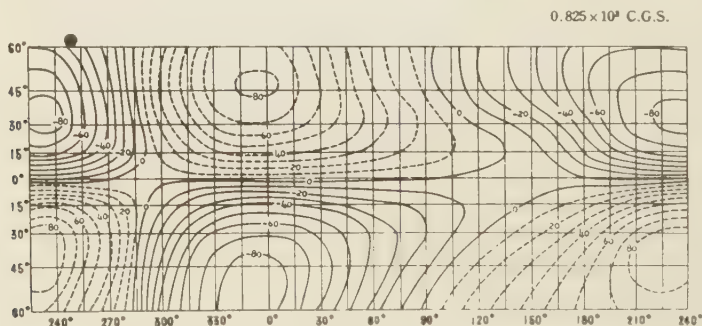


Fig. 4. Similar to Figure 3, but for the S_q field. The symbol shows the position of the Sun.

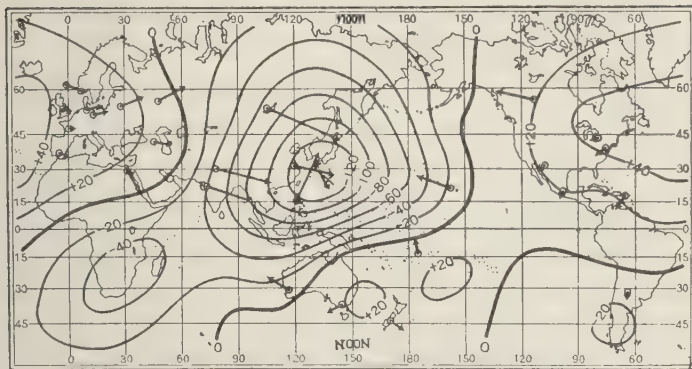


Fig. 5. Equipotential lines of daily magnetic variations at 2h GMT, June 21, 1934.

north focus, the type of the S_q (H) variations was quite different on the two days.

Figures 5 to 8 also indicate that the latitude of the external current focus may differ from that of the corresponding potential focus by 1° to 5° . It is hardly possible at present to judge which focus is the better for the discussion of the changes of ionospheric current system. The position of the current focus cannot at present be determined with an accuracy better than 2° to 3° . The factors on which the accuracy depends are discussed in section 5.

Figure 9 shows the difference between the overhead current systems (Figs. 6 and 8) on June 23 and June 21, 1934. Figure 10 is a corresponding diagram showing the difference as

between September 24 and 23, 1933. The cause of such day-to-day changes is discussed in section 3.

(d) *The seasonal change of latitude of the S_q potential focus.* Ota used the magnetic records of the Second International Polar Year to study the seasonal change of S_q focal latitude in the west Pacific region, which is the most favorable zone as regards the number and location of observatories suitable for the purpose. There he determined the north focal latitude for each day during the 13-month period. Omitting uncertain values, he calculated 30-day means to show the seasonal variation of the focal latitude, with the result shown in Figure 11. This indicates a marked seasonal variation with a range of about 10° —the focus is farthest north (about 39°) when the sun is farthest

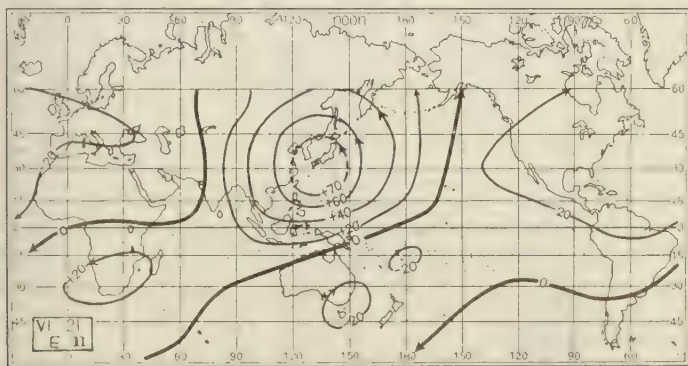


Fig. 6. External electric current system at 2h GMT, June 21, 1934.

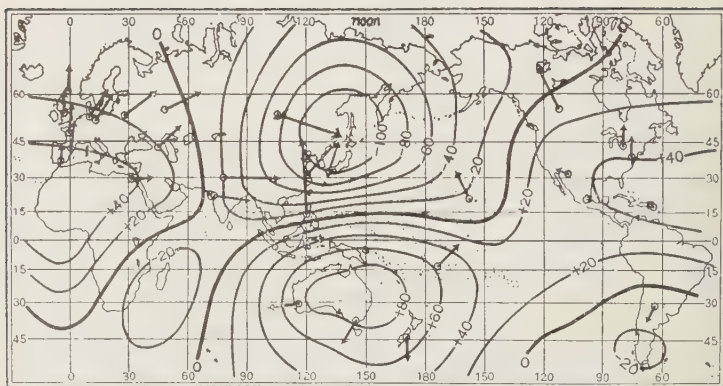


Fig. 7. Equipotential lines of daily magnetic variations at 2h GMT, June 23, 1934.

south, but from March to September it varies only slightly around a value of about 31° . It seems likely that the south focus has an approximately corresponding variation, being most southerly around June and July.

Ota attempted to determine the seasonal variation of the focal latitudes for other zones also, with only moderate success. Further study of the seasonal variation is needed, with better data.

3. THE CAUSE OF THE CHANGES IN THE S_q FIELD

The S_q field changes from day to day [section 2(c)] and seasonally [section 2(d)]. It is a product of dynamo action by winds in the ionosphere; the distribution of the currents produced by the dynamo emf's depends on the dis-

tribution of ionospheric ionization and the resulting conductivity. Ionospheric observations show that there is a considerable seasonal change of ionization, which must greatly affect the S_q current system. From the geomagnetic observations, Maeda [1955; 1957] and Kato [1956; 1957] inferred the ionospheric wind distribution at the solstices and equinoxes, taking account of the anisotropic conductivity. They concluded that at the solstices the wind flow across the equator in opposite directions in different longitudes. The cause of these wind changes must be dynamic (aeronomical or meteorological), not electromagnetic.

The day-to-day changes in the S_q field seem likely to be due to wind changes rather than to changes in the distribution of ionization and conductivity. In the spherical harmonic expres-

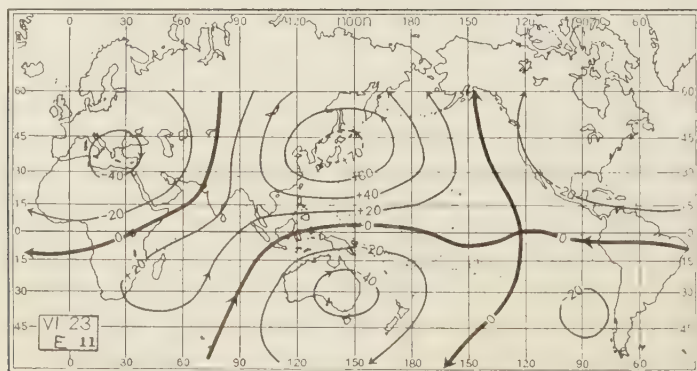


Fig. 8. External electric current system at 2h GMT, June 23, 1934.

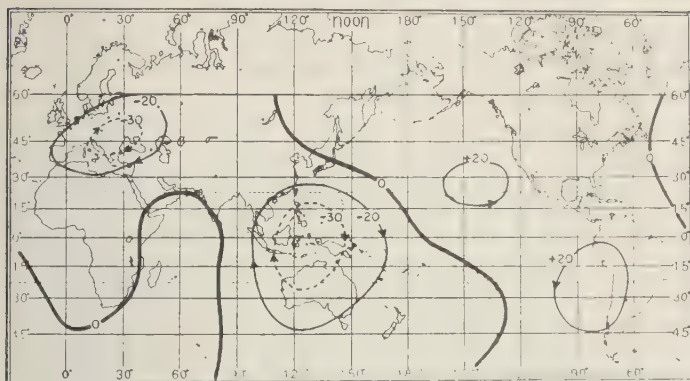


Fig. 9. Difference between the external current systems at 2h GMT, June 23-21, 1934.

ons for the difference between current systems. Figures 9 and 10, the presence of symmetrical terms such as p_1^1 , p_s^1 , p_s^2 is conspicuous, just as the difference between the summer and winter S_a fields. Both Figures 9 and 10 indicate a notable circulation of electronic current across the equator. It seems likely that this is due to a change in the wind system. Without detailed calculations the nature of the change of the wind system cannot be understood, but it may consist of wind circulation across the equator.

4. THE PRACTICAL DETERMINATION OF THE S_a FOCUS

(a) When a focus is surrounded by several stations its position can be determined as the point from which the S_a horizontal force vectors

radiate. Even during the IGY such determination was seldom possible. The northward and southward movements of the focus require a more widespread network for the application of the method than would otherwise be necessary. To determine the focus for a particular UT, on a single day or for monthly or seasonal mean S_a , one must often use stations that at the time are as much as 30° to east or west of the focal meridian. The resulting inaccuracy in the estimated focal position is probably reasonably small.

(b) On the focal meridian at any particular UT the potential reaches its extreme value at the focus. It should be calculated from the values of $S_a(X)$ along this meridian at that UT, but, where such values are lacking, values

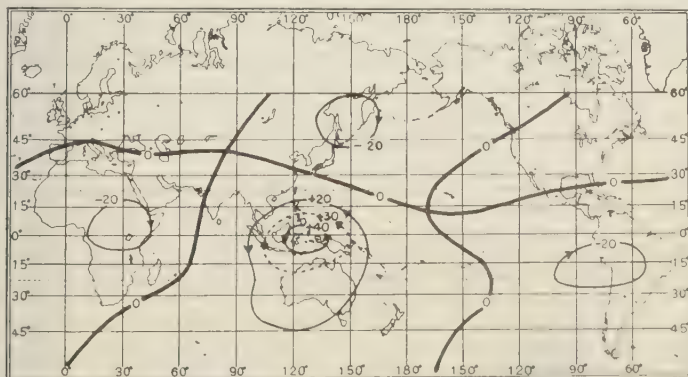


Fig. 10. Difference between the external current systems at 2h GMT, Sept. 24-23, 1933.

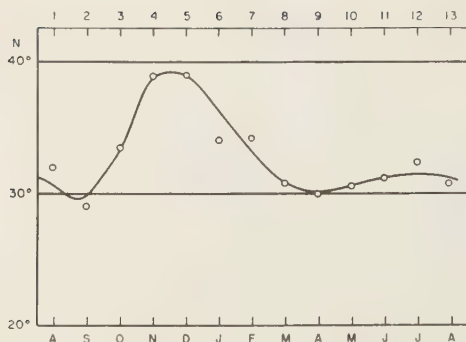


Fig. 11. Seasonal variation of the northern focal latitude in the west Pacific region during the Second Polar Year.

of $S_q(X)$ at 11h local time at adjacent stations within, say, 1 hour difference of longitude may be used instead.

From a curve of $S_q(X)$ as a function of latitude along the focal meridian the focal latitude is determined as the point where $S_q(X)$ changes sign through the zero value. To determine this latitude it is desirable to have more than four available values, some on each side of the focus. Sometimes the available adjacent values are fewer, or all on one side of the focus, or do not give a smooth $S_q(X)$ curve. In such cases *Ota* [1949, 1950] was aided in drawing the curve by a knowledge of the form of curve of $S_q(X)$ for the 10h or 12h meridian in the region of the earth on quiet days. Figure 12 shows some of his results, as communicated at the 1948 Oslo Assembly of the International Association of Terrestrial Magnetism and Electricity.

In studying the S_q focus from the IGY magnetic data the same method can be used. But here, as also in relation to Figure 12, the results are somewhat uncertain on disturbed days [section 5(c)].

5. PROBLEMS CONCERNING THE DETERMINATION OF THE S_q FOCUS

As the S_q potential focus is at the position of maximum or minimum potential, and as the potential varies slowly near such extreme values, a weak anomaly in the S_q distribution can materially change the position of the focus. Hence it is desirable to examine the factors that may thus influence the position.

(a) *The base value of the S_q variation.* The values of $S_q(X)$ are usually reckoned from the daily mean value of X . But from the standpoint of the dynamo theory another choice of base line is better. The choice proposed by *Hasegawa* and *Maeda* [1951] and later by *Maeda* [1953, 1956] was based on a dynamo calculation of the S_q currents, taking the daily mean electromotive force at any station to be zero, and eliminating the daily variation of conductivity. The change of base line is denoted by c_0 (Fig. 13); it is determined for X and Y separately; $C_0(X)$ and $C_0(Y)$ as a function of latitude, as determined from X and also from Y , for summer, winter and the annual mean. $C_0(X)$ has a maximum at the equator, and changes sign at about 35° N and S, at about the focal latitudes of S_q . The numerical value of the potential at the daytime S_q focus is increased by about 45 per cent by the change of X base line by the amount C_0 .

Figure 2 shows two broken lines, lying nearly along the 35° latitude circles, which indicate the latitudes at which a_1 , the first harmonic coefficient of $S_q(X)$, changes sign.

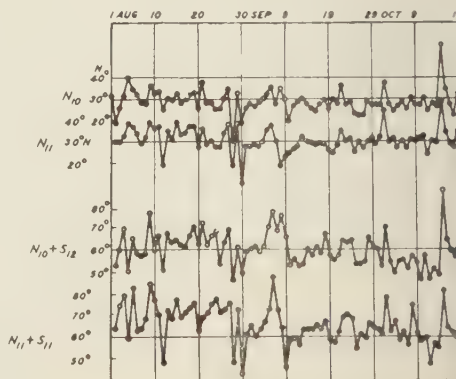


Fig. 12. An example showing the day-to-day focal positions (part of the Second Polar year data).

N_{10} , N_{11} : North focal positions determined by the X curves along the 10h and 11h meridians, respectively.

S_{10} , S_{12} : South focal positions determined by the X curves along the 11h and 12h meridians, respectively.

$N_{10} + S_{12}$: The distance between the foci N_{10} and S_{12} along the meridian.

$N_{11} + S_{11}$: The distance between the foci N_{11} and S_{11} along the meridian.

The open circles indicate less accurate values.

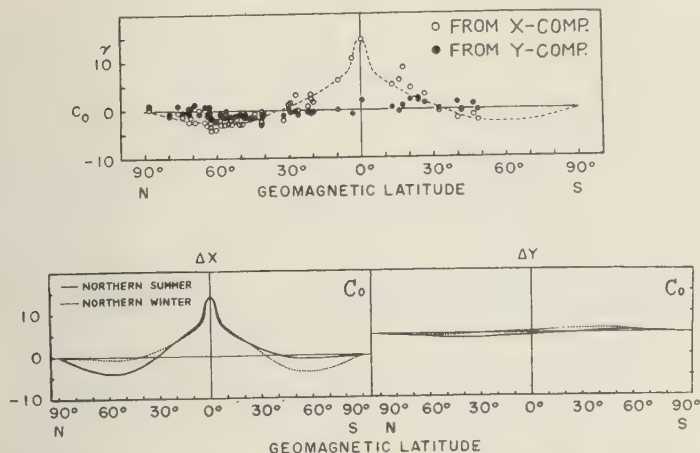


Fig. 13. Latitude distributions of C_0 , which is a quantity showing the departure of daily mean values from base values in the emf of the geomagnetic S_q field, for the mean solstices (above) and equinoctial seasons (below).

It was suggested that in determining the focal position the base value for X should be the right value, or the mean of the sunrise and sunset values. In some cases the base value can be read directly from the records, but in middle latitudes this is not easy. Ota is attempting to determine the day-to-day variations of the focus from the IGY data, using as base value the mean of the sunset and sunrise X data. His preliminary report is given in the Appendix.

(b) *The effect of the internal current system.* The general structure of the crust and the interior of the earth. In the main, the principal spherical harmonic terms in the external and internal parts V_e , V_i of the surface magnetic potential hold similar ratios, and the differences of phase angle, exterior-interior, are only a few degrees. But the relations are less simple for the higher harmonic terms. This departure from similarity may be ascribed to several contributory causes. It may depend partly on the insufficiency and unsatisfactory distribution of the magnetic data, but it may also depend on the nature of the earth's crust and deeper interior. Though it is not unlikely that the V_e and V_i potential foci agree within about 3°, it is desirable to make new analyses of V for S_q into its parts, V_e and v_i , on the basis of the IGY data.

2. *Inequalities within the crust.* Any irregu-

lar distribution of electrical conductivity within the crust will produce a local anomaly in S_q . World-wide studies of S_q average out such local anomalies, but they may affect the determination of the S_q foci at particular epochs of UT. However, as the anomalies seem to affect S_q more in Z than in X and Y , their influence on the focal positions may be small.

3. *The distribution of land and ocean.* The electrical conductivity of a deep ocean will be sufficient to shield the underlying crust from the external varying S_q field, so that some induced currents flow in the ocean. Hence V_i may be expected to vary with UT, owing to the irregular distribution of continents and oceans. The regions of the earth may be roughly classified into continental and ocean hemispheres, and some of the variations of latitude shown on Figure 2 may depend on that distinction.

Sometimes we have a twin structure of the northern focus in the Far East region. Figure 14 shows the chart of the magnetic potential of S_q on September 23, 1933, obtained by means of the method of graphical integration. In this chart we had two foci between 10h and 11h, deduced from observatories in this region. At three stations, Kakioka, Aso, and Zō Sēs, we had records of H variations of a typical equatorial type, showing that the observatories passed south of the focus (say focus I) while

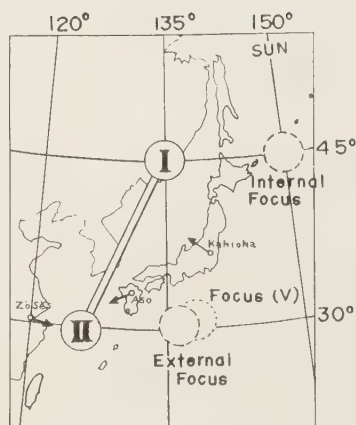


Fig. 14. Example of the twin foci (I) and (II), determined by the integration method. The dotted circle shows the focus in the potential field, represented by a formula with series of spherical harmonics. The broken circles are foci in the separated fields.

the horizontal vectors of the variations described a clockwise rotation, which is characteristic of the daily variations at observatories north of the focus (say focus II).

As the result of calculations made with all available data of the world, the foci of V and also of V_s were found to be nearly on the same latitude as focus II, while the focus of V_i was found to be at the same latitude as focus I, farther north. In other words, focus II is the ordinary one, and focus I is that for the interior electric current. Over the land area to the west, 4 hours later, we found conditions simpler, with a single focus passing between Alibag and Dehra Dun, along the same latitude as focus II. But we cannot be certain that the twin structure of the focus is an effect of the distribution of land and ocean until we examine the effect further by carrying out the analysis of the S_q field not only in this region but also in other parts of the earth.

(c) *The effect of disturbance fields.* The S_q variation of the month is usually defined as the mean of the daily variations on the five most quiet days; therefore it always contains, to some extent, the disturbance variations.

If the electric currents responsible for the SD and the S_q variations flow in the same layer of

the upper atmosphere, the foci will be formed in the combined electric current system, which is represented by V_s of the S field. We expect that electric currents parallel to the meridian near the focal meridian due to the SD field will advance or retard the real foci in longitude, but the latitude effect may be small. To determine the position of focus, the effect of the Dst field on the potential fields must be eliminated. The steady Dst and the steadily changing Dst are eliminated by the ordinary method of obtaining S (solar daily variation field); only irregular changes of the Dst field in the course of the day influence the position of the S field.

In illustrating day-to-day changes of the position of the focus, we find many large departures from the average value during magnetic storms. Except for these extreme cases the effect of Dst on the position of the focus in the monthly or annual mean may be negligible, because the positive and the negative effects seem equally probable. (See Fig. 4.)

The same can be said about the effect of other irregular disturbance fields.

6. CONCLUDING REMARKS

There are many unsolved problems. An essential difficulty is the insufficient and unsatisfactory distribution of observatories in middle latitudes; most other problems are unsolved because we have not worked on them. After examining all conditions, we reach the conclusion that the positions of the foci in the equivalent current system can be adopted as an indication for the foci of the overhead electric current system so far as the mean state of S and the well-calculated S_q on selected days are concerned. As for the day-to-day positions of foci, calculated by the practical method described above, including disturbed days, they may be regarded as revealing the relative variability of the S_q field. They also provide elementary and primary data for studying the various problems in this field.

Kyoto WDC₂₂ for Geomagnetism is attempting to issue the day-to-day position of the foci of equivalent current system of geomagnetic daily variations, if sufficient data are available. We desire the cooperation of all researchers who are interested in this subject, by carrying out

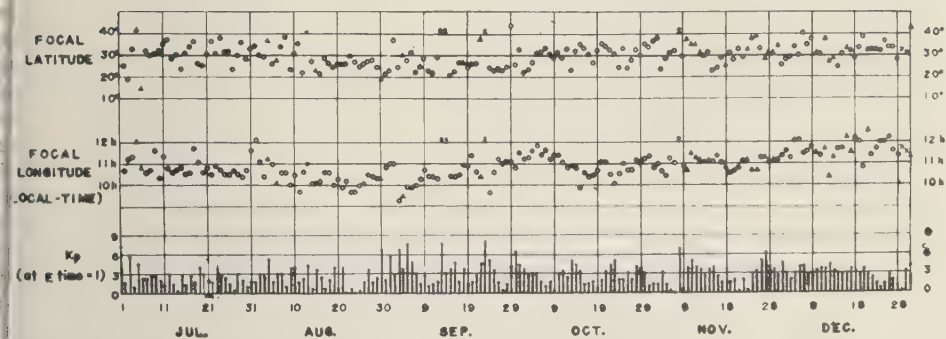


Fig. 15. The day-to-day position of the north focus of S in the Far East region from July 1 to December 31, 1957. Geographic coordinates. Circle, normal; triangle, inexact; x, extrapolated; s, no value, magnetic storm.

Available observatories: C034 Memambetsu, C147 Kakioka, C214 Shimosato, C223 Aso and E553 Muntinlupa.

Similar calculations with data in various regions of the world.

Acknowledgment. The cooperation of S. Chapman in reading this paper and revising the English is gratefully acknowledged.

APPENDIX

A preliminary report on the day-to-day positions of the north focus of S in the Far East Region, by M. Ota. As the base value of the X component, we adopted the mean of the sunrise and the sunset values, which are taken to be the average of X during 3 hours centered at ground sunrise and sunset. Between the main minimum and main maximum points in the Y curve, we determined a point which has the mean of the both extreme values. The time of that point was regarded as showing the focal longitude.

REFERENCES

- Chapman, S., and J. Bartels, *Geomagnetism*, p. 696, Clarendon Press, Oxford, 1940.
- Hasegawa, M., Transactions Oslo Meeting, 1948, *IATME Bull.*, 13, 1950. (Refer to the abbreviated diagrams on p. 431.)
- Hasegawa, M., and H. Maeda, *Rept. Ionosphere Research Japan*, 5, 167, 1951.
- Kato, S., *J. Geomagnetism and Geoelec.*, 8, 24, 1956; 9, 107, 1957.
- Maeda, H., *Rept. Ionosphere Research Japan*, 9, 148, 1955; 10, 49, 1956.
- Maeda, H., *J. Geomagnetism and Geoelec.*, 7, 121, 1955; 9, 86, 1957.
- Namikawa, T., *J. Geomagnetism and Geoelec.*, 9, 212, 1957.
- Ota, M., *Rept. Ionosphere Research Japan*, 3, 27, 1949 (in Japanese); also Transactions Oslo Meeting, 1948, *IATME Bull.* 13, 438, 1950.

(Manuscript received December 8, 1959; revised February 3, 1960.)

Polarization Parameters of the Downcoming Radio Wave

Y. S. N. MURTY¹ AND S. R. KHASTGIR

*University of Calcutta
Calcutta, India*

Abstract. The phase difference between the *normal* and the *abnormal* components of the magnetic vector of the radio wave (i.e., the components in and at right angles to the plane containing the wave normal and the direction of the earth's magnetic field) and the limits of the tilt angle of the major axis of the polarization ellipse (traced out by the electric vector) measured anticlockwise with respect to the direction of the magnetic north for the ordinary and the extraordinary modes of propagation have been obtained on the ray theory of propagation through the ionosphere. The values are given in a table for the ordinary and the extraordinary modes in both the hemispheres for regions below and above the level of ionospheric reflection.

Scott's treatment of the same problem on the ray theory and the results given by Roy and Verma on the basis of the coupled wave equations of Saha and others are reviewed. It is shown that the discrepancies in the results of the polarization parameters obtained by different workers on ray theory are only apparent and arise out of the differences in the forms and notations used in the different formulas. It is also shown that the discrepancies in the limits of the major axis of the polarization ellipse obtained from the ray theory and the wave theory are due to the interchange in the expressions for the amplitude ratio of the *normal* to the *abnormal* components for the ordinary and the extraordinary waves given by Saha and others. The experimental results of Roy and Verma are shown to confirm our theoretical conclusions about the limits of the tilt angle of the polarization ellipse.

1. **Introduction.** The polarization of a radio wave propagated through the ionosphere is usually represented by ρ and ϕ ; ρ is the ratio of the amplitudes of the *normal* to the *abnormal* components of the magnetic vector (i.e., components in and at right angles to the plane containing the wave normal and the direction of the earth's magnetic field), and ϕ is the phase difference between them. If the wave propagation is in the positive direction of the X axis of a right-handed coordinate system and the earth's magnetic field is in the X - Z plane, the state of polarization of the wave can also be represented by θ and ψ , where $\tan \theta = -ih_z/h_y$, h_y and h_z being the magnetic vectors of the wave along the Y and the Z axes and ψ the tilt angle of the major axis of the polarization ellipse as described by the electric vector with respect to the positive direction of the Z axis. The tilt angle is taken as positive when measured anticlockwise on looking toward the direction of propagation, and the direction of magnetic north is taken

as the positive direction of the Z axis. The parameters θ and ψ are related to the parameters ρ and ϕ by

$$\tan 2\psi = -\frac{2\rho \cos \phi}{1 - \rho^2} \quad (1)$$

and

$$\tan^2 \theta = \frac{(1 + \rho^2) \sin 2\psi + 2\rho \cos \phi}{(1 + \rho^2) \sin 2\psi - 2\rho \cos \phi} \quad (2)$$

Following the Appleton-Hartree formulas [Appleton, 1927; Hartree, 1929], theoretical methods for obtaining the polarization parameters were given by Taylor [1934], Bailey [1934], and Scott [1950, 1953]. These methods were based on the ray theory of propagation. Martyn [1935] computed certain dispersion, absorption, and polarization curves for vertical radio-wave propagation in the ionosphere following Bailey's method of conformal representation. Similar curves were also drawn by Ghosh [1938] and later by Singh and Murty [1958] following the same method. The coupled wave equations for vertical propagation in the ionosphere were

¹ Present address: Defence Science Organization, Delhi, India.

given by Försterling [1942], Rydbeck [1944], and Saha, Banerjee, and Guha [1947, 1951]. The identical nature of the equations obtained by these workers was pointed out by Kelso [1953]. Roy and Verma [1955] published a number of polarization curves based on the wave equations of Saha and others along with some experimental results. Mention should be made of the polarization charts given by Snyder and Helliwell [1952]. They plotted the complex polarization given by the magnetoionic theory on the complex plane using normalized parameters related to the electron density and electron collisional frequency. As experimental data were obtained in the form of ellipticity and tilt angle, they computed a chart relating these quantities to the same normalized parameters as those given in the complex polarization chart. They also prepared a nomogram which is helpful in converting the normalized parameters on the two polarization plots to the corresponding electron density and electron collisional frequency. In the recent work of Murty [1959] and Murty and Khashtgir [1959] it has been shown that the expressions for the polarization parameters obtained from the wave equations of Saha and others are exactly the same as those obtained from ray-theory considerations.

There appear to be certain conflicting results, however, in regard to the quadrant of the phase difference between the normal and the abnormal components of the ordinary and the extraordinary waves and also in regard to the limits of the polarization parameters for the downcoming radio wave. Following Bailey's method of obtaining the polarization parameters from the Appleton-Hartree formulas, it is clear that the phase difference ϕ between the normal and the abnormal components of the magnetic vector for the ordinary wave (where $\rho < 1$) below the ionospheric reflection level in the northern hemisphere is in the first quadrant (i.e., between 0 and $\pi/2$). But according to the modified phase-quadrant table given by Scott [1953], who also followed the ray theory, the phase difference ϕ , under the above conditions, is in the second quadrant. From the wave equations of Saha and others the phase difference between the normal and the abnormal components for the ordinary wave, under the same conditions, is in the second quadrant. When the curves for

the polarization parameters given by Taylor, Martyn, Ghosh, and Singh and Murty from ray-theory considerations are compared with the corresponding curves computed by Roy and Verma from the wave equations of Saha and others, two differences appear:

(a) For values of the electron collisional frequency less than the critical collisional frequency, that is, $\nu < \nu_c$, the ray-theory curve showing θ against the electron density N is the mirror image of the corresponding curve drawn by Roy and Verma on wave theory.

(b) For $\nu < \nu_c$, the limits of the tilt angle of the major axis of the polarization ellipse obtained according to the ray theory are different from those obtained by Roy and Verma from wave-theory considerations.

According to Taylor, Bailey, Martyn, Singh and Murty, the tilt angle of the major axis of the polarization ellipse for the ordinary wave, below the ionospheric reflection level in the northern hemisphere, should be within the limits $3\pi/4$ and π , in the second quadrant within the limits $7\pi/4$ and 2π , in the fourth quadrant. Scott agreed with these findings. Roy and Verma, however, concluded from wave-theory considerations that the corresponding tilt angle of the major axis of the polarization ellipse should lie within the limits $\pi/2$ and $3\pi/2$ in the second quadrant, or within the limits $3\pi/2$ and $7\pi/4$, in the fourth quadrant.

The object of the present paper is to explain the above discrepancies. With regard to the quadrant of the phase difference between the normal and the abnormal components obtained by Scott and other workers on ray theory, the discrepancy is due to the difference in the formulas and notations adopted for the periodic field of the radio wave and the complex polarization term. The difference in sign of the polarization parameter θ as given by Roy and Verma on wave theory and by the workers on ray theory is only apparent and arises out of the difference in the sign convention. The discrepancy in the limits of the tilt angle of the major axis of the polarization ellipse obtained on wave theory and on ray theory is due to the interchange of the expressions for the ordinary and the extraordinary complex polarization parameters. Moreover, what Roy and Verma consider

polarization ellipse due to the ordinary wave in their records should actually be that due to the extraordinary wave.

1. *Notations adopted by different workers.* (a) In the present paper, the periodic field at any instant t of the radio wave of angular frequency ω proceeding in the X direction is taken in the form $e^{i\omega t}$ as in the Appleton-Hartree formula. (b) The complex polarization is represented by $R = h_z/h_y = \rho e^{i\phi}$, where ρ is the ratio of the amplitudes of the normal to the abnormal components of the magnetic vector of the wave and ϕ is the phase difference between them.

(c) In the application of the ray treatment by Appleton, Martyn, Ghosh, and Singh and Murty the complex polarization is expressed as $R = h_z/h_y = \rho e^{i\phi}$.

(d) In Scott's treatment on the ray theory, however, the periodic field of the wave is taken in the form $e^{-i\omega t}$, and the complex polarization given by $R = -h_z/h_y = \rho e^{i\phi}$.

(e) In the wave theory of Saha and others considering vertical propagation along the X direction, they have shown that the electric vectors in the Y and Z directions are coupled with the quantities ρ_1 and ρ_2 given by

$$i\rho_1 = \rho e^{i\alpha}$$

$$i\rho_2 = \rho^{-1} e^{-i\alpha}$$

where ρ is the ratio of the amplitudes of the normal and the abnormal components of the magnetic vector, and $\alpha = \pi - \phi$ for the ordinary mode below the ionospheric reflection level in the northern hemisphere, ϕ being the phase difference between the normal and the abnormal components.

(f) With regard to the polarization parameter the workers on the ray theory have taken its positive value to correspond to the *right-handed* wave, the extraordinary component below the ionospheric reflection level in the northern hemisphere, whereas Roy and Verma have taken the positive value of θ to correspond to the *right-handed* or the ordinary component.

(g) In obtaining the polarization curves, on ray-theory considerations, the angle θ' between the direction of propagation and the positive direction of the earth's magnetic field is always

taken as acute, whereas Saha and others have taken θ' to represent the angle between the *upgoing* wave and the positive direction of the earth's magnetic field, so that θ' is obtuse in the northern hemisphere and acute in the southern hemisphere.

(g) It should be noted that the negative sign of the electronic charge is taken into account in the Appleton-Hartree formula for complex polarization, whereas in the coupled wave equations of Saha and others the negative electronic charge is considered at a later stage in the expression for ν_e .

The different forms and notations adopted for the various parameters by different workers are tabulated in Appendix 3.

3. *The quadrant of the phase difference between the normal and the abnormal components of the magnetic vector of the wave.* The complex polarization R of the Appleton-Hartree formula can be written as

$$R = \frac{1}{i\gamma_L} \left[-\frac{\gamma_T^2}{2(1 + \alpha + i\beta)} \pm \sqrt{\frac{\gamma_T^4}{4(1 + \alpha + i\beta)^2} + \gamma_L^2} \right] \quad (3)$$

where

$$\alpha = -p^2/p_o^2 = -mv^2/(4\pi N e^2).$$

$$\beta = p\nu/p_o^2 = (mp\nu/4\pi N e^2).$$

$$\gamma_L = \gamma \cos \theta' = (pp_H \cos \theta')/p_o^2.$$

$$\gamma_T = \gamma \sin \theta' = (pp_H \sin \theta')/p_o^2.$$

N = electron density.

θ' = angle between the direction of propagation and the positive direction of the earth's magnetic field.

$p_H = eH/mc$ = gyromagnetic frequency of the electron.

H = intensity of the earth's magnetic field.

ν = electron collisional frequency.

p = angular frequency of the exploring wave.

m and e = mass and charge, respectively, of an electron.

c = velocity of light.

Representing the complex polarization R as $\rho e^{i\phi}$ and denoting it by R_o and R_z respectively

for the ordinary and the extraordinary waves, it can be shown that

$$R_o + R_x = \frac{i\gamma_T^2 \gamma_L}{1 + \alpha + i\beta} = \rho e^{i\phi} + \frac{1}{\rho} e^{-i\phi} \\ = \frac{2}{\xi + i\eta} = 2a'(\xi - i\eta) \quad (4)$$

where

$$\xi = \nu/\nu_c,$$

ν_c = critical collisional frequency

$$= \frac{p_H \sin^2 \theta'}{2 \cos \theta'} \quad (5)$$

$$\eta = p'/\nu_c,$$

$$p' = p \left(1 - \frac{4\pi N e^2}{m p^2} \right)$$

$$a' = \nu_c^2 / (\nu^2 + p'^2).$$

From (4) we get

$$[\rho + (1/\rho)] \cos \phi = 2a'\xi = 2a'\nu/\nu_c \\ = \text{a positive quantity} \quad (6)$$

and

$$[\rho - (1/\rho)] \sin \phi = -2a'\eta = -2a'p'/\nu_c \\ = \text{a negative quantity } (p' > 0) \quad (7)$$

Since, for the ordinary mode in the northern hemisphere, $\rho < 1$, equations 6 and 7 are satisfied when $0 < \phi < \pi/2$ for $p' > 0$.²

4. *The quadrant of the tilt angle of the major axis of the polarization ellipse traced by the electric vector.* Following Taylor [1934], the major axes of the ordinary and the extraordinary ellipses traced by the electric vectors are inclined to the positive direction of the Z axis (magnetic north) at angles ψ_o and ψ_x given respectively by

$$\tan 2\psi_o = -\frac{2\rho_o \cos \phi_o}{1 - \rho_o^2} \quad (8)$$

and

$$\tan 2\psi_x = +\frac{2\rho_o \cos \phi_o}{1 - \rho_o^2} \quad (9)$$

² This can also be proved from the complex plane representation of the polarization vector R as shown in Appendix 1.

Each of the equations 8 and 9 gives a pair of values for ψ_o (and ψ_x) which are evidently tilt angles of the major and the minor axes with respect to the Z axis. It can be shown that the tilt angles of the major axes of the ordinary and the extraordinary waves with respect to the Z axis are given by

$$\tan \psi_{o(\text{major})} \\ = \frac{(1 - \rho_o^2) - \sqrt{(1 - \rho_o^2)^2 + 4\rho_o^2 \cos^2 \phi_o}}{2\rho_o \cos \phi_o}$$

$$\tan \psi_{x(\text{major})} \\ = -\frac{(1 - \rho_o^2) + \sqrt{(1 - \rho_o^2)^2 + 4\rho_o^2 \cos^2 \phi_o}}{2\rho_o \cos \phi_o}$$

From (10) and (11) we get

$$\tan \psi_{o(\text{major})} \cdot \tan \psi_{x(\text{major})} = 1$$

This gives

$$\psi_{o(\text{major})} + \psi_{x(\text{major})} = (2n + 1)\pi/2$$

This relation was first obtained by A. deBettencourt, and Waterman [1950]. It can be seen from (10) and (11) that $\psi_{o(\text{major})}$ in the northern hemisphere lies between $3\pi/4$ and π in the second quadrant or between $7\pi/4$ and 2π in the fourth quadrant. The corresponding limits for $\psi_{x(\text{major})}$ lie between $\pi/2$ and $3\pi/4$ in the second quadrant or between $3\pi/2$ and $7\pi/4$ in the fourth quadrant. It is therefore concluded that the major axes of the ordinary and extraordinary modes of propagation must both lie in the second or the fourth quadrant.

Table 1 gives the phase quadrants discussed in section 3, and the limits of the tilt angle of the major axes of the polarization ellipses traced by the electric vectors for the ordinary and the extraordinary modes of propagation with the sense of rotation for the two hemispheres discussed in section 4.

5. *Discussion of Scott's treatment and his results.* Scott [1950] derived the expressions for the complex refractive index and polarization vector $e^{-i\phi t}$ for the periodic field of the wave, whereas Appleton and Hartree used $e^{+i\phi t}$ for the same. Further, Scott designated the complex polarization R as $-h_z/h_y$, whereas it was taken as $+h_z/h_y$ by Appleton and Hartree. With this notation Scott [1953] also gave a modified phase quadrant table which showed that the ph

TABLE 1

	Northern Hemisphere		Southern Hemisphere	
Term	$p' > 0$ (Below re- flection level)	$p' < 0$ (Above re- flection level)	$p' > 0$ (Below re- flection level)	$p' < 0$ (Above re- flection level)
Ordinary Mode				
Amplitude ratio	$\rho < 1$	$\rho < 1$	$\rho < 1$	$\rho < 1$
Phase quadrant	$0 < \phi < \pi/2$ (1st quadrant)	$3\pi/2 < \phi < 2\pi$ (4th quadrant)	$\pi < \phi < 3\pi/2$ (3d quadrant)	$\pi/2 < \phi < \pi$ (2d quadrant)
Rotation	Left-handed	Right-handed	Right-handed	Left-handed
Limits of tilt angle	$3\pi/4$ and π (i.e., between mag- netic southwest and magnetic south), or $7\pi/4$ and 2π (i.e., be- tween magnetic northeast and magnetic north)		0 and $\pi/4$ (i.e., between mag- netic north and magnetic north- west), or π and $5\pi/4$ (i.e., be- tween magnetic south and magnetic south-east)	
Extraordinary Mode				
Amplitude ratio	$\rho > 1$	$\rho > 1$	$\rho > 1$	$\rho > 1$
Phase quadrant	$3\pi/2 < \phi < 2\pi$ (4th quadrant)	$0 < \phi < \pi/2$ (1st quadrant)	$\pi/2 < \phi < \pi$ (2d quadrant)	$\pi < \phi < 3\pi/2$ (3d quadrant)
Rotation	Right-handed	Left-handed	Left-handed	Right-handed
Limits of tilt angle	$\pi/2$ and $3\pi/4$ (i.e., between magnetic west and magnetic southwest), or $3\pi/2$ and $7\pi/4$ (i.e., between magnetic east and mag- netic northeast)		$5\pi/4$ and $3\pi/2$ (i.e., between magnetic southeast and magnetic east), or $\pi/4$ and $\pi/2$ (i.e., between magnetic northwest and mag- netic west)	

ifference ϕ_0 for the ordinary wave, below the ionospheric reflection level, in the northern hemisphere, should be in the second quadrant (i.e., between $\pi/2$ and π). It is evident that if the complex polarization is taken as $+h_z/h_y$ and $e^{+ip\psi}$ is used to represent the periodic field of the wave, the phase difference would be in the first quadrant (i.e., between 0 and $\pi/2$).

With the above notation Scott [1953] also obtained the expression³ for the tilt angle of the major axis of the polarization ellipse as

$$\tan 2\psi = +(2\rho \cos \phi)/(1 - \rho^2) \quad (14)$$

Thus for the ordinary wave, below the ionospheric

reflection level, in the northern hemisphere, ϕ_0 being in the second quadrant, the tilt angle ψ_0 is within the limits $3\pi/4$ and π in the second quadrant or within the limits $7\pi/4$ and 2π in the fourth quadrant. These limits agree with the limiting values given by us and earlier by Taylor [1934], Martyn [1935], and Ghosh [1938].

6. Expressions for the ratio of the amplitudes of the normal and the abnormal components obtained from ray-theory considerations and from the wave equations of Saha and others. It has been shown by Murty [1959] and by Murty and Khastgir [1959] that the expressions for the amplitude ratio for the ordinary and the extraordinary waves, on ray theory are given by

$$\rho_o = \frac{a'}{v_c} \left[\frac{v}{\cos \phi_o} - \frac{p'}{\sin \phi_o} \right] \quad (15a)$$

$$\rho_x = \frac{a'}{v_c} \left[\frac{v}{\cos \phi_o} + \frac{p'}{\sin \phi_o} \right] \quad (15b)$$

³ The difference in sign in equations 1 and 14 is only apparent and arises on account of the difference in the forms and notations for the periodic field of the radio wave and the complex polarization as discussed in section 2.

where

$$a' = \nu_c^2 / (\nu^2 + p'^2)$$

$$p' = p[1 - (p_o^2/p^2)]$$

$$\nu_c = (p_H \sin^2 \theta') / (2 \cos \theta')$$

and ϕ_o is the phase difference between the normal and the abnormal components of the magnetic vector for the ordinary wave. Considering the expression for the ordinary wave given in (15a), the phase difference ϕ_o is replaced by $(\pi - \alpha)$, where α is the phase angle of Saha and others. We thus obtain for the ordinary wave:

$$\begin{aligned} \rho_o &= \frac{a'}{\nu_c} \left[\frac{\nu}{\cos(\pi - \alpha)} - \frac{p'}{\sin(\pi - \alpha)} \right] \\ &= -\frac{a'}{\nu_c} \left[\frac{\nu}{\cos \alpha} + \frac{p'}{\sin \alpha} \right] \end{aligned}$$

Since the expression for ν_c in the wave equations of Saha and others is opposite in sign to that given on ray theory, we get the expression for ρ_o in the notations of Saha and others as

$$\rho_o = \frac{a'}{\nu_c} \left[\frac{\nu}{\cos \alpha} + \frac{p'}{\sin \alpha} \right]$$

According to Saha and others, the expressions for the amplitude ratio of the normal and the abnormal components of the radio wave are given by

$$\rho = \frac{1}{\lambda^2} \left[\frac{\xi}{\cos \alpha} - \frac{\eta}{\sin \alpha} \right] \quad (16a)$$

$$\rho^{-1} = \frac{1}{\lambda^2} \left[\frac{\xi}{\cos \alpha} + \frac{\eta}{\sin \alpha} \right] \quad (16b)$$

where

$$\lambda = \xi^2 + \eta^2$$

$$\begin{aligned} \xi &= \frac{\nu}{\nu_c} & \eta &= \frac{p(1 - [p_o^2/p^2])}{\nu_c} \\ & & &= \frac{p'}{\nu_c} \end{aligned} \quad (17)$$

$$p_o^2 = 4\pi N e^2 / m$$

$$\nu_c = \frac{-|p_H| \sin^2 \theta'}{\cos \theta'}$$

Since $a' = \nu_c^2 / (\nu^2 + p'^2)$, it can be easily seen from (17) that $1/\lambda^2 = a'$, so that

$$\rho = \frac{a'}{\nu_c} \left[\frac{\nu}{\cos \alpha} - \frac{p'}{\sin \alpha} \right] \quad (18a)$$

and

$$\rho^{-1} = \frac{a'}{\nu_c} \left[\frac{\nu}{\cos \alpha} + \frac{p'}{\sin \alpha} \right] \quad (18b)$$

According to Saha and others (18a) corresponds to the ordinary and (18b) corresponds to the extraordinary wave. It is thus seen that (18a) for the extraordinary wave according to the wave theory corresponds to (15a) for the ordinary wave according to the ray theory. Similarly, it is evident that (18a) for the ordinary wave obtained on the wave theory corresponds to (15b) for the extraordinary wave obtained on the ray theory. It is, therefore, concluded that owing to the interchange in the expressions for the amplitude ratio, the limits for the tilt angle of the major axes of the polarization ellipse for the ordinary wave obtained by Roy and Verma from the wave equations of Saha and others are the same as those for the extraordinary wave obtained on the ray theory, and vice versa.

The same conclusion may also be drawn from the expressions for the complex polarization of Saha and others as given below.

Saha and others have represented the complex polarization for the ordinary wave as

$$i\rho_1 = \rho e^{i\alpha} = i[G - \sqrt{1 + G^2}]$$

where

$$G = -i/(\xi + i\eta), \quad \xi = \nu/\nu_c, \quad \text{and} \quad \eta = p'/\nu_c$$

Replacing the phase angle α by $(\pi - \phi)$, where ϕ is the phase difference, for comparison with the Appleton-Hartree formula, we get

$$\begin{aligned} i\rho_1 &= \rho e^{i(\pi - \phi)} = -\rho e^{-i\phi} \\ &= i[G - \sqrt{1 + G^2}] \end{aligned} \quad (19)$$

that is,

$$\rho e^{-i\phi} = -i[G - \sqrt{1 + G^2}]$$

It is shown in Appendix 2 that the quantity G can be written as

$$G = -\gamma_\tau^2 / [2\gamma_L(1 + \alpha + i\beta)] \quad (20)$$

where γ_L , γ_T , α , and β have the same significance as in the Appleton-Hartree formula. Using the value of G from (20) in (19), we get

$$e^{-i\phi} = -i \left[\frac{\gamma_T^2}{2\gamma_L(1 + \alpha + i\beta)} - \sqrt{1 + \frac{\gamma_T^4}{4\gamma_L^2(1 + \alpha + i\beta)^2}} \right]$$

since $\gamma_T^4/[4\gamma_L^2(1 + \alpha + i\beta)^2]$ under the radical is the square of $-\gamma_T^2/[2\gamma_L(1 + \alpha + i\beta)]$, we put a negative sign before γ_L when the latter is taken out of the radical. Thus

$$\begin{aligned} e^{-i\phi} &= -i \left[-\frac{\gamma_T^2}{2\gamma_L(1 + \alpha + i\beta)} - \left(-\frac{1}{\gamma_L} \right) \sqrt{\gamma_L^2 + \frac{\gamma_T^4}{4(1 + \alpha + i\beta)^2}} \right] \\ &= \frac{1}{i\gamma_L} \left[-\frac{\gamma_T^2}{2(1 + \alpha + i\beta)} + \sqrt{\gamma_L^2 + \frac{\gamma_T^4}{4(1 + \alpha + i\beta)^2}} \right] \end{aligned}$$

This is the same as the expression for the complex polarization for the extraordinary wave in the Appleton-Hartree formula.

7. *Experimental results of Roy and Verma.* In the experimental studies on the polarization of downcoming radio waves, a pair of crossed loop aerials are placed, one in the direction of the magnetic north and the other at right angles to it. The voltages induced in the two loop aerials are fed into the horizontal and vertical deflection plates of an oscillograph after being separately amplified by identical amplifiers. The voltage induced in the loop placed in the direction of the magnetic north is due to the *abnormal* magnetic vector, and the voltage induced in the other loop is due to the *normal* component of magnetic vector. From the elliptical pattern shown in plate II as ordinary by Roy and Verma [1955], we find that the ratio of the *normal* to the *abnormal* component of the magnetic vector is greater than unity. This corresponds to the extraordinary wave according to the ray theory. Thus, taking the observed ordinary ellipse as extraordinary, it can be concluded that the experimental results of Roy and Verma confirm our theoretical conclusion regarding the limits of the tilt angle.

8. *Conclusions.* We have shown that the differences in the results obtained for the polarization parameters by the different workers on ray theory are only apparent and arise out of the differences in the forms and notations used in the different formulas. We have also shown that the discrepancies in the limits of the tilt angle of the major axis of the polarization ellipse obtained from the ray theory and the wave theory are due to the interchange in the expressions for the amplitude ratio of the *normal* to the *abnormal* components for the ordinary and the extraordinary waves given by Saha and others. The elliptical patterns observed by Roy and Verma are also shown to be in agreement with our theoretical conclusion regarding the tilt angle of the polarization ellipse.

Acknowledgment. Our sincere thanks are due to Mr. S. Datta Majumder for many valuable discussions and particularly for the complex plane representation of the polarization vector given in Appendix 1.

APPENDIX 1

The complex polarization for the ordinary wave can be written as

$$\begin{aligned} R_o &= \frac{1}{i\gamma_L} \left[-\frac{\gamma_T^2}{2(1 + \alpha + i\beta)} - \sqrt{\frac{\gamma_T^4}{4(1 + \alpha + i\beta)^2} + \gamma_L^2} \right] \\ &= +i[\delta + \sqrt{\delta^2 + 1}] \end{aligned}$$

where

$$\delta = \gamma_T^2/[2\gamma_L(1 + \alpha + i\beta)].$$

In the case when $\delta \ll 1$, we get

$$R_o \approx i(1 + \delta + \frac{1}{2}\delta^2)$$

Below the ionospheric reflection level, $(1 + \alpha) < 0$ and β is always positive. In the complex plane representation, $(1 + \alpha)$ is in the negative X direction and $i\beta$ in the positive Y direction. The quantity $(1 + \alpha + i\beta)$ is thus in the second quadrant. Its reciprocal is represented by its mirror image, so that δ , which is equal to some constant multiplied by this reciprocal, lies in the third quadrant. Now $(1 + \delta + \frac{1}{2}\delta^2) \approx 1/(1 - \delta)$. Since δ lies in the third quadrant, $(1 - \delta)$ is obviously in the first quadrant. Therefore its

reciprocal lies in the fourth quadrant. To this, $\pi/2$ should be added, because of the factor $i = e^{i\pi/2}$, to get the resultant R_o . Hence, it can be concluded that the phase difference for the ordinary wave below the ionospheric reflection level in the northern hemisphere must be in the first quadrant (i.e., $0 < \phi < \pi/2$).

APPENDIX 2

According to Saha and others,

$$G = -i/(\xi + i\eta)$$

Since $\xi = \nu/\nu_e$ and $\eta = p'/\nu_e$,

$$G = -i\nu_e/(\nu + ip')$$

Now $p' = p[1 - (p_o^2/p^2)]$, and

$$\nu_e = -\frac{|p_H| \sin^2 \theta'}{2 \cos \theta'}$$

(We have taken θ' as an acute angle for comparison with the ray theory.) Therefore

$$G = \frac{-i\gamma pp_H \sin^2 \theta'}{2\gamma \cos \theta' (p\nu + ip^2 - ip_o^2)}$$

Since $\gamma_T = \gamma \sin \theta'$, $\gamma_L = \gamma \cos \theta'$, and $\gamma = pp_H/p_o^2$,

$$G = \frac{-i\gamma_T^2}{\frac{2\gamma_L}{i} \left(i \frac{p\nu}{p_o^2} - \frac{p^2}{p_o^2} + 1 \right)}$$

Introducing $\alpha = -p^2/p_o^2$ and $\beta = p\nu/p_o^2$, we get

$$G = -\frac{\gamma_T^2}{2\gamma_L(1 + \alpha + i\beta)}$$

APPENDIX 3

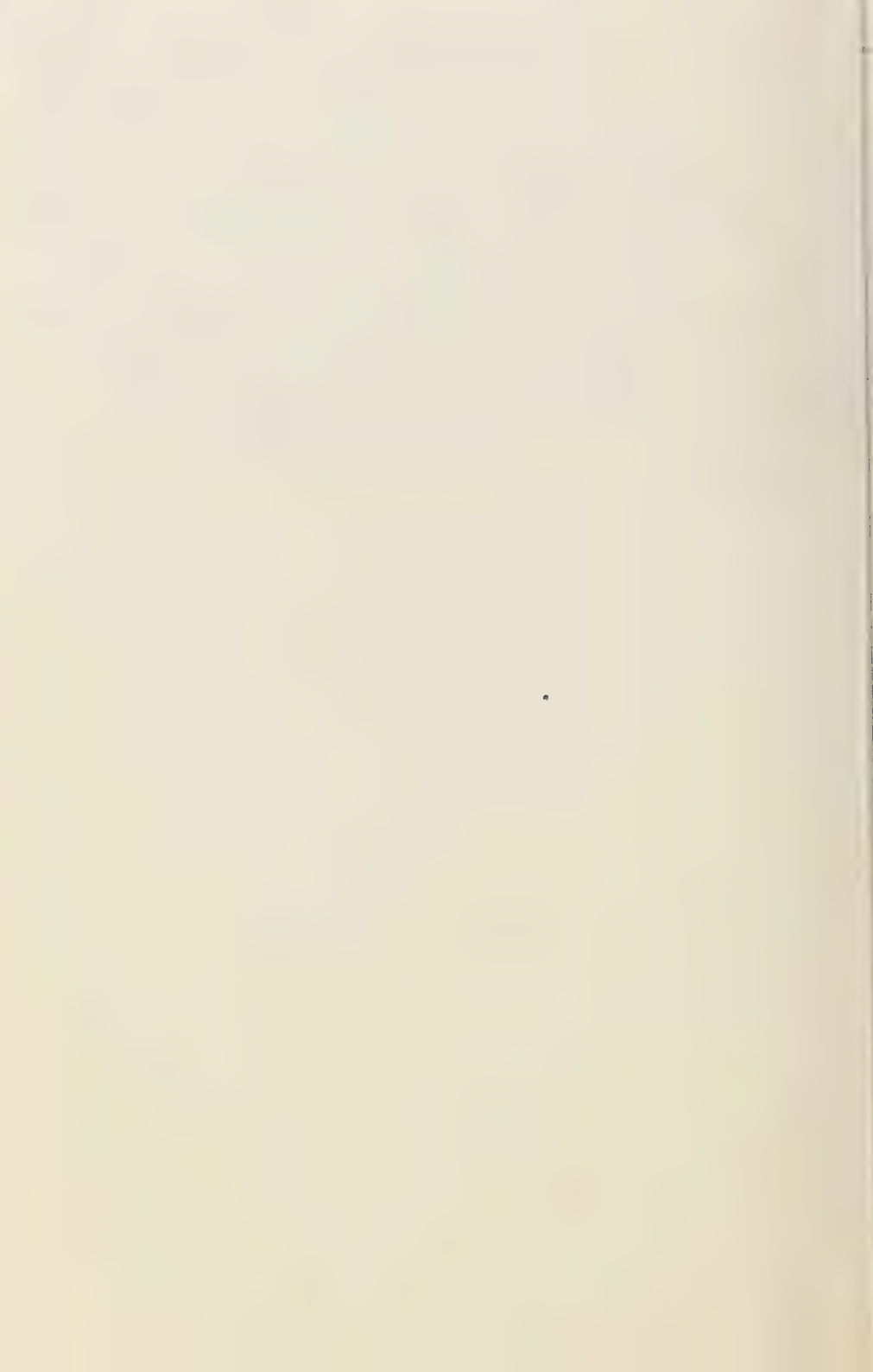
TABLE 2. Notations Adopted by Different Investigators

	Appleton-Hartree	Bailey, Martyn, Ghosh, Singh, and Murty	Murty and Khastgir	Scott	Saha, Banerjee, and Guha
Periodic field of the wave	$e^{ip t}$	$e^{ip t}$	$e^{ip t}$	$e^{-ip t}$	$e^{ip t}$
Ratio of the amplitudes of the <i>normal</i> to the <i>abnormal</i> components of the magnetic vector	...	$R = \frac{\rho}{+h_Z/h_Y}$	$R = \frac{\rho}{+h_Z/h_Y}$	R	R
Complex polarization	$R = +h_Z/h_Y$	$R = \frac{\rho}{+h_Z/h_Y} = \rho e^{-i\phi}$	$R = \frac{\rho}{+h_Z/h_Y} = \rho e^{i\phi}$	$-h_Z/h_Y = R e^{i\phi}$	$i\rho_1 = R e^{i(\pi-\phi)}$ (ordinary)
		(The wave propagation is assumed along the <i>X</i> direction in all cases. ϕ is the phase difference between the <i>normal</i> & the <i>abnormal</i> components.)			
Angle between the direction of propagation and the positive direction of the earth's magnetic field	Acute	Acute	Acute	...	Obtuse
Polarization parameter θ	Negative angles represent left-handed rotation below the ionospheric reflection level.				Positive angles represent left-handed rotation below the ionospheric reflection level.

REFERENCES

- , A. L., J. T. deBettencourt, and A. T. Waterman, Jr., *J. Geophys. Research*, **55**, 53, 1950.
- eton, E. V., URSI papers, Washington, 1927.
- y, V. A., *Phil. Mag.*, **18**, 516, 1934.
- erling, K., *Hochfrequenztechnik u. Elektroakustik*, **59**, 10, 1942.
- h, S. P., *Indian J. Phys.*, **12**, 341, 1938.
- ree, H. R., *Proc. Cambridge Phil. Soc.*, **25**, 47, 1919.
- o, J. M., *J. Geophys. Research*, **58**, 431, 1953.
- yn, D. F., *Phil. Mag.*, **19**, 376, 1935.
- y, Y. S. N., *Sci. and Culture, Calcutta*, **25**, 1959.
- y, Y. S. N., and S. R. Khastgir, *Proc. Natl. Inst. Sci. India, A*, **25**, 00-00, 1959.
- R., and J. K. D. Verma, *J. Geophys. Research*, **60**, 457, 1955.
- Rydbeck, O. E. H., *Chalmers Tek. Högskol. Handl.*, no. 34, 1944.
- Saha, M. N., B. K. Banerjee, and U. C. Guha, *Indian J. Phys.*, **21**, 181, 1947.
- Saha, M. N., B. K. Banerjee, and U. C. Guha, *Proc. Natl. Inst. Sci. India*, **17**, 205, 1951.
- Scott, J. C. W., *Proc. IRE*, **38**, 1057, 1950.
- Scott, J. C. W., *J. Geophys. Research*, **58**, 437, 1953.
- Singh, R. N., and Y. S. N. Murty, *Current Sci. India*, **27**, 161, 1958.
- Singh, R. N., and Y. S. N. Murty, *J. Sci. Research Banaras Hindu Univ.*, **9** (1), 1959.
- Snyder, W., and R. A. Helliwell, *J. Geophys. Research*, **57**, 73, 1952.
- Taylor, Mary, *Proc. Phys. Soc.*, **45**, 245, 1933.
- Taylor, Mary, *Proc. Phys. Soc.*, **46**, 408, 1934.

(Manuscript received June 3, 1959; revised February 18, 1960.) *



VLF Propagation Effects of a *D*-Region Layer Produced by Cosmic Rays

WILLIAM F. MOLER

*Radio Propagation Branch, Signal Propagation Division
U. S. Navy Electronics Laboratory
San Diego 52, California*

Abstract. The single-layered *D*-region model based only on Lyman α photoionization of nitric oxide is inadequate to explain certain aspects of VLF radio propagation. Empirical evidence indicates the existence of a second and lower *D* layer which is important for VLF propagation. It is shown that normal cosmic rays produce sufficient ionization for such a layer. The electron-production and -depletion processes effective below 100 km and the latitudinal distribution of cosmic-ray primaries due to the geomagnetic field are discussed. A series of electron-density profiles obtained from photoionization and cosmic-ray ionization processes is compared with the two-layered *D*-region model deduced from electromagnetic measurements. The calculated phase and amplitude characteristics of VLF signals reflected from the lower cosmic-ray-induced layer during the presunrise hour are in good agreement with those measured.

INTRODUCTION

The most successful electron-production process for explaining the general characteristics of the *D* region is the photoionization of nitric oxide by Lyman- α radiation first suggested by Nicolet [1945]. Following Nicolet's suggestion, Johnston [1958] developed a model for the *D* and *E* regions for which the principal electron-production processes were assumed to be photoionization of NO below 100 km by Lyman α (1216 Å) and photoionization of O₂ above 100 km by Lyman β (4481 Å). Ionization resulting from the Lyman continuum and X radiation of other constituents at relevant heights above 100 km was also considered. This model shows quite good agreement with most radio measurements except for certain aspects of very-low-frequency propagation over long radio paths.

Bracewell and Bain [1952] summarized the results of a series of 16 kc/s propagation experiments made over path lengths from 90 to 535 km. On the shorter paths they found that measured phase changes could be explained in terms of a relatively strong layer *D*₁ which remained at a constant height during the night and descended during the day with decreasing zenith angle. For paths longer than 300 km,

the received signal showed a rapid change in phase during the hour preceding sunrise and the hour after sunset, with high phase stability during the intervening hours. They concluded that reflection from a weak lower layer *D*₂ (which appears about an hour before sunrise and descends to the daytime equilibrium position by sunrise) dominates the propagation mechanism for the longer paths. Figure 1 shows the Bracewell and Bain [1952] model of the diurnal height variations of the layer *D*₁ and *D*₂ observed over Great Britain during the equinoxes.

Van Allen [1952] used cosmic radiation data from rocket soundings to extend the ionization rate curves for cosmic rays to high altitudes for several geomagnetic latitudes. After an examination of these rates, Nicolet [1958] observed that certain features of long-wave radio propagation, especially those of Bracewell, were probably related to cosmic-ray-produced ionization.

The following sections of this paper will discuss the ion-production and -depletion processes in the lowest ionosphere and the electron distributions which result from both Lyman α photoionization of NO and cosmic-ray ionization of other constituents. The last is a brief discussion of the effect of the resulting *D*-region model on VLF propagation characteristics.

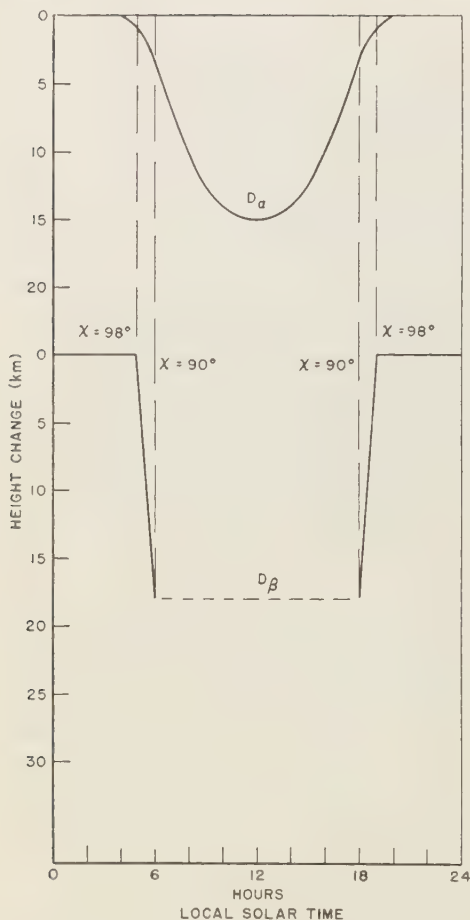


Fig. 1. Diurnal behavior of the ionospheric layers $D\alpha$ and $D\beta$ during the equinoxes, according to Bracewell and Bain [1952].

PRODUCTION AND DEPLETION PROCESSES IN THE D REGION

Ion production. The cosmic-ray primaries are mostly charged particles (80 per cent protons, 19 per cent α particles, and 1 per cent miscellaneous) which are subjected to a force resulting from passage through the geomagnetic field. The force is normal to the trajectory of the particle, causing a path curvature proportional to the momentum of the particle, the path aspect with respect to the magnetic lines, and the intensity of the magnetic field along the

path. Particles approaching the earth from the zenith in polar regions cross few lines of geomagnetic flux and remain on a nearly undeviated course. Those approaching from the zenith in equatorial regions arrive normal to the magnetic lines and experience large deflective forces and path curvatures. The geomagnetic field acts as a large-scale spectrographic filter which causes the extraterrestrial isotropic and homogeneous distribution of cosmic-ray primaries to arrive at the upper atmosphere with a particle density and energy distribution which is a function of geomagnetic latitude and altitude. Consequently the cosmic-ray ionization rate is a function of geomagnetic latitude and altitude.

Van Allen [1952] shows the distribution of altitude of ion production in terms of ion pairs/cm²/sec/atmosphere for four geomagnetic latitudes. The actual ion pair production rate $q(z, \lambda)$ from cosmic rays is then given by

$$q(z, \lambda) = q_0(z, \lambda) \rho(z) / \rho_0$$

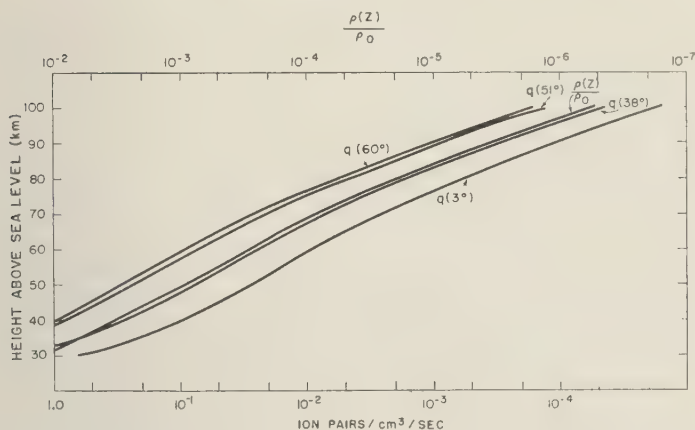
where z is altitude, λ is geomagnetic latitude, $\rho(z)$ is the atmospheric density at z , ρ_0 is sea-level density, and $q_0(z, \lambda)$ is the ion pair production rate normalized to 1 atmosphere. Figure 2 shows the ion pair production rates as a function of altitude for four geomagnetic latitudes. The ratio $\rho(z)/\rho_0$ is from the *Handbook of Geophysics* [1957].

The main daytime source of ion production below 100 km is assumed to be Lyman α photoionization of NO. The rate for this process is a function of altitude and solar zenith angle based on the electron density and recombination coefficient curves calculated by Houston [1957].

The total ion pair production rate q is the sum of the cosmic-ray and photoionization rates and is a function of height, geomagnetic latitude, and solar zenith angle.

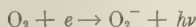
Recombination, detachment, and attachment processes. The processes that have been considered in calculating the electron distribution are photodetachment, associative detachment, radiative attachment, dissociative recombination, three-body ionic recombination, and previously described ionization processes.

Smith, Burch, and Branscomb [1958] determined the photodetachment cross section O_2^- in a simulated 60-km height environment.



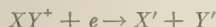
2. The rate of ion production q as a function of altitude for four geomagnetic latitudes λ , and the ratio of air density at height z to the normal sea-level density.

obtained a photodetachment rate ρ of 0.44 attachment/sec/ion for the lower ionosphere. Bates and Massey [1951] proposed the associative detachment process $O_2^- + O \rightarrow O_3 + e$ to account for the slow rate of disappearance of electrons after sunset. The rate coefficient κ has been firmly established, although a value of 10^{-14} cm³/sec for the height interval 70 to 110 km appears reasonable. The radiative attachment process



was examined by Bates and Massey [1951], and was found to have a rate coefficient β of the form $\beta = \beta_0 + cp$ (2) where β_0 is 10^{-14} cm³/sec, c is 1.5×10^{-12} cm³/mb, and p is the partial pressure of O_2 in mb.

The dissociative recombination process



suggested by Bates and Massey [1947] has a rate coefficient α_d which is pressure dependent. Bates and Jones [1954] defined an effective dissociation recombination process without specifying the reactants and calculated α_d to be 10^{-8} cm³/sec at 110 km. For our calculations it is assumed to have a height dependence

$$\alpha_d = ae^{-bz} \quad (3)$$

where a is 1.03×10^{-8} cm³/sec, b is 3.21×10^{-2} /km, and z is the height in kilometers.

The familiar three-body Thomson ionic recombination process has a rate coefficient α_i which is a function of the air pressure, temperature, and mean molecular weight. The molecular weight of air calculated by Miller [1957] and the temperature and pressures in the *Handbook of Geophysics* [1957] were used to compute α_i as a function of height.

The effective recombination coefficient. If it is assumed that advective terms are negligible in the equations that specify the variation of the electron N_e , the positive ion N^+ , and the negative ion N^- particle densities with time are

$$\frac{dN_e}{dt} = q + \rho N^- + \kappa n(O) N^- - \beta N_e n(O_2) - \alpha_d N_e N^+ \quad (4)$$

$$\frac{dN^-}{dt} = \beta n(O_2) N_e - \rho N^- - \kappa n(O) N^- - \alpha_i N^- N^+ \quad (5)$$

$$\frac{dN^+}{dt} = q - \alpha_d N_e N^+ - \alpha_i N^- N^+ \quad (6)$$

where the particle densities of atomic oxygen $n(O)$ and molecular oxygen $n(O_2)$ are those given by Miller [1957].

If the usual assumption of neutral space

charge is made, the negative ion density N^- is $N_e\lambda$ and the positive ion density N^+ is $N_e(1 + \lambda)$, where λ is the negative ion to electron ratio N^-/N_e . [Bates and Massey, 1946]. For steady-state conditions, (5) becomes

$$\beta n(O_2) N_e = \rho N_e \lambda + \kappa n(O) N_e \lambda + \alpha_i \lambda N_e^2 (1 + \lambda) \quad (7)$$

or

$$\lambda = \frac{\beta n(O_2)}{\rho + \kappa n(O) + \alpha_i N_e (1 + \lambda)} \quad (8)$$

for any reasonable combination of α_i , N_e , and λ the third term in the denominator of (8) is small compared with the others, so that

$$\lambda \simeq \frac{\beta n(O_2)}{\rho + \kappa n(O)} \quad (9)$$

The steady-state solution of (6) is

$$N_e = q^{1/2} [(1 + \lambda)(\alpha_d + \lambda \alpha_i)]^{-1/2} \quad (10)$$

Equation 10 is the expression used to compute the electron-density profiles described in the next section. The term $(\alpha_d + \lambda \alpha_i)$ is the effective recombination coefficient α_e of Bates and Massey [1946]. Figure 3 shows α_e as a function

of height for both night and daytime conditions. The negative ion to electron ratio λ is shown for the daytime only.

RESULTS

The electron-density profiles. Figure 4 shows a series of electron-density profiles for four solar zenith angles at four geomagnetic latitudes. The dashed curves indicate the electron densities that would result from Houston's [1958] photoionization process only. The steady-state assumption leads to an estimate of the electron density that is slightly high during the morning and slightly low during the afternoon. It may be seen from the curves that a double-layer structure with two well-defined maxima of ionization exists within the D region for solar zenith angles near 90° . For solar zenith angles less than 90° the two layers are separated by an inflection point rather than by a minimum in the electron density profile. This is similar to the separation between the F_1 and F_2 layers. The profiles support the conclusion of Bracewell [1952] that the daytime D region is composed of two layers.

The electron distributions shown in Figure 4 indicate the ionization produced by cosmic rays only. The daytime curves represent the electron

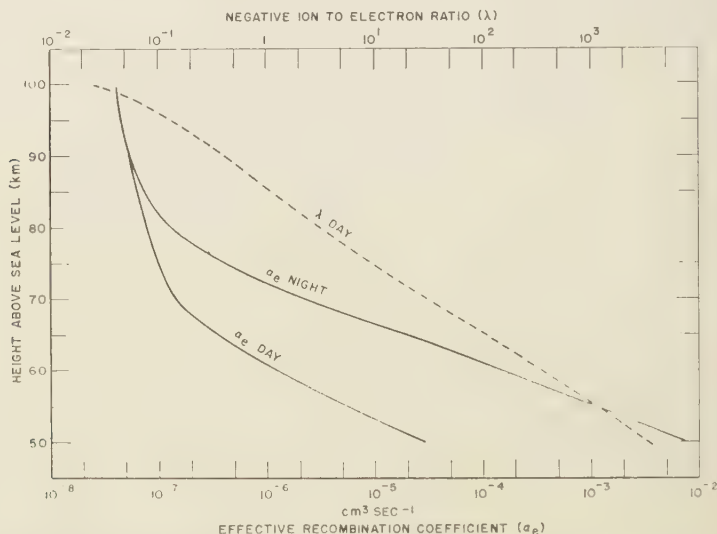


Fig. 3. The day and nighttime effective recombination coefficient α_e as a function of height, and negative ion to electron ratio λ for the daytime, also as a function of height.

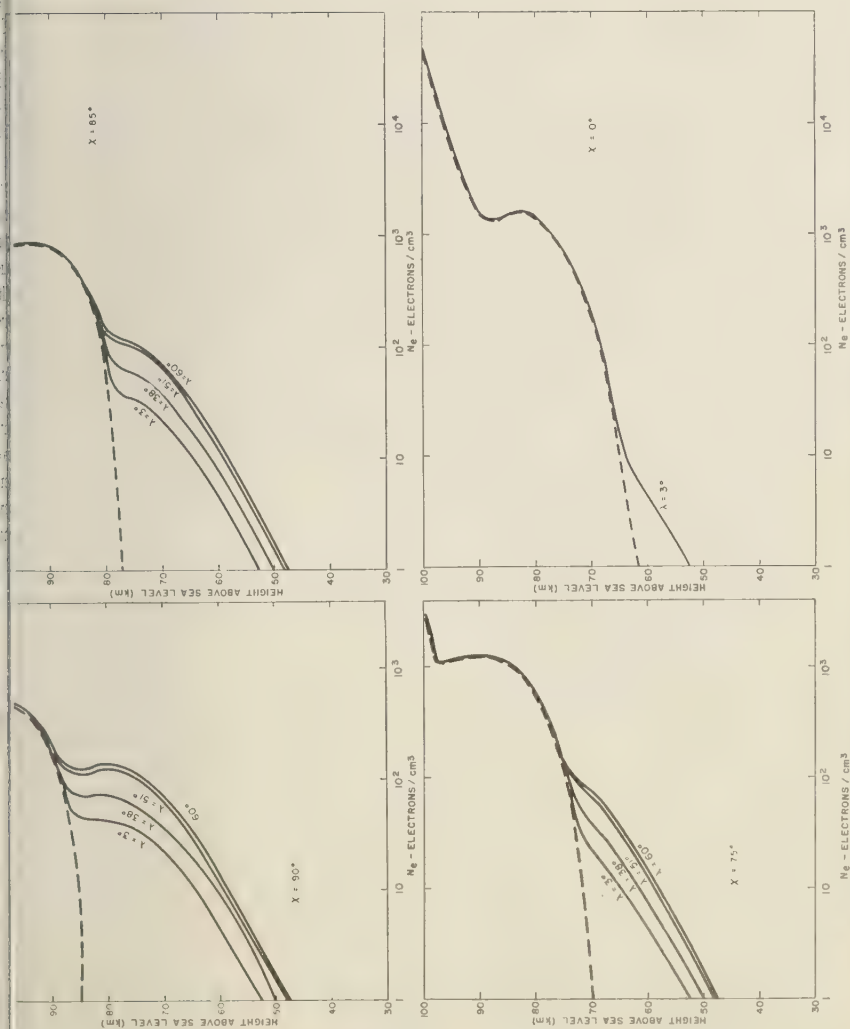


Fig. 4. The electron density resulting from both Lyman α photoionization and from cosmic rays as a function of height for four geomagnetic latitudes (λ) and for solar zenith angles (χ). The dashed curves represent the electron densities resulting from photoionization only.

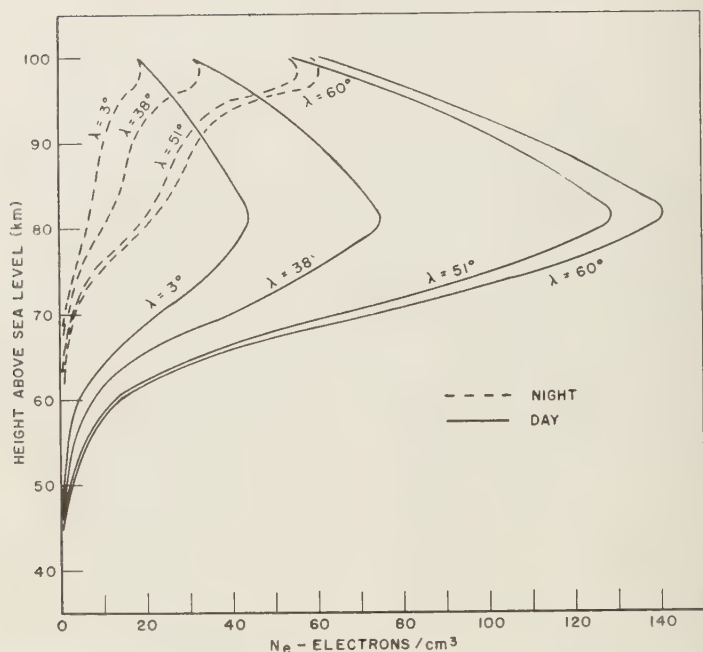


Fig. 5. Electron density resulting from cosmic-ray ionization only, for four geomagnetic latitudes.

densities for solar zenith angles between 90° and 94° when the atmosphere above 50 km is illuminated by visible and infrared radiations. For these zenith angles, the grazing solar rays are depleted of the ionizing ultraviolet radiation on their passage down through the ionosphere and ozonosphere and return with only the energies important for photodetachment.

The D region during sunrise. It is quite easy to understand what must occur when the grazing solar rays first strike the atmosphere at 100 km and then gradually illuminate lower and lower levels as the solar zenith angle decreases. Photodetachment begins immediately with the illumination, and the electron densities produced by cosmic rays quickly change from the night to the day values. The result is that a sharp discontinuity in the electron profile develops at the position of the grazing solar rays. When the illumination reaches the region of negligible daytime electron densities (near 60 km) the sharp discontinuity disappears. At this time the maximum-electron-density gradient in the cosmic-ray-produced layer is at the daytime equi-

librium position at the lowest inflection point of the profile. At ground-level sunrise, photoionization of nitric oxide by Lyman α begins and a second sharp gradient in the electron-density profile is produced.

Figure 6 shows the height of the maximum electron-density gradients produced by photoionization D_α and by cosmic rays D_β as a function of time. The layers represent the ionosphere at the same time of year and location as for *Bracewell* [1952] curves in Figure 1. A comparison of Figure 1 with Figure 6 shows that although there is a 7-km difference in the diurnal height change of layer D_β between the models, the general characteristics of the two are similar.

For the curves in Figure 6, the time for onset of photodetachment as a function of height was calculated using a modified radius of the earth 35 km greater than the earth's mean radius. This was done because observations of E-region sunrise effects made in India [*Mishra* 1952] indicated that there is a delay between the time of arrival of an earth-grazing solar ray and the onset of photodetachment. Anal-

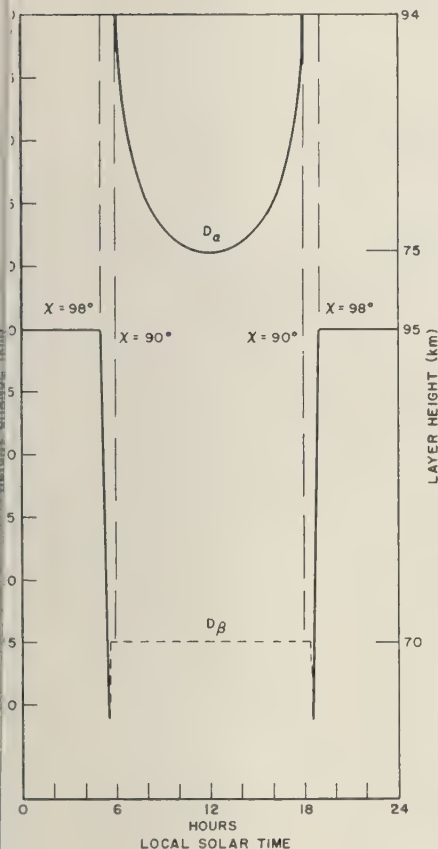


Fig. 6. Diurnal behavior of the height of the maximum-electron-density gradient in the photo-ionization layer, D_α , and the cosmic-ray layer, D_β , during the equinoxes over Great Britain.

shown that photodetachment begins when solar rays become tangent to a surface 35 km above the earth and illuminate the E region. It is assumed that atmospheric turbidity and absorption of low-energy ultraviolet by ozone in the region below 35 km causes a significant reduction of photodetaching energy.

Propagation of 16-km/s waves over a 535-km path. The predicted characteristics of VLF waves propagated by reflection from the cosmic-ray layer D_β were compared with measurements described by the group at the Cavendish Laboratory [Bracewell and Bain, 1952; Bain, Bracewell, Straker, and Wescott, 1952]. A simple propagation

model was used to predict the diurnal phase and amplitude variations of received signals at 16 kc/s. As in the Cavendish group experiment, a vertically polarized wave is transmitted which is assumed to propagate over a 535-km path in Great Britain. The magnetic vector of the wave is horizontal and perpendicular to the plane of propagation. The receiving antenna is a loop in the plane of propagation, so that only the normal component of the field is measured. It is assumed that the total horizontal magnetic field at the receiver consists of the vector sum of the ground wave H_0 and twice the normally polarized one-hop and two-hop sky waves. The sky-wave components are doubled to account for the ground-reflected waves. For constant ground-wave phase and amplitude the total signal vector traces out a loop induction locus [Bracewell, 1952] during the course of the day which represents the diurnal variation of the phase and amplitude of the resultant sky wave.

The magnitude of a single-hop sky wave is [Bain, Bracewell, Straker, and Wescott, 1952]

$$H_1/H_0 = \frac{d \sin i}{sM} ||R|| \quad (11)$$

where i is the angle of incidence of the sky wave at the ground, d is the distance between antennas, s is the equivalent path of the sky wave, M is a ground-wave attenuation factor (0.80), and $||R||$ is the reflection coefficient for the normal component of the vertically polarized sky wave.

The D layer returns VLF waves by a process similar to reflection from a boundary discontinuity rather than by gradual bending because the D -layer ionization density changes by a significant amount within a height comparable to one wavelength [Mitra, 1952]. Then the D region described in this paper may be represented as a sharply bounded homogeneous ionosphere with a superimposed magnetic field. With these restrictions, the expressions for the ionospheric reflection coefficients derived by Wait and Perry [1957] are applicable.

The phase angle between the ground wave and a sky wave is a function of their geometrical path-length difference and of the phase shift of the sky wave on reflection at the ionospheric boundary. The path-length difference, the angle of incidence of the sky wave at the ground and at the ionospheric boundary, and the ionospheric

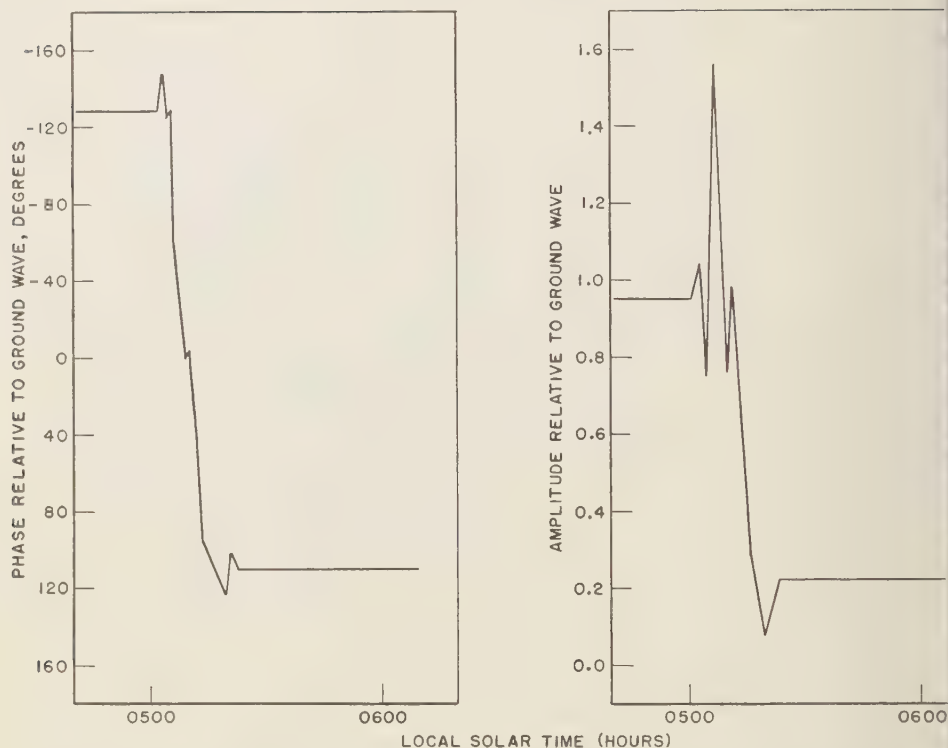


Fig. 7. Diurnal variation of the phase and amplitude, relative to the ground wave, of the 16-kc vertically polarized sky wave (resultant of a one-hop and a two-hop sky wave) propagated over 535-km path over Great Britain during the equinoxes.

reflection coefficients depend critically on the assumed height of reflection. Because of the similarity between the diurnal height variation of the Bracewell-Bain layer D_β (Fig. 1) and the cosmic-ray layer D_β (Fig. 6) we have calculated the phase and amplitude of the received signal with the assumption that reflection takes place at the height of the maximum-electron-density gradient.

Figure 7 shows the variation of the sky-wave phase and amplitude resultants during the pre-sunrise hour. It is assumed that a reversal of the rapid signal phase and amplitude variation occurs during the hour immediately following sunset.

Table 1 is a summary of the empirical propagation characteristics [Bain, Bracewell, Straker, and Wescott, 1952; Bracewell and Bain, 1952], the characteristics predicted by our model, and

those predicted by a modified model which described below.

A comparison of the empirical characteristics with those of our model shows that they agree well for the night ionosphere but differ significantly during the day. The daytime reflective coefficient (0.10) calculated for a reflective height of 70 km is less than half the measured value (0.27). Also, the predicted diurnal phase variation of 239° compared with the measured 200° indicates that the diurnal reflection height change of 25 km is too great. Calculations by others [Wait, 1959] have shown substantial agreement with Bracewell's 18-km diurnal reflective height change, indicating that our assumption that the effective reflection height is at the position of maximum-electron-density gradient may not be adequate. Alternatively, our assumption may be reasonable but the position of the max

TABLE 1. Propagation Characteristics of 16 kc/s Waves over a 535-km Path

	Em- pirical	Model	Modified Model
Reflection height			
Day	74 km	70 km	75 km
Night	92 km	95 km	93 km
Reflection coefficient			
Day	0.27	0.10	0.22
Night	0.55	0.55	0.54
Amplitude of the re- sultant sky wave relative to the ground wave			
Day	0.60	0.25	0.55
Night	1.25	0.98	1.28
Diurnal phase vari- ation of the sky wave relative to the ground wave	200°	239°	197°
At zenith angle at the beginning of the presunrise phase and ampli- tude variation	97°50'	98°	98°

10 km electron-density gradient may be displaced. A inspection of the daytime electron densities shown in Figure 5 indicates that the position of the inflection in the curve is quite sensitive to small changes in the electron density at 70 km. Slight modifications of the reactive process rates and constituent densities could produce changes of the right order of magnitude.

If we modify our model by making the assumption that the daytime reflection height is at 75 km and accept Bracewell's 18-km diurnal height change the daytime reflection coefficient is increased to 0.22 and the amplitude of the resultant sky wave (1.28) is nearly identical to the measured 1.25. The nighttime parameters remain nearly unaffected by the modification.

CONCLUSIONS

The ionization produced at night by cosmic rays forms a layer near 95 km which is capable of reflecting VLF waves. In the daytime, photoionization of nitric oxide by Lyman- α radiation and cosmic-ray ionization of other constituents are the important electron-producing processes in the D region. Each process forms a distinctly separate layer, and the cosmic-ray layer D_β is

below the photoionization layer D_α . The exact height and intensity of the cosmic-ray layer are functions of the geomagnetic latitude.

The ionization densities in layer D_β are sufficient to support the ionospheric propagation of VLF waves. The observed rapid VLF phase and amplitude changes during the pre- and postsunset hours result from the rapid height change of layer D_β with the onset or cessation of photodetachment.

As more detailed information about the electron-production and -depletion rates and constituent densities becomes available, improvement of the electron densities calculated in this paper will be possible.

REFERENCES

- Bain, W. C., R. N. Bracewell, T. W. Straker, and C. H. Westcott, The ionospheric propagation of radio waves of frequency 16 kc/sec over distances of about 540 km, *Proc. IEE*, 99, 250-260, 1952.
- Bates, D. R., and H. S. W. Massey, The basic reactions in the upper atmosphere, I, *Proc. Roy. Soc. London, A*, 187, 261-296, 1946.
- Bates, D. R., and H. S. W. Massey, The basic reactions in the upper atmosphere, II, The theory of recombination in the ionized layers, *Proc. Roy. Soc. London, A*, 192, 1-16, 1947.
- Bates, D. R., and H. S. W. Massey, The negative ion concentration in the upper atmosphere, *J. Atmospheric and Terrest. Phys.*, 2, 1-13, 1951.
- Bracewell, R. N., The ionospheric propagation of radio waves of frequency 16 kc/sec over distances of about 200 km, *Proc. IEE*, 99, 217-228, 1952.
- Bracewell, R. N., and W. C. Bain, An explanation of radio propagation at 16 kc/sec in terms of two layers below E layer, *J. Atmospheric and Terrest. Phys.*, 2, 216-225, 1952.
- Handbook of Geophysics for Air Force Designers*, Geophysics Research Directorate, AFC Research Center, ARDC, U. S. Air Force, 1957.
- Houston, R. E., The effect of certain solar radiations on the lower ionosphere, *J. Atmospheric and Terrest. Phys.*, 12, 225-235, 1958.
- Miller, L. E., Molecular weight of air at high altitudes, *J. Geophys. Research*, 62, 351-365, 1957.
- Mitra, A. P., and R. E. Jones, Recombination in the lower ionosphere, *J. Geophys. Research*, 59, 391-406, 1954.
- Mitra, S. K., *The Upper Atmosphere*, The Asiatic Society, Calcutta, 713 pp, 2nd edition, 1952.
- Nicolet, M., Contribution à l'étude de la structure de l'ionosphère, *Mém. inst. roy. météorol. Belg.*, 19, 1945.

- Nicolet, M., Aeronomie conditions in the mesosphere and lower thermosphere, *Penn. State Univ. Ionosphere Research Lab. Sci. Rept. 102*, April 1, 1958.
- Smith, S. J., D. S. Burch, and L. M. Branscomb, Experimental photodetachment cross section and the ionospheric detachment rate for O^- , *Ann. géophys.*, 14, 225-231, 1958.
- Van Allen, J. A., The nature and intensity of the cosmic radiation, in *Physics and Medicine of the Upper Atmosphere*, University of New Mexico Press, Albuquerque, 1952.
- Wait, J. R., Diurnal change of ionospheric height deduced from phase velocity measurements VLF, *Proc. IRE*, 47, 998, 1959.
- Wait, J. R., and Loris B. Perry, Calculations ionospheric reflections coefficients at very low radio frequencies, *J. Geophys. Research*, 43-56, 1957.

(Manuscript received February 8, 1960.)

The Formation of the *D* Region of the Ionosphere

M. NICOLET¹ AND A. C. AIKIN

*Ionosphere Research Laboratory
Pennsylvania State University
University Park, Pennsylvania*

Abstract. Radiations of solar origin penetrating below 85 km in the terrestrial atmosphere are: (1) X rays of $\lambda < 10$ Å; (2) Lyman α ; and (3) wavelengths greater than 1800 Å. These radiations can ionize: (1) molecular nitrogen and oxygen; (2) nitric oxide; and (3) various atoms such as sodium and calcium. Molecular oxygen and nitrogen are also ionized by cosmic rays. The negative ion to electron ratio is important below 70 km and affects the electron distribution below that altitude. It is possible to explain normal conditions of ionization by cosmic rays and Lyman α . Conditions due to solar flares must be explained by X rays. Above 85 km, the behavior of the ionization is related to the formation of the *E* layer.

1. Introduction. The complexity of studies pertaining to the *D* region of the ionosphere is caused by difficulties in interpreting the observational data and by the fact that several sources of ionization are effective with regard to the different atmospheric constituents involved in region formation.

The ionization of the principal constituents, such as molecular nitrogen and oxygen, cannot be produced by ultraviolet radiation, since their ionization cross sections, not less than 10^{-18} cm², preclude the penetration of such ionizing radiation below 100 km. For ultraviolet radiations to penetrate below 85 km they must have a wavelength greater than 1026.5 Å, corresponding to the first ionization potential of O₂. Furthermore, since the absorption cross section of O₂ in the Schumann-Runge continuum beginning at 1750 Å is more than 10^{-18} cm² between 1700 Å and 2200 Å, the penetration of solar radiation to sufficiently low altitudes can occur only in the atmospheric windows near 1216, 1187, 1167, 1157, 1143, and 1108 Å, and for these unit optical depth is reached at about 10^{20} molecules cm⁻² of vertical column. This corresponds to an altitude of about 75 km for an overhead sun.

In the spectral range 2000 to 1800 Å, the penetration of solar radiation is also possible between the bands of the Schumann-Runge system of O₂. However, ionization by solar radiation

for wavelengths longer than 1800 Å requires constituents for which the ionization potential is very low, such as sodium ($\lambda \leq 2413$ Å) and calcium ($\lambda \leq 2028$ Å). In the region $\lambda < 1220$ Å only nitric oxide and certain atoms have an ionization potential sufficiently low (9.25 eV) to be ionized by ultraviolet solar radiation. Since the absorption cross section of X rays shorter than 10 Å decreases rapidly from 10^{-19} cm² at 10 Å to about 10^{-22} cm² at 1 Å, this spectral range penetrates the entire atmospheric region between 90 and 60 km. Therefore, in addition to photons capable of ionizing nitric oxide and metallic atoms, X rays in the range 1 to 10 Å can contribute to the ionization in the *D* region.

The lower part of the *E* layer, furthermore, can overlap with the ionization of the *D* region. It is known that X rays of wavelength of the order of 35 Å, for which the absorption cross section is 1.3×10^{-19} cm², can produce ionization down to 85 km. It can be shown, however, that such radiations are not important below the mesopause level and need only be considered above 85 km. In fact, the ionospheric region above 85 km must be associated with the formation of the *E* layer by radiations ionizing constituents for which the ionization cross section is not less than 10^{-19} cm².

In addition to the above-mentioned sources of ionization in region *D*, it is shown in this work that it is necessary to consider the effects of cosmic rays. Since the ionization produced by

¹ Present address: R. Mét. Institute, Department of Radiation, Brussels 18, Belgium.

cosmic-ray primaries corresponds to a production of 100 to 300 ion pairs $\text{cm}^{-3} \text{sec}^{-1}$ for 2.5×10^{10} molecules, between geomagnetic latitudes 40° and 60° , the cosmic-ray ionization production is effective below 75 km.

It is the purpose of this work to discuss the ionization processes in region *D* both during normal solar conditions and during solar flares.

2. *The ionization by cosmic rays.* The ionization produced by normal cosmic-ray primaries was considered by Nicolet [1958a] using the ionization rates given by Van Allen [1952].

Let us designate $q_0(\Phi)$ as the ionization rate arising from cosmic-ray primaries in an atmosphere with a number density $n_0 = 2.5 \times 10^{19}$ molecules cm^{-3} at geomagnetic latitude Φ . Above 40 km the ionization rate ($\text{sec}^{-1} \text{cm}^{-3}$) $q(\Phi)$ is given by

$$q(\Phi) = q_0(\Phi)n/n_0 \quad (1)$$

in which n is the molecular concentration at the altitude z .

In order to determine the electron production due to cosmic rays, it is necessary to consider the variation of the effect with latitude and to assume that molecular oxygen and nitrogen have the same ionization coefficient. For example, assuming a mean production rate of 250 ion pairs $\text{cm}^{-3} \text{sec}^{-1}$ at 760 mm of Hg and 20°C , the production rate by cosmic-ray primaries according to (1) is

$$q(\Phi = 50^\circ) = 10^{-17}n \text{ cm}^{-3} \text{sec}^{-1} \quad (2)$$

The variation with latitude (between $\Phi = 0^\circ$ and $\Phi = 60^\circ$) involves a variation of a factor of 10 in q , namely between $1.2 \times 10^{-18}n$ and $1.2 \times 10^{-17}n \text{ cm}^{-3} \text{sec}^{-1}$, that is to say a variation of a factor of 3 in the electron concentration. It should be remembered that conditions ought to be completely different in the auroral zone, and 'abnormal' ionization should be determined in the same way that Bailey [1957, 1959] analyzed the effects of cosmic-ray-flux enhancements in these latitudes. Even at intermediate latitudes some variation can be expected according to variations that have been detected by balloon observations of cosmic-ray intensities. However, it is clear that, for normal conditions, we can use the ionization rate given in (2) by keeping in mind that the latitude effect will cause a

decrease by a factor of 3 from Φ (60°) to the magnetic equator, and an increase which will be of importance in the auroral zone.

The recombination, α , must result from different processes of electron loss, and it is necessary to determine all processes involved in the variation of electron and ion densities. Since there are various processes of electron production and different loss mechanisms with differing recombination coefficients, the recombination must be determined when all ionized constituents and processes are known.

3. *The ionization by X rays.* The principal atmospheric constituents that can be ionized by X rays of $\lambda < 10 \text{ \AA}$ are N_2 , O_2 , and A . Atomic oxygen need not be considered in the mesosphere since it corresponds to a small fraction of O_2 , but may play a particular role in the lower thermosphere. The ionization cross sections can be deduced from the experimental data of Woernle [1930], Messner [1933], Lindh and Nilsson [1945], and Victoreen [1949]. Table 1 gives the absorption cross sections corresponding to a photoelectric absorption associated with the scattering effect. The production of electrons by X rays is due to two different processes. The first is the normal photoelectric effect, in which a photon of energy $h\nu$ is absorbed by an atom which then releases an electron with a certain kinetic energy depending on the ionization potential. In such a process the entire energy of the photon is involved in the ionization process. In addition, the use of the K radiation lines inside the atom can remove other electrons from the same atom (Auger effect) or from another atom (additional photoelectrons of low energy). Several photoelectrons can be produced by a direct photoelectric effect, but the production per photon is limited to a few electrons.

The other ionization process is due to the Compton effect, in which the recoil electron comes from the upper levels of the atoms. Since the ratio of photoelectrons and recoil electrons must, as a first approximation, be equal to the ratio of the absorption and scattering cross sections, it is certain that for $\lambda > 1 \text{ \AA}$ the scattered electrons can be neglected compared with the photoelectrons. But at $\lambda = 0.1 \text{ \AA}$, the ratio in nitrogen is of the order of 120.

In order to compute the efficiency of the ionization by X rays of $\lambda < 10 \text{ \AA}$, let us con-

TABLE 1. Absorption Cross Sections (cm^2) between 0.1 and 10 Å

λ	N_2	O_2	A	Air
0.1	6.64×10^{-24}	7.65×10^{-24}	1.09×10^{-23}	6.89×10^{-24}
0.12	7.02	8.12	1.31	7.30
0.15	7.54	8.81	1.77	7.90
0.20	8.40	1.01×10^{-23}	2.96	8.45
0.25	9.36	1.16	4.86	1.02×10^{-23}
0.3	1.07×10^{-23}	1.39	7.66	1.20
0.4	1.45	2.03	1.66×10^{-23}	1.71
0.5	2.04	3.06	3.10	2.52
0.6	2.91	4.59	5.23	3.72
0.8	5.71	9.51	1.20×10^{-21}	7.56
1.0	1.03×10^{-22}	1.76×10^{-21}	2.27	1.38×10^{-22}
1.2	1.71	2.95	3.83	2.31
1.5	3.23	5.63	7.18	4.37
2.0	7.47	1.31×10^{-21}	1.59×10^{-20}	1.01×10^{-21}
2.5	1.44×10^{-21}	2.51	2.90	1.92
3.0	2.46	4.29	4.67	3.26
3.8			9.71×10^{-20}	
4.0	5.73	9.93	1.10×10^{-20}	6.55
5.0	1.10×10^{-20}	1.90×10^{-20}	1.93	1.26×10^{-20}
6.0	1.87	3.20	3.09	2.13
8.0	4.27	7.22	6.23	4.85
10	8.05×10^{-20}	1.34×10^{-19}	8.37×10^{-20}	9.09×10^{-20}

the average energy W required to produce an ion pair. Since the thresholds of ionization for O_2 and N_2 are about 530 and 400 ev, respectively, the average energy removed from the photoelectron is taken as 500 ev, and the kinetic energy of the electron as $\frac{1}{2}mv^2 = X - 500$, where X denotes the energy of the incident photon; namely 2 kev at 6.2 Å, 3 kev at 4.13 Å, and 6 kev at 2.06 Å. It is clear that the limiting value of W is infinite at zero energy. *Dalgarno and Griffing* [1958] have shown that the average energy per ion pair for electrons in atomic hydrogen is constant for energies above 200 ev and increases rapidly as the energy falls below 200 ev. Therefore, an average energy expenditure can be taken for air as determined by experimental methods. The value adopted is 35 ev [see *Valentine and Curran*, 1958]. Consequently, the following approximate values have been adopted for the number of electrons produced per photon (ionization efficiency):

λ	6 Å	4 Å	2 Å
Efficiency	45	75	165

Data on solar X rays have been obtained by *Friedman, Chubb, Kupperian, and Lindsay* [1958a and b] from rocket measurements during

solar flares and during normal solar conditions. Their results show that solar X-ray radiation must contribute to the ionization of the D region, particularly during solar flares. In fact, the effect of solar X rays was considered as a possibility 25 years ago, for instance by *Müller* [1935], but it was necessary to have rocket observations in order to show that the intensity of such radiations was sufficient for the production of ionization below 85 km. Considering the published data [*Friedman and Chubb*, 1955; *Byram, Chubb, and Friedman*, 1956; *Chubb, Friedman, Kreplin, and Kupperian*, 1957], it is possible to determine the energy available in the X-ray spectrum for various solar conditions. Results of an analysis of observational data are given in Table 2 for three approximate wavelengths. The spectral range between 10 and 1 Å has been subdivided into three ranges for which the absorption cross sections (see Table 1) are $1.0 \times 10^{-21} \text{ cm}^2$ at 2 Å, $6.6 \times 10^{-21} \text{ cm}^2$ at 4 Å, and $2.1 \times 10^{-20} \text{ cm}^2$ at 6 Å. Such a simplification is acceptable in that it corresponds to a variation of a factor of 10 in the energy and to a sufficient approximation to cover the entire spectral range between 1.5 and 8 Å. However, it is also necessary to consider emissions of $\lambda \leq 1$ Å, which

TABLE 2. Variations in the X-Ray Intensities according to Various Solar Conditions
Energies in $\text{erg-cm}^{-2} - \text{sec}^{-1}$.

Condition of the Sun	2 Å	4 Å	6 Å
Completely quiet	10^{-8}	10^{-7}	10^{-6}
Quiet	10^{-7}	10^{-6}	10^{-5}
Lightly disturbed	10^{-6}	10^{-5}	10^{-4}
Disturbed	10^{-5}	10^{-4}	10^{-3}
Special events (flares)	10^{-4}	10^{-3}	10^{-2}
Strong flares	10^{-3}	10^{-2}	10^{-1}

are particularly important during strongly disturbed conditions [Chubb, Friedman, and Kreplin, 1960; Peterson and Winkler, 1959]. For example, an observation of Peterson and Winkler [1959] during a solar flare shows a production of the order of 0.1 to 0.5 electron $\text{cm}^{-3} \text{sec}^{-1}$ near 30 km. High ionization rates at such short wavelengths do not correspond to monochromatic radiations deduced from the ionization of the solar corona (the computation by Elwert [1956a,b] deals only with the emission of coronal lines). The observations of Chubb, Friedman, and Kreplin [1960] show that during a class 2⁺ flare the total flux in the range 0.4 to 0.15 Å was about $2.3 \times 10^{-5} \text{ erg cm}^{-2} \text{sec}^{-1}$ and that the flux per unit energy range decreased by a factor of about 2 for every increase in energy at 5.3 kev. In any event, when X-ray emissions below 1 Å are considered, it is necessary to compare the ionization they produce with the ionization normal for cosmic rays for which the production rate is given by equation 2. Since the ionization coefficient of cosmic-ray primaries at Φ (50°) is of the order of $10^{-17} \text{ sec}^{-1}$ per molecule, let us take this value as the standard value for cosmic-ray-ionization effect so as to make a comparison with X-ray ionization.

For X rays of about 10 kev ($\lambda = 1.2 \text{ Å}$), the energy necessary to equal the production by cosmic rays cannot be less than $3 \times 10^{-6} \text{ e}^{\tau} \text{ erg cm}^{-2} \text{sec}^{-1}$. Therefore, according to the data of Table 2, strongly disturbed solar conditions can increase the ionization above 55 km. If the X-ray energy is of the order of 20 kev ($\lambda = 0.6 \text{ Å}$), however, the energy required to compete with the normal cosmic-ray effect is greater than $2 \times 10^{-6} \text{ e}^{\tau} \text{ erg cm}^{-2} \text{sec}^{-1}$. At higher energies,

from about 30 kev ($\lambda = 0.4 \text{ Å}$) to about 100 kev ($\lambda = 0.12 \text{ Å}$), the X-ray energies needed to lead to ionization rates more important than those produced by cosmic rays are not less than $4 \times 10^{-6} \text{ e}^{\tau} \text{ erg cm}^{-2} \text{sec}^{-1}$ and $8 \times 10^{-6} \text{ e}^{\tau} \text{ erg cm}^{-2} \text{sec}^{-1}$, respectively. Therefore, extreme conditions are needed to modify the normal ionization due to cosmic rays below 50 km, and it is possible to deduce the ionization conditions by using the data of Table 2.

The effective ionization rate coefficient can be determined by using the data of Table 2 together with the absorption cross section and the efficiency of ionization. Table 3 shows the various ionization coefficients for zero optical depth according to various solar conditions. They represent relative ionization rates per unit of energy of 1, 2.5×10^2 , and 10^4 in the spectral ranges 1.5 to 3.3 Å, 3.3 to 5 Å, and 5 to 8 Å, respectively. Values of Table 2 will be used to compute the ionization rates by X-ray radiation versus altitudes above 60 km.

4. *The ionization by Lyman α .* The chromospheric radiation Lyman α at 1215.7 Å is an important solar emission which was suggested by Nicolet [1945] as leading to the ionization of nitric oxide. Lyman α is in the spectral range (9.25 to 12 ev) situated between the ionization and dissociation continua of molecular oxygen and, in particular, in an atmospheric window for which, according to Watanabe, Inn, and Zelikoff [1953], the absorption cross section is $1 \times 10^{-20} \text{ cm}^2$ for molecular oxygen. Other experimental determinations, such as those made earlier by Preston [1940], lead to the same

TABLE 3. Ionization Coefficients, per molecule sec^{-1}

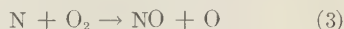
Condition of the Sun	2 Å	4 Å	6 Å
Completely quiet	1.6×10^{-19}	9.8×10^{-18}	2.8×10^{-17}
Quiet	1.6×10^{-18}	9.8×10^{-17}	2.8×10^{-16}
Lightly disturbed	1.6×10^{-17}	9.8×10^{-16}	2.8×10^{-15}
Disturbed	1.6×10^{-16}	9.8×10^{-15}	2.8×10^{-14}
Special events	1.6×10^{-15}	9.8×10^{-14}	2.8×10^{-13}
Strong flares	1.6×10^{-14}	9.8×10^{-13}	2.8×10^{-12}

value, whereas others, such as those of *Lee* [1955] and *Ditchburn, Bradley, Cannon, and Sunday* [1954], give 8.5×10^{-21} cm². Because of such a low value, Lyman α can penetrate to 75 km; and this has been observed by *Byram, Chubb, Friedman, and Gailar* [1953]. Its energy, which now appears to have been determined with an acceptable precision, is between 3 and 4 erg cm⁻² sec⁻¹. In fact, in measurements before 1955 [see *Byram, Chubb, Friedman, and Upperian*, 1958], values as low as 0.1 erg cm⁻² sec⁻¹ were given. In spite of low solar activity, it should be accepted that values greater than 1 erg cm⁻² sec⁻¹ correspond to the real incident flux. Recent spectroscopic observations by *Musey* (private communications) and by *Rense* (private communication) lead to 5 and 3 erg cm⁻² sec⁻¹. A value of 3 erg cm⁻² sec⁻¹ will be considered in our computations as an average value.

Since the mechanism was proposed by *Nicolet* [1945], *Bates and Seaton* [1950] have set forth reasons indicating why it is difficult to consider alternative ionizations due to ultraviolet solar radiation. The experimental values of the absorption and ionization cross sections of NO have been determined by *Watanabe* [1954]. At Lyman α , the ionization cross section of nitric oxide is 2×10^{-18} cm² and the absorption cross section is 2.4×10^{-18} cm².

Negative results of nitric oxide absorption measurements in the atmosphere set upper limits to its concentration. A recent analysis by *Jursa, Wanka, and LeBlanc* [1959] of the solar spectrum leads to the conclusion that the concentration of nitric oxide in the altitude interval 63 to 85 km cannot exceed 10^8 molecules cm⁻³, since the bands of its electronic system are not observed. Such a low value shows that the determination by *Mitra* [1954] of 10^{12} molecules cm⁻³ is not acceptable by a factor of more than 10^4 , and, consequently, his resulting D-layer model likewise will need modification. The estimation made by *Nicolet* [1955a] which was used on the then available low published value of 0.1 erg cm⁻² sec⁻¹ for Lyman α led to a high value of the order of 10^8 molecules cm⁻³ at 80 km. A recent analysis of the photochemistry of nitric oxide made by *Nicolet* [1958b] shows that at the concentration of nitric oxide at 85 km of about 10^{-10} of the total concentration, namely

10^4 molecules cm⁻³. Such a low concentration is far below the value detectable by spectrographic methods. It is therefore necessary to discuss here the determination of the vertical distribution of nitric oxide [*Nicolet*, 1958a]. The most important process is the reaction between atomic nitrogen, produced by X rays, and molecular oxygen, which leads to the formation of NO



even if its rate coefficient a_1 requires a high activation energy.

The coefficient a_1 as determined between 400° and 500°K by *Kistiakowsky and Volpi* [1957] leads to 6.2 kcal for the activation energy. It can be written as follows:

$$a_1 = 1.5 \times 10^{-13} T^{1/2} e^{-6200/RT} \quad (4)$$

The most important process affecting nitric oxide is the reaction with atomic nitrogen, since it must be the principal process leading to nitrogen recombination



Kistiakowsky and Volpi [1957], in a first study of reactions of nitrogen atoms with nitrogen and oxygen oxides, have shown that reaction (5) is very fast and that its lower limit corresponds to a rate coefficient $a_2 \geq 6.6 \times 10^{-10}$ cm³ sec⁻¹. In this case the activation energy of (5) should be less than 3.5 kcal. However, in a recent paper, *Kistiakowsky and Volpi* [1958] consider that a_2 should be greater than 3×10^{-11} cm³ sec⁻¹. Such a high rate leads to a very low value for the activation energy (maximum 0.5 kcal). Therefore, we shall use the following formula

$$a_2 = 1.5 \times 10^{-11} T^{1/2} \quad (6)$$

Comparing the rate coefficients (4) and (6), we obtain the ratio for reactions (3) and (5)

$$n(\text{NO}) = \frac{a_1 n(\text{O}_2)}{a_2} = 10^{-2} n(\text{O}_2) e^{-6200/RT} \quad (7)$$

which leads to the determination of the nitric oxide concentration when nitrogen atoms are sufficiently numerous. It may be pointed out that the activation energy of (3) is less than 0.5 kev and the possible error of (4) would lead to an underestimation of the rate coefficient by one order of magnitude at the mesopause level.

Furthermore, it can be seen that the exponential factor of (7) must be known accurately in order to obtain an exact value in the lower thermosphere, even if there is a systematic error in the pre-exponential factor. Any error in the numerical value of (7) would not appear to change the general picture, but modify the absolute values of nitric oxide concentration in the atmospheric region where the temperature is very low. Therefore, no reliance can be placed on detailed numerical results, because only order-of-magnitude calculations can be made from experimental results for aeronomic problems. For example, the adoption of a concentration of nitric oxide of 10^4 molecules cm^{-3} at 85 km does not exclude the possibility of 10^5 cm^{-3} .

The vertical distribution of nitric oxide given by (7) will be used in the thermosphere, and the distribution, following the atmospheric distributions in the mesosphere, will be adopted for the computation of the ionization by Lyman α . In the computations this radiation will be kept constant even though it is possible that it can vary by a factor of 2 owing to solar activity. Consequently, the photoionization rate coefficient of nitric oxide at zero optical depth is taken as $3.6 \times 10^{-7} \text{ sec}^{-1}$.

5. *The ionization by radiation of $\lambda > 1750$ Å.* From laboratory measurements, absorption cross sections near the threshold can be obtained for Na [Ditchburn, Jutsum, and Marr, 1953] and for Ca [Jutsum, 1954]. At zero optical depth, the photoionization rate coefficients [Nicolet, 1955a] are $1.1 \times 10^{-5} \text{ sec}^{-1}$ and 10^{-6} sec^{-1} for Na and Ca, respectively. These high ionization rate coefficients show that very small concentrations are needed to produce appreciable electron densities at low levels by radiation of $\lambda < 2413$ Å or $\lambda < 2018$ Å.

6. *The ionization of atomic oxygen.* Atomic

oxygen cannot be ionized in the *D* region by solar radiation of $\lambda < 910$ Å, corresponding to its threshold, since molecular oxygen essentially absorbs all this radiation above 100 km. The peak concentration of atomic oxygen is below 100 km, however, and its concentration in the mesosphere is associated with the ozone concentration. Above 50 km, $n(\text{O}) > n(\text{O}_2)$, and atomic oxygen concentration increases with altitude and is not less than 10^{11} atoms cm^{-3} above 65 km in a sunlit atmosphere. At 80 km, a concentration of more than 10^{11} cm^{-3} is maintained even in a dark atmosphere [Nicolet, 1959a]. Therefore, X rays can ionize atomic oxygen, and its ionization rate coefficient is of the values given in Table 3. The importance of the ionization of atomic oxygen in the present connection is that it leads to the production of NO^+ by the ion interchange reaction between O^+ and N_2 (see section 12). Constituents such as Na and Ca, and also O, are possibly important with regard to sporadic effects and nocturnal ionization above 85 km.

7. *The ionization of the E layer.* Since the cross sections between 10^{-10} and 10^{-18} cm^2 with the molecular concentrations of the *E* layer, the spectral range of X rays leading to ionization is between 10 and 100 Å and can be divided as shown in Table 4. The absorption in the range 31 to 10 Å corresponds to the absorption between 100 and 31 Å, but its ionization is small compared to that of 100 to 31 Å.

In addition to X rays, the following ultraviolet radiations are involved in the formation of the *E* layer: Lyman β ionizing O_2 with energy of the order of $0.05 \text{ erg cm}^{-2} \text{ sec}^{-1}$, and Lyman continuum ionizing O and O_2 with energy of the order of $0.05 \text{ erg cm}^{-2} \text{ sec}^{-1}$, according to Toupin (private communication).

Therefore, the origin of the ionization of the

TABLE 4. K Continuum and L Continuum

Mean λ , Å Range, Å	70 90-55	50 55-40	35 40-31
Cross sections:			
Air, cm^2	6.2×10^{-10}	3.0×10^{-10}	1.3×10^{-10}
N_2 , cm^2	5.5×10^{-10}	2.4×10^{-10}	4.7×10^{-10}
O_2 , cm^2	9.3×10^{-10}	4.0×10^{-10}	1.6×10^{-10}
Mean λ , Å	20.5 Å	15.5 Å	11.5 Å
Range, Å	31-16.5 Å	16.5-12.8 Å	12.8-10.3 Å

TABLE 5. Atmospheric Data between 50 and 90 Km

Altitude, km	Temperature, °K	$n(O_2)$, cm^{-3}	$n(NO)$, cm^{-3}	$n(N_2)^*$, cm^{-3}	$n(M)H$, cm^{-2}
50	274	4.93×10^{18}	2.35×10^8	1.83×10^{16}	1.9×10^{22}
52.5	274	3.63	1.73	1.35	1.4
55	274	2.68	1.28	9.97×10^{16}	1.0
57.5	263	2.04	9.72×10^8	7.58	7.6×10^{21}
60	253	1.53	7.31	5.70	5.5
62.5	242	1.14	5.43	4.24	3.9
65	232	8.35×10^{14}	3.99	3.11	2.8
67.5	221	6.05	2.89	2.25	1.9
70	210	4.31	2.06	1.61	1.3
72.5	207	2.94	1.40	1.09	8.7×10^{20}
75	203	1.99	9.48×10^4	7.40×10^{14}	5.8
77.5	200	1.34	6.38	4.98	3.8
80	197	8.93×10^{13}	4.26	3.24	2.5
82.5	193	5.93	2.83	2.21	1.6
85	190	3.90	1.86	1.45	1.1
87.5	191	2.48	1.83	9.24×10^{13}	6.9×10^{19}
90	192	1.59×10^{13}	1.39×10^4	5.93×10^{13}	4.5×10^{19}

* $n(N_2) = 0.7808$ of the total concentration $n(M)$.

layer is different from that of the D layer, and the ionization at the mesopause is affected by the effect of radiations of 31 to 40 Å.

8. *The vertical distribution of constituents and absorption peaks.* In order to study the behavior of the ionization in the D region it is necessary to adopt an atmospheric model. The atmospheric data are taken from tables computed by Nicolet [1959a] on the basis of rocket observations. Table 5 shows the height variation of the numbers of molecules cm^{-3} and molecules cm^{-2} of a vertical column. These data permit the computation of the ionization rate for various radiations by using the following formula:

$$n_j I_{j,\infty} \exp \left[- \sum n_i K_i H \sec \chi \right] \quad (8)$$

where the index j denotes the constituents of species j , I_j is the ionization rate coefficient for the zero optical depth, and the exponential term corresponds to the fraction which is not absorbed at the altitude considered; it is the optical depth τ_λ for an overhead sun multiplied by the solar zenith distance χ .

X rays are absorbed by N_2 and O_2 , and the optical depth τ_λ is

$$\tau_\lambda = n(M) K_\lambda(M) H \quad (9)$$

which $n(M)$ is the total number of particles,

$K_\lambda(M)$ the absorption cross section for air, and H the atmospheric scale height. Lyman α is absorbed by O_2 , and the optical depth τ_λ is

$$\tau_\lambda = n(O_2) K_\lambda(O_2) H \quad (10)$$

in which $n(O_2)$ is the concentration of molecular oxygen, and $K_\lambda(O_2)$ the absorption cross section of O_2 . The unit optical depths for an overhead sun are as follows:

λ , Å	2	4	6	1216
Altitude, km	70	80	87	75

The electron production peak is obtained by differentiating (8), and it corresponds to the condition

$$\sum n_i K_i H = (1 + \beta) \sec \chi \quad (11)$$

in which $\beta = dH/dz$ is the gradient of the scale height H . Since β is small, at the height levels of interest, the altitude of the electronic production peak is approximately the altitude of unit optical depth. From these data it is clear that the ionization by Lyman α occurs in the range of altitudes where is also produced ionization by X rays between 2 and 4 Å.

9. *Equation of ionization.* The conventional equation of ionization is

$$dn_e/dt = q - \alpha n_e^2 \quad (12)$$

in which q is an equivalent production of electrons, n_e , and α denotes an equivalent recombination coefficient or *recombination*. Since the recombination is very high in the D region the ionization conditions can be found by determining the ionization equilibrium given as

$$n_e^2 = q/\alpha \quad (13)$$

Furthermore, since various constituents and various spectral ranges are involved in the electron production, q must be written

$$q = \sum q_i \quad (14)$$

in which q_i represents one of the n contributions, $j = 1, \dots, n$, to the electron production. Also, the recombination α is due to all effects of recombination, and it is necessary to define a specific recombination, α_j ,

$$q_i = \alpha_j n_i^+ n_e \quad (15)$$

in which n_i^+ is the positive ion of the constituent j . According to (15), equation 13 must be replaced by

$$\frac{q_1}{\alpha_1 n_1^+} = \frac{q_2}{\alpha_2 n_2^+} = \dots = \frac{q_n}{\alpha_n n_n^+} \quad (16)$$

or

$$\sum q_i / \alpha_i = n_e \sum n_i^+ \quad (17)$$

since

$$n^+ = n^- + n_e \quad (18)$$

and writing

$$n^- / n_e = \lambda \quad \text{and} \quad n^+ = (1 + \lambda) n_e \quad (18')$$

equation 17 can be written

$$(1 + \lambda) n_e^2 = \sum q_i / \alpha_i \quad (19)$$

instead of the conventional equation 13. It will be noted that the recombination α is different ($\lambda > 1$) from a recombination α_e between positive ions and electrons

$$\alpha n_e^2 \equiv \alpha_e (1 + \lambda) n_e^2 \equiv \sum q_i \quad (20)$$

α_e corresponds to an equivalent production function, $\sum q_i / (1 + \lambda)$.

10. *Negative ions.* The determination of the value of λ , the ratio of negative ions to electrons, has been the subject of many papers. Recently

Mitra [1959] deduced a general expression for the recombination, but his determination may be considered erroneous because it leads to wrong values for λ .

It is necessary to consider the physical parameters which have been determined in the laboratory. Branscomb, Burch, Smith, and Branum [1958] determined the photodetachment cross section of electrons from the negative ion of atomic oxygen and the radiative attachment of electrons to oxygen atoms. At the low energies of electron energies corresponding to the atmospheric temperature in region D , the attachment coefficient $a(O)$ is

$$a(O) = 1.3 \times 10^{-15} \text{ cm}^3 \text{ sec}^{-1}$$

The photodetachment rate coefficient $d(O)$

$$d(O^-) = 1.4 \text{ sec}^{-1}$$

according to the value for the threshold energy of 1.465 \pm 0.05 eV and corresponding to a wavelength of $0.846 \pm 0.003 \mu$. According to (21) and (22), and since $n(O) < 10^{13} \text{ cm}^{-3}$ in the D region, it is clear that

$$\lambda(O) < 10^{-2}$$

and that negative ions of atomic oxygen can be neglected.

The photodetachment of electrons from O_2^- studied by Burch, Smith, and Branum [1958], leads to a photodetachment rate coefficient $d(O_2)$

$$d(O_2) = 0.44 \text{ sec}^{-1}$$

The attachment of slow electrons in molecular oxygen is a three-body attachment, according to Chanin, Phelps, and Biondi [1959]. Since the third body in the atmosphere is also molecular oxygen, and temperature variations can be neglected, the attachment coefficient of electrons to molecular oxygen is taken as

$$a(O_2) = 1.5 \times 10^{-30} n(O_2) \text{ cm}^3 \text{ sec}^{-1}$$

From (24) and (25), the ratio λ is given

$$\lambda = [(1.5 \times 10^{-30}) / 0.44] n^2(O_2)$$

Such a value of λ can be used down to 60 km even if collisional detachment reaches a value of $4 \times 10^{-17} \text{ cm}^3 \text{ sec}^{-1}$, and (26) therefore

nts the equilibrium ratio between negative ions and electrons in a sunlit atmosphere. Its value between 60 and 90 km varies as follows:

Altitude, km	60	70	80	90
λ	7.5	0.63	0.03	8.6×10^{-4}

Figure 1 shows the variation of $\lambda = n^-/n_e$ and $(1 + \lambda) = n^+/n_e$ between 60 and 90 km.

Since the value of $\lambda \leq 0.03$ above 80 km, it is clear that the conventional equation 12 can be written

$$dn_e/dt = q - \alpha_e n_e^2 = \Sigma q_i - \alpha_e n_e^2 \quad (27)$$

which q is the real production function of electrons. α_e now becomes the real recombination, since $n^+ \approx n_e$. But below 80 km the conventional equation must be written

$$\frac{dn_e}{dt} = \frac{\Sigma q_i}{1 + \lambda} - \alpha_e n_e^2 - \frac{n_e}{1 + \lambda} \frac{d\lambda}{dt} \quad (28)$$

if it is assumed that processes dealing with attachment and detachment of electrons are very rapid, $d\lambda/dt$ equals zero. Under such conditions,

$$dn^-/n^- = dn_e/n_e \quad (29)$$

and, therefore, (28) can be written

$$dn_e/dt = \Sigma q_i/(1 + \lambda) - \alpha_e n_e^2 \quad (30)$$

and (30) is the practical equation for the variation of the electron concentration.

11. *The recombination coefficient.* The equivalent recombination, α_e , of equation 30 cannot be determined without a complete analysis of all processes, since several radiations cause the ionization of various constituents in the D region. Empirical values deduced from radio data cannot be adopted, since such values currently deal with estimates which are very uncertain. The values of α_e are not necessarily constant throughout the day, nor should they vary according to the modifications of the layer shape with time. An average curve, such as that of Mitra [1959], is not acceptable, since the difference between the observational data quoted and the mean values adopted is too large.

The calculations made by Houston [1958] for nitric oxide, using a varying recombination from about $5 \times 10^{-6} \text{ cm}^3 \text{ sec}^{-1}$ at 60 km to $10^{-6} \text{ cm}^3 \text{ sec}^{-1}$ near 70 km and $10^{-7} \text{ cm}^3 \text{ sec}^{-1}$ near 90 km,

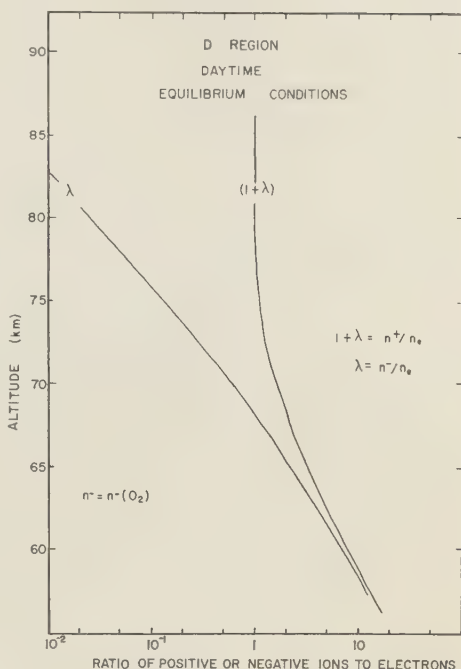


Fig. 1. Variation of λ and $1 + \lambda$ with altitude.

leads to an artificial distribution of the ionization. In fact, such a vertical distribution of the electron density corresponds to any arbitrary minor constituent for which the optical depth is given by the absorption distribution of O_2 and N_2 , subject to the law of recombination that has been assumed.

In order to determine the recombination we may consider the ionization of a constituent, the total ionization being given by equation 19.

The equation for positive ions of species j is

$$\frac{dn_j^+}{dt} = q_j - \alpha_{D,j} n_j^+ n_e - \alpha_{i,j} n_j^+ n^- \quad (31)$$

in which $\alpha_{D,j}$ denotes the recombination coefficient of positive ions with electrons and $\alpha_{i,j}$ is the recombination coefficient of positive ions with negative ions. Equation 31 can be written in the following form since there is only one negative ion to be considered (see section 9):

$$\frac{dn_j^+}{dt} = q_j - (\alpha_{D,j} + \lambda \alpha_{i,j}) n_j^+ n_e \quad (32)$$

However, (32) cannot be written in the practical form of (30) since $n_j^+ < n^+$. In fact, (30) must be equivalent to

$$\sum \frac{dn_i^+}{dt} = \Sigma q_i - n_e \Sigma (\alpha_{D,i} + \alpha_{i,i}) n_i^+ \quad (33)$$

or

$$\frac{dn_e}{dt} = \frac{\Sigma q_i}{1 + \lambda} - \frac{n_e}{1 + \lambda} \Sigma (\alpha_{D,i} + \lambda \alpha_{i,i}) n_i^+ \quad (34)$$

Bates [1950] has shown that dissociative recombination is a process occurring at a much faster rate than other recombination processes involving electrons. Experimental determinations have been made, and in particular the recombination of the molecular ion of nitrogen has been studied recently by *Bialecke and Dougal* [1958] and *Faire and Champion* [1959]. Such determinations lead to a coefficient as high as $5 \times 10^{-7} \text{ cm}^3 \text{ sec}^{-1}$ for N_2 in the *D* region. As far as molecular oxygen is concerned the experimental analysis is not yet complete. However, *Sayers* [1956] gave a value of the order of $4 \times 10^{-8} \text{ cm}^3 \text{ sec}^{-1}$. Nitric oxide ions are certainly an important ionospheric constituent, but their dissociative recombination coefficient is not known. Considering that such an ion should have a long lifetime, its recombination will be considered to be 10 times lower than that of molecular oxygen. Therefore, for a quantitative treatment we have adopted the following values:

$$\left. \begin{aligned} \alpha_D(N_2) &= 5 \times 10^{-7} \text{ cm}^3 \text{ sec}^{-1} \\ \alpha_D(O_2) &= 3 \times 10^{-8} \text{ cm}^3 \text{ sec}^{-1} \\ \alpha_D(NO) &= 3 \times 10^{-9} \text{ cm}^3 \text{ sec}^{-1} \end{aligned} \right\} \quad (35)$$

It is not possible to estimate the value of the coefficients with assurance, since they are temperature dependent. However, we have adopted the approximate ratios 100 : 10 : 1 for the recombination coefficients of N_2 , O_2 , and NO to show how the ionization is affected when various constituents are involved.

Ionic recombination, α_i , has been considered an important process since *Bates and Massey* [1946] gave potent arguments for its inclusion. It can have a value as high as $10^{-7} \text{ cm}^3 \text{ sec}^{-1}$.

Such a value has been adopted as a working value for all constituents.

With the adoption of numerical values for α_i and α_D , all the information required to complete the resulting distribution of the electron concentration has been obtained.

Equation 16 has been used as follows:

$$\begin{aligned} & \frac{q(N_2)}{(10^{-7}\lambda + 5 \times 10^{-7})n^+(N_2)} \\ &= \frac{q(O_2)}{(10^{-7}\lambda + 3 \times 10^{-8})n^+(O_2)} \\ &= \frac{q(NO)}{(10^{-7}\lambda + 3 \times 10^{-9})n^+(NO)} = n_e \quad (36) \end{aligned}$$

and, together with equation 19, leads to the determination of the electron concentration. The values that have been adopted, for example α_i for NO , may be too high, and some inconsistency may, therefore, occur in our results, owing to the fact that only one value has been adopted for α_i . But even a value such as $\alpha_i(NO) = 10^{-8} \text{ cm}^3 \text{ sec}^{-1}$ will not change our arguments. In view of the uncertainty in $n(NO)$ and in $\alpha_i(NO)$, the total uncertainty that must be considered for the determination of the electron concentration is that involved in the ratio $n(NO)/\alpha_i$. Therefore, several experimental results are needed to improve aeronomic results.

12. *The ion-atom interchange.* Bates [1955] first drew attention to the importance of ion-atom interchange in the ionosphere. A process such as

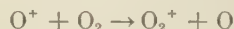


has a relatively large rate coefficient. However, since the activation energy may be important in some instances, *Bates and Nicolet* [1960] consider that ion-atom interchange processes in the upper atmosphere are slower than simple collision theory led us to suppose.

The processes of importance in the ionosphere are, according to *Bates and Nicolet* [1960],



and



In an unexcited colliding system, the only inter

large process transforming molecular ions into atomic ions is



and the only other interchange process suffered by molecular ions is



Since the concentration of atomic nitrogen is small, O_2^+ and N_2^+ are lost by dissociative recombination and not by ion-atom interchange. The disappearance of O^+ ions determined by ion-atom interchange with N_2 and O_2 leads to the production of NO^+ ions. Since O^+ ions are produced by X rays and the Lyman continuum, the origin of NO^+ ions in the *E* layer (and *F* layer) and also their nocturnal concentrations are explained.

13. *Ionization for a quiet sun.* We have determined all values of the various quantities in equation 19 assuming that O_2 , N_2 , and NO are the constituents ionized by cosmic radiation, X rays, and Lyman α . Figure 2 shows the vertical distribution of the electron concentration n_e from 60 km for an overhead sun; n_e increases from about 100 electrons cm^{-3} at 60 km to a peak of about 1500 electrons cm^{-3} at 80 km. Above 85 km, the electron concentration would increase if the tail of the *E* layer were not involved. It will be shown in a later publication that the ionization of the *E* layer by X rays of wavelength 30–35 Å is effective down to 85 km for an overhead sun.

To show the effect of the electron attachment, two curves are given (Figure 2) showing the vertical distributions of positive ions and of the negative ion of molecular oxygen. Negative ions in a sunlit atmosphere are important in the lower part of the *D* region up to 70 km, but are negligible at 80 km. The simultaneous effect of cosmic rays, X rays, and Lyman α is shown by curves giving the vertical distribution of N_2^+ , O_2^+ , NO^+ , and n^+ .

Below 65 km, owing to the adoption of the same ionic recombination coefficient for all constituents, N_2^+ is the most important ion, and N_2 the most important constituent. Above 70 km, n^+ (O_2) $>$ n^+ (N_2), since the dissociative combination coefficient, α_n (O_2), is less than α_n (N_2). It is also clear that ionization by X

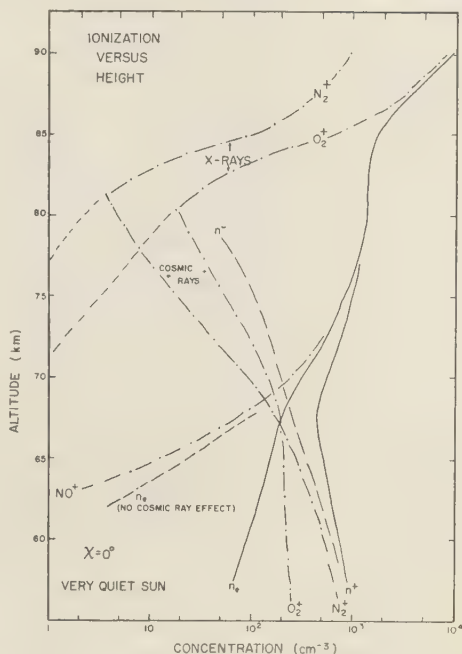


Fig. 2. Concentrations of positive ions (N_2^+ , O_2^+ , NO^+), negative ion (O_2^-), and electrons (n_e) versus altitude for a very quiet sun.

rays does not play a role below 80 km when the sun is quiet. The number of positive ions N_2^+ and O_2^+ due to X rays is negligible. Table 6 shows values of the product n^+n_e at three particular altitudes, 60, 70, and 80 km. From this table it is clear that cosmic rays are the principal radiations causing ionization at 60 km and that Lyman α plays the important role at 80 km.

As far as the altitude of 70 km is concerned, the ionization production is contributed by NO^+ , ionized by Lyman α and O_2^+ and N_2^+ , due to cosmic rays. Since the cosmic-ray-production rate in our computation corresponds to a geomagnetic latitude of about 50°, there will be a variation with latitude near 70 km where the total ionization is very sensitive to fluctuations of the nitric oxide concentration and the intensity of cosmic rays. It is easy to obtain latitude corrections by taking into account the variation of the production function, which varies by a factor 10 between the equator and $\Phi = 60^\circ$.

TABLE 6. n^+n_e at 60, 70, and 80 km

Altitude: 60 km	Cosmic			Lyman α
	Rays	X Rays		
$n^+(\text{O}_2)n_e$	2.1×10^4	1.8×10^1		
$n^+(\text{N}_2)n_e$	4.7×10^4	2.3×10^1		
$n^+(\text{NO})n_e$			3.6×10^4	
Totals	6.8×10^4	4.1×10^1	3.6×10^4	
Total	$6.8 \times 10^4 \text{ cm}^{-6} = (1 + \lambda)n_e^2$			
Altitude: 70 km	Cosmic			Lyman α
	Rays	X Rays		
$n^+(\text{O}_2)n_e$	4.6×10^4	2.8×10^2		
$n^+(\text{N}_2)n_e$	2.9×10^4	9.9×10^1		
$n^+(\text{NO})n_e$			7.9×10^4	
Totals	7.5×10^4	3.8×10^2	7.9×10^4	
Total	$1.54 \times 10^6 \text{ cm}^{-6} = (1 + \lambda)n_e^2$			
Altitude: 80 km	Cosmic			Lyman α
	Rays	X Rays		
$n^+(\text{O}_2)n_e$	2.7×10^4	2.1×10^1		
$n^+(\text{N}_2)n_e$	6.6×10^3	2.9×10^3		
$n^+(\text{NO})n_e$			1.8×10^6	
Totals	3.4×10^4	2.4×10^4	1.8×10^6	
Total	$1.8 \times 10^6 \text{ cm}^{-6} = (1 + \lambda)n_e^2$			

The effect of cosmic rays is shown in Figure 3 by the difference between the curves representing electrons concentrated below 70 km. The minimum electron concentrations should be due to the ionization of Lyman α alone, considering that there is a negligible effect due to cosmic rays. Nevertheless, the gradient of 100 electrons $\text{cm}^{-3} \text{ km}^{-1}$ between 70 km and 75 km is due only to the effect of nitric oxide, and it is not influenced by the cosmic-ray effect.

An essential part of the result is also the fact that there is a peak in the electron concentration between 80 and 85 km. This peak, deduced for an overhead sun, will remain in very nearly the same range of altitudes when the solar zenith angle is between $\chi = 0$ and $\chi = 75^\circ$. The vertical distribution of the ionization is shown in Figure 3. It is clear that the reflection level for 16 kc/s radio waves corresponding to 300 electrons cm^{-3} , which is at 70 km for an overhead sun, goes up to about 75 km for $\chi = 70^\circ$. Near sunrise, ionization conditions for $\chi \geq 80^\circ$ must be studied when considering the time variation due to the rapid change of production after sunrise and the value of the effective recombination before sunset.

14. *Ionization during solar flares.* Considering that the variation of Lyman α cannot be

more than a factor of 4, and that of cosmic rays not more than a factor of 2, except for exceptional events, it is only necessary to study the variations of X rays in determining solar-flare effects. As is easily seen, there is practically no difference in the electron concentration of the E region, if the sun is considered completely quiet or quiet from the values given in Table 2. The conditions, for a lightly disturbed sun, for which the X-ray energies are 10^{-6} , 10^{-5} , and 10^{-4} erg $\text{cm}^{-2} \text{ sec}^{-1}$ at 2, 4, and 6 A, respectively, result in a small effect on the vertical distributions of the ionization below 80 km.

Figure 4 shows how these effects occur when the sun is overhead. The activity of X rays becomes readily apparent when energies are between 10^{-6} and 10^{-3} erg $\text{cm}^{-2} \text{ sec}^{-1}$ for the wavelength range 2 to 6 A. For energies greater than these values, flare conditions become more and more important. Strong flares lead to a very large increase of the ionization.

Evidence that solar X-ray emission produces the necessary ionization, as demonstrated by *Friedman and Chubb* [1955], is provided by the various curves of Figure 4. There is a general

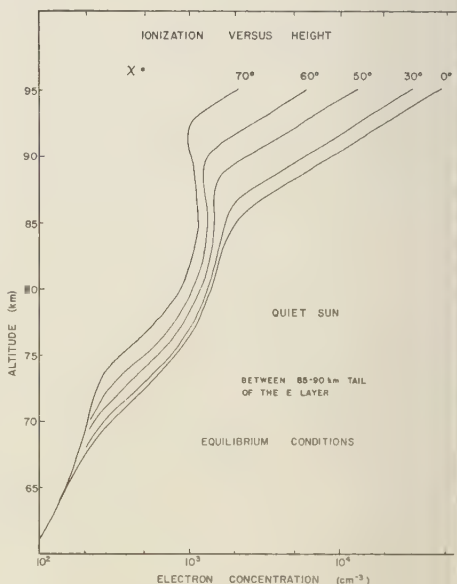


Fig. 3. Variation of the electron concentration with the solar zenith distance when equilibrium conditions are considered.

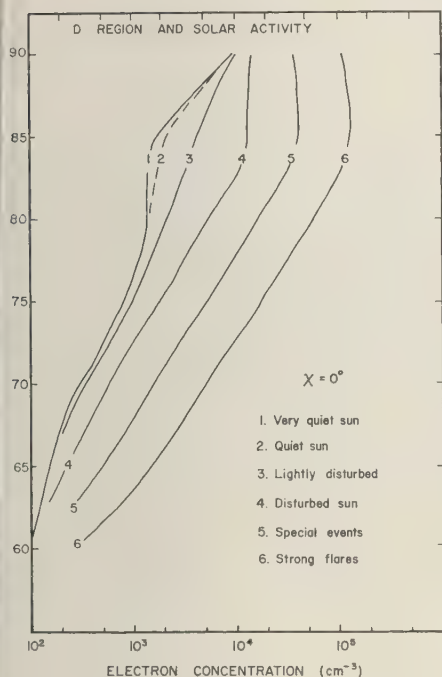


Fig. 4. Variation of the electron concentration according to solar conditions, from very quiet sun to strong solar flares. No effect from 35 to 100 A is considered.

lowering of the layer caused by the increase of the intensity of X rays. When the sun is well disturbed, the average lowering is about 2 km. When there is flare activity, the lowering can easily be as much as 5 km, and during the largest flares, the same electron concentrations are found 10 km below the quieter sun level.

Therefore, X rays are certainly responsible for the ionization during disturbed solar conditions. The rapid increase of the ionization when the energy is greater than 10^{-6} erg cm⁻² sec⁻¹ at 2 A and 10^{-4} erg cm⁻² sec⁻¹ at 6 A would exclude Lyman α in solar-flare effects. On the other hand, it is not possible to account for the formation of the normal D layer with X rays; this must be explained by the ionization of nitric oxide.

The radiations of wavelengths of the order of 6 A can produce a large increase in the ionization near 85 km. The values shown in Figure 4 indicate that an energy of 0.1 erg cm⁻² sec⁻¹

leads to an electron peak of the order of 10^6 cm⁻³, not too different from the peak of the normal E layer.

Such variations in the ionization of the D layer indicate that radio absorption effects are under solar control and sudden or short-duration events in the absorption are directly correlated with solar flares. Since the ratio of the intensities of effective radiations is not necessarily constant, as given in Table 2, the vertical distributions can be distorted from the average curves shown in Figure 4 and the manner in which absorption depends upon the height will be affected according to the variations of the intensities in the spectral range 1 to 10 A.

Below 60 km, the ionization must be explained by cosmic rays and X rays of $\lambda < 1$ A. At such low altitudes the ionization rate corresponding to the absorption peak must be greater than 7×10^{-6} erg cm⁻² sec⁻¹ for $\lambda = 1.2$ A and not less than 2×10^{-4} erg cm⁻² sec⁻¹ for $\lambda = 0.12$ A to compete with the normal ionization by cosmic rays at $\Phi = 50^\circ$.

15. *Conclusions.* This theoretical study of the D region of the ionosphere shows that the ionization processes correspond to a normal ionization of nitric oxide by Lyman α with a resultant electronic peak near 85 km, to cosmic-ray ionization which can be effective below 70 km, and to ionization by X rays of 2 kev or more varying with solar conditions. No effort has been made to follow the observational studies of the D region. Such an analysis would require an interpretation of certain observational data and also the inclusion of other possible sources of ionization such as meteor effects. In fact, it has been shown [Nicolet, 1955b] how meteor atoms may be involved in the ionization, and it is clear that sporadic effects can result from ionized meteor atoms. An ionization of sodium atoms must exist, and near 80 to 85 km the production could be of the order of 10^{-1} cm⁻³ sec⁻¹, but the final electron concentration depends on the recombination of sodium, which is not known.

The term 'D region' is generally used for that part of the ionosphere below the E region. From our analysis it is clear that the separation between these two regions occurs near 85 km at the mesopause level. The tail of the E layer is due to ionization by X rays of $\lambda > 31$ A and, there-

fore, is formed by processes other than those that create the *D* region. At night, such behavior will also be apparent, since there will be negligible electron concentrations below 85 km.

According to our theoretical results, normal conditions lead to three subdivisions of the *D* region. Between 80 and 85 km, there is an electron peak which remains stable until solar activity has increased above a certain level. Between 70 and 75 km, a reflection level can occur, since the electron concentration increases with a gradient of the order of $100 \text{ electrons cm}^{-3} \text{ km}^{-1}$. It must be pointed out that these two persistent regions are subject to variations due to latitude effects and to fluctuations of the solar activity. For example, when the effect of cosmic rays is small, the electron concentrations at 65 and 70 km are 30 and 300 electrons cm^{-3} . At $\Phi = 50^\circ$, the value at 65 km could increase to 150 electrons cm^{-3} . Finally, the effect due to solar flares is a complete transformation of the shape of the normal *D* layer, since concentrations of more than 1000 electrons cm^{-3} can occur at and below 70 km. This corresponds to an increase of not less than 10 times the initial concentration for a strong flare. In the region of 85 km, a complex situation results from the variations of solar activity. The ionization peak disappears in moderate solar activity but may become important when solar flares occur. Concentrations greater than $10^4 \text{ electrons cm}^{-3}$ near 85 km will completely distort the shape of the tail of the *E* layer.

Because of the uncertainties in the rate coefficients involved, the electron concentrations inferred from our theoretical analysis may require certain later modifications. Nevertheless, they give a picture from which it will be possible to find an adequate physical representation of the *D* region when more precise experimental data become available.

Acknowledgments. The research reported in this work has been sponsored by the Geophysical Research Directorate of the Air Force Cambridge Research Center, Air Research and Development Command, under contract AF19(604)-4563, and, in part, by the National Science Foundation under grant G5939.

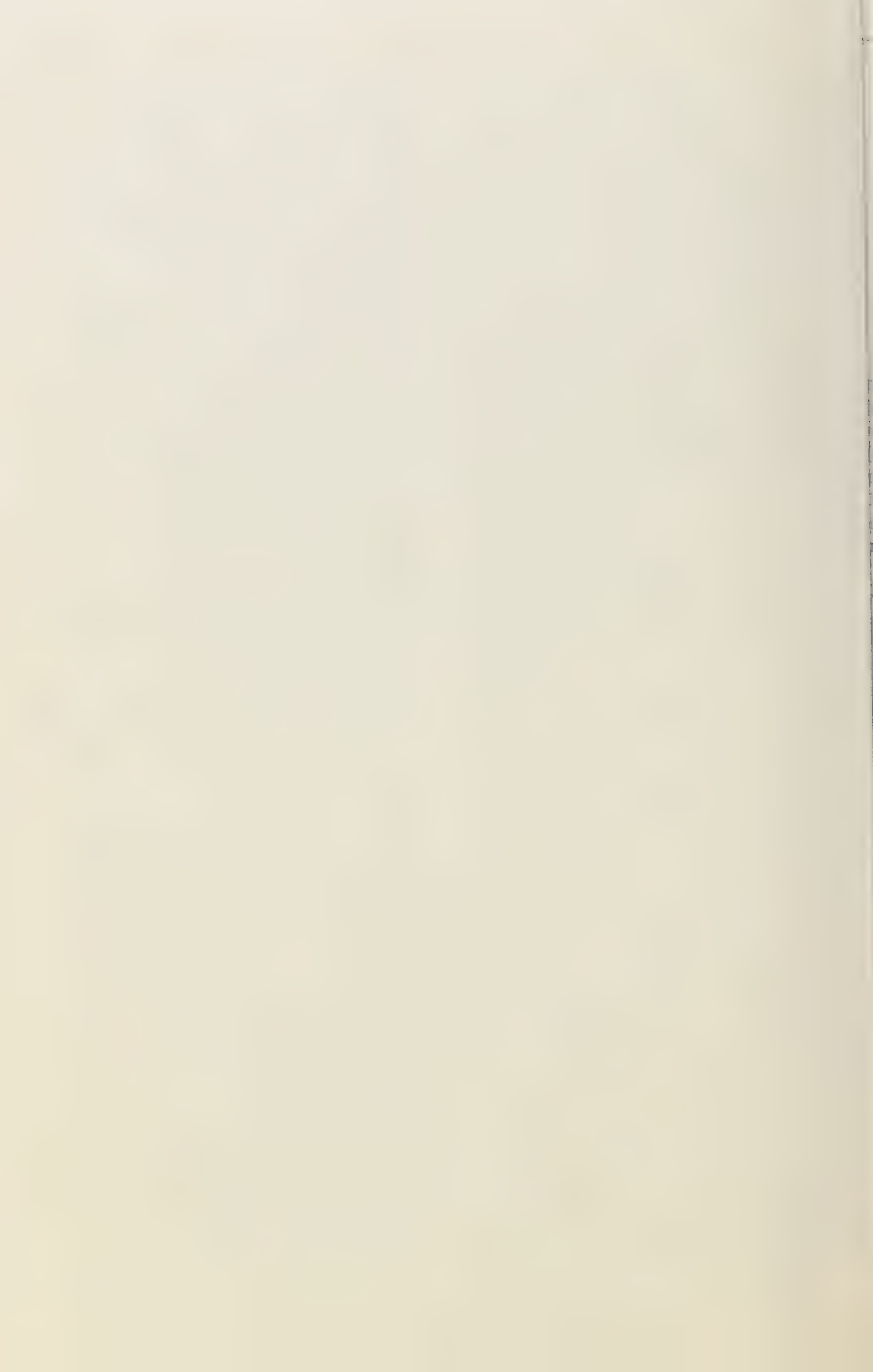
The authors are grateful to Drs. Bates, Bailey, and Branscomb for many stimulating conversations during the preparation of this study. It is also a pleasure to acknowledge the help of Drs. Chubb, Friedman, and Tousey, who provided unpublished

data on solar X-ray and ultraviolet emissions. The authors wish also to thank Mrs. J. Peiffer for making rapidly available the necessary computations throughout a long period.

REFERENCES

- Bailey, D. K., Disturbances in the lower ionosphere observed at VHF following the Solar Flare of 23 February 1956 with particular reference to auroral zone absorption, *J. Geophys. Research*, **62**, 431, 1957.
- Bailey, D. K., Abnormal ionization in the lower ionosphere associated with cosmic-ray flux enhancements, *Proc. IRE*, **47**, 255, 1959.
- Bates, D. R., Dissociative recombination, *Phys. Rev.*, **78**, 492, 1950.
- Bates, D. R., Charge transfer and ion-atom interchange collision, *Proc. Phys. Soc. London*, **A**, **68**, 344, 1955.
- Bates, D. R., and H. S. W. Massey, The basic reactions in the upper atmosphere, *Proc. Roy. Soc. London*, **A**, **187**, 261, 1946.
- Bates, D. R., and M. Nicolet, Ion-atom interchange, *J. Atmospheric and Terrest. Phys.*, **16**, in press, 1960.
- Bates, D. R., and M. J. Seaton, Theoretical considerations regarding the formation of the ionized layers, *Proc. Phys. Soc. London*, **B**, **63**, 129, 1950.
- Bialecke, E. P., and A. A. Dougal, Pressure and temperature variation of the electron-ion recombination coefficient in nitrogen, *J. Geophys. Research*, **63**, 539, 1958.
- Branscomb, L. M., D. S. Burch, S. J. Smith, and S. Geltman, Photodetachment cross-section and the electron affinity of atomic oxygen, *Phys. Rev.*, **111**, 504, 1958.
- Burch, D. S., S. J. Smith, and L. M. Branscomb, Photodetachment of O_2 , *Phys. Rev.*, **112**, 171, 1958.
- Byram, E. T., T. A. Chubb, and H. Friedman, The solar X-ray spectrum and the density of the upper atmosphere, *J. Geophys. Research*, **61**, 251, 1956.
- Byram, E. T., T. A. Chubb, H. Friedman, and N. Gailar, Lyman alpha radiation in the solar spectrum, *Phys. Rev.*, **91**, 1278, 1953.
- Byram, E. T., T. A. Chubb, H. Friedman, and J. E. Kupperian, Jr., Intensity of solar Lyman α and adjacent ultraviolet emission lines, IGY World Data Center A, *IGY Rocket Rept. Ser.* no. 1, 183, 1958.
- Chanin, L. M., A. V. Phelps, and M. A. Biondi, Measurement of the attachment of slow electrons in oxygen, *Phys. Rev. Letters*, **2**, 344, 1959.
- Chubb, T. A., H. Friedman, and R. W. Kreplin, X-ray emission accompanying solar flares. COSPAR Meeting, Nice, January 1960, to be published.
- Chubb, T. A., H. Friedman, R. W. Kreplin, and J. E. Kupperian, Jr., Lyman alpha and X-ray emissions during a small solar flare, *J. Geophys. Research*, **62**, 389, 1957.

- Margno, A., and G. W. Griffing, Energy per ion pair for electron and proton beams in atomic hydrogen, *Proc. Roy. Soc. London, A*, **248**, 415, 1958.
- itchburn, R. W., J. E. S. Bradley, C. G. Cannon, and G. Munday, Absorption cross sections for Lyman α and neighboring lines, in *Rocket Exploration of Upper Atmosphere*, edited by R. L. E. Boyd and M. J. Seaton, Pergamon Press, London, p. 327, 1954.
- itchburn, R. W., P. J. Jutsum, and G. V. Marr, The continuous absorption of light in alkali-metal vapors, *Proc. Roy. Soc. London, A*, **219**, 89, 1953.
- Iwert, G., The X-ray radiation of the solar corona and hot coronal condensations, solar eclipses and the ionosphere, *J. Atmospheric and Terrest. Phys.*, Special Suppl. to **6**, 167, 1956a.
- Iwert, G., Roentgenstrahlung koronaler Kondensation, *Z. Astrophys.*, **41**, 67, 1956b.
- aire, A. C., and K. S. W. Champion, Measurements of dissociative recombination and diffusion in nitrogen at low pressures, *Phys. Rev.*, **113**, 1, 1959.
- riedman, H., and T. A. Chubb, Solar X-ray emission and the height of D-layer during radio fade-out, *The Physics of the Ionosphere*, Physical Society of London, p. 58, 1955.
- riedman, H., T. A. Chubb, J. E. Kupperian, Jr., and J. C. Lindsay, X-ray emission and ultraviolet emission of solar flares, IGY World Data Center A, *IGY Rocket Rept. Ser.*, no. 1, 179, 1958a.
- riedman, H., T. A. Chubb, J. E. Kupperian, Jr., and J. C. Lindsay, X-ray emission of solar flares, IGY World Data Center A, *IGY Rocket Rept. Ser.*, no. 1, 183, 1958b.
- Houston, R. E., The effect of certain solar radiations in the lower ionosphere, *J. Atmospheric and Terrest. Phys.*, **12**, 225, 1958.
- ursa, A. S., Y. Tanaka, and F. LeBlanc, Nitric oxide and molecular oxygen in the earth's upper atmosphere, *Planetary and Space Sci.*, **1**, 161, 1959.
- utsum, P. J., The continuous absorption of light in calcium vapour, *Proc. Phys. Soc. London, A*, **67**, 190, 1954.
- Kistiakowsky, G. B., and G. G. Volpi, Reactions of nitrogen atoms, I, Oxygen and oxides of nitrogen, *J. Chem. Phys.*, **27**, 1141, 1957.
- Kistiakowsky, G. B., and G. G. Volpi, Reactions of nitrogen atoms, II, H_2 , CO, NH_3 , NO, and NO_2 , *J. Chem. Phys.*, **28**, 665, 1958.
- Lee, P., Photodissociation of oxygen as inferred from measured absorption coefficients, *J. Opt. Soc. Am.*, **45**, 703, 1959.
- Lindh, A. E., and A. Nilsson, Ueber das K-Roentgenabsorptionsspektrum von Argon, *Arkiv Mat. Ast. Fysik*, **31B**, no. 11, 1945.
- Messner, R. H., Der Einfluss der chemischen Bindung auf den Absorptionskoeffizienten leichter Elements in Gebiete ultraveicher Roentgenstrahlen, *Z. Physik*, **85**, 727, 1933.
- Mitra, A. P., A tentative model of the equilibrium height distribution of nitric oxide in the high atmosphere and the resulting D-layer, *J. Atmospheric and Terrest. Phys.*, **5**, 28, 1954.
- Mitra, A. P., Time and height variations in the daytime processes in the ionosphere, *J. Geophys. Research*, **64**, 733, 1959.
- Müller, E. A. W., Die Schwächung extraterrestrischen Roentgenstrahlen in der Atmosphäre, *Z. Astrophys.*, **10**, 52, 1935.
- Nicolet, M., Contribution à l'étude de la structure de l'ionosphère, *Mém. inst. météor. belg.*, no. 19, 83, 1945.
- Nicolet, M., The aeronomic problem of nitrogen oxides, *J. Atmospheric and Terrest. Phys.*, **7**, 152, 1955a.
- Nicolet, M., Meteor ionization and the night-time E layer, in *Meteors*, edited by T. R. Kaiser, Pergamon Press, p. 99, London, 1955b.
- Nicolet, M., Ionization by cosmic rays, *Penn. State Univ. Ionospheric Research Sci. Rept.*, **102**, 76, 1958a.
- Nicolet, M., Aeronomic chemical reactions, in Symposium on Upper Atmosphere and Medicine, San Antonio, November 1958b.
- Nicolet, M., La thermosphère, *Ann. géophys.*, **15**, 1, 1959a.
- Nicolet, M., The constitution and composition of the upper atmosphere, *Proc. IRE*, **47**, 142, 1959b.
- Peterson, L. E., and J. R. Winckler, Gamma-ray burst from a solar flare, *J. Geophys. Research*, **64**, 697, 1959.
- Preston, W. M., The origin of radio fade-outs and the absorption coefficient of gases for light of Wavelength 1215.7 Å, *Phys. Rev.*, **57**, 887, 1940.
- Sayers, J., Recent laboratory studies of recombination cross sections, in *Solar Eclipses and the Ionosphere*, Pergamon Press, London, p. 212, 1956.
- Van Allen, J. A., The nature and intensity of the cosmic radiation, in *Physics and Medicine of the Upper Atmosphere*, edited by C. S. White and O. O. Benson, Jr., University of New Mexico Press, Albuquerque, 1952.
- Valentine, J. M., and S. C. Curran, Average energy expenditure per ion pair gases and gas mixtures, *Repts. Progr. in Phys.*, **21**, 1, 1958.
- Victoreen, J. A., The calculation of X-ray mass absorption coefficients, *J. Appl. Phys.*, **20**, 1141, 1949.
- Watanabe, K., Photoionization and total absorption cross section of gases, I, Ionization potentials of several molecules, cross sections of NH_3 and NO, *J. Chem. Phys.*, **22**, 1564, 1954.
- Watanabe, K., E. C. Y. Inn, and M. Zelikoff, Absorption coefficients of oxygen in the vacuum ultraviolet, *J. Chem. Phys.*, **21**, 1026, 1953.
- Woernle, B., Die Absorption langwelliger Roentgenstrahlen von 2-10 ÅE in leichten Elementen, *Ann. Physik*, **5** Folge, **6**, 475, 1930.



Drift Measurements at Kjeller on the Ionospheric F Region

J. BECKEN AND B. MÆHLUM

Norwegian Defence Research Establishment
Kjeller, Norway

Abstract. A study of the drifts and structure of the amplitude pattern of the F_2 echo is presented. Some measurements on the sporadic F echo are also included. All the measurements were made at Kjeller, Norway.

1. *Introduction.* A number of research workers have been concerned with the movements in the E layer during the IGY, using the closely spaced receiver method introduced by Mitra [1949]. Only a few papers, however, have been published on the F_2 layer drifts [Chapman, 1953; Briggs and Spencer, 1954; and Rao, Rao, and Murty, 1959]. Their results may be summarized as follows:

(a) The drifts in the F_2 layer vary from 50 to 150 m/s.

(b) At high latitudes there is an easterly drift near noon and a westerly drift near midnight. Near the equator the drift is shifted 180° .

(c) There exists a positive correlation between the magnitude of the drift and magnetic activity at high latitudes. Near the equator the correlation is negative.

In the studies mentioned, the drift velocities and directions have been deduced from the time shifts between 'similar fades' observed at three closely spaced receivers. The effects of anisometric pattern and nonsystematic drifts have not been taken into account.

During the winter 1958-1959 some measurements were made at Kjeller (60°N , 11.1°E Gr) on the drifts in the F_2 layer by the Mitra [1949] method. The equipment used has been described by Harang and Pedersen [1957]. When analyzing the records the 'full correlation method' [Briggs, Phillips, and Shinn, 1950; Phillips and Spencer, 1955] was used. By this method we obtain information on true systematic drift directions and velocity and on the two-dimensional spatial autocorrelation function of the amplitude pattern of the echo.

In sections 2 and 3 we will describe the results obtained, and in section 4 we will give the results

from a short study of the structure of the fading pattern of sporadic F reflections.

2. *Drift direction and velocity.* Most of the measurements were made during January and February 1959. A frequency of 5.5 Mc/s was used during the day time and a frequency of 2.4 Mc/s during the night. A typical fading record is shown in Figure 1.

Thirty samples were analyzed, and the amplitudes were read every 0.1 second. Record samples of length varying from 40 to 60 seconds were used. The correlation functions were computed by means of an electronic computer.

By the method of analysis used the effect of nonsystematic 'drifts' in the amplitude pattern is removed, so that the 'true drift' can be deduced. In some cases the nonsystematic drift and the true drift were of the same order of magnitude. In those cases there are serious disagree-

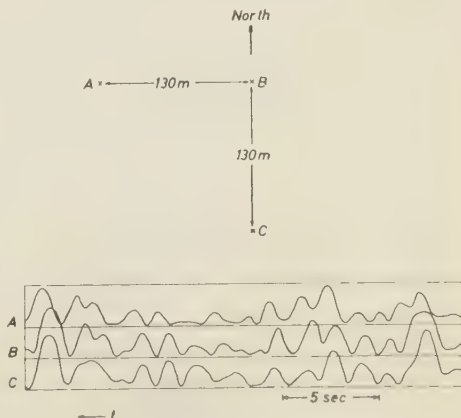


Fig. 1. Typical fading records obtained on the F_2 echo at the three antennas A, B, and C, February 12, 1959, 1705 MET.

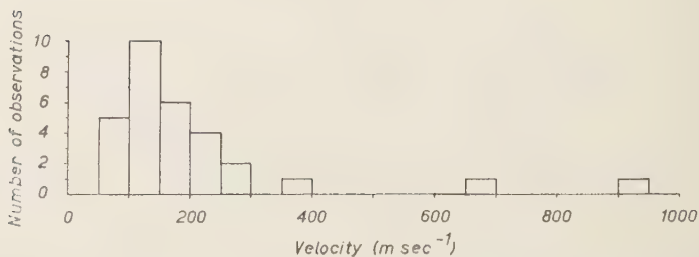


Fig. 2. Distribution of the observed drifts of the F_2 amplitude pattern at Kjeller.

ments between the true drift velocity and the apparent drift velocity deduced from 'similar fades.'

The deduced distribution of the true drifts of the amplitude pattern of the F_2 echo is shown in Figure 2. The mean velocity is 140 m/s, and 90 per cent of the observations are in the interval 50 to 300 m/s. The mean velocity in the F_2 layer near the equator during the winter is approximately 70 m/s [Rao and Rao, 1959]. If we assume that the velocity of the fading pattern over the ground is twice the velocity in the F_2 region, the drift velocities at high latitudes and near the equator are thus of the same order of magnitude.

The diurnal variations of the drift direction during the winter at Kjeller, Cambridge, and Waltair are shown in Figure 3. (The Waltair values are taken from Rao and Rao [1959], and the Cambridge values from Briggs and Spencer [1954]). Near the equator Rao and Rao [1959] observe a steady rotation of the wind vector in the F_2 layer with a periodicity of 24 hours. At Kjeller the drift direction is approximately constant towards the west during the night, changing to east near sunrise. This was confirmed by a series of drift observations performed at Kjeller from June 1 through July 10, 1959, by an automatic drift recorder, 'Phillips recorder' [Phillips, 1952]. During this period all the night observations (21-04 MET) showed drift directions in the sector west to southwest. The same effect may also be seen at Cambridge during the winter (Fig. 3).

Martyn [1955], by assuming that the drifts in the F_2 layer are driven inductively by the geomagnetic current systems in the E region, has derived the following expression for the zonal component of the drift during magnetically quiet conditions:

$$V_z = 2.7 \cdot 10^3 \cdot \sin \theta (1 - 3 \cos^2 \theta) \cdot (\cos \phi) / F_e \quad (1)$$

where ϕ is the hour angle of the sun ($\phi = 0$ at midnight), θ is the geomagnetic colatitude, and F_e is the vertical component of the geomagnetic field. V_z is defined positive when the drift is toward the east.

The theoretical latitude variations of the midnight values of V_z along the meridians 0° and 80° E Gr are shown in Figure 4 together with the zonal component of the observed drift near

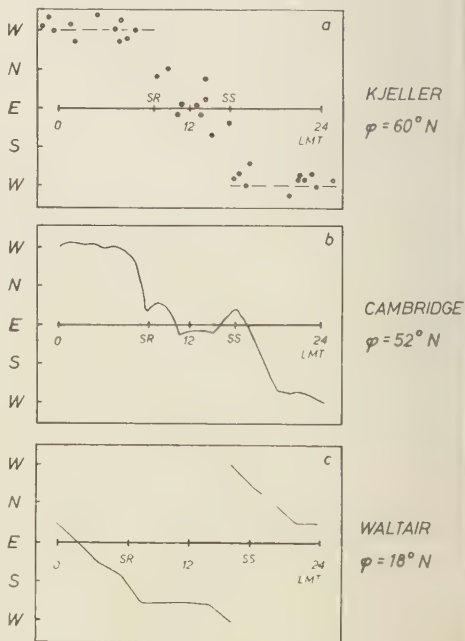


Fig. 3. Diurnal variation of the drift direction of the F_2 amplitude pattern at Kjeller, Cambridge, and Waltair.

midnight (mean values) at Kjeller, Cambridge (after Briggs and Spencer [1954]), and Waltair (after Rao and Rao [1959]). The geomagnetic data used during the computation of V , are taken from Vestine, Laporte, Lange, Cooper, and Hendrix [1948]. The observed drift of the F_2 amplitude pattern at Kjeller has been reduced by a factor of 2. The observed drift velocity at Kjeller is somewhat higher than the theoretical value near midnight. This finding, however, is not unexpected, as all the drift observations are obtained during geomagnetically disturbed conditions. When this effect is taken into account, there is fair agreement between observations and theory.

3. *The structure of the irregularities in the F_2 echo.* The method of analysis [Briggs, Phillips, and Shinn, 1950; Phillips and Spencer, 1955] is based on the assumption that lines for constant spatial autocorrelation are concentric, nonformal ellipses. The axis ratio and the orientation of the major axis of the correlation ellipses have been deduced for all the observations made, and the results are given in Figure 5. The predominant direction of the major axis is north-northwest, and 70 per cent of all observations are in the sector north to northwest. The mean axis ratio is approximately 1.9. No diurnal variation in the orientation or axis ratio could be observed.

As a measure of the scale of the structure in the F_2 pattern we will use the minor semiaxis in the correlation ellipses corresponding to a correlation coefficient of 0.5. The diurnal variation of this 'correlation distance' is shown in Figure 6. There is a clear increase in this parameter during the day, indicating that the F_2 layer is 'smoother' during the day than during the night. The mean value of the correlation distance from

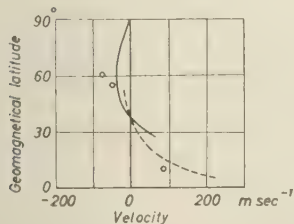


Fig. 4. Latitude variation of V_z (midnight values) along the meridian 80°E Gr (broken line) and 0°.

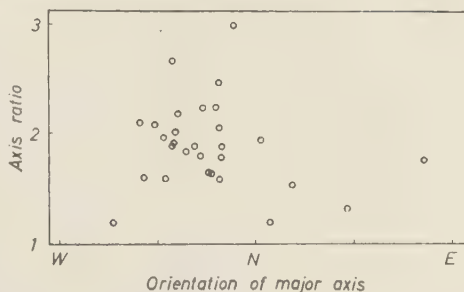


Fig. 5. Orientation of the major axis of the F_2 correlation ellipses vs. axis ratio.

06 through 18 MET is 350 meters, whereas the mean value from 18 through 06 MET is only 150 meters.

4. *The sporadic F echo.* During the period January to February 1958 some measurements were made during the night on the sporadic F echoes at Kjeller. The most frequently occurring type at Kjeller is the 'polar spur' as described by Meek [1949]. The Mitra method was used during the measurements, and frequencies between 5.2 and 5.4 Mc/s were used. The critical frequency of the normal F_2 layer during the same hours was 3.0 to 3.5 Mc/s.

As the F_s echo is normally very spread and shows rapid fading, only a small number of records were usable for detailed analysis.

The deduced axis ratio and the orientation of the major axis in the correlation ellipses of the F_s pattern are shown in Figure 7. The mean orientation of the major axis is 12° west of north. This direction is thought to coincide with the geomagnetic meridian in the proper height range. The mean axis ratio of the correlation ellipses is 3.0, much greater than the corresponding value for the normal F_2 layer.

The correlation distance A has been calculated for the F_s echoes. The observed values of A are plotted in Figure 6 vs. local time. The correlation distances in the F_s pattern are of the same order of magnitude as that of the normal F_2 echo. In order to explain the rapid fading of the F_s echo it is therefore necessary to assume that the systematic and nonsystematic drifts in the F_s amplitude pattern are essentially greater than the drifts in the normal F_2 pattern. It has not been possible to deduce any reliable values for the drifts of the F_s pattern.

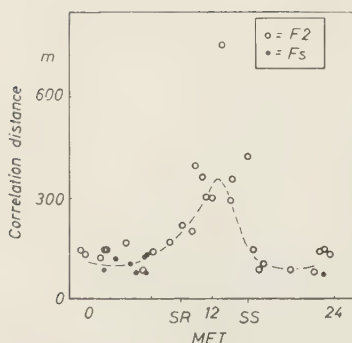


Fig. 6. Diurnal variation of the 'correlation distance' for the F_2 and F_5 amplitude pattern.

5. *Conclusion.* The results from this study of drift and structure in the F region at Kjeller may be summarized:

1. The mean velocity of the amplitude pattern of the F_2 echo is approximately 140 m/s, and most of the observed velocities are between 50 and 300 m/s. No diurnal variation of the drift velocity is observed.

2. There is an almost constant westerly drift in the F_2 layer during the night, changing to east near sunrise.

3. The drift velocities observed near midnight are in fair agreement with the theoretical values of Martyn [1955].

4. The irregularities in the F_2 amplitude pat-

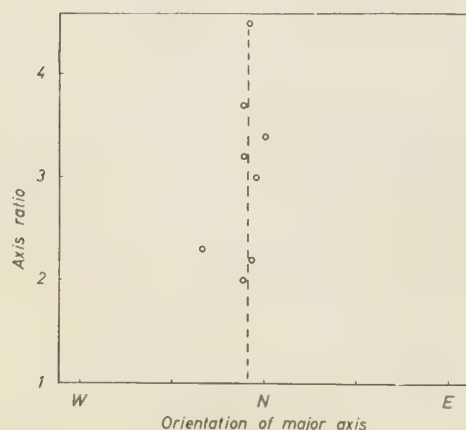


Fig. 7. Orientation of the major axis of the F_2 correlation ellipses vs. axis ratio. The assumed geomagnetic meridian at Kjeller at the 200-km level is indicated by the broken line.

tern are slightly elongated in a direction around north-northwest. The mean axis ratio of correlation ellipses is approximately 1.9. The scale of structure is essentially larger during the day than during the night.

5. The irregularities in the amplitude pattern of the sporadic F echo are elongated in a direction close to the geomagnetic meridian. The mean axis ratio of the correlation ellipses is approximately 3.0. The irregularities in the F_2 amplitude pattern are of the same order of magnitude as the irregularities in the nighttime F_2 pattern.

Acknowledgments. The authors are indebted to Professor L. Harang for providing the measuring equipment, and to colleagues at the NDRE for helpful discussions. The research was sponsored in part by the Air Research and Development Command, through the European Office, under Contract AF 61(052)-228.

REFERENCES

- Briggs, B. H., G. J. Phillips, and D. H. Shinn, The analysis of observations on spaced receivers of the fading of radio signals, *Proc. Phys. Soc. London, B*, **63**, 106, 1950.
- Briggs, B. H., and M. Spencer, Horizontal movements in the ionosphere, *Repts. Progr. Phys.*, **17**, 245, 1954.
- Chapman, J. H., A study of winds in the ionosphere by radio methods, *Can. J. Phys.*, **31**, 120, 1953.
- Harang, L., and K. Pedersen, Drift measurements on the E layer, *J. Geophys. Research*, **62**, 183, 1957.
- Martyn, D. F., *Physics of the Ionosphere*, Physical Society, London, p. 163, 1955.
- Meek, J. H., Sporadic ionization at high latitudes, *J. Geophys. Research*, **54**, 339, 1949.
- Mitra, S. N., A radio method of measuring winds in the ionosphere, *Proc. IEE*, **96**, 441, 1949.
- Phillips, G. J., An apparatus for recording time-delays between radio fading characteristics, *J. Atmospheric and Terrest. Phys.*, **2**, 141, 1952.
- Phillips, G. J., and M. Spencer, The effects of anisometric amplitude patterns in the measurement of ionospheric drifts, *Proc. Phys. Soc. London, B*, **68**, 481, 1955.
- Rao, B. R., and E. B. Rao, Study of horizontal drifts in the F_1 and the F_2 regions of the ionosphere at Waltair, *J. Atmospheric and Terrest. Phys.*, **14**, 94, 1959.
- Rao, B. R., E. B. Rao, and Y. V. R. Murty, Effect of magnetic activity on drifts in the F_2 region, *Nature*, **183**, 667, 1959.
- Vestine, E. H., L. Laporte, I. Lange, C. Cooper, and W. C. Hendrix, Description of the earth's main magnetic field and its secular change, 1905-1945, *Carnegie Inst. Wash. Publ.* **578**, 1948.
- (Manuscript received January 27, 1960; revised February 25, 1960.)

The Absolute Zenith Intensity of [O I] 5577 at College, Alaska

F. E. ROACH

*Boulder Laboratories, National Bureau of Standards
Boulder, Colorado*

AND

M. H. REES

*Geophysical Institute, University of Alaska
College, Alaska*

Abstract. The absolute zenith intensity of [O I] 5577 was measured over College, Alaska, at 5-minute intervals during nights from January 16 to April 8, 1959. A total of 3968 individual readings was obtained. The median intensity is 2.40 kilorayleighs. Eighty per cent of the observations are included within the range from 0.74 to 11.5 kR. A general increase of 5577 intensity occurs with increasing geomagnetic activity.

Introduction. In January 1959, a photometer for the systematic recording of [O I] 5577 zenith intensities was put into service at the Geophysical Institute of the University of Alaska (latitude 64.85°N, longitude 147.83°W, magnetic latitude 64.65°N). The wide range of intensities of 5577 near the auroral zone dictated the use of a logarithmic system, especially since it was planned that the instrument would be unmanned during most of its operation. The present paper reports on results obtained during the first 5 months of use until the encroachment of summer twilight in April 1959.

The photometer. The telescope is identical to the one described by Roach and Pettit [1951]. It has a 5° circular field of view. A Baird type 100 interference filter having a 17 Å bandwidth and half transmission was used to isolate the oxygen green line. The logarithmic response of the system was obtained by adapting a circuit described by Bell and Graham [1952]. A feedback circuit varies the high voltage applied to the photomultiplier tube so as to hold the anode current constant. Changes in the voltage across the tube, representing changes in brightness, are monitored by a continuously running strip chart recorder. The photometer was programmed for automatic operation approximately from civil twilight to civil dawn.

The absolute calibration. Two independent calibration procedures were employed. One method involved use of a calibrated luminescent phosphor, activated by a radioactive material. The brightness of the source (in microlamberts) and the spectral emission curve were supplied by the manufacturer (U. S. Radium Corporation). Using the transmission curve of the filter and the spectral response and luminous efficiency of the photocathode of the tube, the brightness of the source in rayleighs at 5577 Å was obtained. The photometer was calibrated weekly to assure constancy of operation. A set of neutral density filters provided a range of brightness sufficient to establish the calibration curve.

Because of the difficulties inherent in an absolute calibration it was deemed advisable to compare the calibration obtained by the method described above with an independent calibration against a portable calibrating photometer carried by one of us (FER) to several airglow observatories around the world during the IGY [Roach, 1958]. The telescope of the logarithmic photometer was hand-carried to Fritz Peak, Colorado, and the intercalibration was made during a clear night. The calibrations obtained by the two methods differed by 30 per cent. In order to make possible the comparison of the present results with those obtained in the sub-

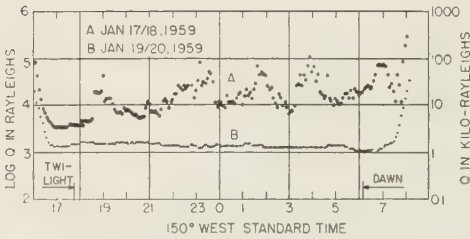


Fig. 1. Time variation of zenith intensity of 5577 A for a magnetically active (A) and a magnetically quiet (B) night at College.

auroral zone during the IGY the Fritz Peak intercalibration is used in this report.

The logarithmic photometer was adjusted to

display a range of almost four decades on chart paper. The inherent precision of the individual readings is therefore not high. Since only the zenith brightness was monitored, corrections for extinction and scattered light were not made; the error introduced by this omission is probably small. The results obtained for the brightness of $[O\ I]\ 5577$ at College indicate that contamination from extraterrestrial light can safely be neglected.

The observations. Examples are shown in the records for two contrasting nights in Figure 1. January 17–18, 1959, was an active night with numerous fluctuations of intensity over a two-fold range; January 19–20 was a ‘quiet’ night.

TABLE 1. Summary of Results: Number of Occurrences

Class, log Q	K									Cumulative	Per Cent Class	Per Cent Cumulative
	0	1	2	3	4	5	6	7	Total			
2.50–2.59		18							18	18	0.5	0.5
2.60–2.69	11	39	37		1				88	106	2.2	2.5
2.70–2.79	22	10	90		10	6			138	244	3.5	6.0
2.80–2.89	0	64	117	17	7	15			220	464	5.5	11.5
2.90–2.99	0	72	101	22	4	12	1	2	214	678	5.4	17.0
3.00–3.09	2	50	110	27	8	7	8	8	220	898	5.5	22.5
3.10–3.19	94	231	78	62	4	17	10	2	498	1396	12.6	35.1
3.20–3.29	23	103	49	76	12	35	46	4	348	1744	8.8	44.0
3.30–3.39	7	62	36	71	40	27	41	7	291	2035	7.3	51.3
3.40–3.49	9	18	41	61	33	18	24	8	212	2247	5.3	56.6
3.50–3.59	10	15	46	96	46	59	46	8	326	2573	8.2	64.8
3.60–3.69	9	0	29	34	45	43	57	3	220	2793	5.5	70.3
3.70–3.79	9	2	34	40	59	42	24	5	215	3008	5.4	75.7
3.80–3.89	19		10	26	53	40	68	14	230	3238	5.8	81.5
3.90–3.99			11	28	40	65	42	26	212	3450	5.3	86.8
4.00–4.09				31	45	30	48	3	157	3607	4.0	90.8
4.10–4.19				2	15	17	65	2	101	3708	2.5	93.3
4.20–4.29				7	15	19	29	5	75	3783	1.9	95.2
4.30–4.39				6	10	10	10	2	38	3821	1.0	96.2
4.40–4.49				2	15	11	7	2	37	3858	0.9	97.1
4.50–4.59				9	5	6	6	0	26	3884	0.7	97.8
4.60–4.69				6	3	13	9	1	32	3916	0.8	98.6
4.70–4.79				2	4	3	0	0	9	3925	0.2	98.8
4.80–4.89				1	11	3	2		17	3942	0.4	99.2
4.90–4.99				1	3		1	1	6	3948	0.2	99.4
5.00–5.09							4	1	5	3953	0.1	99.5
5.10–5.19							1	1	2	3955	0.5	99.9
5.20–5.29							4	2	6	3961	0.2	99.9
5.30–5.39							1	1	2	3963	0.5	99.9
5.40–5.49							2		2	3965	0.5	99.9
5.50–5.59							0		0
5.60–5.69							3		3	3968	0.8	100.0
Total	215	684	789	625	476	509	560	110	3968			

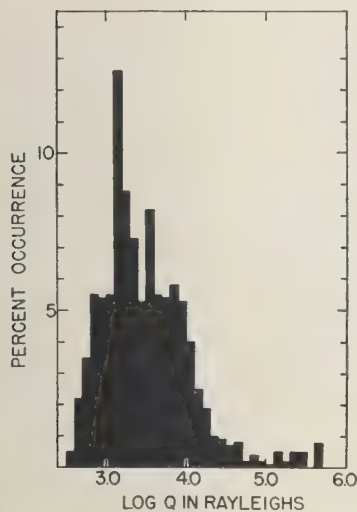


Fig. 2. Histogram showing distribution of 5577 Å zenith intensities for 3968 observations. From column 12 of Table 1.

During which there was little change of intensity. The general intensity level of the first night was more than 10 times that of the second. January 17-18 was a magnetically active night, the College magnetographic records yielding successive 3-hour K values of 4, 4, 5, 6; January 19-20 was magnetically quiet with successive 3-hour K values of 0, 1, 0, 1.

The original records were read for each 5 minutes during the observing night, and the readings were converted to $\log Q$ in rayleighs from the appropriate calibration curve. It was possible to estimate roughly the degree of sky cloudiness from the spectrographic presence of scattered mercury lines from the community lights. Since a preliminary study of cloudy versus clear nights did not indicate any systematic difference in the intensity levels, we have included in a statistical study all observations between astronomical twilight and astronomical dawn. Twilight occurs all night after April 9. A total of 3968 readings during 42 nights included. The number of occurrences according to local magnetic K index and according to uniform $\log Q$ intervals is shown in Table 1.

The statistical distribution of 5577 intensities.

The composite distribution of 5577 intensities at College is shown in histogram form in Fig. 2. The median intensity is at $\log Q = 3.38$ ($Q = 2400$ R). The brightest observation is $\log Q = 5.65$ ($Q = 452,000$ R); the faintest is $\log Q = 2.55$ ($Q = 359$ R). The total spread thus covers a range of a factor of 1260.

Fifty per cent of the intensities lie between 1290 and 6030 R; 80 per cent, between 740 and 115,000 R.

It should be noted that the present sample covers less than 3 months of observations during a post-maximum period in the sunspot cycle. It will be of interest to compare these results with more extensive data that it is hoped will be obtained in the future.

Dependence of 5577 intensity on magnetic activity. Figure 3 is a histogram representation of the occurrence of 5577 absolute intensities for three different groupings of local magnetic activity index, K . The same data are shown in the form of a cumulative probability plot in Figure 4. Two conclusions are obvious: (1) the 'center

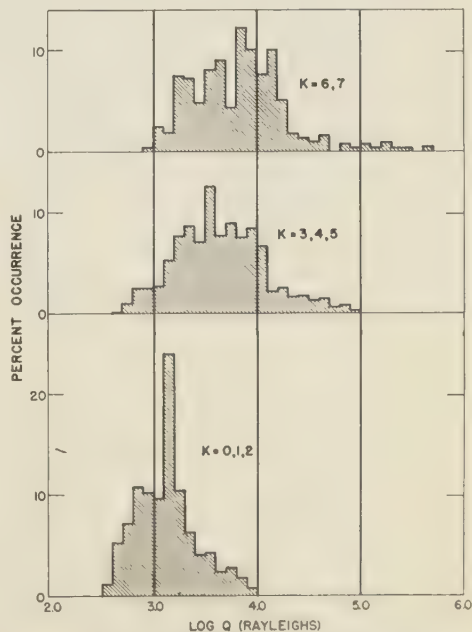


Fig. 3. Distribution of 5577 Å zenith intensities according to three magnetic activity groupings.

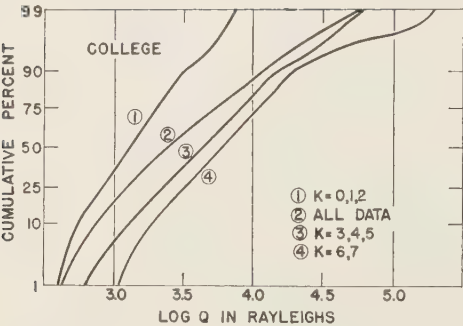


Fig. 4. Distribution of 5577 Å zenith intensities as cumulative per cent occurrence.

of gravity' of the intensity moves steadily higher as the magnetic activity increases; (2) there is a wide range of intensities within each magnetic activity grouping.

In Table 2 and Figure 5 are shown, as a function of K , values of Q corresponding to 10, 25, 50 (median), 75, and 90 per cent occurrence. The general upward trend of intensity with increasing magnetic activity is apparent. It is noted, however, that the increase for the fainter limits (e.g., 10 per cent occurrence) is much smaller than for the brighter limits (e.g., 90 per cent occurrence). The result is a steadily increasing spread in the intensity range as K increases. A convenient measure of the spread is $\{Q(90\%) - Q(10\%)\}$, which is shown plotted against K in Figure 6.

At first glance it might seem that the correlation between 5577 intensity and geomagnetic activity is poor compared with results from other studies of auroral-magnetic correlations.

For example, *Gartlein* [1944] has found a good correlation between the southern extent of visible auroral forms and the planetary magnetic (K_p) index. Two comments are in order.

First, the field of view of the photometer was only 5° , and the result is that the observations give a detailed record of a restricted region and are not necessarily representative of the general conditions. Second the magnetic 'activity,' K , is an index of the total excursion of the magnetic field graph record covering a 3 hour period. Thus a wide range of 5577 intensities might be expected within a given 3-hour interval.

For a general index of 5577 intensity at any given location it might be preferable to use a photometer with a larger field such as the '4'

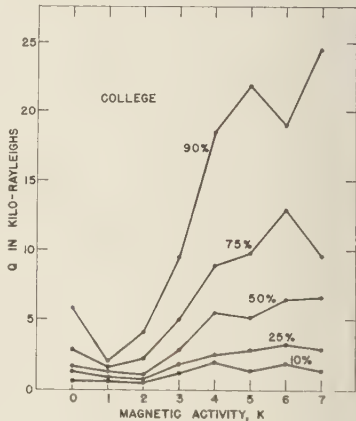


Fig. 5. General increase of 5577 Å zenith intensity with magnetic activity at College. Family of curves is for a sequence of cumulative per cent occurrences.

TABLE 2

	Log Q								
	K = 0	K = 1	K = 2	K = 3	K = 4	K = 5	K = 6	K = 7	
Mode	3.15	3.15	2.85	3.55	3.75	3.95	3.85	3.95	3
10%	2.75	2.80	2.75	3.08	3.30	3.13	3.26	3.14	2
25%	3.11	2.95	2.85	3.25	3.40	3.45	3.51	3.45	2
Median (50%)	3.17	3.12	3.03	3.45	3.75	3.71	3.81	3.82	2
75%	3.45	3.22	3.35	3.70	3.95	3.99	4.11	3.98	2
90%	3.77	3.32	3.61	3.98	4.27	4.34	4.28	4.39	4

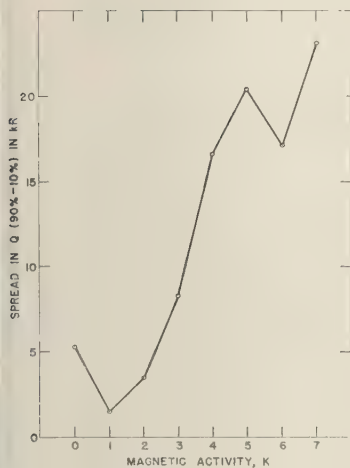


Fig. 6. Spread in 5577 A zenith intensities as a function of magnetic activity at College.

photometer employed by Murcay [1959]. The January 17—18 record illustrates a case in which frequent intensity spikes occur. Such spikes often represent the passage of an auroral feature through the zenith and so correspond to elements of auroral features rather than

representative changes of characteristic intensities.

It should be noted that the magnetic zenith at College is displaced 13° from the geographic zenith. Hence the photometer will miss many auroral features viewed along the magnetic field lines.

Acknowledgment. The research reported in this paper has been supported in part by a grant from the National Science Foundation (Y22.6).

REFERENCES

- Bell, R. E., and R. L. Graham, Wide range logarithmic radiation meter, *Rev. Sci. Instr.*, **23**, 301-304, 1952.
- Gartlein, C., Relation of three-hour-range index K to aurora seen at Ithaca, New York, *Trans. Am. Geophys. Union*, **25**, 533-537, 1944.
- Murcay, W. B., Some properties of the luminous aurora as measured by a photoelectric photometer, *J. Geophys. Research*, **64**, 955-959, 1959.
- Roach, F. E., and Helen Pettit, On the diurnal variation of [O I] 5577 in the nightglow, *J. Geophys. Research*, **56**, 325-353, 1951.
- Roach, F. E., The intercalibration of airglow photometers, *Natl. Bur. Standards Rept.* 5591, 1958.

(Manuscript received February 15, 1960.)

The Intensity of [O I] 5577 in the Subauroral Region as a Function of Magnetic Activity

F. E. ROACH

*Boulder Laboratories, National Bureau of Standards
Boulder, Colorado*

Abstract. The intensity of [O I] 5577 at Fritz Peak, Colorado, and Rapid City, South Dakota, is found to increase with increasing planetary magnetic activity. The nature of the increase is similar to but smaller than that observed in the auroral zone.

Introduction. In the preceding paper [Roach and Rees, 1960] it was shown that the zenith intensity of [O I] 5577 at College, Alaska, has a statistical tendency to increase with increasing magnetic activity. The nature of the relationship between 5577 and the magnetic activity is complex; the minimum intensities increase slightly if at all, but the maxima increase greatly. The result is an intensity spread¹ which varies from 1.5 kilorayleighs for low magnetic activity to 24 kR for the magnetically most active occasions.

The 5577 radiation, being near the peak of the spectral sensitivity curve, is largely responsible for the identification of visible auroras. The results of the preceding paper are thus in agreement with the generally known fact that visible auroras in or near the auroral zone increase in frequency and brightness with increasing magnetic activity.

The question of a magnetic control over 5577 in subauroral zones is pertinent. Until recently the apparent lack of such control has been used in an argument favoring a distinction between airglow and 5577 aurora. If the magnetic control in the subauroral region is similar to that in the auroral zone, namely an increasing spread of 5577 intensity with increasing magnetic activity, its detection may require considerable care in the interpretation of the observational results.

In the present paper we treat some observations made at Fritz Peak, Colorado (latitude 44°01'N; longitude 103°19'W; geomagnetic latitude 53°N), and at Rapid City, South Dakota (latitude 45°49'N; longitude 105°29'W; geomagnetic latitude 54°N).

¹For spread it is convenient to use $Q(90\%)$ minus $Q(10\%)$; see preceding paper.

(latitude 44°01'N; longitude 103°19'W; geomagnetic latitude 53°N), in a fashion similar to the study of the College, Alaska, data in the preceding paper.

The observational data. The absolute zenith intensities of 5577 at Fritz Peak and Rapid City for the period of the IGY have been arranged according to planetary magnetic activity. The results of the breakdown are shown in Tables 1 and 2, where $Q(10)$, $Q(25)$, $Q(50)$, $Q(75)$, and $Q(90)$ refer to the value of the absolute zenith intensity in rayleighs for cumulative occurrences of 10, 25, 50, 75, and 90 per cent. In Figures 1 and 2, $Q(n\%)$ is plotted against K_p .

A comparison with a similar family of curves from data obtained near the auroral zone is possible by reference to Figure 5 of Roach and Rees [1960]. In both the auroral (College) and subauroral zones (Fritz Peak and Rapid City) the increase in the intensity with K at the low-occurrence end (e.g., 10 per cent) is small, whereas the high-occurrence end (e.g., 90 per

TABLE 1. Summary of Statistical Data for Fritz Peak, rayleighs

$\bar{K}_p =$	0.9	2.1	3.0	4.0	4.9	5.8	7.5	All
$\bar{a}_p =$	3.9	7.6	14.8	26.2	44.7	80.0	168.7	
$Q(10)$	198	173	195	230	278	232	229	204
$Q(25)$	249	240	264	295	336	279	285	268
$Q(50)$	338	348	376	388	436	478	670	374
$Q(75)$	445	470	512	510	542	640	1060	502
$Q(90)$	548	615	640	680	690	945	1780	649
$Q(90)-Q(10)$	350	442	445	450	412	713	1551	445

TABLE 2. Summary of Statistical Data for Rapid City, rayleighs

$K_P =$	1	2	3	4	5	6.6	All
$a_p =$	3.6	7.0	14.6	26.5	45.7	112	
$Q(10)$	132	135	153	156	162	141	148
$Q(25)$	191	193	210	194	226	188	198
$Q(50)$	254	256	283	286	337	299	270
$Q(75)$	339	351	382	374	465	518	374
$Q(90)$	426	476	480	466	672	1010	490
$Q(90) - Q(10)$	294	341	327	310	510	869	342

cent) it is striking. The result is that the over-all spread increases with K . The spread in units of $Q(90) - Q(10)$ is shown in Figure 3, which may be compared with Figure 6 of *Roach and Rees* [1960]. In Figure 4 we show a comparison of the relative spread versus magnetic activity for the three stations.

Discussion. The following conclusions may be drawn: (1) high magnetic activity is favorable to the occurrence of high 5577 intensity at Fritz Peak, Rapid City, and College; (2) high magnetic activity does not exclude the possibility of a low 5577 intensity at Fritz Peak, Rapid City, and College; (3) the spread from faint to bright intensities increases with increasing magnetic activity at Fritz Peak, Rapid City, and College; (4) the effect of magnetic activity on the spread of 5577 intensity is initi-

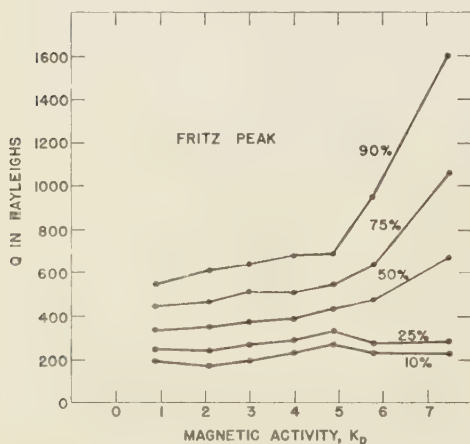


Fig. 1. Variation of 5577 A zenith intensity at Fritz Peak as a function of planetary magnetic activity. Family of curves is for a sequence of cumulative per cent occurrence.

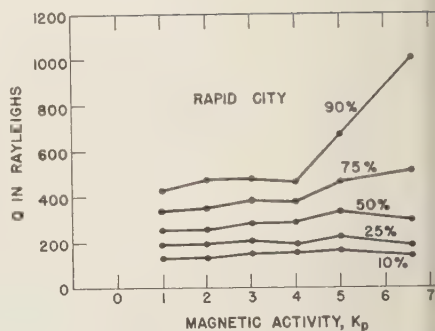


Fig. 2. Variation of 5577 A zenith intensity at Rapid City as a function of planetary magnetic activity.

ated at $K = 1$ (College), $K_P = 4$ (Rapid City) and $K_P = 5$ (Fritz Peak).

In a recent paper, *Sandford* [1959] has made a study of the intensity of 5577 (also 6300 Å) at Invercargill, New Zealand ($\Phi = 52^\circ\text{S}$), as a function of the planetary magnetic activity K_P . His results are based on the photometric spectrograms made during the IGY with a patrol spectrograph. He also finds a general increase of 5577 intensity with magnetic activity. In Figure 5 is shown a comparison of results for Fritz Peak from the present paper with those of Sandford. The abscissa is a_p (rather than K_P). Sandford's results were given in

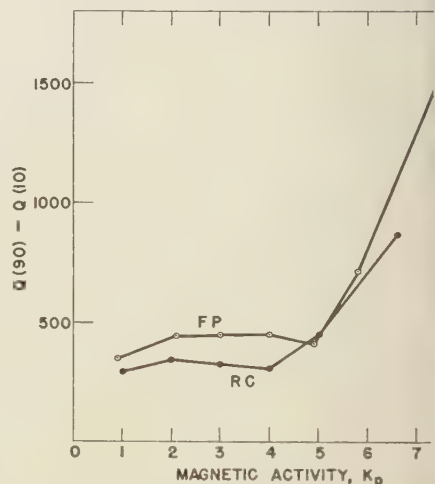


Fig. 3. Variation of spread of 5577 A zenith intensity at Fritz Peak and Rapid City with planetary magnetic activity.

not absolute, intensities, and agreement been forced at the low-intensity end.

It is seen that Sandford finds a much larger increase in 5577 intensity at $\Phi = 52^\circ\text{S}$ than we find at comparable northern geomagnetic latitudes. It seems possible that the discrepancy is due in the difficulty of allowing for reciprocity failure on Sandford's spectrograms. His exposure times varied between 1 and 5 hours, and the assumption of photographic reciprocity over this range of exposures could lead to serious errors [see Roach, McCaulley, Marovich, and Purdy, 1960].

However, the nature of the trend in the two hemispheres is similar, and there is qualitative agreement that the 5577 intensity at geomagnetic latitudes of approximately 50° is affected by planetary magnetic activity.

The following paper presents a study of 5577 intensities at Fritz Peak and local magnetic variations which constitutes a physical extension of the statistical argument in this report.

Conclusions. An examination of the 5577 intensities at Fritz Peak and Rapid City in the subauroral region indicates that low intensities may occur for all degrees of magnetic activity but that the higher 5577 intensities occur at high magnetic activity. The result is

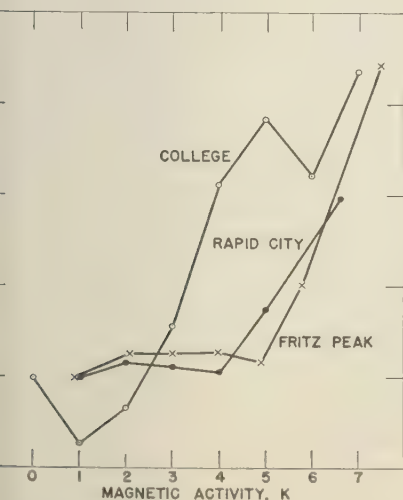


Fig. 4. Variation of relative spread of 5577 A intensity with magnetic activity at College, Rapid City, and Fritz Peak.

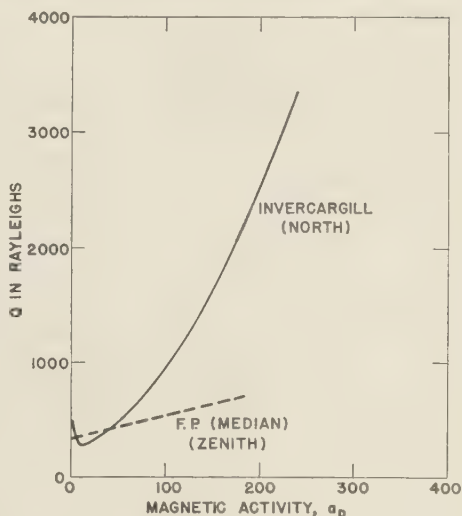


Fig. 5. Comparison of results from this paper (Fritz Peak) with recent results reported by Sandford in the southern hemisphere (Invercargill).

an increasing spread of 5577 intensity with increasing magnetic activity.

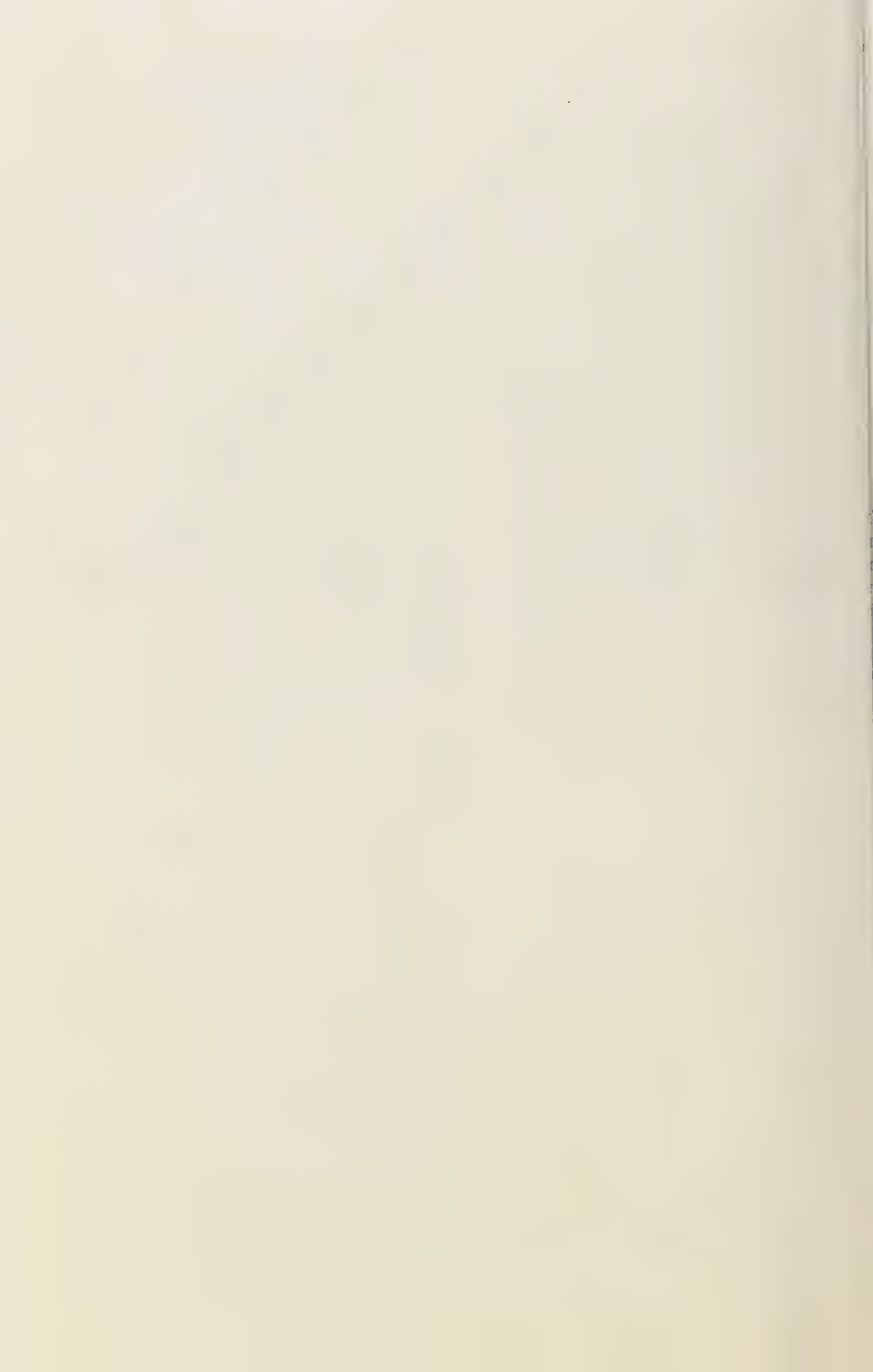
The results by themselves may be interpreted as evidence for the superposition of auroral activity on that of airglow. The fact, however, that the correlation between 5577 intensity and magnetic activity is similar in the auroral and the subauroral regions suggests the alternative hypothesis that there may be a single world-wide excitation mechanism. This hypothesis is discussed in Roach, McCaulley, Marovich, and Purdy [1960].

Sharp breaks in the intensity spread curves (Fig. 4) occur at K indices of 1 (College), 4 (Rapid City), and 5 (Fritz Peak). This is consistent with a movement of auroral activity equatorward from the auroral zone as the magnetic activity increases.

REFERENCES

- Roach, F. E., J. W. McCaulley, E. Marovich, and C. M. Purdy, A comparative study of absolute zenith intensities of [O I] 5577, *J. Geophys. Research*, **65**, 1503-1511, 1960.
- Roach, F. E., and M. H. Rees, The absolute zenith intensity of [O I] 5577 at College, Alaska, *J. Geophys. Research*, **65**, 1489-1493, 1960.
- Sandford, B. P., Studies of the upper atmosphere from Invercargill, New Zealand, *Ann. géophys.*, **15**, 445-452, 1959.

(Manuscript received February 15, 1960.)



A Study of Local Geomagnetic Influence on the [O I] 5577 Nightglow Emission at Fritz Peak

J. W. McCauley and F. E. Roach

National Bureau of Standards, Boulder Laboratories
Boulder, Colorado

AND

S. MATSUSHITA

High Altitude Observatory, University of Colorado

Abstract. A comparison is made of (1) the horizontal magnetic intensity at Leadville, Colorado, and (2) the absolute zenith intensity of [O I] 5577 at Fritz Peak, Colorado. The absolute zenith intensity of 5577 tends to increase as the magnetic ΔH becomes more negative.

Introduction. Previous attempts to correlate magnetic activity with the [O I] 5577 airglow have yielded contradictory results. In a recent study Sandford [1959] has reported an increase in the intensity of [O I] 5577 and [I] 6300 at Invercargill with increasing magnetic activity. (Table 1 gives the coordinates for the stations mentioned in the text.) He finds a greater than 10-fold increase in intensity of 5577, for example, as the planetary magnetic activity increases from 'quiet' ($K_p = 0$) to 'active' ($K_p = 9$). The magnitude of the observed ratio is surprising, since other investigators in the subauroral zone have found little or no correlation between magnetic activity and 5577 airglow intensity. Dufay and Meng Mao-Lin [1947] found a slightly negative correlation at Haute Provence. Roach, Pettit, Williams, St. Amand, and Davis [1953] found that, at Cactus Peak, California, bright 5577 does not occur at a time of 'quiet' magnetic activity. Manning and Pettit [1958] found no evidence for a correlation between magnetic activity and 5577 intensity at Sacramento Peak, New Mexico.

The IGY material from Fritz Peak, Colorado, has recently been studied, and evidence is found for a positive correlation between planetary magnetic activity and the spread of 5577 zenith intensity [Roach, 1960]. In this paper we present a detailed comparison of the absolute zenith intensity of 5577 at Fritz Peak and the

departure of the horizontal magnetic component from quiet conditions at Leadville, Colorado, at a distance of 90 km from Fritz Peak.

The observations and discussion. Records of the D , H , and Z components of the local geomagnetic field were made with a portable Askania variograph at Leadville, Colorado, from July 1, 1957, to January 12, 1959. Geomagnetic variations of all three components were recorded on the same 16-mm films. When the film magnification is 12, the length of a 1-hour period becomes 6 cm and the scale value is 3.1 — 4.0 γ/mm for H and Z , and 0.81 — 0.91 min/mm for D .

The [O I] 5577 observations were made at the Fritz Peak, Colorado, observatory using photo-

TABLE 1. Coordinates of Stations Mentioned in Text

Station	Geographic		Geomagnetic Latitude
	Latitude	Longitude	
Sacramento Peak	32°47'N	105°48'W	42°
Cactus Peak	36°05'N	117°49'W	43°
Fritz Peak	39°54'N	105°29'W	49°
Leadville	39°18'N	106°12'W	49°
St. Michel (Haute Provence)	43°56'N	5°30'E	46°
Invercargill	46°25'S	168°19'E	-52°

electric photometers with interference filters to isolate the emission lines. The deduced intensities in rayleighs refer to the zenith.

The hourly values (value recorded on the hour) of 5577 nightglow intensity were compared with the hourly values of the amplitude of the H component during a corresponding period of observation. To find the relative change in H (ΔH), the solar quiet (S_q) variation (average of variations on the international five quiet days) has been removed from the data. Since insufficient data were available to determine the *disturbed* daily variation (DS), no geomagnetically disturbed periods are included in this study. The lunar daily variation was not considered; it is very small compared with the solar quiet variation.

Figure 1 shows a plot of ΔH in gamma versus Q in rayleighs for 18 nights of observation in November and December 1957. The points plotted are the average ΔH and Q for each 100-rayleigh interval. The crosses indicate the standard deviations of ΔH and Q respectively. These values are given in Table 2. A least-squares solution is indicated by the line in

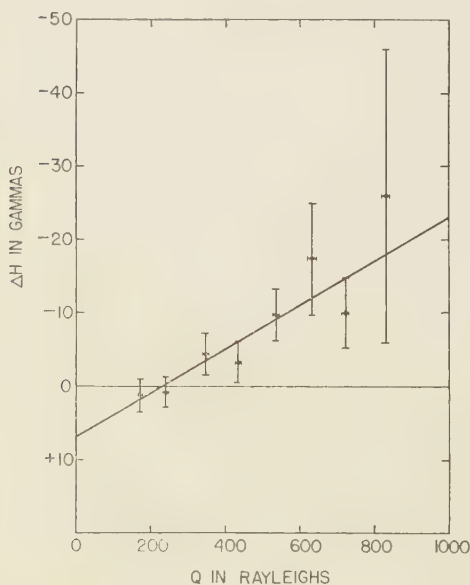


Fig. 1. Relationship between horizontal magnetic intensity (ΔH) and the zenith intensity of [O I] 5577.

TABLE 2

\bar{Q} , rayleighs	$\sigma(\bar{Q})$	$\overline{\Delta H}$, gamma	$\sigma(\overline{\Delta H})$
171	5	+1	2
241	5	+1	2
348	6	-4	3
436	6	-3	3
539	6	-10	4
634	10	-17	8
721	9	-10	5
830	(10)*	-26	(20)*

* Only two observations; entries give total spread.

Figure 1. The empirical solution is given $\Delta H = -0.03Q(\pm 0.006) + 7$. For each 1 rayleigh change in 5577 intensity a change ΔH of 3 gamma is indicated. For the excursion $Q = 0$ to $Q = 1000$ rayleighs, range of ΔH is 30 ± 6 gamma. The computed correlation coefficient is 0.37. As can be seen from the standard deviations, there is considerable scatter in the points. However, the trend is that ΔH becomes more negative as the intensity increases, and the least-squares solution extrapolated to an aurora II (10 kR) would indicate the change in ΔH to be about 30 gamma.

It should be pointed out that the magnitude of ΔH does not necessarily bear a relation to the magnetic index, K . As was mentioned previously, ΔH is measured as a deviation from the 'quiet' variations in H . These quiet variations are composed mainly of the solar quiet (and lunar daily variations) measured at a particular station. On the other hand, the magnetic index, K , given in 3-hour intervals, is specified by the total excursion of the H component during the 3-hour period. As an example of the difference, consider a case in which H is considerably different from quiet-day conditions but remains relatively steady over a given period of time. Then the magnitude of ΔH would be large, since the difference between H and quiet-day conditions is large. The K for this interval would be small, however, since the excursion of H during the interval of time considered is small. Thus, if we translate K to gamma for a given station, we will see no apparent agreement with ΔH unless we measure

the change in ΔH for the same interval of time that we specify K . The difficulty in resolving the magnetic 'fine structure' in the subauroral zone is apparent. A ΔH reflecting high airglow intensity may not necessarily show a high K . This is in agreement with the observation by Roach, Pettit, Williams, St. Amand, and Davis [1953] that a night of very high 5577 intensity at Cactus Peak, California, was associated with low K_p .

A representation of the electric current system in the ionosphere that could produce the observed quiet field is shown by Chapman and Bartels [1951]. The tendency for ΔH to become more negative as the 5577 intensity increases may be interpreted as an increase in the intensity of the overhead electric current with increasing 5577 intensity. This current increase may be due to greater wind velocities or to an increase in the anisotropic electric conductivity. The details will be discussed in another paper.

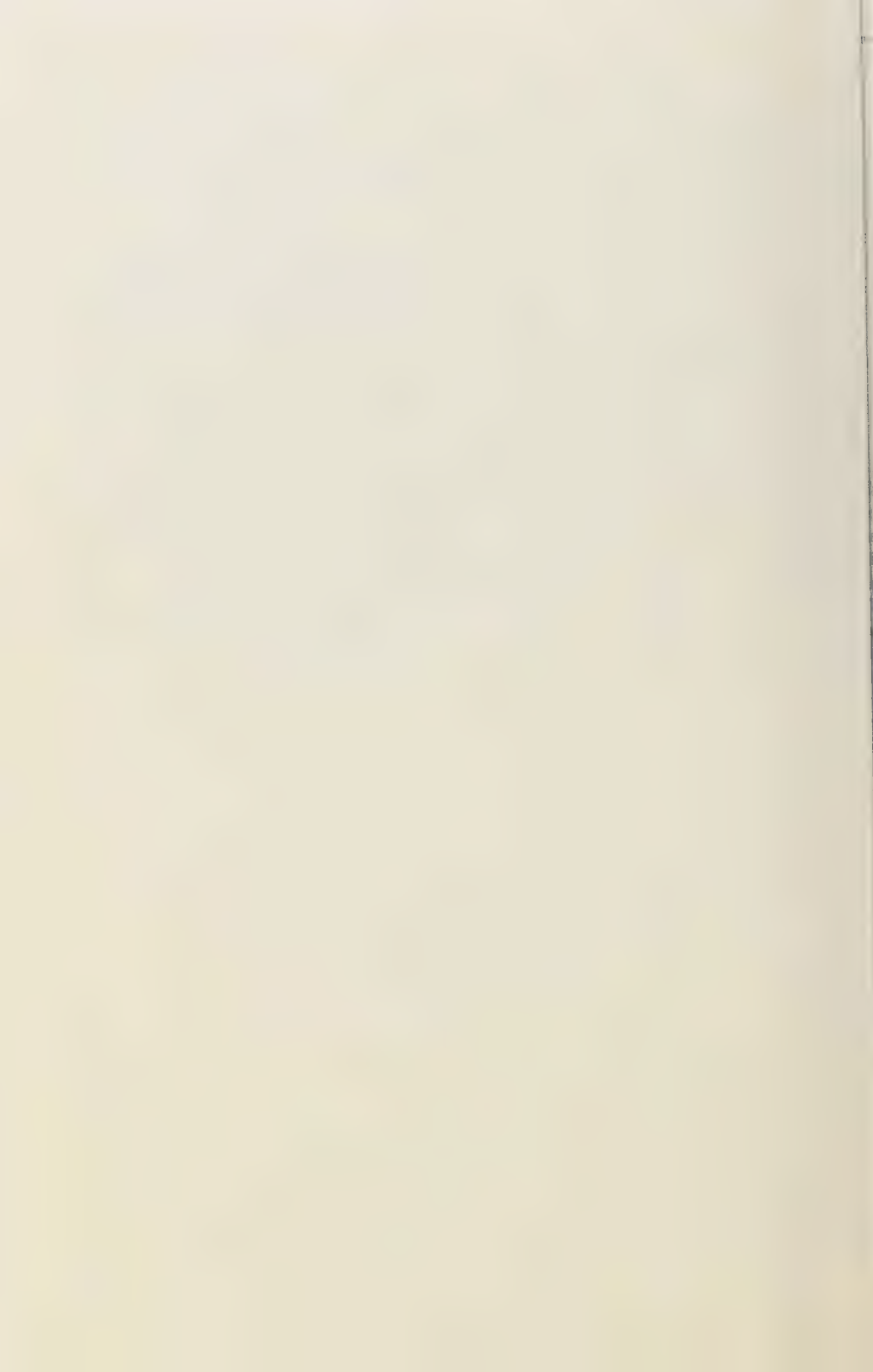
Conclusions. The evidence presented suggests a geomagnetic control of the [O I] 5577 emission in the subauroral zone. We have attempted to isolate the magnetic control effect in the subauroral zone using a more discriminating index than the planetary magnetic figure

used by Sandford [1959] and by Roach [1960]. The result indicates a linear relationship between the magnetic activity defined by ΔH and the 5577 intensity at Fritz Peak, at least up to the visual threshold for extended objects in the green ($Q \sim 1000$ rayleighs).

REFERENCES

- Chapman, S., and J. Bartels, *Geomagnetism*, vol. I, p. 229, Oxford University Press, 1951.
- Dufay, Jean, and Tcheng Mao-Lin, Recherches spectrophotométriques sur la lumière du ciel nocturne dans la région visible, *Ann. géophys.*, **3**, 153-183, 1947.
- Manring, E. R., and H. B. Pettit, The 5577 Å emission in the night airglow from Sacramento Peak, New Mexico, *J. Geophys. Research*, **63**, 39-49, 1958.
- Roach, F. E., The intensity of [O I] 5577 in the subauroral region as a function of magnetic activity, *J. Geophys. Research*, **65**, 1495-1497, 1960.
- Roach, F. E., Helen B. Pettit, D. R. Williams, P. St. Amand, and Dorothy N. Davis, A four year study of [O I] 5577 Å in the nightglow, *Ann. Astrophys.*, **16**, 185-205, 1953.
- Sandford, B. P., Studies of the upper atmosphere from Invercargill, New Zealand, IV, Correlation of the intensity of the forbidden oxygen lines in the airglow and aurora with magnetic activity, *Ann. géophys.*, **15**, 445-452, 1959.

(Manuscript received February 15, 1960.)



A Comparative Study of Absolute Zenith Intensities of [O I] 5577

F. E. ROACH, J. W. McCauley, E. MAROVICH, AND C. M. PURDY

*Boulder Laboratories, National Bureau of Standards
Boulder, Colorado*

Abstract. The statistical distribution of the absolute zenith intensities of [O I] 5577 is compared for four locations at north geomagnetic latitudes 49°, 53°, 65°, and 88°. The distributions are similar in nature at all stations. The median values in rayleighs are 371 (49°), 251 (53°), 2400 (65°), and 630 (88°). The percentage occurrence of intensities greater than the visual threshold is 2.2 (49°), 1.2 (53°), 83 (65°), and 15 (88°). Evidence is presented for and against a single excitation mechanism for both auroral 5577 and airglow 5577.

Introduction. In earlier reports [Roach, McCauley, and Marovich, 1959; Roach, McCauley, and Purdy, 1959], we examined preliminary results of measurements of the zenith intensity of [O I] 5577 at Thule, Greenland (geomagnetic latitude, Φ , = 88°N), at Rapid City, South Dakota (Φ = 53°N), and at Fritz Peak, Colorado (Φ = 49°N). A larger sample of data is now available to us for all three stations. In addition a similar study [Roach and Rees, 1960] at College, Alaska (Φ = 65°N), makes it possible to compare the intensity distributions at two stations in the subauroral zone (Fritz Peak and Rapid City), one close to the auroral zone (College) and one near the geomagnetic pole (Thule).

The observational data. The wide range of observed intensities between the faintest (less than 100 rayleighs) and the brightest (greater than 300,000 rayleighs) indicates the desirability of using logarithms in treating the data. In Table 1 we have collected the pertinent data for the four stations. The total number of individual readings is given in parentheses below the station identification.

A histogram representation of the distributions is shown in Figure 1. The smooth curves are logarithmic normal curves according to the parameters listed in Table 2.

A steady progression to higher intensities occurs in the order Rapid City, Fritz Peak, Thule, and College. This is brought out in Figure 2, in which are shown the smooth logarithmic normal curves normalized to the same rela-

tive peaks. Another form of presentation is the cumulative probability plots of Figure 3. The general impression of all these methods of presentation is that the phenomena are similar at the four stations but with different parameters to define the details.

Logarithmic representations as in Figures 1, 2, and 3 tend to hide the linear spread of the data. The fact that in the auroral zone there is an especially wide over-all spread in the absolute intensities is illustrated in Figure 4, in which $Q(n \text{ per cent})$ is plotted against the geomagnetic latitude for the four stations of the study.

Interstation relationships. From the cumulative plots it is possible to make comparisons between pairs of stations. From the entries in Table 3 we show in Figure 5 plots of Q_n (Thule, Rapid City) versus Q_n (Fritz Peak), and in Figure 6, Q_n (College) versus Q_n (Fritz Peak).

The following relationships describe the data:

$$Q(\text{RC}) = 0.75Q_{FP} - 21$$

$$Q(\text{Thule}) = 1.70Q_{FP} + 9$$

$$Q(\text{College}) = 0.00066Q_{FP}^{2.57}$$

Statistical test of the Chapman reaction. In a recent paper, Barbier [1960] has called attention to the fact that the 5577 intensity distributions at Haute Provence are normal with respect to the cube root of the intensity, Q . This fact is consistent with normality in the distribution of atomic oxygen in the emitting region if the Chapman reaction is responsible for the emission. The reaction involves the triple

TABLE 1

Class, log Q	Fritz Peak (926)	Rapid City (966)	Thule (9732)	College (3968)
1.6-1.7		0.1		
1.7-1.8		0.2		
1.8-1.9		0.6		
1.9-2.0	0.2	1.1		
2.0-2.1	0.3	5.1		
2.1-2.2	2.4	6.2	0.04	
2.2-2.3	7.0	12.1	0.1	
2.3-2.4	11.0	18.5	0.5	
2.4-2.5	15.8	18.3	4.2	
2.5-2.6	18.9	16.7	7.4	1.1
2.6-2.7	19.0	11.3	12.3	5.2
2.7-2.8	13.9	5.6	22.3	7.2
2.8-2.9	6.4	2.1	21.4	10.7
2.9-3.0	2.4	0.8	15.7	10.2
3.0-3.1	2.1	0.4	8.4	9.6
3.1-3.2	0.1	...	4.0	23.9
3.2-3.3	0.1	...	1.1	10.4
3.3-3.4	0.2	0.4	2.3	6.2
3.4-3.5	0.2	0.1	0.3	4.0
3.5-3.6		...		4.2
3.6-3.7		...		2.3
3.7-3.8		0.3		2.7
3.8-3.9				1.7
3.9-4.0				0.7
4.0-4.1				4.0
4.1-4.2				2.5
4.2-4.3				1.9
4.3-4.4				1.0
4.4-4.5				0.9
4.5-4.6				0.7
4.6-4.7				0.8
4.7-4.8				0.2
4.8-4.9				0.4
4.9-5.0				0.2
5.0-5.1				0.1
5.1-5.2				0.5
5.2-5.3				0.2
5.3-5.4				0.5
5.4-5.5				0.5
5.5-5.6				...
5.6-5.7				0.8

collision of three oxygen atoms so that $Q^{1/3} \propto n(O)$. In Figure 7 we show the distribution of 5577 intensities at Fritz Peak and Rapid City according to $Q^{1/3}$. The smooth normal curves show an excellent fit with the observations, in agreement with Barbier's results for Haute Provence.

Discussion. In this section it is proposed to

assemble data pertinent to the question of the physical origin of the excitation of the oxygen atom to the 1S state leading to the emission of 5577 Å. The question has been raised [Roach, McCauley, and Marovich, 1959; Roach, McCauley, and Purdy, 1959; Sandford, 1959] whether a single type of excitation may be responsible for the emission over all the earth. The generally accepted view is that two mechanisms are operating to produce the 5577 night airglow and the 5577 aurora.

The most probable photochemical reaction for the excitation of atomic oxygen to the 1S level is the so-called Chapman reaction:

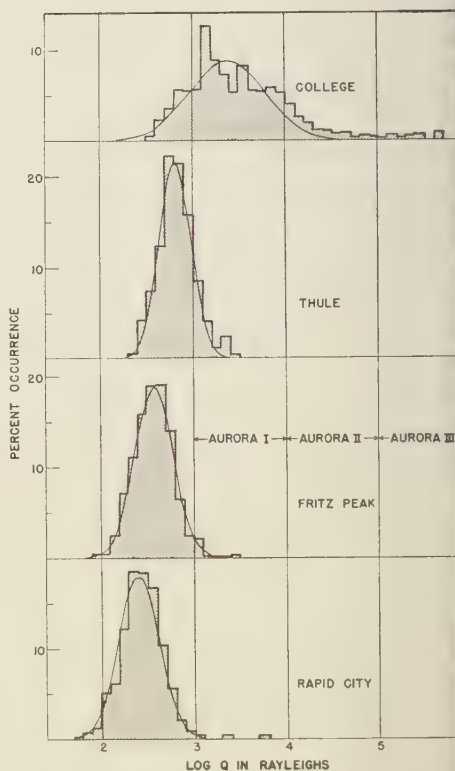
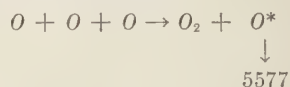


Fig. 1. Histogram distributions of 5577 Å zenith intensities at four stations. Smooth curves are logarithmic normal curves according to the constants in Table 2.

TABLE 2. Parameters for Logarithmic Normal Curves

Parameter	Fritz Peak	Rapid City	Thule	College
Mode, $\log Q$	2.57	2.40	2.80	3.38
$\log Q$	0.21	0.22	0.17	0.40



↓
Herzberg
bands

The energy available for the excitation of either the oxygen molecule or atom is 5.2 ev, more than enough to excite the atom to the 1S state (E. P. = 4.2 ev) or the molecule to the $A^3\Sigma_u^+$ state (E. P. = 4.5 ev) which leads to the Herzberg bands.

The prediction of the quantal output of 5577 from the Chapman reaction is difficult because of the lack of definitive knowledge of the pertinent rate coefficient [Tandberg-Hanssen and Koch, 1959]. That the reaction occurs in the upper atmosphere cannot be doubted; the only question is what part of the emission observed is due to this reaction at a particular place and time. To make the question quantitative let us place the possibilities in four categories:

1. The Chapman reaction is the exclusive source of excitation under what have been loosely called 'airglow' conditions.

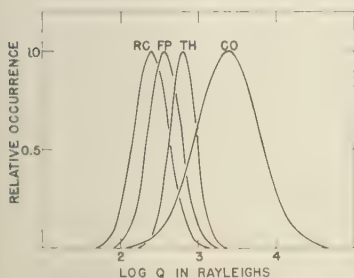


Fig. 2. Smooth distribution curves for four stations. RC = Rapid City; FP = Fritz Peak; TH = Thule; CO = College.

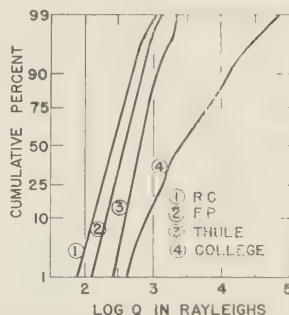


Fig. 3. Cumulative percentage (ordinate) versus $\log Q$ for four stations.

2. The reaction is the major source of excitation in subauroral regions up to intensities of several hundred or even a thousand rayleighs, but 'auroral' excitation may be superimposed under conditions of high magnetic activity.

3. The reaction is a minor source of excitation (say less than 100 R) in subauroral regions, and most of the excitation is of an auroral nature.

4. The reaction contributes insignificantly, if at all, to the excitation under any conditions; the entire world-wide emission is due to some kind of auroral or discharge mechanism.

The observational data do not point unambiguously and uniquely to any one of the above four possibilities.

In Table 4 we have summarized the observational information bearing on the question, and now we will discuss the items seriatim.

1A, 1B. The most comprehensive quantitative study of covariance of various spectral features in the night airglow is due to Barbier [1955]. Of particular interest in the present discussion is a group of emissions which he designates the '5580 group.' Extensive observations over several years have shown conclusively that the radiations coming through the four filters centered on 5580, 5260, 4400, and 3670 Å are covariant.

Of particular interest in this discussion is the combination 5580-3670 Å. Two features of this covariance are pertinent: (1) in general the correlation coefficient between intensity variations of the two radiations is high, better than 0.9; (2) when there is auroral activity there is departure from the general correlation in the

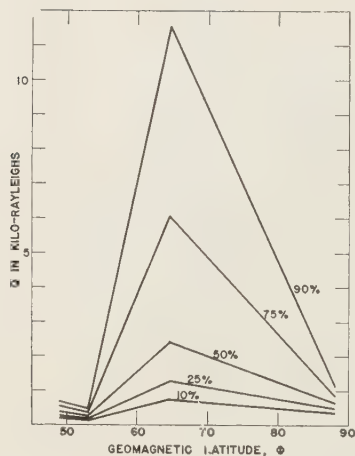


Fig. 4. Intensity of 5577 Å zenith intensity versus geomagnetic latitude for the four stations of this study. Family of curves is for a series of cumulative percentage occurrence.

sense of an enhancement of 3670 with respect to 5580.

The basic difference between the two filters is that the 5580 filter transmits predominantly the 5577 oxygen line whereas the 3670 filter is rather broad and transmits a number of bands including several of the Herzberg bands of O_2 and the three bands of N_2^+ [1-0 (3582 Å), 2-1 (3564), and 3-2 (3549)]. Barbier interprets the two observational results as indicating: (1) the general covariance is due to concurrent changes in the intensity of 5577 and the O_2 Herzberg bands, which is reasonable if both are due to the Chapman reaction; (2) the departure from the normal covariance is due to the enhancement of the N_2^+ bands when auroral conditions are superimposed on normal airglow conditions.

If this interpretation is correct it would be expected that a similar relationship would exist between the 5580 and 4400 filters since the 4400 filter also transmits both O_2 (Herzberg) and N_2^+ bands. No data have been published on this point.

IB. The preceding discussion of Barbier's results calls for an examination of any other simultaneous quantitative measurements of 5577 and one or more of the N_2^+ bands. The strongest N_2^+ band in the first negative group is the O-O band at 3914 Å. Rees [1959] in a study of the

aurora of March 1-2, 1957, at Fritz Peak measured the ratio of intensities of 5577/3914 from the evening hours (before there was any evidence of an aurora) through the night. Visual auroral activity began to develop during the late evening, reaching a maximum just before midnight. Rees selected the 5577 and 3914 reading for northerly zenith distances 70°, 75°, and 80° to make a quantitative study of the two radiations. In Table 5, taken from Rees' study, we show the extreme values of the observed intensities. The minimum intensity of 5577, 282 R at $Z = 70^\circ$, corresponds to about 140 R at the zenith, a value far below the median Fritz Peak value of 371 R. As a matter of fact, from Figure 3 it is found that a 5577 zenith intensity as low as 140 R occurs during only 2 per cent of the time at Fritz Peak. The upper limit of Table 4 is 173 kR for 5577, which corresponds to a visual aurora of International Brightness Coefficient III. Over this entire range (between 3 and 4 decades) of intensity the ratio of intensities 5577/3914 remained closely constant. From a large quantity of data Rees found that this constant ratio was 1.9.

The evidence from Rees' study is that, over range of intensities from faint airglow to bright aurora, and for many variations of auroral form the 5577/3914 ratio was a constant at Fritz Peak on March 1-2, 1957. The constancy of this

TABLE 3. Cumulative Percentage Distributions, log Q , Q

Cumulative Per Cent	Fritz Peak	Rapid City	Thule	College
	2.09	1.88	2.41	2.6
1	123	76	257	436
	2.31	2.12	2.58	2.8
10	204	132	380	740
	2.43	2.25	2.69	3.1
25	269	178	490	1290
	2.57	2.40	2.80	3.3
50	371	251	630	2400
	2.71	2.55	2.91	3.5
75	512	354	812	6020
	2.83	2.69	3.05	4.0
90	675	490	1120	11,500
	3.11	3.05	3.35	4.4
99	1290	1120	2240	64,500

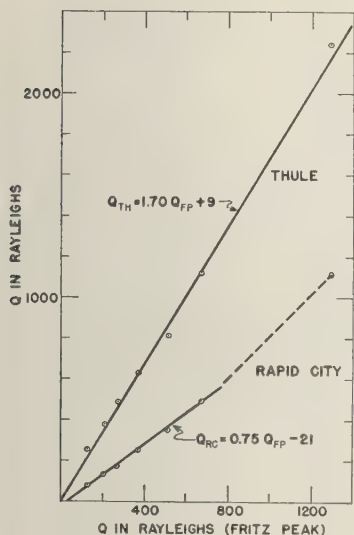


Fig. 5. Relationship between 5577 Å intensity at Fritz Peak and at Thule (upper curve) and at Rapid City (lower curve). Points refer to equal values of cumulative percentage occurrence at the two stations involved.

ratio should be tested over an extended period of time, since the implication of Barbier's analysis (1A, 2A) is that the enhancement of the N_2^+ bands transmitted by his 3670 Å filter is an indication of the occurrence of auroral excitation conditions distinctly different from those exciting the airglow. If, on the other hand, the 5577/3914 ratio is a constant, as found by Rees, then there is an unresolved contradiction between the two sets of data.

Omholt [1957] studied the 5577/3914 intensities at the Yerkes Observatory and found that this ratio seems to be almost constant (within $\pm 20\%$) in all types of aurora. Omholt does not give a numerical value for the ratio, nor does he indicate the lowest absolute intensity to which he observed.

3A. Recently, McCauley and Hough [1959] have studied the detailed structure of low-frequency vertical incidence ionograms made near Boulder. They found an indication of a relationship between the frequency difference of two ionogram features near the 100-km level and the local intensity of 5577 zenith intensities at Fritz Peak.

The significance of their discovery from the standpoint of this paper is that the Chapman reaction does not involve the ionic concentration of the upper atmosphere directly. The McCauley-Hough results suggest the possibility of a reaction involving the charged particles—possibly some kind of a discharge mechanism [Tandberg-Hanssen and Roach, 1959].

McCauley and Hough found that the ionosphere-5577 relationship was not apparent for low 5577 intensities but became measurable at about 450 R. This might be interpreted as a 'break' with the Chapman reaction operative from low 5577 intensities up to 450 R and some kind of discharge mechanism taking over above that intensity.

4A, 4B. It was noted by Barbier [1960] that the 5577 intensities at Haute Provence give a 'normal' distribution with respect to the cube root of the intensity. That this is probably true in general in the subauroral region is evidenced by Figure 7, in which it is shown that at Fritz Peak and at Rapid City a normal (intensity) $^{1/3}$ distribution also occurs. As Barbier points out,

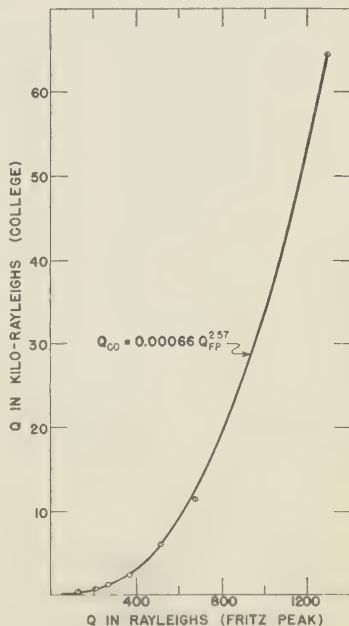


Fig. 6. Relationship between 5577 Å intensity at Fritz Peak and at College. Points as in Figure 5.

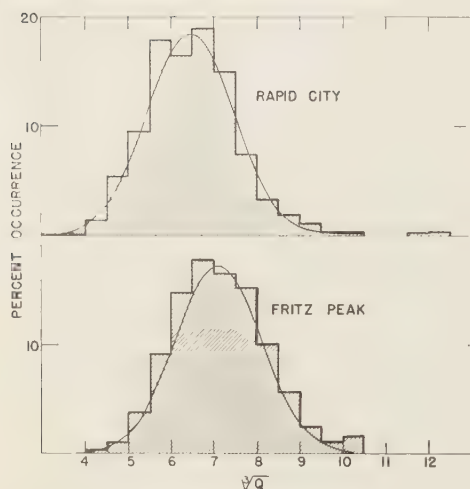


Fig. 7. Histogram representation of the distribution of 5577 Å zenith intensities at Rapid City and Fritz Peak with $Q^{1/2}$ as abscissa. Smooth curves are normal curves with the constants mentioned in the text.

a cube-root intensity normal curve implies atomic oxygen normal distribution leading to the emission.

Such statistical results never, of course, lead to definitive conclusions, but the evidence is consistent with, or at least not inconsistent with, the Chapman reaction.

The 5577 Å distribution curves with respect to the intensity itself are positively skewed. A positively skewed distribution can be converted into a normal one in a number of ways, including using a root as above or a logarithm. In Figure 1 we showed that a logarithmic normal distribution is quite satisfactory for Fritz Peak, Rapid City, and Thule and gives a fair representation for College except at the highest intensities. Actually we have found that the College distribution is well represented by a normal curve with respect to the log log intensity.

But the point of this paper is not the reduction of the distributions to any particular type of normal distribution. The significance is two-fold: (1) from the subauroral region to the auroral region to the geomagnetic pole there is a simple progression of intensity distributions as shown in Figures 1, 2, and 3; (2) all the distributions are sensibly unimodal.

These facts are 'not inconsistent with' the hypothesis that a single mechanism of excitation is operating in both the auroral and the subauroral regions.

5A, 5B. The weakness of many statistical arguments in geophysics is that it is possible to establish only plausibility or consistency and not even approximately a proof. It is with some initial hope that we therefore turn to the matter of magnetic control of 5577 both in its auroral and in its airglow aspects. The existence of the auroral zone having approximate symmetry with respect to the geomagnetic rather than the geographic coordinates of the earth is perhaps the very foundation of all our thinking about auroral mechanisms.

Early attempts to find any general correlation between 5577 Å intensities in the subauroral zone have shown that the correlation is absent or, at least, very small [Dufay and Tchern, Mao-Lin, 1947]. However, the evidence of this series of papers suggests that there is in the subauroral zone a significant magnetic activity-5577 Å relationship.

The effect shown in Figures 1 and 2 of Roach [1960] might be interpreted as the superposition of an auroral mechanism on an airglow mechanism except for the fact that the same kind of result is obtained in the auroral zone. In both regions it is possible to have relatively low 5577 Å intensities with high magnetic activity, but the probability of high intensities increases with magnetic activity, thus leading to an increase in the spread of the 5577 Å intensities as the magnetic activity increases.

We thus have two alternatives: (1) there is a superposition of auroral activity on airglow activity in both the auroral and the subauroral regions, or (2) there is a common mechanism of excitation, the magnetic control being only a statistical one in both regions.

6A, 6B. Auroral 'motions' vary from rapid phenomena in which the whole visible sky is covered in a second or so to slower motions which correspond to wind velocities [Roach, Tandberg-Hanssen, and McGill, 1958] to still slower movements in which an arc may move only a few degrees in a whole night [Roach and Marovich, 1959].

In the early history of our knowledge of the 5577 airglow the authors always gave the in-

TABLE 4. Summary of Observational Data on [O I] 5577

A. Two Mechanisms		B. One Mechanism	
Observational Fact	Reference	Observational Fact	Reference
1. Correlation between 5577 and 3670.	<i>Barbier</i> [1955]	1. Correlation between 5577 and 3914 (N_2^+) over several decades of intensity from 'airglow' to 'auroral.'	<i>Rees</i> [1959]; <i>Omholt</i> [1957]; <i>Murcray</i> [1959]
2. Breakdown of correlation 1A under 'auroral' conditions.	<i>Barbier</i> [1958]	2. Same as 1B.	
3. Break in curve of ionosphere-5577 relationship near 500 R.	<i>McCaulley and Hough</i> [1959]	3. Same as 1B.	
4. Distribution of 5577 intensities in sub-auroral zone is 'normal' with respect to 3 density.	<i>Barbier</i> [1960]; this paper	4. Distribution of 5577 intensities in both auroral and sub-auroral zones is unimodal and approximately normal with respect to logarithm of intensity.	This paper
5. Lack of conspicuous dependence of 5577 intensity on magnetic activity in subauroral zone as contrasted with well-known dependence of auroral activity on magnetic activity.	<i>Dufay and Tcheng Mao Lin</i> [1947]; <i>Barbier</i> [1960]	5. Existence of a statistical dependence of 5577 intensity on magnetic activity which in the subauroral zone is similar to but smaller than that in the auroral zone.	<i>Roach</i> [1960]; <i>McCaulley, Roach, and Matsushita</i> [1960]; <i>Sandford</i> [1959]
6. Rapid time and space fluctuations of visual auroral features in contrast with more steady airglow 5577 intensities.		6. Similarity of 5577 airglow motions and the slower auroral motions.	<i>Roach, Tandberg-Hanssen, and Megill</i> [1958]
7. Differences in general spectra of aurora and airglow based on inspection of spectrograms.		7. Lack of systematic quantitative measurements of relative intensities of spectral features over wide range of intensity and with allowance for reciprocity failure.	

pression that it was a more or less static phenomenon, any variations of intensity that occurred being due to in situ changes. It now appears, however, that the intensity changes in 5577 airglow may be due to dynamic movements of large cells [*Roach, Tandberg-Hanssen, and Megill*, 1958] with velocities similar to some observed in visible auroras and much faster than the movements of some sluggish auroral features [*Roach and Marovich*, 1959]. Very high-speed movements in the 5577 airglow are not likely but cannot be entirely ruled out on the basis of the usual observations with low time resolutions.

7A, 7B. We now discuss a general argument which refers not to 5577 alone but to the entire spectrum.

A well-exposed auroral spectrogram is rich in lines and bands most of which do not appear at

all on even the longest airglow exposure. Thus a casual inspection of two spectrograms, one of an aurora and one of night airglow, would lead one to make an apodictic statement that the two phenomena are completely different. Two comments, however, are in order:

1. There is not just a single *airglow*; there are *airglows*. The several airglows occur at dif-

TABLE 5

Time, MST	Zenith Distance	Intensity, rayleighs		Ratio 5577/3914
		5577	3914	
2050	70°N	282	149	1.89
2346	80°N	173,000	93,200	1.86

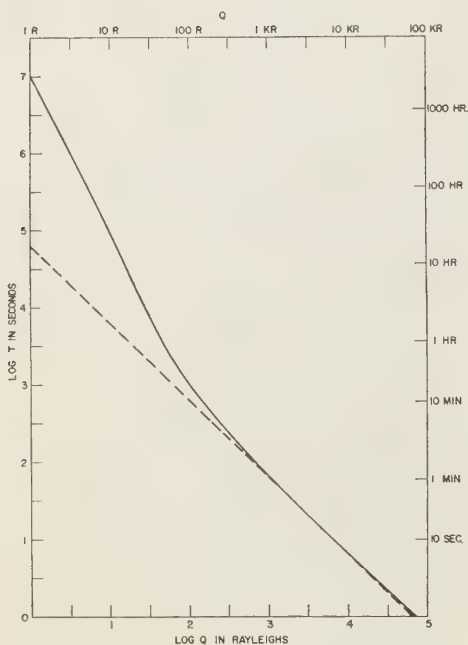


Fig. 8. Reciprocity failure for Eastman 103a F emulsion with IGY patrol spectrograph. Dashed line is for reciprocity between exposure and intensity; solid line is based on empirical use of emulsion indicating need for relatively long exposures for fainter emissions.

ferent heights and are almost certainly due to different mechanisms: OH (70 km?); Na-D (85 km); 5577 and Herzberg O₂ bands (100 km); and 6300 (*F* region?). The present debate is concerned only with 5577.

2. It is difficult, if not impossible, to get quantitative ideas of relative intensities of spectral features from a comparison of aurora and airglow spectrograms or even careful microphotometer tracings because of the effect of reciprocity failure. That this is not a trivial effect will now be shown.

In Figure 8 we show a plot of the exposure time to obtain a just developable photographic image with Eastman 103a F emulsion in conjunction with the IGY patrol auroral spectrograph. (This curve was deduced with the help of a laboratory curve obtained through the courtesy of the Research Laboratories of the Eastman Kodak Company.) The solid curve is

the empirical result, as contrasted with the dashed curve, which would hold if reciprocity between exposure time and light intensity held throughout all intensity levels. The difference between the two curves is severe (note that the plot is on a log-log scale). Reciprocity failure sets in for the 103a F emulsion with the IGY patrol spectrograph for intensities of about 500 R, below which serious distortions in the appearance of spectrograms must occur. For example, a faint line of intensity 1 R ($\log Q = 0$) requires for a just developable image an exposure of 10^7 seconds (1/3 year!) compared with 4×10^4 seconds (11 hours) if reciprocity held. Thus the exposure is increased by a factor of 250 because of the reciprocity failure. An aurora with 5577 having an intensity of 100 kR and another auroral line with an intensity of 1 kR could be obtained showing both lines with an exposure of a few minutes. On the other hand, if the two lines maintained the same intensity ratio and 5577 were 100 R it would be possible to bring out 5577 with reasonable photographic density in an exposure of some hours, but the fainter (1 R) line would be completely invisible.

Another example taken from Figure 8 may be instructive. A just developable image is obtained for 100 R with an exposure of 17 minutes, but for a line one-fourth as bright (25 R) the exposure is 187 minutes (11 times as long) and for a line one-tenth as bright (10 R) the exposure is 1125 minutes, 66 times as long.

An example is presented by the N₂⁺ 3914 band, which is often taken as an index of auroral activity. As was mentioned above, Rees has found with a photoelectric photometer that it maintains a constant intensity ratio to 5577 over a very wide range. Since 3914 is a band, it may be assumed that its *photographic* effect will be spread out so that the effective 3914/5577 ratio may be something like 1:10. In this event, when 5577 has an intensity of 100 R the effective intensity of 3914 is 10 R and will just emerge with an exposure of 19 hours. If 5577 is 500 R, then 3914 (50 R effective) will just show with a 1-hour exposure. 3914 will yield a just developable image in 17.5 minutes when 5577 has an intensity corresponding to an aurora of IBC I (1000 R), and thus with exposures of an hour or more it will show a good photographic density and may be said to be an index

of the occurrence of an aurora. But the index, then, may be the result of the nonlinearity of response of the photographic emulsion rather than the result of a change in the physical excitation mechanisms in the upper atmosphere.

The determination of differences in relative line and band intensities that may exist over the wide range of auroral intensities and types should be based either on careful photoelectric measurements or on photographic measurements made with very careful attention to the quantitative effects of reciprocity failure. Visual inspection of long-exposure spectrograms may lead to inconclusive results.

Conclusions. We have assembled quantitative arguments pertinent to the controversial question of a single or double source of excitation of 5577. We believe that the weight of evidence supports the hypothesis of a single world-wide mechanism. We suggest that such a mechanism may be of a 'discharge' nature, the word *discharge* connoting any type of excitation due to impacts with particles moving with non-thermal velocities. Examples of discharges in this sense are (1) excitation by particles entering the atmosphere from outside with high velocities and (2) excitation by particles that have been locally accelerated to high velocities. The first possibility includes the classical approaches to auroral theory; the second has been examined by Chamberlain [1955] and Seaton [1955] for auroral rays and by Tandberg-Hanssen and Roach [1959] for the airglow.

A suggestion in the 'discharge' category has been made by Gold [1959] that the 5577 emission is associated with leakage from the recently discovered radiation zones, a hypothesis that is attractive because of its rationalization of a semiannual term in the seasonal variation of 5577 intensities [Roach, 1959].

REFERENCES

Barbier, D., Résultats préliminaire d'une photométrie en huit couleurs de la lumière du ciel nocturne, *The Airglow and the Aurorae*, pp. 38-59, Pergamon Press, 1955.
Barbier, D., L'Activité auroral aux basses altitudes, *Ann. géophys.* 14, 334-355, 1958.

Barbier, D., Origine de [O I] 5577 dans la luminescence nocturne, *Ann. géophys.* 16, 1960, in press.
Chamberlain, J. W., Discharge theory of auroral rays, *The Airglow and the Aurorae*, pp. 206-221, Pergamon Press, 1955.
Dufay, Jean, and Tchong Mao-Lin, Recherches spectrophotométrique sur la lumière du ciel nocturne dans la région visible, *Ann. géophys.* 3, 153-183, 1947.
Gold, T., Motions in the magnetosphere of the earth, *J. Geophys. Research*, 64, 1219-1224, 1959.
McCaulley, J. W., and W. S. Hough, A relationship between the lower ionosphere and the [O I] 5577 nightglow emission, *J. Geophys. Research*, 64, 2307-2313, 1959.
Murray, W. B., Some properties of the luminous aurora as measured by a photoelectric photometer, *J. Geophys. Research*, 64, 955-959, 1959.
Omholt, A., Photometric observations of rayed and pulsating aurorae, *Astrophys. J.*, 126, 461-463, 1957.
Rees, M. H., Absolute photometry of the aurora—the ionized molecular nitrogen emission and the oxygen green line in the dark atmosphere, *J. Atmospheric and Terrest. Phys.*, 14, 325-337, 1959; also Ph.D. thesis, University of Colorado, 1958.
Roach, F. E., The night airglow, *Proc. IRE*, 47, 267-271, 1959.
Roach, F. E., and E. Marovich, A monochromatic low-latitude aurora, *J. Research NBS.*, 63D, 297-301, 1959.
Roach, F. E., J. W. McCaulley, and E. Marovich, Origin of [O I] 5577 in the airglow and the aurora, *J. Research NBS.*, 63D, 15-18, 1959.
Roach, F. E., J. W. McCaulley, and C. M. Purdy, Comparison of absolute intensities of [O I] 5577 in the auroral and subauroral zones, *J. Research NBS.*, 63D, 19-20, 1959.
Roach, F. E., and M. H. Rees, The absolute zenith intensity of [O I] 5577 at College, Alaska, *J. Geophys. Research*, 65, 1489-1493, 1960.
Roach, F. E., E. Tandberg-Hanssen, and L. R. Megill, Movements of airglow cells, *J. Atmospheric and Terrest. Phys.*, 13, 122-130, 1958.
Sandford, B. P., Studies of the upper atmosphere from Invercargill, New Zealand, IV, Correlation of the intensity of the forbidden oxygen lines in the airglow and aurora with magnetic activity, *Ann. géophys.*, 15, 445-452, 1959.
Seaton, M. J., Excitation processes in the aurora and airglow, 3, Low latitude aurorae, *The Airglow and the Aurorae*, 5, 225-243, Pergamon Press, 1955.
Tandberg-Hanssen, E., and F. E. Roach, Excitation mechanisms of the oxygen 5577 emission in the upper atmosphere, *J. Research NBS.*, 63D, 319-324, 1959.

(Manuscript received February 15, 1960.)

Lightning and Charge Storage

E. J. WORKMAN, M. BROOK, AND N. KITAGAWA

*New Mexico Institute of Mining and Technology
Socorro, New Mexico*

Abstract. An unusual lightning flash consisting of a record 54 current surges, of which 26 were leader-return-stroke combinations, and having a total duration of 2 seconds, is described. The character of the lightning flash evidences a charge configuration of large extent, thought to consist of from 4 to 6 thunderstorm cells simultaneously active. The electric and photographic evidence indicates path lengths of approximately 9 km (30,000 ft) for the final strokes of the flash.

Introduction. In describing a thunderstorm, one is faced with the elemental problem of how and where in the cloud the electric charge that is supplied to a lightning flash is stored. It is understandable that an active storm, given appropriate energy and moisture conditions, might continue for an indefinite period while producing periodic discharges of negative electricity to the ground. Something like 10 to 30 coulombs of electricity would be involved in each flash, and a time interval of from 5 to 30 seconds between flashes would be sufficient to maintain the supply, provided that suitable disposition could be made of the equal amount of positive electricity generated in the process. The positive charge, that portion complementary to the negative charge which goes to ground, must be diffused into the relatively conductive space of its environment. Perhaps eventually it will be exhibited in the downward flow of the positive electricity observed in fair-weather conditions over the earth. The final disposition of the residual positive charge poses some basic questions which beg solution. Nevertheless, a single flash which carries negative charge to ground is completed in such a short time that it must obtain its electricity from storage, and this involves space limitations.

A lightning flash may consist of many repeated elements, each involving a few coulombs—probably more than 1 and perhaps as high as 10. The dielectric strength of air at atmospheric pressure and under conditions of high liquid-water content may be as low as 10,000 volts/cm. A spherically symmetrical charge in free space would give a field intensity $E = 90 Q/R^2$, where Q is in coulombs, R is in kilometers, and E is in

volts/cm. This means that under this idealized spherical distribution the minimum radius of sphere required to enclose 100 coulombs would be 0.95 km. A more advantageous scheme of packing is not available, because a charge of any shape will give an electric-field intensity $E \geq 90 Q/R^2$, where R is the radius of the circumscribed sphere and E is the maximum field intensity on the surface of the sphere. Numerically, $Q = 111R^2$.

Since the repeated strokes of a flash drain charge from different regions of the cloud, interest develops in the maximum number of repeated strokes one might expect.

Observations. It is important to distinguish, as *Malan* [1956] has done, between leader-return-stroke combinations and minor current surges (or luminosity fluctuations) in the channel. The minor surges have been designated *M* components [*Schonland*, 1956]. The *M* components and leader-return-stroke combinations are not usually distinguishable from one another when photographed by a camera which does not resolve the leaders. A stroke in a multiple flash is defined as a partial discharge which involves a leader-return-stroke sequence [*Malan*, 1956]. In the multiple flash cited by *Malan* there were 48 luminous events, only 16 of which satisfied the above criterion.¹

¹ Frequent reference [for example, *Hagenuth*, 1951] has been made to an early and remarkable photograph of a lightning discharge by *Larsen* [1905], which consists of 40 luminous events over an elapsed time of 0.624 sec. The photograph does not, however, resolve the dart leaders. Since the time interval between the 40 successive events is less than 12 msec in 24 instances, it must be concluded that at least 24 of these events are *M* components [see *Malan*, 1956].

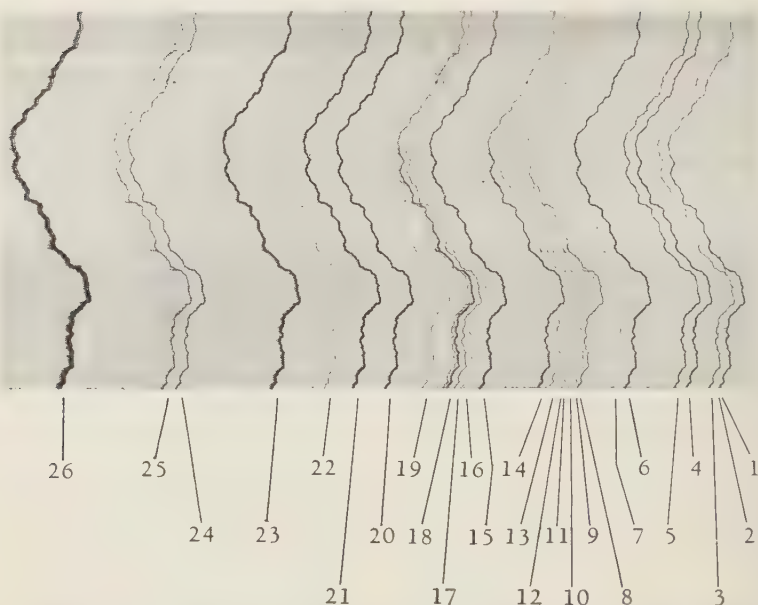


Fig. 1. Photograph of a lightning flash obtained by slowly rotating in a horizontal plane a type K-18, 24-in.-focal-length camera at a uniform rate through an arc of approximately 30° . The effective image velocity at the film is 5 cm/sec. Time increases from right to left.

In the course of observations at Socorro, New Mexico, during the summer of 1959 (July 26, 8 P.M.), the authors photographed a discharge having 26 separate and distinct leader-return-stroke combinations. Fortunately, this exhibition was photographed with two different moving-film cameras, and its electric-field change and luminosity variations were recorded on auxiliary equipment. The photographic presentation is shown in Figures 1 and 2. Figure 1 presents the record on a 'slow' camera of 24-inch focal length, and Figure 2 is a picture of the flash as recorded on a special camera used by the authors for the first time during the 1959 season. The total duration of the flash was 2 seconds. The events represent a record in the number of components, and, in addition, we believe, set a record for total duration.

Not all the leaders are apparent on the reproductions, but 24 of them show on the negatives, the other 2 being lost in halation. The electric and photoelectric records confirm their existence. (Strokes 1 to 3 were inadvertently lost on the electric record.) The character of the 26 strokes

is summarized in Table 1. Elements 7, 14, 15, 18, 20, 21, 23, 25, and 26 have M components, totaling 28. Thus, the total number of current surges involved is at least 54.

Discussion. Unfortunately, we have no way of characterizing this cloud which gave rise to the nocturnal lightning flashes except as it may be inferred from the available meteorological data. The small-convection-cell structure [Workman and Reynolds, 1949] would seem to require, by implication, a relatively large number of cells simultaneously active in this particular case. It is desirable to point out, however, that intra-airmass storms and storms of squall-line type would be expected to deviate very widely in their cellular configuration.

Weather Bureau reports indicate that on the night of July 26 conditions were favorable for orographic development of thunderstorms as moist air was lifted over the east slope of the Manzano Mountains northeast of Socorro. These generative features would favor a lateral development of cells in close phase relationship. A lightning discharge from one center would be

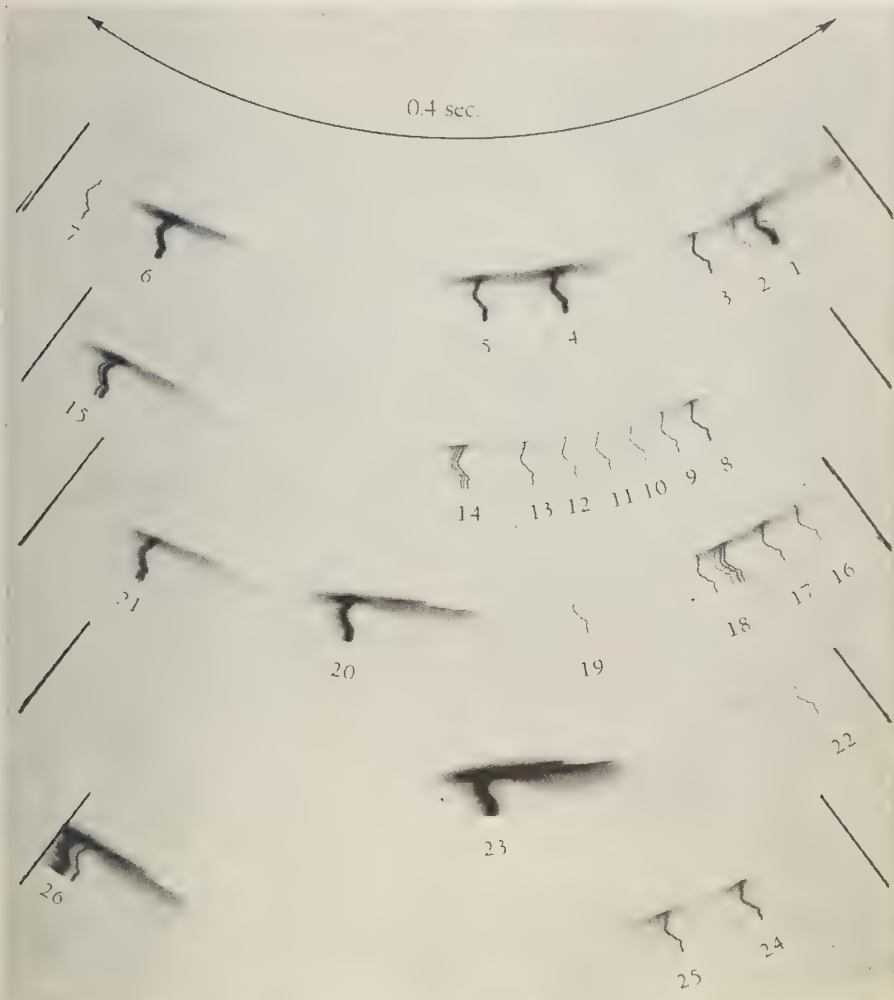


Fig. 2. Photograph of same lightning flash as shown in Figure 1. The photograph was obtained with a camera in which the film rotates with constant velocity in the focal plane of the lens. The successive images are formed on a circle of approximately 8-in. diameter. For reproduction, the circle was cut into $72\frac{1}{2}^\circ$ sectors, each representing 0.4 sec. The film makes one revolution every 2 sec, giving an effective transport speed of approximately 30 cm/sec at the lens.

followed in quick succession by discharges from neighboring centers, some of which would extend to relatively remote parts of the cloud.

The cloud base at the time of the flash here reported was estimated at 3.8 km, or 2.4 km above the terrain. Obviously, the photographic record shows the lower 2.4 km of the path. The

electric record, however, shows the entire duration of the events. If we assume that dart-leader velocity as measured on the photographs is the same inside the cloud, an estimate of the ratio of total length to below-cloud length is obtained. It appears from these ratios that the length of successive strokes increases more or less uni-

TABLE 1. Analysis of the Lightning Discharge of July 26, 1959, 8:00 P.M.

Stroke No.	Time from Previous Stroke, msec	From Photographic Record			From Electric and Photoelectric Record		Ratio t_e/t_p
		Leader		No. of M Components	Duration of Leader, msec: t_e	No. of M Components	
		Type	Duration, msec: t_p				
1	...	stepped	17.2	0	*	*	
2	12.0	dart	0.97	0	*	*	
3	18.0	dart	0.73	0	*	*	
4	70.0	dart	1.45	0	1.7	0	1.17
5	36.5	†	†	0	0.4	0	...
6	152.0	2 darts	{ 2.2 0.35	0	{ 3.6 0.6	0	{ 1.65 1.70
7	38.3	2 darts	{ 0.96 0.4	1	{ 1.8 0.65	1	{ 1.88 1.62
8	104.5	dart	3.3	0	5.5	0	1.66
9	15.5	dart	0.32	0	0.6	0	1.82
10	15.8	dart	0.65	0	1.55	0	2.38
11	16.6	dart	0.4	0	1.1	0	2.75
12	15.7	dart	...	0	...	0	...
13	19.5	dart	0.35	0	1.0	0	2.86
14	29.6	dart	0.49	6	1.5	5	3.06
15	171.5	†	†	2	0.8	2	...
16	56.3	dart	0.95	0	...	0	...
17	19.1	dart	0.7	0	2.0	0	2.85
18	20.4	dart	0.4	5	1.0	5	2.50
19	75.0	dart	0.97	0	2.2	0	2.27
20	107.3	dart	0.96	1	2.8	1	2.82
21	94.0	dart	0.45	3	1.3	2	2.9
22	89.7	dart	0.97	0	2.8	0	2.9
23	150.8	dart	1.9	1	7.0	1	3.68
24	272.0	3 darts	{ 4.8 1.9 0.8	0	{ 18.5 5.0 2.0	0	{ 3.85 2.63 2.50
25	38.7	dart	0.81	5	2.5	3	3.09
26	289.0	dart	4.0	4	13.0	4	3.25
Total	1928			28		24	

* No record.

† Not visible because of halation.

formly with each element. The first path calculated gives approximately 2.9 km for stroke 4 and 9 km for stroke 23. It is important to observe that these numbers represent an estimated path length and not necessarily a vertical distance.

The typical multiple ground flash consists of several strokes (from 2 to 6); the luminous and electric activity is usually most intense for the first stroke, diminishing gradually with the stroke number. For the flash under consideration, no such regularity is immediately apparent. It is possible, however, to divide the 26 strokes into

a number of groups, each of which does exhibit a behavior comparable to that of the typical multiple-stroke discharge. For example, strokes 6 to 14, 15 to 19, 20 to 22, and 23 to 25 each appear to constitute a group in which the luminosity decreases in a regular manner. The duration of each group is also comparable to that of the typical flash. Thus, the flash of July 26 must have involved from 4 to 6 times the cloud volume of a typical flash. Large horizontal displacements of the path within the cloud were no doubt involved. Although quantity of charge cannot be inferred from single-station measure-

ents, one might expect, from the grouping exhibited, that this lightning flash transferred to ground from 4 to 6 times the normal 10 to 30 coulombs.

The relationship between convection and cloud electrification has been firmly established [Reynolds and Brook, 1956; Brook 1957; Moore, Vonnegut, and Botka, 1958]. These studies have shown that rapid convective growth of the clouds is a necessary condition for cloud electrification. It is believed that this unusual exhibition of lightning activity resulted from a storm with an unusually large number of in-phase convective elements, or possibly of very large structural elements. Many other lightning flashes were photographed in this storm, and they were characterized by a relatively large number of strokes, several exceeding 20. The electric and photographic records obtained are therefore consistent with a cellular structure of very large extent. Indeed, it is probable that such storms give rise to the very long radar lightning echoes reported by Ligda [1956].

Acknowledgments. The work here presented involved the coordinated participation of two groups: one sponsored by the Geophysics Branch, Office of Naval Research; the other supported by the National Science Foundation.

REFERENCES

Brook, M., The relationship between the initial radar echo and the initial electric field in iso-

- lated thunderstorm cells, *Proc. Sixth Weather Radar Conf., Mass. Inst. Technol.*, Cambridge, 61-68, 1957.
- Hagenguth, J. H., The lightning discharge, *Compendium of Meteorology*, edited by Thomas F. Malone, Am. Meteorol. Soc., Boston, 136-143, 1951.
- Larsen, A., Photographing lightning with a moving camera, *Ann. Rept. Smithsonian Inst.*, 119-127, 1905.
- Ligda, G. H., The radar observation of lightning, *J. Atmospheric and Terrest. Phys.*, 9, 329-346, 1956.
- Malan, D. J., The relation between the number of strokes, stroke interval, and the total durations of lightning discharges, *Geofis. pura e appl.*, 34, 224-230, 1956.
- Moore, C. B., B. Vonnegut, and A. T. Botka, Results of an experiment to determine initial precedence of organized electrification and precipitation in thunderstorms, *Recent Advances in Atmospheric Electricity*, Pergamon Press, London, 333-360, 1958.
- Reynolds, S. E., and M. Brook, Correlation of the initial electric field and the radar echo in thunderstorms, *J. Meteorol.*, 13, 376-380, 1956.
- Schonland, B. F. J., The lightning discharge, *Handbuch der Physik*, 22, Springer Verlag, Berlin, 576-627, 1956.
- Workman, E. J., and S. E. Reynolds, Electrical activity as related to thunderstorm cell growth, *Bull. Am. Meteorol. Soc.*, 30, 142-144, 1949.

(Manuscript received December 18, 1959; revised February 20, 1960.)

Note on the Recent Climatic Fluctuation in the United States

H. E. LANDSBERG

*Office of Climatology, U. S. Weather Bureau
Washington, D. C.*

Abstract. The monthly, seasonal, and annual temperature means and the annual precipitation totals are compared for the two 25-year periods 1906-1930 and 1931-1955. The data from rural stations with homogeneous records were used. The temperatures in most places show significant rises. Annual rises of 1.5°F are noted over the Great Lakes region and in the mountain states. The average of 48 stations shows an annual rise of 0.8°F between the two time intervals. For the most part, precipitation changes are probably not significant, but a tendency toward lower totals is noted over the mountain states, parts of the Great Plains, and in a sector west of the Appalachians.

A great deal has been written about the climatic change which has become very notable since the beginning of the 20th century. An excellent review of the literature on this subject as been presented by *Baum and Havens* [1956]. A good deal of the earlier literature has suffered, at least for the analyses of United States data, from the difficulty of assessing the magnitude of the natural climatic change. The reason for this is that most of the readily accessible data are for the city stations with records extending over long periods. The observational quality of these records is good because they were made by full-time, well-trained Weather Bureau observers. However, the problems of continuity and exposure of these stations have become overwhelming. Many have been shifted from city sites to airports and have often undergone several exposure changes. In the cities themselves radical environmental changes have often taken place in the surroundings of the weather stations, such as the large expansions of population with accompanying artificial sources of heat. *Mitchell* [1953, 1956] has published several analyses of the influence of these changes on the records. These problems have led to the establishment of a tentative network of benchmark stations [Swartz, 1956]. The records from these stations are still being subjected to a rigorous analysis for homogeneity. When this is completed more definitive material for the study of climatic changes in the United States will be available.

In the meantime it seemed important to base a preliminary analysis on readily available data from rural regions. The reason for this was the increasing number of inquiries received from scientists in allied disciplines, from industry, and from interested laymen. New 25-year temperature and precipitation averages for the interval 1931-1935 have been compiled in the revised issues of 'Climates of the States' [U. S. Weather Bureau, 1959-1960]. These also list, for comparative purposes, the data for representative stations in the States for the interval 1906-1930. Some of these stations are those which are being considered by the Weather Bureau for climatic bench-mark locations. Others are high-quality climatic stations, which for various reasons did not meet the rigid standards for the bench-mark network. Primary among these reasons was that the future continuity of the record was not secure because the station was privately operated. The past records were about as good as are presently available. Only a single first-order Weather Bureau station, Tatoosh Island, Washington, is among the 48 stations so selected.

The seasonal and annual temperature means and the mean precipitation totals were compared for two intervals, 1906-1930 and 1931-1955. The changes are shown in Table 1 for all chosen stations in the 48 contiguous states. The table also shows the standard deviations σ for the annual temperatures. I owe these values of σ to my colleague, Mr. H. C. S. Thom. The table

TABLE 1. Changes in 25-Year Mean Values of Temperature and Precipitation at Selected U. S. Stations

Station	State	Lat. N	Long. W	Temperature Change, °F					Precip. Change		Remarks on Quality of Record		
				Winter	Spring	Summer	Autumn	Year	σ	t		in.	%
Tatoosh Island	Wash.	48°23'	124°44'	+0.9	+0.8	+0.7	+0.6	+0.8*	1.5	+2.6	+1.17	+1.6	Homogeneous
Park Rapids	Minn.	46°54'	95°03'	+0.7	-0.6	+0.8	+0.3	+0.1	2.1	+0.2	+2.79*	+11.7	Homogeneous
Dickinson E.S.	N. Dak.	46°53'	102°48'	+1.0	-0.9	+0.9	+0.2	+0.5	1.8	+1.1	-0.39	-2.4	Homogeneous
Moscow U.	Idaho	46°44'	117°00'	+1.6	+1.2	-0.3	+1.0	+0.8*	1.8	+2.2	+0.78	+3.7	Homogeneous
Chatham E.F.	Mich.	46°20'	86°57'	+3.2	+1.7	+2.5	+1.2	+2.2*	1.6	+6.8	+1.61	+5.0	Homogeneous
Bozeman	Mont.	45°40'	111°03'	+1.7	+1.2	+1.5	+2.3	+1.7*	1.8	+4.6	-0.89	-4.8	Probably homo- geneous
Yellowstone Pk.	Wyo.	44°58'	110°42'	+1.4	+1.2	+1.4	+1.9	+1.5*	1.7	+4.1	-1.31*	-7.7	Homogeneous
Redfield	S. Dak.	44°52'	98°32'	+2.0	+0.7	+2.4	+1.3	+1.8*	2.5	+3.2	-1.90*	-9.8	Probably homo- geneous
Farmington	Maine	44°40'	70°09'	+1.9	+1.3	+1.5	+1.0	+1.4*	1.3	+5.6	+2.65*	+6.3	Homogeneous
Albany	Oreg.	44°35'	123°04'	+1.0	+1.0	+0.2	+0.8	+0.8*	1.4	+2.6	+1.88	+4.8	Probably homo- geneous
Northfield	Vt.	44°08'	72°40'	+2.1	+2.2	+2.4	+1.8	+2.1*	1.2	+8.4	-0.23	-0.7	Homogeneous
Hancock E.F.	Wisc.	44°07'	89°32'	+1.8	+0.7	+1.2	0.0	+0.8*	1.6	+2.2	-1.95	-6.2	Probably homo- geneous
Franklin	N. H.	43°27'	71°40'	+0.9	+0.7	+1.3	+0.8	+0.9*	1.1	+3.6	+2.35*	+6.0	Probably homo- geneous
Blue Hill	Mass.	43°13'	72°07'	+1.4	+1.1	+1.1	+1.1	+1.2*	0.9	+4.4	+0.23	+0.5	Homogeneous†
Geneva	N. Y.	42°53'	77°00'	+1.8	+0.8	+1.5	+0.5	+1.1*	1.3	+3.5	+0.90	+3.1	Homogeneous
Ames	Iowa	42°00'	93°39'	+0.3	-0.7	+0.9	+0.3	+0.3	2.2	+0.06	+0.93	+3.0	1 major shift
Cream Hill	Conn.	41°52'	73°20'	+1.9	+2.5	+1.5	+0.6	+1.6*	1.2	6.4	-2.32	-5.1	Homogeneous
Logan	Utah	41°45'	111°49'	+0.9	+1.6	+0.9	+1.1	+1.0*	1.2	+4.0	-0.82	-4.6	Probably homo- geneous
Kingston	R.I.	41°29'	71°32'	+1.9	+1.5	+1.3	+0.8	+1.4*	1.2	+5.6	-4.79*	-9.7	1 major shift
Wooster E.S.	Ohio	40°47'	81°56'	+0.8	-0.4	+1.0	-0.2	+0.3	1.1	+1.2	-3.39*	-8.7	Probably homo- geneous
Crete	Nebr.	40°37'	96°57'	+0.8	+0.4	+1.9	+0.6	+0.9*	1.9	+2.4	-0.02	0	Homogeneous
Huntingdon	Penna.	40°30'	78°01'	+0.1	-0.2	+0.8	-0.2	+0.4	1.2	+1.2	-0.02	0	Probably homo- geneous
New Brunswick	N. J.	40°28'	74°26'	+1.7	+0.9	+1.0	+1.0	+1.2*	1.1	+4.8	-0.40	-0.9	Homogeneous
Urbana	Ill.	40°06'	88°14'	+2.0	+1.0	+1.9	+1.0	+1.5*	1.4	+4.8	+1.26	+4	Probably homo- geneous
Whitestown	Ind.	40°00'	86°20'	+1.5	+0.3	+1.0	+0.1	+0.8*	1.3	+2.6	-3.32*	-7.4	Homogeneous
Fallon	Nev.	39°27'	118°47'	0.0	-0.3	-1.2	+0.6	-0.2	1.6	-0.65	+0.53	+11	Homogeneous
Woodstock Coll.	Md.	39°20'	76°53'	+0.1	-0.8	+0.5	-0.5	-0.4	1.1	-1.6	+2.62*	+65	Slight in- homogeneity†

Station	State	Lat. N	Long. W	Temperature Change, °F				Precip. Change		Remarks on Quality of Record			
				Winter	Spring	Summer	Autumn	Year	σ		t	in.	%
Dover	Del.	39°10'	75°32'	+1.4	+0.7	+1.0	+0.6	+0.9*	1.1	+3.6	+3.74*	+8.8	Probably homo- geneous
Fayette	Mo.	39°09'	92°41'	+3.0	+1.1	+1.7	+1.7	+1.9*	1.5	+6.1	-2.68*	-8.0	Probably homo- geneous
Hays	Kans.	38°52'	99°20'	+0.7	+0.5	+2.2	+1.0	+1.1*	1.9	+3.0	+0.48	+2.1	Homogeneous
W. Va.	38°48'	81°21'	+2.0	+1.0	+1.9	+1.3	+1.4*	0.8	+6.8	+0.31	+0.7	1 shift	
2	Colo.	38°28'	107°52'	+1.6	+0.9	+2.1	+1.9	+1.6*	1.5	+5.2	-1.72	-16	Homogeneous
Staunton	Va.	38°09'	79°06'	-0.3	-1.0	+0.4	-0.4	-0.4*	0.9	-2.1	+0.65	+1.8	Some slight moves
Greensburg	Ky.	37°16'	85°30'	+1.6	+1.2	+1.8	+0.5	+1.3*	1.1	+5.2	-1.82	-3.3	Probably Homo- geneous
Fayetteville	Ark.	36°05'	49°10'	+0.2	-0.5	+0.6	-0.7	-0.1	1.1	-0.03	+1.54	+3.5	Probably homo- geneous
Grand Canyon	Ariz.	36°03'	112°08'	+1.2	+2.0	+2.3	+2.3	+1.9*	1.2	+7.6	-2.07*	-12.1	Homogeneous
Chandler	Okla.	35°42'	96°54'	+1.2	-0.1	+0.2	+0.1	+0.3	1.2	+1.2	+0.57	+1.7	Some shifts
Salisbury	N.C.	35°40'	80°29'	-0.2	+0.6	+1.2	-0.5	+0.3	0.9	+1.6	-2.47*	-5.0	Probably homo- geneous
Lewisburg E.S.	Tenn.	35°27'	86°48'	0.0	-0.4	+0.5	-0.7	0.0	1.0	0	-1.55	-2.9	1 major shift
Winthrop Coll.	S.C.	34°57'	81°03'	+0.6	+0.3	+0.4	+0.4	+0.5*	0.8	2.6	-1.03	-2.2	Probably homo- geneous
Indio	Calif.	33°43'	116°13'	-0.6	+0.4	-0.5	+0.4	-0.1	0.9	-0.5	+0.09	+2.4	Probably homo- geneous
Mississippi S.U.	Miss.	33°27'	88°47'	+0.8	+0.6	+0.4	+0.2	+0.5*	0.9	+2.6	-6.45*	-11.7	Some shifts
Milledgeville	Ga.	33°05'	83°14'	0.0	-0.8	-0.3	-0.1	-0.4*	0.9	-2.1	-4.42*	-9.0	Probably homo- geneous
Greensboro	Ala.	32°42'	87°35'	+2.0	+1.2	+1.5	+1.2	+1.5*	0.8	+7.8	+0.14	+0.2	Probably homo- geneous
Calhoun E.S.	La.	32°31'	92°20'	+1.2	+1.3	+1.4	+1.1	+1.2*	0.9	+6.3	+0.45	+0.9	Homogeneous
N. Mex. Ag. C.	N. Mex.	32°17'	106°45'	-0.5	+0.5	0.0	-0.2	-0.1	1.1	-0.4	0.0	0.0	Homogeneous
Beeville	Tex.	28°27'	97°42'	+1.1	+0.5	+0.1	+0.4	+0.6*	1.2*	2.4	-1.04	-3.5	Probably homo- geneous
St. Leo's Abbey	Fla.	28°21'	82°15'	+1.2	+0.9	+1.2	+0.8	+1.1*	0.8	7.3	+1.05	+1.9	Homogeneous

* See text.

† J. M. Mitchell, Jr., assisted in determining the correct values for this station.

‡ For a suspicion of an inhomogeneity see *Landsberg, Mitchell, and Crutcher* (1959).

TABLE 2. Summary of Tendency of Temperature Changes at 48 Stations in the Contiguous States

Season	Number of Stations Showing Change		
	Positive	Negative	Zero
Winter	41	4	3
Spring	36	12	0
Summer	43	4	1
Autumn	38	9	1
Year	40	7	1

Range of Annual Change, °F	Number of Stations
-0.5 to -0.1	7
0	1
+0.1 to +0.6	7
+0.6 to +1.0	12
+1.1 to +1.5	13
+1.6 to +2.0	6
+2.1 to +2.5	2

also shows t for the two mean annual temperature values, as obtained from Student's t -test. All values of temperature and precipitation

changes which are significant differences at the 95 per cent probability level have been marked with an asterisk. The quality of the record has been judged solely on the basis of the publication histories [*U. S. Weather Bureau, 1956*]. Further analysis may well change this judgment. With this qualification, the results, especially the temperature comparisons, are quite notable. Forty of the 48 stations show an increase in temperature—overwhelming evidence of a tendency toward warming. The t -test indicates significant for 33 of these but of the 7 stations which had negative change for the annual mean only 2 are barely significant. In 16 positive cases the change between the two means actually exceeds standard deviation. Winter and summer are primarily the seasons of positive trend; it is not so pronounced in spring and autumn. A summary of these tendencies is shown in Table 2.

The approximate distribution of these changes over the country for winter, summer, and the total year is shown in Figures 1 to 3. The area with highest rises is primarily situated over the Great Lakes region. In the annual values the

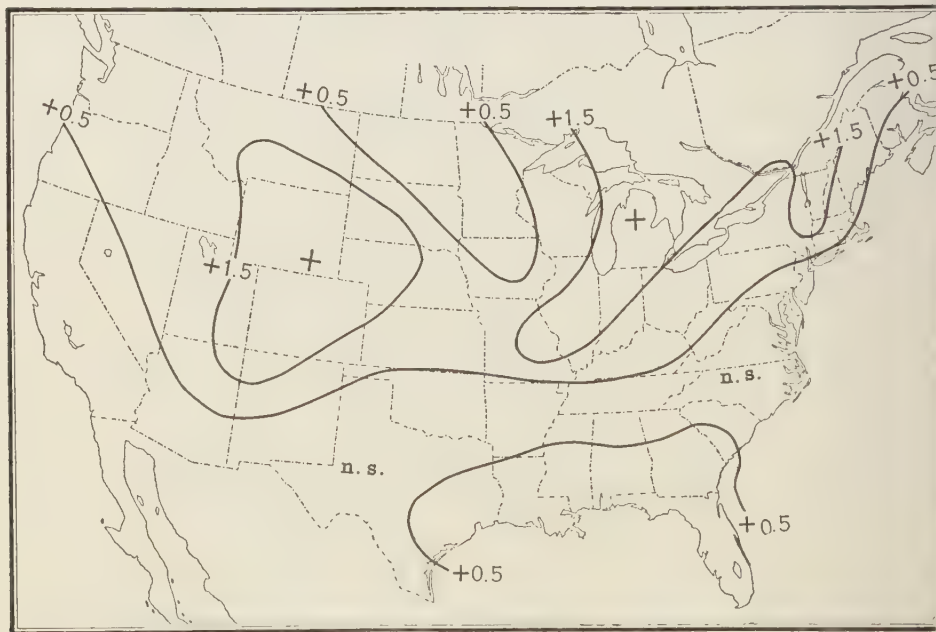
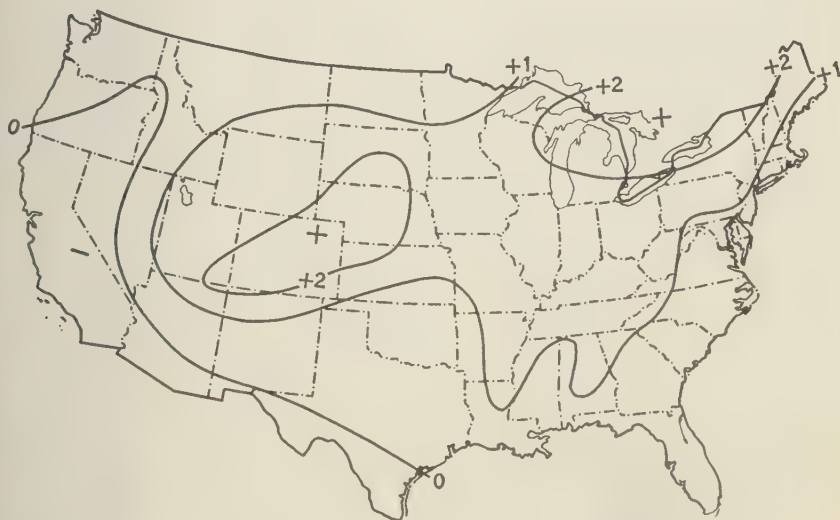


Fig. 1. Change of mean annual temperature (°F) from interval 1906-1930 to 1931-1955 (n.s.: not significant).



g. 2. Approximate change of mean winter temperature ($^{\circ}\text{F}$) from interval 1906-1930 to 1931-1955.



g. 3. Approximate change of mean summer temperature ($^{\circ}\text{F}$) from interval 1906-1930 to 1931-1955.

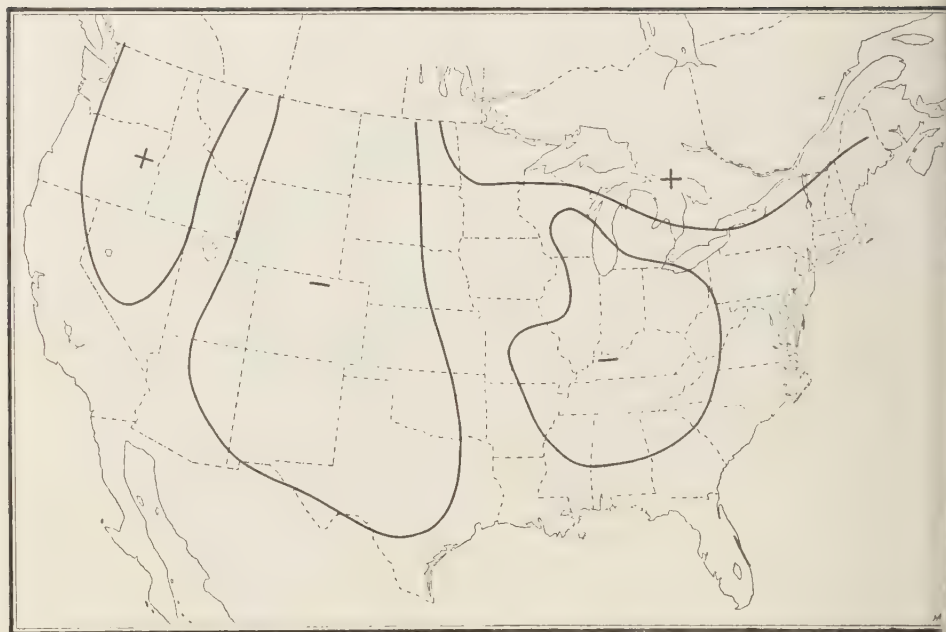


Fig. 4. Tendency of precipitation. Annual totals from interval 1906-1930 to 1931-1955 (most individual values not statistically significant).

is also a rise in the Rocky Mountain region, which has its primary origin in higher summer temperatures. The general rise did not occur in the Southwest, and the change was negative for an area in the southern Appalachians. Some uncertainty is, of course, inherent in the loose network of stations.

If the values of annual temperature change are averaged by zones, it is noted that the higher latitudes have the larger change, as follows:

Stations	>40°N	Average	+1.0°F
in Zone:	35-40°N	Change	+0.7°F
	<35°N		+0.5°F

This is in line with the findings, in other regions of the northern hemisphere, that the warming has been most pronounced in the higher latitudes. For a country-wide average, unweighted by the area represented by the various stations, one obtains a value of 0.8°F.

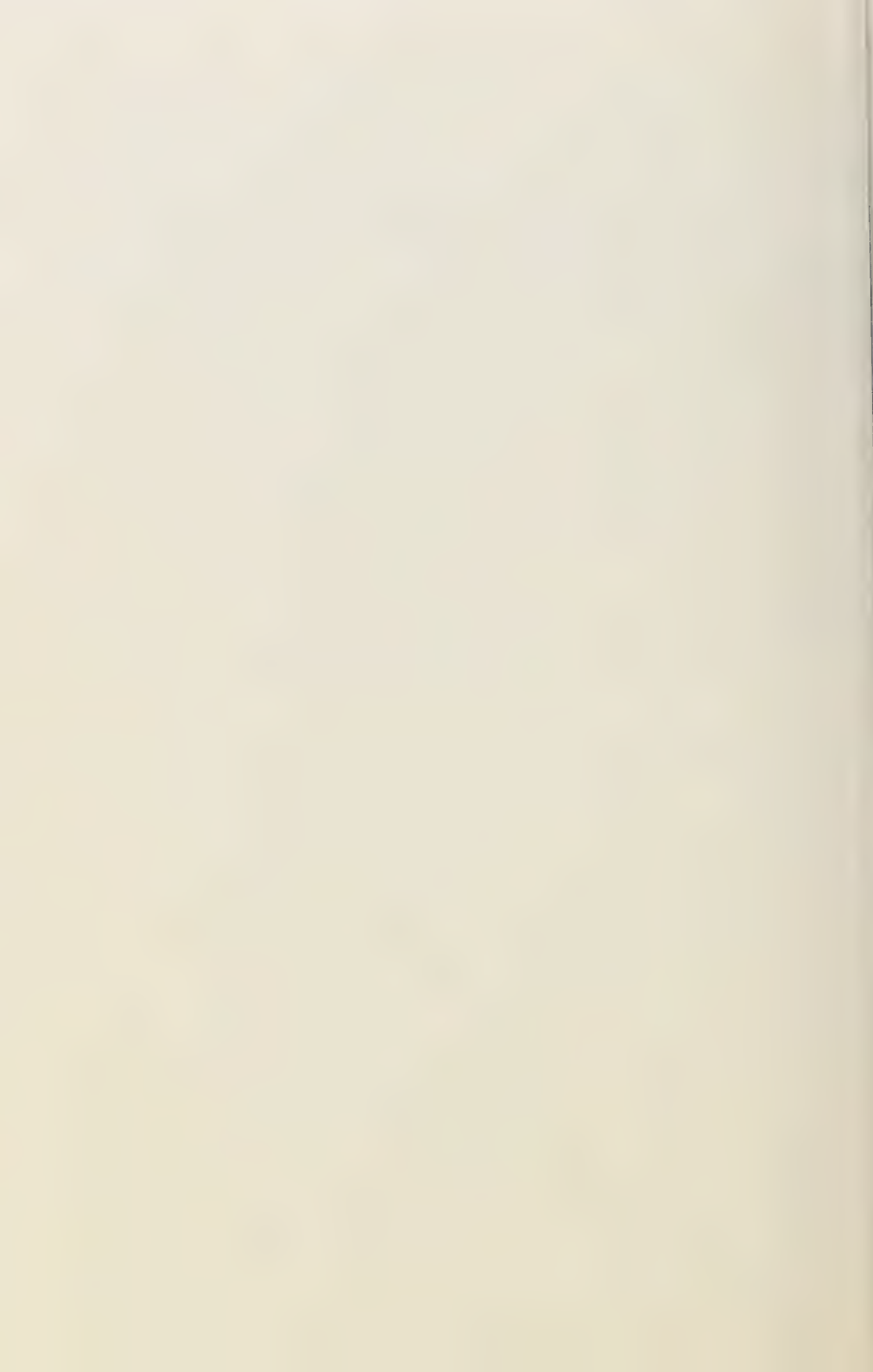
Except for a few stations, the changes of the precipitation totals between the two 25-year intervals are relatively small. Most of them stay

between ± 10 per cent. Even though some of the values are statistically significant changes at the 5 per cent level, as indicated in Table one should not overestimate this because techniques for sampling precipitation are poor. If the sign of the tendency is plotted, we see that there are two areas in the United States where reduction in rainfall was prevalent during the period (Fig. 4). The Great Plains, Rocky Mountains, and Southwest show this tendency. Within two major droughts in the second interval, this is to be expected. The droughts of the mid-thirties and the early fifties are well remembered. Actually it is more surprising that, on the whole, rainfall held up rather well in the second interval. The higher summer temperatures might be more important as indicators of water loss by evapotranspiration than the rainfall variations. Until we have a better estimate of sampling variations, it would seem quite reasonable to state that no major trend in the rainfall conditions of the contiguous States of the Union is noticeable.

REFERENCES

- Am, W. A., and J. A. Havens, Recent climatic fluctuations in the Maritime Provinces, *Trans. 1st N. Am. Wildlife Conf.*, 436-453, 1956.
- Andersberg, H. E., J. M. Mitchell, Jr., and H. L. Bratcher, Power spectrum analysis of climatological data for Woodstock College, Maryland, *Monthly Weather Rev.*, 87, 283-297, 1959.
- Mitchell, J. M., Jr., On the causes of instrumentally observed secular temperature trends, *J. Meteorol.*, 10, 244-261, 1953.
- Mitchell, J. M., Jr., Link warmer climate to city growth, *Heating, Piping Air Conditioning*, 28, 92-95, 118-120, 1956.
- Swartz, J. R., A climatological bench-mark network, *Weatherwise*, 9, 88-89, 106, 1956.
- U. S. Weather Bureau, Climates of the States, *Climatography of the United States*, 60-1 to 50, Washington, variously issued, 1959, 1960.
- U. S. Weather Bureau, *Substation History (by states) Key to Meteorological Records Documentation No. 1.1* Washington, variously issued, 1956.

(Manuscript received February 8, 1960.)



Environmental Photometry in the Antarctic

JOHN M. HOOD, JR.

*U. S. Navy Electronics Laboratory
San Diego 52, California*

Abstract. A series of photometric measurements are presented which were made in November 1958 in transit to and in the McMurdo Sound area, Antarctica. Included are luminance distributions of clear and overcast skies, several measurements of air clarity, the diffuse/total illuminance ratio, and luminances of ice and sea surface details under a typical condition of weather and lighting. A photographic technique is described for measuring meteorological range or air clarity. A value of 73.9 nautical miles for a contrast transmittance of 0.02 on a clear, cloudless day was found. Applications of Fritz's theory to the overcast sky data are discussed.

INTRODUCTION

The immediate purpose of the measurements in the Antarctic was to provide optical environmental data to be used in the specifications for ice reconnaissance television. The data gathered are of a fundamental nature, however, to provide information of use in photography, ocean surveying, cartography, navigation, and meteorology. The principal value of the illuminance charts is in the prediction of visibility of objects in the natural environment. All the measurements were made with cameras, battery-powered photoelectric photometers, or simple visual photometers. Many of the measurements were made from aboard the U. S. Navy icebreaker *U.S.S. Glacier* (AGB-4). The devices used for making these measurements included a General Electric Luckiesh color visual photometer with the daylight color corrected to the internal standard; a photoelectric small-field photometer manufactured by the Photo Research Corporation of Hollywood, California; and a special high-sensitivity photometer designed and built by Akin [1958] of the U. S. Navy Electronics Laboratory. In addition to these photometers, 35-mm film negatives were made with a hand-held K-20 aerial camera. These films in conjunction with the photometers provided a wide selection of environmental luminances in the field.

The records made are not complete descriptions of the environment, and the time span

of the total experimental work does not provide any clues to annual variations in conditions; but the measurements are representative of conditions which commonly prevail during the late spring or early summer.

EXPERIMENTAL PROCEDURE

In providing an accurate picture of the environment, in photometric terms, an old and well-tried technique was used. Photographs of the environmental details of interest were made with the aerial camera, and photographs of an externally located gray scale were included on each roll of film to be later analyzed with the microdensitometer. When an external gray scale is used, most of the difficulty associated with internal scattering in the lens and body of the camera is eliminated and precise control of processing is unnecessary. Accordingly, a series of six painted plaques about 9 inches square were mounted on the after rail of the ship's hangar roof deck. These had a previously measured scale of reflectance values ranging from 10 to 80 per cent. This provided a brightness scale of about 8 to 1 in each of the calibration photographs. Using one of the middle grays for determining the normal exposure, four photographs were made of the scale with a three-stop separation between exposures. With shutter speed error an exposure range of about 500 to 1 was obtained. Densitometry of the 24 steps in the four negatives provides, with some curve fitting, the characteristic curve of the film.

At the time the photographs were being made one of the photometers was used to measure the luminance of certain prominent features of the scenes. In this case a flat snow-covered area and an area of open water in the various leads and polynyi were chosen. This also provided a double check on the validity of the characteristic curve determination, since the ratio of the luminances of these areas should be the same whether measured with a visual or an electronic device or determined from the characteristic curve of the film. Primarily, of course, these measurements provided the absolute scale of luminances for the densitometered details of the film.

Photographs were taken during two flights of the ship's helicopter and on two occasions from aboard the icebreaker. Additional photographs were made ashore at the McMurdo Sound base to increase the variety of landscape detail available on calibrated film. Some of these photographs were analyzed to provide information on atmospheric clarity.

Sky luminance distribution was measured using the three photometers from the roof of the ship's hangar deck and from the ice in the vicinity of the moored ship.

Measurements of the atmospheric clarity or 'meteorological range' were made by two different techniques. The first involved the use of a very sensitive small field photometer which looked into a black cavity at a known distance and detected the luminance of the intervening column of air. Simultaneously, the luminance of the sky near the horizon was measured immediately behind the black cavity. If the so-called equilibrium luminance existed at the point measured in the sky, and if the column of air from the cavity to the photometer was illuminated in the same fashion as the column of air stretching out from the instrument to the horizon, the two measurements yielded a value for meteorological range. Meteorological range, as introduced by Duntley [1948a] and used by Middleton [1952], is specifically defined in terms of the beam attenuation coefficient. Graphical methods for using meteorological range to find the visibility ranges of actual objects are described by Duntley [1948b].

In the second technique for obtaining values of meteorological range the contrast reduction

apparent in the photographic negatives of distant mountains was used. These details were analyzed with a microdensitometer to obtain the luminance values and thus the meteorological range.

CALIBRATION OF PHOTOMETERS AND FILTERS

All photometers and filters were calibrated against a portable diffuse source (Standard Brightness Source, Photo Research Corp., Hollywood, Calif.) having a color temperature of 2360°K and a luminance of 91 foot-candle. This source was compared on several occasions with National Bureau of Standards lamps and found to be stable and reliable as a standard source for field calibration.

The color correction filter used in the internal field of the Luckiesh-Taylor meter was the EK Wratten No. 86, which shifts the color temperature of a 5500°K source to 2360°K. The photometric transmission of this filter was determined by measurement to be 0.549.

TABLE 1. Photometric Detail of
Antarctic Ice Pack
(Nov. 7, 1958; 1300 local apparent time;
174°24'E, 73°54'S)

Description	Luminance (ft-L)
<i>Photograph 2</i>	
Water in wake	730
Small open-water area in wake	550
Highlight on ice block	5640
Highlight on ice block	4270
Flat snow-covered floe	2300
Shadow area in wake	380
Shadowed side of ice block	650
<i>Photograph 3</i>	
Horizon sky	1750
Rippled snow-covered floe (up sun)	1700
Shadow detail in pressure ridge	279
Smooth snow-covered floe	2300
Shadow detail in pressure ridge	410
Rippled snow-covered floe (up sun)	1600
<i>Photograph 4</i>	
Side of ship (27%) (down sun)	1320
Open water in polynya	360
Black ice (newly congealed)	960
Flat snow-covered floe*	1480
Shadow of helicopter*	430

* Values used to compute diffuse/total illuminance ratio.



Fig. 1. Sample of photometrically calibrated pictures of sea ice in early spring. (Date: November 7, 1958. Local apparent time: 1300. Location: $174^{\circ}24'E$, $73^{\circ}54'S$.)

Surface Description	Luminance, ft-L
1. Open water	297
2. Black ice	450
3. Snow-covered ice	2300
4. Vertical side of ship	1000
5. Snow-covered floe	2830

This value was established by the use of a photoelectric photometer (Spectra-Spot Photometer, Photo Research Corporation, Hollywood, Calif.) having a photopic spectral response characteristic, and thus the necessity of forming heterochromatic visual matching of photometric fields was avoided. Alternate readings with and without the filter in front of the objective lens of the photometer of a uniform, hazy horizon sky (color temperature about $5500^{\circ}K$) produced the photometric transmittance ratio directly.

RESULTS

Luminances of environmental detail. Fig. 1 is a sample of the approximately 100 photographs which were made of the antarctic environment. The details measured are marked and identified in the figure title. Additional details measured, but not photographically illustrated in this paper, are listed in Table 1 to demonstrate the ranges of values in luminance. The photometric data which were collected to establish the absolute scale of luminances are listed in Table 2, which also shows

TABLE 2. Photometric Measurement for Calibration of Film

Date	Instrument	Snow, ft-L	Water, ft-L	Ratio
1958				
Nov. 7	L-T meter	2200	330	6.7
Nov. 7	L-T meter	2300	300	7.7
Nov. 11	Spectra	4500	700	6.4
Nov. 7	K20 camera	7.9*

* Average from three sets of measurements in two photographs.

the computed ratios of snow-covered ice water as measured with the photometers as computed from the densitometry of the responding photographs. From measurements made of the helicopter shadow and an immediately adjacent flat snow area, the diffuse/illumination ratio was found to be

$$\text{diffuse/total } E \text{ ratio} = 0.29$$

The air was clear and the sky cloudless in these photographs were made, and the sun at an elevation of about 31°.

Luminance distributions. Luminance in

TABLE 3. Data for Figures 2, 3, 4, and 5

Fig.	Conditions	Elevation	Azimuth Relative to Sun				
			0°	± 45°	± 90°	± 135°	± 180°
			foot-lamberts				
2	Date: Nov. 3, 1958	0° sea	not measured				
	Local apparent time: 0915	0° sky	7500	2000	1000	1700	1000
	Location: 175°30'E, 54°42'S	15°	5500	1500	650	1350	1000
	Sun elevation: 41°	30°	4200	1000	410	1000	1000
	Sky description: Clear	45°		825	370	540	1000
	Ground description: Open sea, no ice	60°		800	450	390	1000
		75°		680	525	420	1000
		90°	500	520	540	560	1000
3	Date: Nov. 7, 1958	0° sea	5800	2000	2900	3200	4000
	Local apparent time: 1900	0° sky	7000	3000	3000	...	5000
	Location: 169°50'E, 73°25'S	15°	2500	1450	1050	1300	1000
	Sun elevation: 10°45'	30°	800	650	500	600	1000
	Sky description: Clear	45°	600	480	570	400	1000
	Ground description: Ice, no wind	60°	500	420	350	350	1000
		75°	440	400	360	360	1000
		90°	580	420	280	320	1000
4	Date: Nov. 9, 1958	0° sea	2810	2480	2900	1240	1000
	Local apparent time: 1535	0° sky	9100	3970	3140	2070	1000
	Location: 170°15'E, 76°33'S	15°	7440	3310	2900	2150	1000
	Sky luminance 2° from the sun:						1000
	17,000	30°	8270	3470	2650	1410	1000
	Sun elevation: 22°30'	45°	3720	2070	2560	1490	1000
	Sky description: Broken stratus	60°	2810	1820	1740	580	1000
	Ground description: Ice, no wind	75°	1410	1000
		90°					1000
			True Azimuth				
		Elevation	180°	235°	270°	315°	0°
5	Date: Nov. 5, 1958	0° sea	430	430	720	500	500
	Local apparent time: 1330	0° sky	1400	2100	1900	1700	0°
	Location: 177°48'E, 66°54'S	15°	1700	1900	1800	1800	0°
	Sun azimuth: 332°	30°	1900	1900	1800	2100	0°
	Sun elevation: 35°30'	45°	2000	2000	1900	2400	0°
	Sky description: Stratus overcast	60°	2200	2200	2000	2400	0°
	Ground description: Ice, no wind	75°	2300	2300	2200	2000	0°
		90°	2600	2500	2400	2300	0°

TABLE 4. Data for Figures 6, 7, and 8

Conditions	Elevation	Azimuth Relative to Sun				
		0°	±45°	±90°	±135°	±180°
		foot-lamberts				
Date: Nov. 10, 1958	0° sea	4540	4130	4130	4130	4550
Local apparent time: 1020	0° sky	4540	2480	3310	3470	4300
Location: 166°15'E, 77°40'S	15°	4630	3960	3390	3800	4960
Sun elevation: 30°15'	30°	7850	4540	4130	4300	5120
Sky description: Overcast	45°	5780	4960	4460	4300	5040
Ground description: Ice, no wind	60°	5130	4880	4380	4460	4960
	75°	4750	4650	4450	4550	4700
	90°	4550	4540	4550	4550	4620
Date: Nov. 12, 1958	0° sea	16,540	7440	6200	7030	6200
Local apparent time: 0910	0° sky	4300	7030	4710	6200	6200
Location: 166°15'E, 77°40'S	15°	4960	2480	3640	5050	4140
Sky luminance 2° from the sun: 4135	30°	2230	1410	2480	2150	3310
Sun elevation: 27°30'	45°	1570	1080	990	1080	1490
Sky description: Thin cirrus	60°	870	830	700	790	740
Ground description: Bay ice, 30-knot wind	75°	780	750	700	620	680
	90°	not measured				
Date: Nov. 14, 1958	0° sea	10,380	4920	5460	5560	5190
Local apparent time: 0940	0° sky	3420	4370	3100	4010	4370
Location: 166°15'E, 77°40'S	15°	2730	1170	890	960	1280
Sky luminance 2° from the sun: 2732	30°	1600	690	600	680	690
Sun elevation: 30°	45°	890	670	510	500	490
Sky description: Clear	60°	620	620	400	380	440
Ground description: Ice, no wind	75°	530	440	360	450	380
	90°	420	...	370	360	...

ments of the sky and, in some cases, the ice or the sea near the horizon were made on seven different occasions. These measurements are shown as polar iso-luminance plots in Tables 3 and 4 and in Figures 2 to 8. The azimuth reference, location, and local apparent time are noted for each set of data as well as incidental notation concerning weather, locale, and sun position. The units of measurement are foot-lamberts.

Atmospheric clarity. Measurements of atmospheric clarity were computed in terms of meteorological range. The relationship of this term to the more familiar beam attenuation coefficient is shown as a special case of the equation for contrast attenuation [Duntley, 1948a], where

$$C_x = (1/50)C_0 = C_0 \exp(-\beta v) \quad (1)$$

$$\ln 50 = \beta v$$

in which C_x is the apparent contrast of an object with the background horizon sky at distance v equal to the meteorological range, C_0 is the inherent contrast, and β is the attenuation coefficient in units of reciprocal length. The photoelectric measurements of meteorological range when the black cavity is used at a relatively short range are computed from the equation [Duntley, 1952]:

$$v = 3.912X/2.3026$$

$$\cdot \log [(B_h - B_0)/(B_h - B_x)] \quad (2)$$

where x is the distance of the black cavity, B_h is the luminance of the horizon sky background (assumed equivalent to the equilibrium luminance for the selected path of sight), B_0 is the inherent luminance of the black cavity, and B_x is the apparent luminance of the black cavity at distance X .

The photographic technique used to determine atmospheric clarity requires that the con-

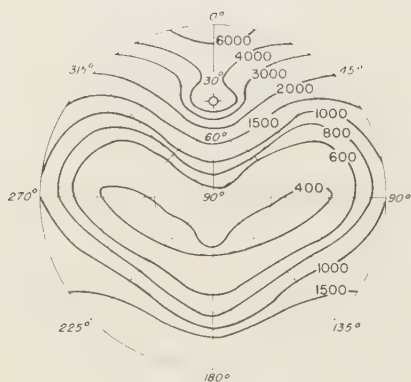


FIG 2

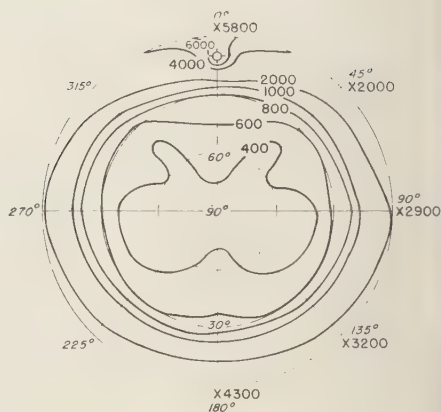


FIG 3

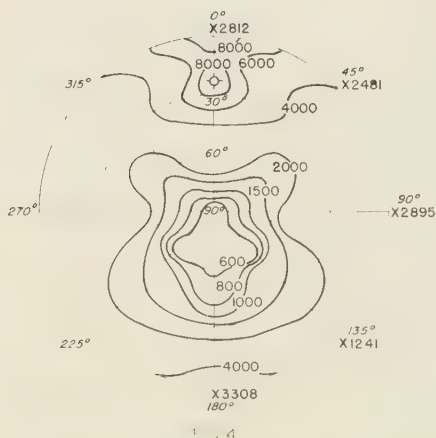


FIG 4

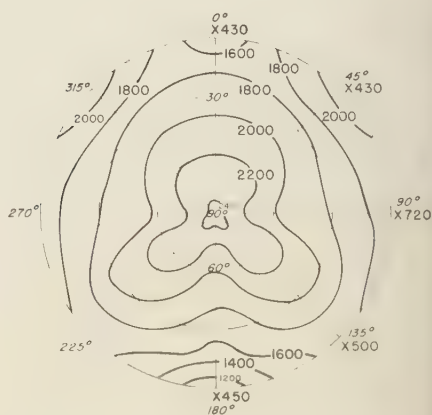


FIG 5

Figs. 2-8. Iso-luminance polar plots of light distributions of the antarctic sky. Note the sea-ice and sea-luminance data measured just below the horizon and recorded just outside the zero elevation grid circle. All data presented have the units of foot-lamberts.

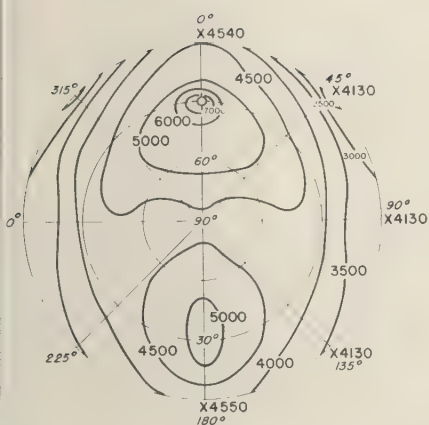


FIG. 6

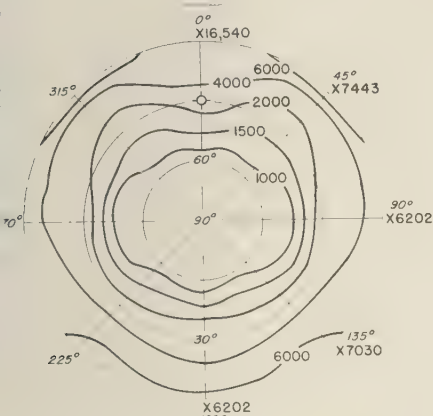


FIG. 7

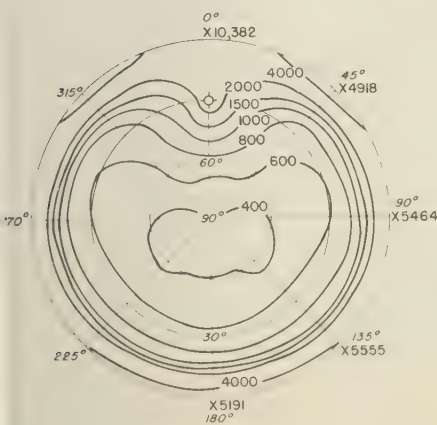


FIG. 8

trast attenuation occurring for a particular target be sufficient to be easily recorded within the range of variation of film densities obtainable in normal photography. A slightly different form of equation 2 is used in this situation. This equation, which states that luminance differences are exponentially attenuated, was used in the form

$$(\Delta B)_x = (\Delta B)_0 \exp(-3.912X/v) \quad (3)$$

where the subscript x refers to the range of the distant target and the subscript 0 indicates the zero range or the inherent luminance difference. In the experimental measurements, Mt. Discovery, 35.3 miles away, was used as the distant target. A hill close to the McMurdo Sound base was used for the 'zero' distance measurements, and the assumption was made that the lighting and composition of the two targets were very similar. This is a reasonable assumption, since both targets were the west sides of partially snow-covered black volcanic cinder cones.

Calculations of v from both techniques are shown in Table 5. The estimate of error for the photographic result was derived from an interpretation of the variance of the gray-scale densitometry data used to construct the characteristic curve for the film. The estimated probability is 0.9 that the range lies between 56 and 88 nautical miles.

DISCUSSION AND CONCLUSIONS

The results presented form a body of data

TABLE 5. Meteorological Range Measurements

Date	Time (-12 zone)	Method	Conditions	Met. Range, naut. mi.
1958				
Nov. 8	1630	Photo- electric	Clear	59
Nov. 10	1045	Photo- electric	Blowing snow, partial white- out	13
Nov. 10	1235	Photo- electric	Blowing snow, partial white- out	14
Nov. 15	1200	Photo- graphic	Very clear	73.9

on the sunlit antarctic environment with clear skies. Within a given scene and at any particular time the range of luminances in ground details was found to be about 19 to 1.

The success in measuring meteorological range with simple photographic materials and equipment suggests that this method should be more widely employed by field investigators where inaccessibility of the area often prevents the establishment of more elaborate instrumentation. The range of 73 miles for meteorological range compared with the theoretical 190 miles for Rayleigh scattering in pure dry air indicates the presence of particulate constituents.

Study of the limited data on luminance distributions did not indicate that there were measurable effects of the presence or absence of the highly reflective ice and snow on the over-all luminance of the clear, cloudless sky. Definitive work will be conducted in the future in an attempt to establish the effects of this secondary lighting on the atmosphere.

Fritz's [1958] techniques for describing the distribution of light from overcast skies and the effects of the terrain reflectance were applied to the data of Figures 5 and 6 to determine the values of h/L for the cloud layers present during those periods. He defines h as the thickness of the cloud layer and L as the mean free path length of photons between scattering events by spherical particles. High values of this ratio indicate thick or dense clouds. For these calculations the terrain reflectance (solid layer of sea ice) was estimated to be 0.8.

Values used in the calculations for the illuminance of the top of the cloud layers were taken from Brown's *Natural Illumination Chart*, [1952]. The best estimate possible from the data shows, for Fig. 5:

$$10 < h/L < 50$$

and for Fig. 6:

$$0.1 < h/L < 1.0$$

Casual inspection of the iso-luminance plots reveals effects of the sun's presence in Figure 6 and the lack of it in Figure 5.

REFERENCES

- Akin, R. H., A portable, transistorized, photomultiplier photometer, *J. Opt. Soc. Am.*, **48**, 238 1958.
- Brown, D. R. E., Natural illumination charts *U. S. Navy BUSHIPS Rept. 374-1*, September 1952.
- Duntley, S. Q., The reduction of apparent contrast by the atmosphere, *J. Opt. Soc. Am.*, **38** 179-191, 1948a.
- Duntley, S. Q., The visibility of distant objects *J. Opt. Soc. Am.*, **38**, 237-249, 1948b.
- Duntley, S. Q., The visibility of submerged objects, Visibility Laboratory, MIT, final report ONR contracts N5ori-07831 and N5ori-07864 and BUSHIPS contract NObs-50378, 31 August 1952.
- Fritz, S., Illuminance and luminance under overcast skies, *J. Opt. Soc. Am.*, **45**, 820-825, 1955.
- Middleton, W. E. K., *Vision Through the Atmosphere*, Univ. Toronto Press, Toronto, 1952.

(Manuscript received December 14, 1959.)

The Thermal Conductivities of Ocean Sediments

E. H. RATCLIFFE

*National Physical Laboratory
Teddington, Middlesex, England*

Abstract. As a part of the measurement of heat flow through the ocean floor, the thermal conductivities of samples of sediment from the Pacific, Atlantic, and Mediterranean areas have been determined in the laboratory by a steady-state method. Average values over a wide range of water content are found to depend more on water content than on solid phase constituents, and conductivities can be read from a diagram if the amount of contained sea water or the wet density of the sediment is known. A graph is included, showing the conductivities of wet, granular materials other than ocean sediment.

INTRODUCTION

Heat flow from the interior of the earth outward through the ocean floor can be estimated if the conductivities and the temperature gradients of the sediments are known. The first estimation of oceanic heat flow by measurements of this kind was made possible by the work of the 1947 Swedish expedition in the *Albatross* [Pettersson, 1949]. The present paper is concerned with thermal conductivity measurements on sediment cores supplied in airtight containers by various expeditions.

Initial steady-state conductivity measurements at this laboratory were carried out by Mr. D. W. Butler on red clays collected in 1950 by the mid-Pacific expedition of the Scripps Institution of Oceanography [Revelle and Maxwell, 1952]. Subsequently the writer made further measurements, on Atlantic sediment cores from a 1952 *R. R. S. Discovery II* expedition [Bullard, 1954], on Mediterranean sediments in 1955, and on a few samples of sediments taken in the southeast Pacific (stations 10, 29, and 32 of the Scripps Institution *Downwind* expedition) [Natl. Phys. Lab. Report, 1958; Von Herzen, 1959]. The latter measurements were made so that the steady-state results might be compared with those obtained from the transient method employed by Von Herzen.

The result of the above work was to show that the major factor in fixing the conductivities was the amount of contained sea water, and that variations in solid phase constituents were relatively unimportant. It therefore seemed pos-

sible to treat ocean sediments collectively, whether of organic or inorganic origin, and from the following graphs and a diagram conductivity assessments can rapidly be made. Measurements on other wet granular materials were also made, and a few results are given for comparison.

APPARATUS AND MEASUREMENT

The apparatus used consisted fundamentally of a flat, circular, metal hot plate, containing an electrical heater, and a pair of water-cooled cold plates (Fig. 1). The plate faces were lapped flat. Thin ebonite rings, externally of the same diameter as the plates, containing ocean sediment or other wet granular material, were positioned as shown. Plate temperatures were measured by fine thermocouples inserted into small holes drilled parallel and near to the plate surfaces. A 120-volt battery was used as energy source; current and voltage were measured potentiometrically. Glass-wool insulation reduced edge losses to a small amount. A vertical load was applied to the top cold-plate assembly. The conductivity values were derived from the usual, steady-state equation, after allowing for heat flow through the ebonite rings. The apparatus was constructed in several sizes: plate diameters approximately 3, 5, and 7½ cm (Fig. 2). The smaller sizes were used for ocean sediment, and, since the plate diameter did not exceed the core diameter from which the samples were sliced, unnecessary manipulation of the sediment was avoided. The apparatus with 7½-cm plates was used for other wet granular materials, such as

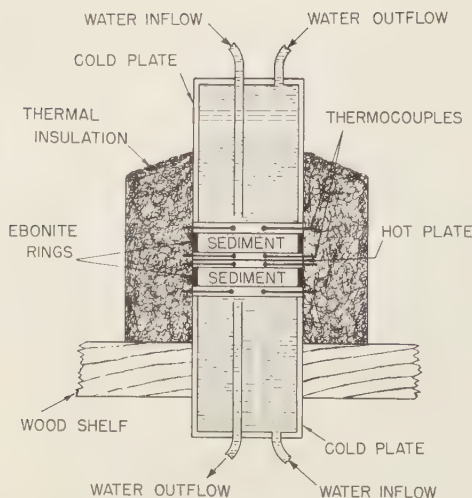


Fig. 1. Disk apparatus (schematic). Thermocouple and heater leads not shown.

copper powder, quartz sand, and diatomaceous earth with added water. Evaporation was prevented by greasing the joints between rings and plates. The accuracy of measurement was assessed at about ± 3 per cent.

The bulk densities of the specimens were determined after test. The specimens were then oven dried at about 100°C and the water content evaluated. In the case of many of the ocean sediments, the chlorine content of dried samples was determined, and the original percentage of sea water in the sample when it was collected was calculated from chlorinity data (assuming that all the chlorine in the sediment was derived from sea water present at the time of collection); thus losses by evaporation could be assessed. Comparison with water-content values obtained by oven drying showed that the chlorine test gave calculated water contents within 1 per cent of those obtained by the direct drying method. The formula used for the calculation was

$$\% \text{ water (wet wt.)} = 50.8C / (1 + 0.508C)$$

where C is the percentage of chlorine by weight on the dry weight of the sample, and the determination is based on the assumption of 3.45

per cent by weight of total salts in sea water and 1.9 per cent chlorine.

CORRECTIONS AND RESULTS

Water loss and temperature coefficient. Most conductivities were determined at mean specimen temperatures between 20°C and 25°C , and these, plotted against water content in Figure 2, lie near a smooth curve, even when the specimen has obviously lost water (often apparently due to migration under gravity during laboratory storage, as in the case of the Atlantic specimen shown, with 20 per cent water content). Hence the conductivity of the sediment before it lost water can always be deduced from the graph if its original water content is known. The shape of the curve for water contents less than 30 per cent, representing mainly an artificial condition for ocean sediment, is not accurately known, but other data for wet, granular material lead one to assume an inflexion in the curve commencing at about this water content.

A correction is needed to reduce the conductivities to deep ocean-bottom temperatures of a few degrees centigrade, and the corrected curve is shown dotted in Figure 3. The temperature coefficient has been calculated from unpublished data by Butler, who measured specimens of Pacific sediments of differing water contents at about 4°C , in a disk apparatus shielded from heat gain by a low-temperature surround, and found approximately a 6 per cent reduction in conductivity from 25°C to 4°C in each case. A

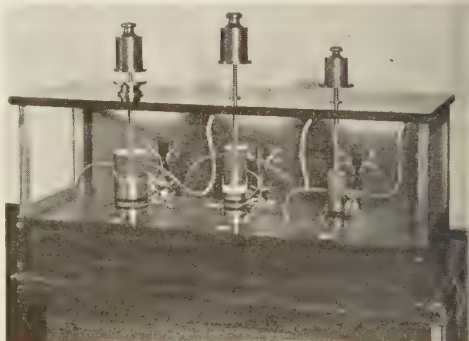


Fig. 2. Cabinet containing three disk thermal conductivity apparatus of similar type but of different sizes.

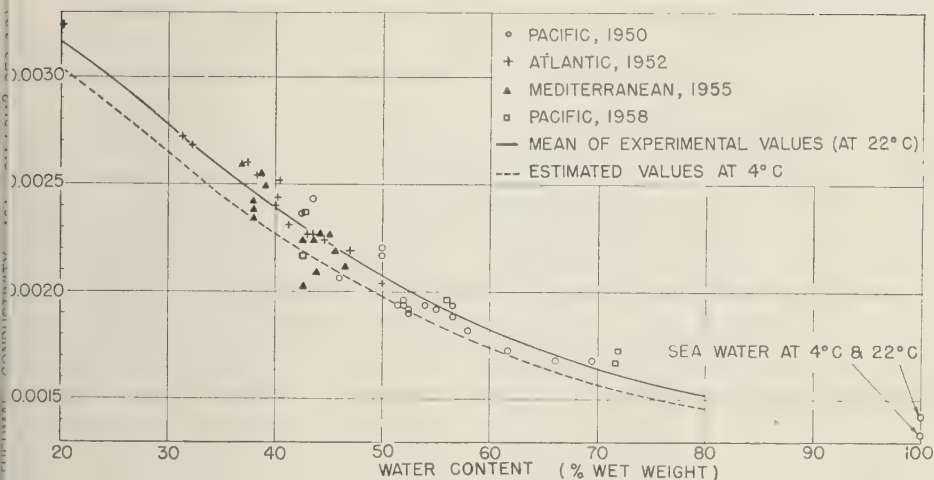


Fig. 3. Ocean sediment. Thermal conductivity (at 1 atm) versus water content by weight.

ilar order of decrease is evident for sea water and pure water [Nukiyama and Yoshizawa, 1934; Challoner and Powell, 1956].

The foregoing values are shown in Table 1. The sea-water points in Figure 3 have been only adopted from the Japanese [who gave $k = 0.4747(1 + 0.00224t)$ over the range 10°C to 71°C , where K is the thermal conductivity in cal/m² hour $^{\circ}\text{C}$, and t the temperature in

$^{\circ}\text{C}$] but the 22°C point has been raised slightly because their results on pure water at this temperature are lower than the more recent (1956) determinations at this laboratory.

Salinity and pressure. Since the difference in the conductivities of pure water and sea water is only a few per cent, a conductivity correction for salinity variations from sediment to sediment is unnecessary. Variations of less than 1

TABLE 1. Ocean Sediment, Water, Sea Water:
Change of Thermal Conductivity with Temperature

Substance	Temperature, $^{\circ}\text{C}$	Thermal Conductivity, cal cm	Decrease in Thermal Con- ductivity over Temperature Range, %	Observer
		$\frac{\text{cm}^2 \text{ sec } ^{\circ}\text{C}}{\times 10^4}$		
Pacific sediment moisture content 52% of wet weight, wet density 1.40 g/cm ³)	25	19.0	5.8	Butler, 1950*
	4	17.9		
Pacific sediment moisture content 66.5% of wet weight, wet density 1.23 g/cm ³)	25	17.0	5.9	Butler, 1950*
	4	16.0		
Sea water	25	14.3	4.2	Nukiyama and Yoshizawa [1934]
	5	13.7		
Sea water	25	14.6	6.2	Challoner and Powell [1956]
	4	13.7		
Sea water	30	14.1	4.3	Nukiyama and Yoshizawa [1934]
	10	13.5		

* Unpublished data.

per cent in the thermal conductivity of sea water for salinity changes of the order of 10 g/kg have been noted [Krümmel, 1907; Barratt and Nettleton, 1929].

The thermal conductivities of the sediment grains are only likely to change by small amounts due to ocean-bottom pressures, and it should be sufficient to consider the change in the conductivity of water alone in estimating the conductivity of the sediment. Approximations to the relative effects of pressure on the conductivities of solid and liquid phases can be obtained from the average values of Birch and Clark [1945] for several water-saturated sedimentary rocks, and from the values of Lawson, Lowell, and Jain [1959] for pure water. These values show, for solid and liquid, respective increases in conductivity of about $\frac{1}{2}$ and 1 per cent for pressure increases of the order of that found at a depth of 1000 fathoms of sea water. A correction of 1 per cent per 1000 fathoms to the measured sediment conductivities at atmospheric pressure appears reasonable.

Bulk density. Figure 4 shows variations in the bulk density of the sediments with their water content. If there is no gas in the sediment, this curve should be of the form

$$\rho = \frac{\rho_s}{1 + (w/100)(\rho_s/\rho_L - 1)} \quad (1)$$

where ρ is the bulk density, ρ_s and ρ_L are the densities of the solid and liquid phases, and w is the

water content (per cent wet weight). Taking $\rho_L = 1.03 \text{ g/cm}^3$ and $\rho_s = 2.35 \text{ g/cm}^3$ yields curve close to the experimental points between water contents of 40 and 70 per cent. In the case of sediments whose water contents are below about 38 per cent, the experimental bulk densities are higher than the ones calculated from the formula. Possibly the few specimens which were so low in water content may have contained sediment of a higher density than average. From a number of tests on grain densities by displacement method, ρ_s was found to vary between about 2.0 and 2.6 g/cm³. Bullard [1954] gave $\rho = 2.32 - 0.0181w$, based on experimental values found by the writer, over a limited range of water content, for Atlantic sediment.

Conductivity diagram. When measurements are not available or speed is essential, working values for thermal conductivity can be obtained from Figure 5 if we know either bulk density or water contents related to the dry or wet state of the sediment. The diagram was constructed by assuming average values for ρ_s and ρ_L and then substituting these in simple theoretical equations similar to (1).

OTHER MATERIALS

It is useful to compare changes of conductivity in ocean sediment over a limited range of water content with similar variations in other granular material over a much wider range of water content. Figure 6 shows some provision

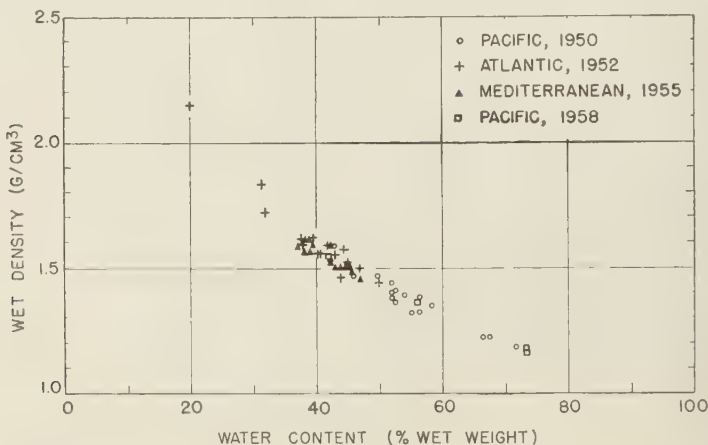
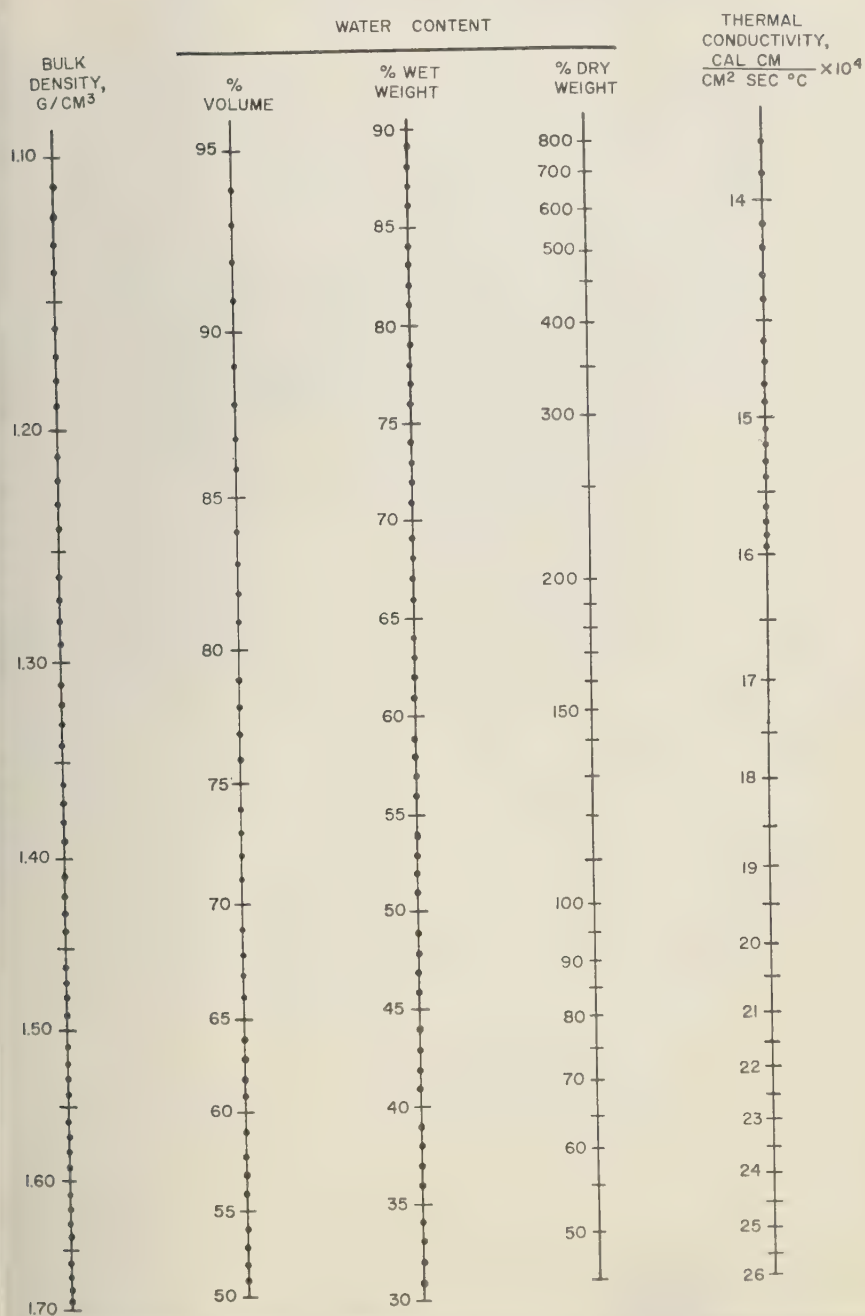


Fig. 4. Ocean sediment. Bulk density versus water content by weight.



g. 5. Ocean sediment. Diagram for assessment of thermal conductivity at 4°C and 1 atmosphere.
Add 1 per cent per 1000 fathoms and 1 per cent per 4°C temperature increase.

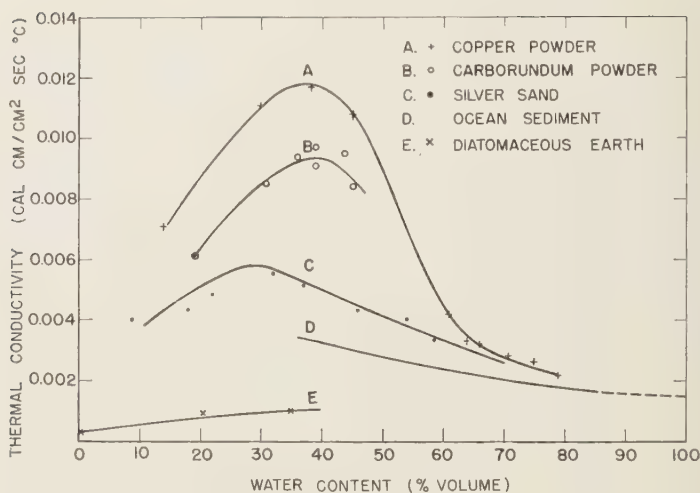


Fig. 6. Wet granular material. Thermal conductivity (at 1 atm) versus water content by volume.

results for the materials studied at the National Physical Laboratory. Experimental points for the ocean sediment curve *D* are not shown, since these are equivalent to those of the curve (at 22°C) given in Figure 3; they are plotted against water content by volume for an average value of density for sediment grains. As the water content is increased from zero, the air between the powder grains is gradually replaced by the higher-conductivity liquid, and the conductivity of the wet powder increases, at first rapidly and then more slowly. Saturation occurs at 30 to 37 per cent content by volume, when all voids are filled. Further additions of water will lead to diminution in solid material per unit volume as this is replaced by liquid, and, if the conductivity of the water is less than that of the grain material, the conductivity of the mix will decrease after saturation point has been reached, to a lower limit, which is the thermal conductivity of water. Loss of contact between the grains may also aid this decrease. The suspension of grains within a continuous phase for high water contents was achieved by mixing the powders with agar and water and testing the specimen in the form of a jelly, the continuous phase having a conductivity close to water. This method is described by Orr and Dallavalle [1954].

It will be seen from Figure 6 that the ratio of

the conductivity of a water/copper powder mix to that of a water/sand mix for a water content of 50 per cent by volume is about 2:1 whereas the ratio of the conductivities of the solid grain is probably of the order 50:1. It is clear that the relatively small differences in the conductivity of ocean sediment grains can be neglected and that the diagram of Figure 5 may be confidently used to obtain conductivity values for diverse sediments.

Details of further work on the conductivity of other wet granular materials, including some in nonaqueous media, are outside the scope of this paper. There is a need for more practical data, for most theories for computing the conductivities of solid/liquid mixes are based on, or are suitable for, only a limited range of materials and conditions.

Acknowledgments. The author is grateful for the interest of Sir Edward Bullard, F. R. S., in the initial work on these sediments, to Dr. R. W. Powell for interest in the later work on other wet granular materials, and to Mr. M. J. Hickman for some helpful suggestions regarding experimental procedure. The work described above has been carried out as part of the research program of the National Physical Laboratory, and this paper is published by permission of the Director.

REFERENCES

- Curatt, T., and H. R. Nettleton, *Intern. Critical Tables*, 5, 218-233, 1929.
- Reh, F., and H. Clark, An estimate of the surface flow of heat in the West Texas Permian Basin, *Am. J. Sci.*, 243A, 69-74, 1945.
- Willard, E. C., The flow of heat through the floor of the Atlantic Ocean, *Proc. Roy. Soc., A*, 222, 408-429, 1954.
- Halloner, A. R., and R. W. Powell, Thermal conductivities of liquids: new determinations for seven liquids and appraisal of existing values, *Proc. Roy. Soc., A*, 238, 90-106, 1956.
- Rümmel, O., *Handbuch der Ozeanographie*, 1, 280, J. Engelhorn, Stuttgart, 1907.
- Lawson, A. W., R. Lowell, and A. L. Jain, Thermal conductivity of water at high pressures, *J. Chem. Phys.*, 30, 643-647, 1959.
- National Physical Laboratory, Teddington, England, The thermal conductivities of three samples of deep-sea clays, *Rept. H4354 d/9.6.58*, 1958.
- Nukiyama, S., and Y. Yoshizawa, The thermal conductivity of sea-water and some water solutions, *J. Soc. Mech. Eng., Japan*, 37, 347, 1934.
- Orr, C., and J. M. Dallavalle, Heat-transfer properties of liquid-solid suspensions, *Chem. Eng. Prog.*, Symposium series no. 9, 1954.
- Pettersson, H., Exploring the bed of the ocean, *Nature*, 164, London, 468-470, 1949.
- Revelle, R., and A. E. Maxwell, Heat-flow through the floor of the eastern North-Pacific Ocean, *Nature*, 170, 199-200, 1952.
- Von Herzen, R., Heat-flow values from the South-Eastern Pacific, *Nature*, 183, 882-883, 1959.

(Manuscript received February 10, 1960.)

Nearshore Ocean Currents off San Diego, California

ROY D. GAUL¹

Marine Advisers, La Jolla, California

AND

HARRIS B. STEWART, JR.²

Geological Diving Consultants, San Diego, California

Abstract. Observations of the trajectories of fields of free-drifting current drogues were made off San Diego, California, on 103 days. This provided data for statistical analysis of the surface current regime in two nearshore areas separated by the entrance to San Diego Bay.

Reduction of the data required corrections for wind drag on the exposed portion of the drogues and for surface current drag on the float system of the subsurface drogues. Corrected subsurface data and surface data at times of low wind speeds were used to determine tidal components. Vector subtraction of tidal currents from total surface currents provided the components of the wind-induced currents. These were then statistically adjusted as derived from the yearly wind distribution, and finally the tidal and wind-induced components were recombined to yield a statistical redistribution of the total surface current.

INTRODUCTION

Between March 1956 and March 1957, 4900 measurements of nearshore ocean currents were made during 103 days at sea by Geological Diving Consultants, Inc., of San Diego, California. These were part of an oceanographic program initiated by the City of San Diego for studying environmental factors pertinent to the design of an ocean outfall system for the disposal of municipal wastes. Currents were measured to a maximum distance of 6 miles from shore off the 17 miles of coast between the Mexican border and Mission Bay, California (Fig. 1). The original field data, details of the field techniques used, and the preliminary results may be found in the report of Geological Diving Consultants to the City of San Diego [Stewart, 1957].

Subsequent biological and geological surveys in the same area, together with analyses of the 1956-1957 current data, were carried out by *San Diego Marine Consultants* [1959]. The present paper is concerned primarily with the

method of analyzing the current data to provide a realistic statistical description of the current regime.

FIELD EQUIPMENT AND METHODS

Free-drifting current crosses or drogues (Fig. 2) were used for measuring the integrated current in the top 2 feet of the water column. Sash weights were used to ballast the system so that about $\frac{1}{2}$ inch of the top of the cross projected above still water level.

Each day before the drogues were released, a temperature-depth profile perpendicular to the shore was obtained with a standard bathythermograph. The slides were examined, and the suspension line on each subsurface drogue was adjusted so that the cross was below the thermocline, if one existed. When no marked thermocline was present, subsurface drogues in the Imperial Beach area were placed at 50 feet or in the deeper area off Point Loma at 100 feet (Fig. 1).

At least three pairs of surface and subsurface drogues were released each day, usually in a line 2000 to 3000 feet long. Release times were noted, release positions were determined from the boat by measuring angles between precisely located

¹ Now at U. S. Navy Hydrographic Office, Washington, D. C.

² Now at U. S. Coast and Geodetic Survey, Washington, D. C.

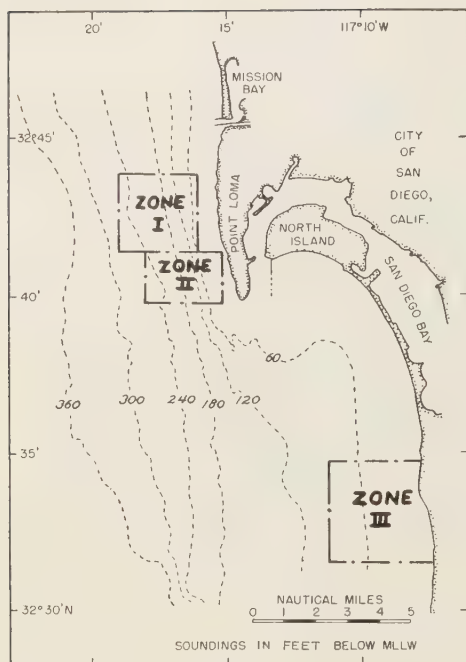


Fig. 1. Division of nearshore region into areas for current data analysis.

stations on shore, and positions were plotted with a three-arm protractor. Position accuracy was within 50 to 100 feet, depending on the distance from shore. Drogues were followed during the day, and successive positions for each drogue were similarly determined. The time interval between successive determinations of the position of any one drogue depended on the number of drogues being followed, the size of the original drogue field, the rate of separation of the drogues, and visibility. Generally the interval was between 10 minutes and 1 hour. Lines connecting the plotted positions for each drogue delineated trajectories from which the data on current speed and direction were obtained. Figure 3 is a sample of these trajectory plots.

Measurements of wind speed and direction were made each hour with a spring-loaded anemometer held approximately 8 feet above the water surface. Hourly observations were also made of the direction and height of sea and swell. Observation periods were always at least 5 hours and averaged more than 6 hours. A

6-day series of consecutive days of operation was made in each of the two areas. There were 8 night operations when lighted drogues and survey beacons were used, 6 days of heavy-weather operations, and continuous operations for periods of 24 and 27 hours in order to observe currents throughout a complete diurnal cycle.

ANALYSIS OF DATA

In order to minimize the misleading or erratic effects of individual drogue motion under locally varying conditions, mean motion of drogue fields was computed, a field being defined as a quasi-synoptic pattern of surface or subsurface drogues. Since drogues were not simultaneously positioned, a space-time adjustment of individual drogue locations to correspond with mean field time was required before the mean speed and direction between two successive fields could be computed.

Differential current drag correction. Included in the initial reduction of subsurface data was a correction for surface current drag on the submerged portion of the subsurface drogue pad (Fig. 2). Under the assumption of nonaccelerated flow, the drag force F_p on the pad can be expressed as

$$F_p = (W/2g)C_D A_p (V_a - V_d)^2 \quad (1)$$

and the force F_d on the current cross or the drag at the level of the subsurface current to be measured is

$$F_d = (W/2g)C_D A_d (V_a - V_d)^2 \quad (2)$$

where

- w = weight of water
- g = acceleration of gravity
- C_D = drag coefficient
- A_p = projected area of pad
- A_d = projected area of drag
- V_a = 'apparent' or measured velocity of the drogue
- V_d = actual velocity of subsurface current
- V_s = velocity of surface current without wind correction

If drag coefficients of the pad and cross are equal, equations 1 and 2 reduce to

$$(V_a - V_d)^2 = A_p/A_d (V_s - V_a)^2 \quad (3)$$

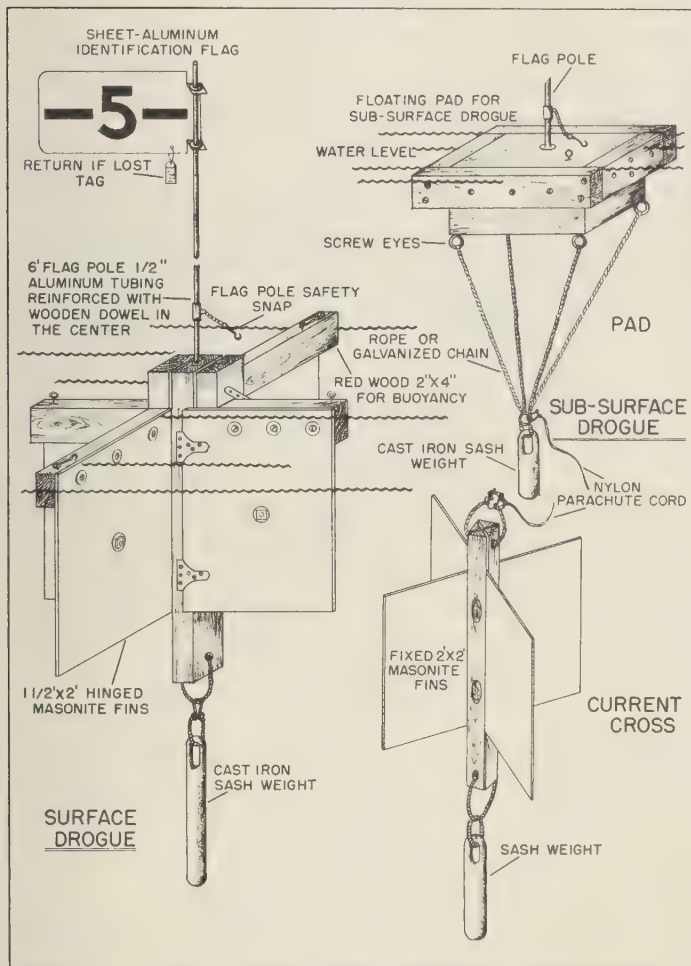


Fig. 2. Surface and subsurface current drogue assemblies.

which was used for adjustment of all subsurface drogue data.

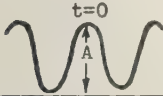
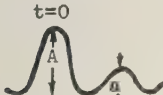
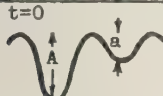
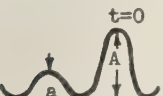
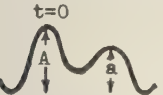
Correction for wind. Several calibrations were made in the ocean and the bay to determine effects of wind drag on the pole and flag superstructure of the drogues. Fluorescein dye was used as a reference for surface drogues. A drogue with a small float ballasted for near-neutral buoyancy was the reference for the subsurface drogues. The effect of the wind was found to be 0.01 and 0.015 of the wind speed for surface and subsurface drogues, respectively.

This adjustment was applied to all current velocity vectors.

TIDAL CURRENTS

Inspection of vertical tidal fluctuations along the coast shows wide variations in wave form and amplitude. These are chiefly dependent upon the various combinations of the lunar and solar components of the tide-producing forces. Much more complex, however, is the horizontal motion of the sea surface near the shore. The tidal components of the total current pattern

TABLE 1. Types of Tides

Form of Curve	Type	Range of 'A' (ft)	Range of 'a' (ft)	Recurrence Frequency* (per cent)
	Ia	4.5-6.0	...	4.5
	Ib	3.0-4.5	...	4.2
	IIa	4.5-6.5	3.5-5.0	3.3
	IIb	3.5-5.0	1.0-3.0	10.2
	IIIa	4.5-6.5	3.5-5.0	3.0
	IIIb	3.5-5.0	1.0-3.0	10.5
	IVa	6.0-8.0	3.0-6.0	32.8
	IVb	4.0-6.0	2.0-4.0	23.1
	IVc	0-4.0	...	4.2
	V	0-6.0	0-4.0	4.2

*Frequencies based on predicted tides for 1958.

per cent for type V and 10 per cent for Ia plus Ib.

Analytical procedure. Tidal currents within each zone in Figure 1 were derived from subsurface currents at depths greater than or equal to 40 feet, supplemented by surface currents observed when wind speeds were less than 5 mph. The vectors were averaged within selected ranges of speed and direction for each 3- to 3.5-hour span of the tidal cycle (Fig. 4). In consideration of the usually transient character of local winds in the area, it was assumed that wind-induced components of current at a depth of 40 feet are not significant; therefore the subsurface currents were considered to be representative of the tidal components.

The end points of individual currents vectors for each type of tide within a zone were used in constructing polar diagrams. Since the volume of data was limited, it was necessary to draw

smooth curves subjectively, as dictated by continuity of form between separate 'ellipses' as well as by the plotted points.

Tidal currents off Point Loma. Tidal ellipses for zone I are shown in Figures 5 through 10. Mean values of plots for types Ia and Ib were almost identical, so the data were combined and a mean ellipse constructed. Most of the data for types II and III happened to fall within a relatively limited range of tidal hour; considerable subjectivity was necessary in the construction of Figures 6 and 7, and consequently the reliability is relatively low for these two types. Data were insufficient for evaluating currents for type V.

The majority of observations taken in zone II are shown in Figures 11 and 12. No attempt has been made to draw tidal ellipses, but it is important to note that practically all observations are in the second and third quadrant, with

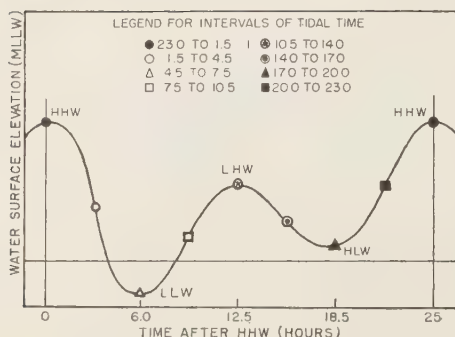


Fig. 4. Tidal wave nomenclature.

southerly speeds near low tide ranging from about 45 to 85 feet per minute (fpm).

Clockwise rotation of the current vectors with time is evident. Of the 50 days of measurements off Point Loma used for the analysis, none revealed a significant contradiction to this conspicuous clockwise rotation. Currents near the time of high tide are northerly. Near low tide they are southerly, with maximum velocities somewhat larger than those at high tide. Maximum velocities generally occur at or before the time of low tide, are southerly, and are highest with type IVa tides (45 fpm average) and lowest with type II (about 12 fpm average).

Tidal currents off Imperial Beach. Tidal current ellipses developed for the area off Imperial Beach are given in Figures 13 through 15. Only for type IV is the ellipse believed to be nearly as reliable as those derived for Point Loma. Poorer coherence is justified for the Imperial Beach data because (1) depths are considerably less, (2) tidal current velocities appear on the average to be less than half those at Point Loma, and (3) observations were made on fewer days when the wind was calm or of low velocity. Any uncertainties involved in the calibration of the subsurface drogue are consequently magnified proportionally, and thus the scatter, which at best we would expect to be large, is increased.

In spite of the uncertainties noted above, several important differences between currents in the two areas are evident. Counterclockwise rotation predominates off Imperial Beach. This phenomenon was verified repeatedly during analysis of the data by following the sequential

rotation of current vectors on individual days. However, clockwise rotation was indicated for a small percentage of the observations. In passing, we might add that significant alteration of the usual current patterns off Imperial Beach seems to exist during periods of marked residual current associated with strong ebb flow from San Diego Bay or with movement into the area of the coastal current usually found at greater distances from shore.

Tidal current velocities are considerably less at Imperial Beach than at Point Loma. Velocities are maximum and southerly at low tide. Highest currents are associated with type I tide, and the maximum is just over 30 fpm compared with 45 fpm at Point Loma.

Net tidal drift and particle trajectories. From a tidal ellipse it is possible to evaluate net tidal drift, that is displacement of a water particle after one complete tidal cycle in the absence of wind. Drift distance, speed, and direction for each tidal type in zones I and II are given in Table 2. These are estimates of average drift considered accurate to within 3 per cent off Point Loma (zone I) and 50 per cent off Imperial Beach (zone III). Note that in all except type IVa, net tidal drift off Point

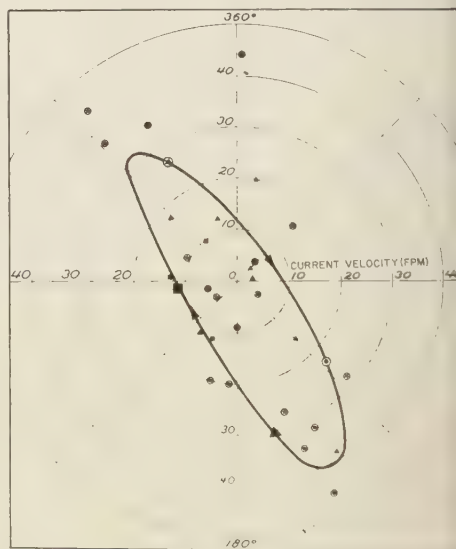


Fig. 5. Type I tidal ellipse off Point Loma (zone I).

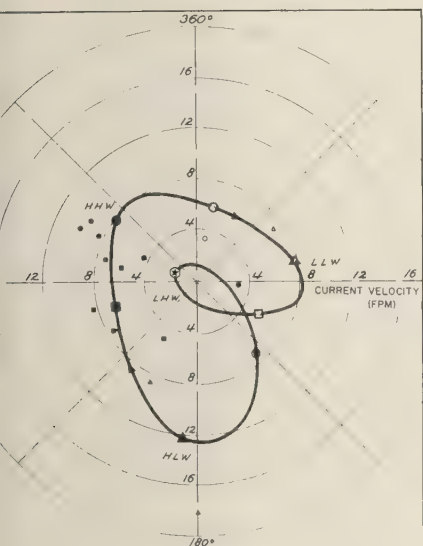


Fig. 6. Type II tidal ellipse off Point Loma (zone I).

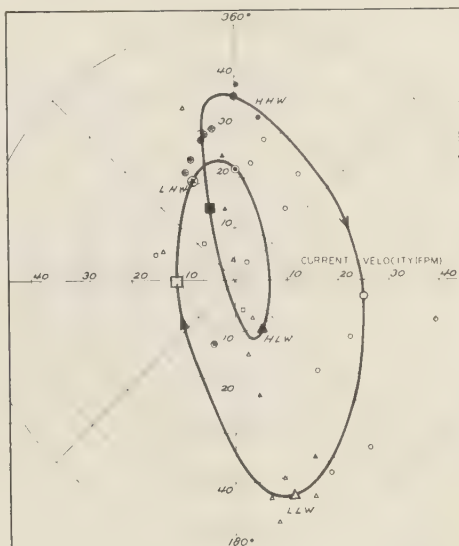


Fig. 8. Type IVa tidal ellipse off Point Loma (zone I).

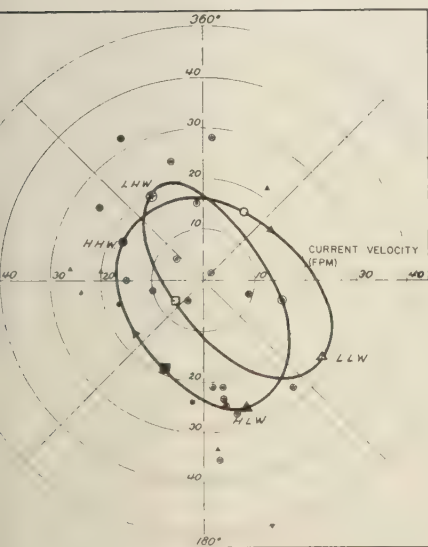


Fig. 7. Type III tidal ellipse off Point Loma (zone I).

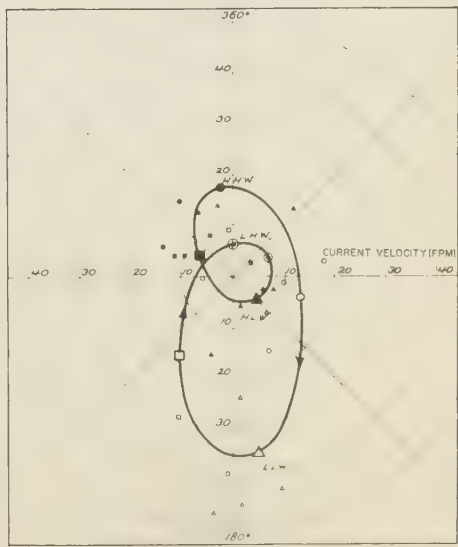


Fig. 9. Type IVb tidal ellipse off Point Loma (zone I).

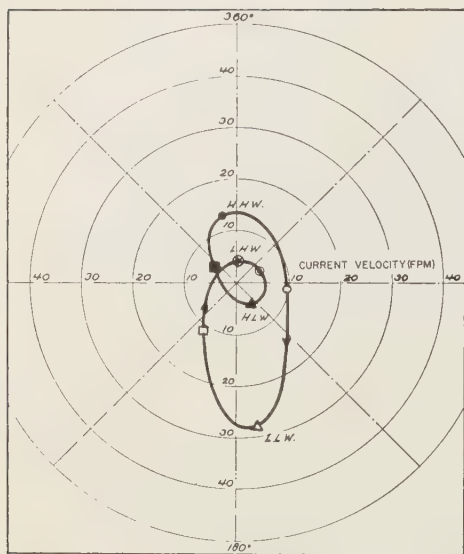


Fig. 10. Type IVc tidal ellipse off Point Loma (zone I) as interpreted from types IVa and IVb.

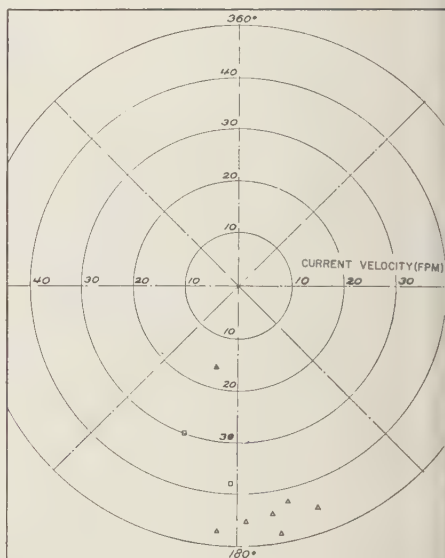


Fig. 12. Type IV tidal currents off Point Lo (Zone II).

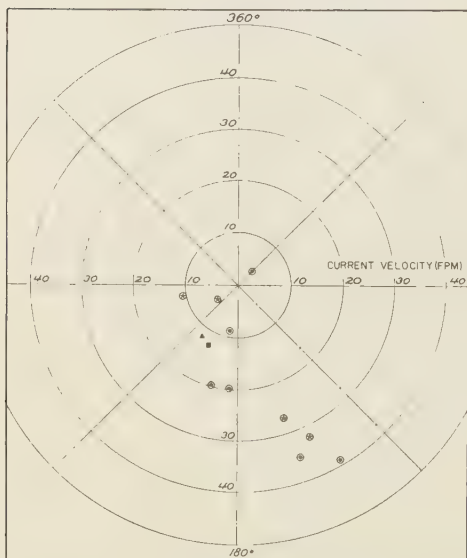


Fig. 11. Type I tidal currents off Point Loma (Zone II).

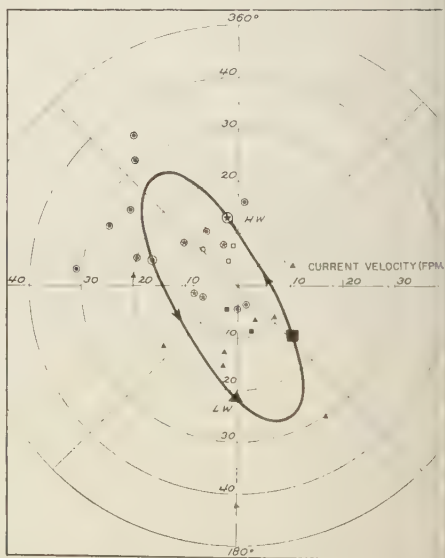


Fig. 13. Types I and III tidal ellipse off Impe Beach (zone III).

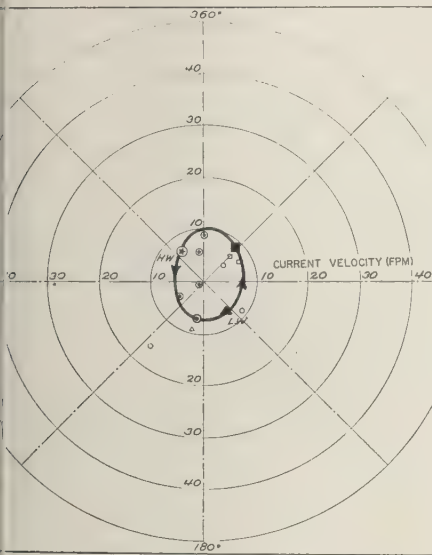


Fig. 14. Type II tidal ellipse off Imperial Beach (zone III).

ona is southerly to southeasterly, whereas off Imperial Beach it appears to be consistently southerly to southwesterly.

Also of interest is the trajectory of a water particle under the influence of tidal currents only. Figure 16 is an example of such a trajectory constructed from a tidal ellipse. Displacement during any increment of time may be determined by placing the origin of the polar diagram (shown in Fig. 16 with the origin at *HLW*) at the initial tidal hour and reading the azimuth and distance to the final hour. From Figure 16, for example, it is seen that a water particle leaving a given location at *HHW* reaches a position approximately 6000 feet toward 80° after 5 hours. Starting at *LHW* it would be 5000 feet due north after 5 hours; and if it began at *HLW* it would travel a maximum of about 1500 feet but would return to approximately the starting position at the end of the 5-hour period.

Yearly distribution of tidal currents. Once tidal ellipses have been constructed from the field data, yearly occurrence frequencies for each type of tide can then be applied as weighting factors to cumulations within desired ranges of speed and direction to provide a meaningful

statistical description. Results of such an analysis are given in Tables 3 and 4 for zone I off Point Loma and zone III off Imperial Beach. The small percentage of time not included in the sum of tidal types for which ellipses were drawn has been distributed within the tabulations.

WIND-INDUCED CURRENTS

To arrive at an estimation of the wind-driven current we must first remove tidal current components from the total current. The present state of knowledge and the limited amount of data are not sufficient to permit an estimation of tidal currents free of the distorting effects of residual currents. If it can be assumed that observations were taken during all variations of residual current influences and, in addition, were taken in direct proportion to the frequency of occurrence of these residuals, then the tidal components including the residual distortion may be subtracted vectorially from the total current to provide the current component due to wind. Since there is no assurance that the present observations constitute an adequate distribution of current sampling, and since there is no means of quantitative evaluation of

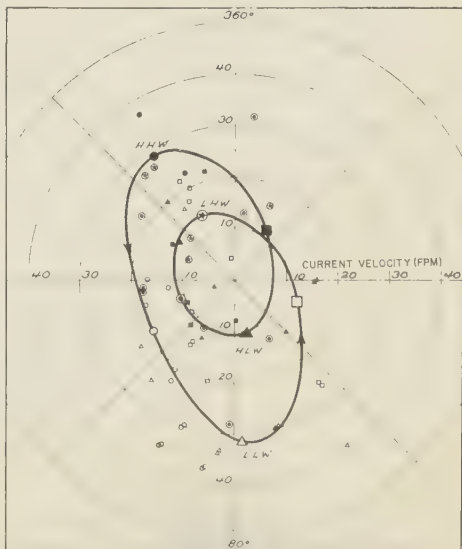


Fig. 15. Type IV tidal ellipse off Imperial Beach (zone III).

TABLE 2. Net Tidal Drift during a 25-Hour Tidal Cycle

Zone	Type of Tide	Speed, fpm	Distance, ft	Direction, degrees
I				
(Pt. Loma)	I	7.0	10,500	170
	II	3.0	4,500	120
	III	4.5	7,000	140
	IVa	4.0	6,000	050
	IVb	4.5	7,000	165
	IVc	3.5	5,500	160
III				
(Imp. Beach)	I & III	3.0	4,500	210
	II
	IV	4.0	6,500	180

the residual components, a wide scatter of points can be expected from such an analysis. In view of the assumed low-recurrence frequency of strong residual components, a comparatively narrow band of values reflecting the mean wind-induced currents should exist.

Theoretical justification for a constant angular deviation between current and wind directions can be made only for steady-state conditions: that is, a steady wind blowing from one direction long enough to have produced an unchanging horizontal and vertical current profile. Even in particular areas of the open ocean where comparatively constant winds prevail it is difficult to obtain consistent quantitative agreement with the renowned Ekman equation [Rossby and Montgomery, 1935]. Ekman himself presented exhaustive mathematical treatises on space-time parameters for current development, with remarks about the effects of shallow water and coastal boundaries [Ekman, 1905, 1928]. Other theoretical treatments by Durst [1924] and Jeffreys [1923], augmented by observational data, seem to support Ekman's contention that over a considerable range of wind speeds there should be an almost linear relationship between the speed of the wind and the speed of the surface current it generates.

Ratio of current to wind speed. The analytical approach taken in this study was the evaluation of the total wind current vector as a function of wind speed and direction. Constant

values of angular deviation dependent upon the mean current and wind vectors were then established. Had sufficient data been available it would have been desirable to investigate angular deviation independently in order to evaluate its variation with changes in the velocity of the wind and current. There is also some question whether the total wind current or only its component in the wind direction would be more likely to retain a constant relationship to wind velocity. These are relatively fine points, however, and their consideration cannot be justified in view of the limited amount and wide distribution of the basic data.

The procedures for zoning and initial processing of the surface current data taken for winds greater than 5 mph are the same as those used in preparing the data for tidal analysis. The data were grouped into 45° sectors of wind direction, and an attempt was made to analyze data from each sector independently, so that some allowance would be made for the effect of the coastline in orienting currents parallel to it.

Surface current observations were not considered unless they were accompanied by simultaneous surface measurements at depths of at least

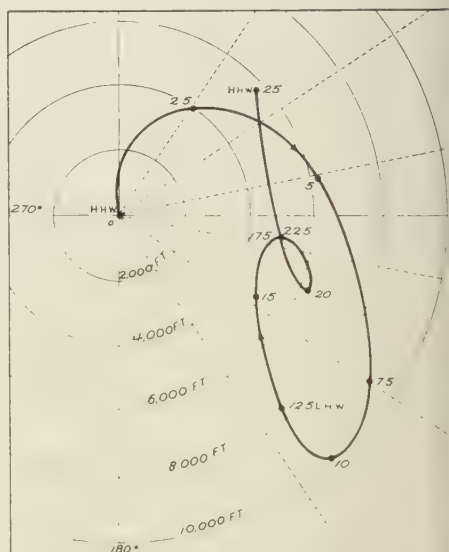


Fig. 16. Type IVa tidal current trajectory Point Loma (zone I).

TABLE 3. Frequency Distribution of Tidal Currents at Point Loma, Zone I

Direction	Velocity Ranges, fpm					Totals
	0-10	10-20	20-30	30-40	40-50	
N	2.8*	6.5	6.6	4.9	...	20.8
NE	4.9	4.0	1.6	10.5
E	5.4	2.4	2.2	10.0
SE	7.0	2.2	4.6	2.4	0.7	16.9
S	1.4	3.4	3.6	4.6	1.5	14.5
SW	2.9	4.4	0.7	8.0
W	4.4	2.9	7.3
NW	3.5	7.0	1.2	0.3	...	12.0
Totals	32.3	32.8	20.5	12.2	2.2	100.0

* Numbers are percentage of total time.

This was done in an effort to minimize the effect of wind distortion of the subsurface tidal currents to which the surface currents were referred. In cases of strong winds blowing for a considerable period of time there is no doubt that currents at 40 feet would not be representative of the tidal component.

To make allowances for the effect of wind distortion on surface current generation, the wind vector for the period of approximately 3 hours preceding and including the time of observation was used. This does not account for water motion existing in one location as the result of winds that had blown previously at other places. Under conditions of more variable and stronger local winds, this effect is likely to be significant. It is possible, for example, that the dominantly northwesterly winds at considerable distances off shore may be largely responsible for the drift factor previously discussed under tidal currents, as well as for some periods of high residual currents.

The ratio of surface current to wind speed—wind factor—was evaluated by obtaining a best fit of straight lines to plots of wind speed versus the speed of the wind current for each onshore sector (wind toward N, NE, E, SE, etc.). In this case the linear relationship between wind speed and induced current previously discussed is assumed. As might be expected, a large scatter was encountered. Wind factors and directions are summarized in Table 5.

It should be emphasized that these results are based on values for a limited amount of data and

are averaged over a wide range of unsteady current and wind directions. There is some doubt as to the possibility of realistically improving or modifying these results until continuous measurements at fixed locations and at several levels below the water surface can be made. The same conclusion was reached after the statistical analysis of over 20,000 surface current observations by *Mandelbaum* [1955, 1957].

Wind factors of the same order of magnitude as those shown in Table 5 were reported by *Rossby and Montgomery* [1935]. This is probably more coincidental than significant, since their observations were primarily of ice drift in the open ocean, and theoretical values were dependent upon many of the same assumptions encountered in the Ekman equation, which for this latitude gives a wind factor of 0.017. On the other end of the scale is the value 0.04 as the wind factor for the very thin surface film determined experimentally by *Van Dorn* [1953]. His work also showed that the direction of wind-induced movement of the surface film is aligned with the wind (current deviation = 0), agreeing with theoretical conclusions of *Ekman* [1928].

Statistical distribution of wind-induced currents. Mean daily wind speed during days of observation was 6.5 mph at Point Loma and 8.6 mph at Imperial Beach, or 25 per cent less at Point Loma. Whether this difference is due chiefly to winds actually being on the average higher at Imperial Beach or simply that windier

TABLE 4. Frequency Distribution of Tidal Currents at Imperial Beach, Zone III

Direction	Velocity Ranges, fpm					Totals
	0-10	10-20	20-30	30-40	40-50	
N	2.6*	8.8	3.5	14.9
NE	4.4	2.3	6.7
E	5.0	2.6	7.6
SE	4.4	4.9	4.4	13.7
S	2.7	4.3	7.3	3.0	...	17.3
SW	1.7	9.2	1.9	12.8
W	1.7	8.9	1.2	11.8
NW	1.7	8.0	5.5	15.2
Totals	24.2	49.0	23.8	3.0	...	100.0

* Numbers are percentage of total time.

TABLE 5. Current Deviation and Wind Factor for Each of Five Onshore Sectors

Area	Wind toward (degrees)	Current Deviation (degrees)	Wind factor (V_w/U)
Point Loma	000	15*	0.048
"	045	25	.034
"	090	15	.028
"	135	10	.023
"	180	-15	.040
Imperial Beach	000	15	.038
"	045	20	.031
"	090	15	.023
"	135	15	.032
"	180	5	.037

* Positive angles indicate current deflection to the right of the wind, negative to the left.

days happened to be sampled there than at Point Loma is unknown. In any event, this difference seems to account for the fact that observed drogue motion (total current) was roughly the same in both areas, whereas analysis has indicated relatively larger tidal influence at Point Loma.

The frequency distribution of winds at Lindbergh Field, San Diego, is summarized in Figure 17. Although winds along the coast are normally stronger than at the weather station inland, no long-term series of wind observations at the coast is available for a quantitative comparison with observations at Lindbergh Field.

Cumulative frequency curves of wind-driven

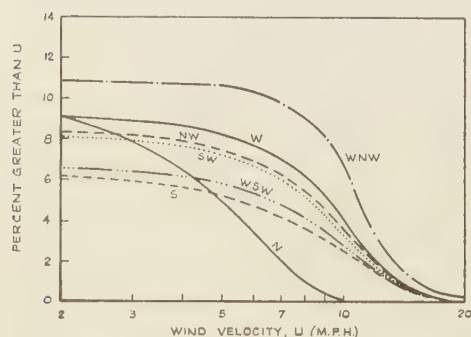


Fig. 17. Cumulative frequency distribution of onshore winds at San Diego (22.5 degree direction sectors).

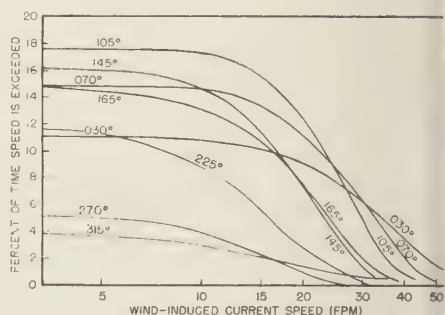


Fig. 18. Cumulative frequency distribution of onshore wind-induced currents off Point Loma (direction sectors). Directions indicated for each curve denote mean current set which includes angular deviation from wind direction.

current velocities have been prepared for both areas (Figs. 18 and 19) by applying the wind factors and angular deviations of Table 5 to the wind-frequency curves of Figure 17. Offshore winds, that is wind toward SW, W, and NW, are quite infrequent, and almost no current observations were made during their occurrence. Consequently, a wind factor of 0.030 and angular deviation of zero are assumed in curves for these directions.

DISTRIBUTION OF ONSHORE SURFACE CURRENTS

The frequency distributions of tidal currents (Table 3) and of wind-induced currents (Figs. 18 and 19) may be combined to give the frequency distribution of total surface current. In view of uncertainties involved in computation of offshore current components, the final analysis summarized below has been restricted to the three 45° ranges of onshore current set (NE, E and SE).

Since tidal and wind-induced current components are considered to be independent, the probability F of individual components occurring simultaneously is

$$F = F_T F_W$$

where F_T is the recurrence frequency of the tidal current and F_W is the cumulative recurrence frequency of the wind-induced current. In order to determine completely the frequency of occurrence of any given current vector it is necessary to sum the probabilities associated with all possible combinations of vectors.

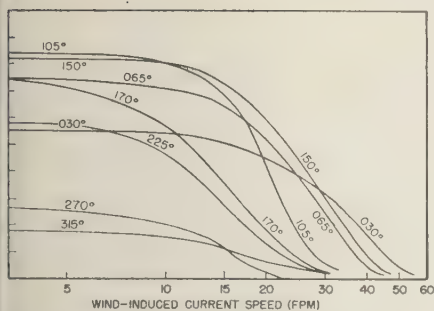


Fig. 19. Cumulative frequency distribution of onshore wind-induced currents off Imperial Beach (direction sectors). Directions indicated for each curve denote mean current set which includes angular deviation from wind direction.

In Figure 20 the yearly cumulative frequency distributions for onshore surface currents are shown for both Point Loma and Imperial Beach. These curves were derived by application of equation 4 to all significant component vector combinations resulting in total currents of 20, 40, 60, and 80 fpm in each of the three onshore directions. Wind vectors corresponding to each total vector in Tables 3 and 4 were computed for each of the total current speeds designated above. F_w was obtained from these vectors by interpolation between the curves of Figures 18

or 19. As an example, consider a total current off Point Loma of 40 fpm to the east and a tidal component of 15 fpm to the NE ($F_T = 0.04$). The required average wind component is 31 fpm toward 109° , which (Fig. 18) gives $F_w = 0.04$ (interpolating between 105° and 145°). The resultant is, then, $F = 0.0016$, which must be summed with the probabilities of all other combinations of component vectors similarly derived for this single total current vector. The final cumulative frequency is obtained by adding this result to values for speeds of 60 and 80 fpm.

SUMMARY AND CONCLUSIONS

Current trajectories observed during a 1-year period with simply constructed, free-drifting drogues in the nearshore region off San Diego, California, were used to evaluate the surface current regime in two regions separated by the mouth of San Diego Bay. Reduction of the data required corrections for wind drag and for surface current drag on the float system for subsurface drogues. A system based on the following assumptions has been presented for the statistical adjustment of computed currents: (1) wind and tide are the primary current-producing factors; (2) tidal currents may be related to form and range of the tidal wave; (3) under local wind conditions the wind seldom exerts a

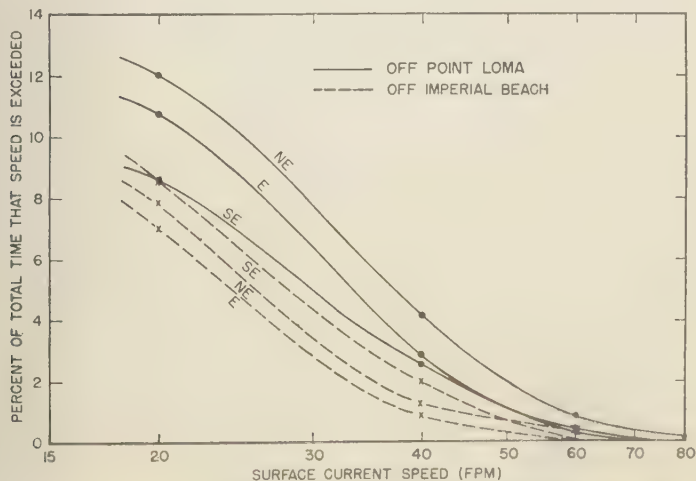


Fig. 20. Cumulative frequency distribution of total surface currents off San Diego, California.

significant effect on currents 40 feet or more below the water surface; (4) wind-to-current ratios and angular deviations of direction may be consistently determined from observed data; (5) historical wind data from an adjacent inland area may be used as a basis for statistical adjustment of observed wind-induced currents; (6) cumulative frequency distributions may be completed by synthesis of component vector probabilities.

Markedly different features in the currents at the two sites separated by less than 20 miles were detected. There is evidence that some of these differences may be directly associated with the flushing of San Diego Bay and with its location between the sites. Rotary currents are evident within both regions, although the southern area displays counterclockwise rotation instead of the usually expected clockwise rotation that prevails at the northern site.

Acknowledgments. The authors wish to express their appreciation to the City of San Diego for permission to publish this report, to Paul L. Horrer for consultation and aid in the statistical study, and to J. F. T. Saur for his advice and encouragement.

REFERENCES

Durst, C. S., The relationship between current and wind, *Quart. J. Roy. Meteorol. Soc.*, 50, 113-119, 1924.

Ekman, V. W., On the influence of the earth's rotation on ocean-currents, *Arkiv Math., Astr. Fys.*, 2, no. 11, 1905.

Ekman, V. W., Eddy-viscosity and skin-friction: the dynamics of winds and ocean-currents, *Meteorol. Soc.*, 2, 161-172, 1928.

Jeffreys, Harold, On the effect of a steady wind on the sea level near a straight shore, *Phil. Mag.*, 46, 114-125, 1923.

Mandelbaum, Hugo, Wind-generated ocean currents at Amram Bank light ship, *Trans. Am. Geophys. Union*, 36, 72-86, 1955.

Mandelbaum, Hugo, Wind influence on a rotational tidal current, *Trans. Am. Geophys. Union*, 38, 867-878, 1957.

Rossby, C. G., and R. B. Montgomery, The kinetic energy of frictional influence in wind and ocean currents, *Papers in Phys. Oceanog. and Meteorol. Mass. Inst. Technol. and Woods Hole Oceanographic Inst.*, 3, No. 3, 1935.

Stewart, Harris B., Jr., Oceanographic studies of the City of San Diego, unpublished report of the Geological Diving Consultants to the City Engineer, San Diego, California, 1957.

San Diego Marine Consultants, Special oceanographic report on San Diego waste disposal system, unpublished report submitted to the City of San Diego, California, 1959.

Van Dorn, W. G., Wind stress on an artificial pond, *J. Marine Research, Sears Foundation*, 19, 249-276, 1953.

(Manuscript received January 8, 1960; revised February 13, 1960.)

A Comparison of Power Spectra of Ocean Waves Obtained by an Analog and a Digital Method

JERRY K. PARKS

Lockheed Missiles and Space Division, Palo Alto, California

Abstract. Power spectra of ocean waves obtained by an analog method are presented. In the analog method, standard laboratory equipment is used and no design or development work is required. A sample power spectrum of an ocean wave pressure record is obtained by the analog method, and this spectrum is compared with a power spectrum obtained by a digital analysis of the same record. The agreement of the spectral shapes and the variances obtained by the two methods is fairly good.

INTRODUCTION

Current theoretical developments in ocean wave analysis are based on methods of random noise analysis [Pierson and Marks, 1952]. Many of the properties of ocean waves, such as propagation, refraction, attenuation, and wave form statistics, have been theoretically derived in terms of the power spectrum of the ocean wave record [Pierson, 1954a; Ehrenfeld and others, 1958]. In order to verify the theory and to apply it to specific problems, one must measure the power spectra of ocean wave records. There are basically two methods of measuring power spectra. They are the digital computer method and the electrical analog method [Blackman and Tukey, 1958]. A number of analog analyzers have been specifically designed to obtain power spectra of ocean waves [Pierson, 1954b; Austin, 1954; Tucker, 1955]. These analyzers have met with varying degrees of success, their use being limited somewhat by development difficulties. As a consequence, the majority of power spectral measurements of ocean waves are made today by the digital method. The purpose of this paper is to describe an analog method of power spectral analysis in which standard laboratory equipment is used, and to show that the spectra obtained by this method compare favorably with the spectra obtained by the digital method.

ANALOG METHOD

The analog method of measuring power spectra to be described here consists essentially of an electronic Fourier analysis of a 20-minute sample of an ocean wave pressure record. The es-

sence of the method is as follows. The pressure variations due to ocean waves are recorded as a function of time on magnetic tape. The magnetic tape is formed into a loop and played back continuously, as a fixed bandwidth filter is swept through the range of frequencies. The electrical output of the filter is converted to power, averaged, and recorded.

There are several important parameters which must be considered in this type of analysis: the filter bandwidth, the loop period, the frequency scanning rate, and the time constant of the power averaging circuit. These parameters cannot be selected independently. Each parameter will be discussed in turn.

Loop period. The fundamental frequency in the Fourier analysis and the constant frequency interval between the Fourier components are functions of the loop period. This frequency interval is often called the elemental bandwidth.

Filter bandwidth. Once the loop period is fixed, the bandwidth of the filter determines the number of Fourier frequency components which fall in the filter passband. The output power of the filter is the sum of the powers associated with each of the Fourier frequency components which lie in the filter band. The power spectrum level, which is the output power of the filter divided by the filter band width, or power per cycle, is an average of the powers associated with those frequency components which happen to be in the filter passband.

A finite sample of a random function will have an abrupt beginning and ending. The effect of the abrupt ends of the sample is to require a slightly different set of Fourier frequency com-

ponents for description of the sample than would be required if the sample were infinite in length. The abrupt ends of the sample cause a perturbation of the true spectral values of the random function. These perturbations of the true spectral values are smoothed when the filter averages over the frequency components which lie in the passband. If too few of the Fourier components are included in the averaging process, a large statistical variation in spectral level can occur from one sample to the next, even though the samples were taken from the same random process with one true spectrum. If too many Fourier frequency components are included in the averaging process, the true spectral variations will be smoothed and detail will be lost.

Time constant of the power-averaging circuit. In the analysis, the output voltage of the filter is squared, averaged over time, and recorded. The time constant of the power-averaging circuit should be approximately the same as the loop period in order that the power variations which occur at the loop repetition rate will be smoothed.

Frequency scanning rate. If the power-averaging circuit is neglected for the moment, the rate of frequency scanning is limited by the finite time required for a resonant signal to be built up in a narrow band-pass filter. This time is several times the reciprocal of the half bandwidth of the filter. The maximum scanning rate in this case would be one which would allow each frequency component to remain in the filter passband for this length of time.

The time constant of the power-averaging circuit places a further restriction on the rate of frequency scanning. If the power variation with time (due to the spectral shape) has frequency components greater than $f_s = 1/2\pi RC$, where RC is the time constant of the power-averaging circuit, these frequency components will be attenuated and the spectrum will be distorted. It is therefore necessary for the scanning rate to be slow enough to insure that the recorded spectral function does not have frequency components above f_s .

ANALOG EQUIPMENT

The original pressure signal was converted to a low-frequency FM signal (300 cps center fre-

quency) and recorded on a 1/4-inch magnetic tape by an Ampex Mod. 600 AM tape recorder. This record is referred to as the 'storage tape.' A Hewlett-Packard model 600B frequency meter was used for demodulating the playback signal of the storage tape. The demodulated pressure signal was available at the recorder output terminal of the frequency meter.

It was desired to analyze the playback of the storage tape, but the available analysis equipment would not respond to the low-frequency signal variations which represented the pressure changes. It was therefore necessary to compress the pressure signal in time by a series of tape re-recordings. With Ampex recording equipment it is possible to compress the recorded signals in this manner because the center frequencies of the FM modulators of the recorder have a definite relationship to the tape speed. Consequently, a tape recorded at one speed can be played back on another recorder at a different speed.

The time compression involved two re-recordings, the formation of a loop, and a recording of the repeated loop signal. Details of the compression scheme and equipment were reported by Parks [1959]. The final tape was a 2500-foot reel which contained approximately 850 loop repetitions. When this tape was played back at 15, 30, and 60 inches per second, the compression of the original record was 512, 1024, and 2048 to 1. A compression ratio of 512 to 1 was selected for the analysis. With this compression ratio, the loop period was 2.5 seconds. The original frequency range of interest in the pressure

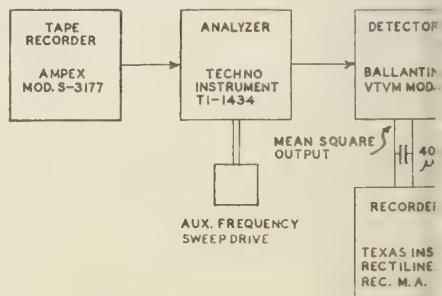


Fig. 1. Block diagram of the instrumentation used in analyzing the time-compressed record.

record was 0.02 to 1 cps. After compression, frequency became 10 to 500 cps. The equipment used in the analysis is listed below.

Item	Use
Recorder, Ampex model 600	Storage tape playback
Electronic frequency converter, Hewlett-Packard model 600B	Demodulation of storage tape playback
Recorder, Ampex model S-3481	Time compression
Recorder, Ampex model S-3177	Time compression
Loop transport, Ampex model S-3559AC	Loop playback
Analyzer, Techno Instrument model T.I-1434	Compressed signal analysis
Mean-square-law detector, Ballantine model 320, V.T.V.M	Conversion of analyzer filter output to power
Recorder, Texas Instrument rectilinear recorder, millimeter	Detector output recorder

Modification of two pieces of equipment in this case was found to be necessary. The modification consisted of adding a capacitor in shunt with the mean-square-law detector output of the Ballantine model 320, and of adding a slow-sweep frequency drive to the analyzer. A block diagram of the instrumentation used to analyze the compressed signal is shown in Figure 1.

In the Techno Instrument analyzer an oscillator signal is mixed with the signal to be analyzed, and the sum signal is passed through a fixed-bandwidth crystal filter. Tuning the oscillator through a range of frequencies is equivalent to sweeping a fixed-bandwidth filter through the range of the input signal frequency.

The output signal of the analyzer is fed into the Ballantine mean-square-law detector where it is squared and averaged. The time constant of the detector is determined by the capacitance and resistance in shunt with the output terminals. A 4000 μ f electrolytic shunt capacitor was used during all the spectral runs. The time constant of the detector and recorder combina-

tion was approximately 2.5 seconds. The dynamic range of the detector is approximately 24 db. The effective bandwidths used in the analysis were 4 cycles and 20 cycles.

THE ANALOG SPECTRA

The spectra. The power spectrum of a 20-minute wave-pressure record made in 53 feet of water in the Gulf of Mexico 1 mile off shore at the western end of St. Andrew State Park, Panama City, Florida, was obtained by means of the analog method described above. Two different resolutions were used in analyzing the record. The results are shown in Figures 2 and 3. Also shown is the relative frequency response of the filter which was used to obtain the accompanying spectrum. The filter responses were made by analyzing a 20-minute calibration record which was carried through the same compression procedure as the pressure record. The calibration tapes were made by recording 0.1- and 0.2-cps sine waves.

The spectral shapes were found to duplicate very well on repeated runs. However, the location of the spectra along the indicated frequency axis did not repeat well. The shifting of the spectra along the frequency axis on repeated runs was due to a slow drift in the analyzer oscillator. The oscillator drift was undoubtedly due to the state of repair of the instrument.

The frequency scale. The spectral frequency scale was determined by analyzing 0.1- and 0.2-cps sine-wave calibration tapes. Some error was introduced because of the oscillator drift, since the analysis required a finite time.

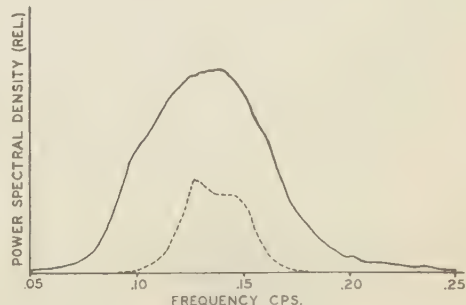


Fig. 2. Power spectrum of wave record obtained by analysis with 20-cycle filter. Filter response of 20-cycle filter (dashed curve).

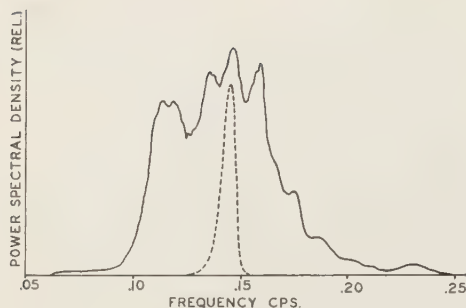


Fig. 3. Power spectrum of wave record obtained by analysis with 4-cycle filter. Filter response of 4-cycle filter (dashed curve).

The variance. The area under the spectrum is a measure of the variance of the pressure record or of the time average of power in the electrical signal. The value of the variance of the pressure record in units of (inches of water)² was determined by playing the compressed tape record directly into the detector (by-passing the analyzer). The shunt capacitor was increased to 8000 μ f for this measurement in order to insure a long time average of power. For the measurement, the recorder was replaced by a dc voltmeter.

The procedure used to determine the variance was as follows. The compressed tape record was played into the detector, and the mean-square output voltage was noted. The output of the detector is a negative voltage which is proportional to the mean square of the input voltage (in this case, -0.81 volts dc). A sine-wave input was then substituted for the compressed tape record input. The amplitude of the sine-wave input was adjusted until the mean-square output voltage again read -0.81 volts dc. The required sine-wave input amplitude was 0.67 volt, peak to peak. The voltage sensitivity of the original wave-pressure record was 0.38 volt per inch of water. The equivalent pressure amplitude of the sine wave was 16.8 inches of water, peak to peak. The variance of a sine wave with this pressure amplitude is $A^2/2 = 35 \text{ in.}^2$. The variance of the pressure record as determined by this method is therefore 35 in.^2 .

The spectral density scale. Spectral density has the units of power per cycle or, in statistical

terms, variance per cycle. The spectral density can be expressed as

$$P(f) = \frac{1}{f_2 - f_1} \frac{\int_{f_1}^{f_2} KP(f) df}{\int_0^\infty KP(f) df} \sigma^2$$

where $P(f)$ is the spectral density and $f_2 - f_1$ is the frequency band of the spectrum in which the spectral density is evaluated. K is a scale constant, and σ^2 is the variance of the record being analyzed.

The spectral density scale of the analog spectrum obtained with the narrow band-pass filter was determined by two methods. One method consisted of evaluating the spectral density of the first hump on the spectrum and using this value to set the spectral density scale. Figure 3 shows the narrow band spectrum reproduced on the real (unscaled) frequency axis. The spectral density of the first hump was calculated by taking the ratio of the shaded area to the total spectral area, multiplying by the measured variance, and dividing by the shaded area bandwidth. The resulting spectral density was 435 $\text{in.}^2 \text{ sec.}$

The spectral density scale was also determined by calculating the spectral density of the filter response curve in Figure 3. The spectral density of the peak of the response curve is equal to the variance of the calibration record divided by the effective bandwidth of the filter, 4 cps. The calculations indicate that the spectral density of the peak of the filter response curve was 435 $\text{in.}^2 \text{ sec.}$ This value is in fairly good agreement with the spectral density scale value determined by the other method. The filter response curve is reproduced in Figure 4 for convenience of comparison.

Confidence intervals. The spectra in Figures 1 and 2 are only estimates of the true power spectra of the random function of time which was analyzed. The abrupt ends of the finite samples introduce spectral components which are not present in the true spectrum of the random function. As a result, the spectral estimates determined by analyzing finite samples differ in shape from one sample to another. According to theory, the spectral estimates

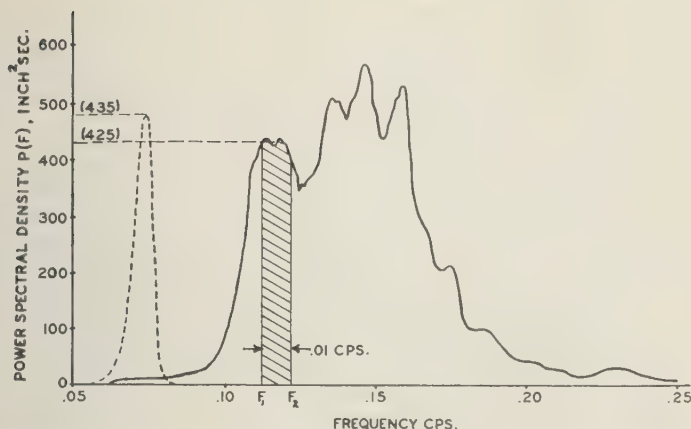


fig. 4. A comparison of the spectral density values of analog spectrum as determined by two methods.

given frequency are distributed as a chi-square distribution with $2N$ degrees of freedom, where N is the number of elemental bands covered by the filter [Pierson, 1954b]. If the spectral density is not a fast changing function of frequency over a frequency interval equal to the bandwidth of the filter, then N is approximately equal to the effective bandwidth of the filter divided by the elemental bandwidth. The elemental bandwidth is $1/T$, where T is the loop period. The spectral estimates in Figures 1 and 2 can be said to be distributed with a chi-square distribution having respectively 100 degrees of freedom and 20 degrees of freedom.

Confidence intervals of the estimated spectral densities can be calculated from a chi-square distribution table. A family of chi-square probability density functions is shown in Figure 5. Figure 5 shows one of the chi-square probability density functions with areas marked off to indicate the manner in which the confidence intervals are calculated. The unshaded area under the curve is 90 per cent of the total area. Ninety per cent of the chi-square values fall within the bounds of this area. The upper and lower bounds of the area can be expressed in terms of the mean, or true, spectral density by dividing by the mean. For chi-square with 100 degrees of freedom the true spectral density $P_T(f)$ is related to the estimated spectral density $P_E(f)$ by the following inequality.

$$0.76P_T(f) < P_E(f) < 1.24P_T(f)$$

Therefore, 90 per cent of the time

$$\frac{P_E(f)}{1.24} < P_T(f) < \frac{P_E(f)}{0.76}$$

The 90 per cent confidence intervals for the spectra in Figures 2 and 3 are

	Upper limit	Lower limit
Wide band	$1.32 P(f)$	$0.81 P(f)$
Narrow band	$1.84 P(f)$	$0.64 P(f)$

A COMPARISON OF THE POWER SPECTRA OBTAINED BY THE ANALOG AND DIGITAL METHODS

The 20-minute wave record that was analyzed by the analog method was also analyzed by the digital method. The digital analysis of the record was done by the Department of Meteorology and Oceanography at New York University.

A chart record was obtained by monitoring the demodulated playback of the storage tape with a Texas Instrument Rectilinear Recording Millimeter. The chart record was marked off at 1.25-sec time intervals, and the ordinates of the record were read and punched on IBM cards. The power spectrum was computed by an IBM 650 computer which was programed [Stevens, 1958] to compute the spectrum by the Tukey method.

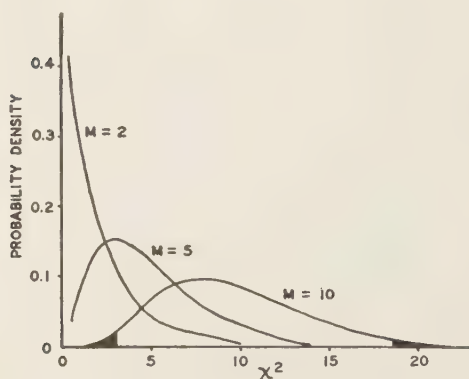


Fig. 5. Probability density functions for chi-square distribution with M degrees of freedom.

In order to make a valid comparison of two spectra, it is necessary that the same resolution be used in obtaining the two spectra. The resolution used in the digital analysis was adjusted to match that of the analog analysis by choosing the digital parameters so that the digital analysis would have the same number of degrees of freedom as the analog analysis. The expression used to calculate the number of degrees of freedom of the digital analysis is [Blackman and Tukey, 1958]

$$M \approx 2(T_n/T_m - 1/3)$$

where T_n is the record length (1200 sec) and T_m is the largest lag. For a 90-lag analysis $T_m = 90(1.25) = 113$ seconds and M 20.6 degrees of freedom. The power spectrum obtained by the 90-lag analysis is represented in Figure 6 by the brokenline curve.

The variance obtained by the digital analysis (21.2 in.²) was only about half that obtained by the analog analysis. The discrepancy was traced to a mistake made in matching the monitoring chart recorder to the demodulator. The use of an incorrect source impedance for the recorder resulted in a poor frequency response in the frequency band of the wave pressure record. The spectrum was corrected for the chart recorder frequency response by making a point-by-point power correction to its spectral values. The variance of the corrected spectrum was obtained by multiplying the uncorrected variance

by the ratio of corrected to uncorrected spectral areas. The resulting variance was 36.2 in.².

The analog spectrum has negligible power between 0.06 cps and the cut-off frequency of the electronics which corresponds to 0.02 cps. A comparison of variances obtained with the two methods, the variance associated with the spectral area to the right of 0.02 cps in the digital spectrum is compared with the variance obtained with the analog method. The two variances are

Variance obtained with the
analog method = 35 in.²

Variance obtained with the
digital method = 34 in.²

Figure 6 shows the analog-determined power spectrum (continuous curve) and the correctly digitally determined power spectrum (dashed broken-line curve). The scales of the spectra are determined by making the areas under the spectra (to the right of 0.02 cps) correspond to their reported variances. The agreement is fairly good.

COMMENTS

The location of the analog spectrum on the frequency axis in Figure 6 is not to be used as a basis for the judgment of the accuracy with which the spectral components can be located on the frequency axis by the analog method. As mentioned above, a slow oscillator drift in the analyzer (not present when the equipment was new) caused repeated analyses of a record to yield identically shaped spectra which were displaced in frequency to the right and to the left of the analog spectrum in Figure 6. The position of the analog spectrum in Figure 6 was chosen for convenience of comparison of spectral shapes.

The compression scheme reported in this paper is not very efficient and would not be satisfactory if a large number of wave records were to be analyzed. If two Ampex FR-100 tape recorders are available, there is a better method. The compression scheme would be as follows: Record 20-minute wave records on an Ampex FR-100 tape recorder at a tape speed of 15 inches per second; cut the tape record from the reel and play it back as a loop at 60 inches per second on an Ampex FR-100 (a holder for the loop of tape 2250 inches long would be required for the playback recorder); record the loop pla-

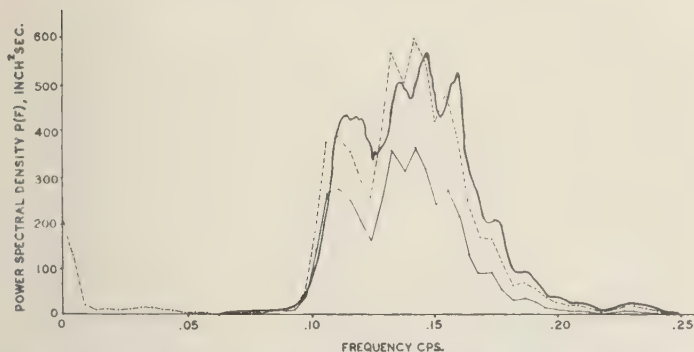


Fig. 6. Power spectra of wave record obtained by analog and digital methods. The continuous line is the analog spectrum, the solid broken-line curve is the uncorrected digital spectrum, and the dashed broken-line curve is the corrected digital spectrum.

on an FR-100 at 17½ inches per second (425 repetitions can be recorded on a 2500-foot loop of tape); play the loop repetition tape back to the analyzer at 30 or 60 inches per second. The corresponding compression ratios would be 1:1 and 1024:1). The FR-100 is available with as many as 14 channels; consequently, a single recording would serve to compress 14 wave records simultaneously. The original wave records could be recorded on one channel at a time for any desired period of time. As many as a hundred 30-minute wave records could be recorded on one reel of tape. Such a method would have an obvious advantage for the storage of the compressed records.

Acknowledgment. The work reported was done by the author while employed by the United States Navy Mine Defense Laboratory, Panama City, Florida.

REFERENCES

Stinson, W. E., A very low frequency recording and analyzing instrument, *NAVORD Rept. 3615*, 1954.
 Ackman, R. B., and J. W. Tukey, The measurement of power spectra from the point of view of communications engineering, *Bell System Tech. J.*, 37, Parts 1 and 2, 1958.

- Ehrenfeld, S., and others, Theoretical and observed results for the zero and ordinate crossing problems of stationary gaussian noise with applications to pressure records of ocean waves, *N. Y. Univ., Coll. Eng., Dept. Meteorol. Oceanog. Tech. Rept.*, 1958.
 Parks, J. K., Power spectra of ocean waves obtained by an analog method using standard laboratory equipment—Comparison of spectra obtained by analog and digital methods, *U. S. Navy Mine Defense Lab., Panama City, Fla., Tech. Paper 158*, 1959.
 Pierson, W. J., An electronic wave spectrum analyzer and its use in engineering problems, *Beach Erosion Board Tech. Mem. 56*, 41–50, 1954a.
 Pierson, W. J., An interpretation of the observable properties of 'sea' waves in terms of the energy spectrum of the gaussian record, *Trans. Am. Geophys. Union*, 35, 747–757, 1954b.
 Pierson, W. J., and W. Marks, The power spectrum analysis of ocean-wave records, *Trans. Am. Geophys. Union*, 33, 834–844, 1952.
 Stevens, R. G., Spectral and cross spectral analysis of two dimensional stationary gaussian time series, *Statistical II, Research Div. Coll. Eng., N. Y. Univ.*, 1958.
 Tucker, M. J., The N. I. O. wave analyzer, *Proc. 1st Conf. Coastal Eng. Instrs.*, Berkeley, Calif., Oct. 1955.

(Manuscript received December 11, 1959; revised February 13, 1960.)

Comparison of Precipitation on Islands of Lake Michigan with Precipitation on the Perimeter of the Lake

F. BLUST AND B. G. DeCOOKE

*U. S. Lake Survey
Detroit, Michigan*

Abstract. A program for measurement of precipitation on certain islands in northeastern Lake Michigan and on the lake's perimeter is described, and an analysis is made of the data collected to date. The analysis indicates that lake surface precipitation computed from the perimeter stations may be greater than the true amount in summer and less in winter. The exposure of the individual precipitation gages on islands is a major factor in the analysis of the data.

Introduction. The U. S. Lake Survey is responsible for studying and evaluating hydrologic phenomena associated with the Great Lakes. In these studies, determining the amount of precipitation which falls on the water areas of the Great Lakes is an important factor.

The Lake Survey computes precipitation per unit area on the lakes from measurements made by the U. S. Weather Bureau at stations located along the perimeters of the lakes. In the computation, weighted precipitation data from the shore stations are summed. It is assumed that precipitation at the shore stations is the same as precipitation on adjacent water areas, but there is considerable evidence that the precipitation on the two areas is significantly different. Horton [1927] gave a detailed discussion of the question and, from a comparison of precipitation measured at Beaver and Mackinaw Islands in northern Lake Michigan with precipitation measured near the shore of the lake at Charlevoix, Petoskey, Mackinaw City, St. Ignace, and Manabwa, Michigan, found the ratio of precipitation over the lake to precipitation at shore stations to be 0.94 in summer and 0.93 in winter. Barber's [1955] data indicated less precipitation on certain islands in western Lake Erie than on the adjacent mainland. Both Horton and Barber noted that a possible cause of reduced over-water precipitation in the summer is reduced thunderstorm activity over the lake—a result of the cooling effect of the water mass in producing a more stable atmosphere over the

lake than over surrounding land areas. Byers and Graham [1949] made a similar observation about Lake Michigan and noted further that in winter the warming effect of the lake encourages greater precipitation on the leeward shore than on the windward shore. Pearson [1958], in a study of observation of precipitation by radar, reported: 'evidence indicated that shower development is less favorable over the lake in summer.'

When the study reported in this article was initiated in 1952, there was strong evidence that the water areas of the Great Lakes receive less precipitation than the land areas. At that time, because of the increasing need for accurate data for hydrologic studies of the Great Lakes and because of the impetus given such studies by the then existing near-record-high levels of the lakes, it was decided to test the accuracy of the Lake Survey method of computing over-water precipitation. In the lake area selected for the test several islands were necessary in order that a network of precipitation gages might be installed. The over-water precipitation measured by these gages would then be compared with precipitation measured simultaneously by gages located on the adjacent shore. It was agreed that the U. S. Weather Bureau, whose responsibility is the measurement of precipitation, would install and maintain the required gages and collect the data, assisted by the Lake Survey, and that the Lake Survey would analyze the data.

Description of the project. After investiga-

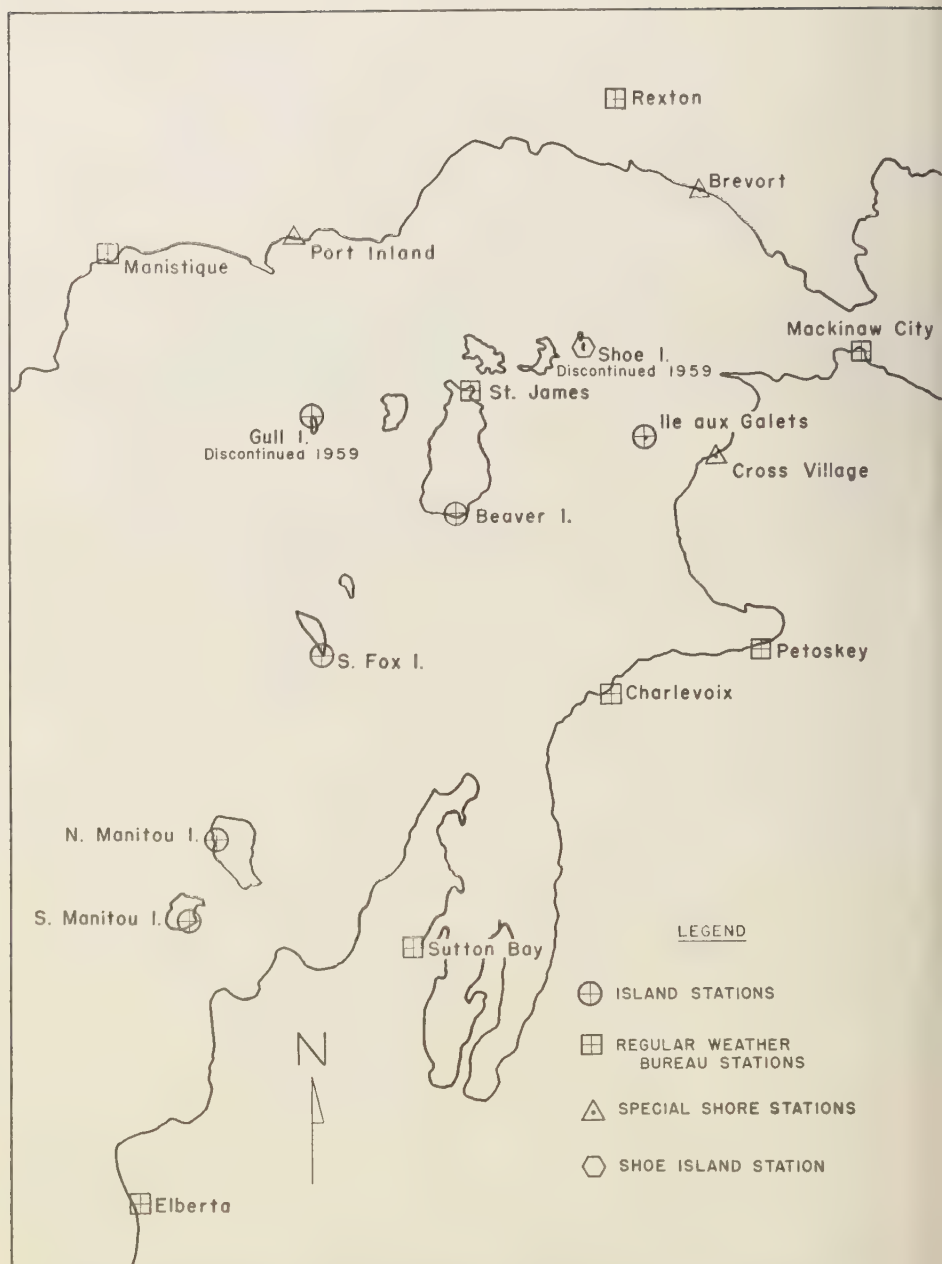


Fig. 1. Map showing locations of precipitation stations in northeastern Lake Michigan.



Fig. 2. A typical island gage installation.

tion of a number of sites, an island group in the northeastern section of Lake Michigan was selected as a suitable site for this study. In October 1952, precipitation gages were installed on six islands in the group. The locations of the gages are shown by circles in Figure 1. These islands vary in shape and size, ranging in area from 6.01 to 72 square miles. The extreme locations are located approximately 65 miles apart. A Sacramento storage precipitation gage equipped with an Alter wind shield was installed on each island (Fig. 2). In addition, records from an existing precipitation station at St. James, Beaver Island (shown by a square in Fig. 1), having a standard 8-inch nonrecording gage equipped with wind shield, were used as land data. Seven regular U. S. Weather Bureau precipitation stations, located near the lake and nearly encompassing the test site, were selected to provide comparative data. These stations are indicated in Figure 1 by squares. Each of the seven stations is equipped with a standard 8-inch nonrecording shielded precipitation gage. At the end of the first year of study it was decided that three new shore stations should be established. Therefore, during the summer of 1953, standard 8-inch nonrecording shielded precipitation gages were installed at the sites indicated by triangles in Figure 1. No further changes were made until October 1956. At that

time a Sacramento storage precipitation gage was installed on Shoe Island (Fig. 1). In the same month anemometers were installed at Sutton Bay, Manistique, Mackinaw City, Elberta, Charlevoix, Beaver Island, Ile aux Galets, Shoe Island, and St. James, and the collection of wind data was started. In December 1958 the anemometers were removed from Beaver Island, Ile aux Galets, Shoe Island, and Charlevoix. In May 1959 the island stations at Gull and Shoe islands were discontinued. A Sacramento storage precipitation gage equipped with an Alter wind shield was installed in May 1959 at a second site on Beaver Island, about half a mile from the original gage installation, and anemometers were installed at both sites. Also in May 1959 a second gage was installed at Ile aux Galets, a few feet from the Sacramento gage. An anemometer was reinstalled at this site. This gage, a standard 8-inch nonrecording shielded precipitation gage, was installed at ground level and ringed with a snow fence.

The reasons for the installation of the Shoe Island gage and the new gages at Beaver Island and Ile aux Galets are described below as part of the analysis of the data.

Inspection of the island gages and measurement of the catches were made semiannually in May and October. Because of the transportation requirements involved in reaching the island sites, inspection of all gages cannot be made on the same day. Hence, the corresponding seasonal periods of record for each of the island gages are often different by a few days. To compare the catch of each island gage with that of the shore gages it is necessary to tabulate the precipitation at each shore station for the period of record at each island station. A composite tabulation of the measured precipitation at shore and island gages from October 1952 through May 1959 is shown in Table 1. The precipitation shown for each shore station under each seasonal period of record is the precipitation measured at that station for the periods of record of the Beaver Island gage.

Analysis of data. It is well established that exposure will affect the amount of precipitation caught by a gage, and as the project progressed there was evidence that exposure might have a major influence on the catches at the island gages. The data in Table 1 show that the catch

TABLE 1. Inches of Precipitation during Period

Island Stations	Oct 1952 to May 1953	May 1953 to Oct 1953	Oct 1953 to May 1954	May 1954 to Oct 1954	Oct 1954 to May 1955	May 1955 to Oct 1955	Oct 1955 to May 1956	May 1956 to Oct 1956	Oct 1956 to May 1957	May 1957 to Oct 1957	Oct 1957 to May 1958	May 1958 to Oct 1958
St. James	14.07	14.67	14.93	14.65	9.68	8.08	12.15	13.33	14.89	14.32	11.58	14.10
South Fox	15.59	15.91	13.10	18.21	8.55	6.09	13.13	11.32	11.66	11.76	11.21	17.06
Gull	14.84	13.61	13.54	14.55	9.95	7.83	14.27	13.23	15.00	12.82	12.12	16.06
Beaver Island	18.82	14.88	16.46	15.14	10.00	8.32	13.62	12.70	15.33	12.65	15.25	16.38
South Manitou	17.09	14.49	14.95	19.63	13.30	7.86	15.49	11.87	16.53	13.54	12.85	14.70
North Manitou	17.34	14.66	14.49	17.86	12.20	6.71	16.15	9.89	14.93	12.09	12.23	13.57
Ile aux Galets	9.61	13.73	9.87	12.79	6.76	5.80	7.81	10.26	10.75	9.74	9.43	12.40
Shoe Island									9.15	10.30	7.13	13.29
Shore Stations												
Manistique	14.18	16.82	14.85	21.01	10.29	12.52	14.77	16.90	14.36	13.26	13.33	16.06
Mackinaw City	13.77	...	13.34	19.50	10.90	9.65	16.07	13.10	15.29	13.90	11.70	15.22
Charlevoix	17.62	14.67	12.48	22.44	12.47	8.17	15.87	11.96	15.03	13.20	12.16	12.16
Sutton Bay	19.87	15.20	16.99	24.18	12.26	7.74	12.63	13.55	14.16	11.44	13.47	13.47
Port Inland	16.49	19.64	8.91	9.65	13.26	16.09	13.69	12.39	12.46	17.39
Brevort Cross	15.32	21.03	11.00	9.65	15.60	15.55	15.87	13.90	13.61	18.15
Village	16.10	15.09	9.07	6.65	14.85	12.05	11.34	14.39	12.25	12.25
Elberta	14.32	21.01	11.43	8.31	14.05	18.22	10.03	12.31	13.76	17.71
Rexton	16.05	15.34	15.23	16.90	9.88	10.34	14.24	17.39	13.71
Petoskey	17.73	12.39	15.40	19.83	10.62	8.46	15.48	14.12	13.83	15.38

at Ile aux Galets was substantially less than the catch at any other of the original six island gages. Ile aux Galets is a low, small island, devoid of vegetation, and the gage there is much less shielded from the wind by topographic features than are the gages at other islands. This was a possible explanation for the deficient catch. Nevertheless, the gage was carefully checked for leakage, and a new gage was installed, as noted above, on Shoe Island, which is similar to Ile aux Galets in that it is low, small, and almost devoid of vegetation. Data obtained from Shoe Island were similar to those obtained from Ile aux Galets, which is additional evidence that greater exposure causes the deficient catch at Ile aux Galets. To further

confirm the effect of exposure, a standard 8-inch Weather Bureau gage was installed on Ile aux Galets in May 1959, as described above. It was expected that precipitation received at the new installation will be less affected by wind passing the gage orifice, and thus a higher catch than that of the storage gage will be obtained.

An exposure index for each of the island shore gages was computed to indicate how extensively the gage was shielded from the wind by topographic features, trees, and buildings in the surrounding area. The horizontal plane of each gage was divided into circular sectors, with the gage orifice at the center, selected so that each sector had topographic features of approximately the same vertical angle (measured at

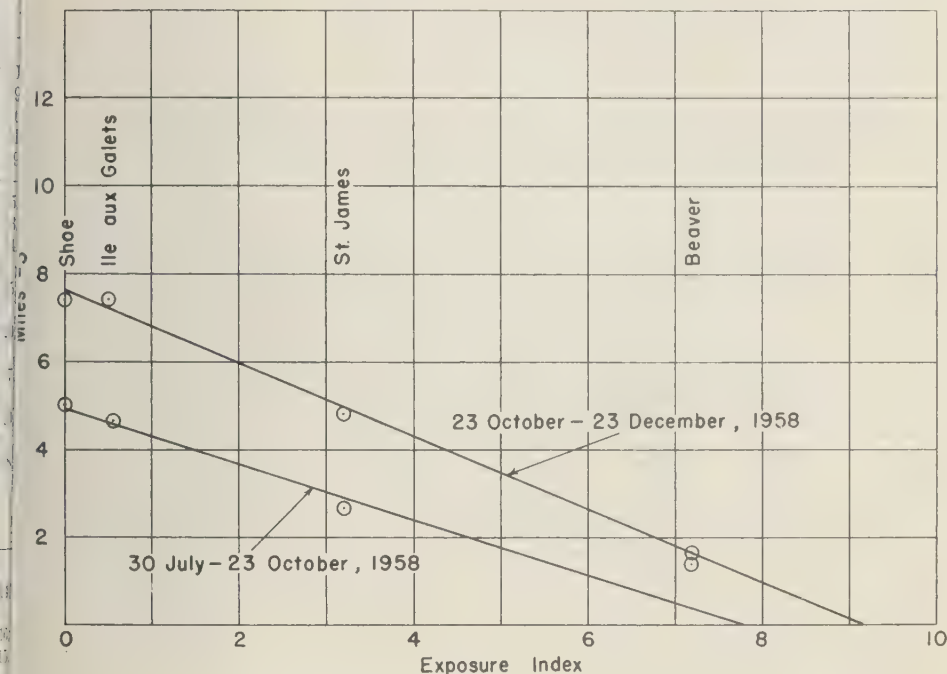


Fig. 3. Mean monthly miles of wind versus exposure index.

(gage orifice) between the horizontal plane and the top of the particular features. The horizontal angle of each circular sector was multiplied by its vertical angle, and the sum of the products so formed, divided by 1000, was considered to be the exposure index for the particular gage. Thus, the gage with the lowest index is least shielded by the surrounding topographic features and is therefore most affected by air turbulence at the gage orifice. Figure 3 is a plot of the mean monthly miles of wind as a function of the exposure index for gages at Shoe Island, Ile aux Galets, St. James, and Beaver Island, based on wind data collected in the summer and fall of 1958. Figures 4 and 5 show the exposure index of each gage plotted against the average seasonal precipitation catch during the period October 1952 to October 1958 for the island and shore stations. Data for the period October 1958 to May 1959 were not used for Figures 4 and 5 so that the winter and summer points would be based on records of approximately the same length. Figure 5 shows that exposure is related

to catch at the island gage sites if areal inequalities of precipitation over the period of record are slight. With a low index, Shoe Island and Ile aux Galets gages recorded much less precipitation than the Beaver Island and South Manitou Island gages, which have high indexes. Figure 4 also shows greater dependence of precipitation on exposure during the winter than during the summer. This is to be expected, since snow is generally more affected by wind than rain is.

The high exposure index at South Fox Island gage presents an anomaly in that the precipitation collected during the winter period was deficient in comparison with exposures and precipitation catches at the other gages. Interception of snow by obstructing objects may account for this deficient catch. However, according to M. A. Kohler of the U. S. Weather Bureau, a topographic effect is a more likely reason, because the experience of that organization indicates that the exposure index of the South Fox Island gage is not high enough to produce the observed

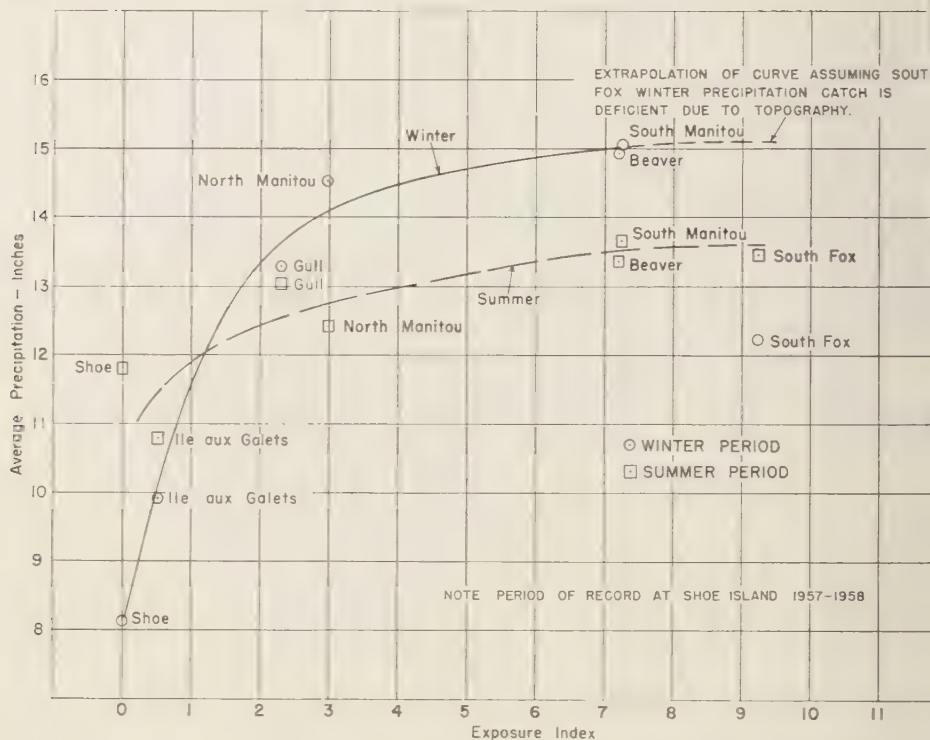


Fig. 4. Seasonal relationship between exposure and average precipitation, 1952-1958, island gages.

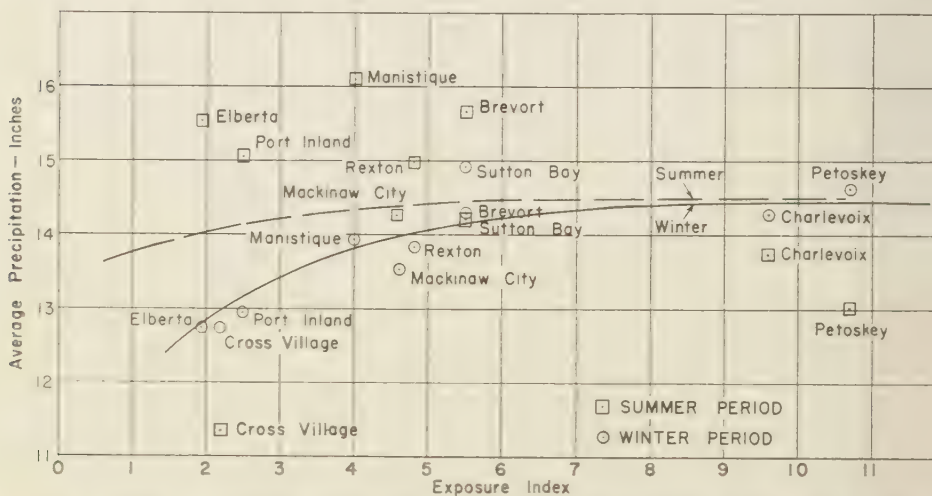


Fig. 5. Seasonal relationship between exposure and average precipitation, shore gages. Period record is 1952-1958, except Rexton 1952-1956, Petoskey 1952-1957, and Elberta 1953-1958.

iciency by interception. It was observed that there is a low hummock to the northwest of the South Fox gage. The hummock does not rise above the elevation of the gage orifice, but it might cause a significant upward deflection of a wind passing the orifice. This topographic feature is not included in the derivation of the exposure index because it lies below a horizontal line through the gage orifice. To investigate the anomaly, a storage gage was installed near the Beaver Island gage in May 1959, as previously noted, in such a position as to duplicate the exposure conditions at the South Fox Island gage without any other apparent influencing topographic feature.

The relationships between the exposure indexes and precipitation at the shore gages (Fig. 1) are more poorly defined than the similar relationships at the island gages. One reason for this is that the island gages can be expected to be subject to higher winds. Another reason may be that wind at the shore gages is more likely to be influenced by topographic features not included in the determination of the exposure indexes.

Since the island gages are located on land masses, their catches may not be representative of over-water precipitation even if the influence of exposure is accounted for. There is the possibility that, although thunderstorm activity may be reduced over the water surface in summer by the cooling effect of the water mass, it may be initiated to some extent over the land masses of the islands. If such a phenomenon has any observable effect, it is reasonable to assume that the degree of the effect is observably related to the size of the island and the direction of prevailing wind. However, a relationship of this kind could not be found nor, in the data col-

TABLE 3. Comparison of Average Seasonal Perimeter Precipitation and Water Area Precipitation, 1952-1958

Season	Precipitation, inches		Percentage of Deviation of Water Area Precipitation from Perimeter Precipitation
	Perimeter	Water Area	
Summer	14.50	13.60	-6.2
Winter	14.45	15.10	+4.5

lected, could any other evidence be found that increased summer shower activity over the islands is significant.

If over the 6-year period of record most of the differences in the seasonal 6-year average precipitation values at the island gages are due to exposure effects, the summer and winter average over-water precipitation values for this period are approximated by the maximum ordinates of the corresponding curves shown in Figure 4. To fulfill the purpose of the investigation, these values must be compared with over-water precipitation values computed from the observed shore-gage data. Table 2 gives the comparison.

The data of Table 2 indicate that the long-period average precipitation on the water area of northeastern Lake Michigan estimated from shore gages is higher than the true precipitation in the summer and lower than the true precipitation in the winter. Further, the seasonal discrepancies are about equal and opposite in sign, so that for the whole year the two estimates are very nearly equal.

Estimates of shore precipitation given in Table 2 are based on observed data uncorrected for exposure effects. It is of interest to estimate the true precipitation along the perimeter of the lake by correcting observed shore data for exposure effects, and to compare the values obtained with the estimated values of precipitation over the water area. Although exposure effects at the shore gages are not clearly defined by the data plotted in Figure 5, the maximum ordinates of the seasonal curves shown in the figure were taken as estimates of true perimeter precipitation. Because of the wide scatter of the points from the curves, particularly for the summer period, this procedure is not entirely consistent with an assumption of equal areal distribution of precipitation. Table 3 shows the seasonal comparison for the 6-year period (1952-1958) of

TABLE 2. Comparison of Average Seasonal Over-Water Precipitation, 1952-1958, Estimated from Island Data and from Shore Data

Season	Precipitation, inches		Percentage of Deviation of Shore Estimate from Island Estimate
	Shore Data	Island Data	
Summer	14.87	13.60	+9.3
Winter	13.86	15.10	-8.2

estimated perimeter precipitation and water area precipitation.

Continuation of project. The collection of data will be continued until October 1962, and the final analysis will be formulated after that time.

Acknowledgments. This project has been conducted as part of the General Investigations program of the United States Army Corps of Engineers by the U. S. Army Engineer District, Lake Survey. The U. S. Coast Guard supplied surface and air transportation to the island sites. Presentation of this report to the American Geophysical Union is by permission of the Chief of Engineers.

REFERENCES

- Horton, R. E., and C. E. Grunsky, *Hydrology of the Great Lakes*, Part III, Appendix II, Chap. I, Report of the Engineering Board of Review of the Sanitary District of Chicago, 1927.
- Verber, J. L., The climates of South Bass Island, western Lake Erie, *Ecology*, *36*, 388-399, 1955.
- Pearson, J. E., The influence of lakes and urban areas on radar observed precipitation echoes, *Bull. Am. Meteorol. Soc.* *39*, 79-82, 1958.
- Byers, H. R., and R. R. Braham, *The Thunderstorm*, U.S. Dept. of Commerce, p. 115, 1949.

(Manuscript received January 7, 1960.)

An Analysis of the Flow of Water in a Shallow, Linear Aquifer, and of the Approach to a New Equilibrium after Intake

J. N. LUTHIN¹

Department of Irrigation, University of California, Davis, California

AND

J. W. HOLMES

Division of Soils, C. S. I. R. O., Adelaide, South Australia

Abstract. The problem of predicting changes in the water table due to changes in the amount of water supplied is analyzed for a specific case. The differential equation describing the situation is

$$(\epsilon/km) \partial\phi/\partial t = \partial^2\phi/\partial x^2 - A/k$$

where ϵ is a storage factor, k the hydraulic conductivity, m the thickness of the aquifer, ϕ the hydraulic head, and A the steady-state loss due to deep seepage and/or evapotranspiration.

The Laplace transformation is used for solving the above equation, subject to an appropriate set of boundary conditions.

Introduction. An investigation of the hydrology of a portion of the upper South-East district of South Australia [O'Driscoll and Shepherd, 1960] suggested that the shallow ground waters were fed from intake areas eastward of the region surveyed. A schematic section of the area, in which homogeneous soil (sand) is assumed for the complete depth of the aquifer, is shown in Figure 1. The essential features of the system are that the flow may be represented approximately by a two-dimensional model, that the water-table surface is initially plane, though sloping, and that the ground water discharges to the Coorong and the sea approximately 25 miles to the west of the intake region. The gradient of the water table is approximately foot per mile except where it dips steeply to the Coorong. The depth of the aquifer seems to be about 100 feet.

The water flowing in the aquifer is replenished by the arrival of surface water at the eastern boundary of the system. There the permeability of the sands is so great that the overland water infiltrates below the surface. The overland flow

occurs in broad sheets of water moving in a northwesterly direction, the several independent streams, however, being divided by low sand dunes running roughly parallel to the coast line. This rather regular system of dunes, which breaks up into an irregular topography of uniform deep sands [Sprigg, 1950] comprises the intake area for the aquifer. The water then begins to flow underground, apparently as a continuous body of water.

The overland flow is markedly seasonal. The simplest description of the system is that water flows into the aquifer during the months of July, August, and September of each year and that there is no flow during the other nine months. In fact, there are some years in which there is intake for longer than this period and other years in which there is no intake at all.

The problem we wished to investigate was the passage of water through the aquifer, assuming it to be taken in at the eastern boundary and eventually discharged into the Coorong Lake on the western boundary. The equipotential and streamline pattern of the aquifer [O'Driscoll and Shepherd, 1960], insofar as it is known, suggested that the system could be approximated by the simple system shown in Figure 1.

This system includes a variety of drainage

¹Fulbright Research Scholar, C.S.I.R.O., Division of Soils, Adelaide, South Australia. On sabbatical leave until March 1959 from the University of California.

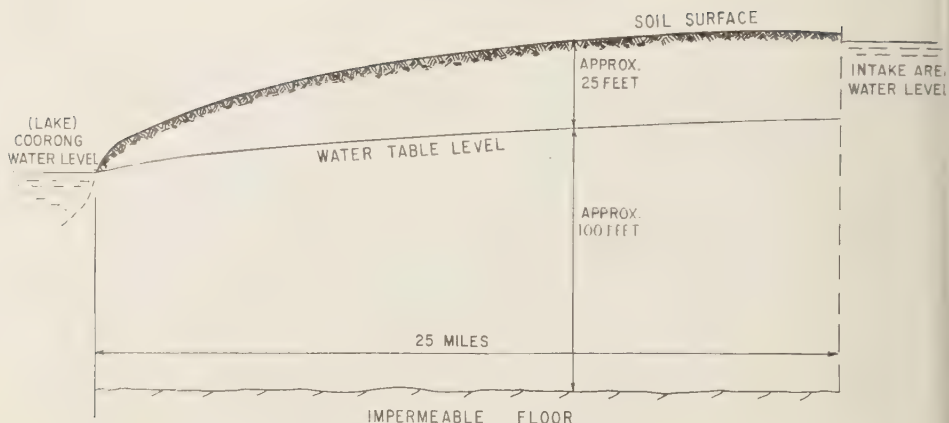


Fig. 1. Schematic section of the shallow aquifer showing intake and discharge areas.

and subirrigation situations, to which the solution given below may be applied. A more extensive analysis of similar problems has been given by Werner [1947].

Water flow in the aquifer. The generalized geometry of the problem is shown in Figure 2. The aquifer has a total horizontal length l and constant depth m . The water discharges at $x = 0$ and is taken into the aquifer at $x = l$. Although there is no evidence that the ground water in our area of study (the upper South-East) is used by the transpiration of plants, or that some is lost by deep seepage, nevertheless such losses will be considered in order to keep the problem as general as possible. Let the rate of loss from either cause be A cm/sec. Then the flow of water in the aquifer [see Boussinesq, 1877; Werner, 1957] is described by

$$(\epsilon/km) \partial \phi / \partial t = \partial^2 \phi / \partial x^2 - A/k \quad (1)$$

where ϵ is the storage coefficient, k (cm/sec) is the hydraulic conductivity of the aquifer (assumed to be constant), ϕ is the hydraulic head, t is time, and m is the thickness of the aquifer; km is called the 'transmissivity'.

Solution of the water flow equation. Consider (Fig. 2) a plane level water table in which the initial hydraulic head ϕ is zero. We shall study the case in which, at time $t = 0$, the hydraulic head at $x = l$ is changed to $\phi = \phi_L$ and is maintained at this value. This system may not be the same as that in the upper South-East district of South Australia, in which the hydrau-

lic head at $x = l$ may be approximately periodic, but the solution can be used as a guide in the development of a program of field investigation.

We therefore have to solve (1) for the initial and boundary conditions.

$$\left. \begin{aligned} \phi &= 0, & 0 < x < l, & t = 0 \\ \phi &= 0, & x = 0, & t > 0 \\ \phi &= \phi_L, & x = l, & t > 0 \end{aligned} \right\} \quad (2)$$

The Laplace transformation of (1) is

$$d^2 \bar{\phi} / dx^2 - q^2 \bar{\phi} = \alpha / p \quad (3)$$

where $q^2 = p/k$, $K = km/\epsilon$, and $\alpha = A/k$. The notation of the Laplace transformation follows that used by Carslaw and Jaeger [1947], whose solutions of many problems of the flow of heat in solids guide the solution given here.

The initial and boundary conditions (2) transform to

$$\bar{\phi} = 0, \quad x = 0, \quad \text{and} \quad \bar{\phi} = \bar{\phi}_L / p, \quad x = l.$$



Fig. 2. Diagram of the aquifer. The source of the water is considered to be at the right hand side at $x = l$. The outlet side is at $x = 0$.

The solution of (3) is

$$\phi = C_1 e^{-qx} + C_2 e^{qx} - \alpha/pq^2 \quad (4)$$

where C_1 and C_2 are constants which have to be evaluated from the boundary conditions. Equation 4 then becomes

$$\phi = \frac{\phi_L}{p} \frac{\sinh qx}{\sinh ql} + \frac{\alpha}{pq^2} \frac{\sinh qx}{\sinh ql} + \frac{\alpha}{pq^2} \frac{\sinh q(l-x)}{\sinh ql} - \frac{\alpha}{pq^2} \quad (5)$$

The inverse transform of (5) is found by expanding the first three terms as a series of exponentials, of which each term is of the form e^{-x^2/p^2} . When this is done, the inverse transform is found to be

$$\begin{aligned} \phi &= \phi_L \sum_{n=0}^{\infty} \operatorname{erfc} \frac{(2n+1)l-x}{2(Kt)^{1/2}} \\ &- \operatorname{erfc} \frac{(2n+1)l+x}{2(Kt)^{1/2}} \\ &+ \alpha K \left[\sum_{n=0}^{\infty} (-1)^n \left\{ t + \frac{(nl+x)^2}{2K} \right\} \right. \\ &\cdot \operatorname{erfc} \frac{nl+x}{2(Kt)^{1/2}} \\ &+ \sum_{n=0}^{\infty} (-1)^n \left\{ t + \frac{(n+1)l-x}{2K} \right\} \\ &\cdot \operatorname{erfc} \frac{(n+1)l-x}{2(Kt)^{1/2}} \\ &+ \sum_{n=0}^{\infty} (-1)^{n+1} (nl+x)(t/\pi K)^{1/2} \end{aligned}$$

$$\begin{aligned} &\cdot \exp \left[-(nl+x)^2/4Kt \right] \\ &+ \sum_{n=0}^{\infty} (-1)^{n+1} \{ (n+1)l-x \} \\ &\cdot (t/\pi K)^{1/2} \exp \left\{ -[(n+1)l \right. \\ &\left. -x]^2/4Kt \right\} - \frac{t}{2} \quad (6) \end{aligned}$$

in which the notation erfc refers to the error function complement, defined by

$$\operatorname{erfc} z = \frac{2}{(\pi)^{1/2}} \int_z^{\infty} e^{-v^2} dv$$

For purposes of generality, (6) includes the term in α which gives the effect of uniform loss of water from the aquifer, either by deep seepage or by transpiration through the plant cover on the land surface. In the particular case which prompted this study, we believe that $\alpha = 0$, and, when we make this assumption, (6) simplifies to

$$\begin{aligned} \phi &= \phi_L \sum_{n=0}^{\infty} \operatorname{erfc} \frac{(2n+1)l-x}{2(Kt)^{1/2}} \\ &- \operatorname{erfc} \frac{(2n+1)l+x}{2(Kt)^{1/2}} \quad (7) \end{aligned}$$

Values of the water-table height ϕ (equation 7) for various times t after the establishment of a new boundary value of $\phi = \phi_L$ at $x = l$ are shown in Figure 3. The values of the parameters used in calculating ϕ are given in Table 1.

The hydraulic conductivity was not measured, and the value assumed is representative of a permeable sand. The amount of water ϵ that

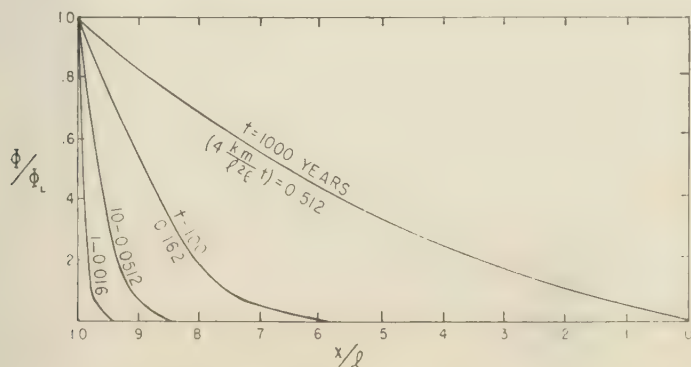


Fig. 3. Height of the water table in the aquifer.

TABLE 1. Numerical Values of the Parameters Used in Making the Plot in Figure 3

Quantity	Symbol	Magnitude
Hydraulic conductivity	k	1×10^{-2} cm/sec
Depth of aquifer	m	3000 cm
Length of aquifer	l	4×10^6 cm
Storage coefficient	ϵ	0.45

must be added to, or removed from, the soil lying above the water table to change the height of the water table by unit distance was determined from the moisture characteristics of samples taken from the soil at one locality only, at a depth of 6 meters.

One of the main features of the aquifer, at once evident from Figure 3, is the long time required for approximate approach to equilibrium. Even after 10 years the water would have moved perceptibly a distance of $2\frac{1}{2}$ miles, with still $22\frac{1}{2}$ miles to go. After 1 year it would have moved perceptibly a distance of less than 1

mile. Such a time scale makes it difficult, of course, to check the computation from any field observations. The scant field data we have indicate an approximate agreement with theory.

REFERENCES

- Boussinesq, J., Essai sur la theorie des eaux courantes, *Mem. Acad. des Sci.*, 23, ser. 2, 680 p. 1877.
- Carslaw, H. S., and J. C. Jaeger, *Conduction of Heat in Solids*, Oxford Univ. Press, 1947.
- O'Driscoll, E. D., and R. G. Shepherd, The hydrology of part of County Cardwell in the upper South-East of South Australia, *S. Australia Dept. of Mines, Rept. of Investigations No.* 1960.
- Sprigg, R. C., The geology of the South-East Province, S. Australia, with special reference to quaternary coast-line migrations and modern beach developments, *Dept. of Mines, Geol. Survey of S. A. Bull.* 29, 1950.
- Werner, P. W., Some problems in non-artesian ground-water flow, *Trans. Am. Geophys. Union* 38, 511-518, 1957.

(Manuscript received May 18, 1959; revised February 11, 1960.)

The Long-Time Response of a Layered Elastic Medium to Explosive Sound¹

J. H. ROSENBAUM

Shell Development Company, Exploration and Production Research Division, Houston, Texas

Abstract. The long-time response of a layered elastic medium is considered for the particular case of a point-source explosion in a liquid layer lying above an infinitely deep liquid bottom. An asymptotic solution, valid for large values of the time variable, is obtained; it expresses the response in terms of harmonic vibrations of the liquid layer. Special emphasis is placed on those vibrations which correspond to waves with small angles of incidence and which, because of radiation into the bottom, decay exponentially with time. However, the well-known guided-wave phenomenon, first discussed by Pekeris in 1948, is also included in the present formulation.

A detailed presentation is made of the method of analysis. This method is applicable to more complicated problems of direct geophysical interest. Numerical results are presented for some typical examples, the behavior of the phase velocity for the lower modes being of particular interest.

INTRODUCTION

The problem of elastic wave propagation from point-source explosions in layered media is of fundamental importance in theoretical seismology. Even for the simplest cases, the mathematical treatment can become quite laborious, and it is necessary for us to choose different methods of analysis depending on what specific features of the problem are of primary interest. Two general methods are apparent. One is the so-called ray treatment [Pekeris, 1948, p. 46 ff.], which amounts to expressing the solution in terms of signals arriving from image sources successively farther removed from the detector. In essence, the layer problem is resolved into a sum of problems of the type in which two semi-infinite media are in contact along a plane. Each of these problems can then in turn be solved exactly by methods derived by Hugoniot [1939], Pekeris [1948], Pekeris and Ingman [1958], and others. However, the evaluation of even a single term of the solution, that is, one 'ray,' requires considerable effort, so that in practice we are restricted to a small

number of images, that is to early arrivals at the detector. The total response at the detector is given as a superposition of contributions, each of which is a function of time and must be evaluated numerically. The solution is exact, but the computation is very laborious; and the solution is not easily interpreted if we are interested in the response at later times, when the interference of the contributions from many images becomes important.

The second method is essentially complementary to the 'ray' approach and treats directly the interference phenomenon due to the superposition of signals from the images. This is the modal or normal coordinate approach [Pekeris, 1948, p. 51 ff.], where the response of the medium to the explosion wave is expressed in terms of the free vibrations of the layers. The solution can then be stated (exactly) as a sum of single integrals (see equation 33 below). These integrals can readily be evaluated by asymptotic methods² as long as the time from the start of the explosion is large compared with the vertical transit time of elastic waves through the layer or layers. This relative ease of calculation and the form of the solution as a sum of oscillatory contributions are the outstanding features of the modal approach.

¹ Publication No. 223, Shell Development Company, Exploration and Production Research Division. Presented at the Fortieth Annual Meeting of the American Geophysical Union, Washington, D. C., May 5, 1959.

² Two of the integrals can be evaluated exactly without difficulty.

In the present paper, we are interested in the long-time response of a layered elastic medium to explosive sound, and thus the modal approach is indicated. The modal approach has been used by many investigators in connection with the problem of refraction shooting in water-covered areas [Erwing, Jardetzky, and Press, 1957]. Such solutions concern the wave-guide type of propagation through water layers over bottom materials in which the velocity of elastic waves is greater than the sound velocity in water. They apply to relatively early signals, which do not radiate into the bottom half-space. The solutions are valid for large values of the horizontal distance r from source to detector and are expressed as asymptotic series in inverse powers of r . The problem to be treated here, however, is of a somewhat different nature. We wish to consider also problems connected with reflection shooting, where the horizontal distance r need not be large. Of particular interest are persistent oscillations often observed in water-covered areas, which may obscure all useful seismic reflections. We shall therefore derive solutions valid for large values of the time variable t and express these solutions as asymptotic series in inverse powers of t . As we pointed out earlier, a convenient modal solution requires precisely that t be large in comparison with the vertical transit time of elastic waves through the layers. Because of the finite propagation velocity of any first-arrival signal, large horizontal distance also implies large time, so that an asymptotic solution in inverse powers of the time variable also includes the long-range refraction solution for the high-velocity bottom.

The case of a point-source explosion in a liquid

layer lying above an infinitely deep liquid bottom, which we treat here, represents one of the simpler examples of the general problem of propagation of elastic waves in layered media. The algebra involved in its solution is relatively tractable, but the solution still exhibits most of the general features of more complicated systems. Thus we can clearly demonstrate the method of analysis, which is also applicable to more difficult elastic-layer problems of direct geophysical interest. A case in point is the reverberation problem referred to above. The simple model with liquid layer and liquid bottom cannot account for such a phenomenon except in cases of extreme velocity (and density) contrasts. There are models of a somewhat more complicated nature than the one treated here, however, which do exhibit this phenomenon. An evaluation of the long-time response of such models to a point-source explosion presents a much more difficult computational problem, but the essential features of the analysis are the same as those given in the present paper.

THE FORMAL SOLUTION

In this section we derive a mathematical expression for the pressure signal obtained in the liquid layer due to a point-source explosion in the layer. The formal solution to the problem appears in the form of a repeated integral, whose reduction to a more convenient form and evaluation will be taken up in later sections of this paper.

A schematic drawing of the configuration of our problem is given in Figure 1. H is the depth of the liquid layer of density ρ_1 and sound velocity c_1 which lies on top of an infinitely deep

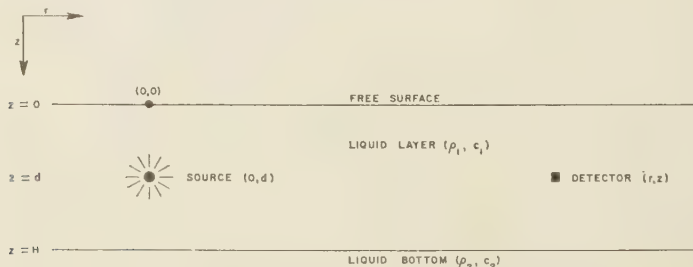


Fig. 1. The two-layer liquid model.

homogeneous liquid bottom of density ρ_2 and sound velocity c_2 . We consider mainly the case of bottom whose sound velocity and density are greater than those of the layer, $c_2 > c_1$ and $\rho_2/\rho_1 < 1$. At a depth d below the free surface, a point source of explosive sound within the layer emits a pressure pulse at time $t = 0$, which is described by an amplitude factor A (at unit distance) and an exponential decay time-constant θ . We introduce cylindrical coordinates, r, ϕ, z , with origin at the free surface directly above the source; r is the radial coordinate parallel to the free surface, and the positive z axis points downward into the medium. Because of symmetry, the problem is independent of the polar angle ϕ .

In the liquid layer, the wave equation

$$\nabla^2 P = (1/c_1^2)(\partial^2 P / \partial t^2) \quad (1)$$

is applicable. Similarly, in the liquid bottom,

$$\nabla^2 P = (1/c_2^2)(\partial^2 P / \partial t^2) \quad (2)$$

The point source of explosive sound emits a pressure pulse, described in the water layer by the formula

$$P(R, t) = \frac{A}{R} [H_u(t - R/c_1)] e^{-(t - R/c_1)/\theta} \quad (3)$$

where $R^2 = r^2 + z^2$, and H_u represents the Heaviside unit step function. The boundary conditions are vanishing pressure at the free surface, $z = 0$; continuity of pressure and displacement at the layer-bottom interface, $z = H$; and the radiation conditions for $r \rightarrow \infty$ and $z \rightarrow \infty$.

The pressure signal P , observed at a point (r, z) in the liquid layer, is then given by the equation*

$$P(r, z, t) = \frac{A}{\pi i} \int_{\gamma - i\infty}^{\gamma + i\infty} \frac{e^{st}}{(s + 1/\theta)} ds \int_0^\infty J_0(kr) k \frac{\sinh \beta_1 d}{\beta_1} \frac{\beta_1 \cosh \beta_1(H - z) + b\beta_2 \sinh \beta_1(H - z)}{\beta_1 \cosh \beta_1 H + b\beta_2 \sinh \beta_1 H} dk \quad (4)$$

for $d \leq z \leq H$. For $0 \leq z \leq d$, interchange z and d in the above equation. Here, $s = i\omega$ is the

Laplace transform variable, ω is the angular frequency, k is the wave number in the radial direction, and γ is real and > 0 .

$$\beta_1 = (k^2 + s^2/c_1^2)^{1/2} \quad (5)$$

$$\beta_2 = (k^2 + s^2/c_2^2)^{1/2}$$

For $\gamma > 0$, the integrand over k has no singularities on the positive real k axis, and (4) may be considered a double integral. Let us now look at the complex s plane when k is real and positive. The square roots β_1 and β_2 have branch points at $\pm ic_1 k$ and $\pm ic_2 k$, respectively; but, since the integrand is an even function of β_1 , only the β_2 branch points need be considered. Cuts are made in the Riemann plane between $\pm ic_2 k$ and ∞ (Fig. 2A), and both the square roots β_1 and β_2 are chosen positive along the real s axis. We find that the integrand of (4) has a pole on the negative real axis at $s = -1/\theta$, and for the case $c_2/c_1 > 1$ it has a set of poles, the so-called normal mode poles, on the imaginary axis between $\pm ic_1 k$ and $\pm ic_2 k$, as indicated by the heavy lines in Figure 2. The normal mode poles are roots of the period equation

$$f = \beta_1 \cosh \beta_1 H + b\beta_2 \sinh \beta_1 H = 0 \quad (6)$$

on the imaginary axis of the top sheet of the s plane (Fig. 2). It is easily demonstrated that on the top sheet of the s plane as drawn in Figure 2A there can be no further roots of the period equation.

REDUCTION OF THE FORMAL SOLUTION TO SINGLE INTEGRALS

In this section we reduce our formal solution, as given by the repeated integral in (4), to a

* It can be shown that the expression $P(r, z, t)$ will vanish at times earlier than the arrival of the first (refracted or reflected) signal.

sum of single integrals. To do this, we shift the branch cuts of the square root β_2 (and paths of integration running along them) into a rapidly converging position in both the complex s and the complex k planes. In so doing we uncover

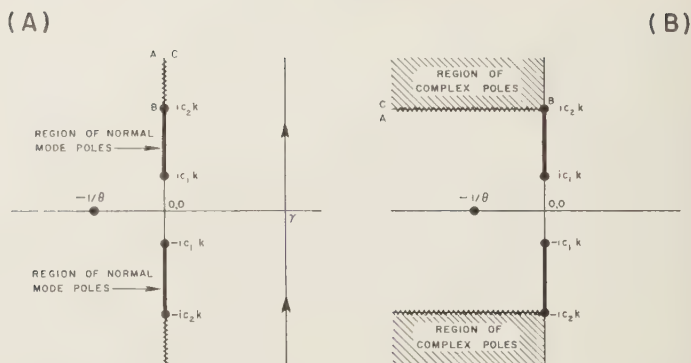


Fig. 2. The principal Riemann surface of the complex s plane for k real and positive. (To convert the ω plane, rotate each figure by an angle of $-\pi/2$ around the origin.)

poles which were originally on the lower Riemann surface of the complex s plane and which generally correspond to vibrations at frequencies lower than the cutoff values of the normal mode vibrations usually considered. When the cuts are drawn in this position, poles of the integrand no longer pass through the branch cuts from one Riemann surface to the other. It then becomes possible in each case to express one of the integrations by means of residues at poles. Two types of integrals are obtained. One type consists of the pressure contributions P_L and P_{BL} , which are monotonically decaying functions of time and are thus of no great interest. The other type consists of the pressure contributions P_N , P_{B2} , and P_{B3} , which can be combined into a single integral P_V . This integral represents vibrations of the water layer.

To obtain a convenient solution valid for large values of the time variable t , we proceed as follows. We interchange the order of integration of equation 4, which is permissible because for $\gamma > 0$ the integrand has no singularities on the positive real k axis. We shift the path of integration over s to the imaginary axis, and, since the integrand of (4) is real on the real s axis, it is very easy to combine the integrals in the lower and upper half-planes into one in the upper half-plane.

Next, we deform the path of integration into the second quadrant of the s plane. The contribution from the arc at infinity vanishes, and we have

$$P = P_L + P_N + P_B$$

P_L is a line integral from 0 to $-\infty$ along the negative real s axis, which avoids the pole $s = -1/\theta$ by a small indentation into the second quadrant. P_N is the contribution due to poles on the positive imaginary s axis, and P_B is the branch line integral around the cut on the positive imaginary s axis (from A to B to C in Fig. 2A). We may combine the integrals on two sides of the cut into one and thus express P_B as an integral from $s = ic_2 k$ to $s = ic_1 k$ on the right-hand side of the cut (path BC).

A digression on the roots of the period equation. Before proceeding with the discussion of the integrals P_L , P_N , and P_B , we digress briefly to investigate the roots of the period equation

$$f = \beta_1 \cosh \beta_1 H + b\beta_2 \sinh \beta_1 H = 0$$

for the case $c_2/c_1 > 1$, and $c_2/c_1 b > 1$, in the second quadrant of the s plane (Fig. 2A). The locus of the roots of $f = 0$ in the s plane for a set of values of k in the k plane are called the dispersion curves of the period equation in the s plane. In this case we choose for the set

$$P = \frac{2A}{\pi} \operatorname{Im} \int_0^\infty J_0(kr) k dk \int_0^\infty \frac{e^{st}}{(s + 1/\theta)} \frac{\sinh \beta_1 d}{\beta_1} \frac{\beta_1 \cosh \beta_1 (H - z) + b\beta_2 \sinh \beta_1 (H - z)}{\beta_1 \cosh \beta_1 H + b\beta_2 \sinh \beta_1 H} ds$$

values in the k plane the positive real k axis. Equation 6 represents a functional relationship between the two complex variables k and s .

At $k = 0$, the roots of $f = 0$ in the second quadrant of the s plane (Fig. 2A) are all on the lower Riemann surface at

$$s = (c_1/2H) \ln [(c_2/c_1 - b)/(c_2/c_1 + b)] + i(c_1/H)(n - 1/2)\pi \quad (9)$$

where $n = 1, 2, \dots$. Expanding around these points, we obtain for the initial derivatives of the dispersion curves at $k = 0$,

$$ds/dk = 0; \quad d^2s/dk^2 = -(c_1^2/s) \cdot \{1 + (bc_2/sH) \cdot [(1 - c_1^2/c_2^2)/(1 - b^2c_1^2/c_2^2)]\} \quad (10)$$

With increasing k , the roots s_n move toward the imaginary axis in a direction of increasing imaginary values. Their motion in the positive imaginary direction, however, is slower than that of the branch point $s = ic_2k$. Thus, they reach the positive imaginary s axis on the lower Riemann surface at points falling between ic_1k and ic_2k which are described by the equation

$$(1 - c_1^2/c_2^2)b^2 \tanh^3 \beta_1 H - \beta_1 H \tanh^2 \beta_1 H - \tanh \beta_1 H + \beta_1 H = 0 \quad (11)$$

where the roots in the second quadrant of the s plane coincide with a similar set of roots in the first quadrant, and the period equation $f = 0$ has double roots. With a further increase in k there are two sets of roots on the positive imaginary axis of the lower Riemann surface. One set moves toward the point ic_2k on the lower sheet; $s \rightarrow ic_1k[(1 - b^2)/(1 - b^2c_1^2/c_2^2)]^{1/2}$ for the lowest mode, and $s \rightarrow ic_1k$ for the higher modes as $k \rightarrow \infty$. The other set moves with increasing k faster than the branch point $s = ic_2k$. These roots therefore appear at the branch point on the upper Riemann surface at the 'cutoff' values

$$s = ic_2k_n \\ s = ic_2(n - 1/2)\pi/H(c_2^2/c_1^2 - 1)^{1/2} \quad (12)$$

These roots are now precisely the normal mode

roots of the period equation, which we considered separately as the contribution P_N . Since at the branch point

$$ds/dk = ic_2$$

and

$$d^2s/dk^2 = -i(c_2^2/c_1^2 - 1)^2 c_2 k H^2 / b^2 \quad (13)$$

we find that upon reaching the upper Riemann surface of the s plane the roots move more slowly than the branch point with increasing k . The poles remain on the positive imaginary s axis and for all modes approach the limiting point $s = ic_2k$ on the top surface as $k \rightarrow \infty$.

Evaluation of P_L . The pressure contribution P_L is given by the expression

$$P_L = \frac{2A}{\pi} \operatorname{Im} \int_0^\infty J_0(kr) k \, dk \cdot \int_0^\infty \frac{e^{s\theta}}{(s + 1/\theta)} \frac{\sinh \beta_1 d}{\beta_1} F_1(s, k) \, ds \quad (14)$$

where

$$F_1(s, k) = \frac{\beta_1 \cosh \beta_1 (H - z) + b \beta_2 \sinh \beta_1 (H - z)}{\beta_1 \cosh \beta_1 H + b \beta_2 \sinh \beta_1 H}$$

This integral is purely real except for the indentation around the pole at $s = -1/\theta$. Evaluation of this contribution yields

$$P_L = 2Ae^{-1/\theta} \int_0^\infty J_0(kr) k \cdot \frac{\sinh \beta_{1\theta} d}{\beta_{1\theta}} F_1(-1/\theta, k) \, dk \quad (15)$$

where the subscript θ signifies evaluation of the functions at $s = -1/\theta$. The integral in (15) can be evaluated numerically. The important feature of the expression, however, is the fact that it does not represent an oscillation but a monotonic decay. This decay is exponential in time and has the same decay time-constant θ as the original pulse.

We note that there is no contribution from P_L when $\theta \rightarrow 0$ (the delta-function source). When $\theta \rightarrow \infty$, that is for the unit step function source, we may express P_L in terms of a series

$$P_L = A \left\{ [r^2 + (z - d)^2]^{-1/2} - [r^2 + (z + d)^2]^{-1/2} + \sum_{n=1}^{\infty} (-1)^{n-1} \left(\frac{1-b}{1+b} \right)^n \cdot [r^2 + (2nH - z - d)^2]^{-1/2} - [r^2 + (2nH - z + d)^2]^{-1/2} - [r^2 + (2nH + z - d)^2]^{-1/2} + [r^2 + (2nH + z + d)^2]^{-1/2} \right\} \quad (16)$$

P_L here corresponds precisely to the sum of the residues at infinity of Cagniard's method as applied to the present problem [Cagniard, 1939; Rosenbaum, 1956].

The normal mode poles. The pressure contribution due to the normal mode poles P_N is obtained in terms of the residues at the poles.

$$F_3(s, k) = \frac{b\beta_2 \sinh \beta_1 d \sinh \beta_1 z}{(\beta_1 \cosh \beta_1 H + b\beta_2 \sinh \beta_1 H)(\beta_1 \cosh \beta_1 H - b\beta_2 \sinh \beta_1 H)}$$

After some algebraic reduction, we write

$$P_N = 4A \operatorname{Re} \sum_n \int_{k_n^0}^{\infty} J_0(kr) k \frac{\exp(s_n t)}{(s_n + 1/\theta)} F_2(s_n, k) dk \quad (17)$$

where

$$F_2(s_n, k) = \frac{\sinh \beta_{1n} d \sinh \beta_{1n} z}{\sinh \beta_{1n} H [\partial/\partial s (\beta_{1n} \cosh \beta_{1n} H + b\beta_2 \sinh \beta_{1n} H)]_n}$$

The summation extends over the $n = 1, 2, \dots$ normal mode solutions of the period equation $f = 0$. The subscripts n also refer to an evaluation of a function at such a solution. The partial derivative in the denominator of F_2 refers to constant k . The change of order of summation and integration is permitted if the number of modes is finite, and on the basis of physical arguments we may certainly ignore very high

modes.⁴ The integrals over k in (17) extend over the n normal mode dispersion curves given by the period equation $f = 0$ which were discussed previously. The lower limit of integration k_n^0 refers to the branch point $s = ic_n$ where the normal mode poles first appear on the upper Riemann surface of the s plane (Figure 2A). Thus

$$k_n^0 = -is_n^0/c_2 = (n - 1/2)\pi/H(c_2^2/c_1^2 - 1)^{1/2} \quad (18)$$

At the upper limit $k \rightarrow \infty, s \rightarrow ic_k$.

The branch line integral. The branch line integral P_B is given by the expression

$$P_B = -\frac{4A}{\pi} \operatorname{Im} \int_0^{\infty} J_0(kr) k dk \int_{ic_k}^{1-i\infty} \frac{e^{st}}{(s + 1/\theta)} F_3(s, k) ds \quad (19)$$

where

The integration over s runs along the right hand side (BC) of the cut in Figure 2A where the phase of β_s is imaginary and positive. Next we shift the path of integration, as well as the branch cut, into the second quadrant of the s plane (Fig. 2B). The integration now extends from $s = ic_k$ to $s = ic_k - \infty$, and the integral converges rapidly for large values of t . The arc at infinity contributes nothing, since $2H \gg z + d$. However, in shifting the path of integration, we pass over complex roots of the period equation

$$f = \beta_1 \cosh \beta_1 H + b\beta_2 \sinh \beta_1 H = 0 \quad (20)$$

whose positions in the second quadrant of the s plane for k real and positive were described

⁴ If the pressure at the source is a continuous function of time, the infinite series in the integrand converges, and the order of integration and summation may be changed directly. Note the corresponding occurrence of logarithmic singularities in the ray theory solution [Pekeris and Longman, 1958; Rosenbaum, 1956].

viously. We note that we do not pass over roots of the equation

$$f = \beta_1 \cosh \beta_1 H - b\beta_2 \sinh \beta_1 H = 0 \quad (20)$$

since $f_2 = 0$ is precisely the period equation $f = 0$ if the definition of the upper and the lower sheet of the s plane is inverted; and the period equation $f = 0$ had no roots in the second quadrant on the upper Riemann surface of the original s plane (Fig. 2A).

On shifting the path of integration of (19) in the s plane to the position shown in Figure 2B, we pass over all roots of the period equation $f = 0$ whose imaginary parts are greater than $c_2 k$; those whose imaginary parts are equal to $c_2 k$ are avoided by means of a small indentation in the path of integration. The branch line integral P_B is now written as

$$P_B = -\frac{4A}{\pi} \operatorname{Im} \int_0^\infty J_0(kr) k dk \\ + \int_{ic_2 k}^{ic_2 k - \infty} \frac{e^{st}}{(s + 1/\theta)} F_2(s, k) ds \\ + 4A \operatorname{Re} \sum_n \int_0^{k_n^1} J_0(kr) k \\ \cdot \frac{\exp(s_n t)}{(s_n + 1/\theta)} F_2(s_n, k) dk = P_{B1} + P_{B2} \quad (21)$$

The s integration in the first integral P_{B1} refers to the path BC in Figure 2B. The function $F_2(s, k)$ in P_{B2} was defined in (17). The limit of integration k_n^1 in P_{B2} refers to points $\operatorname{Im}(s_n^1)$ or k_n^1 , where the roots s_n pass through the branch cut (Fig. 2B).

In order to evaluate the pressure contribution P_{B1} , we introduce a change of variable from s to q

$$q = -s + ic_2 k \quad (22)$$

so that the branch point $s = ic_2 k$ is at the origin of the q plane), and we change the order of integration

$$P_{B1} = \frac{4A}{\pi} \operatorname{Im} \int_0^\infty e^{-qt} dq \int_0^\infty J_0(kr) k \\ \cdot \frac{\exp(ic_2 kt)}{(1/\theta - q + ic_2 k)} F_2(q, k) dk \quad (23)$$

the phase of β_2 along the path BC of Figure

2B (q and k both real and positive) varies from $3\pi/4$ to π , as q varies from 0 to ∞ . When $q = 0$, we see that β_2 vanishes, and so does the numerator of $F_2(q, k)$. Both factors in the denominator of $F_2(q, k)$ become equal to $\beta_1 \cosh \beta_1 H$. The denominator can now vanish when $\cosh \beta_1 H = 0$, that is for $\beta_1 H = i(n - 1/2)\pi$, and the integrand over k becomes infinite at those points. When $q > 0$, neither factor in the denominator of $F_2(q, k)$ can vanish for real values of k , since we avoided poles on the branch cut by small indentations in the path of integration of P_{B1} . Since the integrals over q and k now converge, the change of order of integration carried out above is permissible if we consider the integration over k to extend from $q = \delta$ to $q = \infty$ and let $\delta \rightarrow 0$ in the limit.

For large values of the time t , the integral over q in P_{B1} is converging rapidly. In order to have the integral over k converge rapidly also, we shift the path of integration in the complex k plane to the positive imaginary axis. The principal Riemann surface of the k plane for q real and positive is shown in Figure 3. From equations 5 and 22 we see that β_2 may

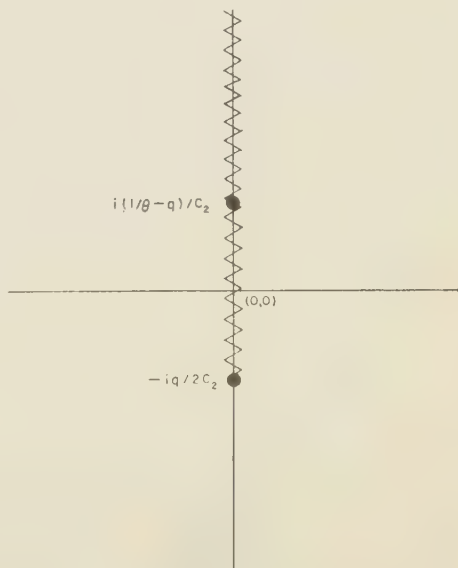


Fig. 3. The principal Riemann surface of the complex k plane for q real and positive.

now be written as

$$\beta_2 = q^{1/2}(k + iq/2c_2)^{1/2}(2/c_2)^{1/2}e^{i3\pi/4} \quad (24)$$

and thus has a branch point at $k = -iq/2c_2$. We cut the k plane along the imaginary axis between the branch point and $i\infty$, as shown in the figure. Depending on whether $1/\theta \geq q$, there is a pole at $k = i(1/\theta - q)/c_2$ on the positive or negative imaginary axis.

The path of integration for P_{B1} in (23) is along the positive real k axis. When $q = 0$, the function $F_3(0, k)$ has double poles at the points k_n^0 along the real k axis. For $q > 0$, one set of poles, corresponding to the roots of the period equation

$$f = \beta_1 \cosh \beta_1 H + b\beta_2 \sinh \beta_1 H = 0 \quad (6)$$

moves into the first quadrant of the k plane; the other set, corresponding to roots of the equation

$$f_2 = \beta_1 \cosh \beta_1 H - b\beta_2 \sinh \beta_1 H = 0 \quad (20)$$

moves into the fourth quadrant. For still larger values of q , the poles in the first quadrant will again return to the real k axis at the points $k = k_n^0$ and then move also into the fourth quadrant. Thus, when we shift the path of integration in the k plane from the real axis to the positive imaginary axis, we must leave a small indentation around the pole at $i(1/\theta - q)/c_2$ whenever it occurs on the positive imaginary axis, and we must also take into account the poles in the first quadrant of the k plane due to the roots of the period equation $f = 0$. The arc at infinity evidently contributes nothing, and we write

$$\begin{aligned} P_{B1} = & \frac{4A}{\pi} \operatorname{Im} \int_0^\infty e^{-at} dq \int_0^{i\infty} J_0(kr) k \\ & \cdot \frac{\exp(i\omega kt)}{(1/\theta - q + ic_2 k)} F_3(q, k) dk \\ & - 4A \operatorname{Re} \sum_n \int_0^{q_n} \frac{\exp[-(q + ic_2 k_n)t]}{(1/\theta - q + ic_2 k_n)} \\ & \cdot J_0(k_n r) k_n F_4(q_n, k) dq = P_{BL} + P_{B3} \end{aligned} \quad (25)$$

where

$$F_4(q, k_n) = \frac{\sinh \beta_{1n} d \sinh \beta_{1n} z}{\sinh \beta_{1n} H [\partial/\partial k (\beta_1 \cosh \beta_1 H + b\beta_2 \sinh \beta_1 H)]_n}$$

Here the limits of integration 0 and q_n^1 in P_{B1} correspond to the interval when the period equation $f = 0$ has roots in the first quadrant of the k plane. The partial derivative $\partial f/\partial k$ in the denominator of $F_4(q, k_n)$ refers to constant q .

Evaluation of P_{BL} . In the first integral of the right-hand side of (25), we set $k = i\xi$; the

$$\begin{aligned} P_{BL} = & -\frac{4A}{\pi} \operatorname{Im} \int_0^\infty e^{-at} dq \int_0^\infty I_0(\xi r) \xi \\ & \cdot \frac{\exp(-c_2 t \xi)}{(1/\theta - q - c_2 \xi)} F_3(q, \xi) d\xi \end{aligned} \quad (26)$$

The repeated line integral is thus purely real except for the indentation around the pole $\xi = (1/\theta - q)/c_2$ on the positive real ξ axis. This pole arises there only in the interval $0 \leq q \leq 1/\theta$. Evaluation of this contribution yields

$$\begin{aligned} P_{BL} = & 4Ae^{-t/\theta} \\ & \cdot \int_0^{1/\theta} I_0(\xi_0 r) \frac{\xi_0}{c_2} F_3(q, \xi_0) dq \end{aligned} \quad (27)$$

where $\xi_0 = (1/\theta - q)/c_2$. Again, the integral in (27) can be evaluated numerically; the important feature of the expression, however, is the fact that it does not represent an oscillation but a monotonic decay. This decay is exponential in time and has the same decay time-constant θ as the original pulse.

It is interesting to note that there will be no contribution from the integral P_{BL} when $\theta \rightarrow \infty$ (the unit step function source) or when $\theta \rightarrow 0$ (the delta-function source).

The oscillatory contribution to the pressure signal. The pressure contributions P_L and P_B which are given by (15) and (27) respectively are signals which represent monotonically decreasing functions of the time and as such are not of primary interest to us here. The pressure contributions P_N (equation 17), P_{B2} (equation 21), and P_{B3} (equation 25) on the other hand are signals which represent vibrations of the liquid layer and thus are of great interest in our present problem. The integrals P_{B2} and P_{B3} represent contributions due to poles which

extensions of the usual, that is, the normal poles to complex values of the frequency. Expressing this in a slightly different way, may say that P_{B2} and P_{B3} are integrals over the sections of the dispersion curves for which horizontal wave number k (or its real part) is less than the cutoff value k^0 . We find that we can express P_N , P_{B2} , and P_{B3} in terms of a single integral from $k = 0$ to ∞ .

Let us first consider P_{B3} (equation 25), and then change the integration over q to an integration over k . Since, from (6) and (22),

$$\begin{aligned} &= -\{(\partial f/\partial k)_a/(\partial f/\partial s)_k(\partial s/\partial q)_k\} dk \\ &= \{(\partial f/\partial k)_a/(\partial f/\partial s)_k\} dk \quad (28) \end{aligned}$$

$$F_5(\omega_n, K) = \frac{\sinh(\alpha_{1n} d/H) \sinh(\alpha_{1n} z/H)}{\sinh \alpha_{1n} [\partial/\partial \bar{\omega}(\alpha_1 \cosh \alpha_1 + b \alpha_2 \sinh \alpha_1)]_n}$$

$$= \frac{\sinh(\alpha_{1n} d/H) \sinh(\alpha_{1n} z/H) [\alpha_{2n}(\alpha_{1n}^2 - b^2 \alpha_{2n}^2)]}{\bar{\omega}_n [\alpha_{1n}^2 \alpha_{2n} + b(\alpha_{1n}^2 c_1^2/c_2^2 - \alpha_{2n}^2) - b^2 \alpha_{2n}^3]}$$

obtain, on inverting the limits of integration,

$$\begin{aligned} &= 4A \operatorname{Re} \sum_n \int_{k_n^1}^{k_n^0} J_0(kr) k \\ &\quad \cdot \frac{\exp(s_n t)}{(s_n + 1/\theta)} F_2(s_n, k) dk \quad (29) \end{aligned}$$

where the path of integration is in the first quadrant of the k plane and is such that q is real and positive. A comparison of the present contribution P_N , P_{B2} , and P_{B3} now shows

$$\begin{aligned} &= P_N + P_{B2} + P_{B3} \\ &= 4A \operatorname{Re} \sum_n \int_0^\infty J_0(kr) k \\ &\quad \cdot \frac{\exp(s_n t)}{(s_n + 1/\theta)} F_2(s_n, k) dk \\ &= -4A \operatorname{Im} \sum_n \int_0^\infty J_0(kr) k \\ &\quad \cdot \frac{\exp(i\omega_n t)}{(1/\theta + i\omega_n)} F_5(\omega_n, k) dk \quad (30) \end{aligned}$$

re

$$F_5(\omega_n, k) = \frac{\sinh \beta_{1n} d \sinh \beta_{1n} z}{\sinh \beta_{1n} H [\partial/\partial \omega(\beta_1 \cosh \beta_1 H + b \beta_2 \sinh \beta_1 H)]_n}$$

It is convenient here to introduce nondimensional units. Let $K = kH$ be the horizontal wave number normalized with respect to the depth of the liquid layer, and let $\tau = t c_1/H$ be the time and $\bar{\omega} = \omega H/c_1$ the angular frequency normalized with respect to the vertical transit time of sound through the liquid layer. Similarly, let $\bar{\theta} = c_1 \theta/H$ be the reduced exponential decay time-constant. Then

$$\begin{aligned} P_V &= -\frac{4A}{H} \operatorname{Im} \sum_n \int_0^\infty J_0\left(K \frac{\tau}{H}\right) K \\ &\quad \cdot \frac{\exp(i\bar{\omega}_n \tau)}{(1/\bar{\theta} + i\bar{\omega}_n)} F_5(\bar{\omega}_n, K) dK \quad (31) \end{aligned}$$

where

$$\alpha_1 = (K^2 - \bar{\omega}^2)^{1/2} = i(\bar{\omega}^2 - K^2)^{1/2} = i\bar{\alpha}_1$$

and

$$\begin{aligned} \alpha_2 &= (K^2 - \bar{\omega}^2 c_1^2/c_2^2)^{1/2} \\ &= i(\bar{\omega}^2 c_1^2/c_2^2 - K^2)^{1/2} = i\bar{\alpha}_2 \end{aligned}$$

The path of integration proceeds from $K = 0$ to $K = K_n^1$ with K real and $\bar{\omega}_n$ in the first quadrant; from $K = K_n^1$ to $K = K_n^0$ with both K and $\bar{\omega}_n$ in the first quadrant; and from $K = K_n^0$ to ∞ with both K and $\bar{\omega}_n$ real and positive. The period equation

$$f = \alpha_1 \cosh \alpha_1 + b \alpha_2 \sinh \alpha_1 = 0 \quad (32)$$

provides relations (dispersion curves) of $\bar{\omega}_n$ as functions of K and can be evaluated numerically.

THE LONG-TIME VIBRATIONS

In the preceding section, we reduced the formal solution of our problem, as given by the repeated integral in equation 4, to a sum of single integrals

$$P = P_V + P_L + P_{BL} \quad (33)$$

This expression is still exact, and the direct numerical evaluation of P_L and P_{BL} , although of minor interest to us, should offer no particular difficulty. A numerical solution of P_V is somewhat more complicated, and for large values of the variable τ an asymptotic evaluation of this integral is indicated. Two methods of solution, the method of steepest descent (saddle-point method) and the method of stationary phase, are apparent. The former method appears to give in general more accurate and, for our purposes, more satisfactory results. The latter method has as one of its advantages the fact that we can obtain an approximate solution for an integral along a *given* path of integration in the complex plane. If this path passes through all the applicable saddle points, the results of the two methods are essentially the same.

A short digression on the method of stationary phase. We discuss very briefly the method of stationary phase as it applies to the evaluation of integrals in the complex plane, which are of interest to us here. The method is based on an evaluation by means of partial integration of sections of a given integral between 'critical points.' The formulas which we shall quote are essentially those derived by *van der Corput* [1936].

An approximate solution is desired for the integral

$$I = \int_{K_1}^{K_2} g(K) \exp [\sigma(K)] dK \quad (34)$$

where K , $g(K)$, and $\sigma(K)$ may be complex quantities, and the path of integration between the limits K_1 and K_2 is prescribed. Let $g(K)$ and $\sigma(K)$ be continuously differentiable to a sufficiently high order; also σ'' does not vanish, and $\sigma'/(\sigma'')^{1/2}$ may be real at only a finite number of points in the interval $[K_1, K_2]$. The primes denote differentiation with respect to K . Then the integral I can be approximated by expansions around 'critical points' in the interval $[K_1, K_2]$. These critical points are the end points K_1 and K_2 and those stationary points (in an extended sense) where $\sigma'/(\sigma'')^{1/2}$ is real and about which $\text{Im} [\sigma'/(\sigma'')^{1/2}]$ changes sign; an end point at infinity does not contribute. Whenever it is desired, we may divide the interval $[K_1, K_2]$ into subintervals. Contributions from end points thus introduced will usually

cancel, unless there is a stationary point in the neighborhood of the new end points.

Ordinarily, the method of stationary phase is applied to integrals where K is real and $\sigma(K)$ is purely imaginary. If $\text{Im} [\sigma'/(\sigma'')^{1/2}]$ is to vanish under those conditions, σ' must vanish and this is the usual condition for a point of stationary phase or for a saddle point. If σ is an analytic function, then in the neighborhood of a saddle point the condition that $\sigma'/(\sigma'')$ is real characterizes a point on a line of steepest ascent from a saddle point. If the critical (stationary) point and the saddle point are not far apart, then $\text{Im} (\sigma)$ is approximately the same for such a critical point as it is for the saddle point, and the saddle-point method and the method of stationary phase should yield approximately the same value of $\text{Im} (\sigma)$.

The vanishing of σ'' characterizes an inflection point, for example, where a line of steepest ascent from one saddle point goes over into a line of steepest descent from another saddle point. When such an inflection point occurs on the path of integration of the integral I , then if the integrand is analytic in the neighborhood of the point, we may avoid the point where $\sigma'' = 0$ by shifting the path of integration in a direction so that we cross the path of steepest descent. There will then be no contribution from the neighborhood of the point where $\sigma'' = 0$ as long as $|\sigma'|$ is sufficiently large there because the magnitude of $y(K) = |\sigma'(K)|/|\sigma''(K)|^{1/2}$ and the magnitude of $|e^{\sigma(K)}|$ in the interval $[K_1, K_2]$ are important in determining how good the approximate solution is. Another way of dealing with points where $\sigma'' = 0$ is to introduce a change of variable $K = u^2$. Then $d\sigma/du = 2K^{1/2}d\sigma/dK$ and $d^2\sigma/du^2 = 2d\sigma/dK + 4Kd^2\sigma/dK^2$, and again we see that there is no difficulty as long as $|d\sigma/dK|$ is sufficiently large.

The contribution due to the end point K_1 given by the integral

$$\begin{aligned} \int_{(K_1)} [g(K_1) + g'(K_1)(h - K_1) \\ + g''(K_1)(h - K_1)^2/2! + \dots] \\ \cdot [1 + \sigma'''(K_1)(h - K_1)^3/3! + \dots] \\ \cdot \exp [\sigma(K_1) + \sigma'(K_1)(h - K_1) \\ + \sigma''(K_1)(h - K_1)^2/2] dh \end{aligned} \quad (35)$$

where the path of integration over h proceeds from K_1 to $[K_1 - \sigma'(K_1)/\sigma''(K_1)]$ to $\{K_1 - \sigma'(K_1)/\sigma''(K_1) \pm i\infty/[\sigma''(K_1)]^{1/2}\}$. The upper or lower sign is used depending on whether in the neighborhood of K_1 the function $\text{Im}[\sigma'/(\sigma'')^{1/2}]$ is positive or negative to the right of K_1 . The contribution due to the end point K_2 is similarly given by the integral

$$\begin{aligned} & \int_{K_2} [g(K_2) + g'(K_2)(h - K_2) \\ & + g''(K_2)(h - K_2)^2/2! + \dots] \\ & \cdot [1 + \sigma'''(K_2)(h - K_2)^3/3! + \dots] \\ & \cdot \exp[\sigma(K_2) + \sigma'(K_2)(h - K_2) \\ & + \sigma''(K_2)(h - K_2)^2/2] dh \end{aligned} \quad (36)$$

The path of integration is from K_2 to $[K_2 - \sigma'(K_2)/\sigma''(K_2)]$ to $\{K_2 - \sigma'(K_2)/\sigma''(K_2) \pm i\infty/[\sigma''(K_2)]^{1/2}\}$. The upper or lower sign is used depending on whether in the neighborhood of K_2 the function $\text{Im}[\sigma'/(\sigma'')^{1/2}]$ is positive or negative to the left of K_2 .

Finally, the contribution due to a stationary point at, say, K_* is given by the integral

$$\begin{aligned} & \int_{-\infty}^{+\infty} [g(K_*) + g'(K_*)h \\ & + g''(K_*)h^2/2! + \dots] \\ & \cdot [1 + \sigma'''(K_*)h^3/3! + \dots] \\ & \cdot \exp[\sigma(K_*) + \sigma'(K_*)h \\ & + \sigma''(K_*)h^2/2] dh \end{aligned} \quad (37)$$

where the upper or lower sign is used depending on whether in the neighborhood of K_* the function $\text{Im}[\sigma'/(\sigma'')^{1/2}]$ is positive or negative to the right of K_* . The integral is defined to be convergent; that is, the variable h is given the proper phase so that (37) converges. Let $C = |C|e^{i\gamma} \neq 0$ where $-\pi < \gamma < \pi$. Then for every polynomial $p(h)$, we set

$$\begin{aligned} & \int_{-\infty}^{+\infty} p(h) \exp(Nh + Ch^2/2) dh \\ & = e^{i\gamma/2} \int_{-\infty}^{+\infty} p(He^{-i\gamma/2}) \\ & \cdot \exp(Ne^{-i\gamma/2}H - |C|H^2/2) dH \end{aligned} \quad (38)$$

We mentioned above that the magnitude of the quantity $|e^{\sigma(K)}|$ in the interval $[K_1, K_2]$ is important in determining how good the asymptotic solution is. Evidently this quantity is minimized when we pass through saddle points and use paths of steepest descent. In the problem which we treat in this paper, $\sigma(K)$ is usually represented by $i\tau(\bar{\omega} - Kr/H\tau)$, and our interest centers not only on obtaining a good approximation for the phase and the exponential decay of the oscillatory pressure contribution but also on getting the best approximation for the frequency $\bar{\omega}$ and the horizontal wave number K as a function of $\tau/H\tau$. When (37), for example, does not go through a saddle point but crosses a path of steepest ascent not very far from the saddle point, it will yield directly an approximation for the value of $\sigma(K) = i\tau(\bar{\omega} - Kr/H\tau)$ at the saddle point; but in order to obtain the proper values of $\bar{\omega}$ and K , we must also find out what their values are at the saddle point. From (37) we see that we cannot get those values to a better accuracy than to the order of the square of the distance from the critical point to the saddle point. In general, therefore, it seems preferable to evaluate the integral P_V (equation 31) directly by the saddle-point method; however, especially for more complicated problems of the present type, if the dispersion curves can be calculated more readily along a given path in the complex plane, then the method of stationary phase may be used to obtain an approximate solution to the problem.

We are now in a position to evaluate asymptotically the integral 31 for P_V for large values of τ . To begin with we shall obtain a limiting solution valid for long times and small horizontal ranges, where the vibrations of the water layer are expressed in terms of pseudostanding plane waves parallel to the boundaries. This solution confirms some well-known results, such as the so-called 'organ pipe formula', but is not of a form convenient for the discussion of other interesting phenomena associated with waves traveling in a horizontal direction. A solution in terms of horizontally traveling waves is derived next. This solution is applicable at larger horizontal distances from the source.

A solution in terms of standing waves in the horizontal direction. We first consider the limiting case of extremely long times, when τ

is so much greater than r/H that the Bessel function $J_0(Kr/H)$ may be considered constant in comparison with the factor $\exp(i\bar{\omega}_n\tau)$. Such a solution is certainly applicable in the vicinity of the shotpoint, $r = 0$. The term $F_s(\bar{\omega}_n, K)$ in (31) will always be considered a slowly varying function compared with $\exp(i\bar{\omega}_n\tau)$, since $\tau \gg 1$ is an essential condition if we want to express our solution in terms of vibrations of the liquid layer. We next apply the method of stationary phase as extended by *Van der Corput* [1935, 1936]. We may consider separately the sections 0 to K_n^1 , K_n^1 to K_n^0 and K_n^0 to ∞ of the path of integration in (31). The point at infinity does not contribute, and since no critical points occur in the neighborhood of K_n^1 and K_n^0 the end point contributions there will cancel. At $K = 0$, the group velocity $U = d\bar{\omega}/dK = 0$ and its derivative $d^2\bar{\omega}/dK^2 \neq 0$, so that a critical point, which is actually a saddle point, coincides with this end point. Finally, there is a point between K_n^0 and ∞ where $d^2\bar{\omega}/dK^2$ vanishes. In *van der Corput's* formulation such a point is not permitted to occur in the interval of integration. If we avoid this point by shifting the path of integration below the real K axis, we shall then find no additional critical points on the shifted path. Thus, as long as in the neighborhood of that point the group velocity $U = d\bar{\omega}/dK$ does not become very small also, we shall have no contribution, in our approximation, from the point where $d^2\bar{\omega}/dK^2$ vanishes.

The contribution at the point $K = 0$ is given by the expression

$$P^* = -\frac{4A}{H} \operatorname{Im} \sum_n \int_0^{\infty e^{i\phi}} \left[Q_1(0) + Q_1'(0)h + Q_1''(0) \frac{h^2}{2!} + \dots \right] \cdot \left[1 + Q_2'''(0) \frac{h^3}{3!} + \dots \right] \cdot \exp [Q_2(0) + Q_2'(0)h + Q_2''(0)h^2/2] dh \quad (39)$$

where

$$Q_1(K) = \frac{J_0(Kr/H)KF_s(\bar{\omega}_n, K)}{(1/\bar{\theta} + i\bar{\omega}_n)}$$

and $Q_2(K) = i\bar{\omega}_n\tau$. The primes designate deriva-

tives with respect to K along the dispersion curves, and $\phi = \pi/2 - 1/2$ [phase $Q_2''(0)$]. The leading term of an asymptotic series in inverse powers of τ , we then obtain

$$P^* = \frac{4A}{H\tau} \sum_n |Q^*| \cos [\operatorname{Re}(\bar{\omega}_n^*)\tau + \psi^*] \cdot \exp [-\operatorname{Im}(\bar{\omega}_n^*)\tau] \quad (40)$$

where

$$Q^* = \frac{\sin(\bar{\omega}_n^* d/H) \sin(\bar{\omega}_n^* z/H)}{(1/\bar{\theta} + i\bar{\omega}_n^*)\bar{\omega}_n^* (\bar{\omega}_n^*)'}$$

and ψ^* is the phase of Q^* . The superscript refers to the evaluation of a function at the point $K = 0$.

We note that the path of integration in (3) proceeds to infinity along a path which coincides with the steepest descent path to terms up to the second order in Q_2 , as expanded around the point $K = 0$. Since the factor $\exp(i\bar{\omega}\tau)$ of (3) vanishes to an exponential order in the first quadrant of the K plane, we could have shifted the path of integration directly into the steepest descent path and obtained, by the method of steepest descent, a solution which is essentially the same as (40).

Since

$$\bar{\omega}_n^* = (n - 1/2)\pi + i1/2 \ln [(c_2/c_1 + b)/(c_2/c_1 - b)] \quad (41)$$

the exponential decay term may be rewritten

$$\exp [-\operatorname{Im}(\bar{\omega}_n^*)\tau] = [(c_2\rho_2 - c_1\rho_1)/(c_2\rho_2 + c_1\rho_1)]^{\tau/2} \quad (42)$$

The expression in brackets is the normal reflection coefficient at the layer-bottom interface and thus P^* precisely represents vertically bouncing waves. The real part of $\bar{\omega}_n^*$ yields the well-known 'organ pipe formula,' which is often referred to in connection with the singing phenomenon. Note that the leading term (4) of the pressure response is independent of τ /the reduced radial coordinate. A dependence τ/H will be introduced only in the higher-order terms of the asymptotic series. Also note that since $\bar{\omega}_n^*$ is a complex quantity, the functions $\sin(\bar{\omega}_n^* d/H)$ and $\sin(\bar{\omega}_n^* z/H)$ cannot vanish except when d or $z = 0$. An explanation for the

readily given. The imaginary part of $\bar{\omega}_n^*$ is a measure of the radiation into the lower medium, and the vibrations of the liquid layer may be considered to be made up of standing and progressive waves in the vertical direction. When $\bar{\omega}_n^*$ is purely real there is no radiation into the bottom, and we have only standing waves in the vertical direction. As $\text{Im}(\bar{\omega}_n^*)$ increases, the radiation into the bottom and the relative importance of the progressive waves in the vertical direction also increase.

A solution in terms of waves traveling in the horizontal direction. In the preceding solution, given by P^* in (40), the long-time vibrations were presented as exponentially decaying standing waves in the horizontal direction. Such a representation is satisfactory very close to the source, where $r/H \sim 0$, or at very long times when $Kr \ll 1$, that is, when we are effectively very close to the source again. In many applications, however, we are interested in the phenomenon at long times at recording positions sufficiently removed from the shotpoint so that r/H is vanishingly small. In other words, it is desirable to extend our solution so that we can observe the effect of traveling waves in the horizontal direction and obtain expressions for the frequency, the exponential decay, and, especially, the apparent horizontal phase velocity as a function of time. To do this, we replace the Bessel function $J_0(Kr/H)$ by its equivalent

$$1/2[H_0^{(1)}(Kr/H) + H_0^{(2)}(Kr/H)]$$

For sufficiently large (Kr/H) we may in turn replace the Hankel functions $H_0(Kr/H)$ by their asymptotic expansions, whose leading terms are given by

$$\begin{aligned} (1) \left(K \frac{r}{H} \right) &\sim \left(\frac{2H}{\pi Kr} \right)^{1/2} \cdot \exp[i(Kr/H - \pi/4)] \\ (2) \left(K \frac{r}{H} \right) &\sim \left(\frac{2H}{\pi Kr} \right)^{1/2} \cdot \exp[-i(Kr/H - \pi/4)] \end{aligned} \quad (43)$$

Substituting this into (31) for P_v , we see that the $H_0^{(1)}$ function corresponds to waves traveling toward the source, and the $H_0^{(2)}$ function corresponds to waves traveling away from the source. We write

$$\begin{aligned} P_v &\sim -2A \left(\frac{2}{\pi r H} \right)^{1/2} \\ &\cdot \text{Im} \sum_n \int_0^\infty \frac{\exp[i(\bar{\omega}_n \tau + Kr/H - \pi/4)]}{(1/\bar{\theta} + i\bar{\omega}_n)} \\ &\cdot F_5(\bar{\omega}_n, K) K^{1/2} dK \\ &- 2A \left(\frac{2}{\pi r H} \right)^{1/2} \\ &\cdot \text{Im} \sum_n \int_0^\infty \frac{\exp[i(\bar{\omega}_n \tau - Kr/H + \pi/4)]}{(1/\bar{\theta} + i\bar{\omega}_n)} \\ &\cdot F_5(\bar{\omega}_n, K) K^{1/2} dK \sim P_{v1} + P_{v2} \end{aligned} \quad (44)$$

First, we employ the method of stationary phase and let $\sigma = i(\bar{\omega}_n \tau \pm Kr/H)$. Then we encounter critical points at the end point $K = 0$ and at those points where $\text{Im}[\sigma' / (\sigma'')^{1/2}] = 0$. The primes refer to derivatives with respect to K along the dispersion curves. As long as σ' does not vanish at the end point $K = 0$, the end-point contributions of P_{v1} and P_{v2} cancel.⁶ Since there are no other critical points for the integral P_{v1} , only those of P_{v2} need be considered. This means that, for the simple problem of a liquid layer overlying an infinitely deep liquid bottom, the long-time response (in the present approximation) may be visualized in terms of outgoing waves only. (This is not necessarily true for similar problems involving more complicated systems of elastic layers.)

We must, of course, note the fact that because of the approximation 43, the expression 44 is not strictly applicable near the point $K = 0$. This is of little consequence, however, as long as our interest centers around contributions from critical (stationary) points for which Kr/H is sufficiently large. When this is not the case, we

⁶ This can be shown in another way by combining P_{v1} and P_{v2} directly. We use the well-known formula $H_0^{(1)}(Kr/H) = -H_0^{(2)}(-Kr/H)$ and find that

$$\begin{aligned} P_v &= -\frac{2A}{H} \text{Im} \sum_n \int_{-\infty}^{+\infty} H_0^{(2)}(Kr/H) \\ &\cdot \frac{\exp[i\bar{\omega}_n \tau]}{(1/\bar{\theta} + i\bar{\omega}_n)} F_5(\bar{\omega}_n, K) K dK \end{aligned}$$

for $\bar{\omega}_n$ an even function of K . The singularity at $K = 0$ is avoided by shifting the path of integration slightly.

may still obtain an accurate solution to our problem by considering higher-order terms of the asymptotic solution given by (39), as mentioned previously. Note that, although in (44) we approximate the Bessel function $J_0(Kr/H)$ by an asymptotic series valid for large values of (Kr/H) , we approximate it in (39) by a convergent expansion around the zero point.

Our problem, then, is to find the stationary points, where $\text{Im} [\sigma'/(\sigma'')^{1/2}]$ vanishes, and hence a solution for P_{V2} (equation 44) by expansions around such points. The condition $\text{Im} [\sigma'/(\sigma'')^{1/2}] = 0$ yields along each dispersion curve a relation of $r/H\tau$ as a function of K . Thus for each mode we can find K and consequently $\bar{\omega}$ as a function of time τ , the reduced horizontal charge to gauge distance r/H being given. Note, however, that these values of $\bar{\omega}$ and K are not the ones which apply to a saddle point unless the stationary points coincide with the saddle points. For our present path of integration, the saddle points and stationary points coincide only when such points occur at $K_n = 0$ or in the interval $[K_n^0 < K_n < \infty]$. We also note that, whereas $r/H\tau$ is always a single-valued function of K_n , the inverse is true in our present approximation only for times later than the arrival of the Airy phase maximum. This time is given by $\tau^A = r/U_n^A H$. U_n^A is the group velocity which corresponds to the point K_n^A on the dispersion curve $[K_n^0 < K_n < \infty]$ where $\sigma'' = dU/dK = d^2\bar{\omega}/dK^2$ vanishes. The Airy phase is of importance in long-range propagation problems and has been discussed in some detail by Pekeris [1948] and others [Ewing, Jardetzky, and Press, 1957] (see also equation 48 below). The method of stationary phase, as applied to the path of integration $[0, K_n^1, K_n^0, \infty]$ with K_n real and positive in the intervals $[0, K_n^1]$ and $[K_n^0, \infty]$, and q_n real and positive in the interval $[K_n^1, K_n^0]$, would indicate then that besides the ground and the water waves [Pekeris, 1948], which are due to stationary points in the normal mode interval $[K_n^0 < K_n < \infty]$, $[(c_1/c_2)(\tau/H) < \tau < \tau^A]$ and which show no exponential decay, there is a pressure contribution at all times $[(c_1/c_2)(\tau/H) < \tau < \infty]$ from the complex mode interval $[0 < K_n < K_n^0]$ which decays exponentially with time.

The dispersion curves have kinks at the points K_n^1 and K_n^0 . Instead of one integral

P_{V2} , we may consider three integrals separately their paths of integration extending from 0 to K_n^1 , K_n^1 to K_n^0 , and K_n^0 to ∞ . The end-point contributions at K_n^1 and K_n^0 cancel as long as a stationary point does not coincide with them. When the stationary point does coincide with an end point, the two end-point contributions are equal and must be added. The resulting expression, however, is the same as if we had expanded directly around the stationary point. (This is analogous to the case treated previously [Rosenbaum, 1959].)

In the interval $[0 < K_n < K_n^A]$, $\text{Im} [\sigma'/(\sigma'')^{1/2}] > 0$ to the right of the stationary point; in the interval $[K_n^A < K_n < \infty]$, $\text{Im} [\sigma'/(\sigma'')^{1/2}] < 0$ to the right of the stationary point. With the aid of the formulas presented earlier in this paper, we can therefore write for the pressure contribution P_{V2} the leading term of an asymptotic series in inverse powers of τ ,

$$P_{V2}(\tau, r/H) = 4A/(\tau H\tau)^{1/2} \cdot \sum_n |Q_n^c| \exp[-L_n\tau] \cdot \cos[\text{Re}(\bar{\omega}_n^c)\tau - \text{Re}(K_n^c)r/H + \psi^c] \quad (45)$$

where

$$L_n = \text{Im}(\bar{\omega}_n^c) - \text{Im}(K_n^c)r/H\tau + i[(\bar{\omega}_n^c)' - r/H\tau]^2/2(\bar{\omega}_n^c)''$$

$$Q_n^c = \frac{F_0(\bar{\omega}_n^c, K_n^c)K_n^c}{(1/\bar{\theta} + i\bar{\omega}_n^c)(\bar{\omega}_n^c)''K_n^c)^{1/2}}$$

$\psi^c = \text{phase}(Q_n^c) + \pi$ for $[0 < K_n^c < K_n^A]$ and

$$\psi^c = \text{phase}(Q_n^c) \text{ for } [K_n^A < K_n^c < \infty]$$

The superscript c refers to the evaluation of the function at the stationary point on the n th dispersion curve, and $-\pi < \text{phase}(\bar{\omega}_n^c) \leq \pi$.

Because of the definition of a stationary point the nondimensional exponential decay function of the n th mode, L_n , is real and positive and thus does indeed represent the exponential decay with time of the vibration. Note that in the interval $[0 < K_n < K_n^1]$, $\text{Im}(K_n) = 0$, so that

$$L_n = \text{Im}(\bar{\omega}_n^c) + i[(\bar{\omega}_n^c)' - r/H\tau]^2/2(\bar{\omega}_n^c)'' \quad (46)$$

In the interval $[K_n^0 < K_n < \infty]$, $\text{Im}(K_n) =$

1 ($\bar{\omega}_n$) = 0 and $(\bar{\omega}_n^*)^e = r/H\tau$, so that

$$L_n = 0 \quad (47)$$

at is, in the normal mode region the vibrations do not decay exponentially with time.

Expression 45 is not uniformly valid for all values of the parameters. As was mentioned earlier, for K_n/H sufficiently small, the approximation 43 for the Hankel function breaks down, and we should consider higher-order terms (39) in order to get a dependence of our solution on the radial coordinate r . Another difficulty arises when the stationary point is near the Airy phase point K_n^A , where σ'' vanishes. Now σ' is also small in the neighborhood of K_n^A , and our method of solution must be modified. We follow the procedure employed by Pekeris [1948] for the analogous case of an asymptotic solution in inverse powers of r ; expanding around the point K_n^A where $\sigma'' = 0$, we obtain the leading term

$$v_2^A = 2A \left(\frac{2\pi}{rH} \right)^{1/2} \left(\frac{2}{r} \right)^{1/3} \cdot \sum_n S_n^A \text{Ai} \left\{ \frac{2^{1/3} \tau^{2/3} [U_n^A - r/H\tau]}{[(d^2 U/dK^2)_n^{1/3}]^A} \right\} \cdot \cos(\bar{\omega}_n^A \tau - K_n^A r/H - \psi^A) \quad (48)$$

where

$$S_n^A = \left\{ \frac{\sin(\bar{\alpha}_{1n} d/H) \sin(\bar{\alpha}_{1n} z/H) [\alpha_{2n}(\bar{\alpha}_{1n}^2 + b^2 \alpha_{2n}^2)] K_n^{1/2}}{[\bar{\omega}_n [\bar{\alpha}_{1n}^2 \alpha_{2n} + b(\bar{\alpha}_{1n}^2 c_1^2/c_2^2 + \alpha_{2n}^2) + b^2 \alpha_{2n}^3] (d^2 U/dK^2)_n (1/\bar{\theta}^2 + \bar{\omega}_n^2)^{1/2}} \right\}^A$$

$$\psi^A = [\pi/4 + \tan^{-1}(\bar{\omega}_n^A \bar{\theta})]$$

and Ai designates the Airy function. (For its definition, see McLachlan [1955].) As before, U is the group velocity and the superscript A refers to the evaluation of a function at the point K_n^A where the group velocity has a minimum; that is, $dU/dK = d^2\bar{\omega}/dK^2$ vanishes. The water wave arrives with zero amplitude, since its onset corresponds to an end point at infinity. For the ground wave arrival the stationary point coincides with the point K_n^0 ; the function $F_b(\bar{\omega}_n, K_n)$ vanishes because of the factor α_{2n} in the numerator (see equation 31) and so does the leading term of our solution for P_{V2} as given by (45). Evaluation of the next higher term of the asymptotic expansion (either directly or as the sum of two end-point con-

tributions) leads to a term of order $r^{-1/2} \tau^{-3/2}$, which does not vanish. This is analogous to the discussion presented previously [Rosenbaum, 1959]. A stationary point at K_n^0 corresponds to the time of the first refraction arrival $\tau = (c_1/c_2)(r/H)$, and thus the first nonvanishing term is of order r^{-2} . There will also be monotonically decaying contributions from P_L and P_{BL} . All this agrees with the previous results, where the first-arrival signal was evaluated asymptotically in inverse powers of r . Indeed, as far as the entire normal mode interval [$K_n^0 < K_n < \infty$] is concerned, our present solution is comparable in all respects with the large-distance asymptotic solutions of Pekeris [1948] and Rosenbaum [1959].

As mentioned previously, the values of $\bar{\omega}^e$ and K^e obtained above are generally not the ones we are looking for, unless the critical points coincide with the saddle points. The latter condition along our path of integration may occur at $K = 0$ and in the normal mode interval [$K_n^0 < K_n < \infty$]. For critical points in most of the interval [$0 < K_n < K_n^1$] the second-order corrections made to obtain values of $\bar{\omega}_n$ and K_n at the saddle points, which we discussed previously, yield satisfactory results. For critical points in the remaining interval of integration such corrections are rather poor, and the results we obtain do not seem to agree well with the

solution of the problem by the saddle-point method. However, on the whole, the differences between the results obtained by the saddle-point method and the method of stationary phase are not serious.

We now consider the asymptotic solution of (44) by the saddle-point method. From the end point $K_n = 0$ we proceed to infinity along a path of steepest descent, which for $r/H\tau > 0$ proceeds for P_{V2} from $K_n = 0$ tangent to the negative imaginary axis into the third quadrant; for P_{V1} it proceeds from $K_n = 0$ tangent to the positive imaginary axis into the first quadrant of the K plane. As before, these end-point contributions cancel. Next we look for saddle points over which we should pass as we integrate P_{V2} from ∞ in the third quadrant of the K plane

to ∞ in the first quadrant when $1 > r/H\tau > 0$, or to ∞ in the fourth quadrant when $c_2/c_1 > r/H\tau > 1$. The integration of P_{V1} proceeds from ∞ in the first quadrant to ∞ in the first quadrant for all values of $r/H\tau$, and, as before, this integral appears to yield no significant contribution. (Contributions appear possible and could arise because of roots of the denominator of F_6 in the first quadrant. Such roots correspond to branch points; and branch line integrals, which we must shift into steepest descent paths, remain. See also the case of the low-velocity, high-pressure bottom later on.)

The actual evaluation of P_{V2} proceeds as follows. The condition for a saddle point is given by

$$\bar{\omega}' = d\bar{\omega}/dK = r/H\tau \quad (49)$$

and this can be written in terms of only the single variable α_{1n} (where $\bar{\alpha}_1$ is the nondimensional vertical wave number in the liquid layer) as

$$\frac{r}{H\tau} = \left[\frac{1 - (c_1^2/c_2^2)b^2 \tanh^2 \alpha_{1n}}{1 - b^2 \tanh^2 \alpha_{1n}} \right]^{1/2} \cdot \left[\frac{b^2 \tanh^3 \alpha_{1n} - \alpha_{1n} \tanh^2 \alpha_{1n} - \tanh \alpha_{1n} + \alpha_{1n}}{(c_1^2/c_2^2)b^2 \tanh^3 \alpha_{1n} - \alpha_{1n} \tanh^2 \alpha_{1n} - \tanh \alpha_{1n} + \alpha_{1n}} \right] \quad (50)$$

For a given value of $r/H\tau$, the equation is solved for α_{1n} by iteration on an electronic computer.

Since

$$\alpha_{2n} = -\alpha_{1n}/(b \tanh \alpha_{1n}) \quad (51)$$

and

$$\bar{\omega} = \left[\frac{\alpha_2^2 - \alpha_1^2}{1 - c_1^2/c_2^2} \right]^{1/2} \quad (52)$$

$$K = \left[\frac{\alpha_2^2 - (c_1^2/c_2^2)\alpha_1^2}{1 - c_1^2/c_2^2} \right]^{1/2}$$

values of α_{2n} , $\bar{\omega}_n$, and K_n at a saddle point are readily calculated. The solution for P_{V2} for a given value of $r/H\tau$ follows from an expansion around the saddle point (or points). The final expressions are essentially the same as those given by (45), and we shall use these for our solution. Note that the term

$$i[(\bar{\omega}_n')^2 - r/H\tau]^2/2(\bar{\omega}_n'')$$

which occurs in L_n , is now identically zero. As

before, the contribution due to the Airy phase is given by (48).

The position of the saddle points and the paths of steepest descent for the case $c_2/c_1 > 1$, which we are treating here, is as follows. For $0 < r/H\tau < r/H\tau^A$, there is one saddle point through which we must pass in the first quadrant of the K plane.^{*} The steepest descent path goes through this saddle point at an angle ϕ where $0 < \phi < \pi/2$. At the Airy phase point $r/H\tau^A$, we have a saddle point of order 2 on the real K_n axis. Our steepest descent path enters along a ray at angle $5\pi/6$ and leaves along a ray at angle $\pi/6$. For $r/H\tau < r/H\tau^A$, there are two saddle points on the real K_n axis through which we must pass. One is located between K_n^0 and K_n^A . Its contribution is the so-called ground wave [Pekeris, 1948]; the steepest descent path goes through this saddle point at an angle of $-\pi/4$. The other is located between K_n^A and ∞ . Its contribution is the

so-called water wave [Pekeris, 1948]; the steepest descent path passes through this saddle point at an angle of $\pi/4$. For $1 < r/H\tau < c_2/c_1$, we pass through only one saddle point on the real axis; it is located between K_n^0 and K_n^A . This contributes the ground wave before the direct water arrival. We note that our path always ends in the correct quadrant of the K plane. Since $\bar{\omega}_n \rightarrow K_n$ as $K_n \rightarrow \infty$, the integrand of P_{V2} (see equation 44) vanishes to an exponential order in the first quadrant of the K_n plane when $r/H\tau < 1$, and in the fourth quadrant when $r/H\tau > 1$.

Finally, there is the question whether we can shift our original path of integration into the steepest descent paths without encountering singularities whose contributions are significant. Two points appear to be of special importance in this respect: the branch point at K_n^0 , where

^{*} There may be others, but this one is associated with the least exponential decay and is therefore the most important one.

vanishes, and a branch point along the real axis between K_n^1 and K_n^0 , where

$$b^2 \tanh^3 \alpha_{1n} - \alpha_{1n} \tanh^2 \alpha_{1n} - \tanh \alpha_{1n} + \alpha_{1n} = 0 \quad (53)$$

and where $(d\bar{\omega}_n/dK_n)$ becomes infinite; we can verify this by comparing (50) with the denominator of (31). (The branch points given by equation 53 correspond to the critical points described by equation 11.) We draw branch cuts from these points to infinity in the fourth quadrant. For $r/H\tau < c_2/c_1$, that is for times later than the first arrival, the steepest descent paths do not seem to encounter either branch point, and thus our solution is that given by the saddle-point contributions discussed above.

THE LOW-VELOCITY BOTTOM AND OTHER CASES OF INTEREST

Before proceeding with a discussion of numerical examples of the solution obtained in the previous section, we shall discuss briefly the modal solution for a liquid layer over a bottom whose sound velocity is slower than that of the layer, that is, the case $c_2/c_1 < 1$. We shall also mention briefly the case of the source or the detector located in the bottom, as well as the case of a deep rigid reflector.

For the case $c_2/c_1 < 1$, the expression for the branch line integral which corresponds to P_{BL} (equation 26) is considerably more complicated and includes terms which, although they are not oscillatory in time or radial distance, do exhibit a harmonic dependence on depth.⁷ The oscillatory part of the pressure contribution, P_r , is again an integral of the form of equation 41. The dispersion curves are as follows: At $\bar{\omega} = 0$,

$$\bar{\omega} = (n - 1/2)\pi + i(1/2) \cdot \ln [(c_2/c_1 + b)/(c_2/c_1 - b)] \quad (54)$$

or the case $(bc_1/c_2 < 1)$, and

$$\bar{\omega} = n\pi + i(1/2) \cdot \ln [(c_1/c_2 + 1/b)/(c_1/c_2 - 1/b)] \quad (55)$$

or the case $(bc_1/c_2 > 1)$. In either case,

⁷ The contribution P_{BL} has its maximum at $\bar{\omega} = (c_1/c_2)(r/H)$ and may well be an important feature of a pressure record.

$$\frac{d\bar{\omega}}{dK} = 0, \quad \text{and} \quad \frac{d^2\bar{\omega}}{dK^2} = \frac{1}{\bar{\omega}} \left[1 - \frac{i}{\bar{\omega}} \frac{bc_2}{c_1} \frac{(c_1^2/c_2^2 - 1)}{(b^2 c_1^2/c_2^2 - 1)} \right] \quad (56)$$

As $K \rightarrow \infty$, $\bar{\omega} \rightarrow K$ and $\alpha_1 \rightarrow i\pi$. As before, $n = 1, 2, 3 \dots$ signifies the various modes. For the case $(bc_1/c_2 > 1)$, there is actually a lowest mode, $n = 0$, for which $\bar{\omega}$ is purely imaginary for all values of K . This mode does not yield an oscillatory pressure contribution and is in fact included in the evaluation of the integral P_{BL} .

The integral P_r (see equation 44) is evaluated asymptotically by the method of stationary phase or the saddle-point method. Equation 50 is again applicable in case the saddle-point method is used. For the case $(bc_1/c_2 < 1)$ we must pass through two saddle points. One has a value of $\text{Re}(\bar{\omega}) = (n - 1/2)\pi$ and $K = 0$ at $r/H\tau = 0$, and $\bar{\omega}$ and K change relatively slowly with increasing $r/H\tau$. The other yields values of $\bar{\omega} \rightarrow \infty$, $K \rightarrow \infty$ at $r/H\tau = 1$, and $\bar{\omega}$ and K drop rapidly with decreasing $r/H\tau$. As we may expect, the exponential decay associated with contributions of the former saddle point is less for small values of $r/H\tau$ but greater for larger values of $r/H\tau$ than the exponential decay for contributions of the latter saddle point. The latter saddle point also yields solutions for incoming waves, that is for the integral P_r (see equation 44), but the exponential decay associated with such waves is large. For the case $(bc_1/c_2 > 1)$ we need consider only one saddle point for the entire interval $[0 < r/H\tau < 1]$.

If the detector is located in the bottom but the source is in the layer, the formal solution for the pressure response is given by the expression

$$P = \frac{A}{2\pi i} \int_{\gamma-i\infty}^{\gamma+i\infty} \frac{e^{st}}{(s+1/\theta)} ds \int_0^\infty J_0(kr)k \cdot \frac{\exp[-\beta_2(z-H)] \sinh \beta_1 d}{(\beta_1 \cosh \beta_1 H + b\beta_2 \sinh \beta_1 H)} dk \quad (57)$$

where $(0 < d \leq H < z)$. When the source is in the bottom but the detector is in the layer $(0 < z \leq H < d)$, we interchange z and d in the above expression. The solution proceeds essentially as for the case of both source and detector in the layer. The oscillatory pressure signal, corresponding to (31), is given for the

case ($0 < d \leq H < z$) by the expression

$$P_v = -\frac{2A}{H} \operatorname{Im} \sum_n \int_0^\infty J_0(Kr/H) K \cdot \frac{\exp(i\bar{\omega}_n \tau)}{(1/\bar{\theta} + i\bar{\omega}_n)} F_6(\bar{\omega}_n, K) dK \quad (58)$$

where

$$F_6(\bar{\omega}_n, K) = \frac{\exp[-\alpha_{2n}(z-H)/H] \sinh(\alpha_{1n} d/H) [\alpha_{2n}(\alpha_{1n}^2 - b^2 \alpha_{2n}^2)]}{\bar{\omega}_n [\alpha_{1n}^2 \alpha_{2n} + b([c_1^2/c_2^2] \alpha_{1n}^2 - \alpha_{2n}^2) - b^2 \alpha_{2n}^3]}$$

For $(z-H)/H \ll c_2\tau/c_1$, the asymptotic evaluation of (58) proceeds as before, and $\exp[-\alpha_{2n}(z-H)/H]$ expresses the pressure variation as a function of detector depth. For $(z-H)/H$ not $\ll c_2\tau/c_1$, we must include $\exp[-\alpha_{2n}(z-H)/H]$ in the asymptotic evaluation. A saddle point is now given by the condition that

$$i \left(\frac{d\bar{\omega}_n}{dK} \pm r/H\tau \right) - \left(\frac{z-H}{H\tau} \right) \frac{d\alpha_{2n}}{dK} = 0 \quad (59)$$

the upper and lower sign referring to P_{v1} and P_{v2} , respectively (see equation 44). Equation 59 can of course be rewritten as an equation in terms of the single variable α_{1n} only.

Finally, we should like to mention briefly the case of the liquid layer of depth H_1 lying on top of a liquid layer of depth H_2 , which in turn rests on top of a perfectly rigid boundary (Fig. 4). For source and detector in the upper layer (subscript 1), we obtain for the pressure response at the detector the following formal solution:

$$P = \frac{A}{\pi i} \int_{\gamma-i\infty}^{\gamma+i\infty} \frac{e^{st}}{(s+1/\bar{\theta})} ds \int_0^\infty J_0(kr) k \cdot \frac{\sinh \beta_1 d}{\beta_1} F_7(s, k) dk \quad (60)$$

where

$$F_7(s, k) = \frac{\beta_1 \cosh \beta_1(H_1 - z) \cosh \beta_2 H_2 + b\beta_2 \sinh \beta_1(H_1 - z) \sinh \beta_2 H_2}{\beta_1 \cosh \beta_1 H_1 \cosh \beta_2 H_2 + b\beta_2 \sinh \beta_1 H_1 \sinh \beta_2 H_2}$$

For $H_2 \gg H_1$, it is convenient to expand $F_7(s, k)$ as follows:

$$\begin{aligned} F_7(s, k) &= \frac{\beta_1 \cosh \beta_1(H_1 - z) + b\beta_2 \sinh \beta_1(H_1 - z)}{\beta_1 \cosh \beta_1 H_1 + b\beta_2 \sinh \beta_1 H_1} \\ &+ \frac{2\beta_1 \beta_2 \sinh \beta_1 z}{(\beta_1 \cosh \beta_1 H_1 + b\beta_2 \sinh \beta_1 H_1)^2} \exp(-2\beta_2 H_2) \\ &- \frac{2\beta_1 \beta_2 \sinh \beta_1 z (\beta_1 \cosh \beta_1 H_1 - b\beta_2 \sinh \beta_1 H_1)}{(\beta_1 \cosh \beta_1 H_1 + b\beta_2 \sinh \beta_1 H_1)^3} \exp(\beta_2 H_1) \exp[-4\beta_2 H_2] \\ &+ \dots \end{aligned} \quad (61)$$

We see that the first term describes the case of a liquid layer lying on top of an infinitely deep liquid bottom; the second term describes all signals which have been reflected once from the deep rigid boundary, the third term a signals which have been reflected twice from the

deep rigid boundary, and so forth. An expansion of this type, which we may call a partial ray expansion, should be of some interest for seismological problems, since it allows us to treat multiples from a deep reflector separately and to consider at the same time the multiple reflections in a shallow layer as an interference phenomenon. We note that in the solution of, say, the first deep reflection, that is the second term of the expansion of $F_7(s, k)$, we are dealing with double roots of the period equation in the denominator. This introduces an additional complication over the problem of the source (or detector) located in the infinitely deep bottom, which we discussed in the preceding paragraph. This complication may be considered to be due to the greater number of ray paths from source to detector (images), whose interference with one another we are observing.

DISCUSSION OF NUMERICAL RESULTS

In this section we present numerical values for the quantitative discussion of the solution obtained in the previous sections. We have evaluated, principally by means of (50), examples of each of the following four possible cases

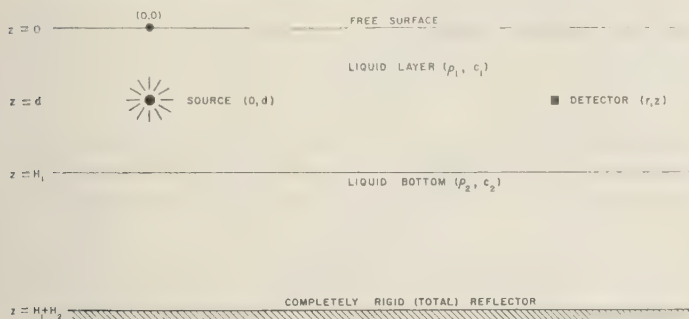


Fig. 4. Two liquid layers lying on top of a rigid reflector.

1. $c_2/c_1 > 1$, $c_2/c_1 b > 1$; 2. $c_2/c_1 > 1$, $c_2/c_1 b < 1$;
 3. $c_2/c_1 < 1$, $c_2/c_1 b > 1$; 4. $c_2/c_1 < 1$, $c_2/c_1 b < 1$.

All except case 2 represent conditions that may be encountered in actual seismic problems; case 2 has been included because it presents some interesting features which are similar to those that may arise in more complicated problems of layered elastic media. We note that cases 1 and 2 involve the phenomenon of total reflection. That is, there exists an angle of incidence for plane waves in the liquid layer beyond which all plane waves are totally reflected from the layer-bottom interface. Cases 2 and 3, on the other hand, involve the phenomenon of total transmission across the layer-bottom interface. That is, there exists an angle of incidence for plane waves in the liquid layer, the so-called Brewster angle, for which plane waves in the layer are totally transmitted into the bottom. We see that for cases 1 and 3 plane waves normally incident upon the bottom interface from above are reflected without a change of phase; for cases 2 and 4 they are reflected with a phase change of 180° . As we may surmise, these differences have an important influence on the oscillatory pressure signal P_V observed at the detector.

Before proceeding with a discussion of the numerical results, we introduce the nondimensional horizontal phase velocity $V_n(\tau, r/H)$ for the n th mode at time τ and horizontal range r/H . We may define this quantity as the instantaneous velocity, $d(r/H)/d\tau$, with which a phase of zero pressure travels in the radial direction. We see that

$$V_n(\tau, r/H) = \text{Re}(\bar{\omega}_n^c)/\text{Re}(K_n^c) \quad (62)$$

where the superscript c refers to an evaluation of the functions $\bar{\omega}$ and K at a saddle point.

Figures 5 to 11 are plots of the parameters of interest for the case of a bottom material whose sound velocity and density are much higher than those of the water layer,

$$c_2/c_1 = 4, \quad \rho_2/\rho_1 = 1/b = 2.7.$$

The lowest three modes $n = 1, 2, 3$ have been considered. Figures 5, 7, and 9 present the exponential decay factor L (see equation 45), the frequency $\text{Re}(\bar{\omega})$, and the horizontal wave number $\text{Re}(K)$, as functions of $r/H\tau$ in the region of partial radiation, that is, at times later than the Airy phase maximum. Figure 11 shows values of the group velocity $U = r/H\tau$ and the horizontal phase velocity V as functions of the horizontal wave number K for the three modes $n = 1, 2, 3$ in the normal mode region, that is, for times earlier than the Airy phase maximum. Note that in Figure 11 $\bar{\omega} = VK$, the Airy phase corresponds to the minimum in the group velocity (U) curves, and values to the left (right) of each minimum correspond to the ground (water) wave contributions discussed by Pekeris [1948]. Figures 6, 8, and 10 are plots of the inverse of the phase velocity, $1/V$, as functions of $r/H\tau$. It is interesting to note that for the lowest mode, $n = 1$ (Fig. 6), the slope of the curve $1/V$ versus $r/H\tau$ at long times (small $r/H\tau$) differs markedly from that of the case of the rigid bottom (see Appendix), whose slope is unity and thus agrees precisely with results obtained with the aid of ray path or wave-front construction in the liquid layer. Now values of $(1/V)/(r/H\tau) = H\tau/rV$ also correspond to

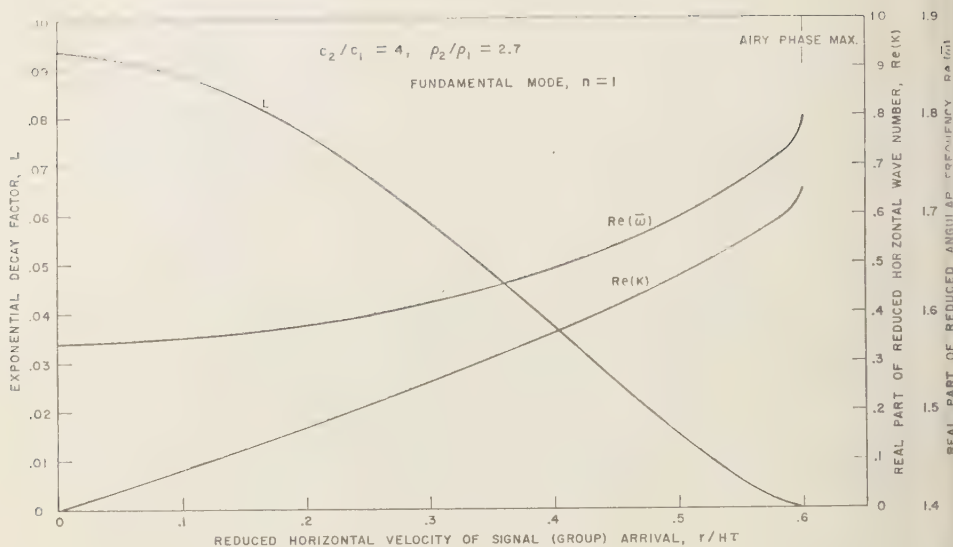


Fig. 5. Frequency, wave number, and exponential decay factor for late arrivals.

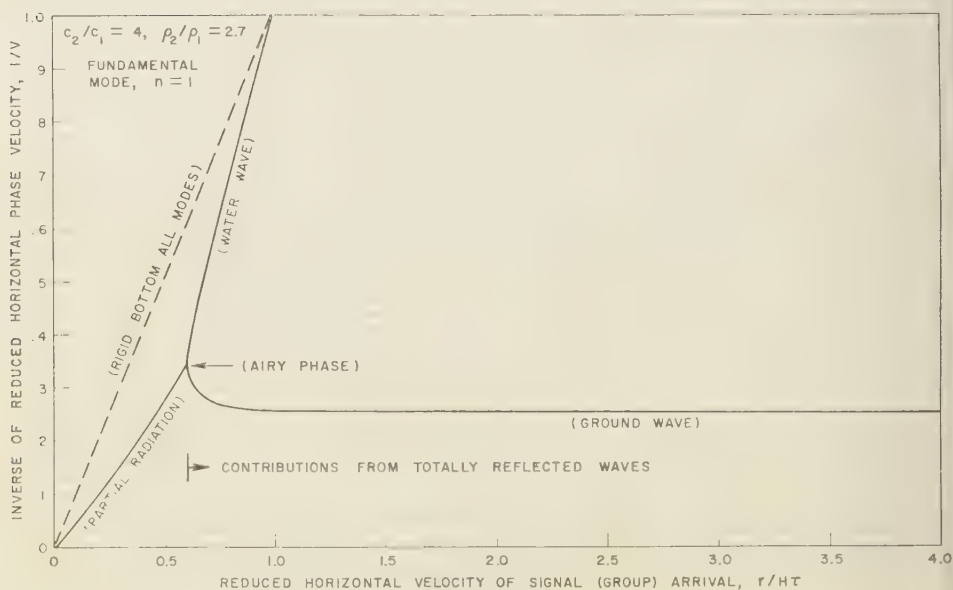


Fig. 6. Phase velocity-arrival time curves.

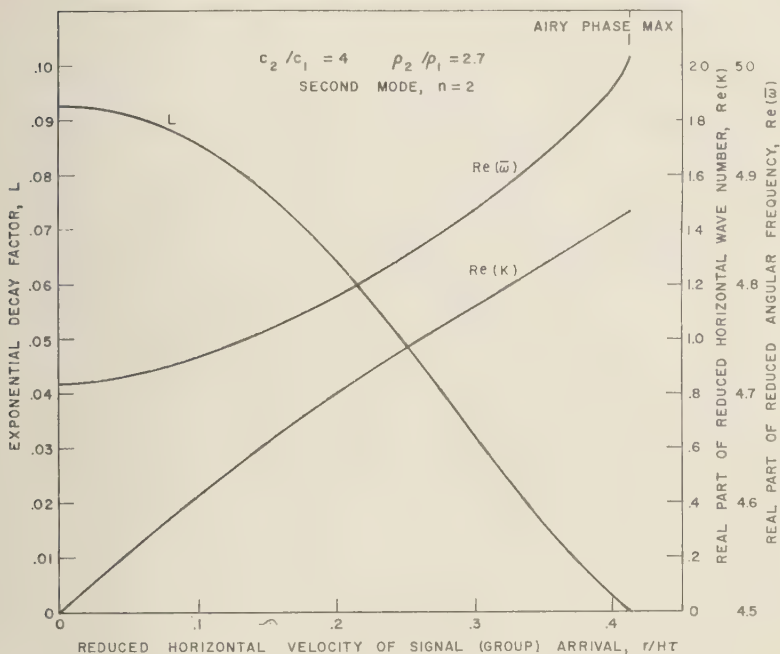


Fig. 7. Frequency, wave number, and exponential decay factor for late arrivals.

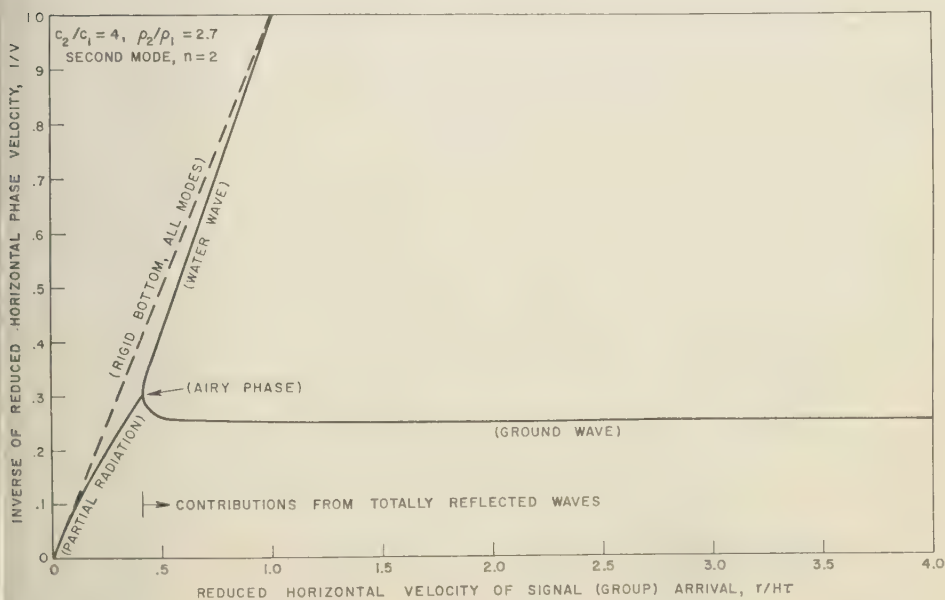


Fig. 8. Phase velocity-arrival time curves.

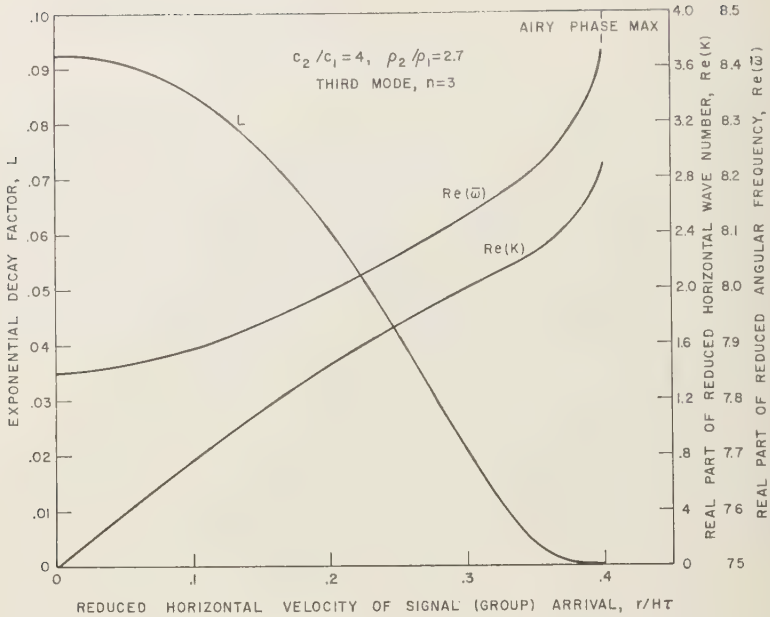


Fig. 9. Frequency, wave number, and exponential decay factor for late arrivals.

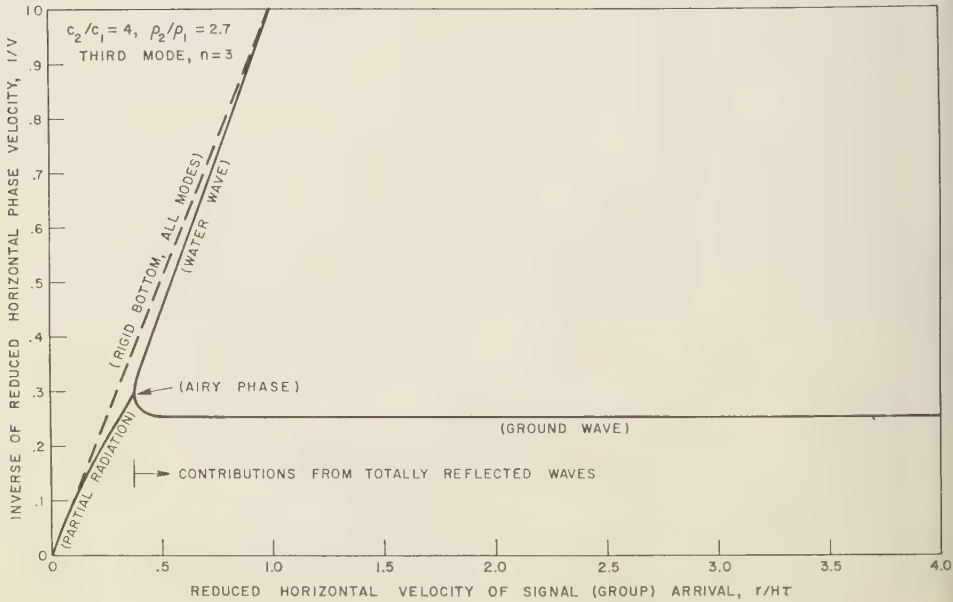


Fig. 10. Phase velocity-arrival time curves.

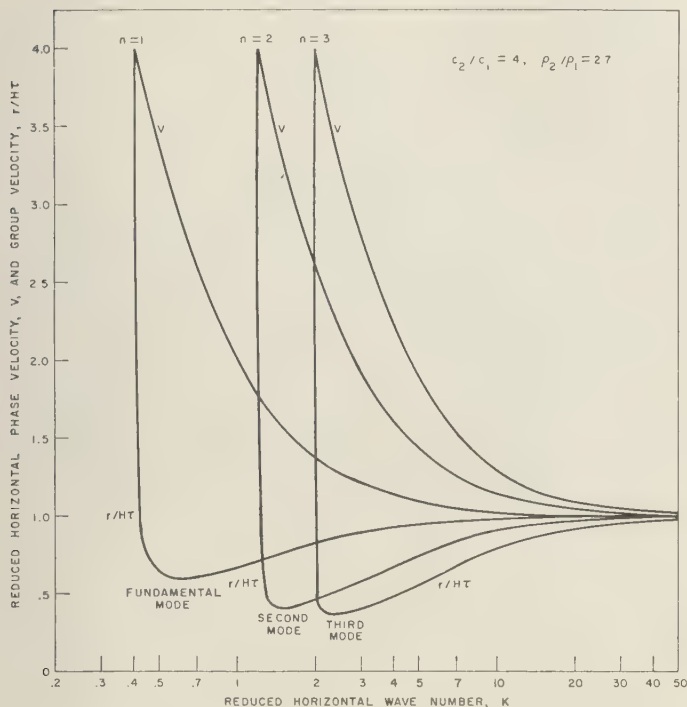


Fig. 11. Real (normal mode) dispersion curves for the two-layer liquid model.

slopes of the usual t^2 versus x^2 plots (in reduced units).⁸ Thus if we used only the lowest mode, $n = 1$, of the high-velocity bottom case in Figure 6 to determine the sound velocity in the liquid layer, we should obtain a value which is definitely larger than the sound velocity c_1 in the layer, but still much smaller than the sound velocity c_2 in the bottom. Note, however, that for the higher modes, $n = 2$ and $n = 3$ (Figs. 8 and 10), the curve $1/V$ versus $r/H\tau$ approaches the rigid bottom case for small values of $r/H\tau$. This is not surprising, since high-frequency asymptotic solutions are known to lead to the results of geometrical acoustics [Friedlander, 1958].

In Figures 12 to 18 the same parameters as shown in Figures 5 to 11 are plotted for the

case of a bottom material whose sound velocity and density are only moderately higher than those of the water layer,

$$c_2/c_1 = 1.24, \quad \rho_2/\rho_1 = 1/b = 2.$$

Here the normal mode region occupies a less prominent position as far as the time variable is concerned. Because of the smaller acoustic contrast at the bottom interface, radiation into the bottom at later times is considerably greater than in the previous case, and this is shown by the increased magnitude of the exponential decay factor L in Figures 12, 14, and 16. Note that at later times (small values of $r/H\tau$) the phase velocities for the lower modes of the present model do not differ much from the rigid bottom case (Figs. 13, 15, and 17).

The preceding examples treated case 1, that is, the case where $c_2/c_1 > 1$ and $c_2/c_1 b > 1$. We now discuss very briefly case 4 where $c_2/c_1 < 1$ and $c_2/c_1 b < 1$. The lowest mode for such a

⁸ We could, for example, define an apparent (reduced) sound velocity c of the medium as obtained from the slope a nondimensional x^2 versus t^2 plot, by the equation $c = (Vr/H\tau)^{1/2}$.

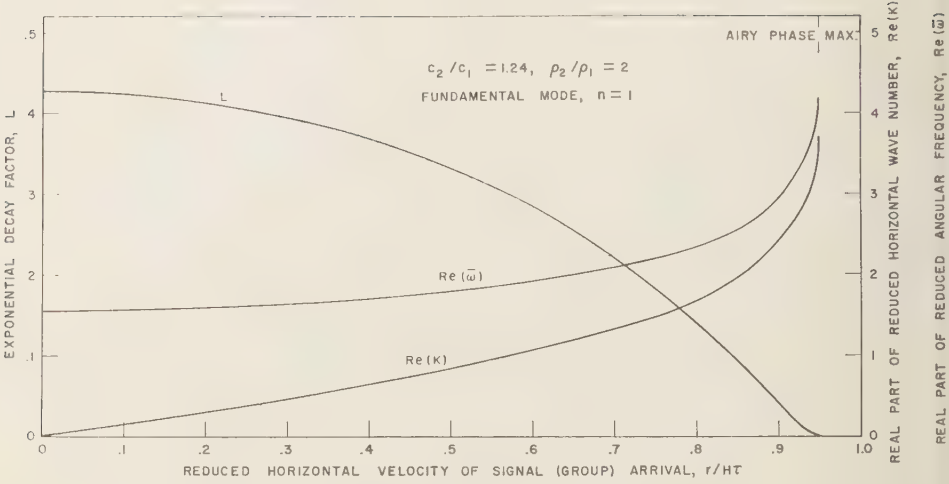


Fig. 12. Frequency, wave number, and exponential decay factor for late arrivals.

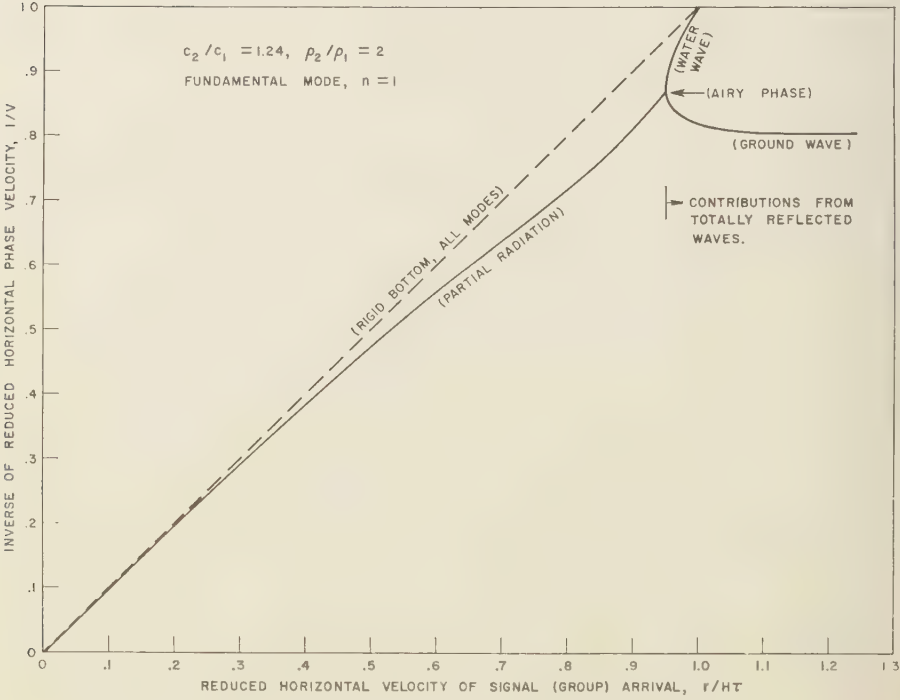


Fig. 13. Phase velocity-arrival time curves.

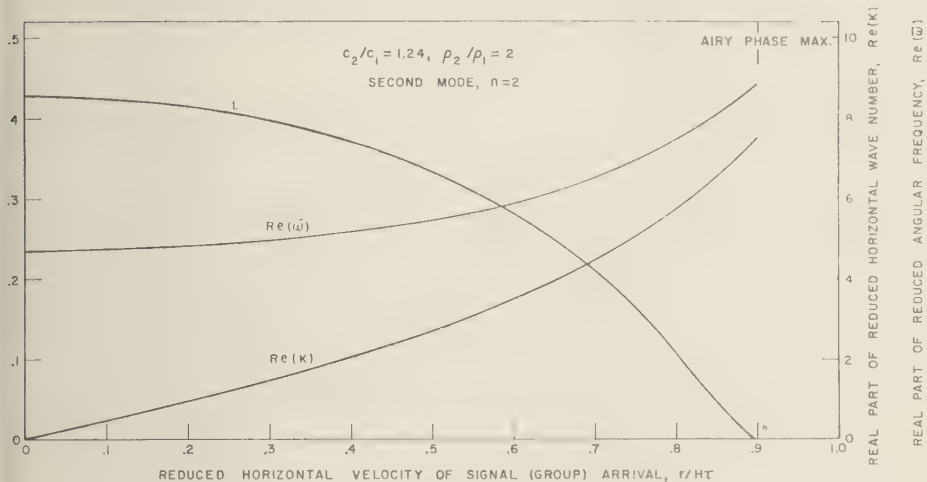


Fig. 14. Frequency, wave number, and exponential decay factor for late arrivals.

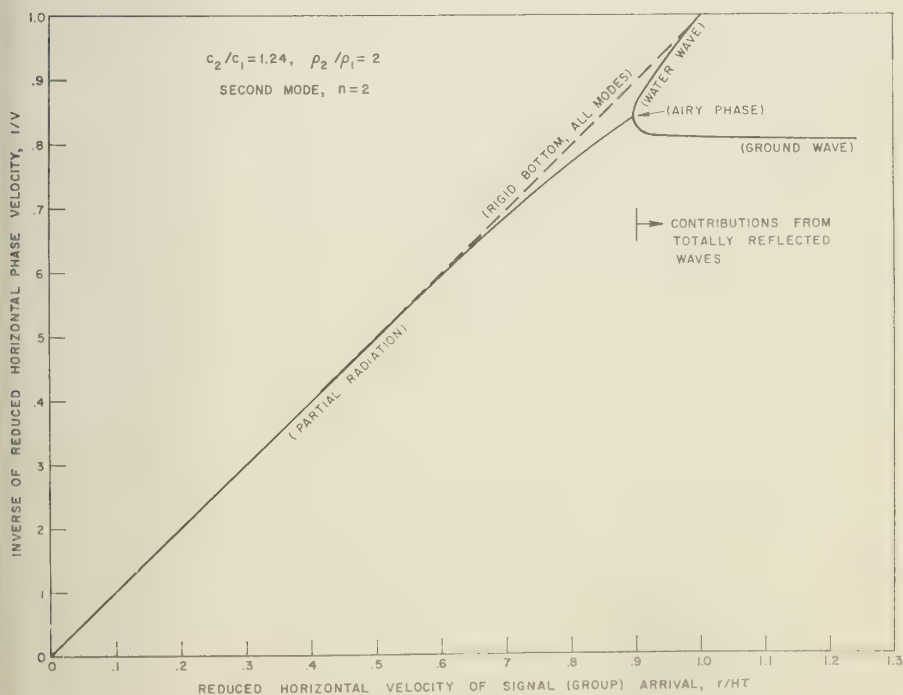


Fig. 15. Phase velocity-arrival time curves.

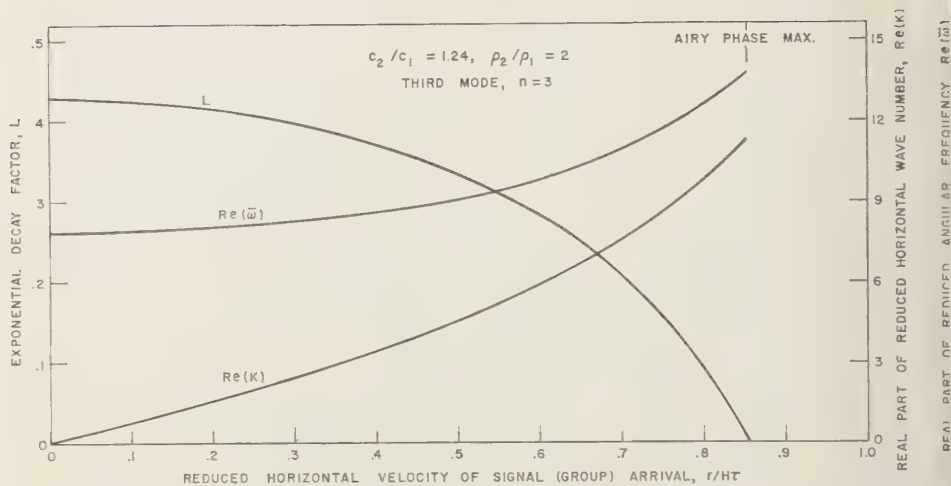


Fig. 16. Frequency, wave number, and exponential decay factor for late arrivals.

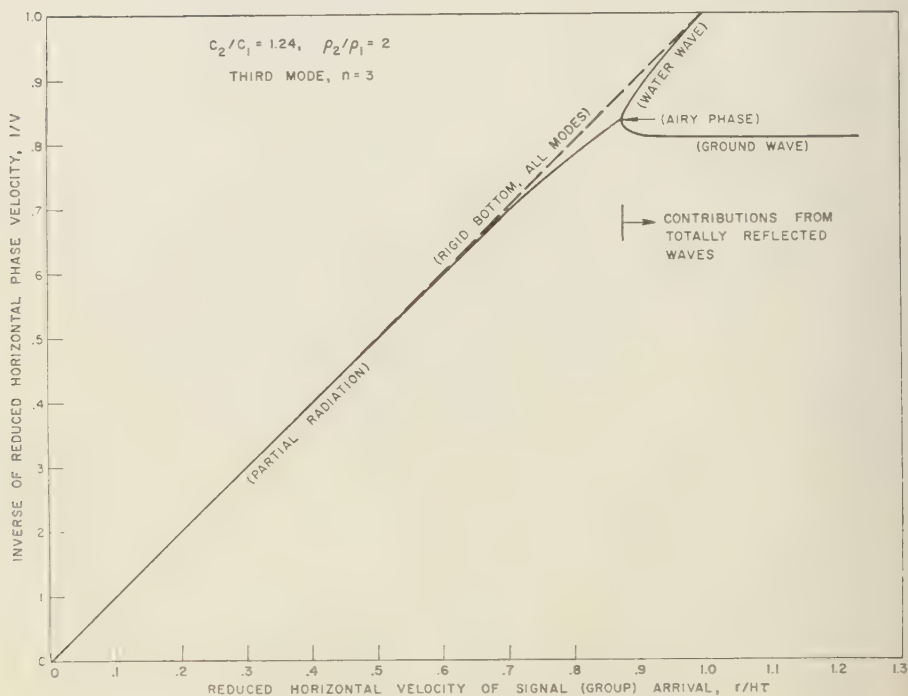


Fig. 17. Phase velocity-arrival time curves.

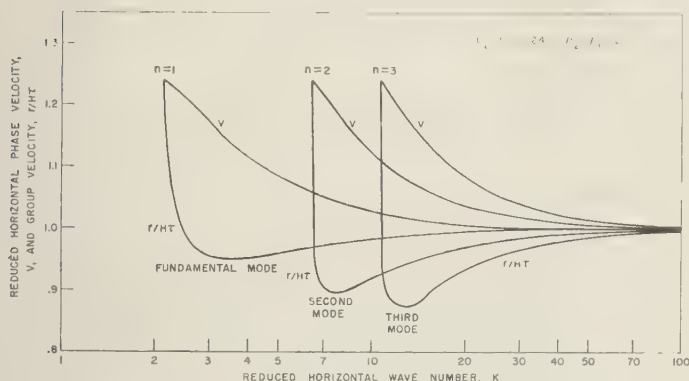


Fig. 18. Real (normal mode) dispersion curves for the two-layer liquid model.

case is illustrated in Figures 19 and 20, where the parameters $c_2/c_1 = 0.120$ and $\rho_2/\rho_1 = 1/b = 1.4$ have been chosen. Here the exponential decay of the oscillatory signals sets in with the first arrival at $r/H\tau = 1$. Because of the relatively large acoustic contrast at the bottom interface, the exponential decay factor L remains relatively small (Fig. 19). The curve of $1/V$ versus $r/H\tau$ (Fig. 20) shows no perceptible difference from the case of a completely rigid or a completely free bottom interface.

Case 3, that is, $c_2/c_1 < 1$, $c_2/c_1 b > 1$, is illustrated by the graphs in Figures 21 to 26 for the two lowest modes, $n = 1$ and 2, of the case $c_2/c_1 = 0.8$ and $\rho_2/\rho_1 = 1/b = 1.4$. Figures 21 and 24 are plots of the exponential decay factor L associated with two applicable saddle points in the first quadrant of the K plane. Of course the significant contribution to the observed oscillatory signal is the one involving the smaller value of L , and this is indicated by the solid lines in Figures 21 to 26. Around $r/H\tau = 0.60$ for mode $n = 1$, and around $r/H\tau = 0.625$ for mode $n = 2$, the two contributions have equal exponential decay. A very interesting aspect is exhibited by the more rapidly decaying (dashed) curves at $r/H\tau = 0$, which indicate for each mode a standing wave with a finite complex wave number K . This standing wave arises from the superposition of horizontally incoming and outgoing waves. Mathematically, the vanishing of $r/H\tau$ results here from the condition that

$$b^2 \tanh^3 \alpha_{1n} - \alpha_{1n} \tanh^2 \alpha_{1n} - \tanh \alpha_{1n} + \alpha_{1n} = 0 \quad (63)$$

(see equation 50) rather than the condition that $K = 0$.

The curves of $1/V$ versus $r/H\tau$ plotted in Figures 23 and 26 show that the ratio $H\tau/rV$ for the solid curves for small values of $r/H\tau$ is less and for large values of $r/H\tau$ is greater than that of the rigid bottom model. We notice again that this difference becomes less for the higher modes. Although the dashed line in Figures 23 and 26 indicates a finite horizontal phase velocity at $r/H\tau = 0$, this is not what we would actually observe. The interference of the incoming and outgoing waves would result in an apparent horizontal phase velocity which approaches ∞ as $r/H\tau$ approaches 0.

The last example is the somewhat unrealistic case 2, $c_2/c_1 > 1$, $c_2/c_1 b < 1$. This is illustrated (Figs. 27 to 30) for the lowest mode, $n = 1$, of the case $c_2/c_1 = 2$, $\rho_1/\rho_2 = b = 4$. We see that we have here all the features of cases 1 and 3 combined. The complexity of the curves for this relatively simple problem serves to indicate what we may expect in the case of more complicated systems of elastic layers.

In Table 1 we have listed the initial slopes, as $K \rightarrow 0$ and $r/H\tau \rightarrow 0$, of $1/V$ versus $r/H\tau$ curves, such as were plotted in Figures 6, 8, 10, 13, 15, 17, 20, 23, 26, and 29. Values of $(1/V)/(r/H\tau) = H\tau/rV$,⁹ which also correspond to the slopes of nondimensional t^2 versus x^2 plots, as mentioned earlier, are listed for the first three modes, $n = 1, 2, 3$, for each case, and a comparison is made with the rigid (or free)

⁹ According to the definition given in footnote 8, $H\tau/rV = 1/c^2$.

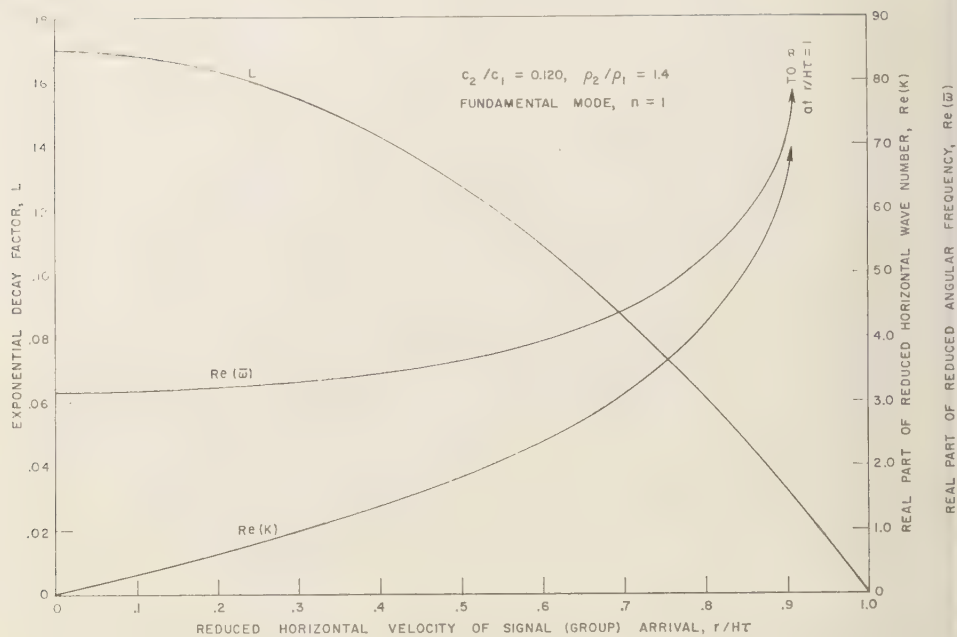


Fig. 19. Frequency, wave number, and exponential decay factor for a very low velocity bottom.

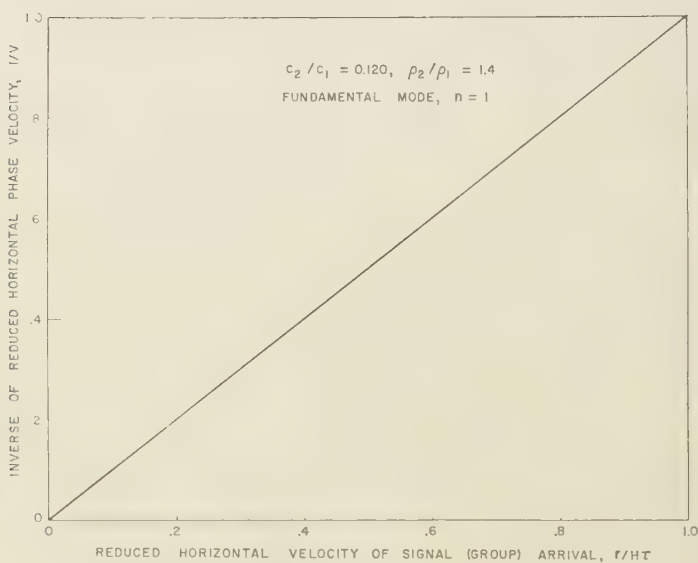


Fig. 20. Phase velocity-arrival time curve.

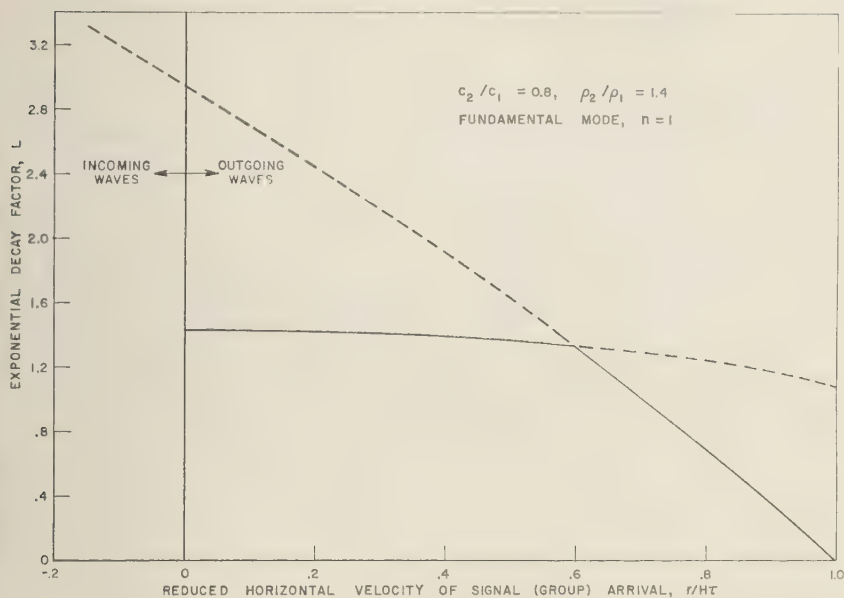


Fig. 21. Exponential decay for a low-velocity bottom.

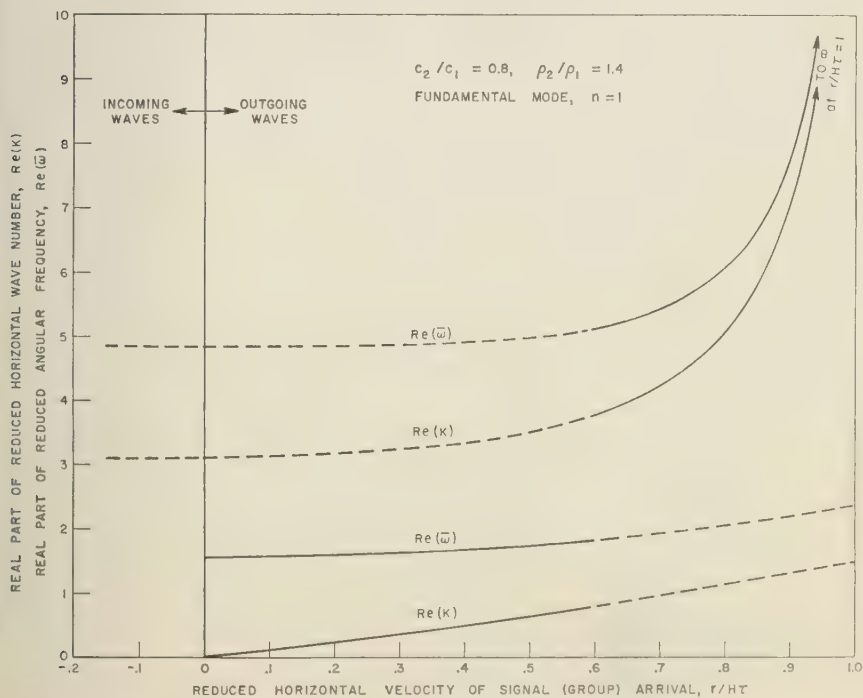


Fig. 22. Frequency and wave number for a low-velocity bottom.

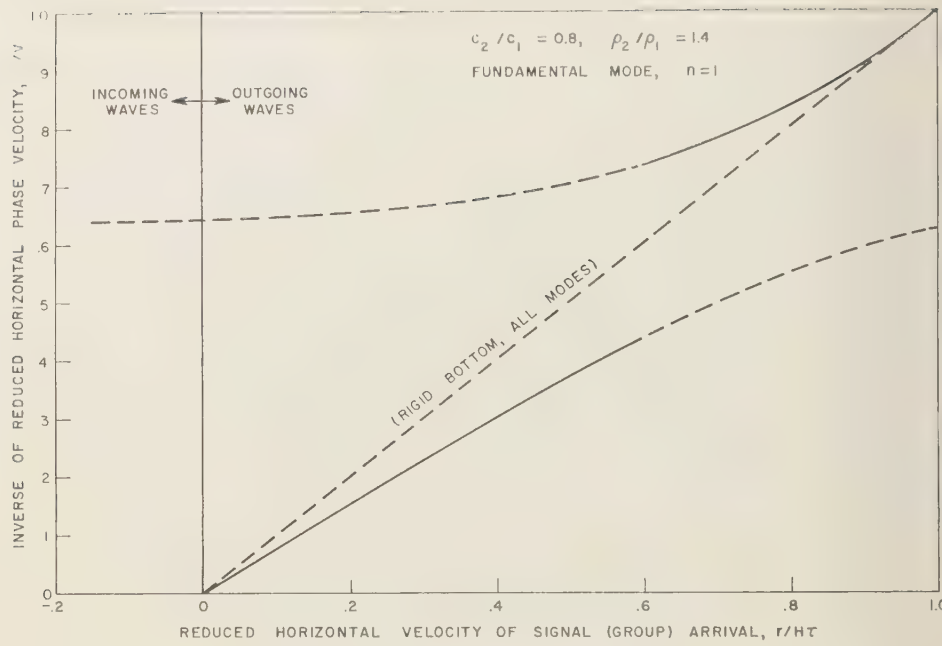


Fig. 23. Phase velocity-arrival time curves.

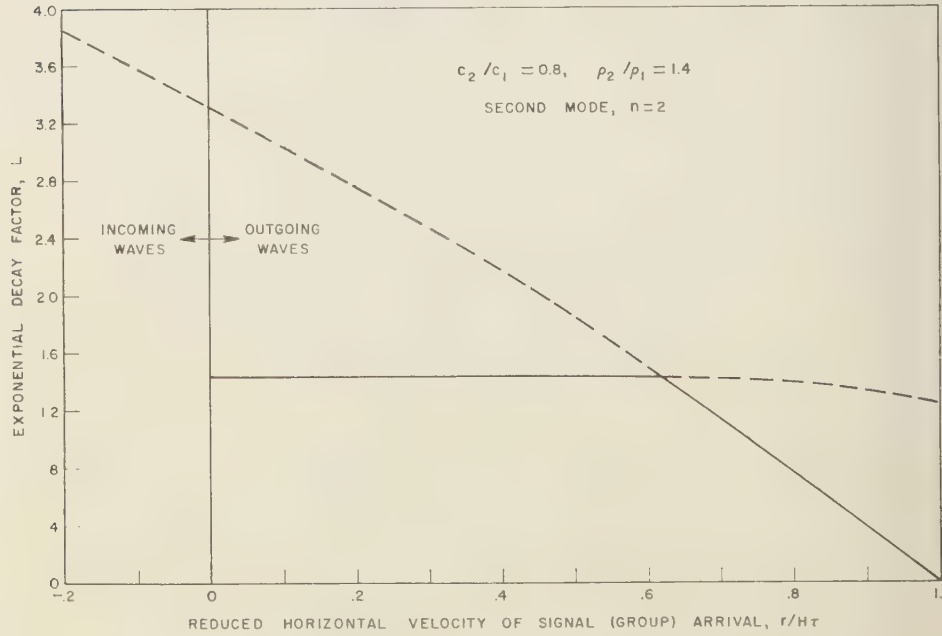


Fig. 24. Exponential decay for a low-velocity bottom.

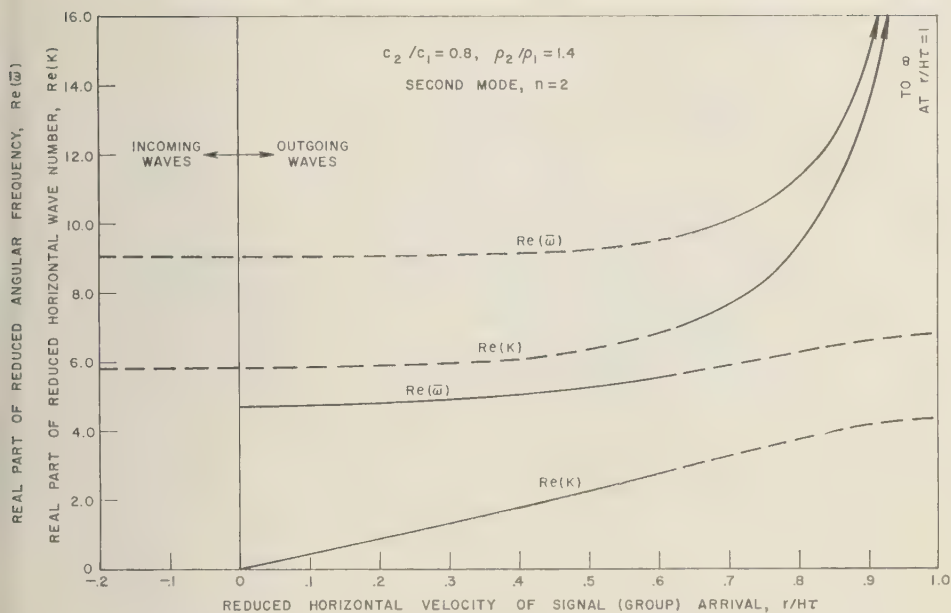


Fig. 25. Frequency and wave number for a low-velocity bottom.

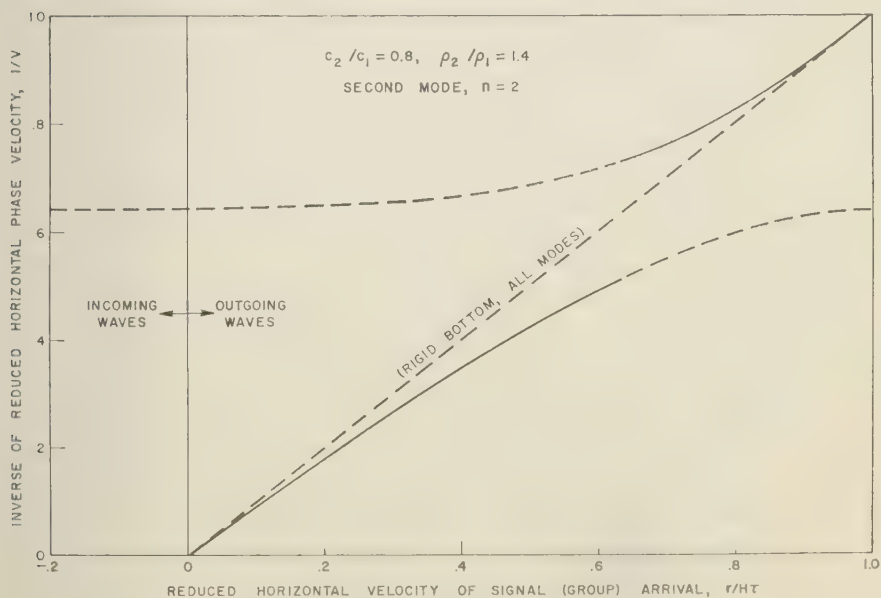


Fig. 26. Phase velocity-arrival time curves.

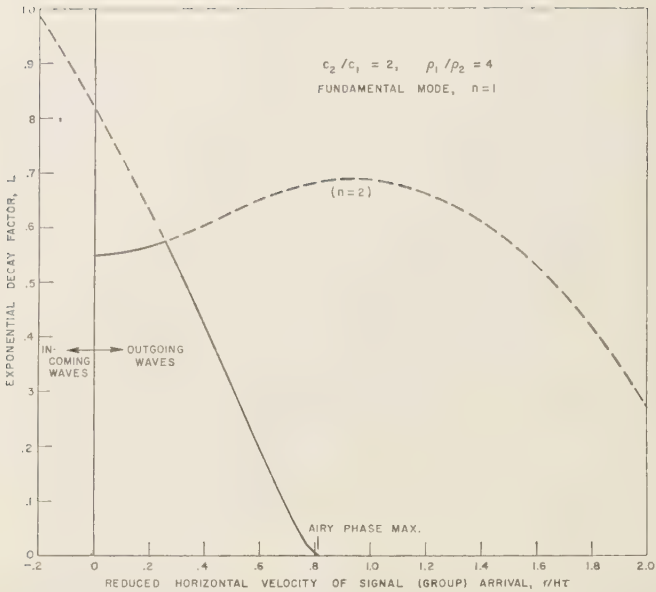


Fig. 27. Exponential decay for a high-velocity, low-density bottom. (Note that one of the curves actually belongs to the next higher mode.)

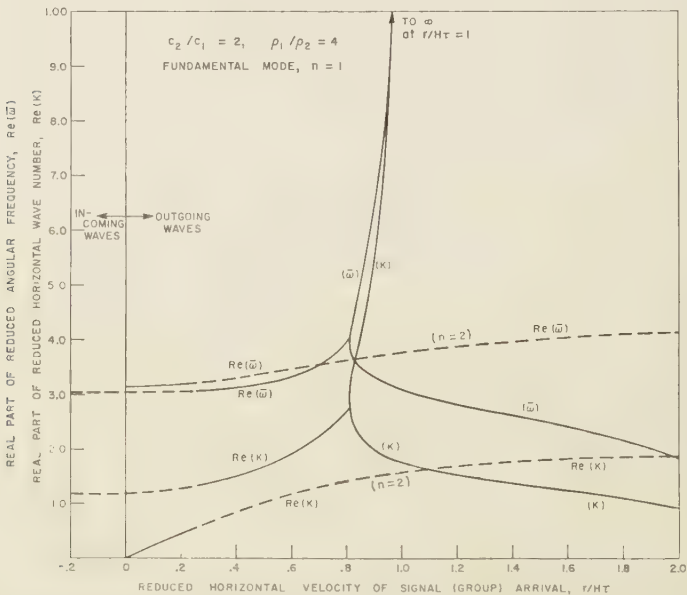


Fig. 28. Frequency and wave number for a high-velocity, low-density bottom. (Note that one of the curves actually belongs to the next higher mode.)

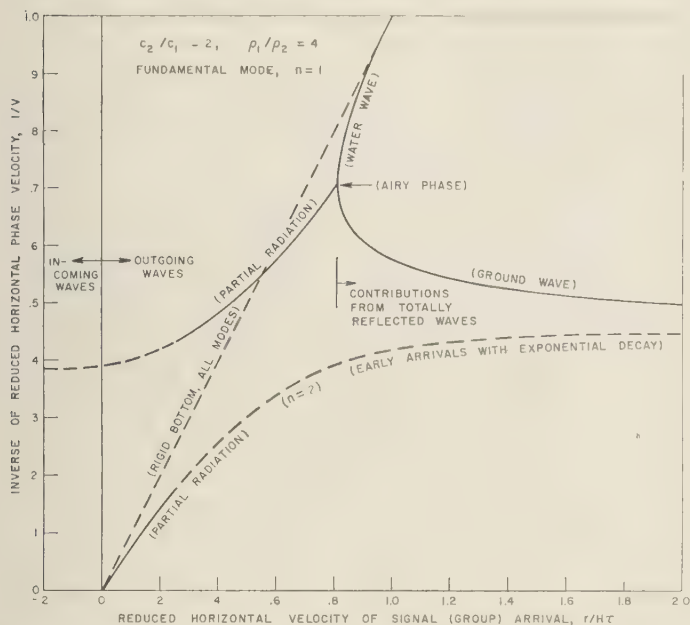


Fig. 29. Phase velocity-arrival time curves. (Note that one of the curves actually belongs to the next higher mode.)

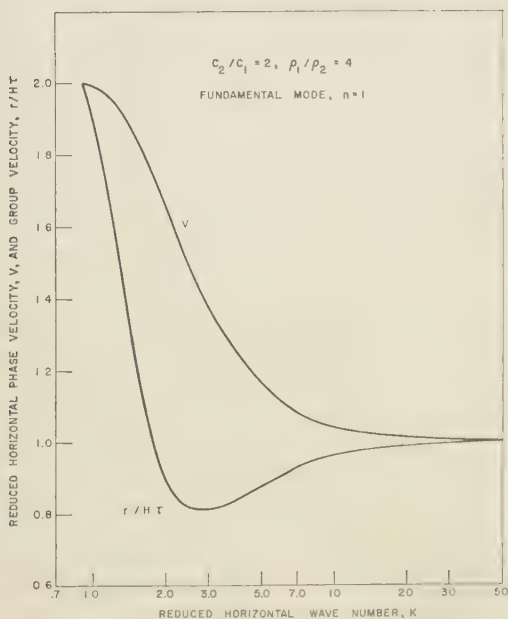


Fig. 30. Real (normal mode) dispersion curves for the two-layer liquid model.

TABLE 1. Values of the Function ($H\tau/rV$) as $K \rightarrow 0$ and $r/H\tau \rightarrow 0$

c_2/c_1 Velocity Ratio	$1/b = \rho_2/\rho_1$ Density Ratio	$\kappa = c_2/c_1 b$ Acoustic Impedance Ratio	n Mode	Liquid Layer, over		
				Liquid Bottom	Constant Normal Impedance Bottom	Rigid (or Free) Bottom
4	2.7	10.8	1	0.530	0.997	1
			2	.918	~ 1	1
			3	.968	~ 1	1
1.24	2	2.48	1	0.973	0.930	1
			2	.997	.990	1
			3	.999	.996	1
1.18	1.4	1.652	1	0.945	0.825	1
			2	.994	.963	1
			3	.998	.936	1
0.8	1.4	1.12	1	0.783	0.470	1
			2	.920	.656	1
			3	.965	.798	1
2	0.25	0.500	1	0.756	0.955	1
			2	.913	.989	1
			3	.958	.995	1
0.12	1.4	0.168	1	~ 1	0.997	1
			2	~ 1	.999	1
			3	~ 1	~ 1	1

bottom model and the case of a bottom exhibiting constant normal impedance independent of frequency. (See Appendix.) The numbers listed in Table 1 were calculated by means of the formula

$$(H\tau/rV)^e = \{\text{Re}(\bar{\omega}')/[\bar{\omega}'']^2 \text{Re}(\bar{\omega})\}^e \quad (64)$$

which follows immediately from (45) or from an evaluation of V from the higher-order terms of (39). As before, the superscript e refers to an evaluation of the functions at the end point $K = 0$.

We note from Table 1 that in all cases the agreement with the rigid or free bottom model, and therefore with the ray or wave-front picture, becomes better as we go to higher modes. This, of course, is what we expect. A comparison of results from the liquid bottom and a bottom interface of constant normal impedance shows clearly that, even for waves at near normal incidence, the liquid bottom cannot be considered to be locally reacting in most cases, but that the sound-velocity contrast has a strong influence on the behavior of the phase velocity of the lower modes.

The schematic phase velocity-arrival time curves (Fig. 31) illustrate how the calculated

horizontal phase velocity for the lower mode of a high-velocity bottom, case 1, differs from the results of simple ray or pulse-front arguments. On the basis of a simple ray picture, which does not take into account phase shifts on reflection and interference, we should expect the dashed-line dispersion curve $W\bar{A}G$ for the trapped waves and the dashed-line dispersion curve $\bar{A}O$ for the partially radiated waves. The line $W\bar{A}O$ has a slope of unity, and $G\bar{A}$ is parallel to the abscissa $r/H\tau$ at $1/V = c_1/c_2$. The point \bar{A} would correspond to the Airy phase, and the entire ground wave $G\bar{A}$ would have a phase velocity equal to the velocity of sound in the bottom. The actual trapped mode dispersion curve for case 1, the solid curve GAW , approaches the curve $G\bar{A}W$ for the higher modes, for which ray arguments are more applicable, and similarly the solid curve AO approaches $\bar{A}O$. It is interesting to note that for case 1 (Figs. 6, 8, 10, 13, 15, 17), the calculated phase velocities (solid curve in Fig. 31) at a point in time corresponding to \bar{A} are somewhat greater than the velocity of sound in the bottom, while at A they are somewhat less. For the more complicated case 2 (Fig. 29), however, the phase velocities at times corresponding to A and to \bar{A} are somewhat less than the velocity of sound in the bottom.

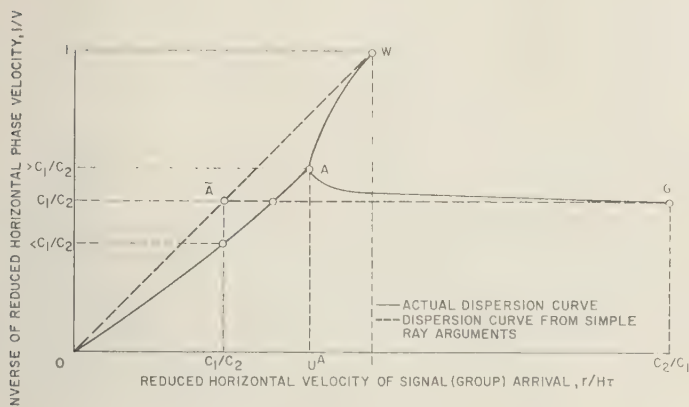


Fig. 31. Phase velocity-arrival time curves.

The significance of an Airy phase as the transition *in time* from unattenuated to attenuated mode propagation (or vice versa) is quite general as long as the trapped mode in question exists over a finite interval of real values of $\bar{\omega}$ and K , and thus for a finite interval of time. The Airy phase then corresponds to the condition that with increasing (or decreasing) time, two saddle points along the real K axis merge and separate again into two saddle points in the complex K plane. This also means that for a pulse problem there is continuity in time of the parameters $\bar{\omega}$, K , V , etc., as we pass from unattenuated to attenuated mode propagation.

It follows directly from the discussion in the introduction that our long-time solution (45) may also be written as a large horizontal distance solution. To do this, we need only replace τ by $r/H)/ (r/H\tau)$. Because of the saddle-point condition (49), $r/H\tau$ is equal to the horizontal group velocity U , if we extend the definition of group velocity to apply also to exponentially decaying signals.

In conclusion, we should like to comment briefly on the representation of the pressure response in terms of damped oscillations, which we have used in this paper. It is evident that a progressive harmonic plane wave which is damped, that is, which decays exponentially with time when observed at a fixed point, will also increase exponentially with distance at constant time in the direction of propagation. For a steady-state harmonic problem, such a

solution would naturally lead to conceptual difficulties, but for the point-source pulse problem of the type considered here, no difficulty arises. The disturbance is always limited to a finite region of the space-time domain; all contributions to the solution which are associated with arrival times earlier than those obtained from the shortest time path must vanish. This can be shown rigorously, for example, when we solve (4) or (57) by the ray expansion discussed in the introduction. It is therefore quite permissible to express the response of the medium to a point-source explosion as a sum of oscillations which decay exponentially in time, even though such solutions individually are not proper for the steady-state harmonic problem. On the other hand, the usefulness of our solution and the precision with which the parameters $\bar{\omega}$, K , L , V , etc., for a given mode can be defined at any time depend on how good the asymptotic solution is, that is, for example, how rapidly the path of steepest descent drops down in the neighborhood of a saddle point. This will in turn depend upon the specific layered elastic model under consideration.

APPENDIX: THE RIGID BOTTOM AND THE BOTTOM INTERFACE OF CONSTANT NORMAL IMPEDANCE

For comparison with the analysis presented in the main part of the paper, we briefly derive

here the normal mode solution to the problems of sound propagation in a liquid layer which rests on top of a perfectly rigid bottom and a

for P_L , and vanishes for the delta-function source. The second integral corresponds to (equation 18), and, since $\beta_1 H = (K^2 - \bar{\omega}^2)^{1/2}$, $i(n - 1/2)\pi$, we may write it in the form

$$P_N = \frac{4A}{H} \operatorname{Im} \int_0^\infty J_0(Kr/H) K \cdot \sum_n \exp(i\bar{\omega}_n \tau) \frac{\sin(n - 1/2)\pi z/H \sin(n - 1/2)\pi d/H}{(1/\bar{\theta} + i\bar{\omega}_n)\bar{\omega}_n} dK \quad (\text{A})$$

bottom which exhibits a constant normal impedance independent of frequency.

The rigid bottom. The formal solution may be written as

$$P = \frac{4G}{H} \sum_n \frac{\sin[(n - 1/2)\pi z/H] \sin[(n - 1/2)\pi d/H] \cos[(n - 1/2)\pi(\tau^2 - r^2/H^2)^{1/2}]}{(\tau^2 - r^2/H^2)^{1/2}} \quad (\text{A})$$

$$P(r, z, t) = \frac{A}{\pi i} \int_{\gamma-i\infty}^{\gamma+i\infty} \frac{e^{st}}{(s + 1/\theta)} ds \cdot \int_0^\infty J_0(kr) k \frac{\sinh \beta_1 d}{\beta_1} \cdot \frac{\cosh \beta_1(H - z)}{\cosh \beta_1 H} dk \quad (\text{A-1})$$

The integrand is an even function of the square root β_1 . We change order of integration, combine the paths of integration in the lower and upper s half-planes into one in the upper half-plane, and shift the path of integration to the negative real s axis. We obtain the expression

$$P(r, z, t) = 2Ae^{-t/\theta} \int_0^\infty J_0(kr) k \cdot \frac{\sinh \beta_{1\theta} d}{\beta_{1\theta}} \frac{\cosh \beta_{1\theta}(H - z)}{\cosh \beta_{1\theta} H} dk - 4A \operatorname{Re} \int_0^\infty J_0(kr) k \cdot \sum_n \frac{e^{s_n t}}{(s_n + 1/\theta)} \cdot \frac{\sinh \beta_{1n} z \sinh \beta_{1n} d}{(s_n H/c_1^2)} dk \quad (\text{A-2})$$

where the subscript θ refers to an evaluation of the functions at $s = -1/\theta$, and the subscript n refers to an evaluation of the functions at the roots of the period equation $f = \cosh \beta_1 H = 0$; that is $\beta_1 H = i(n - 1/2)\pi$, and $n = 1, 2, \dots$.

The first integral in (A-2) is analogous to (16)

where $\bar{\omega}_n = [K^2 + (n - 1/2)^2 \pi^2]^{1/2}$. We introduce the Hankel functions and solve the integral by the saddle-point method or by method of stationary phase. However, for a delta-function source the integral is easily evaluated in closed form. We obtain

where $G = A\bar{\theta}(A \rightarrow \infty, \bar{\theta} \rightarrow 0)$, and P vanishes for $[r^2 + (z - d)^2]^{1/2}/H\tau < 1$.

For the case of a fluid slab, that is, a fluid layer with two free surfaces, the formal solution is given by the expression

$$P = \frac{A}{\pi i} \int_{\gamma-i\infty}^{\gamma+i\infty} \frac{e^{st}}{(s + 1/\theta)} ds \int_0^\infty J_0(kr) k \cdot \frac{\sinh \beta_1 d \sinh \beta_1(H - z)}{\beta_1 \sinh \beta_1 H} dk \quad (\text{A-})$$

The solution proceeds as for the rigid bottom case. The roots of the period equation $f = \sinh \beta_1 H = 0$ are now being $\beta_1 H = in\pi$.

Bottom with constant normal impedance independent of frequency. We define the acoustic impedance ratio $\kappa = P/(\rho_1 c_1 v_z)$, where P is the pressure and v_z is the particle velocity in the z direction at the layer-bottom interface. The formal solution to our problem is then given by the expression

$$P(r, z, t) = \frac{A}{\pi i} \int_{\gamma-i\infty}^{\gamma+i\infty} \frac{e^{st}}{(s + 1/\theta)} ds \int_0^\infty J_0(kr) k \frac{\sinh \beta_1 d}{\beta_1} \cdot \frac{\beta_1 \cosh \beta_1(H - z) + \frac{s}{\kappa c_1} \sinh \beta_1(H - z)}{\beta_1 \cosh \beta_1 H + \frac{s}{\kappa c_1} \sinh \beta_1 H} dk \quad (\text{A-})$$

which is again an even function of the square root β_1 . We proceed as above and obtain

$$\begin{aligned} \psi(r, z, t) = & \frac{2A}{H} e^{-t/\theta} \int_0^\infty J_0(Kr/H) K \frac{\sinh \alpha_{1\theta} d/H}{\alpha_{1\theta}} \\ & \frac{\alpha_{1\theta} \cosh \alpha_{1\theta} \left(\frac{H-z}{H} \right) - \frac{1}{\kappa \theta} \sinh \alpha_{1\theta} \left(\frac{H-z}{H} \right)}{\alpha_{1\theta} \cosh \alpha_{1\theta} - \frac{1}{\kappa \theta} \sinh \alpha_{1\theta}} dK \\ & - \frac{4A}{H} \operatorname{Im} \sum_n \int_0^\infty J_n(Kr/H) K \frac{\exp(i\bar{\omega}_n \tau)}{(1/\theta + i\bar{\omega}_n)} \\ & \frac{\sinh \alpha_{1n} z/H \sinh \alpha_{1n} d/H \left(\frac{\bar{\omega}_n^2}{\kappa^2} + \alpha_{1n}^2 \right)}{\left[\bar{\omega}_n \left(\frac{\bar{\omega}_n^2}{\kappa^2} + \alpha_{1n}^2 \right) - iK^2/\kappa \right]} dK. \quad (A-7) \end{aligned}$$

The first integral is analogous to P_L (see equation 6), and the second integral corresponds to ψ (see equation 32). The period equation $= \alpha_1 \cosh \alpha_1 + i(\bar{\omega}/\kappa) \sinh \alpha_1 = 0$ has roots in the first quadrant of the $\bar{\omega}$ plane. At $K = 0$, for

$$> 1, \bar{\omega}_n^* = (n - 1/2)\pi + i \ln [(\kappa + 1)/(\kappa - 1)]^{1/2},$$

$$< 1, \bar{\omega}_n^* = n\pi + i \ln [(1 + \kappa)/(1 - \kappa)]^{1/2}; \quad (d\bar{\omega}_n/dK)^* = 0,$$

$$(d^2\bar{\omega}_n/dK^2)^* = -(1/\bar{\omega}_n^*)[1 + i\kappa/\bar{\omega}_n^*(\kappa^2 - 1)].$$

As $K \rightarrow \infty$, $\bar{\omega}_n \rightarrow K$. An asymptotic solution valid for large values of τ , of the second integral in equation A-7, can again be obtained by means of the saddle-point method or the method of stationary phase as given in the main part of this paper.

Acknowledgments. The numerical solutions by the saddle-point method were obtained on an Ecom 120 electronic computer by Dr. A. S. Ginzburg. Numerical results for use with the method of stationary phase were obtained by Messrs. W. Strickler and B. Tasini. The author is also grateful to Drs. A. S. Ginzburg, G. W. Postma, and E. Strick of the Shell Development Company for many helpful discussions.

REFERENCES

- Cagniard, L., *Réflexion et réfraction des ondes sismiques progressives*, Gauthier-Vilars, Paris, 1939.
- Ewing, W. M., W. S. Jardetzky, and F. Press, *Elastic Waves in Layered Media*, McGraw-Hill, New York, Chap. 4, 1957.
- Friedlander, F. G., *Sound Pulses*, Cambridge Univ. Press, Chap. 3, Sec. 9, 1958.
- McLachlan, N. W., *Bessel Functions for Engineers*, 2nd ed., Clarendon Press, Oxford, p. 205, 1955.
- Pekeris, C. L., Theory of propagation of explosive sound in shallow water, *Geol. Soc. Am. Mem.* 27, October 15, 1948.
- Pekeris, C. L., and I. M. Longman, Ray theory solution of the problem of propagation of explosive sound in a layered liquid, *J. Acoust. Soc. Am.*, 30, 323-328, 1958.
- Rosenbaum, J. H., Shockwave propagation in shallow water, I, *NAVORD Rept.* 4353, U. S. Naval Ordnance Laboratory, White Oak, Maryland, 1956.
- Rosenbaum, J. H., A note on the propagation of a sound pulse in a two-layer liquid medium, *J. Geophys. Research*, 64, 95-102, 1959.
- Van der Corput, J. G., Zur Methode der stationären Phase, I, *Compositio Math.*, 1, 15-38, 1935; II, *ibid.*, 3, 323-372, 1936. (See also Erdelyi, A., *Asymptotic Expansions*, Dover Publications, New York, Chap. 2, 1956.)

(Manuscript received December 22, 1959.)

Letters to the Editor

The Production of Tritons and C^{14} in the Terrestrial Atmosphere by Solar Protons

J. A. SIMPSON

*Enrico Fermi Institute for Nuclear Studies and Department of Physics
University of Chicago
Chicago 37, Illinois*

Recently *Begemann* [1959] has confirmed the results of *Craig* [1957] and *Begemann and Libby* [1957] that the natural production rate of tritons is greater than might be expected from production by the cosmic-ray flux in the atmosphere. Two mechanisms have been considered to explain this discrepancy: (a) accretion of solar-produced tritons by the earth, as suggested by B. Feld and J. Arnold; and (b) additional production by the low-energy component of the cosmic radiation at times of minimum solar activity. The integrated flux of primary cosmic-ray particles varies with solar activity, and by a factor of 2 to 4 during a solar-activity cycle.

The purpose of this note is to point out a third source, namely, intense fluxes of energetic solar protons which could produce tritons and C^{14} in the terrestrial atmosphere at times near the maximum of the solar-activity cycle. Within the past two years it has become clear that large solar flares not only produce rarely observed bursts of relativistic particles such as the event of February 23, 1956 [*Meyer, Winckler, and Simpson*, 1956], but also frequently contribute enormous fluxes of solar-flare protons with an energy range not extending above 400 mev, and hence not observable in cosmic-ray detectors located deep within the atmosphere. The existence of these solar protons was required to explain the large increases in ionospheric absorption of cosmic radio noise [*Reid and Leinbach*, 1959] and the absorption of forward-scatter radio signals [*Bailey*, 1959]. These protons were first directly detected at balloon altitudes [*Anderson, Arnoldy, Hoffman, Peterson, and Winckler*, 1959] and in nuclear emulsions [*Ney, Winckler, and Freier*, 1959;

Freier, Ney, and Winckler, 1959]. The extension of these nonrelativistic proton fluxes to normally forbidden geomagnetic latitudes as low as 51° (Chicago) has been investigated [*Fenton and Simpson*, 1959].

A solar flare of importance 3 to 3+ in a typical event is followed within 1 to 5 hours by the arrival at earth of a large solar proton flux that continues for more than 50 hours to bombard the entire atmosphere over the polar caps and down to latitudes of approximately 65° . Lower latitudes are reached during geomagnetic storms. A typical integral energy spectrum is $1/E^4$ in the approximate range 80 to 400 mev. A typical average flux at the top of the atmosphere is 10^4 protons/cm² sec. On the basis of data by *Reid and Leinbach* [1959] and by *Bailey* [1959], it appears that approximately 30 events of this type occurred during the present solar cycle.

We may estimate the contribution of these solar protons to triton production within one solar cycle from the following facts:

1. Not much is known about the energy dependence of triton production by nucleons. We do know, however, that an average cosmic-ray proton will have an energy of approximately 4 bev and lose this energy in the atmosphere by producing mesons, electrons, and electromagnetic radiation, and the nucleonic component. For our estimate we assume that tritons and C^{14} are products of the nucleonic component. For the relative yield R_1 of tritons by 100-Mev solar protons to 4-bev cosmic-ray protons, we estimate the ratio $R_1 \approx 5 \times 10^{-2}$.

2. The fraction R_2 of the time that solar protons irradiate the polar regions during the 11-year solar activity cycle is $R_2 \approx 1.4 \times 10^{-2}$.

3. The fraction R_4 of the terrestrial atmosphere accessible to solar protons compared with the 4-bev cosmic-ray proton flux is $R_4 \geq 0.1$.

4. The ratio of the solar proton flux to averaged 4 beV cosmic-ray proton flux is $R_4 \approx 5 \times 10^4$.

From these estimates, we compute the ratio R of triton production by solar protons to triton production by cosmic radiation. Thus,

$$R = R_1 R_2 R_3 R_4 \approx 3.5$$

The fact that triton production by nonrelativistic solar protons may be of the same order as production by cosmic radiation suggests that this might account for excess triton production, even though there is a large uncertainty in this ratio.

Because of their solar-flare origin, these events are centered in time about the maximum of solar activity. On the other hand, we know that the primary cosmic-ray spectrum changes with the solar cycle, so that the greatest contribution of low-energy cosmic-ray particles is present at the minimum of solar activity. Consequently a significant anticorrelation of triton production with the solar-activity cycle, such as looked for by Begemann [1959], may not be present during cycles of unusually intense solar activity.

Terrestrial triton production by solar protons must also be accompanied by additional C^{14} production from the secondary neutrons in the atmosphere. This may present a difficulty, since the present C^{14} production in the atmosphere is roughly in agreement with estimates derived from neutron density, and the total cosmic-ray flux. However, it should be noted that both the present solar cycle and the previous cycle were unusually active periods—no solar cycles over the past century display com-

parable levels of solar activity. Since the triton half-life is of the order of 11 years, and much shorter than the C^{14} half-life, the C^{14} production rate may, therefore, average out to a lower long-time production rate than estimates from the data in this solar cycle alone would indicate.

The existence of a well-defined region in the atmosphere for production of tritons and C^{14} by solar protons, namely, an atmospheric depth less than 50 g/cm² (an atmospheric pressure of 3 to 4 cm Hg), may have interesting applications to the problems of atmospheric mixing in the polar regions.

The writer appreciates a discussion with Dr. Anthony Turkevich, who added the suggestion that short-lived Be^7 might also be detected after these solar events.

REFERENCES

- Anderson, K. A., R. Arnoldy, R. Hoffman, Peterson, and J. R. Winckler, *J. Geophys. Research*, **64**, 1133-1147, 1959.
 Bailey, D. K., *Proc. IRE*, **47**, 255, 1959.
 Begemann, F., *Z. Naturforsch.*, **14A**, 334-342, 1959.
 Begemann, F., and W. F. Libby, *Geochim. et Cosmochim. Acta*, **12**, 277, 1957.
 Craig, H., *Phys. Rev.*, **105**, 1125, 1957.
 Fenton, K. B., and J. A. Simpson, Enrico Fermi Institute Document EFINS-60-7, in press.
 Freier, P. S., E. P. Ney, and J. R. Winckler, Balloon observations of solar cosmic rays on March 26, 1958, *J. Geophys. Research*, **64**, 685-688, 1959.
 Meyer, P., E. N. Parker, and J. A. Simpson, *Phys. Rev.*, **104**, 768, 1956.
 Ney, E. P., J. R. Winckler, and P. S. Freier, *Phys. Rev. Letters*, **3**, 183, 1959.
 Reid, G. C., and H. Leinbach, *J. Geophys. Research*, **64**, 1801-1805 (and references therein) 1959.

(Received March 9, 1960.)

Observed Magnetic Effects from Meteors¹

ALVIN W. JENKINS, JR., AND CHARLES A. PHILLIPS, JR.

*Denver Research Institute, Denver University
Denver, Colorado*

AND

ELWOOD MAPLE

*Geophysical Research Directorate
Air Force Cambridge Research Center
Bedford, Massachusetts*

correlation between geomagnetic fluctuations and meteoric activity was reported by Kalashnikov [1949], who used sensitive fluxmeters and a photographic recording technique. In his work, he noted an increase in the number of pulses in the vertical component over dates of meteor showers. Hawkins [1958], using more sensitive equipment also sensitive to the vertical component, attempted to correlate these with visual meteors. His results were tentative, indicating only such correlation as might be expected statistically. A real discrepancy thus exists between the results of these two workers. Hawkins has pointed out, however, that Kalashnikov's results may not be significant, since the correlation he noted is not much greater than that expected to occur accidentally. A preliminary analysis of data recently available from the IGY program concerned with audio fluctuations in the geomagnetic field is to indicate that meteoric activity and the average level of the fluctuations are related.

The subaudio program is a study of geomagnetic fluctuations in the 1- to 50-cps range. Two mutually perpendicular coils are used to detect variations in the magnetic field. The resulting electrical signals are amplified and recorded on magnetic tape. The tape is later played back through filters which analyze each signal into six approximately octave frequency bands. The filtered signals are rectified and integrated for the 15 minutes of recording time

provided each hour, resulting in a single number indicative of the average level of the geomagnetic fluctuations for each frequency band for each hour. The program has been active for more than a year, with five recording stations gathering data. Only recently, however, has the reduction equipment been put into operation, so that only a small fraction of the data so far appears in reduced form.

A striking feature of the activity levels thus far available is the occurrence of occasional large increases in the frequency band centered at 1.5 cps. In particular, the data from the Denver, Colorado, recording station show an increase in this band of about 5 or 6 times the usual level on the night of December 12-13, 1959. Since this is also approximately the expected time of the maximum of the Geminid meteor shower, a connection between the two events was suggested.

In Figure 1 the average of the nighttime activity levels in the 1.5-cps band for the north-south component of the geomagnetic field at Denver are plotted for October, November, and December 1959 (6 p.m.-5 a.m. local time). The sensitivity of this band is limited to 0.3 mV by instrument noise. Also shown is an average hourly meteor rate. It was determined by averaging over all counts listed for the particular date in Interim Report 28-29, Harvard University Radio Meteor Research Program (kindly supplied by Dr. Fred Whipple, Smithsonian Astrophysical Observatory). This report lists visual meteor counts, as reported to the American Meteor Society, going back to the early 1900's. The correlation between the two

¹This work supported by Air Force Cambridge Research Center under contract AF 19(604) 2204.

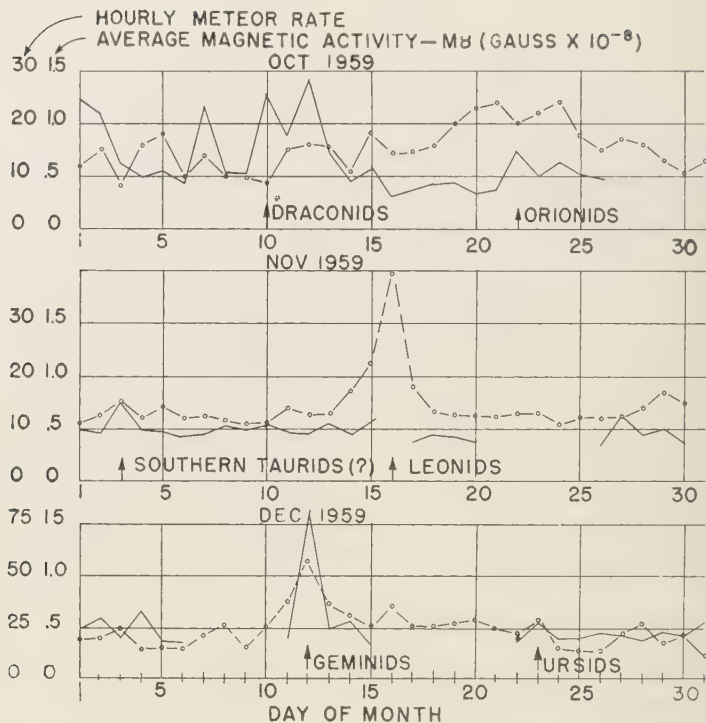


Fig. 1. Average of nighttime geomagnetic activity level in the 1.5-cps band at Denver (solid curve) and average hourly meteor rate. Breaks in activity-level curve correspond to dates for which no recordings were made. Approximate times of showers are indicated.

appears to be more than could reasonably be expected to occur accidentally.

The Geminid shower appears strongly in both plots. The Leonid shower is exaggerated in the meteor rate curve, since years of maximum activity are included in the average. Unfortunately, the recording station was not operating on November 16; however, the peak on November 15 is the highest activity level between November 3 and November 27. The Orionids appear in both curves, the meteor rate curve being broadened by the averaging process. An interesting feature of the curves is the large peak in the average magnetic variation on October 10–12. This time corresponds to the maximum of the Draconids, a periodic shower not included in the hourly meteor rate average, but one which should have been active in 1959. (There is considerable doubt as to the strength of the Draconid shower in 1959, the meteoric

orbit suffering a large perturbation from Jupiter since its last appearance.)

For every major shower in the interval (with the possible exception of the Leonids) there is either a pronounced or a noticeable peak in the geomagnetic activity level in the 1–5 cps band. There are also a few peaks that apparently do not correspond to peaks in the meteoric activity, but, since the entire magnetic activity in this frequency range does not, certainly, derive solely from meteors, such peaks could reasonably be expected. In addition, the peaks designated as coincident with shower dates have a special character significantly different from other peaks. The peaks that fall on October 10, 22, and December 12 and 23, occur in the 1.5-cps band and to a lesser extent in the 2.75-cps band. Above this they do not appear at all. The peaks on October 1, 7, and 12 and December 4 appear in all bands, 1.5–40 cps. The

er peaks are probably associated with local unusually active thunderstorm centers.

The same general behavior is exhibited by the east-west component. The peaks in the east-west component are lower in amplitude; however, the 'background' activity is also lower for this channel. The signal from the vertical coil varies much less from day to day than the horizontal component. Only very slight increases are observed in the vertical component over shower maxima. There is also a somewhat smaller correlation between the second frequency band (centered at 2.75 cps) of the north-south and east-west component and meteoric activity. Above 5 cps, no correlation is apparent.

A comparison with the Tucson 3-hour K in-

dices for December indicates little correlation with the activity levels. A magnetic bay is indicated for 0359, December 12, from the Tucson data.

Analysis will be continued as more data become available. Correlation with records from other sites will also be studied. The results of the complete analysis will be made available when completed.

REFERENCES

- Kalashnikov, A. G., (*Soviet Research in Phys.*)
Doklady Akad. Nauk SSSR, 66, 3, 1949.
Hawkins, G. S., *J. Geophys. Research*, 63, 467, 1958.

(Received February 25, 1960; revised
March 14, 1960.)

Ionospheric Backscatter Observation at 440 Mc/s¹

V. C. PINEO, L. G. KRAFT, AND H. W. BRISCOE

*Lincoln Laboratory, Massachusetts Institute of Technology
Lexington 73, Mass.*

Gordon [1958] has described a technique for investigating certain characteristics of the ionosphere using a powerful radar to detect backscatter from free electrons. By this technique, Bowles [1958, 1959] has obtained backscattered returns from the F_2 region at 41 Mc/s.

In recent experiments at the MIT Lincoln Laboratory Millstone Hill radar in Westford, Massachusetts, ionospherically backscattered returns have been observed at heights ranging from under 100 km to about 800 km.

The radar transmitter was operated at a peak pulse output power of 1.2 megawatts. The pulse length was 500 microseconds at pulse repetition frequencies of 100 and 50 cps. The antenna is an 84-foot-diameter paraboloid with a gain of about 37 db and a 2° beamwidth. The transmitted polarization was right circular. Left circular polarization was received. The receiver noise figure was about 6 db. The receiver bandwidth is adjustable, and, for the experiments described here, a bandwidth of 3 kc/s was used. Square-law detection was used in receiving. A digital encoder sampled the receiver output at intervals of 250 microseconds. The digitalized output from the receiver was processed by a high-speed real-time computer which is part of the Millstone radar system. Computer-integration techniques were used to improve the apparent signal-to-noise ratio.

The backscattered returns resemble noise when viewed on an A-scope display of the receiver output. The highest signal-to-noise ratios are obtained with the antenna beam pointing vertically upward. However, the signal intensities are usually high enough to be observed down to elevation angles as low as 15°.

One proof that the observed returns are from the ionosphere is that the range changes in the expected manner as the elevation of the antenna beam is changed. Operation at low elevation angles has made it possible to obtain returns from E -region heights that would have been obscured by ground clutter with the antenna beam in the vertical position. Vertical-incidence soundings, however, because of the reduced radar range, result in returns from great heights.

Measurements have been made of the variation with height of relative received signal power over the height range 90 to about 800 km. Signal-to-noise ratios versus height profiles shown in Figures 1 and 2 were taken at antenna elevation angles of 90° and 15°, respectively. The measured values of the signal-to-noise ratio shown in these figures have not been adjusted for differences in distance to the indicated heights. It should be emphasized that the

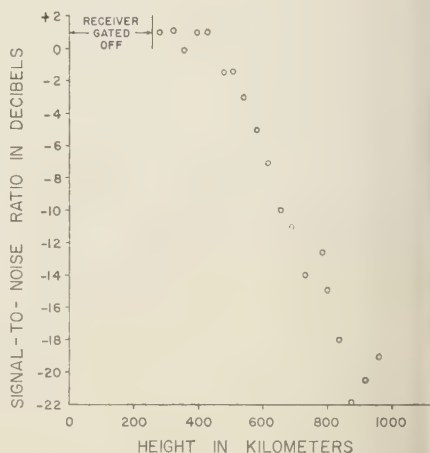


Fig. 1. Signal-to-noise ratio vs. height of vertical-incidence backscatter, observed at 440 Mc/s, 1407 hr, 75° west time, February 5, 1960.

¹ The work reported in this paper was performed by Lincoln Laboratory, a center for research operated by Massachusetts Institute of Technology with the joint support of the U. S. Army, Navy, and Air Force.

sults represent only afternoon wintertime conditions in the ionosphere above the observation e.

Frequency spectrum measurements of vertical-incidence backscatter from the ionosphere were made by sampling the received signal intensity at a number of frequencies in a band about 30 kc/s wide centered on the transmitted frequency. A 50-second integration routine was performed by the digital computer at several frequencies. The results of the spectrum measurements for a height of 315 km are shown in Figure 3 with an indicated spectrum width at the half-power points of about 11 kc/s. This observed frequency spectrum width is roughly 10 per cent of that predicted by Gordon [1958] on the basis of Doppler broadening by thermal motion of free electrons.

There has not as yet been any attempt to correlate the experimental results presented here

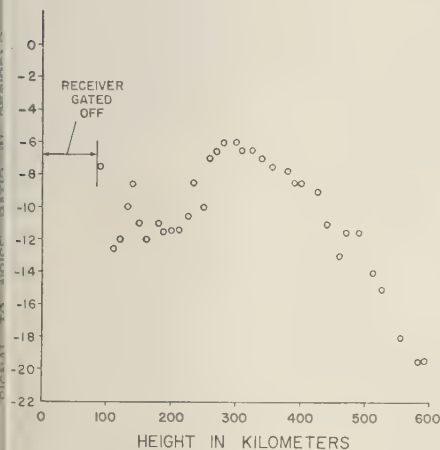


Fig. 2. Signal-to-noise ratio vs. height of observation (elevation angle of antenna beam = 15°), observed at 440 Mc/s during the period 1415 to 1419 hr, 75° west time, February 8, 1960.

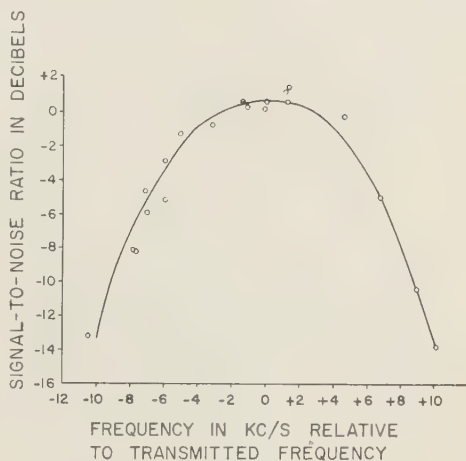


Fig. 3. Frequency spectrum of vertical-incidence backscatter from a height of about 315 km, observed at 440 Mc/s during the period 1400 to 1530 hr, 75° west time, February 5, 1960.

to electron temperatures or to any other parameters of the ionosphere, but it is planned that from data now in hand or easily obtainable to attempt to plot the electron-density profile of the ionosphere to heights above 800 km and to determine the variation in the frequency spectrum width with height.

REFERENCES

- Bowles, K., Observation of vertical incidence scatter from the ionosphere at 41 Mcps, *Phys. Rev. Letters*, 1 (12), 454-455, 1958.
- Bowles, K., Incoherent scattering by free electrons as a technique for studying the ionosphere and exosphere: Observations and theoretical considerations, *Nat. Bur. Standards Rept.* 6070, September 18, 1959.
- Gordon, W. E., Incoherent scattering of radio waves by free electrons with application to space exploration by radar, *Proc. IRE*, 1824-1829, 1958.

(Received March 9, 1960.)

Further Discussion of Paper by F. D. Stacey, 'The Possible Occurrence of Negative Nitrogen Ions in the Atmosphere'

D. R. BATES

*Department of Applied Mathematics
The Queen's University of Belfast, Northern Ireland*

In the controversy on N_2^- ions [Stacey, 1959; Bates, 1959] misunderstanding has arisen on the significance of the excess energy, ϵ , of the ion with respect to the normal molecule. The assumption that ϵ is positive does not imply that there are no states in which N_2 has an affinity for an electron. In the case of helium, for example, ϵ is certainly positive, but nevertheless He^- exists [Holstien, 1951].

If ϵ for nitrogen were negative N_2^- ions could not be formed and destroyed rapidly in radiationless transitions; and it would be difficult to understand why they have not been detected in the gas phase in the laboratory. Moreover, the arguments which Bates and Massey [1946, 1947] used to show that O^- ions cannot have an appreciable influence on the effective recombina-

tion coefficient in the F' layers would then be applicable to N_2^- ions.

REFERENCES

- Bates, D. R., Discussion of paper by F. D. Stacey, *J. Geophys. Research*, **64**, 2469, 1959.
Bates, D. R., and H. S. W. Massey, The basic reactions in the upper atmosphere, I, *Proc. R. Soc. London, A*, **187**, 261-296, 1946; II, **192**, 1-1947.
Holstien, E., Some investigations on the stability of the negative helium ion, *Arch. Math. Nat. videnskab.*, **51** (5), 1-9, 1951.
Stacey, F. D., The possible occurrence of negative nitrogen ions in the atmosphere, *J. Geophys. Research*, **64**, 979-981, 1959.
Stacey, F. D. Author's reply to D. R. Bates, *Geophys. Research*, **64**, 2470, 1959.

(Received February 20, 1960.)

A Convenient Method of Getting Representative Ionospheric Heights

G. A. M. KING

*Geophysical Observatory
Christchurch, New Zealand*

Several organizations are reducing ionograms and electron-density profiles on a routine basis. Most of them use electronic computers. Some workers do not have access to a computer, yet would like profiles representative of monthly conditions for each hour of the day, as a basis for theoretical studies.

A convenient method of getting these data is proposed here:

First, draw $h'f$ curves representative of monthly conditions at each hour. Then, reduce these 24 curves to true height profiles.

The representative $h'f$ curves are prepared as follows: For the particular hour, trace every $h'f$ curve for the month onto a single piece of paper. Now, draw a smooth median curve through them. It is surprisingly easy to do this if the median is counted in a direction perpendicular to the slope of the resulting curve. The figure shows a rather difficult example.

The reduction to true heights can be done

by any of the standard methods, but the ten-point methods of Shinn-Kelso [Thomas, 1959] and Schmerling [1958] are especially suitable, being very quick and quite accurate enough for this purpose. One person can comfortably produce a complete month's data in 24 working hours—an hour to a profile.

In this way, representative data can be obtained even though individual ionograms are unusable on account of sporadic E , absorption, and equipment failure. Further, at high latitudes, where spread F renders a large fraction of ionograms unreducible, representative profiles can still be prepared by dotting in 'upper limit' and 'lower limit' curves, and giving them a half weight in the median count.

It is worth noting that there is considerable variability between records taken all at the same hour. Some of it is caused by traveling disturbances. If the variability is so great that it is unreasonable to draw a median $h'f$ curve,

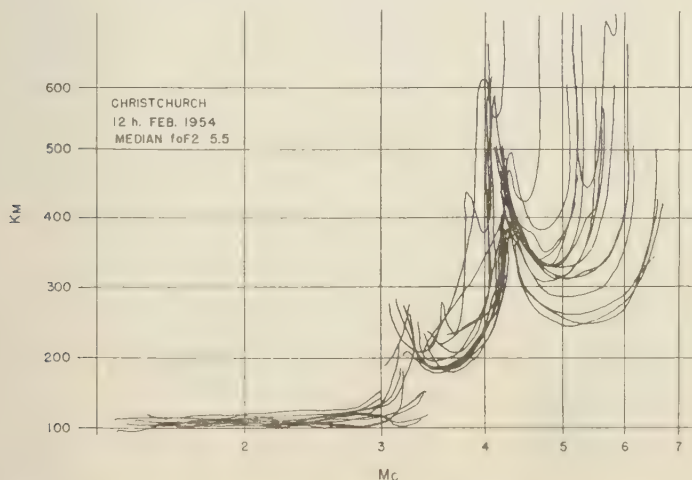


Fig. 1. Overlapped virtual height curves before median curve is drawn in.

the concept of 'representative data' surely does not apply.

Schmerling and Thomas [1956] have described a method of normalizing virtual height curves, followed by averaging, to obtain representative data. The median technique described here would seem to be much quicker, and so more suitable for general use.

This method arose from discussions with C. H. Cummack, and was developed for routine use at the Geophysical Observatory, Christchurch, New Zealand.

REFERENCES

- Schmerling, E. R., *An easily applied method for the reduction of h' , f records to N , h profiles*, *J. Atmospheric and Terrest. Phys.*, **12**, 8-11, 1958.
- Schmerling, E. R., and J. O. Thomas, *The distribution of electrons in the undisturbed F2 layer of the ionosphere*, *Phil. Trans. Roy Soc. London A*, **248**, 609-20, 1956.
- Thomas, J. O., *Distribution of electrons in the ionosphere*, *Proc. IRE*, **47**, 162-175, 1959.

(Received February 12, 1960.)

Discussion of Paper by Mahdi S. Hantush, 'Analysis of Data from Pumping Wells near a River'

R. G. KAZMANN

P.O. Box 451, Stuttgart, Arkansas

This is an interesting, but extremely theoretical, paper in the field of hydrogeology [Hantush, 1959]. The paper is important inasmuch as it typifies the approach of an increasing number of authors to hydrogeologic problems: the publication of more or less elegant mathematical or analog solutions that result in new techniques which do not appear to be an improvement over existing methods, either in simplicity or reliability of results, when applied to real situations.

Geology and hydrogeology are, basically, applied sciences. The geological environment through which the water moves rarely, if ever, corresponds exactly to the postulates of the mathematics or analog. We must, therefore, learn by experience exactly where the limitations of our theoretical approaches are to be found and interpret the differences between the facts and our theories as resulting from these limitations.

In dealing with a river infiltration situation, we find that the transmissibility and the effective distance to the line of recharge are critical. The storage coefficient, especially next to the river, is usually of little or no importance, because after the initial period the great bulk of the pumped water will come from the river via the aquifer. The apparent coefficient of storage of the aquifer near the river will consequently appear to increase indefinitely—it will neither be a constant nor reach a constant value, as is assumed by the author.

Dr. Hantush proposes a method for determining T , S , and the effective distance to the line of recharge by analyzing the time-drawdown relationship at individual observation wells. In the method a 'point of inflection' and the 'maximum drawdown' determined at each well from observations of the water level are used. From a practical standpoint it is no mean

feat to select, accurately, a point of inflection and a 'maximum' drawdown from a hydrograph plotted on semilog paper. This is a matter of judgment and experience.

The author recognizes this problem and he then outlines a procedure for determining the value of t at the point of inflection, making, in the process, two simplifying approximations in order to predetermine the shape of the curve for various values of $\beta^2 u$ (see equations 15 and 16). The mathematical treatment contains too many approximations and simplifying assumptions for the writer to be sure that he understands the practical implications of the procedure. The illustrative example has been carefully studied to see how it works out in practice.

The statement is made that with the passage of time the coefficients (presumably T and S) tend to attain their uniform values (p. 1929). If there is recharge from the river, this is incorrect. T will approach an apparent uniform value, but apparent S will continue to increase. Maybe this is why the slopes and points of inflection computed by the author do not correspond to anything directly obtainable from the plotted points.

The standard method involves the use of Figures 5 and 6: Select the drawdowns at 500 minutes, make a drawdown-distance semilog plot, and compute the transmissibility. It is readily found to be about 137,000 gpd/ft. (The author obtains an average of 151,000 gpd/ft and a minimum value of 139,000 gpd/ft.) The effective distance to the line of recharge is found to be more than 145 and less than 190 feet from the discharging well (Dr. Hantush's figures range from 80 to 165 feet, but he gives an average of 141 feet). The data used in the writer's computation are given in Table A.

Comparison of the south profile of the cone

TABLE A

Parameter	Well Number						
	1S	1W	1N	2W	2S	2N	3N
r (ft)	19.3	32	50	62	57	100	130
s (ft)	2.90	2.13	1.58	1.32	1.35	0.80	0.67

$$Q = 1,000,000 \text{ gpd.}$$

of depression with the other profiles conclusively proves recharge—it is steeper. As a check, a parallel computation can be made by using the data for 1000 minutes. Virtually the same results are obtained. A corroborative computation can also be made by using a point on the profile of the cone of depression which was used for the computation of transmissibility: Compute S for that point, using the Theis formula, at $t = 500$. Repeat this procedure for $t = 900$. Two apparent values of S are obtained: 0.36 and 0.57, respectively. This would indicate that recharge occurred during the test, since the porosity of an alluvial formation rarely exceeds 0.35 and the increase of apparent S with duration of pumpage has been found to mean recharge.

Even the author's procedure showed a variation of apparent S with time (Table 3). If t , is plotted against S , there is clear evidence that an increase in S is associated with an increase

in t . This throws doubt on the 'average' value $S = 0.116$ given by the author. This value is the apparent value reached after operating for a period of time between 39 and 45 minutes and the writer believes that use of this coefficient to evaluate the water supply available from the aquifer would yield misleading results.

A field procedure should yield conclusive answers to the following questions, when applied to pumping wells near a river: (1) Does infiltration of river water to the aquifer occur as a result of pumping a well which taps the aquifer? (2) If so, what is the effective distance to the line of recharge? (3) What is the effective transmissibility of the aquifer? (4) Is there any reason to believe that the properties of the aquifer differ importantly from those assumed in deriving the formulas, thus making it desirable that additional information be obtained before using the coefficients derived from the tests?

It remains to be demonstrated that the author's procedure offers any advantage over procedures now in general use, either in facility of application or reliability of results.

REFERENCE

- Hantush, M. S., Analysis of data from pumping wells near a river, *J. Geophys. Research.* 66: 1921-1932, 1959.

(Received January 27, 1960.)

Author's Reply to the Preceding Discussion

MAHDI S. HANTUSH

*New Mexico Institute of Mining and Technology
Socorro, New Mexico*

Kazmann makes the following observations:

1. *It is important to establish the occurrence of induced infiltration when pumping near a river.*

A considerable part of Kazmann's discussion is devoted to describing known procedures for demonstrating that river infiltration took place during the pumping test cited by the author. This demonstration is important but irrelevant to the object of the present paper, in which the distance of river recharge is assumed.

2. *The storage coefficient is of little or no importance after the initial period of pumping.*

The length of the initial period and the relative amount of water derived from storage are to be considered if any conclusion with regard to the importance of storage is to be drawn. The critic's statement is true only if the pumping installation is very close to the river and the formation supplying the water is of small T and large T . The percentage of discharge of a well (q_s) from storage, if the well is near a river, is given by *Glover and Balmer* [1954]:

$$q_s/Q = \text{erf} [z(S/4Tt)^{1/2}]$$

where erf is the error function, and the other symbols are as given in the original paper. A well tapping an aquifer of $T = 0.1 \text{ ft}^2/\text{sec}$ and $S = 0.2$, and whose effective distance to the river is about a mile (say, 5000 ft), will at the end of 5 years of continuous pumping withdraw 1 per cent of its discharge from storage. The result will be 58 per cent if the well has a $z = 0.000 \text{ ft}$. Obviously, these values are greater during the 5-year period of operation. To make the percentage of the rate of withdrawal from storage insignificant, if one may call 7 per cent of the well discharge of no importance, it would be necessary either to operate the first

well continuously for a period of 125 years or the second well for 500 years.

3. *The assumption of an ultimate uniform value of S is incorrect if there is river recharge.*

If one obtains T and z and then computes the apparent values of S from observed drawdowns through the use of equation 1 instead of the Theis formula, he will find that S approaches a definite value as time progresses. This value (specific yield of formation) can be extrapolated by using a plot of computed values of S versus time.

The indefinite increase of the apparent value of S , on which Kazmann bases his conclusion, must be the result of associating the Theis formula with a flow system to which it does not apply.

The assumption of constant values of the formation coefficients is a weakness in all known procedures now in use. If used carefully, a procedure which employs the same basic assumptions as presently known procedures do, and which avoids the use of data collected in a period when the basic assumptions are most seriously violated, will undoubtedly give more reliable results than procedures in which the use of such vitiating data cannot be avoided.

4. *The author's procedure uses predetermined curves and requires experience and judgment in its application.*

Judgment and experience would seem to be desirable in any undertaking. Known methods of analysis have proved successful if used wisely. Judgment and experience are needed in fitting observational data to Theis's predetermined type curve [*Wenzel*, 1942], to *Jacob's* [1950] predetermined straight line, to *Kazmann's* [1946] predetermined set of curves, to *Hantush's* [1956] predetermined curve, and to *Kazmann's*

[1948] predetermined curve, as well as as to the extrapolation of the direction of the latter curve to obtain its intersection with the zero-drawdown axis. (References which are not listed below are found in the original paper.)

In the author's procedures, both the point of inflection and the value of the maximum drawdown are not selected, as Kazmann seems to have understood; rather, they are computed. Admittedly, the author's statement with regard to the location of the inflection point is not very clear. It should have read (see col. 2, p. 1925): 'The position of the inflection point is not known *until the tangent line is constructed*. The tangent line is. . . .' The maximum drawdown is computed by using the method of least squares (see equation 27), which method can be shown to give a close approximation of s_m even though the data at hand include points that are not represented by equation 15. The point of inflection is located on the tangent line by using equation 14, Table 1, and equation 12, successively. The location of this point can be checked by using the second method for obtaining t_i (see equation 18). As pointed out by the author, with a little experience one may obtain a satisfactory answer on the first trial. If there is any objection to the author's procedure, it should have been directed to the construction of the tangent line, which may require a little experience. Kazmann [1948], in what he calls 'standard procedure,' uses the same procedure in extrapolating the direction of the curve in his drawdown-distance semilog plot.

5. *The author's treatment is highly theoretical, for it contains too many simplifying assumptions.*

Known methods which have been successfully used are based on exactly the same conventional assumptions. Both equation 15 and equation 16 are better approximations than are provided by any known method in use, because, if such an approximation is resorted to, the author retains more terms in the series expansions of $W(u)$.

In the standard procedure that Kazmann used, T is computed from a drawdown-distance semilog plot constructed from drawdowns at an arbitrarily chosen time $t = 500$ min by utiliz-

ing the properties of Theis's approximate formula for relatively large time; namely,

$$s = (2.3Q/4\pi T) \log_{10} (2.25Tt/r^2 S)$$

A look at Figures 5 and 6 of the original paper shows that at $t = 500$ min, the river recharge has already taken place. Consequently, the Theis formula is inapplicable, and the value of T thus obtained has no validity. In the standard procedure one cannot use equation 13 of the Rorabaugh procedure [1956] by selecting drawdowns at an arbitrarily chosen time, unless that time is sufficiently long to give reasonable assurance of a steady-state flow.

6. *An increase of S with time is inferred from a plot of t_i versus S .*

The value of t_i depends on the formation coefficients, as well as on the location of the observation well (see equation 9). According to the location of the well, a larger value of t_i may very well be associated with a smaller value of S .

Contrary to Kazmann's conclusion, the author's Table 3 shows that the value (S/T) is fairly uniform after $t = 130$ min. This is because a plot of u_i versus (r^2/t_i) should theoretically exhibit a straight-line relationship if (S/T) is constant. That this plot is approximately a straight line is readily seen if the values of u_i and r^2/t_i from Table 3 are used.

7. *The average value of S (0.116) obtained by the author is the apparent value of S reached within 39 to 45 min; therefore, known procedures do not give misleading results.*

By using adjusted values of drawdown (s') at $t = 45$ min [Stramel, Lane, and Hodson, 1958, p. 47] and the value of $T = 137,000$ gpd/ft (obtained by Kazmann), the following values of apparent S (each of which is the largest in the interval 39 to 45 min, because of using the largest value of t and the smallest value of T) are computed from the Theis formula:

Parameter	Well Number						
	1S	1W	1N	2W	2S	2N	3N
s'	2.47	1.65	1.12	0.83	0.82	0.39	0.34
app. S	0.051	0.077	0.083	0.094	0.113	0.096	0.065

These values would have been still smaller and the average value of $T = 151,000$ gpd/ft. is used. Such values do not warrant Kazmann's conclusion. A look at Figure 5 shows that the observed drawdown at $t = 45$ min is very close to the curve for which the author obtained $S = 0.114$ and $T = 149,000$ gpd/ft. That is why the apparent value of S for well 1 coincided with the author's value.

If the formation coefficients are not reasonably uniform during the early period of pumping (a condition which is generally recognized to be true), the analysis of data collected during that period by using any procedure based on the conventional assumptions will yield erroneous results. The author is confident that fitting Theis's type curve to a composite drawdown curve for the wells in question in the period $t < 130$ min, where the recharge, apparently at least, does not take place, is virtually impossible. Even when the analysis is carried out on each well separately, a good fit is very difficult to obtain.

If the analysis is performed on these wells by using Theis's graphical method, the scatter of the values of T and S is enormous, with values of T ranging from 280,000 to 450,000 gpd/ft. and values of S ranging from 0.0015 to 0.015. Knowing the field conditions, can one rely on these values in estimating water supply and in predicting future water levels?

8. *The author's procedure is not easier nor has it any advantage over procedures now in use.*

Ease of application is not a criterion of adequacy. Kazmann [1946] uses one observation well and obtains the effective distance by fitting the observational data to a set of type curves. He then obtains T and S from data collected in the early period of pumping using Theis's graphical method. In this period, the variation of the formation coefficients is generally recognized to be very large, in which case Theis's graphical method is known a priori to give poor results. In Kazmann's procedure [1948] more than two wells are required to obtain the effective distance; T cannot be determined if steady-state drawdowns are not observed. In the author's procedure, on the other hand, the use of data where the variation of T and S is most severe is avoided; observed steady-state drawdowns are not required; and T , S , and z can be determined by using one or more observation wells.

REFERENCES

- Glover, R. E., and G. G. Balmer, River depletion resulting from pumping a well near a river, *Trans. Am. Geophys. Union*, 35, 768-770, 1954.
 Hantush, M. S., Analysis of data from pumping tests in leaky aquifers, *Trans. Am. Geophys. Union*, 37, 702-714, 1956.

(Received February 20, 1960.)

Gravity Anomalies over a Buried Step

A. M. BANCROFT

Dominion Observatory, Ottawa, Canada

Bott and Smith [1958] give the following formulas for three-dimensional and two-dimensional anomalies, respectively:

$$d_0 = (48\sqrt{5}/125)(\Delta g_T/U_{xz})$$

$$d_0 = (3\sqrt{3}/8)(\Delta g_T/U_{xz})$$

where d_0 is the maximum possible depth to the top of the anomaly-producing body, Δg_T is the total anomaly and U_{xz} is the maximum horizontal gradient. It should be noted that these formulas are also valid as the *exact* depths to a point source and an infinite horizontal line source, respectively.

In the case of a 'stepped' anomaly, the derivation of maximum depth is particularly straightforward if we assume that the anomaly is due to a semi-infinite step of depth d and thickness t (Fig. 1).

We have

$$\Delta g_T = 2\pi G\sigma t$$

and

$$U_{xz} = 2G\sigma \log_e (1 + t/d)$$

where σ is the density contrast and G the gravitational constant. If we write

$$d_0 = (1/\pi)(\Delta g_T/U_{xz})$$

we can rearrange to obtain an expression for the depth

$$d = \frac{t}{\exp(t/d_0) - 1}$$

It can be seen that, as t decreases to very small values, d increases and tends to the value d_0 . The maximum depth to the step is therefore d_0 ; the actual depth is likely to be considerably less than d_0 for reasonable values of σ .

The expression for d_0 gives both the exact depth to a semi-infinite horizontal thin plate and the maximum possible depth to the top of *any* body producing the anomaly. The general argu-

ment is implicit in a paper by *Tatevosyan* [1958].

The advantage of the formula for a step is that in cases where it is applicable it gives a smaller value of d_0 than either of the formulas of *Bott and Smith*. Also, the relation between actual depth and d_0 is very easily applied.

The expressions for d and d_0 were originally derived for use in the interpretation of the Bouguer anomalies in the vicinity of Holleford Ontario (Fig. 2). The probability that an ancient meteorite crater underlies the area has been discussed by *Beals* [1957, 1958]. It is sufficient for the purposes of this communication to note that the gravity observations were made by staff members of the Dominion Observatory in 1955, after a study of air photographs had revealed an unusual circular depression a little over a mile in diameter. A geological reconnaissance suggested that the shallow topographic depression (about 100 feet) was underlain by a deeper bedrock basin. The rocks outcropping in the central area and the region to the south are typically Ordovician limestones, whereas the Precambrian rocks exposed elsewhere are mainly granites and gneisses with some crystalline limestone.

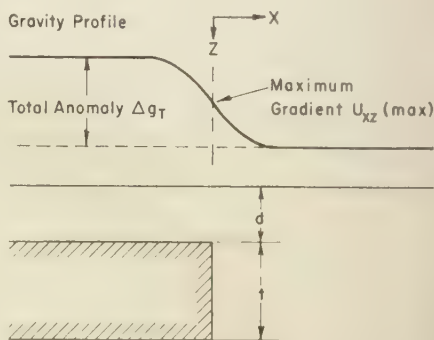


Fig. 1. Gravity anomalies over a buried step.

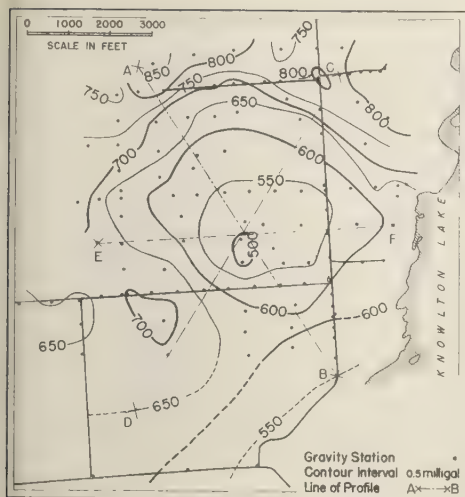


Fig. 2. Bouguer gravity map of Holleford, Ontario.

The gravity measurements were undertaken in order to determine the nature and dimensions of this basin prior to diamond-drilling operations. The Bouguer anomaly map provided striking confirmation that the circular topographic depression was indeed a bedrock feature. The negative anomaly indicated that for the most part this basin was filled with material lighter than the rocks exposed at the surface.

Quantitative interpretation of the anomalies is rendered difficult because the density variations of the known rocks do not explain the anomaly. The Ordovician limestones which overlie the feature have a mean density of 2.70 g/cm^3 (with a standard deviation of 0.010 g/cm^3 for 19 samples) and the Precambrian granites and gneisses which underlie the area have a mean density of 2.61 g/cm^3 (s.d. = 0.011 g/cm^3). In trying to assign an over-all density for the Precambrian in this area, we must also remember that there is a proportion of crystalline limestone (density = $2.80 \pm 0.008 \text{ g/cm}^3$). It can be seen that it is unlikely that the densities of the Ordovician limestones and Precambrian rocks as a whole differ significantly. Hence the negative anomaly is caused by material whose nature and density is unknown, and anything more than an elementary interpretation is unwarranted.

It is here that the method described at the beginning of this note can be used to advantage. Despite the fact that the Holleford feature is decidedly not two-dimensional, the uncertainties justify the approximation.

Without going into any unnecessary attempts to find the 'regional' in this area, we can quickly ascertain that the total anomalies of about 2 mgal are associated with maximum anomaly gradients of about 2 mgal/kilofeet. Then the maximum possible depth to the top of the low-density material is

$$d_0 \approx 300 \text{ feet}$$

If we estimate that the density contrast between the low-density material and its surroundings is probably somewhere between 0.1 and 0.4 g/cm^3 , this implies that its thickness t is between 400 and 1600 feet. The corresponding values of d are 150 feet and 10 feet.

The implications of such an elementary interpretation are that between 650 feet and 1600 feet of drilling would need to be undertaken to penetrate the lower-density material completely and reach undisturbed bedrock. Because of all the uncertainties concerning the nature and form of the materials at depth, this estimate cannot be improved by a more sophisticated interpretation, although such a study may give an illusion of greater accuracy.

Subsequent drilling operations [Beals, 1957] showed that, within the boundaries of the feature, it was possible to drill to a depth of over 1100 feet without reaching the undisturbed Precambrian. A fuller discussion can be found in the cited papers and a forthcoming comprehensive report.

REFERENCES

- Beals, C. S., A probable meteorite crater of great age, *Sky and Telescope*, 16, 526-528, 1957.
- Beals, C. S., Fossil meteorite craters, *Sci. American*, 199, 33-39, 1958.
- Bott, M. H. P., and R. A. Smith, The estimation of the limiting depth of gravitating bodies, *Geophys. Prospecting*, 6, 1-10, 1958.
- Tatevosyan, L. K., Several features of the deep structure of the earth's crust in Azerbaydzhan from gravimetric data, *Izvest. Akad. Nauk SSSR, Ser. Geofiz.* no. 5, 643-647, 1958.

(Received, January 12, 1960; revised February 23, 1960.)

Abstracts of the papers presented at the
Pacific Southwest Regional Meeting, American Geophysical Union
Los Angeles, California, February 4-5, 1960
listed in the order of the last name of the first author

HENRY W. ANDERSON (Pacific Southwest Forest and Range Experiment Station, U. S. Forest Service, Berkeley, Calif.) *Three Years of 'Operation Wet-Blanket' Progress.* 'Operation Wet-Blanket,' the term given by the late E. A. Colman to the California Co-operative Snow Management Program, is now in its fourth year. Its objective is to develop and test methods of managing the forests and other lands in California's snow zone for improved water yield. Study has shown that the snow zone is quite open and that brush makes up a significant part of the zone. Snow accumulation and melt are widely different on various topographic and forest sites—these differences are best characterized in terms of the energy received and radiated. Winds during snowfall, largely from the south and southwest, play an important part in where the snow accumulates in relation to forest openings. Evaporation from snow is greatest from exposed ridges and least under forest canopies. Logging in strips, in blocks, and by selection cutting; the way slash is treated; and the removal of brush have been found to affect snow accumulation, snowmelt, and water yield. A wall-and-step forest is proposed as 'ideal forest' for snow accumulation and delayed water yield on north and south slopes. The wall would be made by cutting east-west strips successively to the south. On east and west slopes L-shaped openings are proposed for maximum snow accumulation.

EDUARDO BASSO (University of Chile and National Electric Company of Chile, Santiago, Chile) *Estimating Sedimentation in Rapel Reservoir in Chile.* For the Rapel Dam project (390,000 kw) near Santiago, Chile, on which construction is about to start (1959) it was very important to compute the rate of sediment transport into the future reservoir site.

Less than two years of suspended-sediment measurements were available at two river cross sections. For this period, relatively complete measurements were made once a month at these two cross sections and a sample of water near the shore was taken every day. The system of sampling is briefly discussed.

The correlation between the monthly and daily samples was found to be satisfactory. Since the sediment samples were taken in a period of sub-normal runoff, they were judged to be not representative. In order to extend the results, a correlation was established between sediment and

water discharge. In contrast to the normal sediment rating curves, a good correlation was found and the sediment rating curve could be extended over the entire 17 years of flow measurements.

For estimating bed load transport, the formula of Meyer Peter, Du Bois, Shields, and Einstein were used. The results vary widely, but the total rate was low in comparison with the rate of suspended-load transport. It was possible to conclude that sediment problems were not serious in this case.

R. H. BROOKS (Western Soil and Water Conservation Research Branch, U. S. Department of Agriculture, Fort Collins, Colo.) *Induced Unsaturated Flow in a Sloping Aquifer of Constant Thickness.* The relationship of capillary pressure as a function of elevation for steady one-dimensional flow through a homogeneous porous medium was applied to a two-dimensional system. The system consisted of a two-dimensional model, feet thick, 24 feet long, and 1½ inches wide, filled with two sands of different properties. These sands abruptly joined each other in the model. The model was elevated to an angle of 30° with the horizontal causing essentially saturated flow down the slope through the first sand. The second sand had a greater permeability; therefore, unsaturated flow occurred through the remainder of the model.

A theoretical relationship, developed from the steady one-dimensional two-phase system, was used to predict the locus of points where the capillary pressure equals zero. A comparison was made of the experimental results and theory.

FRED A. CAMP (Department of Water and Power, City of Los Angeles, Calif.) *Pictorial Reconnaissance of the Los Angeles Aqueduct Watershed.* A pictorial reconnaissance covering about 5200 square miles of alpine-terrain watershed in the southwest portion of Lahontan area and south east portion of the Central Valley, Sierra Nevada Mountain range, in California is presented. About 70 per cent of the data were collected on the watershed of the City of Los Angeles.

ARNOLD COURT (Pacific Southwest Forest and Range Experiment Station, U. S. Forest Service, Berkeley, Calif.) *Reliability of Hourly Precipitation Data.* Properly exposed, calibrated, and evaluated, the customary 8-inch diameter, weigh-

ing rain gage yields hourly precipitation values with standard errors of about .01 inch, so that reliability within .02 inch can be assumed. But, two identical gages 10 feet apart on a windy hill-top can differ consistently in catch by 50 per cent of the smaller. Four pairs of identical gages, exposed side by side at four sites in Santa Barbara County, Calif., January-April 1959, were studied.

This report is the outgrowth of a cooperative effort of the Pacific Southwest Forest and Range Experiment Station, Forest Service, U. S. Department of Agriculture, with the Statistical Laboratory of the University of California and the Department of Water Resources of the State of California.

G. DE JOSSELIN DE JONG (College of Engineering, University of California, Berkeley, Calif.) *Macrostructural Dispersion in Stratified Aquifers*. If a miscible fluid-fluid displacement occurs in an aquifer, with a stratification pattern which repeats itself a sufficient number of times, the macrostructural dispersion approaches a normal law. For the computation of the dispersion coefficients, it is necessary to determine the probability distribution of the deviation from mean travel time and mean travel path for the individual transitions from one layer to another. The computation of the cumulative effect of these transitions is then straightforward and is shown for a schematized case of sand lenses imbedded in a clay deposit. The dispersion coefficients are expressed explicitly as functions of the geometry and the permeabilities of the stratified system.

JAMES G. EDINGER (Department of Meteorology, University of California, Los Angeles, Calif.) *The Influence of Terrain and Thermal Stratification on Flow in the Planetary Boundary Layer*. Wind velocities in the lowest 5 km at Santa Monica, California, during the summer season, are analyzed. The mean flow is observed to consist of two separate regimes, one below the inversion, somewhat resembling a channel flow, and one above the inversion approximating an Ekman spiral. The diurnal oscillation about this mean flow is observed to be more complex than a simple sea-land breeze circulation at a coastline. Analysis of the data indicates that this complex circulation can be closely approximated by the superposition of two diurnal oscillations, one originating at the coastline, the other at the southern slopes of the inland mountain ranges.

JACK GREEN (Aero-Space Laboratories, Missile Division, North American Aviation, Inc., Downey, Calif.) *Lunar Volcanism as Related to Lunar Exploration*. Defluidization of the moon's interior is believed to have triggered expansion and contraction processes on a regional scale in a relatively cool and rigid lunar crust. The resulting zones of weakness served to localize calderas of

explosion and collapse. The deeper nucleation of bubbles in a magma column, coupled by a greater degree of viscosity in the upper portions of the magma column, is thought to contribute to the origin of calderas of great dimension. Terrestrial analogs of lunar craters are illustrated. Accepting volcanism as a major lunar process, surface rock froths—pumice, reticulate, and scoria—may be abundant. Maria lithologies may include basalt and tachylite; non-maria lithologies may include welded tuff, rhyolite, andesite, and obsidian. Also, certain minerals which can sublime in the absence of oxygen and which have low vapor pressures may accrete on the lunar surface, particularly in eternally shadowed zones. Many of these minerals may contain elements of high neutron capture cross section.

BEN L. GROVER, JAMES T. LIGON (University of California, Riverside, Calif.), AND DON KIRKHAM (Iowa State College, Ames, Iowa) *Operational Characteristics of the Laterals near the Edge of a Drainage System*. A glassbead-glycerol drainage model was used to evaluate the operational characteristics of the two outside tile laterals of a drainage system. It was found that the shape and position of the surface of saturation was essentially the same between the two outside laterals as it was between the second and third laterals and hence between any other pair of adjacent laterals in the drainage system.

It was also found that the discharge of the second lateral in the system was of the same form as was found for center laterals of the drainage system. The discharge of the outside lateral was the same as the second during the early part of the drainage cycle but remained at a higher value during the latter part of the cycle. In practical or in experimental work, the single tile or ditch lateral at the edge of the experimental area is an adequate guard for those experiments on tile discharge, and the area between the two outside laterals can be used for water table measurements.

WARREN A. HALL AND NATHAN BURAS (College of Engineering, University of California, Los Angeles, Calif.) *The Dynamic-Programming Approach to Optimum Water Resources Planning*. Dynamic programming is an analytical technique which has been developed recently. It was successfully applied in various branches of engineering and is now being adapted to the field of water resources engineering.

In planning the development and utilization of water resources, one is very often confronted with the situation in which a finite amount of water has to be allocated among several competing demands. Obviously, a finite amount can be divided among several activities in an infinite number of ways, each distinct way defining an allocation policy. The optimal policy, or the solution of the problem, is conceptually arrived at by comparing

all possible policies. The number of policies to be compared is intolerably large; however, dynamic programing provides the necessary mathematical simplification which effectively permits the accomplishment of this comparison. By this process, a specific problem, e.g., how best to allocate the runoff volume of a river and/or how best to allocate the storage volume in a reservoir, is imbedded in a general class of problems. The solution to the general problem is readily obtained, with the specific solution included.

In this paper, the mathematical model for water resources planning is derived and discussed as an engineering problem.

L. C. HALPENNY, K. J. DECOOK AND D. K. GREENE (Water Development Corporation, Tucson, Ariz.) *Infiltration from Flood of October 30-31, 1959, along Salt River, Maricopa County, Arizona.* Following heavy rains on the Salt and Verde River watersheds, 7085 acre-feet of water was spilled from Granite Reef Dam and three wasteways above Phoenix. The flood water moved through the Phoenix area on October 30-31 along the normally dry Salt River. A slope-area measurement at 40th Street in Phoenix showed a peak discharge of about 4000 ft³/sec.. The flow reached only to 7th Avenue in Phoenix, much of it having been impounded by gravel quarrying pits and other obstructions that occupy 10 to 15 per cent of the bottom land.

Measurements of infiltration rates of the impounded water were made at ten localities in a 16-mile reach between October 31 and November 25. The average rate at all localities for the 26-day period was 0.46 feet per day. The minimum volume of impounded water accounted for by infiltration was 3150 acre-feet in 26 days; on November 25 several hundred acre-feet remained in the pits. An analysis of the total inflow indicated that about 3600 acre-feet were lost from the moving water during 2 days of flow.

MAHDI S. HANTUSH (New Mexico Institute of Mining and Technology, Socorro, N. M.) *Modification of the Theory of Leaky Aquifers.* The theory of leaky aquifers as currently known involves, among other things, the assumption that the storage in the semiconfining beds is small and therefore may be neglected. Frequently, however, the semiconfining beds, although of very low permeabilities, may yield significant amounts of water from storage. The present paper deals with flow problems in which the storage in the semiconfining beds is taken into consideration. The more general solutions thus obtained describe more closely the physical flow systems.

NORMAN B. HUME, CHARLES G. GUNNERSON, AND CHARLES E. IMEL (Bureau of Sanitation, City of Los Angeles, Calif.) *Characteristics and Effects of Hyperion Effluent in Santa Monica Bay, Cali-*

fornia. The City of Los Angeles' Hyperion sewage treatment plant has since 1949 discharged effluent into Santa Monica Bay through a 1-mile outfall into 50 feet of water. Present flow is 260 million gallons per day. Bacterial control is maintained by chlorination. The quantities of suspended solids, grease, detergent, heavy metals, nutrients, and vitamin B₁₂ have been determined. Resulting phenomena are (1) an inshore water of about 20 square miles in area differing from normal coastal water in salinity and temperature, (2) increased standing crop of plankton, particularly dinoflagellates, diatoms, and copepods, and (3) establishment of faunal zones and enrichment in the benthos which are reflected in the numbers of bottom fish.

A 7-mile outfall has discharged 5 million gallons per day of digested sludge and effluent at 320 feet since 1957. While some evidence of this discharge is found in the water column, the major effects are on the bottom: (1) *Capitella capitata* populations have developed in some areas to approximately 200,000 individuals or 6000 g/m², (2) a probable increase in numbers of fish, and (3) periodic buildup and removal of stabilized sludge, largely down a submarine canyon.

C. E. JACOB (P. O. Box 347, Northridge, Calif.) *Ground-water Mounds in Two-Layered Aquifers.* This is a study of flow in systems of two layers, a top one of low permeability and high storativity and a bottom one of high permeability and low storativity, coupled hydraulically across their common interface. Partial differential equations are obtained for non-steady flow in such a two-layered system into which water is recharged at non-uniform and varying rates over all or part of the aquifer. Various lateral boundary conditions are specified for both linear and radial systems.

Finite difference equations are obtained as approximations of the differential equations. Solutions are obtained in certain illustrative cases by electronic analog computer. Examples of actual ground-water mounds are studied in the light of this theory.

S.-K. KAO (Department of Meteorology, University of California, Los Angeles, Calif.) *Stationary Flow in the Planetary Boundary Layer with an Inversion and a Sea Breeze.* An analysis is made of the effects of an inversion layer and a sea breeze on the stationary flow in a planetary boundary layer. It is shown that an intense temperature inversion virtually acts as a boundary surface which separates a planetary boundary layer into two layers. In the lower layer the flow is primarily driven thermally whereas in the upper layer the flow is similar to that in a boundary layer of a homogeneous fluid. A simple model is constructed to bring out the effects of the temperature inversion and the sea breeze on the stationary

low. A comparison of the observations and the model is made.

WILLIAM W. KELLOGG (Planetary Sciences, Rand Corporation, Santa Monica, Calif.) *The Dynamics of the Upper Atmosphere as Revealed by Rockets and Satellites*. In recent years upper-atmospheric research with rockets and satellites has raised new questions concerning the motions and energy balance in the upper atmosphere. Of particular interest are the seasonal changes in circulation in the mesosphere and lower ionosphere in polar regions and the reaction of the upper atmosphere to solar disturbances. Considerations of energy balance during the winter night indicate that there are energy sources other than sunlight.

E. C. LAFOND (U. S. Navy Electronics Laboratory, San Diego, Calif.) *Vertical Oscillations of Temperature Structure in the Sea off San Diego*. The vertical oscillations and variability in the temperature structure of the ocean area off San Diego have been under investigation by the U. S. Navy Electronics Laboratory for many years, first through repeated bathythermograph lowerings, then with strings of thermistor beads and, more recently, with isotherm followers. The latter instruments automatically give a continuous depth recording of any desired isotherm.

It has been found that the isotherms in the shallow, summer thermocline fluctuate virtually all the time. Of the significant vertical oscillations of a central isotherm in the thermocline, half are greater than 7.2 feet and half have periods greater than 7.6 minutes.

Since the waves refract, they usually proceed in a general shoreward direction. The theoretical speeds (c) of two-layer (h, h') water (ρ, ρ') internal waves were evaluated by the approximate expression,

$$c = \left[\left(\frac{ghh'}{h + h'} \right) \left(\frac{\rho - \rho'}{\rho} \right) \right]^{1/2}$$

for the observed water properties. The computed speeds agreed closely with the observed shoreward speeds of internal waves which, at the measurement site, had an average speed of 0.31 knot.

The major internal waves occurred at moving water mass boundaries; that is, sudden changes in the thermocline level produced by the advancing mass were accompanied by a series of large internal waves. The first wave was usually the largest and subsequent ones became progressively smaller. The water mass boundaries were in turn related to tidal circulation. A knowledge of internal waves helps in the understanding of related physical processes and the causes of temperature variability in the sea.

W. B. LANGBEIN (U. S. Geological Survey,

Washington, D. C.) *The Salinity and Hydrology of Closed Lakes*. Closed lakes have no outlet and therefore are salty. The classic explanation of the salt content of closed lakes is that the salt load continuously accumulates. Except for the precipitation of the less soluble salts, the total content is the aggregate salt input during the life of the lake—the length of time since the lake last overflowed as an open lake. However, an examination of available data for closed lakes shows that the mass of salts may increase or decrease with fluctuations in water level. These data tend to support a theory that the salt content of closed lakes is in balance between the input brought in by the rivers and the wastage of salts either by wind action or by coverage of sediments. In accordance with these data and this theory, it is shown that the salinity of closed lakes can be related very closely to their hydrologic environment. These data suggest, therefore, that a closed lake does not have a grand birth at some past epoch. Rather, the theory suggests that a lake dies a little and is reborn a little with each fluctuation in water level.

W. F. LIBBY (Department of Chemistry, University of California, Los Angeles, Calif.) *Tritium and Hydrology*. The concentration of tritium (produced by cosmic rays or bombs) in rain water may be used for solving problems in hydrology. Recent data are presented, and a plan for measurement of tritium in rain water on a world-wide basis is described. One or two examples of the application of the method to specific hydrological problems are given.

EUGENIE LISITZIN (Merentutkimuslaitos, Finland) AND JUNE G. PATTULLO (Scripps Institution of Oceanography, University of California, La Jolla, Calif.) *The Principal Causes of the Seasonal Variation in Sea Level*. During the IGY, sea level was recorded not only along the coast but also on numerous islands in the Pacific. These data give a fairly detailed picture of the seasonal oscillation in sea level in this ocean, revealing new features. In low and temperate latitudes, the steric levels, which reflect the seasonal variation in density of the water, agree remarkably well with the departures of the recorded level; but in higher latitudes the principal cause of the oscillation is the variation in air pressure. Conditions are, in other words, *isostatic*, at least in the central parts of the ocean. The differences between the higher and lower latitudes lies in the relative effects of the two factors; the boundary between the zones, in the northern hemisphere, runs approximately along the latitude of 40°N. Each term has a maximum amplitude of the order of 10 cm, but their phases are different. The steric term has a maximum in fall (September–October in the northern hemisphere); the barometric term leads to highest levels in winter (December–January in the north). Comparable phase relationships but somewhat

smaller amplitudes prevail in the southern hemisphere.

W. D. McMILLAN AND R. H. BURGY (Department of Irrigation, University of California, Davis, Calif.) *Interception Loss in Grass*. The entire plant-soil system must be considered in evaluating interception loss from a wetted vegetative canopy, since evaporation from wetted leaf surfaces may replace all or part of normal transpirational use.

During the summer and fall of 1959, field studies were conducted to measure interception loss in an actively transpiring grass cover. A pair of floating lysimeters was installed in a field of perennial rye grass. The grass cover on and around each lysimeter was alternately wetted by sprinkling, and records were obtained of total water use by the wet-leaf and dry-leaf systems. Soil moisture and soil temperature conditions were similar in the lysimeters and in the surrounding field area during the treatment period. No significant difference in total water use by the wet-leaf and dry-leaf systems was observed, indicating that a net loss by interception did not occur.

R. WILLIAM NELSON (General Electric Company, Richland, Wash.) *In-Place Measurement of Permeability in Heterogeneous Media*. An *in situ* method for measurement of permeability in heterogeneous, saturated soils is presented. The permeability is found through an analysis of the piezometric-head distribution of the existing flow regime when combined with a few permeability determinations.

The method is based on a general theory, presented in three dimensions for saturated flow in a heterogeneous media. When the permeability is considered as the dependent variable, the expression to be solved is a first-order quasi-linear partial differential equation. A method of solution can be obtained through an extension of Lagrange's method utilizing a system of subsidiary differential equations. Through consideration of the identity of two of the Lagrange subsidiary equations in modified form with the three-dimensional stream function, a special interrelationship is shown. This interrelationship has special significance with respect to the boundary condition. It is shown that, if the arbitrary or boundary function satisfies part of the subsidiary differential equations, no unique solution exists. In the physical problem this requirement for uniqueness indicates that the permeability measurements taken in the field for a boundary condition cannot be measured along a stream tube. This condition is needed, since the boundary condition must include the permeability at one point in every stream tube making up the flow system under analysis.

HANS R. PRUPFACHER (Department of Meteorology, University of California, Los Angeles, Calif.) *On the Supercooling of Diluted Aqueous Solutions*.

The freezing depression of water due to the presence of a solute is an experimentally well-investigated and thermodynamically well-understood problem. The freezing point of a solution is, in this case, defined as the temperature at which the solution of a certain concentration is in equilibrium with ice.

However, the purpose of this study was to abandon the equilibrium problem and to investigate the nonequilibrium problem. For this reason the supercooling limit of aqueous solutions has been determined.

In the present study, solutions of various salts mostly alkali halides, have been investigated. The concentration of the solutions were: 10^{-5} , 10^{-4} , 10^{-3} , 10^{-2} , 10^{-1} , 1, 3 mole/l. Out of these solutions, droplets of 1 to 2 mm in diameter were prepared, and three methods have been used to freeze them: (1) The drops were frozen on the junction of a thermocouple; the junction was covered with a thin glass layer coated with silicon oil; (2) The drops in groups of a hundred were frozen at the interface of two organic liquids (paraffin oil and CCl_4 , or paraffin oil and fluorocarbon-75); (3) The solutions were sprayed into a cold chamber.

The experiments so far have shown that certain salts are able to reduce the supercooling of pure water, but others have no effect or increase the supercooling range. The effects are strongly concentration-dependent. An especially pronounced reduction of the supercooling of pure water (rise of 10° to 15°C) was found in the case of ammonium fluoride. It is tentatively suggested that this rise is due to a combined action of the ions on the surrounding water molecules, the ammonium ion introducing tetrahedral coordination among the water molecules, the fluoride ion causing a hindered rotation of the water molecules due to hydrogen-bond formation. It is finally of importance that ammonium fluoride forms mixed crystals with ice.

JOSEPH L. REID (Scripps Institution of Oceanography, University of California, La Jolla, Calif.) *The Differences in Temperature, Salinity, and Density between the North Pacific and the North Atlantic Oceans in the Upper Thousand Meters*. The North Atlantic is warmer, saltier, and denser in its upper thousand meters than the North Pacific. The differences in the means in the region from the equator to 60°N are 2.64°C , 0.79 ‰, and $35 \times 10^{-5} \text{ g/cm}^3$. Averaged at particular levels and along zonal bands of 10° width, differences of 7°C are found, for example, at 600 meters between 30° and 40°N . At 400 meters between 30° and 40°N the average salinity difference is 1.8 ‰. The greatest density difference is found between 50°N and 60°N at the surface, where the average difference in winter is $140 \times 10^{-5} \text{ g/cm}^3$.

This remarkable difference stems first from the greater rate of evaporation minus precipitation in the North Atlantic, but the indirect effects are

probably greater than the direct effects. In the high latitudes of the Pacific, the salinity is low, and even in winter the surface waters never sink more than 100 meters. The cold waters mix sopsynally to the south where at 25°N they constitute the intermediate water at about 900 meters. This water is both cool (5° to 8°C) and low in salinity (34.00 to 34.40 ‰).

In the high latitudes of the North Atlantic the surface water in summer is high in temperature and in salinity, though not so high as in the tropics. Winter cooling increases the density so much that the surface waters sink to more than 1000 meters, carrying downward and then southward the colder, less saline water. This water is replaced from the surface waters of the South Atlantic via the South Equatorial Current. These waters are warm (more than 20°C at the surface) and saline (more than 36 ‰).

The North Pacific thus retains the high-latitude water of low salinity and low temperature within its upper thousand meters. The North Atlantic does not retain this water, and thus the large differences in temperature, salinity, and density occur.

FRANCIS S. RILEY AND STANLEY N. DAVIS (Department of Geology, Stanford University, Stanford, Calif.) *A Tiltmeter to Measure Surface Subsidence around a Pumping Artesian Well.* A portable liquid-level tiltmeter was developed to measure the local subsidence occurring around a pumping artesian well. The device consists of two identical pots, connected by 150 feet of hose and partially filled with water. Minute changes in the relative elevations of the pots are observed by reference to the common water level, which is measured to 0.0001 inch in each pot by a needle-tipped electric probe attached to a micrometer screw.

An improvement over this basic instrument has been achieved by connecting, at the middle of the hose, a displacement device consisting of a cylinder and micrometer-actuated piston. Screwing down the micrometer displaces water from the cylinder, raising the water level equally in both pots. The micrometer is read when the rising water level contacts, in turn, each of the electric probes, which have been pre-set at convenient heights. A gradual change in the difference between the two readings indicates tilting. The hydromechanical magnification, achieved by using a relatively small-diameter piston, increases the sensitivity to 5.0×10^{-3} inch.

Preliminary field tests revealed tilting caused by pumping, superimposed on tidal and other effects. The feasibility of determining the elastic and hydraulic properties of aquifers by tiltmeter tests is being investigated.

MARGARET K. ROBINSON (Scripps Institution of Oceanography, University of California, La Jolla, Calif.) *Mean Temperature Interpolation by IBM*

Computer. Our experience has shown that when dealing with temperature data erratically distributed in time and space, interpolation in time gives more consistent and reliable estimates of seasonal variation than interpolation in space. However, it has always been necessary to do such analyses graphically and subjectively.

Recently, a program for interpolation of missing monthly mean temperatures for selected depths has been written and is now being tested on the UCLA IBM 709 computer. The temperature data being used are bathythermograph and reversing thermometer observations in the Northeast Pacific which have already been analyzed and results published.¹

The program is based on the fact that at any given location in the ocean there is a dominant mean seasonal cycle, representative of each level. These may vary slightly from year to year but their general shape is a smooth curve. Over limited areas the shapes of the seasonal curves are similar, although the mean temperature and annual range change with latitude and longitude.

Results obtained by computer are compared graphically and statistically with those previously obtained by subjective methods.

GUNNAR I. RODEN (Scripps Institution of Oceanography, University of California, La Jolla, Calif.) *On the Variation of Oceanographic and Meteorological Variables along the California Coast.* Monthly anomalies of sea-surface temperature, salinity, air temperature, cloudiness, wind, precipitation, and runoff are investigated. The autocorrelation and energy of each variable and the cross correlation between each pair of variables are determined and interpreted.

Sea-surface temperatures are persistent, on the average, for from 4 to 8 months, air temperatures about 5 months, salinities off southern California about 12 months, off central and northern California about 4 months. Local wind anomalies are persistent about a year and cloudiness and precipitation anomalies about a month. Runoff anomalies appear to be persistent for about 3 months.

There is a fairly good coherence between sea-surface temperature and air-temperature records and between precipitation and runoff. In the coastal waters off the northern part of the state there is also a good relation between runoff and salinity and sea-surface temperature and salinity. Off Southern California, no such relation is found. There is almost no coherence between air-temperature and precipitation records and only a slight coherence between sea-surface temperature and precipitation. The local wind and cloudiness do not correlate well with any of the other variables.

¹ Robinson, M. K., *Bull. Scripps Inst. Oceanog. Univ. Calif.*, 7 (1), 1957.

STANLEY A. SCHUMM (Department of Geology, University of California, Berkeley, Calif.) *The Shape of Alluvial Stream Channels in Relation to Sediment Type.*²

The weighted mean percentage of silt-clay in the bed and banks of stable alluvial stream channels is used as a parameter (M) descriptive of sediment type. Silt-clay is defined as sediment smaller than 0.074 mm. As the percentage of silt-clay in banks and bed increases, the shape of stream channels expressed as a width-depth ratio (F) decreases according to the equation, $F = 255 M^{-1.08}$. Neither mean annual discharge nor mean annual floods affects this relationship, in spite of the importance of discharge to the absolute width and depth of a channel.

Downstream changes in width and depth of a stream channel are greatly influenced by the type of sediment. As M increases downstream along a river, the depth increases more rapidly and the width less rapidly with discharge, than if M were constant, and the width-depth ratio decreased. Conversely, as M decreases downstream the depth increases less rapidly and the width more rapidly, with discharge, than if M were constant, and the width-depth ratio increased.

Unstable channels may be recognized by changes in the width-depth ratio. In general, aggrading channels have a higher width-depth ratio than is indicated by M , and degrading channels have a lower width-depth ratio than is indicated by M .

R. E. STEVENSON (University of Southern California, Los Angeles, Calif.) *The Summer Climatic Environment of the Yorkshire Coast of England.* The coastal climate of Yorkshire has long been described by laymen and scientists alike as invigorating, healthful, and bracing. Indeed, the inhabitants claim that their unusual longevity and vigor are due to the rigorous qualities of the climate. An investigation of the oceanographic and meteorologic characteristics of the coast during the summer months of 1959 revealed the basic reasons for these subjective statements.

The Yorkshire coast is at a latitude where it is under the influence of frequent gradient winds

from the northeast. The air involved in the flow has three sources, each of which result in different climatic effects. At sea, along the coast, there is a band of cool water which varies in width from 10 to 15 nautical miles. This water mass is caused by tidal mixing, and, although the turbulence occurs each day, the consequent cooler water is more pronounced in the warmer months. The combination of northeasterly gradient winds and the water adjacent to the coast has profound effects on the coastal climate.

R. B. TIBBY AND R. D. TERRY (Allan Hancock Foundation for Scientific Research, University of Southern California, Los Angeles, Calif.) *Visual Transparency and the Vertical Transmission of Light of Inshore Waters off Southern California.* In any investigation of the consequences of man-made alterations in the marine environment, one of the problems is the amount of light which penetrates the sea and which is available for photosynthesis and other photochemical changes is of some concern. The inshore waters off the coast of Southern California are being used to a constantly increasing degree as a receptacle for debris which directly or indirectly may be attributed to man's activities. The biological consequences of this practice may be profound—in particular, as they may relate to modifications in the basic production of organic matter.

The present study is a comparison of the Secchi disk and the hydrophotometer as a measure of visual transparency and optical clarity. Each method has its own special utility: the first as an indicator of transparency as it may appear to the layman and as it may readily demonstrate the extent of man's influence; the second as a more precise measure of the amount of light reaching any particular depth and of the nature of the dissolved or suspended material.

Within a distance of 8 miles from the shore of Southern California, visual transparencies varied from about 2 to 70 feet, and the vertical transmission exponents ($I/I_0 = e^{-k'z}$) from 0.10 to 0.30. The reasons for the variations are discussed and the role of man's activities described.

Although a rough, nearly straight-line relationship between Secchi disk readings and the optical measurements can be described, the correlation is poor. Furthermore, readings by one method cannot be associated with inaccuracies inherent in either method transferred directly to the other, for reasons of method.

² Publication authorized by the Director, U. S. Geological Survey.

Geomagnetic and Solar Data

J. VIRGINIA LINCOLN

*CRPL, National Bureau of Standards
Boulder, Colorado*

FINAL RELATIVE SUNSPOT NUMBERS FOR 1959

The final sunspot numbers are based on observations made at the Zurich Observatory and its two branch stations at Arosa and Locarno, and supplemented by series furnished by a large

number of cooperating observatories. The most important of these are: Royal Greenwich Observatory, Herstmonceux; Observatoire Royal de Belgique, Uccle; Astrophysikalisches Observ-

TABLE 1. Final Relative Sunspot Numbers for the Whole Disk of the Sun for 1959

Day	Jan.	Feb.	Mar.	Apr.	May	June	July	Aug.	Sep.	Oct.	Nov.	Dec.
1	221	141	158	243	120	152	147	194	290	65	136	170
2	225	141	151	242	112	133	118	210	256	76	121	165
3	229	140	151	174	113	152	138	213	202	89	97	160
4	231	137	146	159	105	166	158	225	161	101	103	163
5	243	128	152	124	112	162	136	212	148	115	91	142
6	238	114	148	108	138	180	127	207	152	128	98	147
7	247	124	150	107	156	181	120	179	135	130	114	141
8	246	90	155	136	188	192	131	175	136	115	131	145
9	245	87	164	161	238	188	129	170	157	103	136	94
10	224	100	156	177	262	160	127	155	141	91	142	89
11	218	100	148	197	287	172	133	180	155	87	153	82
12	203	101	126	189	276	176	135	160	170	81	154	75
13	192	106	159	178	257	165	160	125	148	78	149	73
14	128	129	173	193	227	170	180	139	151	102	137	88
15	120	133	216	174	204	158	176	144	161	96	127	123
16	143	144	225	153	182	172	190	157	130	116	113	113
17	168	170	228	126	187	161	193	166	87	107	83	107
18	179	170	230	114	198	174	195	174	100	116	73	117
19	202	175	234	117	185	182	184	182	120	111	69	134
20	240	160	238	135	187	173	160	180	149	108	65	133
21	255	163	230	128	151	162	132	200	143	111	70	131
22	278	171	208	138	145	170	94	204	157	129	110	126
23	270	186	194	186	149	188	113	205	143	135	131	122
24	261	190	178	186	143	157	108	217	155	143	151	116
25	255	181	199	203	178	180	118	212	132	137	162	121
26	252	176	190	204	188	184	134	220	110	126	161	124
27	263	163	178	175	177	186	156	231	102	128	157	132
28	239	186	173	172	132	160	181	274	91	129	151	127
29	213		217	160	99	158	182	301	87	129	161	136
30	167		233	141	106	147	193	292	86	131	175	127
31	143		248		131		190	284		141		153
Mean	217.4	143.1	185.7	163.3	172.0	168.7	149.6	199.6	145.2	111.4	124.0	125.0

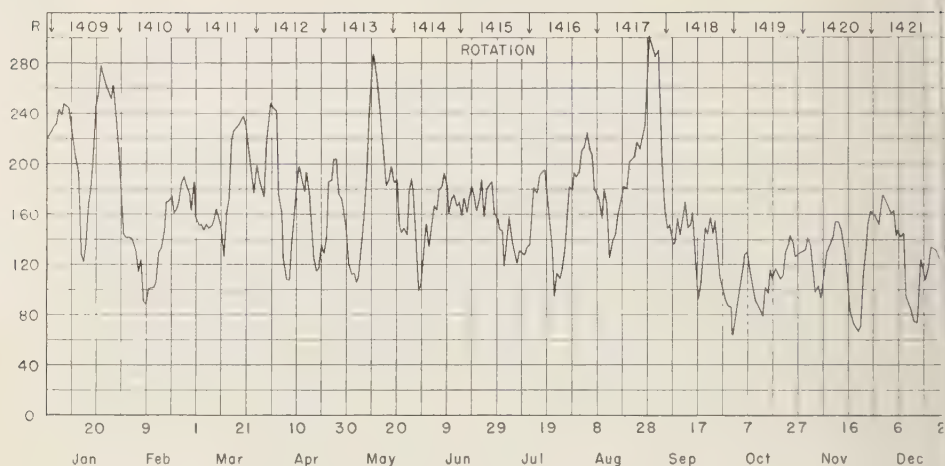


Fig. 1. Daily relative sunspot numbers for 1959.

TABLE 2 Daily Number of Sunspot Groups for 1959

Day	Jan.	Feb.	Mar.	Apr.	May	June	July	Aug.	Sep.	Oct.	Nov.	Dec
1	19	15	16	17	11	12	16	12	21	9	12	9
2	19	15	15	19	8	10	15	15	18	9	11	8
3	20	14	12	14	11	12	15	14	16	10	10	10
4	17	14	15	13	11	12	15	19	13	11	9	10
5	19	15	13	12	12	12	13	20	13	10	8	8
6	24	11	14	9	14	12	12	16	14	10	8	11
7	20	14	14	8	14	15	10	15	12	9	12	8
8	21	10	14	11	14	12	11	15	13	8	12	9
9	21	10	16	14	17	14	10	15	14	9	9	9
10	20	8	16	17	18	12	11	13	11	9	12	6
11	20	11	16	15	15	15	13	16	11	8	10	9
12	19	11	14	13	15	14	10	14	12	6	9	6
13	21	10	17	14	17	13	12	11	10	6	9	5
14	13	12	15	15	14	14	14	13	11	9	9	8
15	12	13	20	14	15	14	11	13	13	10	11	10
16	16	13	18	12	13	17	13	14	12	12	10	10
17	15	16	17	10	15	16	12	11	7	12	8	10
18	17	14	18	11	17	16	15	14	8	11	8	10
19	17	15	16	11	17	15	16	13	10	10	9	10
20	17	14	15	14	19	15	15	12	11	11	9	10
21	18	16	15	11	14	14	14	14	11	12	7	10
22	17	14	14	13	13	15	10	13	13	11	10	11
23	17	14	16	19	14	16	13	14	11	11	11	12
24	15	15	14	17	9	12	12	16	14	11	12	12
25	17	12	15	20	12	16	13	16	10	12	9	12
26	18	14	15	21	13	15	12	17	9	7	9	10
27	21	14	13	14	15	17	11	15	10	9	8	14
28	22	17	13	15	8	14	13	16	9	9	10	13
29	19	14	12	10	15	14	17	17	9	11	9	14
30	17	17	9	10	15	15	15	16	10	11	10	14
31	16		19		11		15	16		11		15
Mean	18.2	13.2	15.4	13.8	13.4	14.0	12.9	14.7	11.9	9.8	9.7	10.1

GEOMAGNETIC AND SOLAR DATA

SELECTED GEOMAGNETIC AND SOLAR DATA

Kp, Ci, Cp, Ap, K_{Fr}, R_z, and Selected Days
January 1960

Day ¹	3-hr range indices Kp^2								Sum	Prel. ³ Ci	Cp^4	Ap^5	3-hr range indices K_{Fr}^6		Prov. ⁷ R_z
	1	2	3	4	5	6	7	8					Values	Sum	
1 Q	1+	2-	1+	1+	1-	0+	0+	0+	7+	0.0	0.1	4	2221 0000	07	136
2 Q	1-	1+	1o	1+	2o	1+	2-	1-	10o	0.1	0.2	5	0210 1110	06	110
3 q	2o	3-	1+	1+	2o	2o	1o	1o	13+	0.1	0.3	6	1321 1101	10	133
4	2o	2o	3o	3o	3o	3-	1o	1+	18o	0.6	0.6	10	1222 3221	15	156
5	3o	5-	4o	3+	4+	3+	3-	4o	29+	1.1	1.1	24	2422 4223	21	158
6	4-	3+	2-	1+	2-	2-	2o	1+	17-	0.5	0.5	9	3310 1120	11	174
7 q	1-	2-	2+	3-	2o	2-	1+	1o	13+	0.2	0.3	6	0123 1221	12	167
8 q	2o	2o	1-	1+	1-	1+	2-	2-	11+	0.2	0.2	5	1101 0110	05	153
9 Q	1+	2o	1+	1o	1-	0+	1-	1o	8+	0.1	0.1	4	1111 0010	05	150
10 D	1+	2+	5o	5+	5-	6-	6-	5+	35+	1.6	1.5	43	1244 5553	29	127
11 D	4o	3+	5-	4+	5o	4o	3o	3-	31o	1.2	1.2	27	4443 4332	27	143
12	3+	2+	3o	2+	3+	3+	3-	4-	24o	1.0	0.9	15	3131 2233	18	108
13	2o	3-	2o	2-	1+	1+	4-	3+	18o	0.8	0.6	10	1332 0133	16	108
14 D	5+	4+	5o	5-	4o	3o	5+	6-	37+	1.6	1.5	42	4354 4345	32	118
15 D	6+	5+	4-	3+	3+	3+	2o	1+	29-	1.2	1.3	30	5432 3310	21	112
16 q	1o	2+	0+	0+	1-	1+	1o	4-	11-	0.5	0.3	6	1200 0103	07	119
17	3o	3+	2+	2-	4o	3+	2-	2+	22-	0.9	0.8	14	2222 4323	20	117
18	2o	2+	6-	5-	4+	2+	3-	3-	27-	1.2	1.1	23	2255 5332	27	89
19	3+	2o	1o	2o	2+	2o	2-	2-	16o	0.5	0.4	8	3112 2212	14	80
20	2-	3+	3o	4+	3+	4o	3-	2+	25-	1.1	0.9	17	1334 3332	22	94
21 D	6o	4+	4o	5o	5o	5o	6-	5o	40o	1.7	1.6	50	5445 5434	34	103
22	4o	3+	4-	5o	3o	3o	2o	3-	27-	1.1	1.0	20	3345 3322	25	134
23	2+	3+	4-	3-	4-	3+	4-	3+	26o	1.0	1.0	18	2322 3232	19	138
24	3+	4-	3o	4-	4-	3+	3-	3-	26o	0.9	1.0	18	3334 3322	23	130
25	2+	3-	2o	2o	2+	3o	3-	1+	18+	0.6	0.5	10	2212 2221	14	152
26	2-	2+	2o	2+	2-	2o	1o	2o	15o	0.2	0.3	7	1312 1122	13	209
27	3o	3+	2-	3-	2o	1+	0+	1+	16-	0.3	0.5	9	3312 2101	13	186
28 q	2o	1o	1o	2-	2o	1o	3-	1+	13-	0.2	0.3	6	2011 2132	12	159
29	3o	3o	3+	3+	3+	2-	1o	1+	20o	0.7	0.7	12	3223 3211	17	193
30 Q	0+	0o	0+	1+	0+	0+	0+	0o	3o	0.0	0.0	2	0000 0000	00	178
31 Q	0+	1o	1-	1+	1o	1o	0+	0+	6o	0.1	0.1	3	0100 1100	03	178
Means:										0.69	0.67	15			139.1
No. of days:										31	31	31			31

¹ Five quiet days (Q), ten quiet days (Q or q), five disturbed days (D) selected by Committee on Characterization of Magnetic Disturbances, J. Veldkamp, Kon. Nederlandsch Meteorologisch Instituut, DeBilt, Holland.

² Geomagnetic planetary 3-hour-range indices *Kp* prepared by Committee on Characterization of Magnetic Disturbances, J. Bartels, Chairman, University, Göttingen, Germany.

³ Preliminary magnetic character figures, *Ci*, prepared by J. Veldkamp.

⁴ Magnetic character figures, *Cp*, prepared by J. Bartels.

⁵ Average amplitudes *Ap* (unit 2γ), prepared by J. Bartels.

⁶ Fredericksburg 3-hour-range indices *K* (*K*9 = 500γ); scale values of variometers in γ, mm: *D* = 2.7, *H* = 2.5, *Z* = 2.8; prepared by Robert E. Gebhardt, Observer-in-Charge, Fredericksburg Magnetic Observatory, Corbin, Virginia.

⁷ Provisional sunspot numbers (dependent on observations at Zurich Observatory and its stations at Locarno and Arosa) prepared by M. Waldmeier, Swiss Federal Observatory, Zurich, Switzerland.

atorium Potsdam; Sonnenobservatorium Kanzelhöhe, Kärnten; Statne Observatorium Skalnaté Pleso; Observatoire de Belgrade; Observatoire de Bucarest; Observatoire National, Athens; Observatorium Istanbul; Osservatorio Astrofisico, Arcetri; Osservatorio Astronomico Monte Mario, Rome; Osservatorio Astrofisico, Catania; Observatorio del Ebro, Tortosa; Tokyo Astronomical Observatory.

The final sunspot numbers for the whole disk of the sun are given in Table 1 and are likewise presented in graphical form in Figure 1. By the vertical arrows in the upper edge of this figure, the limits of the successive solar rotations are indicated. Solar activity was still at a very high level from the beginning of the year to the beginning of September. Compared with the corresponding period of the previous year only the months of February, April, and July show appreciably lower sunspot numbers. It is not until the first days of September that solar activity shows its first large and persistent drop

after the maximum of 1957.9. Nevertheless at the end of 1959 sunspot activity was even higher than during a medium-sized sunspot maximum. The yearly mean of the relative numbers amounts to 159.0 against 184.8 in 1958. Table 2 gives the numbers of sunspot groups on each day for the year 1959. The yearly mean of the group numbers is 13.1 against 14.9 in 1958. From 1958 to 1959 sunspot numbers have decreased by 14 per cent, group numbers by 12 per cent.

More details about the solar activity and the distribution and development of the individual spot groups will be given in 'Die Sonnenaktivität im Jahre 1959' (*Astron. Mitt. Eidgenöss. Sternwarte Zürich*, no. 229) and in 'Heliographische Karten der Photosphäre für das Jahr 1959' (*Publ. Eidgenöss. Sternwarte Zürich*, 11, fasc. 4).

M. WALDMEIER

SWISS FEDERAL OBSERVATORY

Zurich, Switzerland, February 20, 1960

Late Letter to the Editor

Initial Results of the TIROS I Meteorological Satellite

W. G. STROUD

*Goddard Space Flight Center
National Aeronautics and Space Administration
Washington, D. C.*

At 06h 50m, April 1, 1960, TIROS I meteorological satellite was injected into orbit over the North Atlantic. The characteristics of the satellite operation are shown in Table 1.

TABLE 1.

Launch vehicle	Thor-Able II
Payload weight	264 lbs
Stabilization	Spin; at 10 rpm
Inclination	48.4 degrees
Apogee	466 statute miles
Perigee	431 statute miles
Period	99.24 sec
Data Acquisition Sites	Ft. Monmouth, N. J., and Kaena Point, Oahu, Hawaii, 65-ft antennas, 30-db gain at 235 mcs.

The satellite, a 19-inch high pill box, 42 inches in diameter, is covered with solar cells which supply the power required for operation. The sensors are two vidicon-based TV systems with different lens components. Table 2 summarizes the camera characteristics.

TABLE 2.

Item	Camera	
	Wide	Narrow
Lens field	104	12.7 degrees
Lens aperture	f/1.8	f/1.5
Shutter speed	1.5	1.5 millisecc
Lines per frame	500	500
Frame readout	2	2 sec
Video bandwidth	62.5	62.5 kcs
Area viewed from		
Vertical (approx)	750	65 miles sq.
Shades of grey (design)	8	8
Shades of grey (practice)	5-6	5-6

The satellite has performed quite well in all respects, yielding picture data of the cloud patterns and distributions over wide areas of the sunlit portions of the earth. The camera operation has been commanded from the ground stations to transmit images directly when the satellite is near the station and looking at the sunlit earth or to store data of a remote part of the earth and play them back when near the acquisition site. Some trouble has been incurred in the

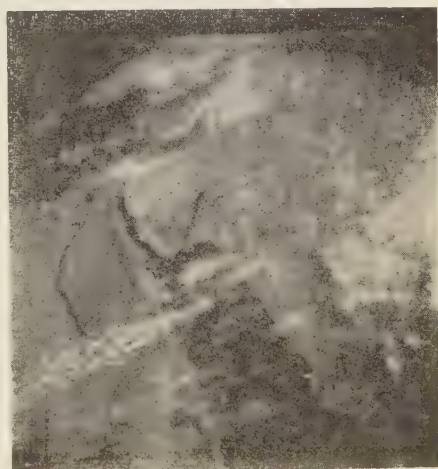


Fig. 1. This photograph was taken by the wide-angle camera in TIROS I during the 43 orbit at about 06h 00m (EST) on April 4, 1960, from an altitude of about 450 miles. The satellite was over the Red Sea, the dark area in the center foreground, looking downward to the northwest. The Gulfs of Suez and Aqaba are the two spikes at the top of the Red Sea. The Nile River lies to the left of the Sea.

narrow angle remote television chain so that at present such pictures are not being obtained.

The kind of data being received is illustrated in Figures 1 and 2. These rough pictorial data

show great promise in the realization of the satellite as a practical research tool.

(Received April 19, 1960.)

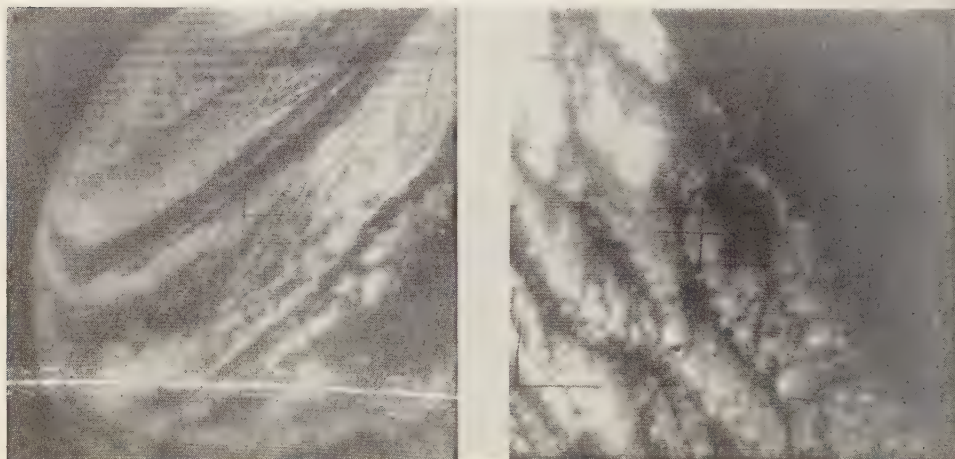


Fig. 2. These pictures were taken over the Pacific Ocean at the Hawaiian station as the satellite passed between the Islands and the West Coast of the United States. The picture on the left, taken by the wide-angle camera, portrays a broad circulation pattern over the ocean. The one on the right, taken by the narrow-angle camera one minute earlier, shows the cloud structure within this pattern.

Corrigendum

The authors, Messrs. J. L. Stearn and H. Richardson, have called attention to an error in the first line of the mathematical material in their Letter to the Editor, 'A Variant Least-Squares Method of Solution of a System of Ob-

servation Equations,' in the April issue of this *Journal*. On page 1308, in the first line equation in column one, an equals sign was omitted. This should read

$$F = v' W v + V' \overline{W} V.$$



AMERICAN GEOPHYSICAL UNION

1515 Massachusetts Avenue, N.W., Washington 5, D. C.

Established by the National Research Council in 1919 for the development of the science of geophysics through scientific publication and the advancement of professional ideals.

QUALIFICATIONS FOR MEMBERSHIP

The membership of the AGU shall consist of Members, Associate Members, Student Members, and Corporation Members.

Those eligible as candidates for election to the grade of MEMBER shall be:

MEMBER (a) Persons who have made an active contribution to geophysical research through observation, publication, teaching, or administration. Definite evidence should be presented to the Membership Committee. "Publication" may include books, articles, unpublished manuscripts, inventions, or development of geophysical instruments.

(b) Persons who have made active practical application of geophysical research. It should be shown that the nominee's work has not been purely routine, but that it has tended to create new knowledge of, or to broaden or strengthen the application of, geophysical research. In general, the minimum qualifications for membership will be not less than three years of professional experience in some phase of geophysics.

(Continued on next page)

Cut along this line

APPLICATION FOR MEMBERSHIP

Please refer to qualifications on reverse side and designate below type of membership desired:

Member (\$10) ☐

Associate (\$10) ☐

Student (\$4.50) ☐
(1960)

Application forms for Corporation Membership are available upon request.

1. Surname First Name Middle Name

2. Preferred mailing address for publications

Permanent address

3. Place Month Day Year of Birth 4. Country of citizenship/naturalization

5. Nature of work and title and/or military rank; name and address of organization with which you are associated.

6. Check section or sections with which affiliation is desired.

- | | |
|--|---|
| <input type="checkbox"/> Geodesy | <input type="checkbox"/> Oceanography |
| <input type="checkbox"/> Seismology | <input type="checkbox"/> Volcanology, Geochemistry, and Petrology |
| <input type="checkbox"/> Meteorology | <input type="checkbox"/> Hydrology |
| <input type="checkbox"/> Geomagnetism and Aeronomy | <input type="checkbox"/> Tectonophysics |

7. **EXPERIENCE (List below, use added sheets as necessary)**

Dates: From To Name and address of organization Title, duties, nature of work

8. **EDUCATION (List Below, use added sheets as necessary)**

Dates: From To School Address Major Subject Degree, if any; year
(over)

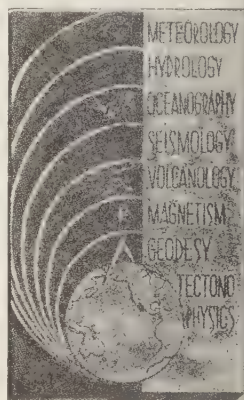
(Continued from previous page)

Those eligible as candidates for election to the grade of ASSOCIATE MEMBER shall be:

ASSOCIATE MEMBER Persons who have an active interest in physical processes of the Earth or technical assistance in the application of geophysics. In general, the minimum qualification for associate membership will be acceptable training or experience in some field of geophysics or allied science.

CORPORATION MEMBER Corporations and other interested organizations shall be eligible as candidates for election to CORPORATION MEMBERSHIP. They shall have the privilege of designating a representative who has the rights and privileges of Members (use special form).

STUDENT MEMBER Those eligible as candidates for election to the grade of STUDENT MEMBER shall be persons who are graduate or undergraduate students in residence at least half-time and who are specializing in the geophysical sciences. Teaching or research assistants enrolled in more than half of a full-time academic program may also be eligible for Student Membership. Student Members shall have all the privileges of Members except that they shall not vote or hold office.



Cut along this line

*9. References: Please list below names and addresses of two or three references; include members of the AGU or others who know you well.

*10. Titles of technical contributions or publications, particularly those in the geophysical sciences, and where published.

*11. Brief statement of any special interests or qualifications in the geophysical sciences.

Date _____
Written Signature _____

12. (STUDENT MEMBERS ONLY) The person whose signature appears above is known to me and is a student majoring in _____ (subject) at _____

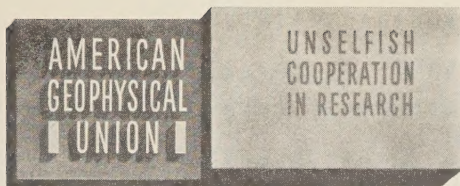
(Name of college or university) expected to graduate in _____ (year) with the degree of _____

☐ He is a full-time student, or ☐ a teaching or research assistant enrolled in more than half of a full-time academic program.

(Signature of faculty sponsor) ☐ Check here if faculty sponsor is a member of AGU and willing to act as a regular sponsor for associate membership as well.

(Typed or printed name of sponsor) (Title) _____

* Applicants for student membership may omit Questions 9, 10, and 11, but must fill in Question 12. Please return form with check or money order payable to American Geophysical Union, 1515 Massachusetts Ave., N.W., Washington 5, D. C.



INFORMATION CONCERNING CORPORATION MEMBERSHIP

The American Geophysical Union is a non-profit scientific organization established by the National Research Council. It is the American National Committee of the International Union of Geodesy and Geophysics, and its Executive Committee is the Committee on Geophysics of the National Research Council.

Extracts from the Statutes:

Article 3. Membership—The membership of the American Geophysical Union shall be as follows:

- (e) *Corporation Members*—Corporations and other organizations interested in geophysics elected by the Executive Committee of the Union. The designated representative of each such organization shall enjoy the privileges of a Member.

(Continued on next page)

Cut along this line

American Geophysical Union

PROPOSAL FOR CORPORATION MEMBERSHIP

To the Executive Committee, American Geophysical Union
1515 Massachusetts Ave., N.W., Washington 5, D. C.

Gentlemen:

As an indication of our interest in the aims and activities of the American Geophysical Union, and to assist in maintaining and extending its program of publication and other work in the development of the geophysical sciences, the undersigned applies for Corporation Membership in the AGU and, until further notice, agrees to pay annual dues, currently at the rate of \$100 per unit of corporation membership, in accordance with the information set forth above.

Company or Organization _____

By _____ Title _____

(Signature)

(over)

(Continued from previous page)

Extracts from the By-Laws:

- (2) . . . Members of class (e) shall pay dues of not less than \$100 for each calendar year; . . .
- (21) One copy of each issue of (a) the *Transactions*, (b) *Journal of Geophysical Research*, (c) any published *List of Members and Officers*, and (d) any other publication which may be approved for *free distribution* to the membership by the Executive Committee of the Union, shall be sent to each . . . Corporation Member. . . . Each . . . organization in good standing may purchase any available publication of the Union at a discount from printed price list to non-members. The General Secretary is authorized to establish discounts for sales of publications.

Action of the Executive Committee, November 29, 1946:

- (1) A list of corporation members shall be published on one or more pages immediately after the final page of text in each issue of the *Transactions*.
- (2) A list of corporation members shall be included in the Membership Directory as a distinct unit.

AMERICAN GEOPHYSICAL UNION

1515 Massachusetts Ave., N.W.
Washington 5, D. C.

Cut along this line

Address _____

City _____ State _____

General fields of activity _____

The following person is designated as our representative in this membership _____

_____ Title _____

Number of units of membership desired (this will be taken as one unless otherwise indicated) _____

Place _____

Date _____

Contents

(Continued from back cover)

	PAGE
Lightning and Charge Storage..... <i>E. J. Workman, M. Brook, and N. Kitagawa</i>	1513
Note on the Recent Climatic Fluctuation in the United States.... <i>H. E. Landsberg</i>	1519
Environmental Photometry in the Antarctic..... <i>John M. Hood, Jr.</i>	1527
The Thermal Conductivities of Ocean Sediments..... <i>E. H. Ratcliffe</i>	1535
Nearshore Ocean Currents off San Diego, California <i>Roy D. Gaul and Harris B. Stewart, Jr.</i>	1543
Comparison of Power Spectra of Ocean Waves Obtained by an Analog and a Digital Method..... <i>Jerry K. Parks</i>	1557
Comparison of Precipitation on Islands of Lake Michigan with Precipitation on the Perimeter of the Lake..... <i>F. Blust and B. G. DeCooke</i>	1565
An Analysis of the Flow of Water in a Shallow, Linear Aquifer, and of the Approach to a New Equilibrium after Intake..... <i>J. N. Luthin and J. W. Holmes</i>	1573
The Long-Time Response of a Layered Elastic Medium to Explosive Sound <i>J. H. Rosenbaum</i>	1577
Letters to the Editor:	
The Production of Tritons and C^{14} in the Terrestrial Atmosphere by Solar Protons..... <i>J. A. Simpson</i>	1615
Observed Magnetic Effects from Meteors <i>Alvin W. Jenkins, Jr., Charles A. Phillips, Jr., and Elwood Maple</i>	1617
Ionospheric Backscatter Observation at 440 Mc/s <i>V. C. Pineo, L. G. Kraft, and H. W. Briscoe</i>	1620
Further Discussion of Paper by F. D. Stacey, 'The Possible Occurrence of Nega- tive Nitrogen Ions in the Atmosphere'..... <i>D. R. Bates</i>	1622
A Convenient Method of Getting Representative Ionospheric Heights <i>G. A. M. King</i>	1623
Discussion of Paper by Mahdi S. Hantush, 'Analysis of Data from Pumping Wells near a River'..... <i>R. G. Kazmann</i>	1625
Author's Reply to the Preceding Discussion..... <i>Mahdi S. Hantush</i>	1627
Gravity Anomalies over a Buried Step..... <i>A. M. Bancroft</i>	1630
Abstracts of the papers presented at the Pacific Southwest Regional Meeting, American Geophysical Union, Los Angeles, California, February 4-5, 1960....	1632
Geomagnetic and Solar Data..... <i>J. Virginia Lincoln</i>	1639
Late Letter to the Editor:	
Initial Results of the TIROS I Meteorological Satellite..... <i>W. G. Stroud</i>	1643
Errigendum..... <i>J. L. Stern and H. Richardson</i>	1644

Contents

	PAGE
Balloon Study of High-Altitude Radiations during the International Geophysical Year.....	J. R. Winckler 13
Observations of the Van Allen Radiation Regions during August and September 1959, Part 1.....	R. L. Arnoldy, R. A. Hoffman, and J. R. Winckler 13
Particle Fluxes in the Inner Radiation Belt.....	Stanley C. Freden and R. Stephen White 13
Cosmic-Ray Characteristics Registered in Chacaltaya during Unusually High Solar Activity.....	I. Escobar, E. Maldonado, N. W. Nerurkar, and R. Romero 13
The Influence of the Solar Radiation Pressure on the Motion of an Artificial Satellite	Peter Musen 13
Properties of the Solar Wind during Sunspot Minimum.....	A. L. Licht 13
Observations of the Aurora Australis at New Zealand Antarctic Stations during IGY.....	T. Hatherton and G. G. Midwinter 14
Observations of Geomagnetic Fluctuations in the Period Range 0.3 to 120 Seconds	Hugo Benioff 14
Studies on Sudden Commencements of Geomagnetic Storms Using IGY Data from United States Stations.....	S. Matsushita 14
On the Position of the Focus of the Geomagnetic S_q Current System....	M. Hasegawa 14
Polarization Parameters of the Downcoming Radio Wave	Y. S. N. Murty and S. R. Khastgir 14
VLF Propagation Effects of a D -Region Layer Produced by Cosmic Rays	William F. Moler 14
The Formation of the D Region of the Ionosphere.....	M. Nicolet and A. C. Aikin 14
Drift Measurements at Kjeller on the Ionospheric F Region	J. Becken and B. Mæhlum 14
The Absolute Zenith Intensity of [O I] 5577 at College, Alaska	F. E. Roach and M. H. Rees 14
The Intensity of [O I] 5577 in the Subauroral Region as a Function of Magnetic Activity.....	F. E. Roach 14
A Study of Local Geomagnetic Influence on the [O I] 5577 Nightglow Emission at Fritz Peak.....	J. W. McCaulley, F. E. Roach, and S. Matsushita 14
A Comparative Study of Absolute Zenith Intensities of [O I] 5577	F. E. Roach, J. W. McCaulley, E. Marovich, and C. M. Purdy 15

(Continued inside back cover)